UCLA
UCLA Electronic Theses and Dissertations

Title

Studies Pertaining to Amide Bond Activation, Small Molecule Therapeutics, Cyclic Allenes, and Chemical Education

Permalink

Author

Knapp, Rachel

Publication Date

2022

Peer reviewed|Thesis/dissertation

UNIVERSITY OF CALIFORNIA

Los Angeles

Studies Pertaining to Amide Bond Activation, Small Molecule Therapeutics,

Cyclic Allenes, and Chemical Education

A dissertation submitted in partial satisfaction of the

requirements for the degree Doctor of Philosophy

in Chemistry

by

Rachel R. Knapp

2022

ABSTRACT OF THE DISSERTATION

Studies Pertaining to Amide Bond Activation, Small Molecule Therapeutics,

Cyclic Allenes, and Chemical Education

by

Rachel R. Knapp

Doctor of Philosophy in Chemistry

University of California, Los Angeles, 2022

Professor Neil Kamal Garg, Chair

This dissertation describes the development of reaction methodologies that utilize unconventional building blocks in chemical synthesis. One major effort involves the nickel-catalyzed net hydrolysis of traditionally inert amide C–N bonds to give carboxylic acids. Additionally, the development of synthetic routes to afford structurally complex bioactive compounds are reported. Specifically, these include the synthesis of a small library of furanoindoline compounds for structure-activity relationship studies related to the treatment of Alzheimer's disease and an alternative synthesis of the nucleobase found in the FDA-approved

COVID-19 antiviral remdesivir. Finally, investigations into strained heterocyclic allenes are described. These studies have allowed for highly reactive cyclic allene intermediates to be utilized strategically in the regioselective and enantiospecific synthesis of a diverse array of densely functionalized heterocycles. Furthermore, a synthetic approach toward the synthesis of alstilobanine A is reported, where the key step hinges on a cycloaddition of an azacyclic allene intermediate. Each of the new strategies presented are expected to expand the synthetic toolbox by leveraging unique reactivity.

Chapter one describes the development of a nickel-catalyzed net hydrolysis of amides. The methodology strategically employs a nickel-catalyzed esterification using 2-(trimethylsilyl)-ethanol, followed by a fluoride-mediated deprotection in a single-pot operation. The selectivity and mildness of this transformation are demonstrated through competition experiments and the net-hydrolysis of a complex valine-derived substrate. This strategy addresses a limitation in the field with regard to functional groups accessible from amides using transition metal-catalyzed C–N bond activation.

Chapters two and three detail the synthesis of bioactive compounds. Chapter two specifically describes the synthesis of a small library of furanoindoline analogs for structure-activity relationship studies on the inhibition of neutral sphingomyelinase-2 and acetylcholinesterase, enzymes implicated in Alzheimer's disease. The syntheses employ a key interrupted Fischer indolization reaction where the furanoindoline product is elaborated to generate a number of analogs. Identification of the dual inhibitors represents a promising new therapeutic approach to Alzheimer's disease. Chapter three describes an alternative approach to the unnatural nucleobase fragment found in remdesivir (Veklury®), an FDA-approved antiviral for the treatment of COVID-19. The route relies on the formation of a cyanoamidine intermediate, which undergoes

a Lewis acid-mediated cyclization to yield the desired nucleobase. The approach is strategically distinct from prior routes and could further enable the synthesis of remdesivir and other small-molecule therapeutics.

Chapters four and five are concerned with the investigation of cyclic allene intermediates. Chapter four describes an experimental and computational study of azacyclic allenes, including the synthesis of several substituted azacyclic allene precursors, subsequent allene generation, and trapping in cycloadditions. Additionally, the computational studies performed provide insight into the underlying reasons for the observed regioselectivities and enantiospecificities. Chapter five details experimental studies of oxacyclic. Specifically, the development of a precursor to 3,4-oxacyclohexadiene and subsequent allene trapping in (4+2), (3+2), and (2+2) cycloadditions is disclosed. Additionally, the first asymmetric synthesis of a silyl triflate cyclic allene precursor was achieved, as well as enantiospecific trapping of the allene. These studies highlighted the potential for cyclic allenes to be valuable building blocks the asymmetric synthesis of heterocycles.

Chapter six illustrates the development of an alternative precursor toward strained cyclic allenes and alkynes. Our studies of strained cyclic allenes revealed that, in some cases, silyl triflate precursors were inaccessible. This study shows that silyl tosylates can serve as alternative precursors to strained cyclic allenes and alkynes.

Chapter seven details a strategy for the total synthesis of alstilobanine A, a monoterpene indole alkaloid. Our approach hinges on a key (4+2) Diels–Alder reaction between an acetoxy-substituted azacyclic allene intermediate and a pyrone. This cycloaddition forms two key C–C bonds and sets three of the four stereocenters found in the natural product. Current efforts to synthesize the natural product are detailed. If successful, these studies should provide efficient

iv

access to alstilobanine A and demonstrate the utility of cyclic allenes in complex molecule synthesis.

Finally, chapter eight is a contribution to chemical education. The chapter outlines a new course centered around transition-metal catalysis in modern drug discovery. The course was designed to illustrate the central role of organic chemistry in driving small-molecule drug development and was taught by graduate students with mentorship from a faculty member. Additionally, experts in the fields of catalysis and drug discovery served as guest lecturers throughout the duration of the course. This chapter reflects on the experience of creating and developing the course, and aims to motivate the creation of future courses that unify fundamental concepts with applications and career outcomes.

The dissertation of Rachel Rose Knapp is approved.

Kendall N. Houk

Abigail Gutmann Doyle

Yi Tang

Neil Kamal Garg, Committee Chair

University of California, Los Angeles

2022

"The future belongs to those who believe in the beauty of their dreams."

– Eleanor Roosevelt

For my parents, Teri & Rick

TABLE OF CONTENTS

CHAPTER SEVEN:

LIST OF FIGURES

CHAPTER ONE

CHAPTER THREE

CHAPTER FOUR

CHAPTER FIVE

LIST OF SCHEMES

LIST OF TABLES

LIST OF ABBREVIATIONS

α	alpha
β	beta
γ	gamma
λ	wavelength
μ	micro
π	pi
δ	chemical shift
Δ	heat
(Het)	hetero
AcOH	acetic acid
Al	aluminum
app.	apparent
aq.	aqueous
Ar	aryl
B	boron
B3LYP	Becke, 3-parameter, Lee–Yang–Parr (functional)
$BF_3 \cdot Et_2O$	boron trifluoride etherate
Bn	benzyl
Boc	*tert*-butyloxy carbonyl
BOX	bis(oxazoline)
br	broad
Br	bromide
BRSM	based on recovered starting material
Bu	butyl
n-Bu	butyl (linear)
t-Bu	*tert*-butyl
c	concentration for specific rotation measurements
°C	degrees Celsius
calcd	calculated
Cbz	carboxybenzyl
CCDC	Cambridge Crystallographic Data Centre
CCSD(T)	Coupled Cluster Single Double Triple
Cl	chloride

cm	centimeter
cod	1,5-cyclooctadiene
conc.	concentration
Cp	cyclopentadienyl
CREST	conformer-rotamer ensemble sampling tool
Cy	cyclohexyl
DABCO	1,4-diazabicyclo[2.2.2]octane
DART-MS	Direct Analysis in Real Time – Mass Spectroscopy
dba	dibenzylideneacetone
d	doublet
dd	doublet of doublets
ddd	doublet of doublet of doublets
ddt	doublet of doublet of triplets
dq	doublet of quartets
dr	diastereomeric ratio
dt	doublet of triplets
δ	chemical shift
DFT	density functional theorem
dist	distortion
DMAP	4-dimethylaminopyridine
dmdba	3,5,3',5'-dimethoxydibenzylideneacetone
DME	1,2-dimethoxyethane
DMF	*N,N*-dimethylformamide
DMS	Doering-Moore-Skattebøl
DMSO	dimethyl sulfoxide
ε	dielectric constant
E_a	activation energy
EDC	1-ethyl-3-(3-dimethylaminopropyl)carbodiimide
ee	enantiomeric excess
equiv	equivalent
er	enantiomeric ratio
ESI	electrospray ionization
Et	ethyl
EtOAc	ethyl acetate

η	eta
Fe	iron
FT	Fourier transform
g	gram(s)
h	hour(s)
HCl	hydrochloric acid
HF	Hartree Fock
HFIP	1,1,1,3,3,3-hexafluoro-2-propanol
Het	heterocycle
HMPA	hexamethylphosphoramide
HOMO	highest occupied molecular orbital
HRMS	high resolution mass spectroscopy
Hz	hertz
int	interaction
IR	infrared (spectroscopy)
i-Pr	iso-propyl
J	coupling constant
kcal/mol	kilocalories to mole ratio
KHMDS	Potassium hexamethyldisilazide
Leu	leucine
L	liter
LDA	lithium diisopropylamide
LUMO	lowest unoccupied molecular orbital
m	multiplet or milli
m	meta
M	molar
m/z	mass to charge ratio
Me	methyl
Mg	magnesium
MeOH	methanol
MHz	megahertz
min	minute(s)
mm	millimeter
mol	mole(s)

mp	melting point
N_2	nitrogen gas
Ni	nickel
NMR	nuclear magnetic resonance
NO_3	nitrate
NOESY	Nuclear Overhauser Enhancement Spectroscopy
o	ortho
ORTEP	Oak Ridge Thermal-Ellipsoid Plot Program
p	para
Ph	phenyl
PHOX	phosphinooxazoline
Phth	phthalimides
ppm	parts per million
q	quartet
quant	quantitative
quint	quintet
rac	racemic
rt	room temperature
R_f	retention factor
s	singlet
sat.	saturated
SFC	supercritical fluid chromatography
SIPr	1,3-bis(2,6-diisopropylphenyl)imidazolin-2-ylidene
SMD	solvation model based on density
Sn	tin
SSA	shield-solvation analysis
t	triplet
temp	temperature
TBAF	tetrabutylammonium fluoride
TES	triethylsilyl
TESCl	triethylsilyl chloride
Tf	trifluoromethanesulfonyl
THF	tetrahydrofuran
TLC	thin layer chromatography

TMSCl	trimethylsilyl chloride
tol	tolyl
Ts	*p*-toluenesulfonyl (tosyl)
TS	transition state
UV	ultraviolet
val	valine
w/w	weight by weight
wt%	percentage by mass
ZPVE	zero-point vibrational energy
Yb	ytterbium
Zn	zinc

ACKNOWLEDGEMENTS

I attribute my success in graduate school to a mixture of incredibly supportive individuals, hard work, and luck. Throughout my time in the Garg lab, I have been fortunate to have unequivocal support from my family, friends, and colleagues. The failures and mistakes have been met with successes, breakthroughs, and surprise in myself many times with regard to my own abilities. It is impossible to recognize every formative experience in this dissertation, but I hope to do my best to recognize those who played the largest roles in my career thus far.

It is only fitting for my acknowledgements to begin where my passion for organic synthesis sparked, in Prof. Chad Eichman's organic chemistry course at Loyola University Chicago. I remember being in a phase of my life where, for the first time, I had no idea what I wanted to do and my future was filled with uncertainty. This was until I began my organic chemistry classes where Chad introduced the applications of this field of science. I became fascinated with the subject and applied to work as an undergraduate researcher in Chad's lab. This has never been confirmed but I believe I only got the position because I was the first student to respond to his email regarding the opening. Through this experience, I got a first-hand look into what research entailed. There were many mistakes, failed reactions, and general confusion about what I was doing but nonetheless, Chad believed in my future and was a huge advocate for success in graduate school. I remember the day I got into UCLA and immediately sent him an email to which he replied, the environment "will set you up for success."

Upon arriving at UCLA, I immediately joined the Garg group and never left. This is where I owe the majority of my development as a chemist, professional, and most importantly a critical thinker to Prof. Neil Garg. Neil is a remarkable mentor and advocate for all of his students. Over the past five years, Neil has always believed in me and taken a hands-on approach to shaping my

development as a scientist. He has an incredible ability to identify any problem and form a logical, stepwise approach to solving it. Between chemistry challenges, paper writing, presentation preparation, Neil has patiently worked with me to solve any challenge I've faced. Furthermore, I think Neil has made the largest impression on me of how to be a leader. During my third year, Neil became the Chair of the chemistry department. This is obviously a role with an unbelievable amount of responsibility but took a major turn with the COVID-19 pandemic. Throughout all this, Neil led the chemistry department as well as our group through an extremely uncertain time while maintaining a sense of concern for me as an individual. I am grateful through all of the craziness of 2020 that I was able to work closely with Neil through a collaboration with the Gates Foundation. I owe much of my current and future success to Neil and I am immensely grateful for his unwavering support and belief in me over the past five years.

I would also like to acknowledge the rest of my doctoral committee: Professors Ken Houk, Abigail Doyle, and Yi Tang. Their collective support, advice, and mentorship throughout my graduate career was invaluable, and I thank them for serving on my committee.

One of the most important components of the Garg lab is the people. Every member of the lab has left a lasting impression on me. With many, I have formed lifelong friendships. I am indebted to all the help and mentorship I've received over the years and truly believe I could not have succeeded in this program without them.

Postdoctoral scholars occupy a unique niche in our laboratory environment. With their PhD shaped from another group culture, they bring a new way of thinking to the Garg lab and provide new perspectives. In my five years, I have had the opportunity to overlap with and learn from a number of strong postdoctoral scholars. When I first joined the group, Drs. Sophie Racine and Maude Giroud were examples of strong women in chemistry. It was inspirational to see them

towards the end of their time in academia and move onto prestigious positions, truly a reflection of all of their hard work throughout the years. There was of course another postdoc in the group at the time, Dr. Evan Darzi. Darzi and I worked side-by-side in lab and this gave me daily exposure to his "lab hacks." I learned a great deal from him throughout the years, not only in lab techniques, but also with personal problems. I'll always remember our Friday afternoon (aka philosophical Friday) carpool where we discussed anything from the week's seminar speaker to how to be the best labmate. It is also exciting to see his career path following academia. Evan has always set an example of prioritizing family as well as career and this is an attribute I hope to have through my next chapter.

Later in my graduate school career, Drs. Logan Bachman and Veronica Tona arrived. Shortly after their arrival, the campus shut down due to the pandemic; however, I was lucky to work closely with each of them through a collaboration with the Sarpong lab and the Gates Foundation. We bonded over hours of Zoom calls and worked to solve many challenging problems with real world applications. With all of the pressure behind this project, I admired their work ethic and extensive chemistry knowledge. In my final year, I overlapped with Drs. Nathan Adamson and Daniel Nasrallah. I've had the opportunity to work on a total synthesis project with Nathan, where I am thankful to bounce many ideas off him and always received encouragement when solving challenging chemistry. Both Nathan and Dan have demonstrated their strong synthetic chemistry skills were readily apparent but more so, was their ability to serve as teachers for the group.

This now brings me to the Garg lab graduate students. I remember vividly my first day in lab and meeting everyone. The room-by-room introductions where a bit overwhelming but I was met with a sense of eagerness to be part of this group. I knew immediately the culture was special

and there was undeniable support for each other's success. We uphold our "work hard play hard mentality" and are exceptional, well-rounded individuals.

My first year in the Garg lab was in part characterized by the especially strong graduating class of Emma Baker-Tripp, Junyong Kim, and Elias Picazo. They were all powerhouses in lab and excellent role models on how to navigate graduate school. Fortunately, I was able to work directly next to Elias Picazo and continually felt his unbreakable optimism. During our year of overlap, I was continually the subject of many hazing activities, but always knew Eli had my back (aside from conceiving the nickname 'Freshman' for me my first year).

I am grateful to have overlapped with the Class of '19, Lucas Morrill, Joyann Barber, and Bryan Simmons. I think this class exhibited the widest range of personalities and it was fun to see how they all traversed the experiences of graduate school. Lucas is by far the wittiest person I have come across and provided endless entertainment in lab. He also held himself (and others) to an extremely high standard and had the experience to back this standard up. Joyann was one of the most positive people to overlap with in the Garg lab and emphasized the importance of a work-life balance. And finally, Bryan falls into my frenemy category. With our desks and hoods being next to each other, I spent more time with him in those two years than with anyone else in my life at the time. Through this time, we learned a lot about each other and our conversations ranged from Italian food favorites to hockey stats. While our conversations were mostly friendly, we had plenty of "no talking periods" when he was too sassy. Bryan can come off a little too harsh at times, but I'm grateful that he has always had an eye out for me. Whether he was helping me figure out housing, guiding me in writing a detailed SI, or helping me with job interviews, Bryan has been a huge support throughout my time here. I know I can call him with any problem, and he will answer.

The next class had the largest role in shaping the Garg lab culture and was comprised of Jordan Dotson, Rob Susick, Jacob Dander, and Michael Yamano. Jordan was a pillar of support with me throughout my candidacy exam and is an example of how an individual can be exceptionally intelligent without having an ego. I'm immensely grateful for him being such a great teacher and for having patience with me. After my first year, I was moved into the same room as Jacob, and this was also the start of a blossoming friendship. Jacob and I joke that our supreme personalities stem from our down-to-earth Mid-Western upbringing, but I also believe as friends, we balance each other – the yin to my yang. Whether Jacob was validating my emotions, or I was trying to make sense of his fifth-year uncertainty through astrology readings, there was never a time where we were both unhinged (okay maybe onetime in the glovebox room). Jacob pushed me to be the best version of myself and I am forever grateful for all of our thought-provoking conversions. Finally, Michael has had one of the largest influences on my success in graduate school. He was my mentor when I first joined the group and played an immense role in my development as a chemist. I always found it unfair to compete with his photographic memory but found this pushed me to work harder to even have a chance to compete. Outside of chemistry, I consider Michael one of my good friends. While on paper we might not be that similar, I think our competitive nature and joy of being correct bonds us. Although we don't work together anymore, I know Michael will continue to be a mentor to me.

I was fortunate to have an outstanding class above me. Their willingness to provide advice throughout the years and help with navigating graduate school was incredibly valuable. Melissa Ramirez was example of a person with incredible work ethic. To see her balance working in two groups while always being available to help with any question I may have had and be a pilar of positivity was truly inspirational. Sarah Anthony was the go-to for any kind of operational question

in the group. As a long time Garg lab resident, she knew the ins and outs and also had a great relationship with Neil – Sarah was the master of "reading Neil's mind," a very-sought after skill. No matter the circumstance, she would take time out of her day to help you; this included helping me to secure my future job where I am excited to continue to be colleagues. Tim Boit is one of the most talented scientists I have come across. He is truly an expert on an unbelievable number of subjects and was a great resource for me to bounce ideas off. Besides being a personal library, Tim is a great friend. We got to know each other very well when working together in 5234 and sharing our lab shifts during the shutdown. He has a constant supply of conversational topics that consumed the hours of time we spent in lab together and created many inside jokes – by the way, I know it was him on the LL Bean website. I'm excited to see how his future unfolds back on the East Coast.

Now I can say without a doubt, I went through graduate school with two of the best possible individuals, Jason Chari and Francesca Ippoliti. Jason has one of the sweetest, positive souls and has always been a pillar of support for me. I remember going through candidacy in the same office together where we would poke our heads out from our desks every few hours to check on one another. Besides having an incredible passion for chemistry, Jason also is an amazing athlete. It is inspirational to see the way Jason lives his life and I strive to emulate these attributes. Francesca has not only been one of the most positive people I have met, but has also provided an amazing sense of comfort for me over the past five years. Having a fellow Minnesotan in the group has offered a little slice of home. Also, her general stability and composure in life has helped through some of my own hectic periods. No matter the problem, whether it be regarding chemistry or personal, she has always approached everything with an aspirational sense of composure. While she is usually one of the most put-together people I know, she knows how to have a heck of a good

time. From bachelorette parties to holiday parties, Fran is the life of the party and lights up any room.

Over the years the group has taken on many forms, and I am so happy to see where the group is today. While conducting experimental research is crucial for any group, I have found there has been a major shift to personal development as well. The past two years have been filled with extreme cultural uncertainty and major current events. Through all of this, the younger classes have persisted and succeed in what is an already extremely challenging environment. They are both amazing scientists and amazing people.

The class directly under me brought me two of my best friends, Katie Spence and Milauni Mehta. There is no possible way to put our relationship into a paragraph, but I'll try my best. Over the past four years, we have seen each other grow and have supported one another across all facets of life. The foundation to our friendship is truly unique, as they understand me on a level many other people don't. I have always felt I can always be myself around Katie and Milauni and they are my loudest cheerleaders (really Milauni is the loudest). We have made so many wonderful memories from our morning hood catchups, trips to San Jose and Minneapolis, nights on Katie's roof, and many more. It is hard for me to imagine a life where I don't see Katie and Milauni every day, but I know they are off on amazing paths, and I can't wait to see all their success.

The third member of the '23 class includes Andrew Kelleghan. Andrew is a modern-day renaissance man. Everyone knows him for his strong synthetic chemistry skillset, but he also has knack for crafting (displayed by his wooden computer stand), cooking (specifically meal prepping), and witty podcasts. Despite his expertise, Andrew is one of the most approachable people I know and his help over the last four years has been invaluable.

The current third-year class comprises of Matt McVeigh, Laura Wonilowicz, and Ana Bulger. Matt's kindhearted personality brings a calming nature to the group. His calmness is met with a strong curiosity for chemistry, and I see Matt sparking a number of new projects for the group and being a role model for creative thinking. Luckily, Laura and I have been able to work in the same room for the past year where we have become great friends. Laura has an incredible sense of humor (like mine of course) and has made my last year in the lab full of funny memes, gory podcasts, and a beacon of support. Over the past year, I have seen Laura tackle candidacy and work through challenging chemistry, especially when working with lithium. Through this she has transitioned into becoming a leader and I'm excited to see all of her future accomplishments. Finally, I had the honor of working closely with Ana Bulger. Ana is an exceptional chemist and an even more exceptional friend. She is incredibly thoughtful and puts reasoning behind every decision she makes, a quality I am working on myself. I am lucky to have had the chance to mentor her and see her grow into the leader she is today.

Dominick Witkowski, Arismel Tena-Meza, and Luca McDermott comprise the current second years in the group. Dominick has set the bar high by not only developing a challenging project but taking on computational chemistry. Luca is one of the most enthusiastic students I have come across, and this positivity is contagious– it is hard to ever be in a bad mood when Luca is around. Finally, Arismel is a passionate chemist with an unmatched work ethic. Her appreciation for the applications of chemistry is infectious and I know she will make a remarkably successful medicinal chemist after graduate school.

The first years of our group, Georgia Scherer and Jordan Gonzalez possess all of the attributes necessary to succeed in the Garg lab: optimism, hard work, and a willingness to be a team-player. I look forward to seeing their future successes.

Outside of the Garg lab, I have been fortunate to have an unbelievable amount of support. My closest friends, Shelby, Maureen, Tayva, Waverly, and Alexandra, have not completely understood what I am working on, but have blindly supported every decision I have made. I am grateful they take me for who I am and empower me to be myself.

My partner, Gregg, entered my life at an interesting point – I had completed the majority of the hurdles of my PhD and was in the process of applying to jobs. Throughout this period, he offered nothing but support and was a source of logic. His approach to life continues to be an inspiration for me and he brings out all the best sides of me. I'm excited to see what our next chapter holds.

Finally, I would like to thank my parents, Teri and Rick. Without their support and encouragement there is no way I could possibly be where I am today. They both always say they have no idea where the side of me to pursue a PhD came from, but to me it is very clear. My mom, from the day I was born, has always been a strong leader. Growing up, she managed to balance an exceptional career, while being an amazing mother. She is a model of genuine authenticity and has one of the hardest work ethics I know. I am fortunate to have such an incredible, strong person as my mom and I aspire to be just like her every day. My dad has always been an example of limitless positivity. He has an outlook on life that inspires me to not only be myself but also to create good in the world. His warm persona is felt by all of those around him and I strive to resemble his nature. Over the past five years, there have been many ups and downs, phone calls of me sharing success and also moments of panic, but through it all my parents have always answered and been my rock. Thank you for letting me follow my dreams.

Chapter 1 is a version of Knapp, R. R.; Bulger, A. S.; Garg, N. K. *Org. Lett.* **2020**, *22,* 2833–2837. Knapp and Bulger were responsible for experimental work.

Chapter 2 is a version of Bilousova, T.; Simmons, B. J.; Knapp, R. R.; Elias, C. J.; Campagna, J.; Melnik, M.; Chandra, S.; Focht, S.; Zhu, C.; Vadivel, K.; Jagodzinska, B.; Cohn, W.; Spilman, P.; Gylys, K. H.; Garg, N. K.; John, V. *ACS Chem. Biol.* **2020**, *15*, 1671–1684. Simmons and Knapp were responsible for the organic synthetic experimental work. Bilousova, Campagna, Melnik, Chandra, Focht, Zhu, Vadivel, Jagodzinska, Cohn, Spilman, and Gylys were responsible for the biological experiments.

Chapter 3 is a version of Knapp, R.; Tona, V.; Okada, T.; Sarpong, R.; Garg, N. K. *Org. Lett.* **2020**, *22*, 1–5. Knapp and Tona were responsible for experimental work.

Chapter 4 is a version of Barber, J. S.; Yamano, M. M.; Ramirez, M.; Darzi, E. R.; Knapp, R. R.; Liu, F.; Houk, K. N.; Garg, N. K. *Nat. Chem.* ***2018, 10, 953–960.*** Barber, Yamano, Darzi, and Knapp were responsible for experimental work. Ramirez and Liu were responsible for the computational studies.

Chapter 5 is a version of Yamano, M. M.; Knapp, R. R.; Ngamnithiporn, A.; Ramirez, M.; Houk, K. N.; Stoltz, B. M.; Garg, N. K. *Angew. Chem., Int. Ed.* ***2019***, *58, 5653–5657.* Yamano, Knapp, and Ngamnithiporn were responsible for experimental work. Ramirez was responsible for the computational studies

Chapter 6 is a version of McVeigh, M. S.; Kelleghan, A. V.; Yamano, M.; Knapp, R. R.; Garg, N. K. *Org. Let.* **2020**, *22,* 4500–4504. McVeigh, Kelleghan, Yamano, and Knapp were responsible for experimental work.

Chapter 7 is unpublished material.

Chapter 8 is a version of Chari, J. V.; Knapp, R. R.; Boit, T. B.; Garg, N. K. *J. Chem. Educ.* **2022**, *99*, 1296–1303. Chari, Knapp, Boit, and Garg were responsible for the manuscript.

BIOGRAPHICAL SKETCH

Education:

University of California, Los Angeles, CA
- Ph.D. in Organic Chemistry, anticipated Spring 2022
- NIH Predoctoral Fellow, August 2019–Present
- Current GPA: 3.90/4.00

Loyola University Chicago, Chicago, IL
- B.S. in Biochemistry, 2017
- Cumulative GPA: 3.57/4.00, *Cum laude*

Professional and Academic Experience:

Graduate Research Assistant: University of California, Los Angeles, CA
- Advisor: Prof. Neil K. Garg; July 2017 – Present
  - Developed Diels–Alder cycloadditions and 1,3-dipolar cycloadditions with 3,4-azacyclohexadiene and 3,4-oxacyclohexadiene for the synthesis of diverse heterocyclic products.
  - Achieved the first asymmetric synthesis of an allyl substituted 3,4-oxacyclohexadiene precursor and studies the transfer of chirality in cycloadditions.
  - Investigated and developed a synthetic route towards the indole alkaloid, alstilobanine A, whereby the core structure is rapidly accessed via a (4+2) cycloaddition with an azacyclic allene.
  - Established a general method for the conversion of amides to carboxylic acids using nickel-catalyzed activation of the amide C–N bond.
  - Generated a small library of heterocyclic compounds for structure-activity relationship studies related to the inhibition of neutral sphigomyelinase-2 and acetylcholinesterase for the treatment of Alzheimer's disease.
  - Identified an alternative route to synthesize pyrrolo[2,1-f][1,2,4]-triazin-4-amine, the nucleobase found in remdesivir, an FDA approved antiviral compound for the treatment of COVID-19.
  - Proposed new synthetic routes to select pharmaceuticals with the overall goal of decreasing manufacturing costs (collaboration with the Sarpong Laboratory and the Bill and Melinda Gates Foundation).
  - Designed and synthesized a photo-affinity probe of ATGlistatin to uncover its protein target and role in ferroptosis rescue.

Summer Course Instructor: University of California, Los Angeles, CA
- Chem 101: Catalysis in Modern Drug Discovery; Summer 2020, Summer 2021
  - Designed a new upper-level elective course at UCLA focused on transition-metal catalysis in the drug development process.

Graduate Teaching Assistant: University of California, Los Angeles, CA
- Undergraduate organic chemistry laboratory sections; Fall 2017 – Spring 2018.
  - Taught students the laboratory analytical techniques necessary to conduct organic chemistry research.

Undergraduate Research Assistant: Loyola University Chicago, Chicago, IL
- Advisor: Prof. Chad C. Eichman; January 2015 – May 2017
  - Studied new, environmentally-friendly routes to synthesize redox active iron catalysts.

Honors and Awards:
- Alfred R. Bader Award for Student Innovation, Merck KGaA, 2021.
- Ralph and Charlene Bauer Award, UCLA, 2021.
- 2020 Educational Innovation Award, UCLA, 2020.
- Michael E. Jung Excellence in Teaching Award, UCLA, 2020.
- NIH – Ruth L. Kirschstein National Research Service Award (NRSA) Predoctoral Fellowship, NIH, 2019–2022.
- UCLA University Fellowship, 2017–2018.
- *Cum laude*, Loyola University Chicago, 2017.
- Damen Scholarship, Loyola University Chicago, 2013–2017.
- Mulcahy Fellowship, Loyola University Chicago, 2015–2017.
- Women's Undergraduate Leadership Award Nominee, Loyola University Chicago, 2017.
- Social Innovation/Entrepreneurship Fellowship, Loyola University Chicago, 2016.
- Casseretto Scholarship, Loyola University Chicago, 2015.
- Provost Fellowship, Loyola University Chicago, 2015.

Publications:
1. **Catalysis in Modern Drug Discovery: Insights from a Graduate Student Taught Undergraduate Course.** Jason V. Chari, [‡] Rachel R. Knapp, [‡] Timothy B. Boit and Neil K. Garg. *J. Chem. Educ.* **2022**, *99,* 1296–1303.
2. **Cyanoamidine Cyclization Approach to Remdesivir's Nucleobase.** Rachel R. Knapp, [‡] Veronica Tona, [‡] Taku Okada, Richmond Sarpong, and Neil K. Garg. *Org. Lett.* **2020**, *22*, 8430–8435.
3. **Treating a Global Health Crisis with a Dose of Synthetic Chemistry.** Melissa A. Hardy, Brandon A. Wright, Logan Bachman, Timothy B. Boit, Hannah M. S. Haley, Rachel R. Knapp, Robert F. Lusi, Taku Okada, Veronica Tona, Neil K. Garg, and Richmond Sarpong. *ACS Cent. Sci.* **2020**, *6*, 1017–1030.
4. **Silyl Tosylate Precursors to Cyclohexyne, 1,2-Cyclohexadiene, and 1,2-Cycloheptadiene.** Matthew S. McVeigh, Andrew V. Kelleghan, Michael M. Yamano, Rachel R. Knapp, and Neil K. Garg. *Org. Lett.* **2020**, *22*, 4500–4504.
5. **Dual Neutral Sphigomyelinase-2/Acetylcholinesterase Inhibitor for the Treatment of Alzheimer's Disease.** Tina Bilousova, Bryan J. Simmons, Rachel R. Knapp, Chris Elias, Jesus Campagna, Mikhail Melnik, Sujyoti Chandra, Samantha Focht, Chunni Zhu, Kanagasabai Vadivel, Barbara Jagodzinska, S Whitaker-Cohn, Patricia Spilman, Karen Gylys, Neil K. Garg, and Varghese John. *ACS Chem. Bio.* **2020**, *15*, 1671–1684.
6. **Nickel-Catalyzed Conversion of Amides to Carboxylic Acids.** Rachel R. Knapp, Ana S. Bulger, and Neil K. Garg. *Org. Lett.* **2020**, *22*, 2833–2837.
7. **Cycloadditions of Oxacyclic Allenes and a Catalytic Asymmetric Entryway to Enantioenriched Cyclic Allenes.** Michael M. Yamano, Rachel R. Knapp, Aurapat Ngamnithiporn, Melissa Ramirez, K. N. Houk, Brian M. Stoltz, and Neil K. Garg. *Angew. Chem., Int. Ed.* **2019**, *58*, 5653–5657.
8. **Diels–Alder Cycloadditions of Strained Azacyclic Allenes.** Joyann S. Barber, [†] Michael M. Yamano, [†] Melissa Ramirez, Evan R. Darzi, Rachel R. Knapp, Fang Liu, K. N. Houk, and Neil K. Garg. *Nat. Chem.* **2018**, *10*, 953–960.

[†] Authors Contributed Equally.

CHAPTER ONE

Nickel-Catalyzed Conversion of Amides to Carboxylic Acids

Rachel R. Knapp, Ana S. Bulger, and Neil K. Garg.

Org. Lett. **2020**, *22*, 2833–2837.

1.1 Abstract

We report the conversion of amides to carboxylic acids using non-precious metal catalysis. The methodology strategically employs a nickel-catalyzed esterification using 2-(trimethylsilyl)ethanol, followed by a fluoride-mediated deprotection in a single-pot operation. This approach circumvents catalyst poisoning observed in attempts to directly hydrolyze amides using nickel catalysis. The selectivity and mildness of this transformation is shown through competition experiments and the net-hydrolysis of a complex valine-derived substrate. This strategy addresses a limitation in the field with regard to functional groups accessible from amides using transition-metal catalysis and should prove useful in synthetic applications.

1.2 Introduction

Despite being well known for their pronounced stability, amides have recently become valuable synthetic building blocks in transition-metal-catalyzed reactions.[1] An array of carbon–carbon and carbon–heteroatom bond-forming reactions using amides have now been disclosed using palladium,[2] rhodium,[3] or nickel[4] catalysis. Figure 1.1 highlights several functional group conversions beginning from amides that can now be achieved using non-precious metal catalysis.[4a–c,4g,4l,4n,4s] Although several methodologies have been reported in recent years, one of the most fundamental transformations, namely the conversion of amides to carboxylic acids,[5] has

not yet been disclosed using transition-metal catalysis. We report a means to achieve this transformation using nickel catalysis.
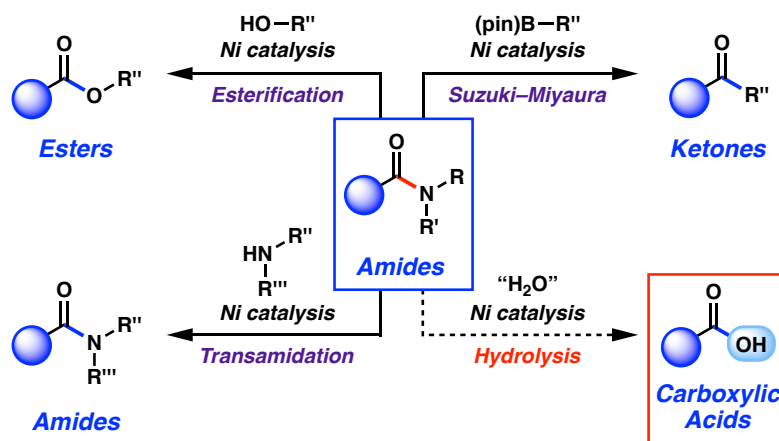
Figure 1.1. Select examples of recent advances in the nickel-catalyzed activation of amides.

1.3 Reaction Discovery and Optimization

Our studies commenced with attempts to modify our previously established protocol for the conversion of amides to esters.[4a,4l] Specifically, we evaluated the activation of amide **1.1** using Ni(cod)$_2$ and the *N*-heterocyclic carbene ligand SIPr, with water as a nucleophile (Figure 1.2). Unfortunately, we did not observe formation of the desired product, benzoic acid (**1.2**). This was surprising, given that many oxygen nucleophiles have been used in nickel-catalyzed amide esterification reactions. To further assess if the direct conversion to the carboxylic acid was possible, additional experiments were performed involving the nickel-catalyzed esterification of amide **1.1** using MeOH as the nucleophile. In the absence of any additive, the reaction proceeded as expected to give ester **1.3** in 85% yield. However, when the reaction was carried out with 0.5 equivalents of benzoic acid (**1.2**) as an additive, the esterification failed, indicative of catalyst poisoning. Recognizing the incompatibility of the carboxylic acid functional group with the catalyst system, we sought to develop an alternative strategy to effect the conversion of amides to carboxylic acids using nickel catalysis.

1.1 → **1.2**

MeOH
Ni(cod)$_2$, SIPr
toluene, 80 °C, 16 h

1.1 → **1.3**

Additive	Remaining 1.1[a]	Yield of 1.3[a]
–	15%	85%
benzoic acid (0.5 equiv)	>99%	0%
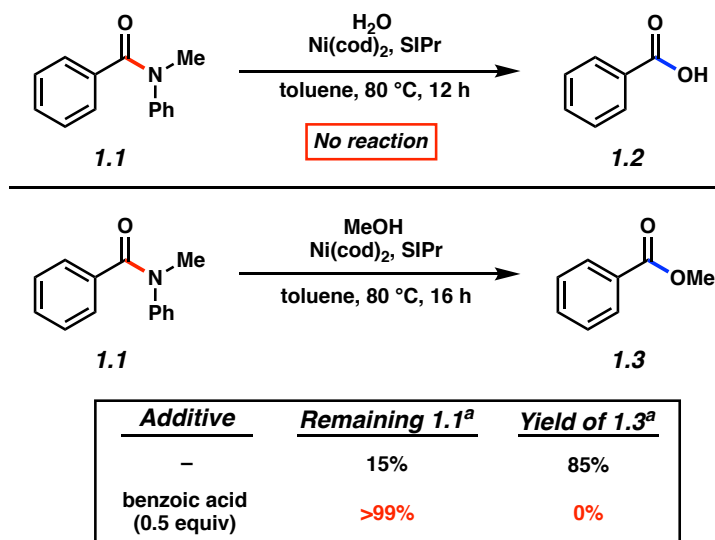
Figure 1.2. Initial studies and control experiments for the nickel-catalyzed hydrolysis of amides. Conditions: amide **1.1** (1.0 equiv), Ni(cod)$_2$ (10 mol%), SIPr (10 mol%), methanol or water (1.2 equiv), and toluene (1.0 M) heated at 80 °C for 12 or 16 h in a sealed vial under an atmosphere of N$_2$. [a]Yields were determined by ^{1}H NMR analysis using 1,3,5-trimethoxybenzene as an external standard.

An alternative one-pot approach to achieve the amide to carboxylic acid conversion was conceived, as depicted using amide substrate **1.4** (Table 1.1). Strategically, this was designed to proceed by nickel-catalyzed esterification to give protected carboxylic acid **1.5** which would then be deprotected in the same reaction vessel through the addition of a mild fluoride source. Table 1.1 shows select key results using two types of nucleophiles, each bearing a silyl group. Although the use of trimethylsilanol (TMS–OH) as a nucleophile failed to generate the desired ester intermediate **1.5** (entry 1), the use of 2-(trimethylsilyl)ethanol (TMS-ethanol, **1.7**) proved more fruitful (entries 2 and 3). For example, using standard reaction conditions at a temperature of 80 °C, the conversion of amide **1.4** to carboxylic acid **1.6** could be achieved in 83% yield using a straightforward esterification / TBAF-mediated deprotection protocol (entry 2).[6] Increasing the temperature to 110 °C gave naphthyl carboxylic acid **1.6** in a slightly improved yield of 87% (entry 3).

Table 1.1. Optimization of Reaction Conditions

entry	alcohol	temp. (°C)	yield of 1.5[a]	yield of 1.6[a]
1	TMS-OH	80	0%	–
2	TMS-ethanol (*1.7*)	80	0%	83%
3	TMS-ethanol (*1.7*)	110	0%	87%
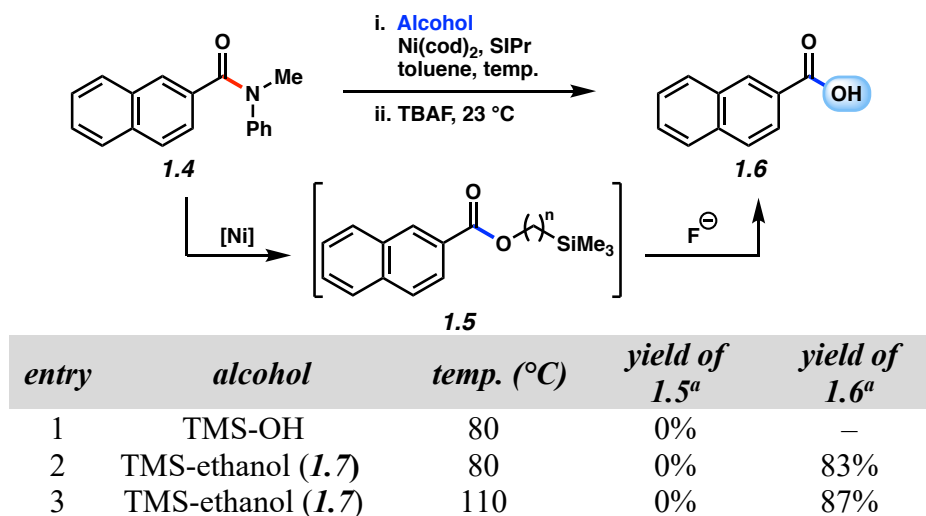
Conditions: amide **1.4** (1.0 equiv), Ni(cod)$_2$ (10 mol%), SIPr (10 mol%), alcohol (1.25 equiv), and toluene (1.0 M) heated at 80–110 °C for 24 h in a sealed vial under an atmosphere of N$_2$; TBAF (2.5 equiv) at 23 °C for 2 h. [a]Yields were determined by ^{1}H NMR analysis using 1,3,5-trimethoxybenzene as an external standard.

1.4 Scope of Methodology

Having identified an operationally-simple means to achieve the nickel-catalyzed conversion of amides to carboxylic acids, we evaluated several benzamide derivatives[7] in the methodology (Figure 1.3). The use of the parent naphthyl substrate **1.4** (Table 1.1) furnished 2-naphthoic acid (**1.6**) in 90% isolated yield. Benzoic acids **1.2**[8] and **1.10**–**1.12** could also be accessed through this transformation. The formation of carboxylic acids **1.11** and **1.12**, in 84% and 79% yield, respectively, highlights the tolerance of electron-withdrawing and electron-donating groups. Additionally, use of a quinoline substrate gave rise to **1.13** in 60% yield, thus demonstrating the tolerance of the methodology toward an important nitrogen-containing heterocycle.
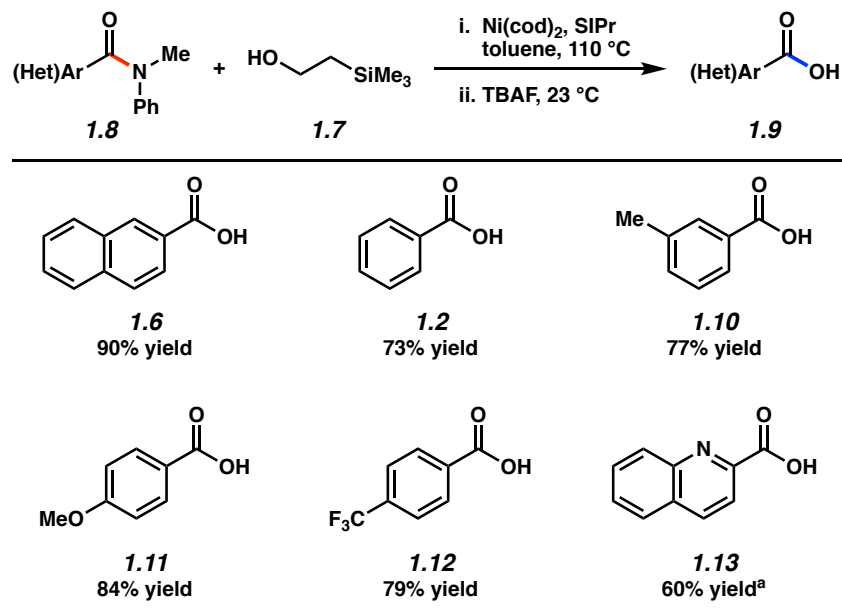
Figure 1.3. Scope of the amide substrate**.** Conditions: amide **1.8** (1.0 equiv), Ni(cod)$_2$ (10 mol%), SIPr (10 mol%), **1.7** (1.25 equiv), and toluene (1.0 M) heated at 110 °C for 24 h in a sealed vial under an atmosphere of N$_2$; TBAF (2.5 equiv) at 23 °C for 2 h. Yields reflect the average of two isolation experiments. [a]Yield was determined by ^{1}H NMR analysis using 1,3,5-trimethoxybenzene as an external standard.

As shown in Table 1.2, variation of the amide *N*-substituents was also possible. The use of benzamide **1.14a**, bearing an *n*-butyl group in place of a methyl group, afforded benzoic acid (**1.2**) in 77% yield (entry 1). Additionally, the more sterically encumbered *N*-isopropyl benzamide seen in **1.14b** (entry 2) and the indoline present in **1.14c** (entry 3) were tolerated. Moreover, tosyl derivative **1.14d** could be employed in the methodology to provide **1.2** in 71% yield (entry 4).

Table 1.2. Variation of the *N*-Substituents.
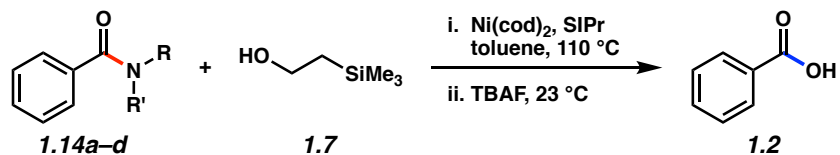
entry	substrate	yield
1	**1.14a**	77%
2	**1.14b**	60%
3	**1.14c**	56%
4	**1.14d**	71%

Conditions: amide **1.14a–d** (1.0 equiv), Ni(cod)$_2$ (10 mol%), SIPr (10 mol%), **1.7** (1.25 equiv), and toluene (1.0 M) heated at 110 °C for 24 h in a sealed vial under an atmosphere of N$_2$; TBAF (2.5 equiv) at 23 °C for 2 h. Yields reflect the average of two isolation experiments.

1.5 Selectivity Studies

Competition experiments were performed to gauge substrate-based selectivity for the nickel-catalyzed conversion of amides to carboxylic acids (Figure 1.4). The first involved benzamide **1.1** and cyclohexyl amide **1.15**, which gave selective reaction of **1.1** to furnish net-hydrolyzed product **1.2** in 86% yield. Aliphatic amide **1.15** was recovered in quantitative yield. We also performed a competition experiment using tertiary amide **1.1** and secondary amide **1.16**.

6

This led to selective reaction of **1.1** to give benzoic acid (**1.2**), with quantitative recovery of secondary amide **1.16**. The ability to preferentially manipulate subclasses of amides through selective conversion to carboxylic acids should prove useful in synthetic applications.

Selectivity for Aromatic over Aliphatic Amides

Selectivity for Tertiary over Secondary Amides
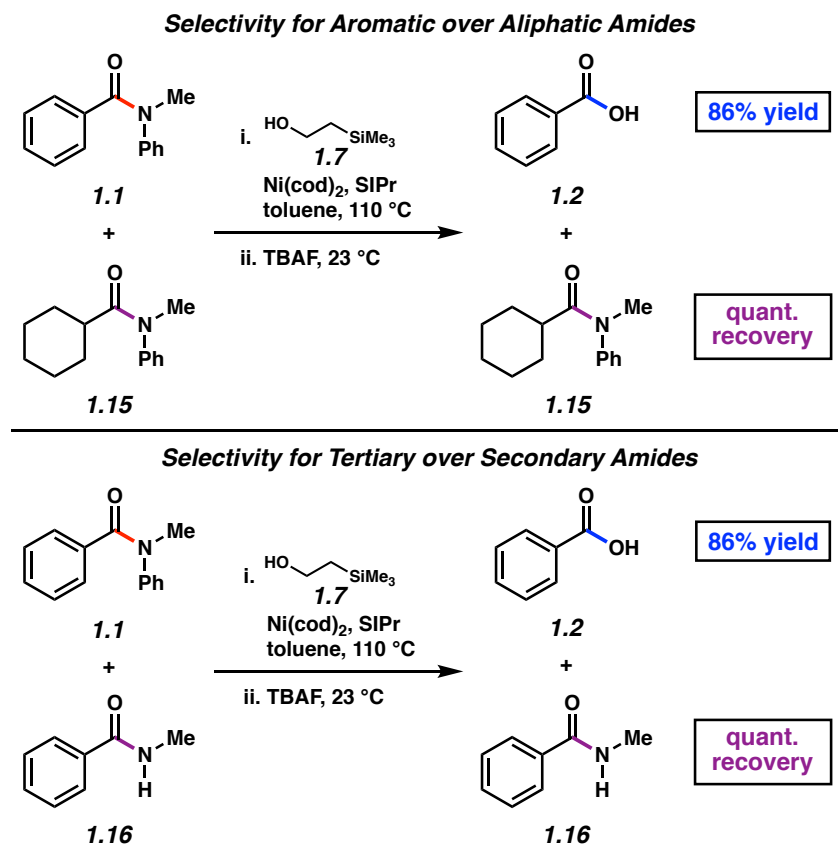
Figure 1.4. Competition experiments demonstrate substrate selectivity. Conditions: amide **1.1** (1.0 equiv), **1.15** or **1.16** (1.0 equiv), Ni(cod)$_2$ (10 mol%), SIPr (10 mol%), **1.7** (1.25 equiv), and toluene (1.0 M) heated at 110 °C for 24 h in a sealed vial under an atmosphere of N$_2$; TBAF (2.5 equiv) at 23 °C for 2 h. Yields reflect the average of two isolation experiments.

One further evaluation of the methodology to assess mildness and selectivity is shown in Figure 1.5. Substrate **1.17** (derived from L-valine)[4a] bearing an amide, an ester, and an epimerizable stereocenter, was subjected to our typical reaction protocol. This gave benzoic acid (**1.2**) and amine **1.18** in 67% and 72% yield, respectively. Of note, amine **1.18** was recovered in 99% ee and the ester functional group remained intact. As classical hydrolysis conditions are often

incompatible with esters and epimerizable stereocenters,[5] this result underscores the mild nature of our strategy for the conversion of amides to carboxylic acids.
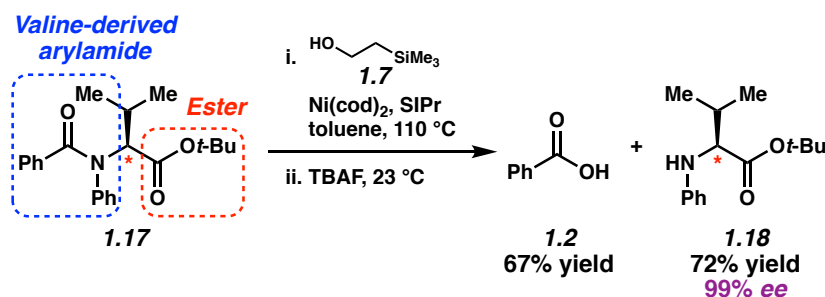
Figure 1.5. Cleavage of a valine-derived amide in the presence of an ester. Conditions: amide **1.17** (1.0 equiv), Ni(cod)$_2$ (20 mol%), SIPr (20 mol%), **1.7** (1.25 equiv), and toluene (1.0 M) heated at 110 °C for 24 h in a sealed vial under an atmosphere of N$_2$; TBAF (2.5 equiv) at 23 °C for 2 h. Yields reflect the average of two isolation experiments.

1.6 Conclusion

We have developed an operationally-simple procedure to convert amides to carboxylic acids using non-precious metal catalysis. The methodology strategically circumvents catalyst poisoning through the use of a nickel-catalyzed esterification, followed by a fluoride-mediated deprotection in a single-pot operation. We have demonstrated that a variety of amides with aryl groups and *N*-substituents can be employed in this transformation. Additionally, we have shown the process can be utilized to cleave amides in a mild and selective manner. This strategy offers a practical means to convert subclasses of amides to carboxylic acids while addressing a limitation with regard to functional groups accessible using transition-metal-catalyzed reactions of amides.

1.7 Experimental Section

1.7.1 Materials and Methods

Unless stated otherwise, reactions were conducted in flame-dried glassware under an atmosphere of nitrogen and commercially obtained reagents were used as received. (Trimethylsilyl)ethanol (**1.7**) was obtained from Combi-Blocks and distilled and sparged with N_2 for ≥10 min prior to use. Tetrabutylammonium fluoride was obtained from Sigma Aldrich. Ni(cod)$_2$ and SIPr were obtained from Strem Chemicals and degassed by sparging with N_2 for ≥10 min prior to use. Toluene was obtained from Fisher Scientific and purified by distillation over CaH_2 then taken through five freeze-pump-thaw cycles prior to use. 1,3,5-Trimethoxybenzene was obtained from Alfa Aesar and used as received. Reaction temperatures were controlled using an IKAmag temperature modulator, and unless stated otherwise, reactions were performed at room temperature (approximately 23 °C). Thin-layer chromatography (TLC) was conducted with EMD gel 60 F254 pre-coated plates (0.25 mm for analytical chromatography and 0.50 mm for preparative chromatography) and visualized using a combination of UV light, anisaldehyde, iodine, and potassium permanganate staining techniques. Silicycle Siliaflash P60 (particle size 0.040–0.063 mm) was used for flash column chromatography. ^{1}H NMR spectra were recorded on Bruker spectrometers (400, 500, and 600 MHz) and are reported relative to residual solvent signals. Data for ^{1}H NMR spectra are reported as follows: chemical shift (δ ppm), multiplicity, coupling constant (Hz), integration. Determination of enantiopurity was carried out on a Mettler Toledo SFC (supercritical fluid chromatography) using a Daicel ChiralPak IA-3 column. Optical rotations were measured with a Rudolph Autopol III Automatic Polarimeter.

*Note: Supporting information for the syntheses of amides **1.1**, **1.4**, **1.14a–d**, **1.17**, and **1.21–24** have been published and spectral data match those previously reported.*

1.7.2 Experimental Procedures

1.7.2.1 Initial Experiments for Amide Hydrolysis
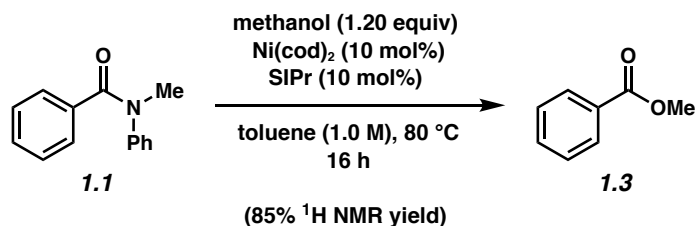
Representative Procedure for Figure 1.2. A 2-dram vial containing amide **1.1** (40.9 mg, 0.194 mmol, 1.00 equiv) and a magnetic stir bar was charged with Ni(cod)$_2$ (5.33 mg, 0.019 mmol, 10.0 mol%) and SIPr (7.56 mg, 0.019 mmol, 10.0 mol%) in a glove box. Subsequently, toluene (0.19 mL, 1.0 M) and then methanol (9.40 µL, 0.232 mmol, 1.20 equiv) were added. The vial was sealed with a Teflon-lined screw cap, removed from the glove box, and stirred at 80 °C in a preheated aluminum block for 16 h. After cooling to 23 °C, the mixture was diluted with hexanes (0.5 mL) and filtered over a plug of silica gel (10 mL of EtOAc eluent). The volatiles were removed under reduced pressure and the yield was determined by ^{1}H NMR analysis with 1,3,5-trimethoxybenzene as an external standard.

Any modifications of the conditions shown in the representative procedure above are specified in Figure 1.2.

1.7.2.2 Optimization and Relevant Control Experiments
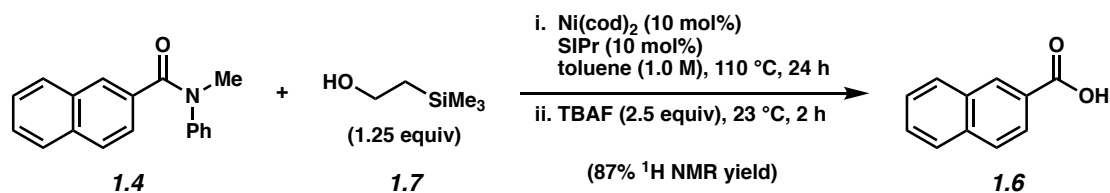
Representative Procedure for the net hydrolysis of amides from Table 1.1. (Entry 3 is used as an example). A 2-dram vial containing amide **1.4** (40.0 mg, 0.153 mmol, 1.00 equiv) and a magnetic stir bar was charged with Ni(cod)$_2$ (4.21 mg, 0.015 mmol, 10 mol%) and SIPr (3.00 mg, 0.015 mmol, 10 mol%) in a glove box. Subsequently, toluene (0.15 mL, 1.0 M) and TMS-ethanol (**1.7**) (27.4 μL, 0.191 mmol, 1.25 equiv) were added. The vial was sealed with a Teflon-lined screw cap, removed from the glove box, and stirred at 110 °C in a preheated aluminum block for 24 h. After cooling to 23 °C, TBAF (0.383 mmol, 2.50 equiv) was added to the reaction mixture. The resulting mixture was stirred for 2 h. The mixture was quenched with 1.0 M HCl (2.0 mL) and diluted with water (5 mL). The layers were then separated and the aqueous layer was extracted with EtOAc (3 x 6 mL). The combined organic layers were then dried over Na$_2$SO$_4$, filtered, and concentrated under reduced pressure. The yield was determined by ^{1}H NMR analysis with 1,3,5-trimethoxybenzene as an external standard.

Any modifications of the conditions shown in the representative procedure

above are specified in Table 1.2.

Using the representative procedure, albeit without the addition of TBAF, a series of control experiments were performed to optimize the nickel-catalyzed esterification using TMS-ethanol

(**1.7**). Key results are shown in Table 1.3. The control experiments indicate the desired transformation is nickel-catalyzed, as no desired ester product was generated.

Table 1.3. Relevant Control Experiments

	Experimental Results	
Reaction Conditions	*1.4*	*1.5*
TMS-ethanol (1.25 equiv), Ni(cod)$_2$ toluene (1.0 M), 110 °C	100%	0%
TMS-ethanol (1.25 equiv), SIPr (10 mol%) toluene (1.0 M), 110 °C	100%	0%
TMS-ethanol (1.25 equiv) toluene (1.0 M), 110 °C	100%	0%

Yields were determined by ^{1}H NMR analysis using 1,3,5-trimethoxybenzene as an external standard.

1.7.2.3 Scope of Methodology
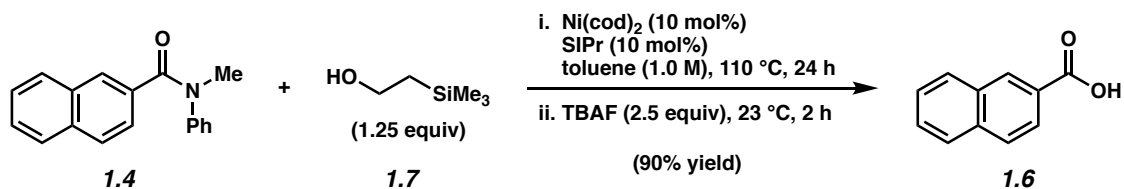
Representative Procedure (net-hydrolysis of amide 1.4 is used as an example).

Carboxylic Acid 1.6 (Figure 1.3). A 2-dram vial containing amide **1.4** (50.6 mg, 0.194 mmol, 1.0 equiv) and a magnetic stir bar was charged with Ni(cod)$_2$ (5.33 mg, 0.0194 mmol, 10 mol%) and SIPr (7.56 mg, 0.0194 mmol, 10 mol%) in a glove box. Subsequently, toluene (0.20 mL, 1.0 M) and then TMS-ethanol (34.7 µL, 0.242 mmol, 1.25 equiv) were added. The vial was sealed with a Teflon-lined screw cap, removed from the glove box, and stirred at 110 °C in a preheated aluminum block for 24 h. After cooling to 23 °C, TBAF (0.485 mmol, 2.50 equiv) was added to the reaction mixture. The resulting mixture was stirred for 2 h. Once the reaction was complete, the mixture was quenched with 1.0 M HCl (3.0 mL) and diluted with water (5 mL). The layers were separated and the aqueous layer was extracted with EtOAc (3 x 10 mL). The combined organic layers were then dried over Na$_2$SO$_4$, filtered, and concentrated under reduced pressure. The crude residue was purified by flash chromatography (5:1 hexanes:EtOAc + 1% acetic acid) to yield carboxylic acid product **1.6** (30.0 mg, 90% yield, average of two experiments) as a white solid. Carboxylic acid **1.6** R$_f$ 0.55 (5:1 hexanes:EtOAc + 1% acetic acid). ^{1}H NMR (500 MHz, DMSO-d_6): δ 8.59 (s, 1H), 8.08 (dd, J = 7.2, 1.4, 1H), 8.02–7.97 (m, 1H), 7.95–7.87 (m, 2H), 7.66–7.60 (m, 1H), 7.60–7.54 (m, 1H). Spectral data match those previously reported.[9]
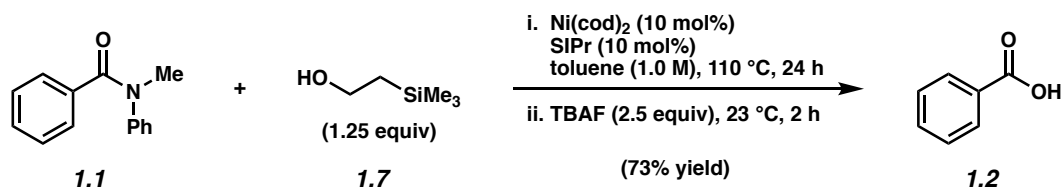
Carboxylic Acid 1.2 (Figure 1.3). Purification by flash chromatography (5:1 hexanes:EtOAc + 1% acetic acid) generated carboxylic acid **1.2** (21.4 mg, 73% yield, average of two experiments) as a white solid. Carboxylic acid **1.2**: R_f 0.22 (2:1 hexanes:EtOAc + 1% acetic acid). ^{1}H NMR (300 MHz, CDCl$_3$): δ 8.15 (dd, J = 8.3, 1.3, 2H), 7.65–7.61 (m, 1H), 7.49–7.45 (m, 2H). Spectral data match those previously reported.[9]
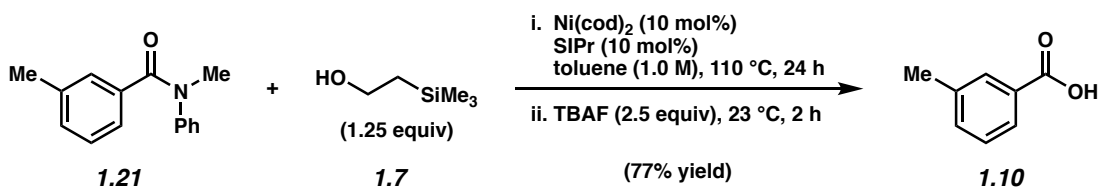
Carboxylic Acid 1.10 (Figure 1.3). Purification by flash chromatography (5:1 hexanes:EtOAc + 1% acetic acid) generated carboxylic acid **1.10** (24.4 mg, 77% yield, average of two experiments) as a white solid. Carboxylic acid **1.10**: R_f 0.54 (5:1 hexanes:EtOAc + 1% acetic acid). ^{1}H NMR (600 MHz, CDCl$_3$): δ 7.96–7.90 (m, 2H), 7.45–7.41 (m, 1H), 7.39–7.35 (m, 1H), 2.43 (s, 3H). Spectral data match those previously reported.[10]
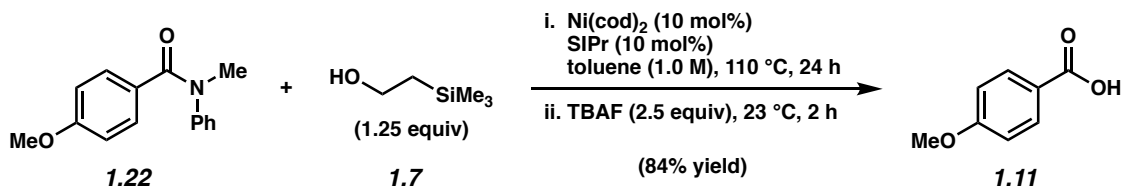
Carboxylic Acid 1.11 (Figure 1.3). Purification by flash chromatography (5:1 hexanes:EtOAc + 1% acetic acid) generated carboxylic acid **1.11** (28.7 mg, 84% yield, average of two experiments) as a white solid. Carboxylic acid **1.11**: R_f 0.33 (5:1 hexanes:EtOAc+ 1% acetic acid). ^{1}H NMR

(500 MHz, DMSO-d_6): δ 7.85 (d, J = 8.5, 2H), 6.97 (d, J = 8.5, 2H), 3.78 (s, 3H). Spectral data

match those previously reported.[9]
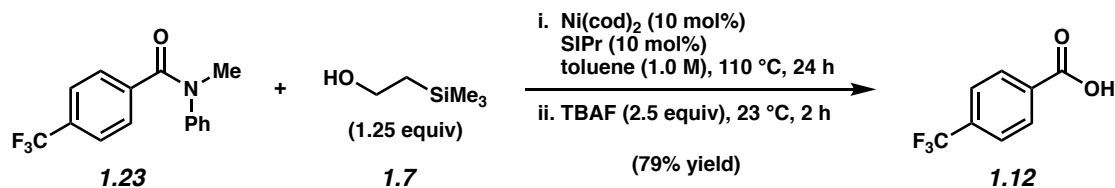
Carboxylic Acid 1.12 (Figure 1.3). Purification by flash chromatography (5:1 hexanes:EtOAc +

1% acetic acid) generated carboxylic acid **1.12** (26.9 mg, 79% yield, average of two experiments)

as a white solid. Carboxylic acid **1.12**: R_f 0.31 (2:1 hexanes:EtOAc + 1% acetic acid). ^{1}H NMR

(600 MHz, DMSO-d_6): δ 8.10 (d, J = 8.1, 2H), 7.84 (d, J = 8.6, 2H). Spectral data match those

previously reported.[9]
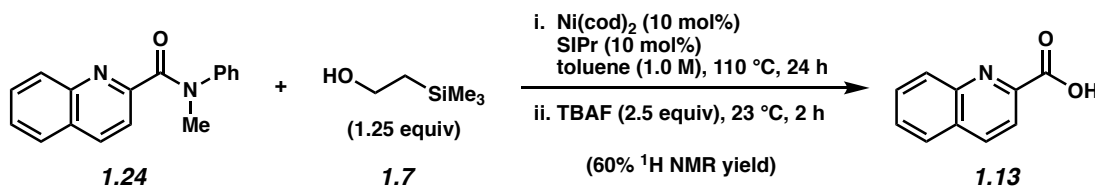
Carboxylic Acid 1.13 (Figure 1.3). ^{1}H NMR (600 MHz, DMSO-d_6) of crude reaction mixture: δ

8.13 (d, J = 8.25, 1H), 7.93 (d, J = 8.25, 1H), 7.85 (d, J = 7.66, 1H), 7.81 (d, J = 8.25, 1H), 7.67–

7.63 (m, 1H), 7.75–7.46 (m, 1H). Spectral data of the crude mixture of carboxylic acid **1.13** match

those previously reported.[11]
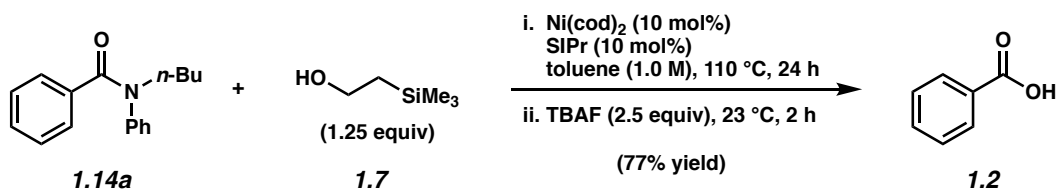
Carboxylic Acid 1.2 (Table 1.2). Purification by preparative thin-layer chromatography (5:1

benzene:EtOAc + 0.1% acetic acid) generated carboxylic acid **1.2** (21.1 mg, 77% yield, average

of two experiments) as a white solid. Carboxylic acid **1.2**: R_f 0.22 (2:1 hexanes:EtOAc + 1% acetic

acid). ^{1}H NMR (300 MHz, CDCl$_3$): δ 8.15 (dd, J = 8.3, 1.3, 2H), 7.65–7.61 (m, 1H), 7.49–7.45

(m, 2H). Spectral data match those previously reported.[9]
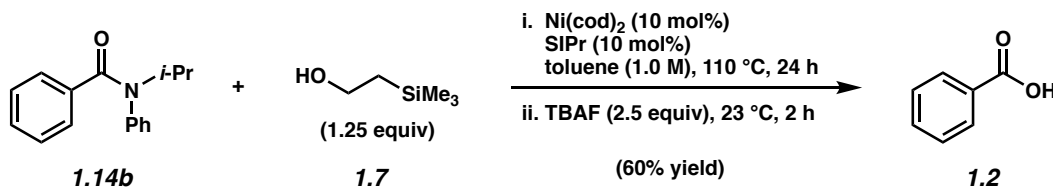
Carboxylic Acid 1.2 (Table 1.2). Purification by preparative thin-layer chromatography (5:1

benzene:EtOAc + 0.1% acetic acid) generated carboxylic acid **1.2** (16.6 mg, 60% yield, average

of two experiments) as a white solid. Carboxylic acid **1.2**: R$_f$ 0.22 (2:1 hexanes:EtOAc + 1% acetic

acid). ^{1}H NMR (300 MHz, CDCl$_3$): δ 8.15 (dd, J = 8.3, 1.3, 2H), 7.65–7.61 (m, 1H), 7.49–7.45

(m, 2H). Spectral data match those previously reported.[9]
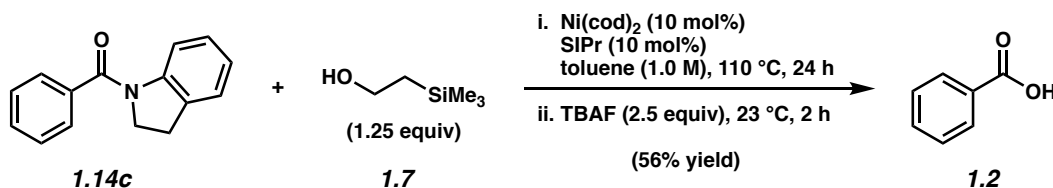
Carboxylic Acid 1.2 (Table 1.2). Purification by preparative thin-layer chromatography (1:1:3

benzene:EtOAc:DCM) generated carboxylic acid **1.2** (17.2 mg, 56% yield, average of two

experiments) as a white solid. Carboxylic acid **1.2**: R$_f$ 0.22 (2:1 hexanes:EtOAc + 1% acetic acid).

^{1}H NMR (300 MHz, CDCl$_3$): δ 8.15 (dd, J = 8.3, 1.3, 2H), 7.65–7.61 (m, 1H), 7.49–7.45 (m, 2H).

Spectral data match those previously reported.[9]
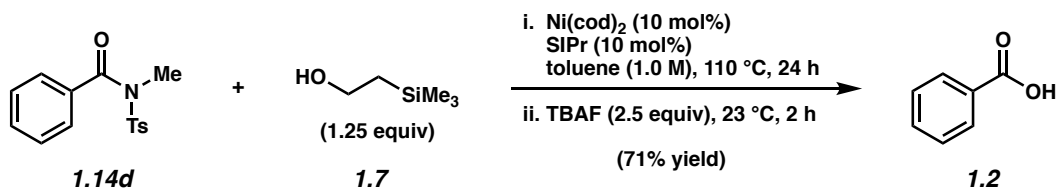
Carboxylic Acid 1.2 (Table 1.2). Purification by preparative thin-layer chromatography (1:1:2 benzene:EtOAc:DCM) generated carboxylic acid **1.2** (16.9 mg, 71% yield, average of two experiments) as a white solid. Carboxylic acid **1.2**: R_f 0.22 (2:1 hexanes:EtOAc + 1% acetic acid). ^{1}H NMR (300 MHz, CDCl$_3$): δ 8.15 (dd, J = 8.3, 1.3, 2H), 7.65–7.61 (m, 1H), 7.49–7.45 (m, 2H). Spectral data match those previously reported.[9]

1.7.2.4 1.0 mmol-Scale Reaction
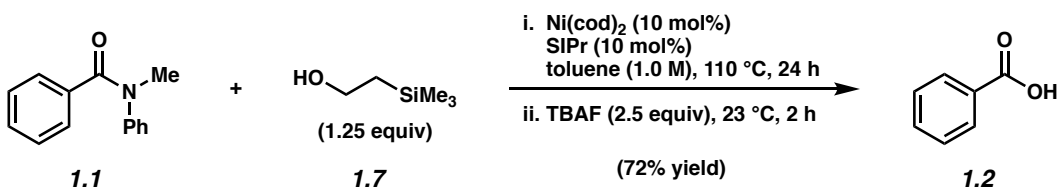
Carboxylic Acid 1.2 (Table 1.2). A 2-dram vial containing amide **1.1** (220 mg, 1.0 mmol, 1.0 equiv) and a magnetic stir bar was charged with Ni(cod)$_2$ (28.6 mg, 0.10 mmol, 10 mol%) and SIPr (40.7 mg, 0.10 mmol, 10 mol%) in a glove box. Subsequently, toluene (1.0 mL, 1.0 M) and then TMS-ethanol (187 μL, 1.25 mmol, 1.25 equiv) were added. The vial was sealed with a Teflon-lined screw cap, removed from the glove box, and stirred at 110 °C in a preheated aluminum block for 24 h. After cooling to 23 °C, TBAF (2.50 mmol, 2.50 equiv) was added to the reaction mixture. The resulting mixture was stirred for 2 h. Once the reaction was complete, the mixture was quenched with 1.0 M HCl (5.0 mL) and diluted with water (10 mL). The layers were separated and the aqueous layer was extracted with EtOAc (3 x 15 mL). The combined organic layers were then dried over Na$_2$SO$_4$, filtered, and concentrated under reduced pressure. The crude residue was

purified by flash chromatography (20:1 hexanes:EtOAc + 1% acetic acid) to yield carboxylic acid product **1.2** (91.0 mg, 72% yield, average of two experiments) as a white solid. Spectral data match those previously reported for carboxylic acid **1.2** (see page 14).

1.7.2.5 Competition Experiments
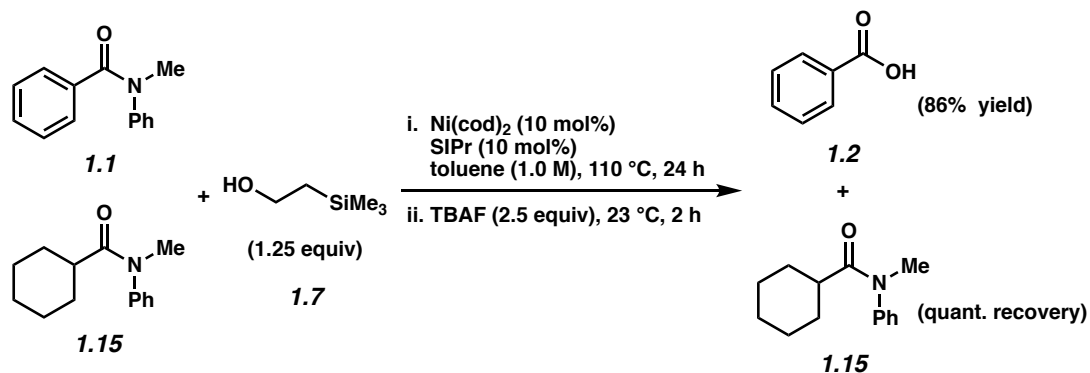
Selectivity for Aromatic over Aliphatic Amides (Figure 1.4). A 2-dram vial containing amide **1.1** (52.4 mg, 0.248 mmol, 1.0 equiv), amide 1.15 (53.9 mg, 0.248 mmol, 1.0 equiv) and a magnetic stir bar was charged with Ni(cod)$_2$ (6.82 mg, 0.025 mmol, 10 mol%) and SIPr (9.69 mg, 0.025 mmol, 10 mol%) in a glove box. Subsequently, toluene (0.25 mL, 1.0 M) and then TMS-ethanol (44.4 µL, 0.310 mmol, 1.25 equiv) were added. The vial was sealed with a Teflon-lined screw cap, removed from the glove box, and stirred at 110 °C in a preheated aluminum block for 24 h. After cooling to 23 °C, TBAF (0.620 mmol, 2.5 equiv) was added to the reaction mixture. The resulting mixture was stirred for 2 h. The mixture was quenched with 1.0 M HCl (3.0 mL) and diluted with water (5 mL). The layers were separated and the aqueous layer was extracted with EtOAc (3 x 10 mL). The combined organic layers were then dried over Na$_2$SO$_4$, filtered, and concentrated under reduced pressure. Spectral data match those previously reported for carboxylic acid **1.2** (see page 14).
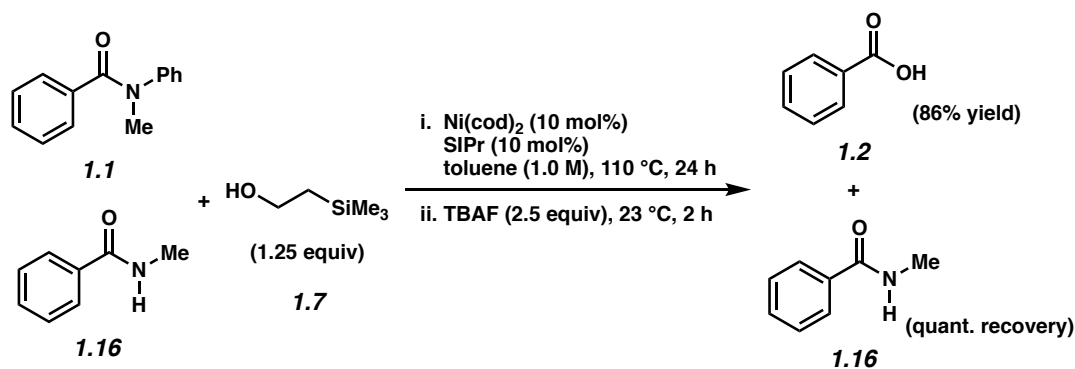
Selectivity for Tertiary over Secondary Amides (Figure 1.4). A 2-dram vial containing amide **1.1** (54.0 mg, 0.256 mmol, 1.0 equiv), amide **1.16** (34.2 mg, 0.253 mmol, 0.99 equiv) and a magnetic stir bar was charged with Ni(cod)$_2$ (7.03 mg, 0.026 mmol, 10 mol%) and SIPr (9.98 mg, 0.026 mmol, 10 mol%) in a glove box. Subsequently, toluene (0.26 mL, 1.0 M) and then TMS-ethanol (45.8 μL, 0.320 mmol, 1.25 equiv) were added. The vial was sealed with a Teflon-lined screw cap, removed from the glove box, and stirred at 110 °C in a preheated aluminum block for 24 h. After cooling to 23 °C, TBAF (0.64 mL, 0.639 mmol, 2.50 equiv) was added to the reaction mixture via syringe. The resulting mixture was stirred at 23 °C for 2 h. Then, the mixture was quenched with 1.0 M HCl (4.0 mL) and diluted with water (3 mL). The layers were separated and the aqueous layer was extracted with EtOAc (3 x 10 mL). The combined organic layers were then washed with saturated NaCl (15 mL), dried over Na$_2$SO$_4$, filtered, and concentrated under reduced pressure. Spectral data match those previously reported for carboxylic acid **1.2** (see page 14).

1.7.2.6 Selective Cleavage of Aryl Amide in the Presence of an Ester
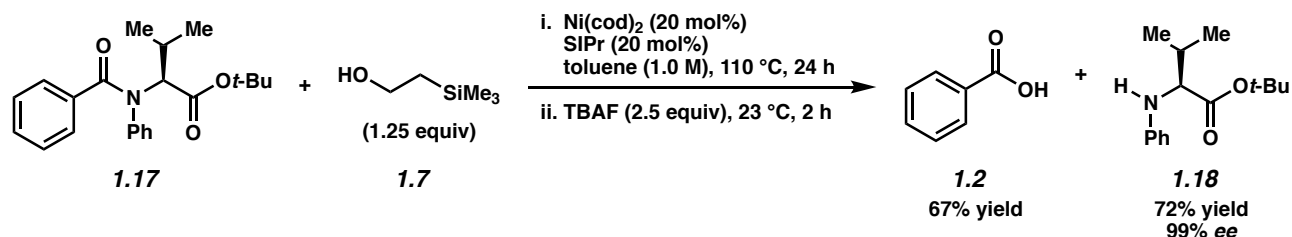
Carboxylic Acid 1.2 and Amine 1.18 (Figure 1.5). A 2-dram vial containing amide **1.17** (50.9 mg, 0.144 mmol, 1.0 equiv) and a magnetic stir bar was charged with Ni(cod)$_2$ (7.92 mg, 0.029 mmol, 20 mol%) and SIPr (11.3 mg, 0.029 mmol, 20 mol%) in a glove box. Subsequently, toluene (0.14 mL, 1.0 M) and then TMS-ethanol (25.8 µL, 0.180 mmol, 1.25 equiv) were added. The vial was sealed with a Teflon-lined screw cap, removed from the glove box, and stirred at 110 °C in a preheated aluminum block for 24 h. After cooling to 23 °C, TBAF (0.360 mmol, 2.5 equiv) was added to the reaction mixture. The resulting mixture was stirred for 2 h. Then, the mixture was quenched with water (6.0 mL) and diluted further with water (5 mL). The layers were separated and the aqueous layer was extracted with EtOAc (3 x 10 mL). The combined organic layers were then dried over Na$_2$SO$_4$, filtered, and concentrated under reduced pressure. The crude residue was purified by preparative thin-layer chromatography (5:1 hexanes:EtOAc + 1% acetic acid) to yield carboxylic acid product **1.2** (11.8 mg, 67% yield, average of two experiments) as a white solid and amine **1.18** (25.7 mg, 72% yield, 99% *ee*, average of two experiments) as a clear oil. Spectral data matched those previously reported.[4a] Carboxylic acid **1.2**: R$_f$ 0.22 (2:1 hexanes:EtOAc + 1% acetic acid). Amine **1.18**: R$_f$ 0.24 (9:1 hexanes:EtOAc). ^{1}H NMR (300 MHz, CDCl$_3$): δ 7.16 (m, 2H), 6.71 (m, 1H), 6.63 (m, 2H), 4.14 (br s, 1H), 3.75 (m, 1H), 2.09 (o, *J* = 5.6, 1.1, 1H), 1.43 (s, 9H), 1.03 (dd, *J* = 6.7, 4.3, 6H). Spectral data match those previously reported.[4a]

1.8 Spectra Relevant to Chapter One:

Nickel-Catalyzed Conversion of Amides to Carboxylic Acids

Rachel R. Knapp, Ana S. Bulger, and Neil K. Garg.

Org. Lett. **2020**, *22*, 2833–2837.
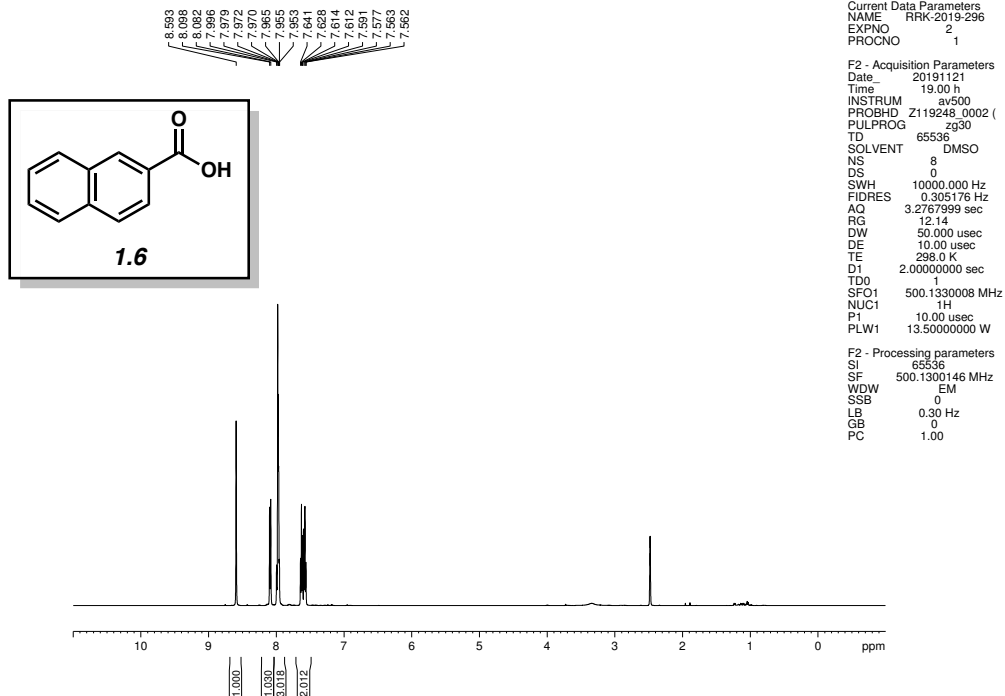
Figure 1.6. ^{1}H NMR (500 MHz, CDCl$_3$) of compound **1.6**.

Figure 1.7. ^{1}H NMR (500 MHz, CDCl$_3$) of compound **1.2**.

7.943
7.942
7.941
7.939
7.938
7.937
7.936
7.923
7.437
7.425
7.424
7.423
7.382
7.369
7.357

2.429

Current Data Parameters
NAME   RRK-2019-241
EXPNO   2
PROCNO   1

F2 - Acquisition Parameters
Date_   20190911
Time   19.12
INSTRUM   av600
PROBHD 5 mm BB5
PULPROG   zg30
TD   65536
SOLVENT   CDCl3
NS   8
DS   0
SWH   12376.237 Hz
FIDRES   0.188846 Hz
AQ   2.6476543 sec
RG   181
DW   40.400 usec
DE   6.50 usec
TE   294.8 K
D1   2.00000000 sec
TD0   1

======== CHANNEL f1 ======
NUC1   1H
P1   22.00 usec
PL1   -1.00 dB
PL1W   31.62277603 W
SFO1   600.1336008 MHz

F2 - Processing parameters
SI   65536
SF   600.1300288 MHz
WDW   EM
SSB   0
LB   0.30 Hz
GB   0
PC   1.00

Me — (structure) — O, OH

1.10

10 9 8 7 6 5 4 3 2 1 0 ppm

1.999   0.964 3.137
        1.054

Figure 1.8. ^{1}H NMR (500 MHz, CDCl$_3$) of compound **1.10**.

7.862
7.844
6.984
6.966

3.781

Current Data Parameters
NAME   RRK-2019-223
EXPNO   3
PROCNO   1

F2 - Acquisition Parameters
Date_   20190903
Time   17.45
INSTRUM   drx500
PROBHD 5 mm bb-Z 800
PULPROG   zg30
TD   65536
SOLVENT   DMSO
NS   8
DS   0
SWH   10000.000 Hz
FIDRES   0.152588 Hz
AQ   3.2767999 sec
RG   101.6
DW   50.000 usec
DE   6.00 usec
TE   294.8 K
D1   2.00000000 sec
TD0   1

======== CHANNEL f1 ======
NUC1   1H
P1   13.30 usec
PL1   0 dB
SFO1   500.3330020 MHz

F2 - Processing parameters
SI   32768
SF   500.3300220 MHz
WDW   EM
SSB   0
LB   0.30 Hz
GB   0
PC   1.00

MeO — (structure) — O, OH

1.11

10 9 8 7 6 5 4 3 2 1 0 ppm

1.987 2.000   3.028

Figure 1.9. ^{1}H NMR (500 MHz, CDCl$_3$) of compound **1.11**.

23
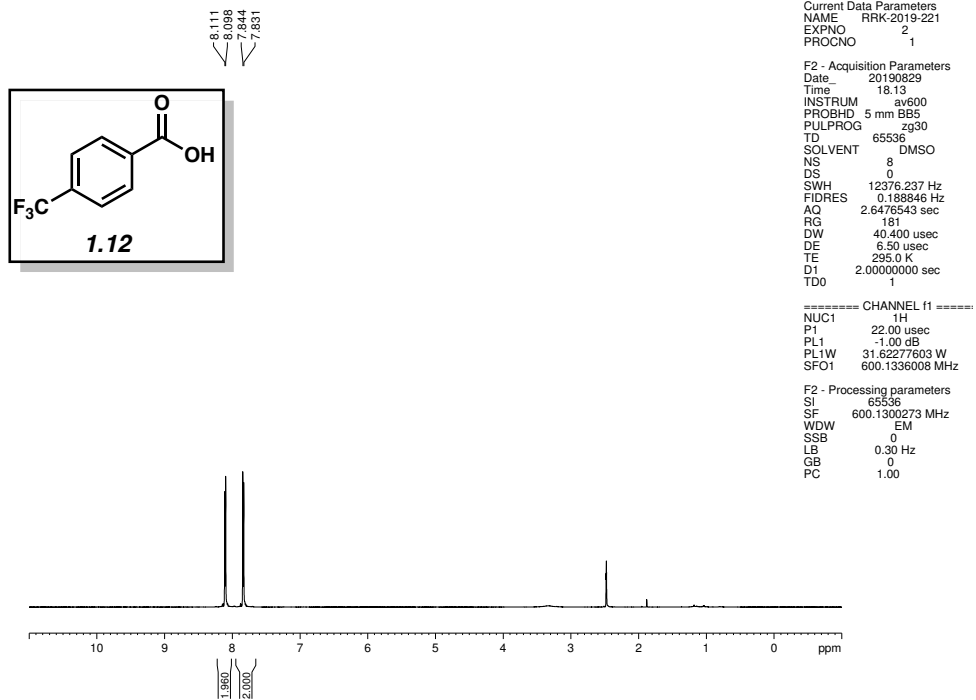
Figure 1.10. ^{1}H NMR (500 MHz, CDCl$_3$) of compound **1.12**.
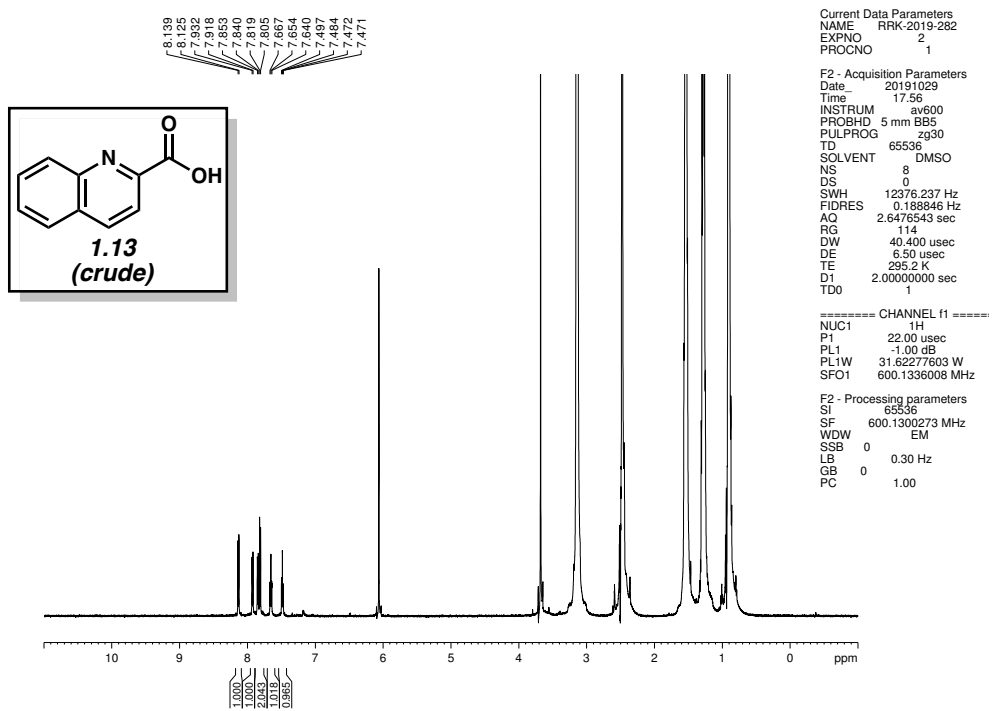
Figure 1.11. ^{1}H NMR (500 MHz, CDCl$_3$) of compound **1.13**.

24

NMR peak labels: 7.191, 7.166, 7.162, 7.138, 6.738, 6.735, 6.714, 6.693, 6.689, 6.686, 6.652, 6.648, 6.623, 6.620

4.144, 3.764, 3.747

2.181, 2.158, 2.136, 2.116, 2.113, 2.094, 2.090, 2.071, 2.051, 2.026, 1.432, 1.059, 1.036, 1.014

Current Data Parameters
NAME   ASB-2020-004
EXPNO   50
PROCNO   1

F2 - Acquisition Parameters
Date_   20200114
Time   18.36
INSTRUM   av300
PROBHD 5 mm PABBO BB-
PULPROG   zg30
TD   65536
SOLVENT   CDCl3
NS   8
DS   0
SWH   5995.204 Hz
FIDRES   0.091480 Hz
AQ   5.4657025 sec
RG   228.1
DW   83.400 usec
DE   6.00 usec
TE   300.0 K
D1   2.00000000 sec
TD0   1

======= CHANNEL f1 =====
NUC1   1H
P1   14.00 usec
PL1   0 dB
PL1W   9.31909847 W
SFO1   300.1318008 MHz

F2 - Processing parameters
SI   65536
SF   300.1300124 MHz
WDW   EM
SSB   0
LB   0.30 Hz
GB   0
PC   1.40

Integration values: 1.996, 0.991, 2.011, 0.968, 1.001, 1.027, 9.000, 6.058

Figure 1.12. ^{1}H NMR (500 MHz, CDCl$_3$) of compound **1.18**.

1.9 SFC Traces

Compound	SFC Method Column/Temp. Abs. Wavelength	Sovlent	Method Flow Rate	Retention Times (min)	Enantiomeric Ratio (er)
rac-1.18	Daicel ChiralPak IA-3/35 °C λabs = 210 nm	2% isopropanol in CO$_2$	3.5 mL/min	2.20/2.75	50:50
1.18	Daicel ChiralPak IA-3/35 °C λabs = 210 nm	2% isopropanol in CO$_2$	3.5 mL/min	2.35/2.87	100:0
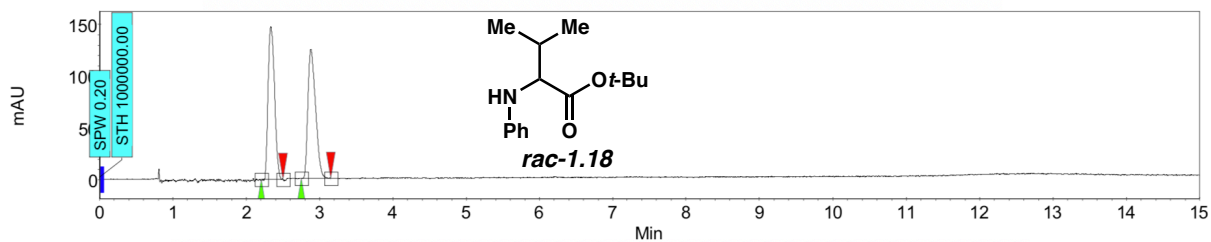
Figure 1.13. SFC trace of **rac-1.8**.
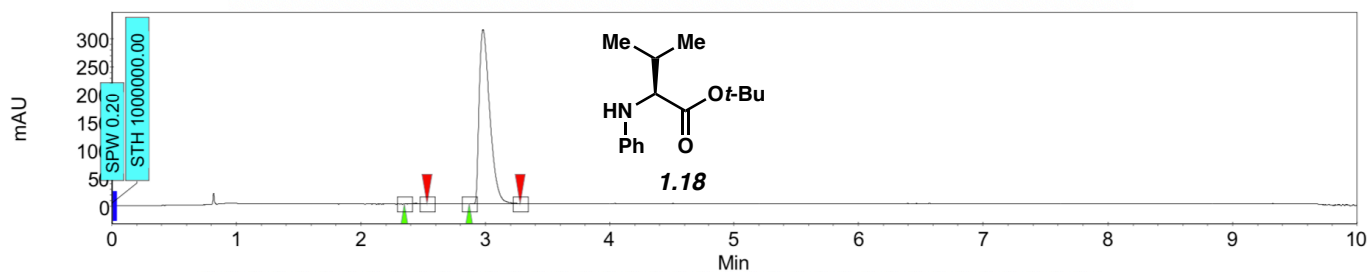
Index	Name	Start	Time	End	RT Offset	Quantity	Height	Area	Area
		[Min]	[Min]	[Min]	[Min]	[% Area]	[µV]	[µV.Min]	[%]
2	UNKNOWN	2.20	2.33	2.50	0.00	50.06	147.5	15.1	50.060
1	UNKNOWN	2.75	2.88	3.15	0.00	49.94	124.8	15.0	49.940
Total						100.00	272.3	30.1	100.000

Figure 1.14. SFC trace of **1.18**.

Index	Name	Start	Time	End	RT Offset	Quantity	Height	Area	Area
		[Min]	[Min]	[Min]	[Min]	[% Area]	[µV]	[µV.Min]	[%]
2	UNKNOWN	2.35	2.44	2.53	0.00	0.16	0.9	0.0	0.161
1	UNKNOWN	2.87	2.98	3.28	0.00	99.84	312.3	30.7	99.839
Total						100.00	313.2	30.8	100.000

26

1.10 Notes and References

(1) For recent reviews, see: (a) Dander, J. E.; Garg, N. K. Breaking amides using nickel catalysis. *ACS Catal.* **2017**, *7*, 1413–1423. (b) Meng, G.; Shi, S.; Szostak, M. Cross-coupling of amides by N–C bond activation. *Synlett* **2016**, *27*, 2530–2540. (c) Takise, R.; Muto, K.; Yamaguchi, J. Cross-coupling of aromatic esters and amides. *Chem. Soc. Rev.* **2017**, *46*, 5864–5888. (d) Kaiser, D.; Bauer, A.; Lemmerer, M.; Maulide, N. Amide activation: an emerging tool for chemoselective synthesis. *Chem. Soc. Rev*. **2018**, *47*, 7899–7925.

(2) For Pd-catalyzed amide C−N bond activations, see: (a) Li, X.; Zou, G. Acylative Suzuki coupling of amides: acyl-nitrogen activation via synergy of independently modifiable activating groups. *Chem. Commun.* **2015**, *51*, 5089−5092. (b) Yada, A.; Okajima, S.; Murakami, M. Palladium-catalyzed intramolecular insertion of alkenes into the carbon−nitrogen bond of β-lactams. *J. Am. Chem. Soc.* **2015**, *137*, 8708−8711. (c) Meng, G.; Szostak, M. Palladium-catalyzed Suzuki−Miyaura coupling of amides by carbon−nitrogen cleavage: general strategy for amide N−C bond activation. *Org. Biomol. Chem.* **2016**, *14*, 5690−5705. (d) Meng, G.; Szostak, M. General olefin synthesis by the palladium-catalyzed Heck reaction of amides: sterically-controlled chemoselective N−C activation. *Angew. Chem., Int. Ed.* **2015**, *54*, 14518−14522. (e) Meng, G.; Szostak, M. Sterically controlled Pd-catalyzed chemoselective ketone synthesis via N−C cleavage in twisted amides. *Org. Lett.* **2015**, *17*, 4364−4367. (f) Liu, C.; Meng, G.; Liu, Y.; Liu, R.; Lalancette, R.; Szostak, R.; Szostak, M. *N*-Acylsaccharins: stable electrophilic amide-based acyl transfer reagents in Pd-catalyzed Suzuki−Miyaura coupling via N−C cleavage. *Org. Lett.* **2016**, *18*, 4194−4197. (g) Lei, P.; Meng, G.; Szostak, M. General method for the Suzuki−Miyaura cross-coupling of amides using commercially available, air- and moisture-stable palladium/NHC (NHC = *N*-heterocyclic

carbene) complexes. *ACS Catal.* **2017**, *7*, 1960−1965. (h) Liu, C.; Liu, Y.; Liu, R.; Lalancette, R.; Szostak, R.; Szostak, M. Palladium-catalyzed Suzuki−Miyaura cross-coupling of *N*-mesylamides by N−C cleavage: electronic effect of the mesyl group. *Org. Lett.* **2017**, *19*, 1434−1437. (i) Liu, C.; Meng, G.; Szostak, M. *N*-Acylsaccharins as amide-based arylating reagents via chemoselective N−C cleavage: Pd-catalyzed decarbonylative Heck reaction. *J. Org. Chem.* **2016**, *81*, 12023−12030. (j) Meng, G.; Shi, S.; Szostak, M. Palladium-catalyzed Suzuki−Miyaura cross-coupling of amides via site-selective N−C bond cleavage by cooperative catalysis. *ACS Catal.* **2016**, *6*, 7335−7339. (k) Cui, M.; Wu, H.; Jian, J.; Wang, H.; Liu, C.; Stelck, D.; Zeng, Z. Palladium-catalyzed Sonogashira coupling of amides: access to ynones via C−N bond cleavage. *Chem. Commun.* **2016**, *52*, 12076−12079. (l) Wu, H.; Li, Y.; Cui, M.; Jian, J.; Zeng, Z. Suzuki coupling of amides via palladium-catalyzed C−N cleavage of *N*-acylsaccharins. *Adv. Synth. Catal.* **2016**, *358*, 3876−3880. (m) Shi, S.; Szostak, M. Decarbonylative cyanation of amides by palladium catalysis. *Org. Lett.* **2017**, *19*, 3095−3098. (n) Lei, P.; Meng, G.; Ling, Y.; An, J.; Szostak, M. Pd-PEPPSI: Pd-NHC precatalyst for Suzuki−Miyaura cross-coupling reactions of amides. *J. Org. Chem.* **2017**, *82*, 6638−6646. (o) Meng, G.; Szostak, R.; Szostak, M. Suzuki−Miyaura cross-coupling of *N*-acylpyrroles and pyrazoles: planar, electronically activated amides in catalytic N−C cleavage. *Org. Lett.* **2017**, *19*, 3596−3599. (p) Meng, G.; Lalancette, R.; Szostak, R.; Szostak, M. *N*-Methylamino pyrimidyl amides (MAPA): highly reactive, electronically-activated amides in catalytic N−C(O) cleavage. *Org. Lett.* **2017**, *19*, 4656−4659. (q) Osumi, Y.; Szostak, M. *N*-Acylsuccinimides: twist-controlled, acyl transfer reagents in Suzuki−Miyaura cross-coupling by N−C amide bond activation. *Org. Biomol. Chem.* **2017**, *15*, 8867−8871. (r) Lei, P.; Meng, G.; Ling, Y.; An, J.; No lan, S. P.; Szostak, M. General method for the Suzuki−Miyaura cross-

coupling of primary amide-derived electrophiles enabled by [Pd(NHC)(cin)–Cl] at room temperature. *Org. Lett.* **2017**, *19*, 6510−6513. (s) Li, X.; Zou, G. Palladium-catalyzed acylative cross-coupling of amides with diarylboronic acids and sodium tetraarylborates. *J. Organomet. Chem.* **2015**, *794*, 136−145. (t) Liu, C.; Li, G.; Shi, S.; Meng, G.; Lalancette, R.; Szostak, R.; Szostak, M. Acyl and decarbonylative Suzuki coupling of *N*-acetyl amides: Electronic tuning of twisted, acyclic amides in catalytic carbon−nitrogen bond cleavage. *ACS Catal.* **2018**, *8*, 9131−9139. (u) Meng, G.; Szostak, M. Palladium/NHC (NHC = *N*-heterocyclic carbene)-catalyzed β-alkyl Suzuki cross-coupling of amides by selective N−C bond cleavage. *Org. Lett.* **2018**, *20*, 6789−6793. (v) Shi, S.; Szostak, M. Decarbonylative borylation of amides by palladium catalysis. *ACS Omega* **2019**, *4*, 4901−4907. (w) Zhou, T.; Li, G.; Nolan, S. P.; Szostak, M. [Pd(NHC)(acac)Cl]: well-defined, air-stable, and readily available precatalysts for Suzuki and Buchwald−Hartwig cross-coupling (transamidation) of amides and esters by N−C/O−C activation. *Org. Lett.* **2019**, *21*, 3304−3309. (x) Rahman, M. M.; Buchspies, J.; Szostak, M. *N*-Acylphthalimides: efficient acyl coupling reagents in Suzuki–Miyaura cross-coupling by N–C cleavage catalyzed by Pd-PEPPSI precatalysts. *Catalysts* **2019**, *9*, 129. (y) Liu, C.; Lalancette, R.; Szostak, R.; Szostak, M. Sterically hindered ketones via palladium-catalyzed Suzuki–Miyaura cross-coupling of amides by N–C(O) activation. *Org. Lett.* **2019**, *21*, 7976–7981. (z) Li, G.; Zhou, T.; Poater, A.; Cavallo, L.; Nolan, S. P.; Szostak, M. Buchwald–Hartwig cross-coupling by air- and moisture-stable [Pd(NHC)(allyl)Cl] pre-catalysts: catalyst evaluation and mechanism. *Catal. Sci. Technol.* **2020**, *10*, 710–716.

(3) Meng, G.; Szostak, M. Rhodium-catalyzed C–H bond functionalization with amides by double C–H/C–N bond activation. *Org. Lett.* **2016**, *18*, 796–799.

(4) For nickel-catalyzed reactions proceeding with cleavage of the amide C−N bond, see: (a) Hie, L.; Fine Nathel, N. F.; Shah, T. K.; Baker, E. L.; Hong, X.; Yang, Y.-F.; Liu, P.; Houk, K. N.; Garg, N. K. Conversion of amides to esters by the nickel-catalysed activation of amide C−N bonds. *Nature* **2015**, *524*, 79−83. (b) Weires, N. A.; Baker, E. L.; Garg, N. K. Nickel-catalysed Suzuki−Miyaura coupling of amides. *Nat. Chem.* **2016**, *8*, 75−79. (c) Baker, E. L.; Yamano, M. M.; Zhou, Y.; Anthony, S. M.; Garg, N. K. A two-step approach to achieve secondary amide transamidation enabled by nickel catalysis. *Nat. Commun.* **2016**, *7*, 11554. (d) Simmons, B. J.; Weires, N. A.; Dander, J. E.; Garg, N. K. Nickel-catalyzed alkylation of amide derivatives. *ACS Catal.* **2016**, *6*, 3176−3179. (e) Shi, S.; Szostak, M. Nickel-catalyzed diaryl ketone synthesis by N−C bond cleavage: direct Negishi cross-coupling of primary amides by site-selective *N,N*-di-Boc activation. *Org. Lett.* **2016**, *18*, 5872−5875. (f) Shi, S.; Szostak, M. Efficient synthesis of diaryl ketones by nickel-catalyzed Negishi cross-coupling of amides via carbon−nitrogen bond cleavage at room temperature accelerated by solvent effect. *Chem. Eur. J.* **2016**, *22*, 10420−10424. (g) Hie, L.; Baker, E. L.; Anthony, S. M.; Desrosiers, J.-N.; Senanayake, C.; Garg, N. K. Nickel-catalyzed esterification of aliphatic amides. *Angew. Chem., Int. Ed.* **2016**, *55*, 15129−15132. (h) Dey, A.; Sasmal, S.; Seth, K.; Lahiri, G. K.; Maiti, D. Nickel-catalyzed deamidative step-down reduction of amides to aromatic hydrocarbons. *ACS Catal.* **2017**, *7*, 433−437. (i) Ni, S.; Zhang, W.; Mei, H.; Han, J.; Pan, Y. Ni-catalyzed reductive cross-coupling of amides with aryl iodide electrophiles via C−N bond activation. *Org. Lett.* **2017**, *19*, 2536−2539. (j) Medina, J. M.; Moreno, J.; Racine, S.; Du, S.; Garg, N. K. Mizoroki−Heck cyclizations of amide derivatives for the introduction of quaternary centers. *Angew. Chem., Int. Ed.* **2017**, *56*, 6567−6571. (k) Hu, J.; Wang, M.; Pu, X.; Shi, Z. Nickel-catalysed retro-hydroamidocarbonylation of aliphatic amides to olefins. *Nat. Commun.* **2017**,

8, 14993. (l) Weires, N. A.; Caspi, D. D.; Garg, N. K. Kinetic modeling of the nickel-catalyzed esterification of amides. *ACS Catal.* **2017**, *7*, 4381−4385. (m) Shi, S.; Szostak, M. Nickel-catalyzed Negishi cross-coupling of *N*-acylsuccinimides: stable, amide-based, twist-controlled acyl transfer reagents via N−C activation. *Synthesis* **2017**, 3602−3608. (n) Dander, J. E.; Baker, E. L.; Garg, N. K. Nickel-catalyzed transamidation of aliphatic amide derivatives. *Chem. Sci.* **2017**, *8*, 6433−6438. (o) Huang, P.-Q.; Chen, H. Ni-catalyzed cross-coupling reactions of *N*-acylpyrrole-type amides with organoboron reagents. *Chem. Commun.* **2017**, *53*, 12584−12587. (p) Deguchi, T.; Xin, H.-L.; Morimoto, H.; Ohshima, T. Direct catalytic alcoholysis of unactivated 8-aminoquinoline amides. *ACS Catal.* **2017**, *7*, 3157−3161. (q) Dander, J. E.; Giroud, M.; Racine, S.; Darzi, E. R.; Alvizo, O.; Entwistle, D.; Garg, N. K. Chemoenzymatic conversion of amides to enantioenriched alcohols in aqueous medium. *Commun. Chem.* **2019**, *2*, 82. (r) Wang, H.; Zhang, S.; Hong, X. Computational studies on Ni-catalyzed amide C–N bond activation. *Chem. Commun.* **2019**, *55*, 11330–11341. (s) Mehta, M. M.; Boit, T. B.; Dander, J. E.; Garg, N. K. Ni-catalyzed Suzuki–Miyaura cross-coupling of aliphatic amides on the benchtop. *Org. Lett.* **2020**, *22*, 1–5. (t) Yu, C.; Matsuo, Y. Nickel-catalyzed deaminative acylation of activated aliphatic amines with aromatic amides via C–N bond activation. *Org. Lett.* **2020**, *22*, 950–955.

(5) (a) Steiger, R. E. α-Aminodiethylacetic acid. *Org. Synth.* **1942**, *22*, 13. (b) Brown, R. S.; Bennet, A. J.; Slebocka-Tilk, H. Recent perspectives concerning the mechanism of H_3O^+- and OH^- promoted amide hydrolysis. *Acc. Chem. Res.* **1992**, *25*, 481–488. (c) Smith, M. B.; March, J. "Aliphatic nucleophilic substitution." *March's Advanced Organic Chemistry*, John Wiley & Sons, Inc. **2001**, 474–477. (d) Slebocka-Tilk, H.; Neverov, A.; Brown, R. S. Proton inventory

study of the base-catalyzed hydrolysis of formamide. Consideration of the nucleophilic and general base mechanisms. *J. Am. Chem. Soc.* **2003**, *125*, 1851–1858.

(6) See section 1.7.2.3 for experimental details.

(7) Consistent with prior studies, this methodology using Ni/SIPr requires the use of benzamide-type substrates. Density functional theory (DFT) calculations suggest the presence of an aromatic ring attached to the carbonyl enables nickel coordination and amide C–N bond cleavage; see reference 3a.

(8) Reaction was also run on a 1.0 mmol scale, affording benzoic acid (**1.2**) in 72% isolated yield.

(9) Bhunia, S. K.; Das, P.; Nandi, S.; Jana, R. Carboxylation of aryl triflates with CO_2 merging palladium and visible-light-photoredox catalysts. *Org. Lett*. **2019**, *21*, 4632–463.

(10) Kobaysashi, K.; Kondo, Y. Transition-metal-free carboxylation of organozinc reagents using CO_2 in DMF solvent. *Org. Lett*. **2009**, *11*, 2035–2037.

(11) Yoshida, M.; Katagiri, Y.; Zhu, W.; Shishido, K. Oxidative carboxylation of arylaldehydes with water by a sulfoxylalkyl-substituted *N*-heterocyclic carbene catalyst. *Org. Biomol. Chem.* **2009**, *7*, 4062–4066.

CHAPTER TWO

Dual Neutral Sphingomyelinase2/Acetylcholinesterase Inhibitors for the

Treatment of Alzheimer's Disease

Tina Bilousova, Bryan J. Simmons, Rachel R. Knapp, Chris J. Elias, Jesus Campagna, Mikhail Melnik, Sujyoti Chandra, Samantha Focht, Chunni Zhu, Kanagasabai Vadivel, Barbara Jagodzinska, Whitaker Cohn, Patricia Spilman, Karen H. Gylys, Neil K. Garg*, and Varghese John.*

2.1 Abstract

We report the discovery of a novel class of compounds that function as dual inhibitors of the enzymes neutral sphingomyelinase 2 (nSMase2) and acetylcholinesterase (AChE). Inhibition of these enzymes provides a unique strategy to suppress the propagation of tau pathology in treatment of Alzheimer's disease (AD). We describe the key SAR elements that affect relative nSMase2 and/or AChE inhibitor effects and potency, in addition to the identification of two analogs that suppress the release of tau-bearing exosomes in vitro and in vivo. Identification of these novel dual nSMase2/AChE inhibitors represents a new therapeutic approach to AD and has the potential to lead to the development of truly disease-modifying therapeutics.

2.2 Introduction

Alzheimer's disease (AD) is the most prevalent age-related neurodegenerative disorder and, currently, there are no effective disease-modifying therapies available for the treatment of AD. The number of AD cases in the US is ~5.8 million patients and this number is expected to rise to 50 million by 2050. The estimated global socioeconomic costs of AD and related dementias are predicted to reach \$2 trillion by the year 2030.[1]

AD brain tissue is characterized by the presence of senile plaques composed mainly of aggregated amyloid-β peptide (Aβ), neurofibrillary tangles (NFTs) composed of pathological forms of the microtubule-stabilizing protein tau, chronic neuroinflammation, and loss of neurons.[2] Clinically, it is thought that the underlying mechanisms of disease are initiated as early as 20 years before the onset of signs and symptoms. During this asymptomatic period, proteopathic proteins are believed to accumulate, leading to structural alterations and the neuronal dysfunction and loss that leads frequently to Mild Cognitive impairment (MCI). MCI then progresses to full-blown AD-related memory deficits, decline of other cognitive skills, and in advanced AD, the inability to participate in activities of daily living.[3]

While the exact mechanisms of disease progression have not been fully elucidated, it is thought that increased Aβ production at the synapse and/or impaired clearance, results in synaptic loss. Contemporaneously and in conjunction with Aβ accumulation, there is hyperphosphorylation and oligomerization of tau that eventually leads to neuronal toxicity, NFT formation, and neuronal cell death. Diseased neurons can release these toxic phosphorylated forms of tau (p-tau) in proteopathic seeds, which can then be taken up by surrounding or interconnected neurons, leading to templating and propagation of the pathological aggregates in prion-like fashion. The propagation of the disease follows a spatiotemporal pattern with Aβ plaques first appearing in the basal forebrain, then the frontal, temporal and occipital lobes of the cortex. NFTs form in the locus coeruleus and in the allocortex of the medial temporal lobe.[4] Both Aβ and tau pathologies spread through the brain during disease progression.[2]

Given the importance of tau, significant attention is now being paid to the mechanisms of pathological tau spread in AD with the goal of identifying targets for novel therapies to prevent disease progression.[5] Historically, Aβ pathology has been thought to be causative in AD,[6,7] but

multiple clinicopathological evaluations, as well as recent in vivo imaging studies, suggest that the cognitive status of AD patients correlates most closely with region-specific brain atrophy and distribution of the hyper-phosphorylated and aggregated pathological forms of tau that lead to the formation of NFTs.[8,9,10,11] Longitudinal studies have confirmed that propagation of tau pathology correlates significantly with cognitive decline.[12,13] These data suggest that suppression of propagation of tau pathology in AD may have a disease-modifying effect.

Prompted by the findings described above, we undertook a screening effort to identify inhibitors of tau propagation. As will be discussed further below, this led to the discovery of dual inhibitors of two important enzymes: neutral sphingomyelinase 2 (nSMase2) and acetylcholine esterase (AChE), a key enzyme implicated in AD. In our in vitro studies, the identified dual inhibitors prevented the spreading of tau in cell culture systems using assays we have previously reported.[14]

NSMase2 is an enzyme responsible for hydrolysis of sphingomyelin to ceramide/phosphatidylcholine and has been implicated in the spread of AD pathology. Pharmacological inhibition or genetic depletion of nSMase2 has been shown to suppress progression of both Aβ and tau pathology in animal models.[15,16,17] nSMase2 activity plays an important role for normal brain function, but its activity increases with age leading to dysregulation in sphingomyelin turnover.[18,19,20,21,22] There is over-activation of nSMase2 in AD, and brain ceramide levels have been found to be elevated in AD patient cerebrospinal fluid (CSF), compared to age-matched control subjects.[23] The ceramide/sphingomyelin imbalance is greater in individuals that express apolipoprotein E4 (ApoE4), the major genetic risk factor for sporadic, late onset AD.[24] NSMase2 is a key enzyme involved in biogenesis of brain exosomes through the Endosomal Sorting Complex Required for Transportation (ESCRT)-independent pathway.[25]

Brain exosomes are a type of extracellular vesicle (EV), that are 40-150 nm in diameter and are released by brain cells when multivesicular endosomes fuse with the plasma membrane.[25,26] They are involved in normal brain function, but a subset produced by the ESCRT-independent pathway involving nSMase2 have been shown to carry disease-propagating proteopathic seeds, such as tau oligomers, in AD.[14,15,17,27] Tau oligomers have been found to be associated with neuronal exosomes in both cell culture medium and transgenic AD/tauopathy model brain tissue, as well as in AD patient plasma and CSF.[15,28,29,30,31,32,33]

Despite recent progress, the current armamentarium of nSMase2 inhibitors have poor drug-like properties and oral brain permeability.[34,35] Thus, our initial goal was to identify nSMase2 inhibitors that overcome these limitations for the development of preclinical candidates for AD. Using an nSMase2 inhibitor screening assay, we identified a novel furoindoline compound 'validated hit'. Further structural alterations of this initial hit generated compounds that resulted in the identification of novel dual inhibitor analogs that not only inhibit nSMase2 activity, but also inhibit acetylcholinesterase (AChE) enzyme activity and suppress p-tau propagation.

AChE inhibitors (AChEIs) are currently one of only two classes of FDA-approved AD therapeutics; they have demonstrated amelioration of symptoms in AD, being most effective in mild and moderate AD.[36] Inhibition of AChE leads to increased levels of acetylcholine (ACh) at the synapse and in brain parenchyma, and provides support for cholinergic synaptic plasticity even during progressive loss of cholinergic innervation from the basal forebrain.[37] However, AChEI's treatment only provides short term benefits in AD and does not block the progression of the disease.

The dual nSMase2/AChE inhibitors we describe herein represent a new therapeutic paradigm and could be a game changer for the treatment of AD. These agents have the potential

to be disease-modifying by suppressing disease progression through exosome-mediated tau propagation, while also providing symptomatic relief through support of ACh-mediated cognitive enhancement. Interestingly, in mild to moderate AD, there is significantly decreased cholinergic activity and high levels of p-tau in CSF-derived exosomes, thus treating patients in these stages of the disease with dual nSMase2/AChE inhibitors could be highly beneficial.[33] We propose a mechanism of action for these dual inhibitors involving nSMase2 mediated suppression of tau oligomer release in brain exosomes by presynaptic neurons,[38] increased ACh levels at the synapse through AChE inhibition, along with the suppression of tau oligomer uptake through ACh receptors by postsynaptic neurons.[39]

2.3 Screening for and Optimization of Selective nSMase2 and Dual nSMase2/AChE Inhibitors

We initiated the present study by screening a compound library for their effect on nSMase2 activity. Using an Amplex Red neutral sphingomyelinase enzyme activity assay several hits were identified that inhibited $\geq$60% nSMase2 activity at a concentration of 50 μM, as shown in the scatterplot (Figure 2.1a). The known nSMase2 inhibitor cambinol[14] was used as a positive control for the screening assay. After retesting, one hit (Figure 2.1a) was validated and selected for further hit-to-lead optimization.
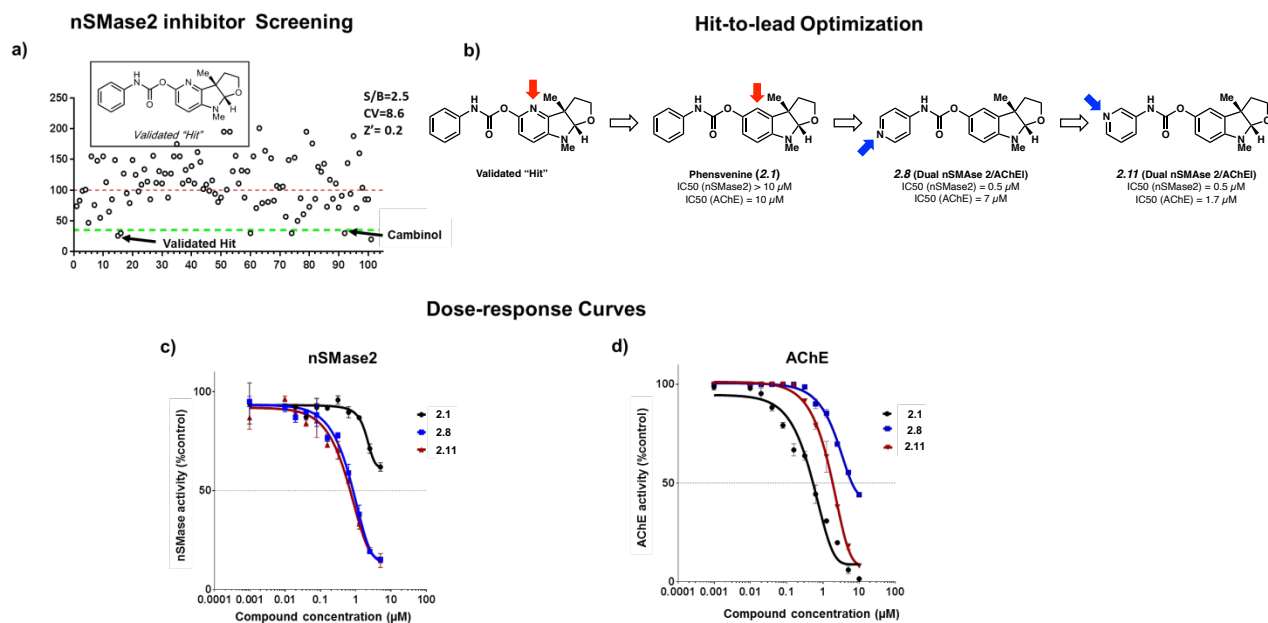
Figure 2.1. Screening and identification of novel dual nSMase2/AChE inhibitors: a) nSMase2 inhibitor screening using Amplex Red-coupled assay revealed several hits that inhibited activity ≥60%; b) hit-to-lead optimization of the validated hit shows removal of the nitrogen group from the furoindoline aryl ring (red arrow) and addition of nitrogen to the carbamate phenyl ring at either the 3 or 4 positions (blue arrow) results in enhanced potency for nSMase2 inhibition and varied AChE inhibition; c) Dose-response analysis for compounds **2.1**, **2.8**, and **2.11** in the nSMase2 assay; and d) Dose-response analysis for compounds **2.1**, **2.8**, and **2.11** in the AChE assay.

Optimization efforts led to the synthesis and evaluation of analogs. Our synthetic approach to the validated hit and analogs will be described subsequently, but a summary of our optimization effort leading to key dual inhibitor analogs **2.8** and **2.11** is shown in Figure 2.1b. Given the structural similarity between the validated hit and known AChE inhibitor phensvenine (**2.1**) we initially prepared this analog to check if it was also an nSMase2 inhibitor. Dose-response analysis revealed that phensvenine (**2.1**) indeed has nSMase2 inhibitory activity (Figure 2.1c) but is a more potent inhibitor of AChE with an IC_{50} = 0.5 µM (Figure 2.1d). In contrast, the dual inhibitors **2.8** and **2.11** were more potent nSMase2 inhibitors (IC_{50} = 0.5 µM) with varying AChE inhibitory activity (Figure 2.1c & 2.1d). Interestingly, replacement of the oxygen in the furoindoline ring of

phensvenine (O → N-CH$_3$), as seen in phenserine, results in the loss of any detectable nSMase2 inhibitory activity (IC$_{50}$ >50 μM).

The synthesis of the validated hit and analogs were made possible by using the interrupted Fischer indolization reaction and variants thereof.[40] As an example, the interrupted Fischer indolization route to (–)-phensvenine (**2.1**) is shown in Scheme 2.1. Treatment of aryl hydrazine **2.17** and lactol **2.18** with acetic acid furnished furoindoline **2.19** in 67% yield. Subsequent *N*-methylation provided **2.23**. At this stage, the enantiomers could be resolved using chiral SFC. As depicted for the (–)-enantiomer, *O*-deprotection was achieved using BBr$_3$, thus furnishing (–)-**2.26**. Lastly, treatment with NaH and phenylisocyanate furnished (–)-phensvenine (**2.1**). It should be noted that (–)-enantiomers were specifically targeted given the known stereospecificity of phenserine for AChE inhibition.[41]
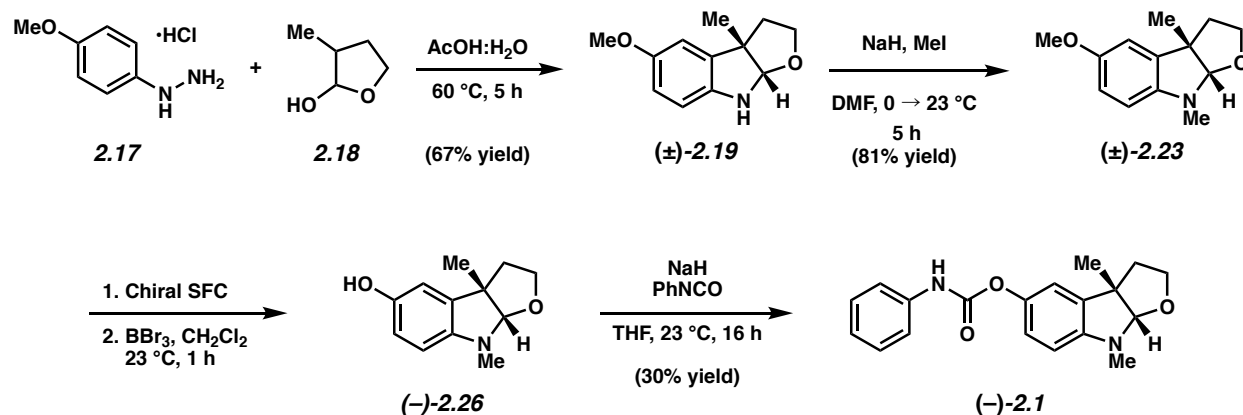
Scheme 2.1. Synthesis of (–)-Phensvenine (**2.1**).

The synthetic route was readily amenable to the synthesis of analogs, particularly by exploiting intermediate (–)-**2.26** as a means to access different carbamate substitution patterns. Scheme 2.2 provides an example, in the context of the synthesis of analog (–)-**2.8**. Alcohol (–)-**2.26** readily underwent reaction with **2.29** to furnish carbonate (–)-**2.30**. Upon treatment with 4-

aminopyradine (**2.32**), (–)-**2.8** was obtained in 61% yield. The syntheses of other carbamate analogs are provided in Section 2.9.
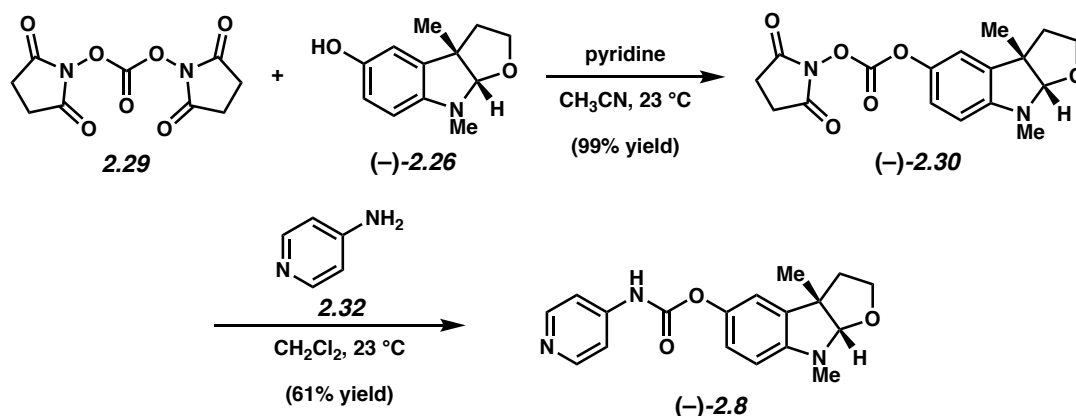
Scheme 2.2. Synthesis of Furoindoline Analog (–)-**2.8**.

Scheme 2.3 shows the routes used to prepare two analogs bearing substitution on the furoindoline ring. Interrupted Fischer indolization using hydrazine **2.20** and lactol **2.21** proceeded smoothly to give **2.22** as a mixture of diasteromers in racemic form. Upon methylation, diastereomers **2.24** and **2.25** were accessed and could be separated by silica gel chromatography. Each diastereomer was then elaborated through a sequence involve separation by chiral SFC, demethylation, and carbamate formation. This delivered (–)-**2.9** and (–)-**2.10**, respectively for biological evaluation.
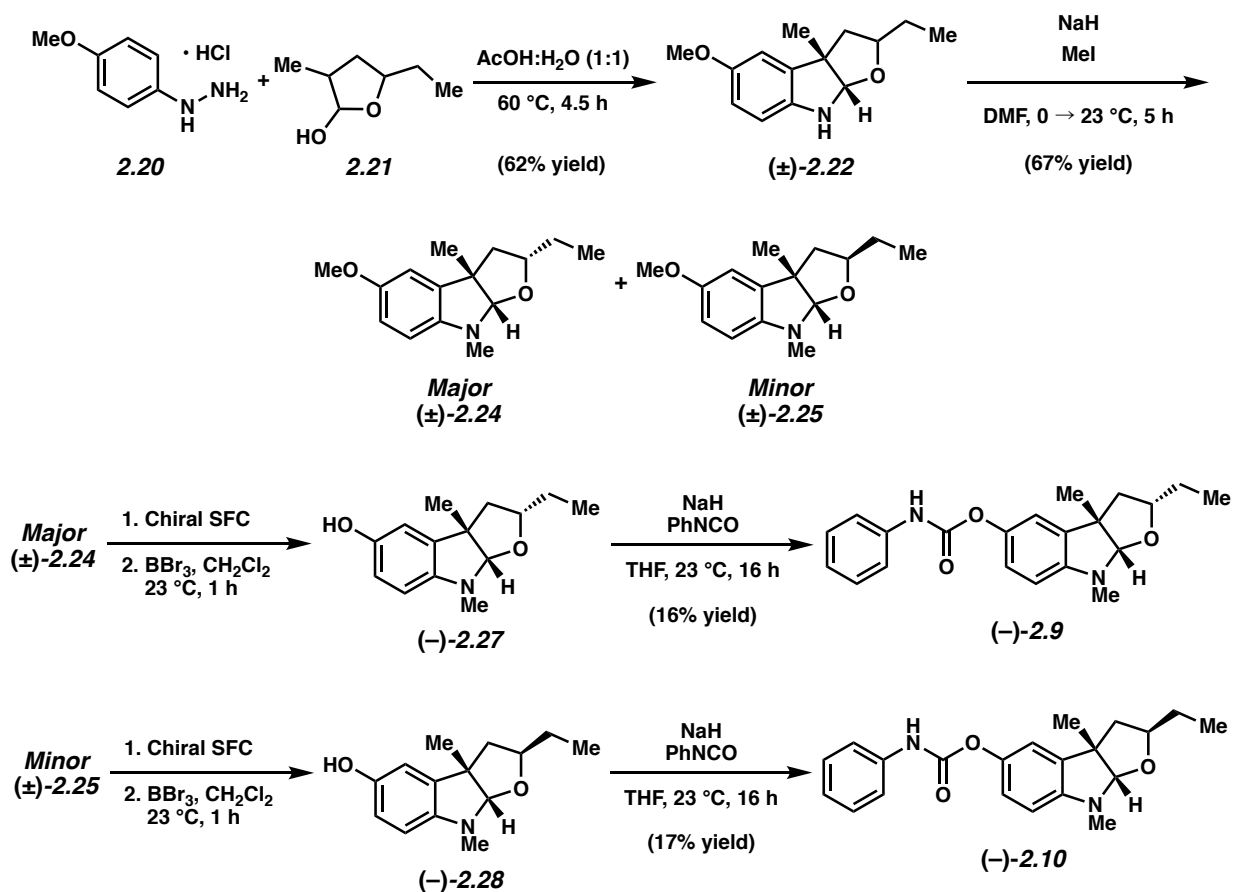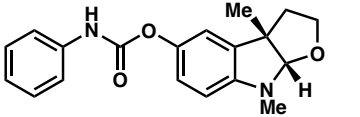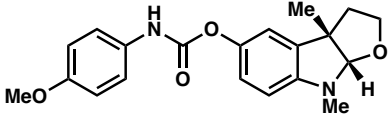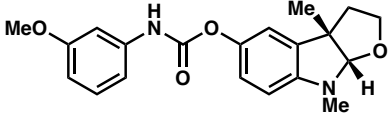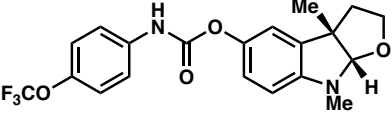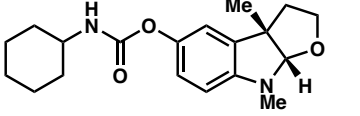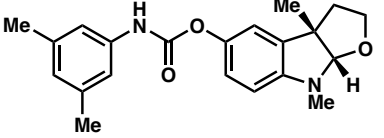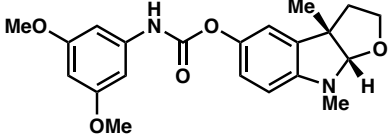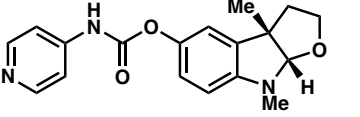
Scheme 2.3. Synthesis of Furoindoline Analogs (–)-**2.9** and (–)-**2.10**.

In total, sixteen analogs were prepared as part of the optimization efforts. The structures of these analogs, dose-response analysis results, predicted brain permeability data, and binding efficiency to human serum albumin (HSA) are shown in Table 2.1. Our SAR analysis reveals structural elements in this series required for enhanced nSMase2 and/or AChE inhibition. Substitutions in the carbamate phenyl ring pointed to a critical role for positions 3 and 4 as key control elements for nSMase2 and/or AChE inhibition. Substitution in the 4-position leads to increased selectivity for nSMase2 inhibition (such as for compounds **2.2, 2.4** and **2.8**). In contrast, substitution in the 3-position leads to increased selectivity for AChE inhibition (such as **2.3** and **2.11**). Introduction of electron donating groups (**2.3**, **2.6**, and **2.7**) at position 3 increased potency of AChE inhibition, while an electron withdrawing group (such as in **2.14**) resulted in decreased

potency. Importantly, replacement of the phenyl ring with a pyridyl ring in the carbamate moiety generally decreased potency of AChE inhibition and markedly enhanced potency for nSMase2 inhibition (e.g. **2.8**, **2.11**, **2.12**). Most of the analogs (except **2.4**) showed high predicted brain permeability by *in silico* StarDrop analysis and in a parallel artificial membrane permeability assay (PAMPA). A low degree of binding to human serum albumin (HSA) measured for most of the compounds, especially **2.8**, **2.11**, **2.12**, and **2.13**.

Table 2.1. Structure and Characteristics of Carbamate Furoindoline Analogs.

Compound #	Structure	MW (g/mol)	IC$_{50}$ nSMase2 (μM)	IC$_{50}$ AChE (μM)	CNS perm (PAMPA)	cLogP	HSA (% unbound)
2.1		324.15	>1	0.5	3.2	3.69	12
2.2		354.16	0.7	3.6	2	3.73	15
2.3		354.16	1	0.1	2.3	3.73	10
2.4		408.13	2.7	>5	0.7	4.84	33
2.5		330.19	3.4	0.3	2.8	3.66	17
2.6		352.18	3.6	0.2	3.1	4.68	4
2.7		384.17	2	0.3	1.8	3.75	9
2.8		325.14	0.5	7	1.9	2.86	28

2.9		352.18	>5	2.5	3	4.73	7
2.10		352.18	5	3.7	3.2	4.73	5
2.11		325.14	0.5	1.7	1.8	2.86	31
2.12		325.14	0.8	>5	1.9	2.86	28
2.13		343.13	0.6	>5	1.3	2.65	31
2.14		343.13	0.9	>5	2	3.1	21
2.15		392.13	5	>5	2.2	4.94	7
2.16		337.42	>5	>5	NA	NA	NA

A summary of the dual nSMase2/AChE inhibition SAR from our optimization efforts is summarized in Figure 2.2. Key points are as follows: (1) replacement of nitrogen in the furoindoline ring of the validated hit yields **2.1** (phensvenine), which is a dual inhibitor showing weak nSMase2 inhibition ($IC_{50} > 10$ μM) but potent AChE (IC_{50}=0.5 μM) inhibition;[42] (2) phenserine, a commercially available potent AChE inhibitor, displays loss of nSMase2 inhibitory activity (IC_{50} >50 μM; not depicted); (3) the 4-pyridyl ring in the carbamate group leads to **2.8**, a dual inhibitor with ~14-fold increased selectivity for nSMase2 inhibition ($IC_{50} =$ 0.5 μM) over

44

AChE inhibition (IC_{50} = 7 µM); and (4) the 3-pyridyl carbamate compound **2.11** was a dual inhibitor with ~3-fold increased selectivity for nSMase2 (IC_{50} = 0.5 µM) and AChE (IC50 = 1.7 µM) inhibition. The mode of inhibition by the dual inhibitors (shown below) of both enzymes allows for comparison of dual activity using IC_{50} values.[39,41] Based on the SAR, the two dual inhibitors, **2.8** and **2.11**, with 10- and 3-fold selectivity for nSMase2 inhibition over AChE, respectively, were further evaluated in *in vitro* and *in vivo* assays for exosomal tau release.
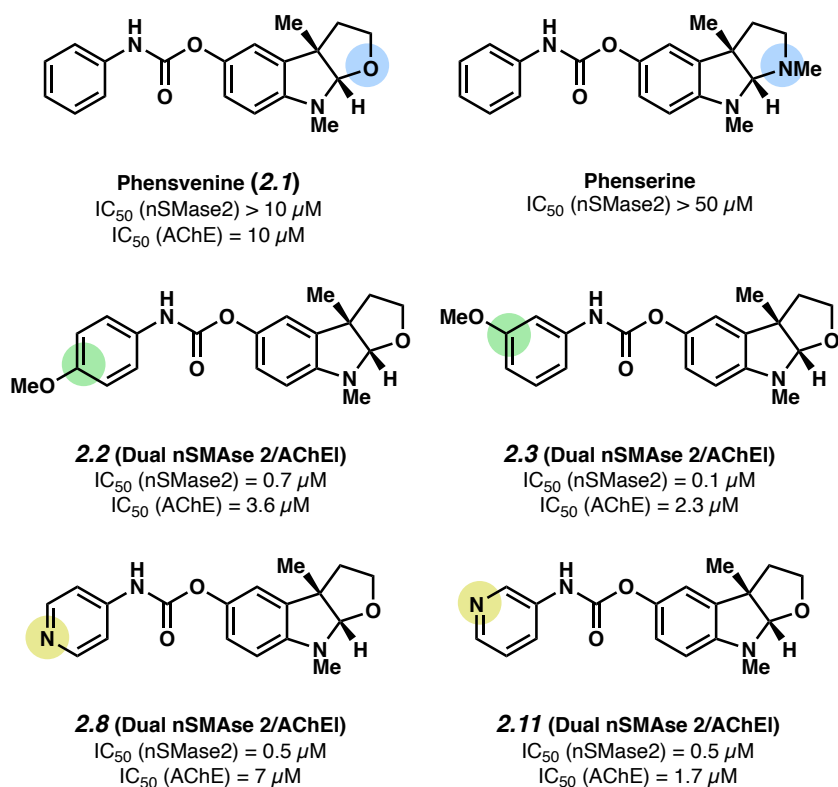
Figure 2.2. Key structure–activity relationships (SAR) control elements for inhibition of nSMase2 (blue highlight) and AChE (green or yellow highlight) activity are indicated.

2.4 Mechanism of nSMase2 Inhibition by the Novel Furoindoline Compounds

To determine the type of nSMase2 inhibition by compounds **2.8** and **2.11**, kinetics assays were performed. As shown in Figures 2.3a and 2.3b, increasing concentrations of compounds **2.8** and **2.11** resulted in decreasing K_m (the Michaelis constant) values as well as concomitant decreases in V_{max} (the maximum rate) indicative of a non-competitive mechanism of inhibition of nSMase2. Thus, it can be concluded that both compounds bind to the enzyme distal from the active site and can inhibit enzyme-substrate cleavage.

Molecular docking analysis (see the Section 2.12 for details) was performed using a recently published crystal structure of the nSMase2 catalytic domain (pdb: 5UVG).[43] We found that both **2.8** and **2.11** could bind to nSMase2 at the distal DK-switch (Asp-Lys) site away from the substrate sphingomyelin site, and thus in concordance with the kinetic analysis, could non-competitively inhibit the enzyme activity through modulation of the DK-switch. This is similar to what we have previously published with the known nSMase2 inhibitor cambinol, which was also shown by molecular docking and simulation to bind the nSMase2 catalytic domain in the DK-switch region and prevent enzyme activation by likely keeping the switch in the 'off' position.[14] Molecular Dynamics (MD) simulation was performed to determine the binding free energy of compound **2.8** binding to nSMase2. Compound **2.8** stays at the DK-switch site of nSMase2 through the 50 ns simulation with an estimated binding energy of -14.3 kcal/mol. An AMBER16 package was used to perform the MD simulation.

	5 μM	1 μM	0.5 μM	0.1 μM	0
Vmax	160.4	344.7	417.8	451.6	512.3
Km	39.97	87.60	67.12	51.11	77.08

	5 μM	1 μM	0.5 μM	0.1 μM	0
Vmax	162.1	291.4	404.8	456.8	533.2
Km	42.22	66.33	70.53	51.30	75.87
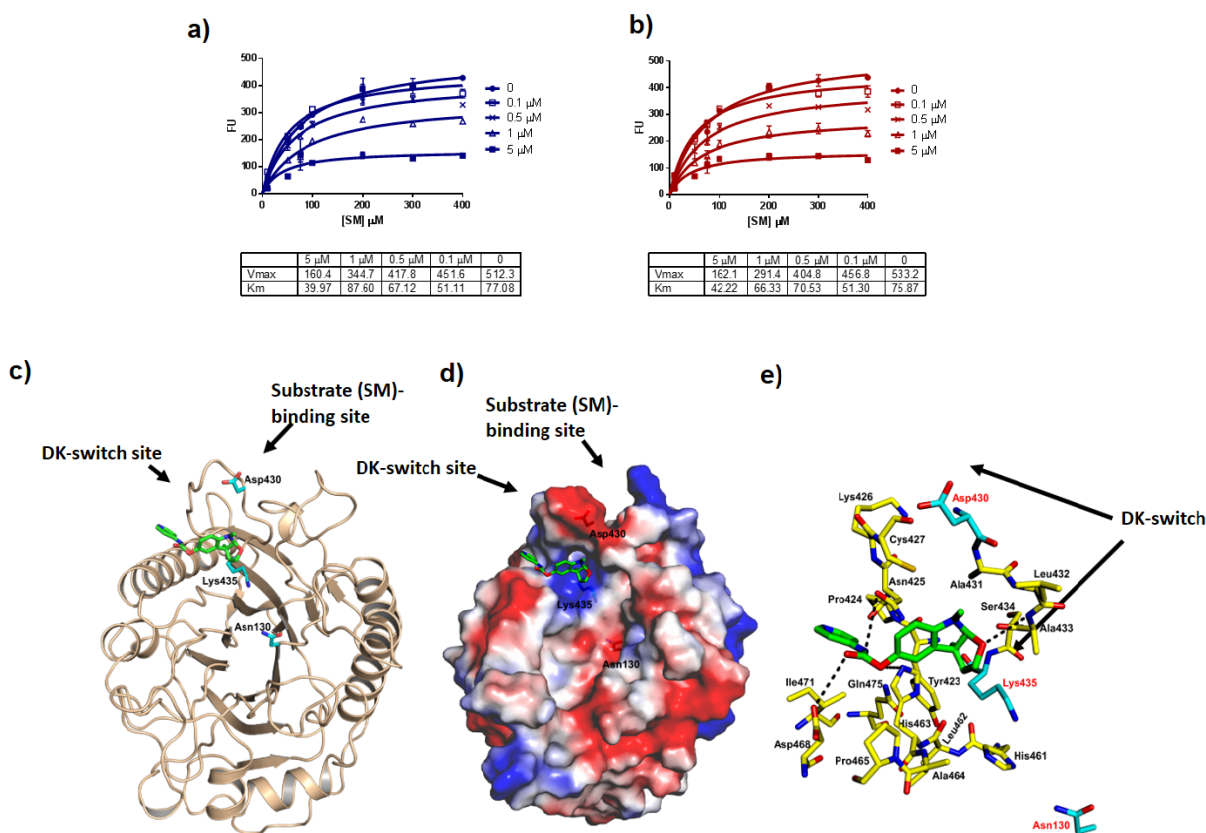
Figure 2.3. Mechanism of nSMase2 inhibition by compounds **2.8** and **2.11**. Kinetics of enzyme inhibition by compounds **2.8** (a) and **2.11** (b) are shown. The rate of the reaction is plotted against substrate concentration at four different concentrations of the inhibitors; corresponding values for V_{max} and K_m are presented in the tables below the graphs. c) Modeling of **2.8** and **2.11** (green) binding to the catalytic domain of nSMase2 predicts compound binding preferably near the DK-switch site than the substrate binding site. d) Molecular surface representation of the nSMase2 catalytic domain with **2.8** and **2.11** (green) bound near the DK-switch; the color representations are blue for positive charge, red for negative charge, and white for neutral charge. e) The nSMase2 residues (yellow) within a 5 Å radius surrounding inhibitors **2.8** and **2.11** (green); H-bonding between the inhibitor and nSMase2 is shown by dashed lines (black).

2.5 In vitro Inhibition of Tau Seed Propagation by Dual nSMase2/AChE Inhibitors

We previously developed a cell culture system based on a well-known tau RD biosensor cell line (tau biosensors) for testing inhibitors of tau propagation.[14] Using known nSMase2 inhibitors cambinol and GW4869, we had demonstrated the role of the nSMase2-dependent pathway of EV biogenesis in tau transmission from donor to recipient cells in this non-neuronal

cell model using two different in vitro assays – the Donor plus Recipient (D+R) assay and the EV-mediated transfer (EMT) assay. [14]

The principles of the D+R and EMT assays are presented in schematic form in Figures 2.4a and 2.4b, respectively. Our data demonstrates that treatment with **2.8** or **2.11** at a concentration of 20 µM significantly suppresses tau seed transfer from donor to recipient cells in the D+R and EMT assays (Figures 2.4a, 2.4b and Section 2.12). Shuttling by tau-bearing EVs is not the only pathway of tau seed transfer between cells in vivo or when donor and recipient cells are growing together in vitro, as in the D+R assay. In contrast, the EMT assay lets us isolate the effect of the inhibitors on EV-mediated tau seed transmission, which can explain the profound difference in the magnitude of FRET fluorescence density by dual nSMase2/AChE inhibitor **2.11** between the assays - 19.5% decrease from dimethyl sulfoxide (DMSO) treated cells in D+R assay and 41.3% decrease in EMT assay.

We characterized EVs purified from the seeded donor cells growing in the presence of our dual inhibitor compounds, **2.8** and **2.11**, or DMSO control. Successful purification of EVs was confirmed by tunable resistive pulse sensing (TRPS) (Figures 2.4c), transmission electron microscopy (TEM) (Figures 2.4d), and western blotting analysis with known exosomal markers (Figures 2.4e). Treatment with dual nSMase2/AChE inhibitor **2.8** or **2.11** did not affect EV size distribution, but decreased the concentrations of exosomal-type small EVs (Figures 2.4c). Levels of exosomal markers CD63, CD81, and syntenin-1 were reduced in EVs purified from **2.8** - and **2.11** - treated cells in comparison with the DMSO treated donors (Figures 2.4e). Relatively high suppression of tau transfer by **2.11** compared to **2.8** in the EMT assay may be related to the greater AChE inhibitory activity of **2.11** in conjunction with its nSMase2 inhibition and the role of dual inhibitory activity in exosome-mediated transfer of tau seeds.

D+R assay

EMT assay

Characterization of donor cell - derived EVs
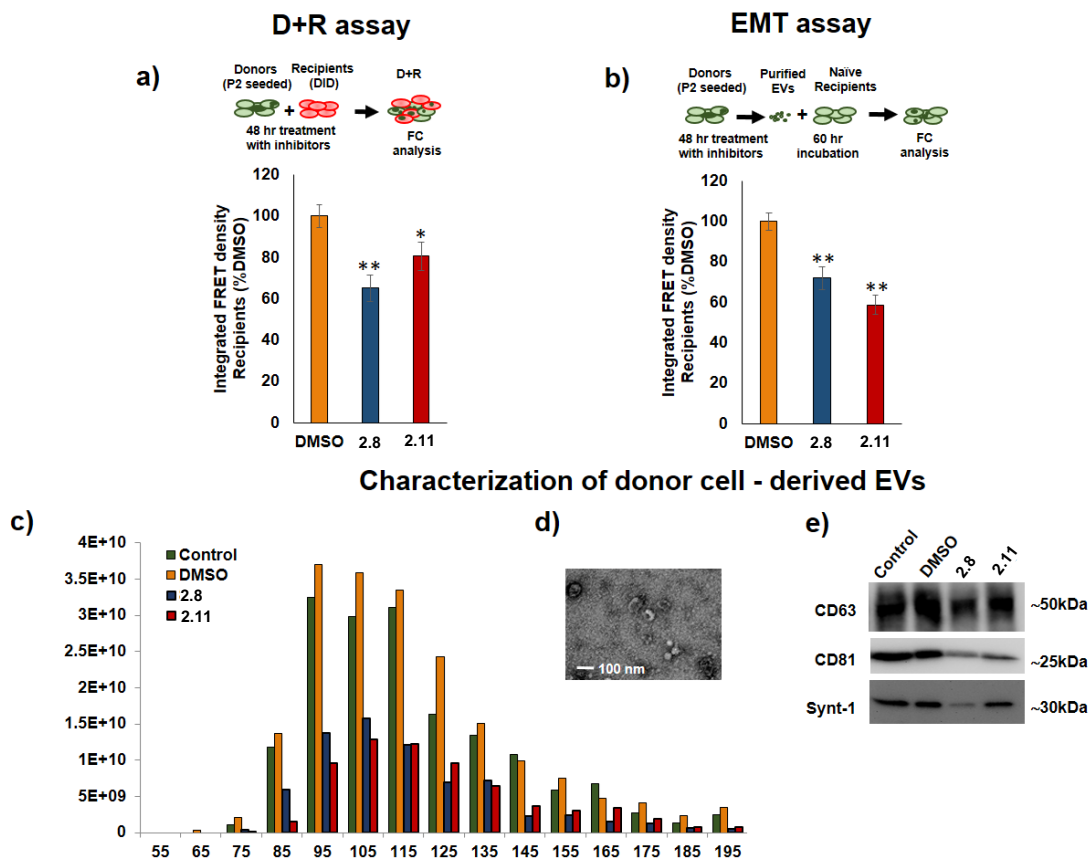
Figure 2.4. Dual nSMase2/AChE inhibitors **2.8** and **2.11** suppress tau propagation from donor to recipient cells in vitro. The assay scheme for each assay is presented at the top of the figure. a) Donor plus recipient (D+R) assay results are shown. Compounds **2.8** and **2.11** at a concentration of 20 µM or a corresponding volume of DMSO were added to the D+R cultures for 48 hrs. Levels of FRET signal were analyzed in recipient cells using flow cytometry. Combined data from three independent experiments are presented. b) EV-mediated tau seed transfer (EMT) assay results are shown. Compounds **2.8** and **2.11** at 20 µM concentration or DMSO were added to donor cell culture medium and then donor cell-derived EVs were purified and transfected to recipient cells. Levels of FRET signal were analyzed in recipient cells using flow cytometry. Four technical replicates were used for each experimental condition. Combined data from three independent experiments is presented. The histograms represent integrated FRET density per each treatment group (mean ± SEM). c) Size distribution and concentrations of the donor-derived EV samples were analyzed by Tunable Resistive Pulse Sensing (TRPS). d) Donor-derived EVs were imaged using transmission electron microscopy (TEM). e) Western blot representative images for exosomal markers are shown. The same volume of EV fractions derived from a similar number of donor cells or control tau biosensor cells treated with Lipofectamine 2000 (Control) were loaded per well and probed against exosomal markers CD63, CD81, and Syntenin-1. Statistics were performed using One-way ANOVA with post hoc Bonferroni and Holm multiple comparison test was used for statistical analysis: * $p<0.05$, ** <0.01.

49

Cell viability and/or rate of proliferation may have an effect on tau seed transfer from donor to recipient cells through different mechanisms. Thus, we evaluated effects of tau seeding and treatment with nSMase2/AChE inhibitors on donor cell number and viability. Twenty-four hour exposure to AD human brain synaptosomal extracts decreased the rate of the donor cell survival in the next passage compared to cells treated with lipofectamine 2000 (see Section 2.12). We have not determined the specific mechanisms of cell death in tau-seeded donor cultures. It is possible that a subset of tau-bearing EVs affected by nSMase2 inhibitors are apoptotic exosome-like vesicles (AEVs) that - in contrast to apoptotic bodies - represent a subtype of exosomes originating from multivesicular endosomes (MVE) at the early apoptotic phase. AEV biogenesis is controlled by the ESCRT-independent sphingosine1-phosphate (S1P)/S1PRs signaling pathway, and can be partially inhibited by nSMase2 inhibitor GW4869.[44] Interestingly, AChE inhibitors are known to protect different cell types, including HEK293T, from apoptosis,[45] and thus dual inhibitor **2.11** with greater AChE inhibition could potentially indirectly suppress AEV production. However, treatment of donor cells with **2.11** for 48 hours didn't affect donor cell numbers or survival compared to DMSO or to compound **2.8** treated donor cells (see Section 2.12). We also hypothesize that other factors may contribute to the greater effect of **2.11** on tau seed transfer in the EMT assay. A recent report suggests that intracellular uptake of tau can be mediated by the muscarinic acetylcholine receptors (mAChR) M1 and M3.[39] Thus, accumulation of tau oligomers in the synapse may exacerbate the cholinergic deficit in AD through suppression of ACh uptake via mAChR M1/M3 receptors on postsynaptic terminals. Based on similar reasoning, inhibition of AChE could have a direct effect on tau seed uptake through the increased levels of ACh in the synapse and postsynaptic M1/M3 receptor occupancy.

Our preliminary experiments using rivastigmine, a potent AChE (but not a nSMase2) inhibitor, reveals that inhibition of AChE may partially suppress EV-mediated transfer from donor to recipient cells (Section 2.12) providing further support to our hypothesis. Thus, the dual nSMase2/AChE inhibitors **2.8** and **2.11** may simultaneously effect both tau seed release and uptake.

2.6 Brain Pharmacokinetics for Lead Compounds

Our goal was to identify a brain permeable dual nSMase2/AChE inhibitor analog for further testing. We therefore performed pharmacokinetic (PK) analysis on the leads **2.8** and **2.11** to determine brain permeability using wild type mice. The compounds were subcutaneously (SQ) injected at a dose of 20 mg per kg of body weight (mpk). Brain and plasma samples were collected 1, 2, and 4 hours after dosing. Our PK analysis revealed that **2.8** and **2.11** reached peak brain levels (C_{max}) around one hour after SQ dosing and brain levels were detectable for both compounds 4 hours after injection (Figure 2.5a).

To carefully evaluate brain compound levels at the C_{max} (1 hour) time point, 20 mpk SQ dosing of compounds **2.8** and **2.11** was performed again using 6 mice per group. Average brain level of the compounds at the peak was equal to 61 ng/g (~0.2 μM) and 262 ng/g (~0.8 μM) for compounds **2.8** and **2.11,** respectively (Figure 2.5b). This data confirmed good brain permeability of the lead compounds as was predicted by *in silico* and PAMPA analysis described earlier (Table 2.1). Compound **2.11** showed higher average brain levels compared to **2.8,** and the brain levels corresponded to ~ 2-fold IC_{50} for nSMase2 and ~0.5-fold for AChE.

Brain pharmacokinetics
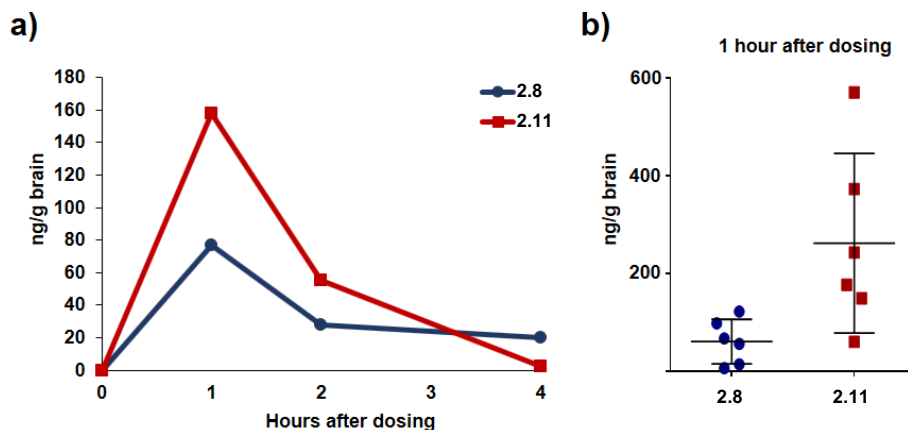
Figure 2.5. Pharmacokinetic analysis for lead compounds **2.8** and **2.11**. a) Mice were subcutaneously (SQ) injected with 20 mg/kg of compound **2.8** or **2.11**; animals were sacrificed 1, 2, and 4 hours after dosing (n=1 animal per time point). b) Mice were dosed as in (a), but n = 6 per compound and sacrificed 1 hour after dosing. Compound levels in brain tissue were analyzed using an LC-MS/MS method.

2.7 Inhibition of Brain EV Release by the Dual nSMase2/AChE Inhibitors in a Rapid In vivo Assay

The chronic inflammation that is reported in AD and tauopathy models is characterized by elevated levels of pro-inflammatory cytokines in brain parenchyma, including interleukin 1β (IL1β), known to induce nSMase2 activity through the IL1-Receptor 1 (IL1-R1).[46] Neuroinflammation and upregulation of IL1β signaling is linked with an early stage of tauopathy development; blocking of IL1β signaling in the 3xTg mouse AD model attenuates tau pathology and rescues cognition.[47,48,49] It was demonstrated that striatal injection of IL1β to wildtype mice induced release of astrocyte-derived EVs into the blood, resulting in peripheral acute cytokine responses[50] which can be suppressed by pre-treatment with nSMase2 inhibitors.[33,34,35]

In order to rapidly test our dual nSMase2 inhibitors in vivo, we used the Tau P301S (PS19 line) tauopathy mouse model.[47] For our in vivo assay there were 4 groups: group I (control) received SQ injection of vehicle (DMSO) and intracerebroventricular (ICV) injection of another

vehicle (0.0006% BSA in PBS, pH 7.4) an hour after SQ treatment; group II (IL1β) received SQ injection of vehicle and unilateral ICV injection of 0.2 ng of IL1β an hour later; group III (8/IL1β) – SQ treatment with 20 mg/kg of **2.8** and ICV injection of 0.2 ng of IL1β; group IV - SQ treatment with 20 mg/kg of **2.11** and ICV injection of 0.2 ng of IL1β. The one-hour interval between treatment with the inhibitors and IL1β ICV injection was chosen based on the brain PK analysis presented above. All animals were sacrificed at 3 hours after compound or vehicle treatment and 2 hours after ICV injection of IL1β. Brain EVs were purified as previously described.[51]

Size distribution and concentration of brain EVs were analyzed using the TRPS method. There were no significant differences in EV size distribution between experimental groups (Figure 2.6a). As previously reported,[51] the collected fraction (F2) consists mostly of small exosome-size EVs with a mode equal to 80±5 nm based on TRPS analysis. A high abundance of exosome-sized EVs was confirmed by TEM analysis (Figure 2.6c). As expected we found that ICV injection of IL1β significantly increased the concentration of small EVs (size 50-150 nm) purified from the brain, more than 2 times that of the control (Figure 2.6b). Dual nSMase2/AChE inhibitors **2.11** suppressed IL1β-induced exosomal release to the control level (Figure 2.6b), while the less brain-permeable dual inhibitor **2.8** did not induce the same level of suppression.

Rapid in vivo assay: brain EV size distribution and concentration (TRPS analysis)

a) EV concentration (particles /ml) vs particle size (nm), with Control, IL1β, 2.8/IL1β, 2.11/IL1β groups.

b) Exosome-size EVs (50-150 nm), EV concentration (% control).

Brain EV characterization and cargo analysis

c) TEM image, 100 nm scale.

d) Western blot: Control (1 2 3), IL1β (4 5 6), 8/IL1β (7 8 9 10), 2.11/IL1β (11 12 13); CD63 ~50kDa, Synt-1 ~35kDa, Bin1 (iso1) ~75kDa, CD11b ~170kDa, GLAST-1 (frag) ~30kDa, Tau ~60kDa.

e) Densitometry analysis: CD63, Synt-1, tau, GLAST-1, CD11B, Bin1.

Figure 2.6. Dual nSMase2/AChE inhibitor **2.11** diminished IL1β-induced brain EV release in the rapid in vivo assay. Tau P301S (line PS19) mice were treated with compound **2.8** or **2.11** subcutaneously (SQ) at 20 mg/kg one hour before IL1β injection (unilateral ICV injection of 0.2 ng). Two hours after IL1β injection, brain tissue was collected and used for brain EV isolation. a) Size distribution and concentrations of the brain EV samples were analyzed by Tunable Resistive Pulse Sensing (TRPS). b) Average concentrations of 50-150 nm size EVs from each treatment condition were compared. c) A representative transmission electron microscopy (TEM) image of the brain EV fraction is shown. d) Representative images of western blot (WB) analysis of EV fractions from individual animals is shown; membranes were probed against exosomal markers (CD63 and syntenin-1), tau protein, and cell-type specific markers (astrocytic glutamate-aspartate transporter GLAST1, microglia marker CD11b, and neuronal isoform of Bridging Integrator 1, BIN1). e) Densitometry analysis of the WB images is shown. Histograms represent average relative signal intensity per each treatment group (mean ± SEM). Statistical analysis was performed using one-way ANOVA with post hoc Bonferroni and Holm multiple comparison tests: #-$P < 0.05$ and ## - $P < 0.01$ compared to control group, treated with vehicles for SQ and ICV injections, * - $P < 0.05$ and ** - $P < 0.01$ compared to IL1β group.

Biochemical analysis of brain-derived EVs (Figures 2.6d & 2.6e) confirmed that pretreatment with lead compound **2.11** led to a significant reduction of exosomal marker CD63 in exosome-enriched F2 fractions compared to the group treated only with IL1β. In contrast to

significant changes in common exosomal marker CD63, levels of syntenin-1, a marker of a specific exosomal subpopulation generated through the Syndecan-Syntenin-ALIX pathway[52] were not different between the groups (Figures 2.6d & 2.6e). These results confirm that IL1β stimulation and nSMase2 inhibition have effects on specific populations of exosomes.

Our data suggest that the nSMase2-dependent pathway of exosome biogenesis is involved in tau-bearing exosome production in PS19 mice. Tau levels in the F2 fraction showed a strong trend of being elevated in animals treated with IL1β, with the average tau level being around 6 times higher in the IL1β-treated group compared to the control group (Figures 2.6d & 2.6e). Pretreatment with **2.11** significantly reduced IL1β-induced tau release by exosomes. The lead compound **2.8** was less effective in this study. The known variability of tau load between PS19 mice likely accounts for the lack of statistical significance despite the high magnitude of tau changes.

Multiple brain cell types express IL1-R1, including subpopulations of neurons, astrocytes, choroid plexus cells and ependymal cells;[53] thus, the nSMase2-mediated exosomal release by different types of brain cells can be affected differently in response to acute increases in intracerebral IL1β concentration. We used a couple of cell-type specific markers to assess the origin of the IL1β/nSMase2 sensitive exosomal population. We found that levels of astrocytic glutamate-aspartate transporter (GLAST) and microglial marker CD11b were significantly elevated in F2 fractions isolated from IL1β-treated animals. GLAST is known to be sensitive to papain, the enzyme we used for gentle brain tissue dissociation. Therefore, we used a 30 kDa fragment of GLAST instead of full-length protein for the analysis.[54] Pretreatment with the dual nSMase2/AChE inhibitor **2.11** significantly reduced the level of astrocyte-derived exosomes and showed the same trend for microglia-derived exosomes, but the difference in CD11b levels

between IL1β and 11/IL1β groups was not significant (Figures 2.6d & 2.6e). This finding correlates with previously demonstrated IL1β-induced nSMase2-mediated production of astrocyte-derived exosomes in wild type mice.[34,35] Microglia play an important role in tau spread,[15,55] and inhibition of microglial nSMase2-dependent exosome release suppresses tau propagation in mouse models.[15] The low levels of microglia response in our rapid in vivo assay may be attributed to saturation of microglia responses in 5-6 month old PS19 mice. Microglia activation is already detectable in 3 mo old PS19 mice and precedes astrogliosis.[47]

Recently, Bridging Integrator 1 (BIN1), a known genetic risk factor for AD, was connected to tau seed release through exosomes in human AD and male PS19 mice.[56] We analyzed levels of BIN1 in our F2 samples. Neuronal BIN1 isoform 1, but not microglia specific isoform 2, were highly enriched in the F2 fractions (Figure 2.6d). As in the case of exosomal tau, we found a high magnitude increase in exosome-associated BIN1 upon IL1β stimulation that was lower in the compound **2.11** treated group, but no statistically significant changes were found due to the high variability of individual levels of BIN1 within each group (Figure 2.6d). This data suggests that nSMase2 and BIN1 could be a part of the same exosomal pathway responsible for tau release and spread in AD.

Overall, our rapid in vivo assay results demonstrate the effectiveness of novel dual AChE/nSMase2 inhibitor **2.11** in suppression of IL1β-induced release of tau-bearing exosomes in tauopathy model.
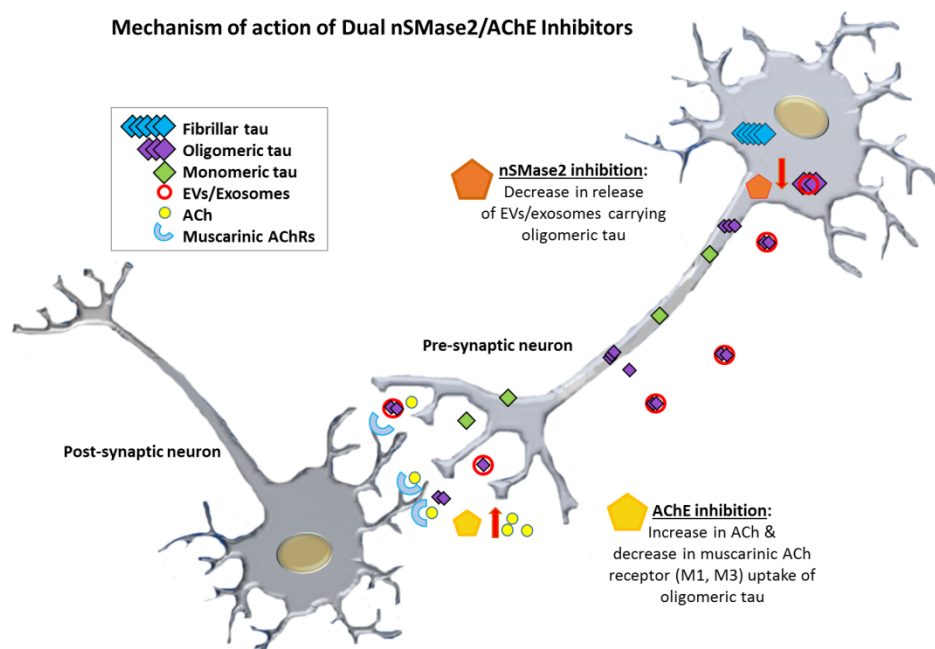
Figure 2.7. A putative mechanism for dual nSMase2/AChE inhibition and suppression of EV/exosome-mediated propagation of tau pathology wherein nSMase2 inhibition suppresses exosome biogenesis while AChE inhibition reduces exosome uptake and cholinergic support.

2.8 Conclusions

Our discovery of a novel class of potent nSMase2/AChE dual inhibitors presents an opportunity for further development of these agents as a new therapeutic approach to the treatment of Alzheimer's disease. Our data supports the ability of the dual inhibitors to suppress tau propagation in vitro and release of tau carrying exosomes in vivo in an AD model. These dual nSMase2/AChE inhibitors would enhance cholinergic synaptic plasticity, reduce neuroinflammation,[37] and most importantly suppress exosome-mediated tau propagation and tau uptake mediated through the M1/M3 muscarinic ACh receptors.[39] This combination of effects is unique, has not been evaluated previously in the disease and clearly differentiate these agents from currently available AChE inhibitors for the treatment of AD. In concert, these mechanisms of action have the potential to not only address symptoms of AD by enhancing cholinergic activity

but also to suppress cell-to-cell tau propagation, (Figure 2.7), significantly altering an underlying

cause of AD and thus be truly disease-modifying.

2.9 Experimental Section

2.9.1 Materials and Methods

Unless stated otherwise, reactions were conducted in flame-dried glassware under an atmosphere of N_2 and commercially obtained reagents were used as received. Sodium hydride, boron tribromide, boron trichloride, phenyl isocyanate, *N,N'*-disuccinimidyl carbonate (**2.29**), cyclohexyl isocyanate, 3,5-dimethylphenyl isocyanate, 3,5-dimethoxyphenyl isocyanate, 3-aminopyridine (**2.33**), 4-aminopyridine (**2.32**), and 4-(trifluoromethyl)aniline (**2.37**) were obtained from Sigma-Aldrich. Hydrazine (**2.17**), 4-methoxyphenyl isocyanate, 3-methoxyphenyl isocyanate, and *N*-ethylmethylamine (**2.37**) were obtained from Oakwood Products, Inc. 4-(trifluoromethyl)phenyl isocyanate and 3-amino-5-fluoropyridine (**2.35**) were obtained from Combi-Blocks. Methyl iodide was obtained from Alfa Aesar. Reaction temperatures were controlled using an IKAmag temperature modulator, and unless stated otherwise, reactions were performed at room temperature (approximately 23 °C). Thin-layer chromatography (TLC) was conducted with EMD gel 60 F254 pre-coated plates (0.25 mm for analytical chromatography and 0.50 mm for preparative chromatography) and visualized using a combination of UV, anisaldehyde, iodine, and potassium permanganate staining techniques. Silicycle Siliaflash P60 (particle size 0.040–0.063 mm) was used for flash column chromatography. ^{1}H NMR spectra were recorded on Bruker spectrometers (500 MHz) and are reported relative to residual solvent signals. Data for ^{1}H NMR spectra are reported as follows: chemical shift (δ ppm), multiplicity, coupling constant (Hz), integration. Data for ^{13}C NMR are reported in terms of chemical shift (125 MHz). ^{19}F NMR spectra were recorded on Bruker spectrometers (at 376 MHz) and reported in terms of chemical shifts (δ ppm). Data for IR spectra were recorded on a Perkin-Elmer UATR Two FT-IR spectrometer and are reported in terms of frequency absorption (cm^{-1}). DART-MS spectra were

collected on a Thermo Exactive Plus MSD (Thermo Scientific) equipped with an ID-CUBE ion source and a Vapur Interface (IonSense Inc.). Both the source and MSD were controlled by Excalibur software v. 3.0. The analyte was spotted onto OpenSpot sampling cards (IonSense Inc.) using volatile solvents (e.g. chloroform, dichloromethane). Ionization was accomplished using UHP He (Airgas Inc.) plasma with no additional ionization agents. The mass calibration was carried out using Pierce LTQ Velos ESI (+) and (–) Ion calibration solutions (Thermo Fisher Scientific). Optical rotations were measured with a Rudolph Autopol III Automatic Polarimeter. Any modification of the conditions shown in the representative procedures are specified in the corresponding schemes.

*Note: Supporting information for the syntheses of lactol **2.18**[57] and ethyl lactol **2.21**[58] used in*

Table 2.1 have been previously reported.

2.9.2 Experimental Procedures

2.9.2.1 Syntheses of Indoline Substrates

Representative Procedure for the synthesis of indoline substrates from Table 2.1.

((±)-2.19 is used as an example).
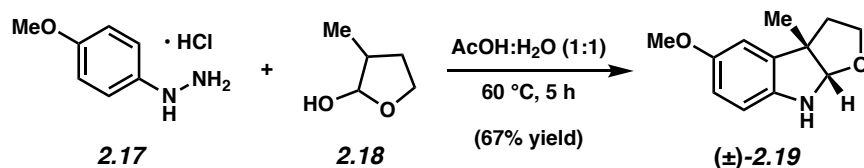
Indoline (±)-2.19. A 250 mL round-bottom flask containing a magnetic stir bar was charged with lactol **2.18** (3.37 g, 33.1 mmol, 1.00 equiv) followed by a solution of AcOH:H$_2$O (1:1, 170 mL, 0.200 M). Hydrazine **2.17** (5.78 g, 33.1 mmol, 1.00 equiv) was added and an air condenser attached to the flask. The reaction mixture was then placed into a pre-heated oil bath at 60 °C and stirred

for 5 h. After the allotted time, the reaction mixture was taken out of the oil bath and allowed to cool to 23 °C over 20 min. The reaction mixture was then diluted with EtOAc (20 mL) and transferred to a separatory funnel. EtOAc (50 mL) and deionized water (50 mL) were then added, followed by a solution of saturated aqueous $NaHCO_3$ (450 mL). The layers were separated and the aqueous layer extracted with EtOAc (3 x 50 mL). The combined organics were washed with saturated aqueous NaCl (50 mL) and dried over $MgSO_4$. The volatiles were then removed under reduced pressure, and the crude residue was purified by flash column chromatography (3:1 Hexanes:EtOAc) to yield indoline (±)-**2.19** (67% yield) as a red solid. Spectral data match those previously reported.[57]
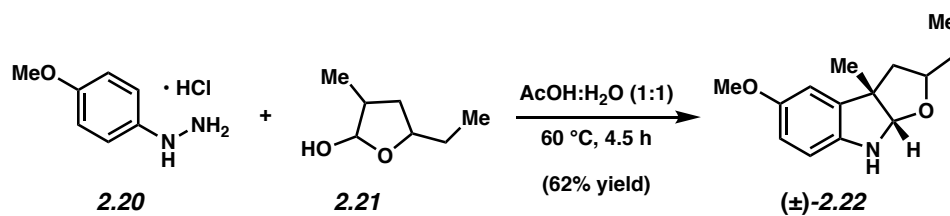
Indoline (±)-2.22. Purification by flash column chromatography (4:1 Hexanes:EtOAc) yielded indoline (±)-**2.22** (62% yield) as an amorphous solid in a 1.5:1 ratio of diastereomers.

2.9.2.2 Methylation of Indoline Substrates

**Representative Procedure for the methylation of indoline substrates from Table 2.1.
((±)-2.23 is used as an example).**

Indoline (±)-2.23. A 100 mL round-bottom flask containing a magnetic stir bar was charged with indoline (±)-**2.19** (4.52 g, 22.0 mmol, 1.00 equiv) and the flask was flushed with N_2 for 5 min. DMF (22.0 mL, 1.00 M) was added and the reaction mixture cooled to 0 °C over 10 min under an N_2 atmosphere. NaH (60% dispersion in mineral oil, 1.90 g, 48.5 mmol, 2.20 equiv) was added in one portion and the reaction was left to stir for 30 min at 0 °C. MeI (3.30 mL, 52.9 mmol, 2.40 equiv) was then added dropwise over 3 min. After stirring for 30 min at 0 °C, the reaction mixture was warmed to 23 °C and allowed to stir for 5 h. The reaction mixture was then transferred to a separatory funnel with deionized H_2O (30 mL) and CH_2Cl_2 (30 mL), sequentially. The layers were separated and the aqueous layer was extracted with CH_2Cl_2 (3 x 50 mL). The combined organic layers were washed with deionized H_2O (3 x 50 mL), saturated aqueous NaCl (50 mL), and dried over Na_2SO_4. The volatiles were removed under reduced pressure, and the crude residue was purified by flash chromatography (5:1 Hexanes:EtOAc) to yield indoline (±)-**2.23** (3.92 g, 81% yield) as a colorless oil. Spectral data match those previously reported.[57] Chiral Preparative SFC: 21.2 x 250 mm Chiral Technologies AD-H SFC column, 7% i-PrOH, 40.0 mL/min, λ = 210 nm, 40 °C, nozzle pressure = 100 bar CO_2, t_{R1} = 3.2 min, $[\alpha]^{26.5}_D$ +58.67° (c = 0.10, CH_2Cl_2); t_{R2} = 5.1 min, $[\alpha]^{27.8}_D$ –40.00° (c = 0.10, CH_2Cl_2).
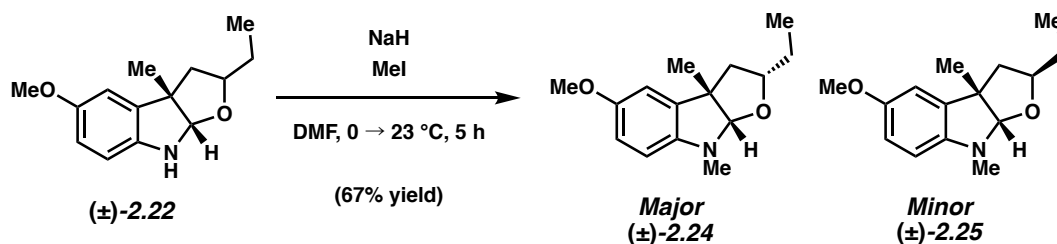
Indolines (±)-2.24 and (±)-2.25. Purification by preparative thin-layer chromatography (15:1 Hexanes:EtOAc) yielded indolines (±)-**2.24** and (±)-**2.25** (67% yield) in a 1.5:1 ratio of diastereomers as amorphous solids. Indoline (±)-**2.24 (major)**: R_f 0.50 (5:1 Hexanes:EtOAc); ^{1}H NMR (500 MHz, CDCl$_3$): δ 6.84–6.66 (m, 2H), 6.31 (d, J = 8.3, 1H), 4.95 (s, 1H), 3.99 (app. p, J = 6.74, 1H), 3.75 (s, 3H), 2.90 (s, 3H), 2.16 (dd, J = 6.5, 12.3, 1H), 1.87 (dd, J = 6.5, 12.3, 1H), 1.43–1.35 (m, 4H), 1.27–1.18 (m, 1H), 0.82 (t, J = 7.3, 3H); ^{13}C NMR (125 MHz, CDCl$_3$): δ 152.9, 143.7, 138.0, 112.1, 110.4, 107.0, 106.5, 80.3, 56.2, 52.4, 45.6, 32.5, 28.8, 24.4, 10.7; IR (film): 2958, 2935, 1596, 1497, 1280 cm^{-1}; HRMS-APCI (m/z) [M + H]$^+$ calcd for C$_{15}$H$_{22}$NO$_2$, 248.16451; found 248.16371. Chiral Preparative SFC: 21.2 x 250 mm Chiral Technologies AD-H SFC column, 4% i-PrOH, 40.0 mL/min, λ = 210 nm, 40 °C, nozzle pressure = 100 bar CO$_2$, t_{R1} = 2.4 min, $[\alpha]^{25.3}_D$ +62.00° (c = 0.10, CH$_2$Cl$_2$); t_{R2} = 3.4 min. $[\alpha]^{26.7}_D$ –96.00° (c = 0.10, CH$_2$Cl$_2$).

Indoline (±)-**2.25 (minor)**: R_f 0.55 (5:1 Hexanes:EtOAc); ^{1}H NMR (500 MHz, CDCl$_3$): δ 6.68–6.65 (m, 2H), 6.28 (d, J = 8.4, 1H), 5.05 (s, 1H), 3.76 (s, 3H), 3.59 (m, 1H), 2.88 (s, 3H), 2.19 (dd, J = 4.4, 11.9, 1H), 1.70–1.58 (m, 2H), 1.50–1.43 (m, 4H), 0.86 (t, J = 7.5, 3H); ^{13}C NMR (125 MHz, CDCl$_3$): δ 152.7, 145.3, 136.7, 112.1, 110.6, 105.3, 105.2, 80.4, 56.2, 53.0, 47.1, 31.7, 27.8, 25.1, 10.4; IR (film): 2958, 2923, 1596, 1498, 1279 cm^{-1}; HRMS-APCI (m/z) [M + H]$^+$ calcd for C$_{15}$H$_{22}$NO$_2$, 248.16451; found 248.16385. Chiral Preparative SFC: 21.2 x 250 mm Chiral Technologies AD-H SFC column, 4% i-PrOH, 40.0 mL/min, λ = 210 nm, 40 °C, nozzle pressure

= 100 bar CO_2, t_{R1} = 2.1 min, $[\alpha]^{27.5}_D$ +105.33° (c = 0.10, CH_2Cl_2); t_{R2} = 2.9 min. $[\alpha]^{28.0}_D$ –91.33° (c = 0.10, CH_2Cl_2).

The configuration of (±)-**2.24** and (±)-**2.25** was verified by 2D-NOESY (500 MHz, $CDCl_3$), as the following correlations were observed:

Major
2.24

Minor
2.25
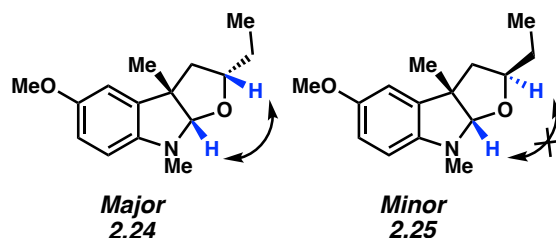
2.9.2.3 Removal of Protecting Groups

Representative Procedure for the deprotection of substrates (–)-2.26, (–)-2.27, and (–)-2.28 from Table 1. ((–)-2.26 is used as an example).

(–)-2.23

BBr₃

CH_2Cl_2, 23 °C, 1 h

(–)-2.26
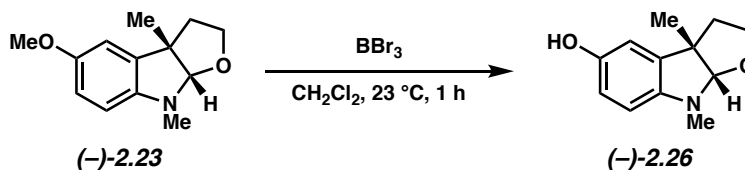
Indoline (–)-2.26. A 1-dram vial containing a magnetic stir bar was charged with indoline (–)-**2.23** (15.0 mg, 0.0680 mmol, 1.00 equiv) and the vial was flushed with N_2 for 5 min. CH_2Cl_2 (860 uL, 0.080 M) was added and the reaction mixture was left to run at 23 °C. BBr_3 (1.00 M in CH_2Cl_2, 340 uL, 0.340 mmol, 5.00 equiv) was added dropwise over 1 min and the reaction was stirred at 23 °C for 1 h. After the allotted time, the volatiles were removed under N_2. MeOH (2.00 mL) was then added to the vial and the reaction mixture was allowed to stir for 5 min. The reaction was then concentrated under reduced pressure and the resulting residue was suspended in deionized water (3 mL). The suspension was then transferred to a separatory funnel with EtOAc (2 mL). A saturated aqueous solution of $NaHCO_3$ (5 mL) was added and the layers were separated. The aqueous layer

was then extracted with EtOAc (3 x 5 mL). The combined organic layers were washed with saturated aqueous NaCl (5 mL) and dried over Na_2SO_4. The volatiles were then removed under reduced pressure, and the crude residue was used in the subsequent step without further purification.
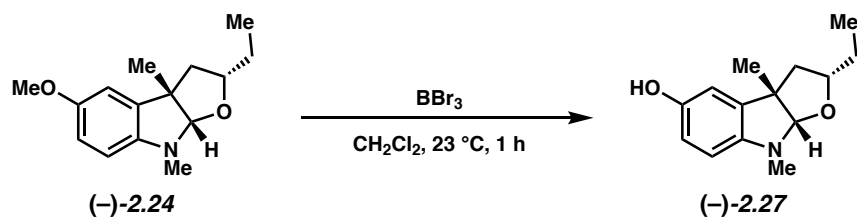
Indoline (–)-2.27. Following the representative yielded indoline (–)-**2.27**. The crude residue was used in the subsequent step without further purification.
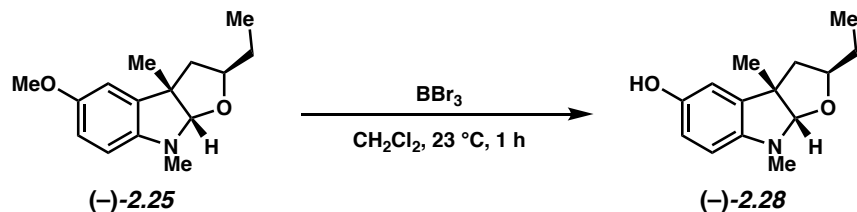
Indoline (–)-2.28. Following the representative procedure yielded indoline (–)-**2.28**. The crude residue was used in the subsequent step without further purification.

2.9.2.4 Carbamoylation

Representative Procedure A for the synthesis of carbamates from Tables 2.1. ((–)-2.1 is used as an example).

(–)-*2.26*   (30% yield)   (–)-*2.1*
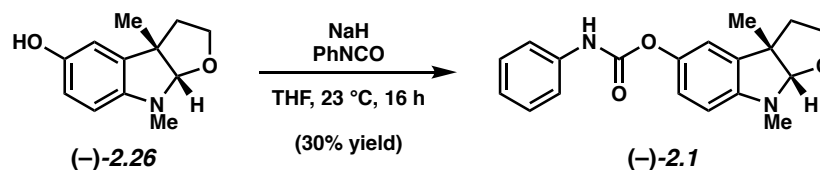
Carbamate (–)-2.1. A 1-dram vial containing a magnetic stir bar was charged with indoline (–)-**2.26** (10.0 mg, 0.0490 mmol, 1.00 equiv) was added and the vial was flushed with N_2 for 5 min. The material was then dissolved in THF (244 uL, 0.200 M) followed by the addition of NaH (60% dispersion in mineral oil, 1.0 mg, 0.024 mmol, 0.50 equiv) in one portion under a constant flow of N_2. PhNCO (6.9 mg, 6.4 uL, 0.058 mmol, 1.2 equiv) was then added dropwise over 1 min and the reaction was stirred at 23 °C for 16 h. After the allotted time, the reaction was quenched by addition of a saturated aqueous solution of $NaHCO_3$ (5 mL) and transferred to a separatory funnel with EtOAc (5 mL). The layers were separated and the aqueous layer was then extracted with EtOAc (3 x 5 mL). The combined organic layers were washed with saturated aqueous NaCl (5 mL) and dried over Na_2SO_4. The volatiles were then removed under reduced pressure, and the crude residue was purified by preparative thin-layer chromatography (1:1 Hexanes:EtOAc, 2% Et_3N) to yield carbamate (–)-**2.1** (9.2 mg, 30% yield) as a brown solid. Carbamate (–)-**2.1**: R_f 0.45 (1:1 Hexanes:EtOAc); $[\alpha]^{31.0}_D$ –39.34° (c = 0.10, CH_2Cl_2). Spectral data match those previously reported.[59]

Representative Procedure B for the synthesis of carbamates from Table 1. ((–)-2.30 is used as an example).
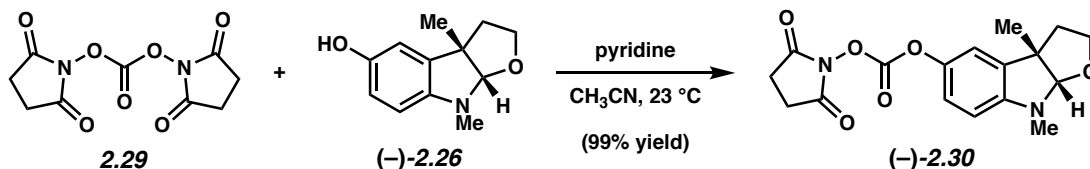
Carbonate (–)-**2.30**. A 1-dram vial containing a magnetic stir bar was charged with indoline (–)-**2.26** (75.0 mg, 0.370 mmol, 1.00 equiv) and the vial was flushed with N_2 for 5 min. The material was then dissolved in CH_3CN (730.0 uL, 0.500 M) and stirring began at 23 °C. Pyridine (59.0 uL, 0.730 mmol, 2.00 equiv) was added in one portion under a constant flow of N_2 followed by carbonate **2.29** (230.0 mg, 0.910 mmol, 2.50 equiv) in one portion. The reaction was then left stirred at 23 °C for 18 h. After the allotted time, the reaction was diluted with CH_2Cl_2 (1.0 mL) and the solid that precipitated was collected by vacuum filtration over filter paper. The solid precipitate was then rinsed with CH_2Cl_2 (3 mL). The filtrate was concentrated under reduced pressure and the residue was then suspended in EtOAc (5 mL) and transferred to a separatory funnel. The organic layer was washed sequentially with 5% aqueous citric acid (2 x 3 mL) and saturated aqueous NaCl (5 mL), and then dried over Na_2SO_4. The volatiles were then removed under reduced pressure to yield carbonate (–)-**2.30** (125.3 mg, 99% yield) as a white foam. Carbonate (–)-**2.30**: mp: 46–49 °C; R_f 0.38 (1:1 Hexanes:EtOAc); ^{1}H NMR (500 MHz, CDCl$_3$): δ 6.96 (dd, J = 2.3, 8.3, 1H), 6.94 (d, J = 2.3, 1H), 6.28 (d, J = 8.3, 1H), 5.09 (s, 1H), 3.96 (ddd, J = 1.6, 7.2, 8.7, 1H), 3.46 (ddd, J = 5.2, 8.7, 11.1, 1H), 2.90 (s, 3H), 2.86 (s, 4H), 2.11 (ddd, J = 1.6, 5.2, 12.1, 1H), 2.04 (ddd, J = 7.2, 11.1, 12.1, 1H), 1.45 (s, 3H); ^{13}C NMR (125 MHz, CDCl$_3$): δ 168.7, 151.0, 149.2, 142.9, 135.9, 119.8, 115.3, 105.3, 104.5, 67.4, 52.5, 41.7, 31.1, 25.6, 24.7; IR

(film): 2942, 2868, 1818, 1741, 1215 cm^{-1}; HRMS-APCI (m/z) [M + H]$^+$ calcd for $C_{17}H_{19}N_2O_6$, 347.12376; found 347.12356; $[\alpha]^{31.0}{}_D$ −52.01° (c = 0.10, CH_2Cl_2).

Carbamate (−)-**2.12**. A 1-dram vial containing a magnetic stir bar was charged with carbonate(−)-**2.30** (10.0 mg, 0.029 mmol, 1.00 equiv) was added and the vial was flushed with N_2 for 5 min. The material was then dissolved in CH_2Cl_2 (600 uL, 0.0500 M) and stirring began at 23 °C. Amine **2.31** (5.4 mg, 0.057 mmol, 2.0 equiv) was then added in one portion under a constant flow of N_2. The reaction was then stirred at 23 °C for 18 h. After the allotted time, the volatiles were removed under reduced pressure and the crude residue was purified by preparative thin-layer chromatography (1:1 Hexanes:EtOAc) to yield carbamate (−)-**2.12** (6.0 mg, 64% yield) as an amorphous solid. Carbamate (−)-**2.12**: R$_f$ 0.63 (1:5 Hexanes:EtOAc); ^{1}H NMR (500 MHz, CDCl$_3$): δ 8.33–8.32 (m, 1H), 8.30 (br. S, 1H), 8.00 (d, J = 8.4, 1H), 7.72–7.68 (m, 1H), 7.02 (ddd, J = 1.0, 4.9, 7.4, 1H), 6.92–6.89 (m, 2H), 6.32 (d, J = 8.3, 1H), 5.09 (s, 1H), 3.96 (ddd, J = 1.6, 7.3, 8.8, 1H), 3.50 (ddd, J = 5.3, 8.8, 11.2, 1H), 2.92 (s, 3H), 2.14 (ddd, J = 1.3, 5.3, 11.9, 1H), 2.08–2.02 (m, 1H), 1.47 (s, 3H); ^{13}C NMR (125 MHz, CDCl$_3$): δ 152.6, 151.6, 148.6, 148.1, 142.2, 138.6, 135.6, 121.0, 119.3, 116.7, 112.6, 105.6, 104.8, 67.5, 52.5, 41.8, 31.3, 24.8; IR (film): 3180, 2955, 2925, 1746, 1588 cm^{-1}; HRMS-APCI (m/z) [M + H]$^+$ calcd for $C_{18}H_{20}N_3O_3$, 326.14992; found 326.15099; $[\alpha]^{26.8}{}_D$ −102.7° (c = 0.10, CH_2Cl_2).

Carbamate (–)-**2.2**. Following representative procedure A yielded carbamate (–)-**2.2** (13.4 mg, 52% yield) as a white solid. Carbamate (–)-**2.2**: mp: 140–143 °C; R_f 0.56 (1:1 Hexanes:EtOAc); ^{1}H NMR (500 MHz, CDCl$_3$): δ 7.38–7.31 (m, 2H), 6.90–6.86 (m, 4H), 6.86–6.83 (m, 1H), 6.32–6.27 (d, 1H), 5.08 (s, 1H), 3.95 (ddd, J = 1.5, 7.3, 8.7, 1H), 3.79 (s, 3H), 3.45 (ddd, J = 5.2, 8.7, 11.1, 1H), 2.90 (s, 3H), 2.13 (ddd, J = 1.4, 5.2, 11.9, 1H), 2.02 (ddd, J = 7.2, 11.3, 11.3, 1H), 1.45 (s, 3H); ^{13}C NMR (125 MHz, CDCl$_3$): δ 156.3, 153.0, 148.3, 142.5, 135.5, 130.8, 121.0, 120.7, 116.7, 114.4, 105.6, 104.8, 67.5, 55.6, 52.5, 41.8, 31.3, 24.7; IR (film): 3311, 2958, 1717, 1512, 1196 cm^{-1}; HRMS–APCI (*m/z*) [M + H]$^+$ calcd for C$_{20}$H$_{23}$N$_2$O$_4^+$, 355.16523; found, 355.16422; [α]$^{30.7}_D$ –62.65° (*c* = 0.10, CH$_2$Cl$_2$).
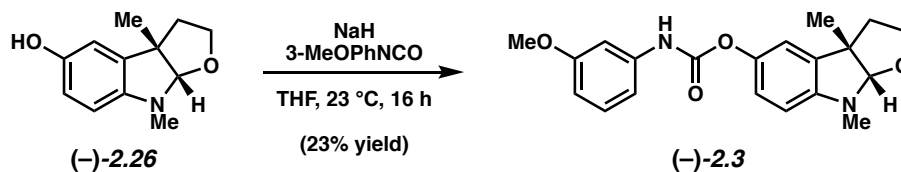
Carbamate (–)-**2.3**. Following representative procedure A yielded carbamate (–)-**2.3** (12.0 mg, 23% yield) as a colorless oil. Carbamate (–)-**2.3**: R_f 0.65 (1:1 Hexanes:EtOAc); ^{1}H NMR (500 MHz, CDCl$_3$): δ 7.21 (app. T, J = 8.2, 2H), 6.92–6.85 (m, 4H), 6.67–6.63 (m, 1H), 6.31 (d, J = 4.2, 1H), 5.09 (s, 1H), 3.96 (ddd, J = 1.5, 7.3, 8.7, 1H), 3.80 (s, 3H), 3.50 (ddd, J = 5.2, 8.7, 11.1, 1H), 2.90 (s, 3H), 2.14 (ddd, J = 1.4, 5.2, 11.9, 1H), 2.03 (ddd, J = 7.2, 11.3, 11.3, 1H), 1.46 (s, 3H); ^{13}C NMR (125 MHz, CDCl$_3$): δ 160.4, 152.5, 148.3, 142.2, 138.9, 135.4, 129.8, 120.9, 116.5, 110.8, 109.7, 105.4, 104.7, 104.2, 67.3, 55.3, 52.3, 41.6, 31.2, 24.6; IR (film): 3301,

2928, 1746, 1611, 1494, 1196 cm^{-1}; HRMS–APCI (*m/z*) [M + H]$^+$ calcd for C$_{20}$H$_{23}$N$_2$O$_4^+$, 355.16523; found, 355.16429; [α]$^{25.2}$$_D$ –32.00° (*c* = 0.10, CH$_2$Cl$_2$).

Carbamate (–)-**2.4**. Following representative procedure A yielded carbamate (–)-**2.4** (3.2 mg, 11% yield) as a white solid. Carbamate (–)-**2.4**: mp: 138–140 °C; R$_f$ 0.69 (1:1 Hexanes:EtOAc); ^{1}H NMR (500 MHz, CDCl$_3$): δ 7.47 (d, *J* = 4.2, 2H), 7.19 (d, *J* = 4.0, 2H), 6.90–6.85 (m, 2H), 6.31 (d, *J* = 4.3, 1H), 5.09 (s, 1H), 3.96 (ddd, *J* =1.5, 7.3, 8.7, 1H), 3.50 (ddd, *J* = 5.2, 8.7, 11.1, 1H), 2.91 (s, 3H), 2.13 (ddd, *J* = 1.4, 5.2, 11.9, 1H), 2.04 (ddd, *J* = 7.2, 11.3, 11.3, 1H), 1.46 (s, 3H); ^{13}C NMR (125 MHz, CDCl$_3$): δ 152.5, 145.0, 142.1, 136.3, 135.5, 123.56, 121.4, 121.5, 120.8, 120.5 (q, *J* = 293), 119.7, 117.4, 105.4, 104.6, 67.3, 52.3, 41.6, 31.1, 24.6; ^{19}F-NMR (376 Hz, CDCl$_3$): δ   –58.2; IR (film): 3322, 2929, 1719, 1549, 1497 cm^{-1}; HRMS–APCI (*m/z*) [M + H]$^+$ calcd for C$_{20}$H$_{20}$F$_3$N$_2$O$_4^+$, 409.13697; found, 409.13604; [α]$^{30.2}$$_D$ –35.35° (*c* = 0.10, CH$_2$Cl$_2$).
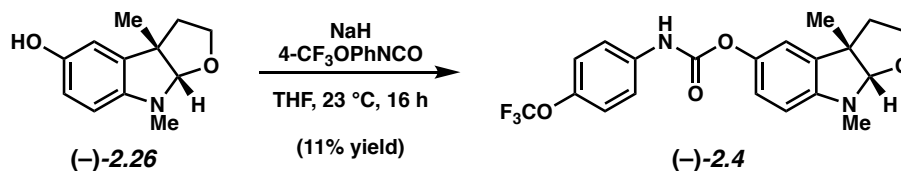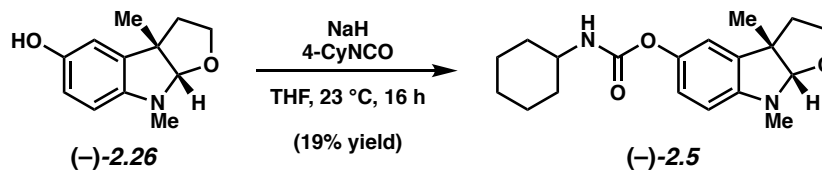
Carbamate (–)-**2.5**. Following representative procedure A yielded carbamate (–)-**2.5** (5.6 mg, 19% yield) as a white solid. Carbamate (–)-**2.5**: mp: 130–133 °C; R$_f$ 0.61 (1:1 Hexanes:EtOAc); ^{1}H NMR (500 MHz, CDCl$_3$): δ 6.83–6.80 (m, 2H), 6.27 (d, *J* = 4.0, 1H), 5.06 (s, 1H), 4.83–4.82 (m, 1H), 3.94 (ddd, *J* = 1.5, 7.3, 8.7, 1H), 3.57–3.54 (m, 1H), 3.48 (ddd, *J* = 5.2, 8.7, 11.1, 1H), 2.89 (s, 3H), 2.12 (ddd, *J* = 1.4, 5.2, 11.9, 1H), 2.05–1.99 (m, 3H),

1.74–1.71 (m, 2H), 1.64–1.60 (m, 1H), 1.44 (s, 3H), 1.41–1.32 (m, 2H), 1.25–1.17 (m, 3H); ^{13}C

NMR (125 MHz, CDCl$_3$): δ 154.7, 148.0, 143.0, 135.3, 120.9, 116.8, 105.6, 104.8, 67.5, 52.5,

50.2, 41.7, 33.5, 31.4, 25.6, 24.9, 24.7; IR (film): 3314, 2928, 1712, 1493, 1198 cm^{-1}; HRMS–

APCI (m/z) [M + H]$^+$ calcd for C$_{19}$H$_{27}$N$_2$O$_3^+$, 331.20162; found, 331.20025; [α]$^{28.7}$$_D$ –130.69° (c =

0.10, CH$_2$Cl$_2$).

Carbamate (–)-**2.6**. Following representative procedure A yielded carbamate (–)-**2.6** (10.2 mg,

20% yield) as an amorphous solid. Carbamate (–)-**2.6**: R$_f$ 0.68 (1:1 Hexanes:EtOAc); ^{1}H

NMR (500 MHz, CDCl$_3$): δ 7.07 (s, 2H), 6.90–6.85 (m, 2H), 6.73 (s, 1H), 6.33–6.29 (m, 1H), 5.09

(s, 1H), 3.96 (ddd, J = 1.5, 7.3, 8.7, 1H), 3.50 (ddd, J = 5.2, 8.7, 11.1, 1H), 2.91 (s, 3H), 2.29 (s,

6H), 2.14 (ddd, J = 1.4, 5.2, 11.9, 1H), 2.04 (ddd, J = 7.2, 11.3, 11.3, 1H), 1.46 (s, 3H); ^{13}C

NMR (125 MHz, CDCl$_3$): δ 152.6, 148.2, 142.4, 138.9, 137.4, 135.4, 125.5, 120.9, 116.6, 116.4,

105.4, 104.7, 67.4, 52.3, 41.6, 31.2, 24.6, 21.4; IR (film): 3308, 2923, 1748, 1497, 1195 cm^{-1}; HRMS–APCI (m/z) [M + H]$^+$ calcd for C$_{21}$H$_{25}$N$_2$O$_3^+$, 353.18597; found, 353.18496; [α]$^{29.4}$$_D$ –
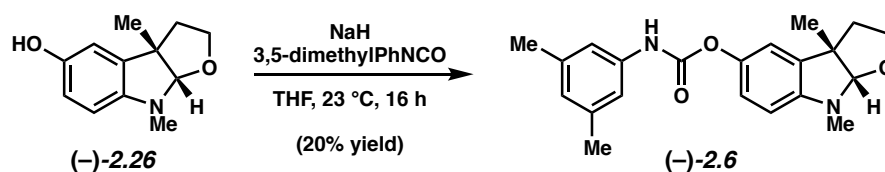
39.34° (c = 0.10, CH$_2$Cl$_2$).
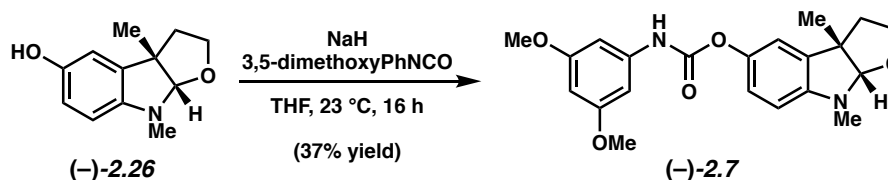
Carbamate (–)-**2.7**. Following representative procedure A yielded carbamate (–)-**2.7** (14.0 mg,

37% yield) as a white solid. Carbamate (–)-**2.7**: mp: 67–69 °C; R$_f$ 0.56 (1:1 Hexanes:EtOAc); ^{1}H

NMR (500 MHz, CDCl$_3$): δ 6.90–6.83 (m, 3H), 6.72–6.65 (m, 2H), 6.30 (d, J = 4.2, 1H), 6.21 (t,

J = 2.2, 1H), 5.08 (s, 1H), 3.96 (ddd, J = 1.5, 7.4, 8.8, 1H), 3.77 (s, 6H), 3.50 (ddd, J = 5.2, 8.7,

11.1, 1H), 2.91 (s, 3H), 2.13 (ddd, J = 1.4, 5.2, 11.9, 1H), 2.04 (ddd, J = 7.2, 11.3, 11.3, 1H), 1.45

(s, 3H); ^{13}C NMR (125 MHz, CDCl$_3$): δ 161.2, 152.4, 148.3, 142.2, 139.4, 135.4, 120.9, 116.5,

105.4, 104.7, 96.8, 96.2, 67.3, 55.4, 52.3, 41.6, 31.2, 24.6; IR (film): 3306, 2936, 1749, 1615, 1202

cm^{-1}; HRMS–APCI (m/z) [M + H]$^+$ calcd for C$_{21}$H$_{25}$N$_2$O$_5{}^+$, 385.17580; found, 385.17580; [α] $^{30.8}$

$_D$ –56.00° (c = 0.10, CH$_2$Cl$_2$).

(–)-2.27 → (–)-2.9

NaH, PhNCO, THF, 23 °C, 16 h, (16% yield)
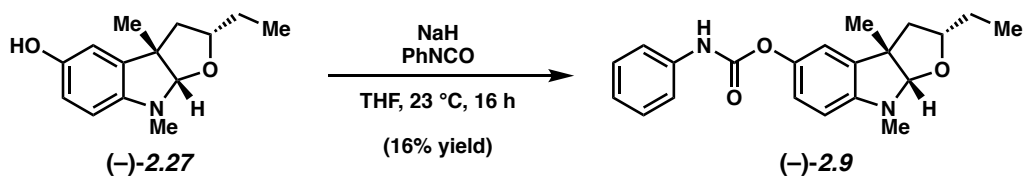
Carbamate (–)-2.9. Following representative procedure A yielded carbamate (–)-**2.9** (8.5 mg,

16% yield) as a clear oil. Carbamate (–)-**2.9**: R$_f$ 0.73 (1:1 Hexanes:EtOAc); ^{1}H NMR (500 MHz,

CDCl$_3$ δ 7.45–7.40 (m, 2H), 7.36–7.30 (m, 2H), 7.13–7.07 (m, 1H), 6.90–6.84 (m, 3H), 6.34 (d, J

= 8.4, 1H), 5.0 (s, 1H), 4.00 (ddd, J = 6.8, 6.8, 13.6, 1H), 2.93 (s, 3H), 2.16 (dd, J = 12.2, 6.6, 1H),

1.87 (dd, J = 12.5, 6.9), 1.47–1.40 (m, 1H), 1.38 (s, 3H), 1.32–1.22 (m, 1H), 0.83 (t, J = 7.6, 3H);

^{13}C NMR (125 MHz, CDCl$_3$): 152.5, 146.8, 142.4, 137.6, 137.2, 129.1, 123.7, 120.6, 118.7, 116.4,

106.7, 105.7, 80.2, 52.1, 45.7, 31.8, 28.6, 24.2, 10.6; IR (film): 3313, 2961, 1722, 1496, 1198 cm^{-1}; HRMS-APCI (m/z) [M + H]$^+$ calcd for C$_{21}$H$_{25}$N$_2$O$_3$, 353.18597; found 353.18462. [α]$^{24.2}$ $_D$ –

49.33° (c = 0.10, CH$_2$Cl$_2$).

(–)-2.28 → (–)-2.10

NaH, PhNCO, THF, 23 °C, 16 h, (17% yield)
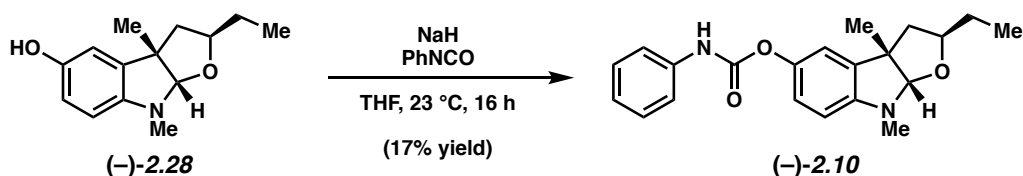
Carbamate (–)-2.10. Following representative procedure A yielded carbamate (–)-**2.10** (10.5 mg,

17% yield) as a clear oil. Carbamate (–)-**2.10**: R$_f$ 0.55 (5:1 Hexanes:EtOAc); ^{1}H NMR (500 MHz,

CDCl$_3$): δ 7.47–7.40 (m, 2H), 7.37 (m, 2H), 7.13–7.06 (m, 1H), 6.93–6.83 (m, 3H), 6.30 (d, 1H),

5.10 (s, 1H), 3.68–3.60 (m, 1H), 2.91 (s, 3H), 2.20 (dd, J = 4.4, 12.0, 1H), 1.72–1.54 (m, 3H),

1.53–1.46 (m, 1H), 1.44 (s, 3H), 0.87 (t, 3H); ^{13}C NMR (125 MHz, CDCl$_3$): 152.5, 148.4, 142.1,

137.6, 135.9, 129.2, 123.8, 120.7, 118.7, 116.4, 105.0, 104.5, 80.2, 52.7, 47.1, 31.1, 27.5, 25.1,

10.3; IR (film): 3314, 2962, 1724, 1498, 1200 cm^{-1}; HRMS-APCI (m/z) [M + H]$^+$ calcd for

C$_{21}$H$_{25}$N$_2$O$_3$, 353.18597; found 353.18482. [α]$^{21.4}$$_D$ –27.33° (c = 0.10, CH$_2$Cl$_2$).

Carbamate (–)-2.8. Following representative procedure B yielded carbamate (–)-**2.8** (108.3 mg,

61% yield) as a white solid. Carbamate (–)-**2.8**: mp: 164.0–166.0 °C; R$_f$ 0.18 (1:4

Hexanes:EtOAc); ^{1}H NMR (500 MHz, CDCl$_3$): δ 8.50 (dd, J = 1.6, 4.7, 2H), 7.39 (dd, J = 1.6, 4.7,

2H), 7.22–7.20 (m, 1H), 6.89–6.86 (m, 2H), 6.31 (d, J = 8.1, 1H), 5.10 (s, 1H), 3.97 (ddd, J = 1.5,

7.1, 8.7, 1H), 3.50 (ddd, J = 5.1, 8.7, 11.1, 1H), 2.91 (s, 3H), 2.13 (ddd, J = 1.5, 5.1, 12.1, 1H),

2.04 (ddd, J = 7.1, 11.1, 12.1, 1H), 1.46 (s, 3H); ^{13}C NMR (125 MHz, CDCl$_3$): 152.1, 150.9, 148.7,

145.1, 142.0, 135.7, 120.8, 116.4, 112.7, 105.5, 104.8, 67.5, 52.5, 41.8, 31.2, 24.8; IR (film): 3165,

2960, 1749, 1594, 1494 cm^{-1}; HRMS-APCI (m/z) [M + H]$^+$ calcd for C$_{18}$H$_{20}$N$_3$O$_3$, 326.14992;

found 326.14971. [α]$^{24.8}$$_D$ –50.00° (c = 0.10, CH$_2$Cl$_2$).
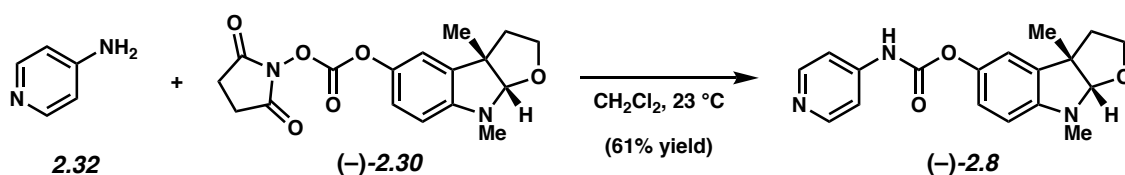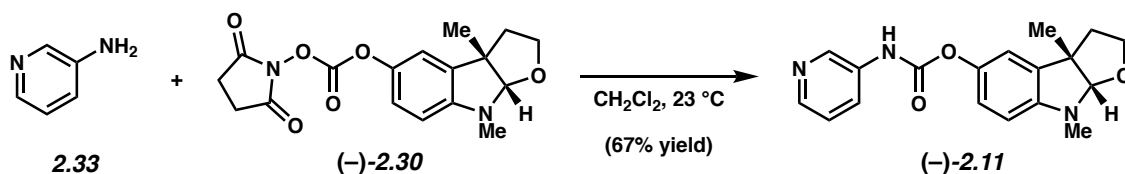
Carbamate (–)-**2.11**. Following representative procedure B yielded carbamate (–)-**2.11** (7.5 mg,

67% yield) as a white solid. Carbamate (–)-**2.11**: mp: 131.0–133.6 °C;

R_f 0.24 (1:5 Hexanes:EtOAc); ^{1}H NMR (500 MHz, CDCl$_3$): δ 8.56 (d, J = 8.6, 1H), 8.35 (dd, J = 1.3, 4.8, 1H), 8.06 (br. d, J = 6.6, 1H), 7.28 (dd, J = 4.8, 8.6, 1H), 6.90–6.68 (m, 2H), 6.31 (d, J = 8.1, 1H), 5.09 (s, 1H), 3.96 (ddd, J = 1.3, 7.2, 8.6, 1H), 3.50 (ddd, J = 5.1, 8.6, 11.0, 1H), 2.91 (s, 3H), 2.13 (ddd, J = 1.3, 5.1, 12.0, 1H), 2.04 (ddd, J = 7.2, 11.0, 12.0, 1H), 1.46 (s, 3H); ^{13}C NMR (125 MHz, CDCl$_3$): δ 152.8, 148.6, 145.0, 142.2, 140.4, 135.7, 134.8, 126.0, 123.9, 120.9, 116.5, 105.5, 104.8, 67.5, 52.5, 41.8, 31.3, 24.8; IR (film): 3187, 2931, 1745, 1497, 1197 cm^{-1}; HRMS–APCI (m/z) [M + H]$^+$ calcd for C$_{18}$H$_{20}$N$_3$O$_3$$^+$, 326.14992; found, 326.15073; $[\alpha]_D^{24.3}$ –52.70° (c = 0.10, CH$_2$Cl$_2$).

Carbamate (–)-2.13. Following representative procedure B yielded carbamate (–)-**2.13** (2.7 mg, 23% yield) as an amorphous solid. Carbamate (–)-**2.13**: R_f 0.38 (1:5 Hexanes:EtOAc); ^{1}H NMR (500 MHz, CDCl$_3$): δ 8.43 (d, J = 2.4, 1H), 8.34 (d, J = 5.7, 1H), 8.14 (br. t, J = 6.3, 1H), 7.34 (br. s, 1H), 6.91–6.87 (m, 2H), 6.32 (d, J = 8.2, 1H), 5.10 (s, 1H), 3.97 (ddd, J = 1.7, 7.3, 8.8, 1H), 3.50 (ddd, J = 5.3, 8.8, 11.0, 1H), 2.92 (s, 3H), 2.13 (ddd, J = 1.3, 5.3, 12.0, 1H), 2.05 (ddd, J = 7.3, 11.0, 12.0, 1H), 1.47 (s, 3H); ^{13}C NMR (125 MHz, CDCl$_3$): δ 151.7, 150.2, 148.8, 148.2, 147.14, 147.10, 141.8, 137.2 (J = 20.3), 135.8, 120.8, 116.3, 113.4, 105.5, 104.7, 67.4, 52.5, 41.8, 31.2, 24.8; ^{19}F NMR (376 Hz, CDCl$_3$): δ –148.00; IR (film): 3238, 2926, 2870, 1753, 1620 cm^{-1}; HRMS–APCI (m/z) [M + H]$^+$ calcd for C$_{18}$H$_{19}$N$_3$O$_3$F$^+$, 344.14050; found, 344.14163; $[\alpha]_D^{28.4}$ –62.70° (c = 0.10, CH$_2$Cl$_2$).

Carbamate (–)-2.14. Following representative procedure B yielded carbamate (–)-**2.14** (6.0 mg, 61% yield) as a colorless oil. Carbamate (–)-**2.14**: R_f 0.38 (1:1 Hexanes:EtOAc); ^{1}H NMR (500 MHz, CDCl$_3$): δ 8.29–8.22 (m, 1H), 8.21 (d, J = 2.5, 1H), 7.99 (br. d, J = 9.3, 1H), 6.89–6.86 (m, 2H), 6.31 (d, J = 8.3, 1H), 5.10 (s, 1H), 3.97 (ddd, J = 1.6, 7.3, 8.7, 1H), 3.50 (ddd, J = 5.2, 8.7, 11.1, 1H), 2.91 (s, 3H), 2.13 (ddd, J = 1.3, 5.2, 12.1, 1H), 2.05 (ddd J = 7.2, 11.1, 12.1, 1H), 1.47 (s, 3H); ^{13}C NMR (125 MHz, CDCl$_3$): δ 160.8, 158.7, 152.5, 148.7, 142.0, 135.9 (J = 6.6), 135.7, 133.1, 132.9, 128.5, 120.8, 116.4, 113.4, 113.2, 105.5, 104.7, 67.4, 52.5, 41.8, 31.2, 24.7; ^{19}F NMR (376 Hz, CDCl$_3$): δ –125.26 (d, J = 10.5); IR (film): 3243, 2959, 2925, 1748, 1601, 1197 cm^{-1}; HRMS–APCI (m/z) [M + H]$^+$ calcd for C$_{18}$H$_{19}$N$_3$O$_3$F$_1^+$, 344.14050; found, 344.14028; [α]$^{31.0}$$_D$ –57.33° (c = 0.10, CH$_2$Cl$_2$).
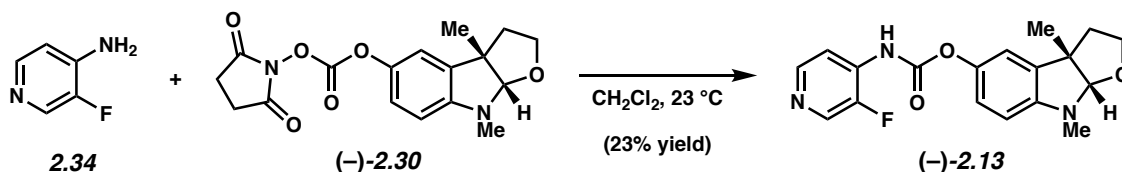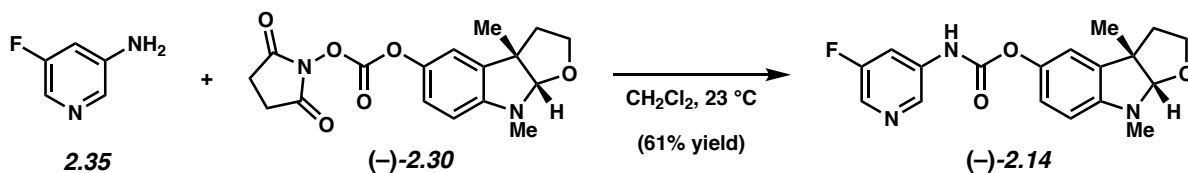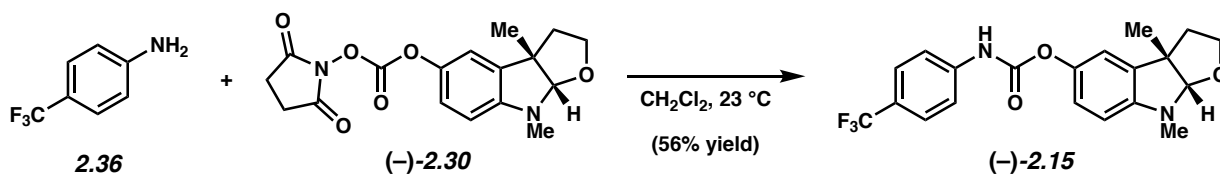
Carbamate (–)-2.15. Following representative procedure B yielded carbamate (–)-**2.15** (6.3 mg, 56% yield) as a white solid. Carbamate (–)-**2.15**: mp: 193.0–195.0 °C; R_f 0.72 (1:1 Hexanes:EtOAc); ^{1}H NMR (500 MHz, CDCl$_3$): δ 7.59–7.54 (m, 4H), 7.07 (br. s, 1H), 6.90–6.87 (m, 2H), 6.31 (d, J = 8.4, 1H), 5.10 (s, 1H), 3.96 (ddd, J = 1.5, 7.3, 8.8, 1H), 3.50 (ddd, J = 5.2, 8.8, 11.1, 1H), 2.91 (s, 3H), 2.13 (ddd, J = 1.5, 5.2, 12.0, 1H), 2.04 (ddd, J = 7.3, 11.1, 12.0, 1H), 1.46 (s, 3H); ^{13}C NMR (125 MHz, CDCl$_3$): δ 152.4, 148.6, 142.1, 140.9, 135.7, 126.6 (q, J = 3.7), 125.8, 125.6, 125.3, 123.2, 120.9, 118.3, 116.5, 105.5, 104.8, 67.5, 52.5, 41.8, 31.3,

24.7; ^{19}F NMR (376 Hz, CDCl$_3$): δ –62.03; IR (film): 3352, 2885, 1719, 1615, 1117 cm^{-1}; HRMS–

APCI (*m/z*) [M + H]$^+$ calcd for C$_{20}$H$_{20}$N$_2$O$_3$F$_3$$^+$, 393.14205; found, 393.14164; [α] $^{30.7}$ $_D$ –58.03°

(*c* = 0.10, CH$_2$Cl$_2$).

Carbamate (–)-**2.16**. Following representative procedure B yielded carbamate (–)-**2.16** (6.0 mg,

72% yield) as a colorless oil. Carbamate (–)-**2.16**: R$_f$ 0.54 (1:1 Hexanes:EtOAc); ^{1}H

NMR (500 MHz, CDCl$_3$): δ 6.81 (app. d, *J* = 8.3, 2H), 6.28 (d, *J* = 8.7, 1H), 5.06 (s, 1H), 3.94

(ddd, *J* = 1.5. 7.3, 8.7, 1H), 3.50–3.39 (m, 3H), 3.04–2.97 (m, 3H), 2.89 (s, 3H), 2.13 (ddd, *J* = 1.5,

5.1, 12.0, 1H), 2.01 (ddd, *J* = 7.3, 11.3, 12.0, 1H), 1.44 (s, 3H), 1.25–1.16 (m, 3H); ^{13}C

NMR (125 MHz, CDCl$_3$): δ 155.6, 155.4, 148.0, 143.4, 135.3, 121.0, 116.78, 116.81, 105.6, 104.9,

67.5, 52.5, 44.1, 41.7, 34.3, 33.8, 31.4, 24.7, 13.4, 12.7; IR (film): 2963, 2931, 1717, 1614, 1396

cm^{-1}; HRMS–APCI (*m/z*) [M + H]$^+$ calcd for C$_{16}$H$_{23}$N$_2$O$_3$$^+$, 291.17032; found, 291.16895; [α] $^{30.9}$
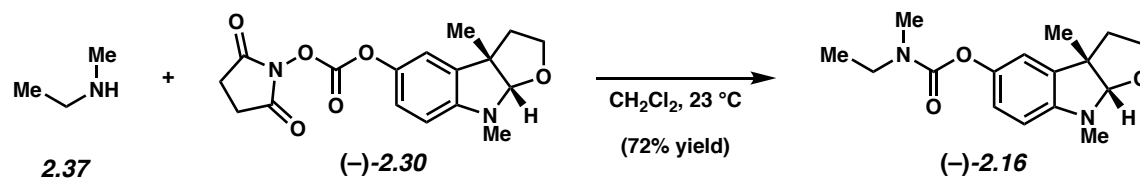
$_D$ –53.97° (*c* = 0.10, CH$_2$Cl$_2$).

*Note: (–)-**2.16** was obtained as a mixture of rotamers. These data represent empirically observed*

chemical shifts from the ^{13}C-NMR spectrum.

2.10 Spectra Relevant to Chapter Two:

Dual Neutral Sphingomyelinase2/Acetylcholinesterase Inhibitors for the

Treatment of Alzheimer's Disease

Tina Bilousova, Bryan J. Simmons, Rachel R. Knapp, Chris J. Elias, Jesus Campagna, Mikhail Melnik, Sujyoti Chandra, Samantha Focht, Chunni Zhu, Kanagasabai Vadivel, Barbara Jagodzinska, Whitaker Cohn, Patricia Spilman, Karen H. Gylys, Neil K. Garg*, and Varghese John.*
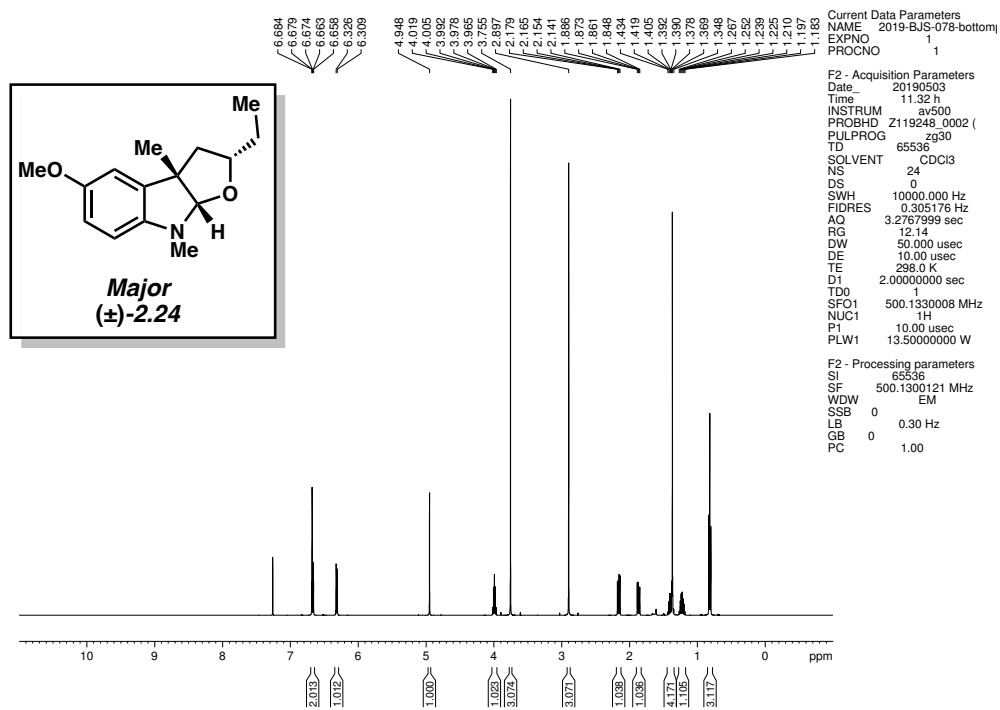
Figure 2.8. ^{1}H NMR (500 MHz, CDCl$_3$) of compound **2.24**.
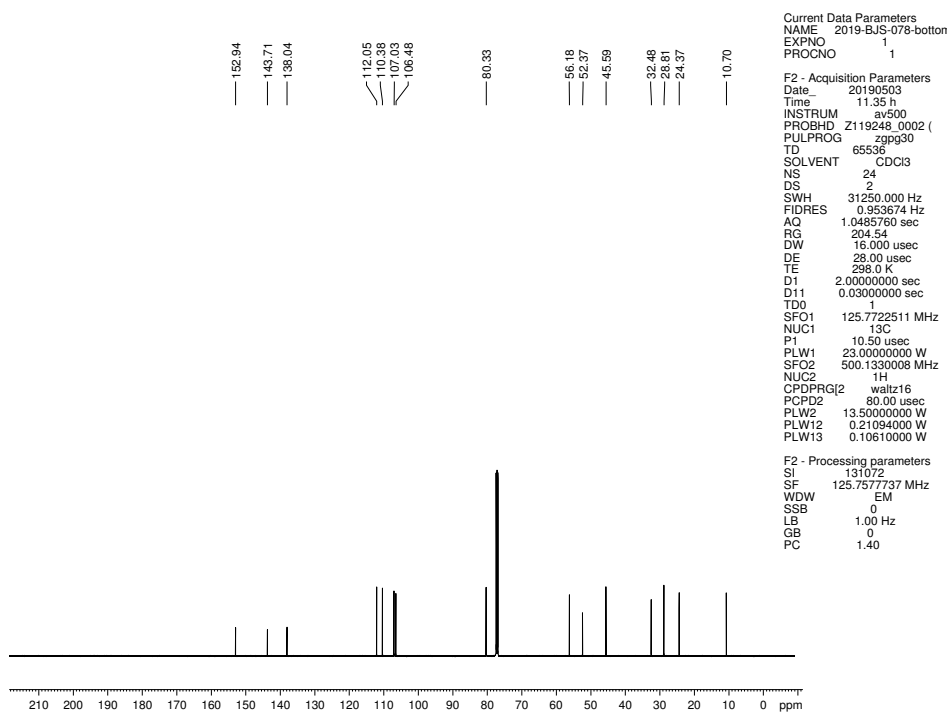
Figure 2.9. ^{13}C NMR (125 MHz, CDCl$_3$) of compound **2.24**.
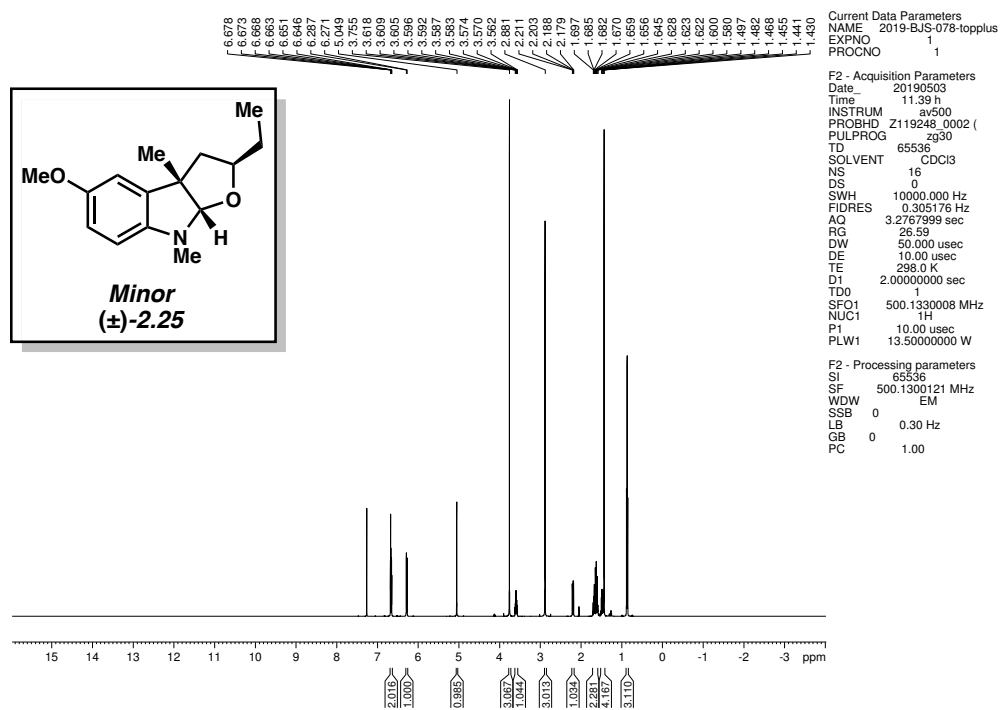
Figure 2.10. ^{1}H NMR (500 MHz, CDCl$_3$) of compound **2.25**.
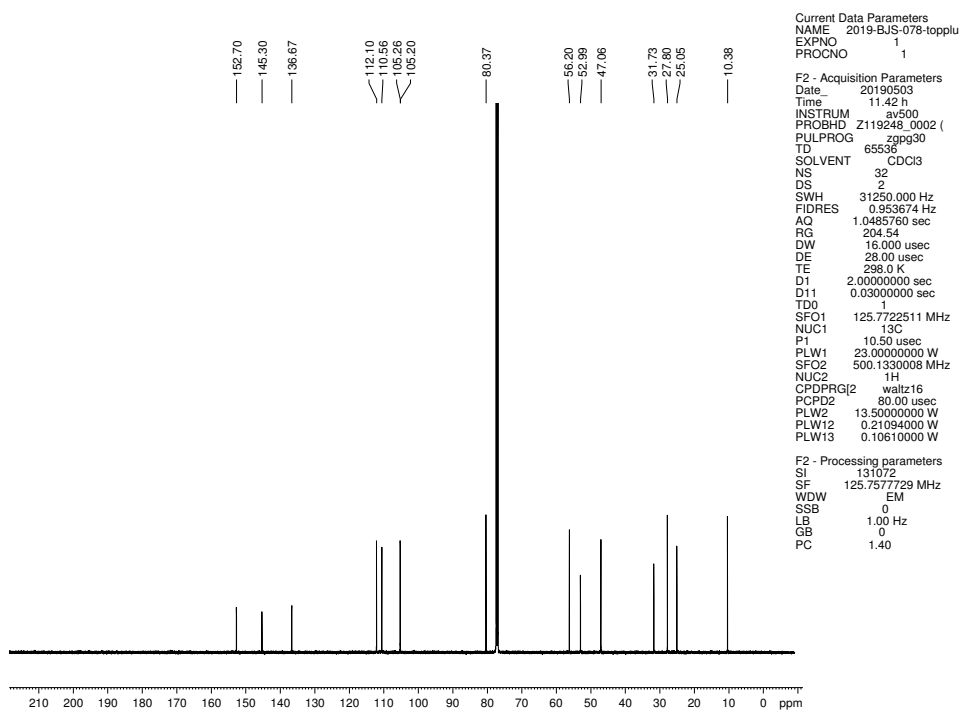
Figure 2.11. ^{13}C NMR (125 MHz, CDCl$_3$) of compound **2.25**.
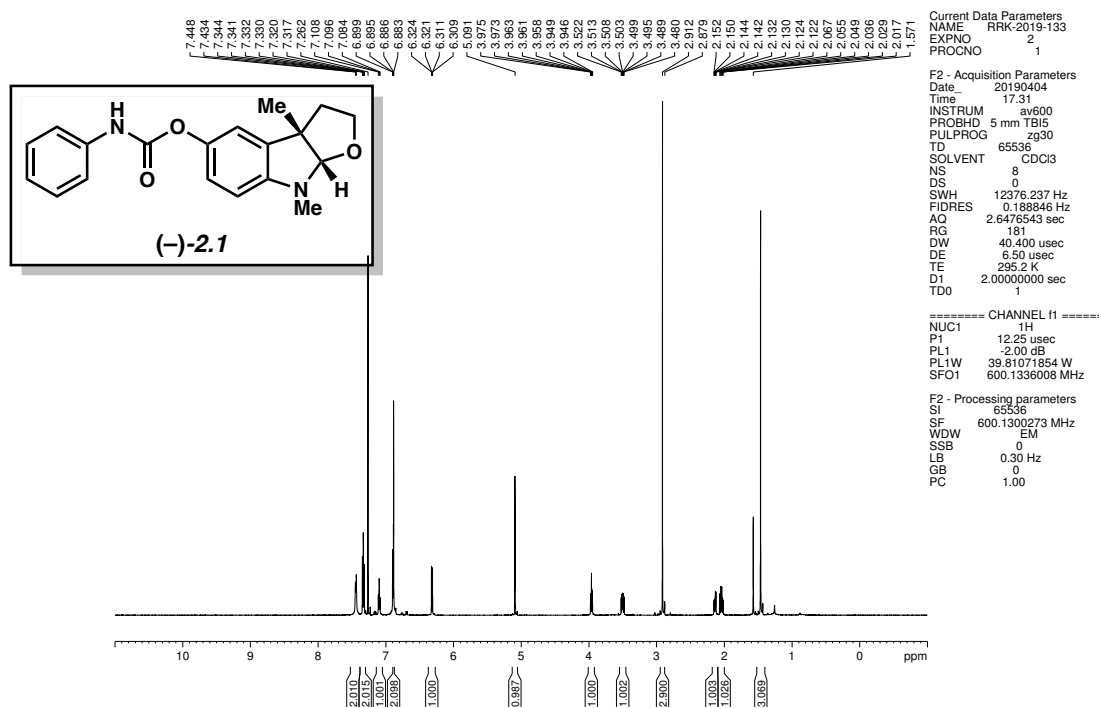
Figure 2.12. ^{1}H NMR (600 MHz, CDCl$_3$) of compound (–)-**2.1**.
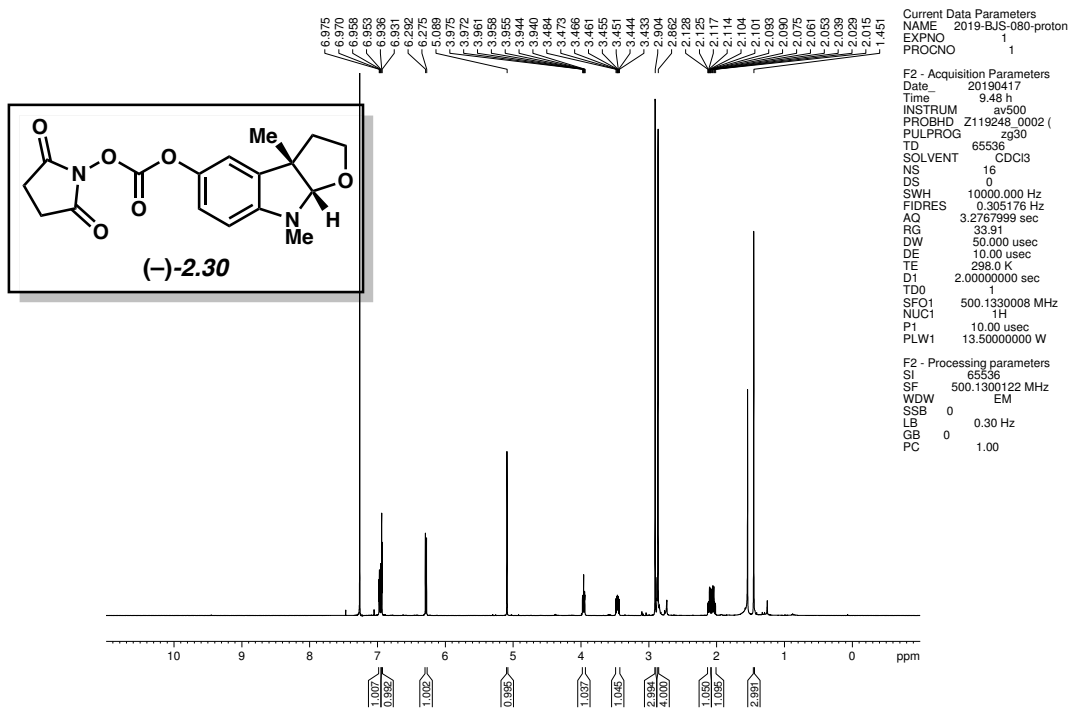
Figure 2.13. ^{1}H NMR (500 MHz, CDCl$_3$) of compound (–)-**2.30**.
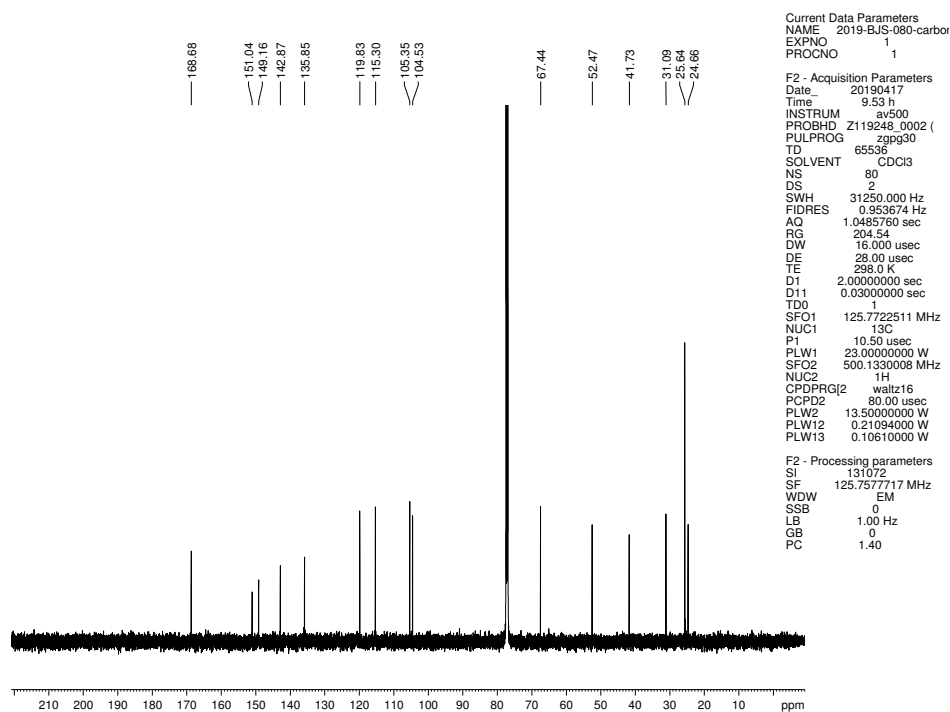
Figure 2.14. ^{13}C NMR (125 MHz, CDCl$_3$) of compound (–)-**2.30**.

Figure 2.15. ¹H NMR (500 MHz, CDCl₃) of compound (–)-**2.12**.

Figure 2.16. ¹³C NMR (125 MHz, CDCl₃) of compound (–)-**2.12**.

7.349, 7.333, 6.887, 6.882, 6.877, 6.870, 6.857, 6.852, 6.311, 6.306, 6.298, 6.293, 5.078, 3.966, 3.963, 3.951, 3.948, 3.946, 3.934, 3.931, 3.786, 3.513, 3.503, 3.496, 3.491, 3.486, 3.481, 3.474, 3.463, 2.901, 2.143, 2.141, 2.133, 2.130, 2.119, 2.117, 2.109, 2.107, 2.059, 2.045, 2.041, 2.037, 2.022, 2.013, 1.998, 1.450

Current Data Parameters
NAME   RRK-2019-144-proton
EXPNO   1
PROCNO   1

F2 - Acquisition Parameters
Date_   20190417
Time   10.18 h
INSTRUM   av500
PROBHD Z119248_0002 (
PULPROG   zg30
TD   65536
SOLVENT   CDCl3
NS   16
DS   0
SWH   10000.000 Hz
FIDRES   0.305176 Hz
AQ   3.2767999 sec
RG   30.07
DW   50.000 usec
DE   10.00 usec
TE   298.0 K
D1   2.00000000 sec
TD0   1
SFO1   500.1330008 MHz
NUC1   1H
P1   10.00 usec
PLW1   13.50000000 W

F2 - Processing parameters
SI   65536
SF   500.1300146 MHz
WDW   EM
SSB   0
LB   0.30 Hz
GB   0
PC   1.00

1.914 3.009 1.006 0.997 0.997 1.007 3.004 1.000 3.006 1.004 1.013 3.001

Figure 2.17. ^{1}H NMR (500 MHz, CDCl$_3$) of compound (–)-**2.2**.

156.13, 152.83, 148.21, 142.40, 135.36, 130.67, 120.83, 120.57, 116.57, 114.32, 105.43, 104.66, 67.34, 55.52, 52.34, 41.62, 31.18, 24.61

Current Data Parameters
NAME   RRK-2019-144-carbo
EXPNO   1
PROCNO   1

F2 - Acquisition Parameters
Date_   20190417
Time   10.23 h
INSTRUM   av500
PROBHD Z119248_0002 (
PULPROG   zgpg30
TD   65536
SOLVENT   CDCl3
NS   80
DS   2
SWH   31250.000 Hz
FIDRES   0.953674 Hz
AQ   1.0485760 sec
RG   204.54
DW   16.000 usec
DE   28.00 usec
TE   298.0 K
D1   2.00000000 sec
D11   0.03000000 sec
TD0   1
SFO1   125.7722511 MHz
NUC1   13C
P1   10.50 usec
PLW1   23.00000000 W
SFO2   500.1330008 MHz
NUC2   1H
CPDPRG[2   waltz16
PCPD2   80.00 usec
PLW2   13.50000000 W
PLW12   0.21094000 W
PLW13   0.10610000 W

F2 - Processing parameters
SI   131072
SF   125.7577892 MHz
WDW   EM
SSB   0
LB   1.00 Hz
GB   0
PC   1.40

Figure 2.18. ^{13}C NMR (125 MHz, CDCl$_3$) of compound (–)-**2.2**.
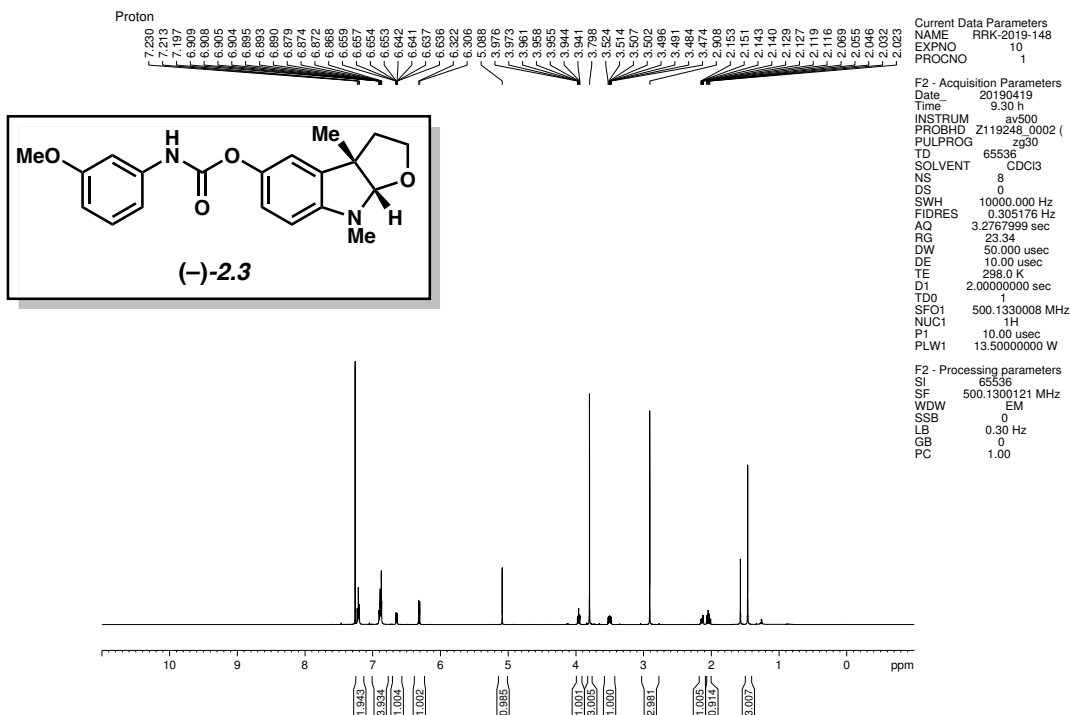
Figure 2.19. ^{1}H NMR (500 MHz, CDCl$_3$) of compound (–)-**2.3**.
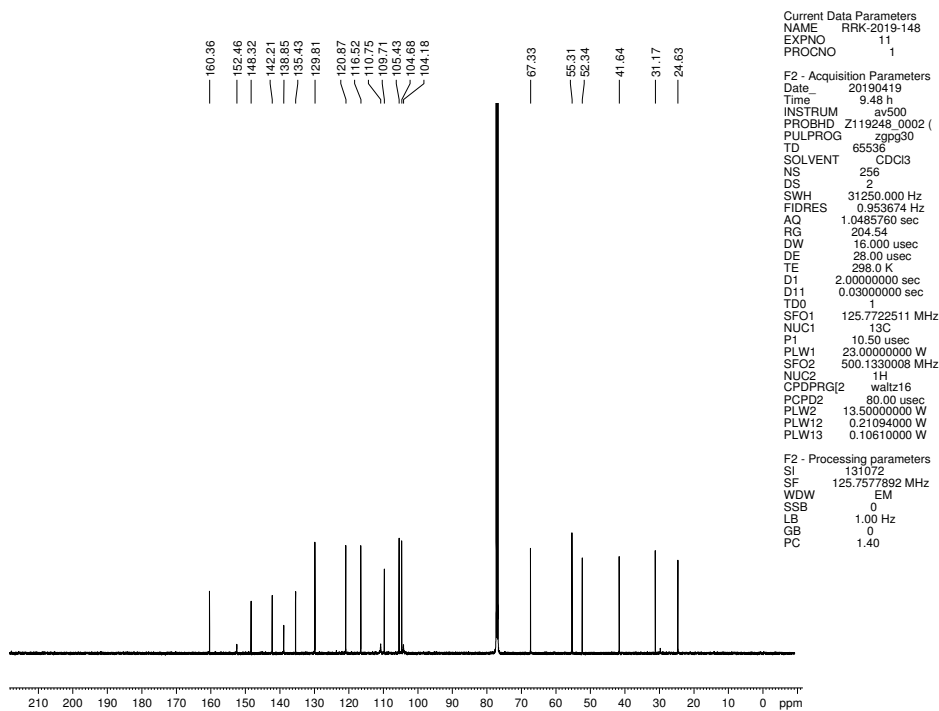
Figure 2.20. ^{13}C NMR (125 MHz, CDCl$_3$) of compound (–)-**2.3**.
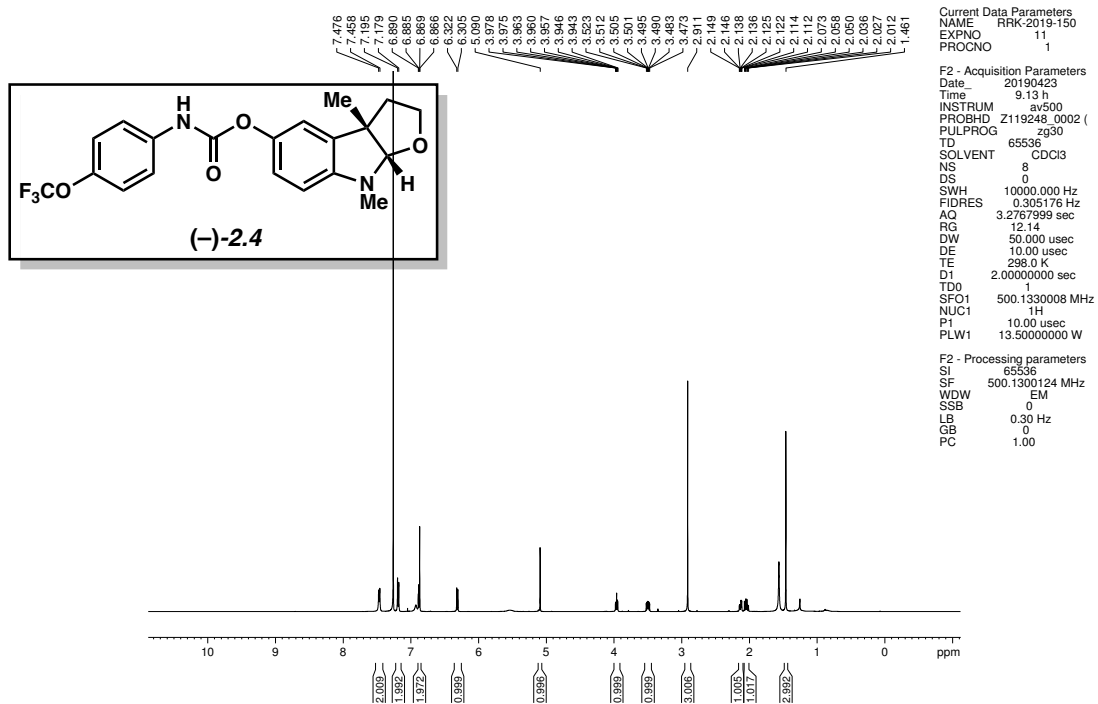
Figure 2.21. ^{1}H NMR (500 MHz, CDCl$_3$) of compound (–)-**2.4**.
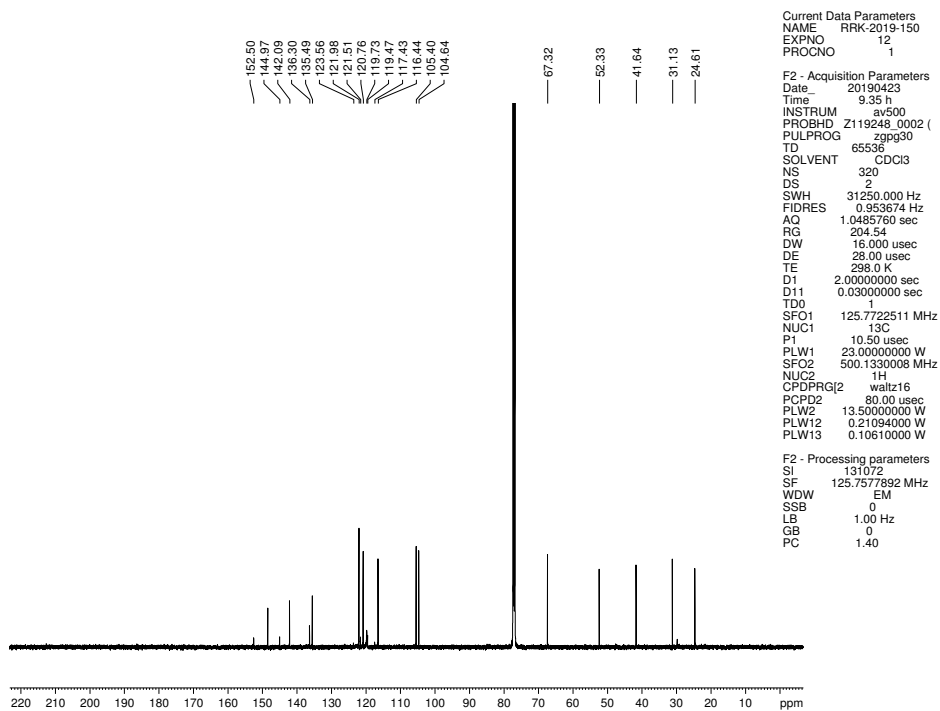
Figure 2.22. ^{13}C NMR (125 MHz, CDCl$_3$) of compound (–)-**2.4**.
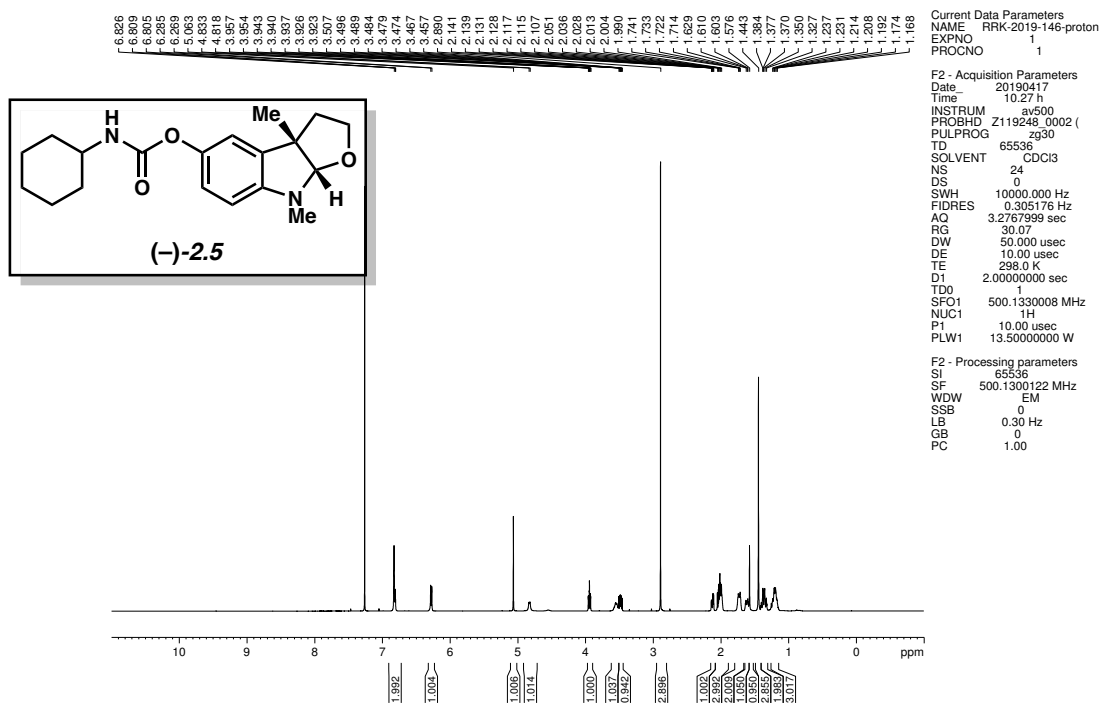
Figure 2.23. ^{1}H NMR (500 MHz, CDCl$_3$) of compound (–)-**2.5**.
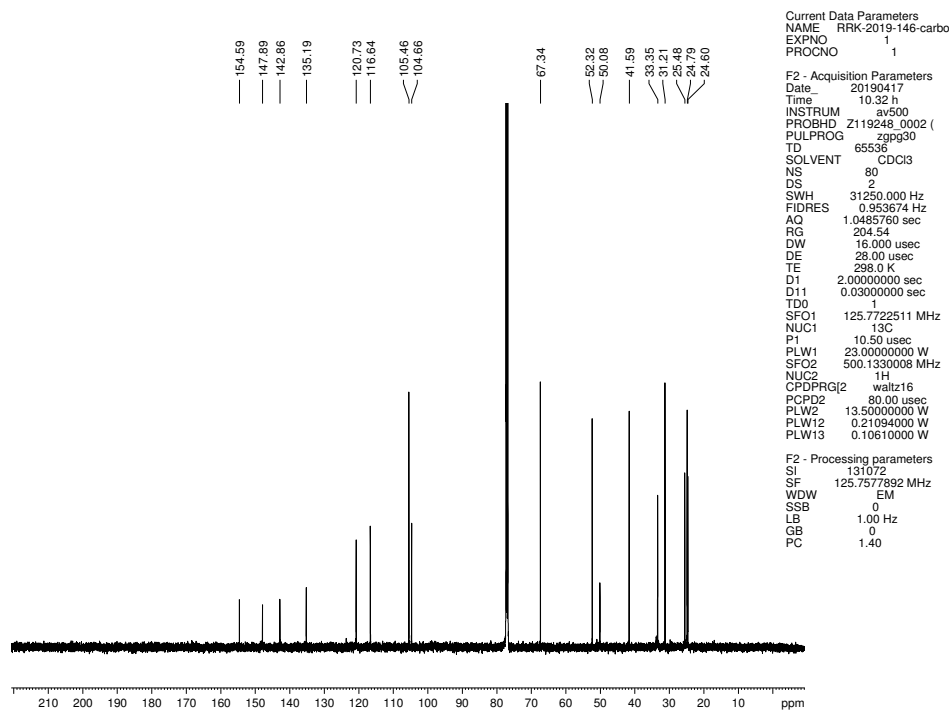
Figure 2.24. ^{13}C NMR (125 MHz, CDCl$_3$) of compound (–)-**2.5**.
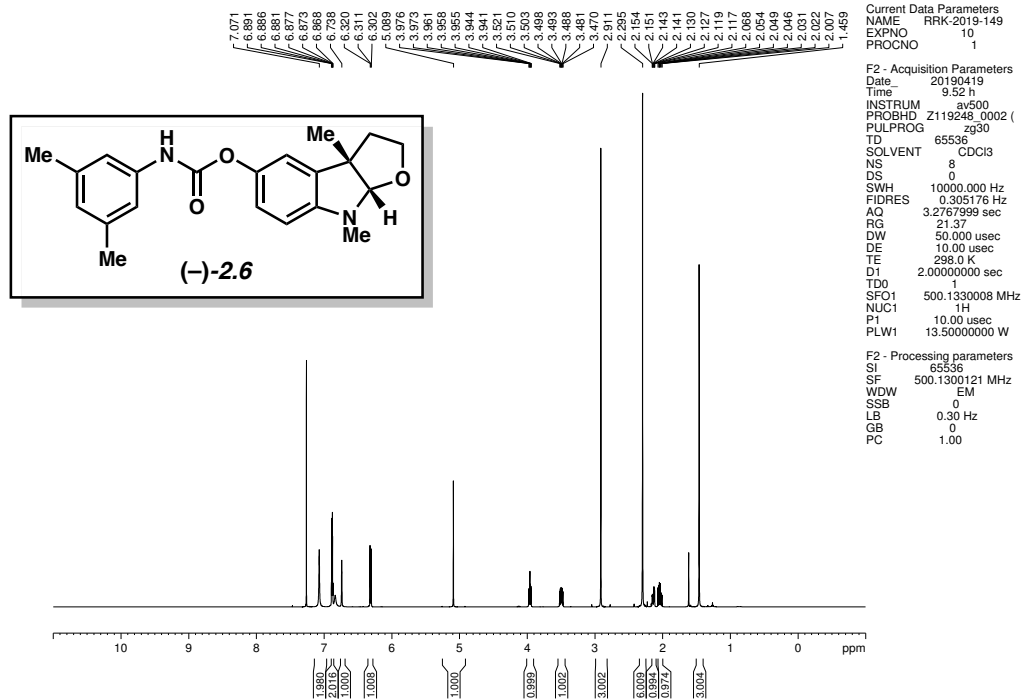
Figure 2.25. ^{1}H NMR (500 MHz, CDCl$_3$) of compound (−)-**2.6**.
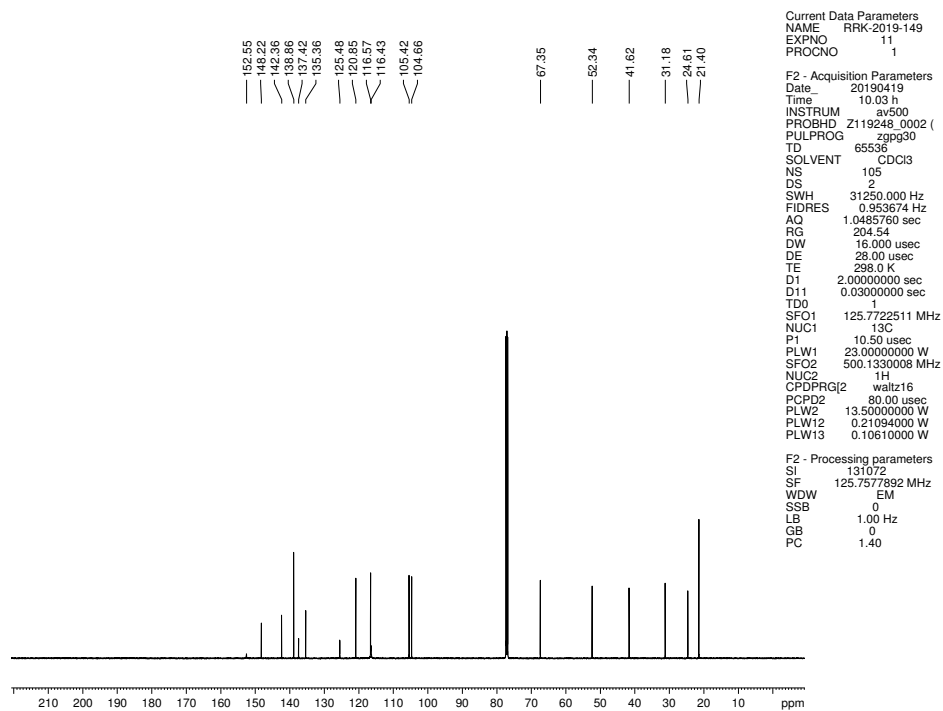
Figure 2.26. ^{13}C NMR (125 MHz, CDCl$_3$) of compound (−)-**2.6**.
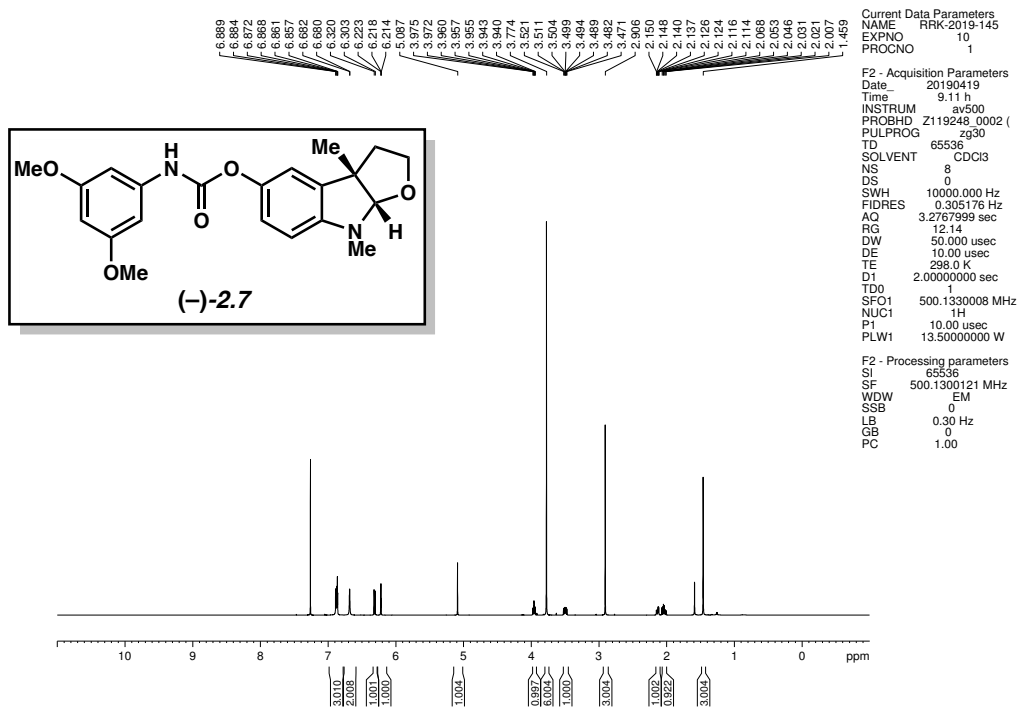
Figure 2.27. ^{1}H NMR (500 MHz, CDCl3) of compound (–)-**2.7**.
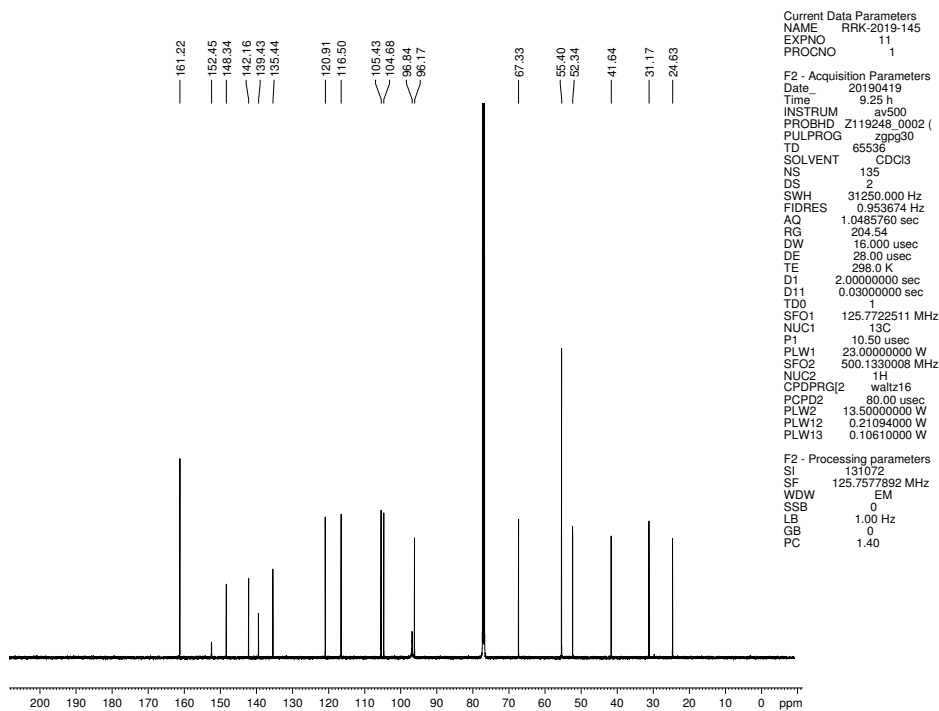
Figure 2.28. ^{13}C NMR (125 MHz, CDCl3) of compound (–)-**2.7**.
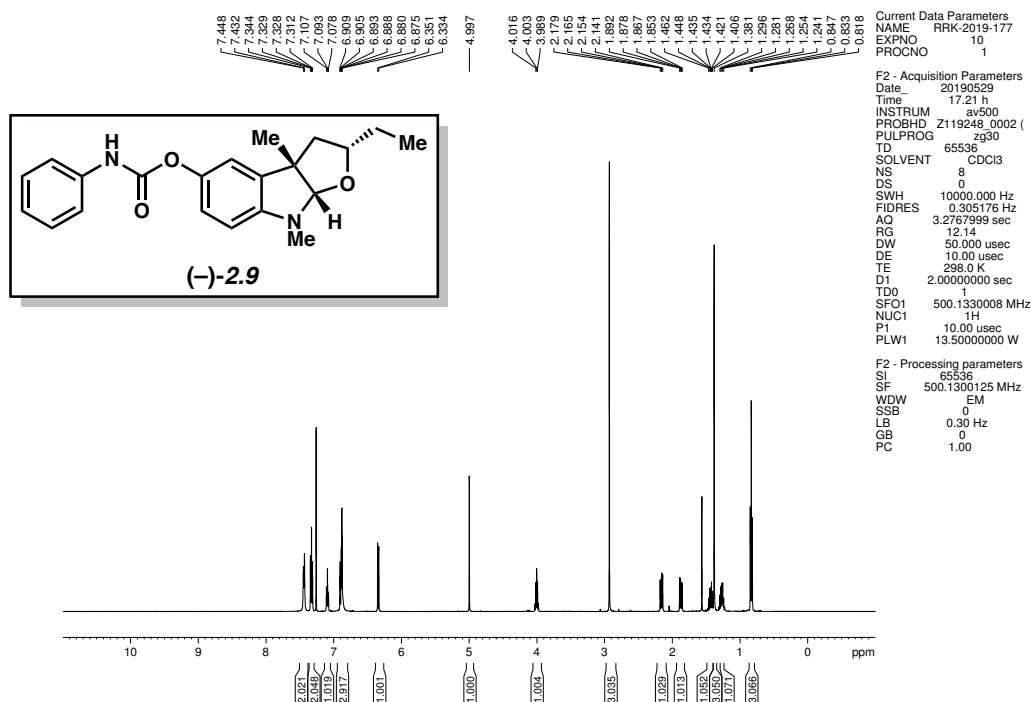
Figure 2.29. ^{1}H NMR (600 MHz, CDCl$_3$) of compound (–)-**2.9**.
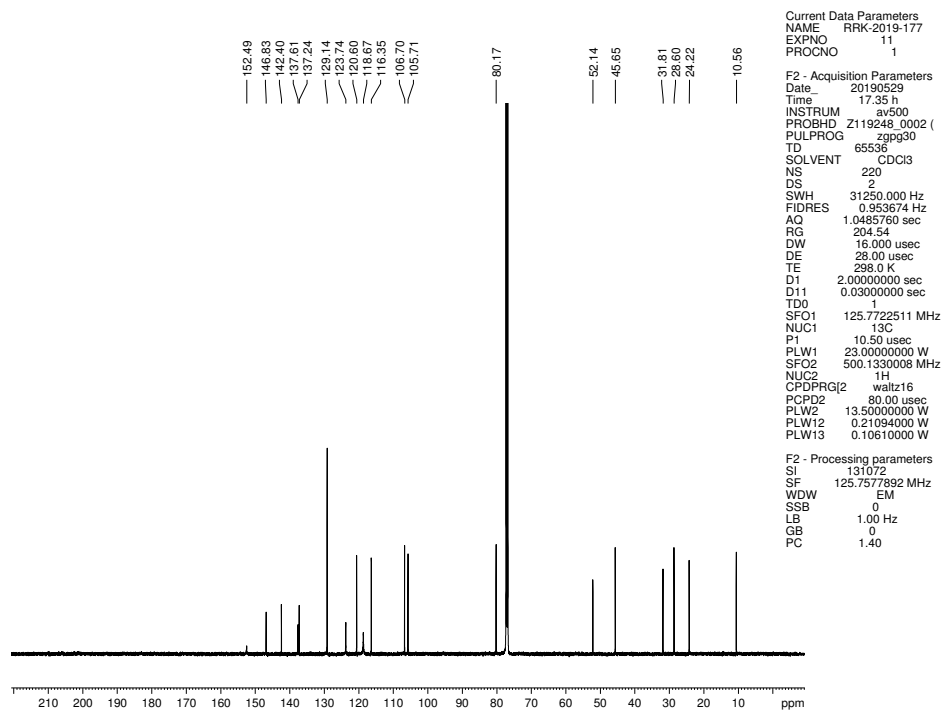
Figure 2.30. ^{13}C NMR (125 MHz, CDCl$_3$) of compound (–)-**2.9**.
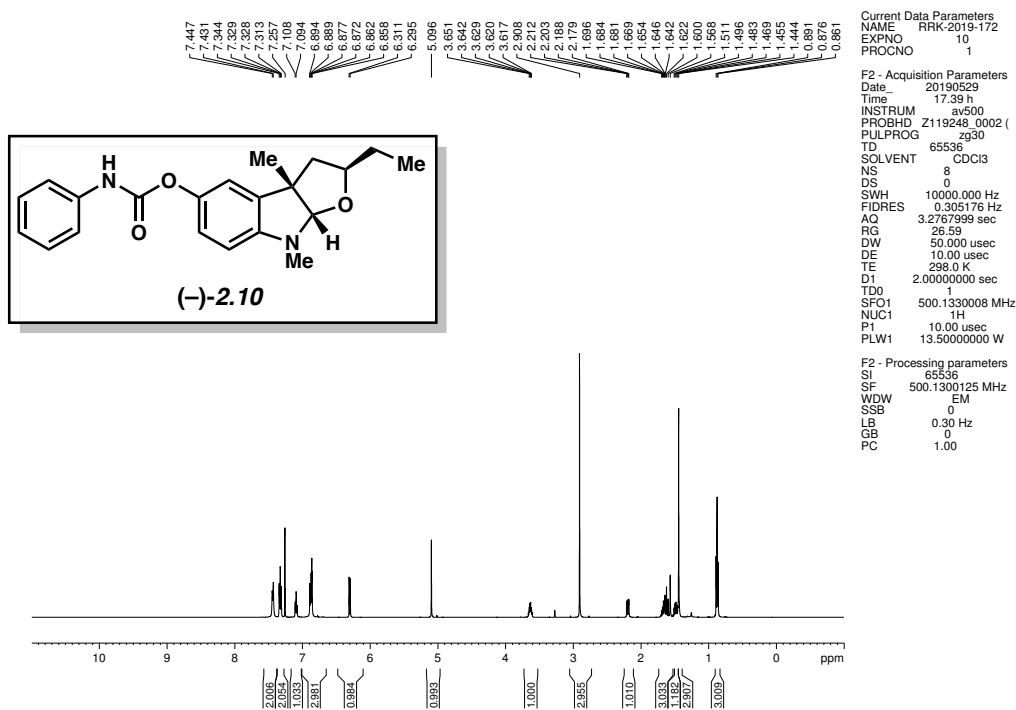
Figure 2.31. ^{1}H NMR (500 MHz, CDCl$_3$) of compound (–)-**2.10**.
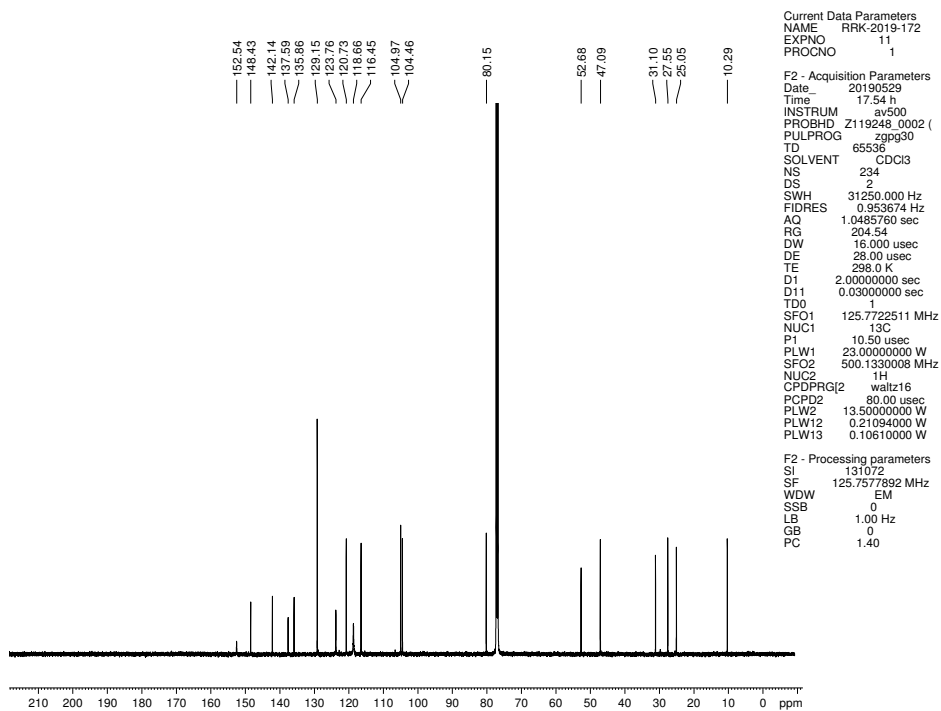
Figure 2.32. ^{13}C NMR (125 MHz, CDCl$_3$) of compound (–)-**2.10**.
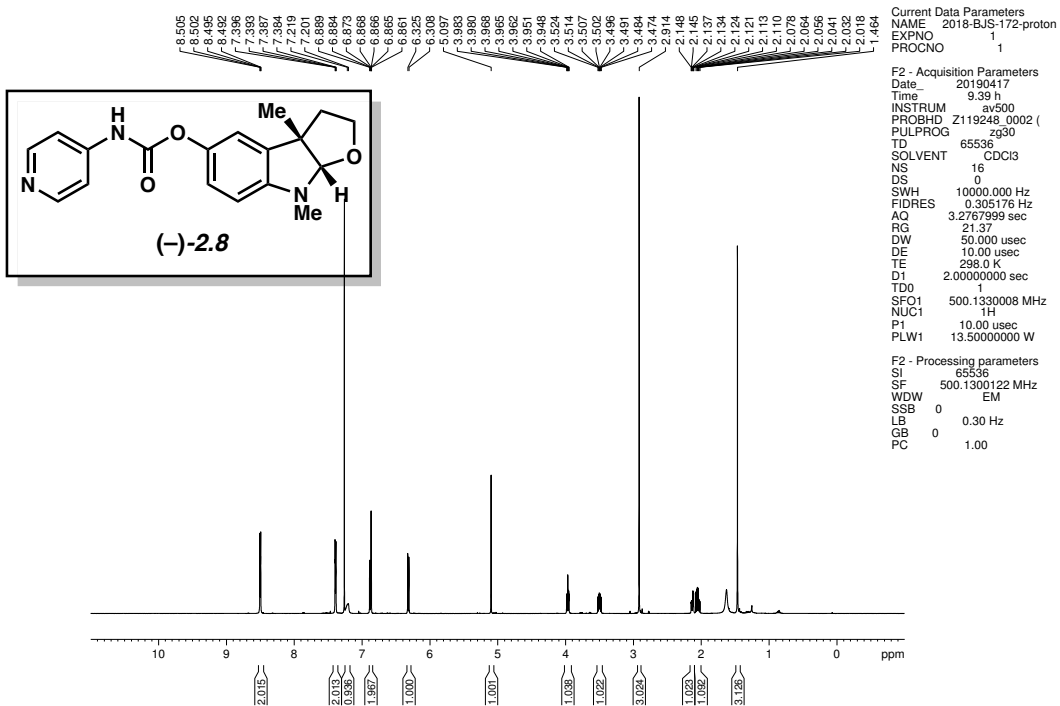
Figure 2.33. ^{1}H NMR (500 MHz, CDCl$_3$) of compound (–)-**2.8**.
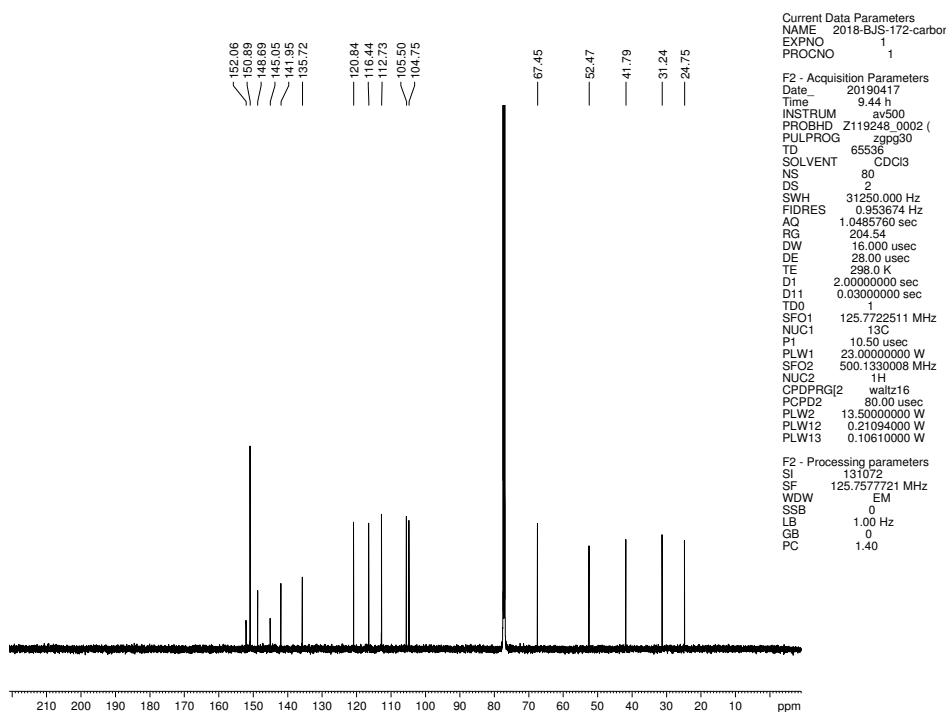
Figure 2.34. ^{13}C NMR (125 MHz, CDCl$_3$) of compound (–)-**2.8**.
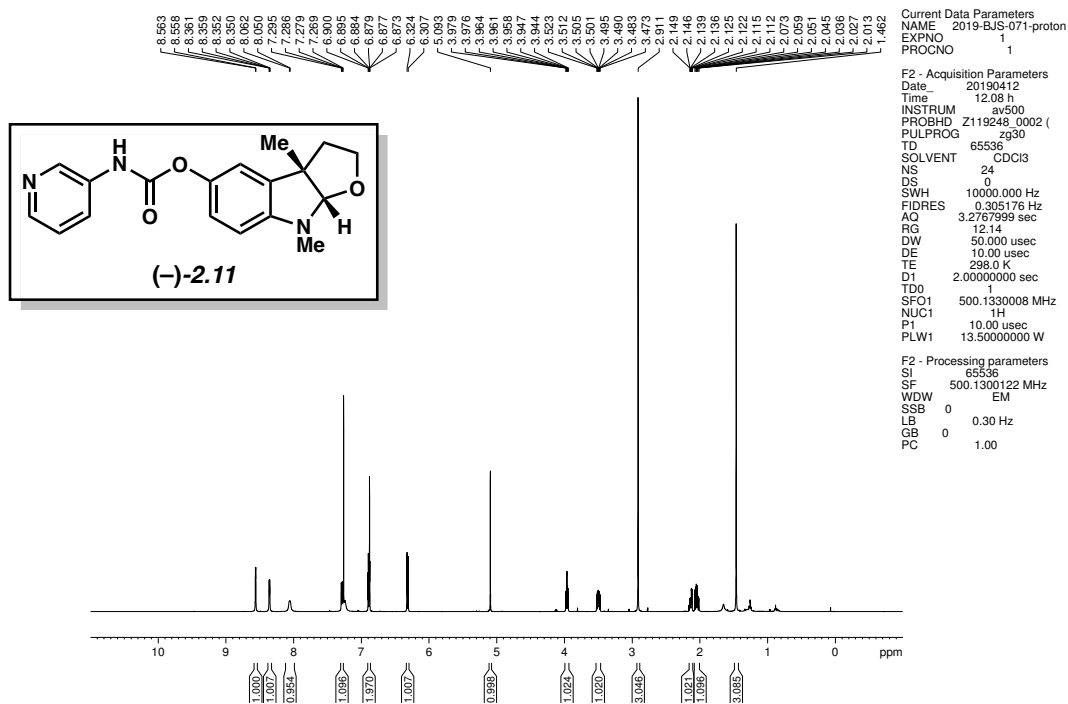
Figure 2.35. ^{1}H NMR (500 MHz, CDCl$_3$) of compound (–)-**2.11**.
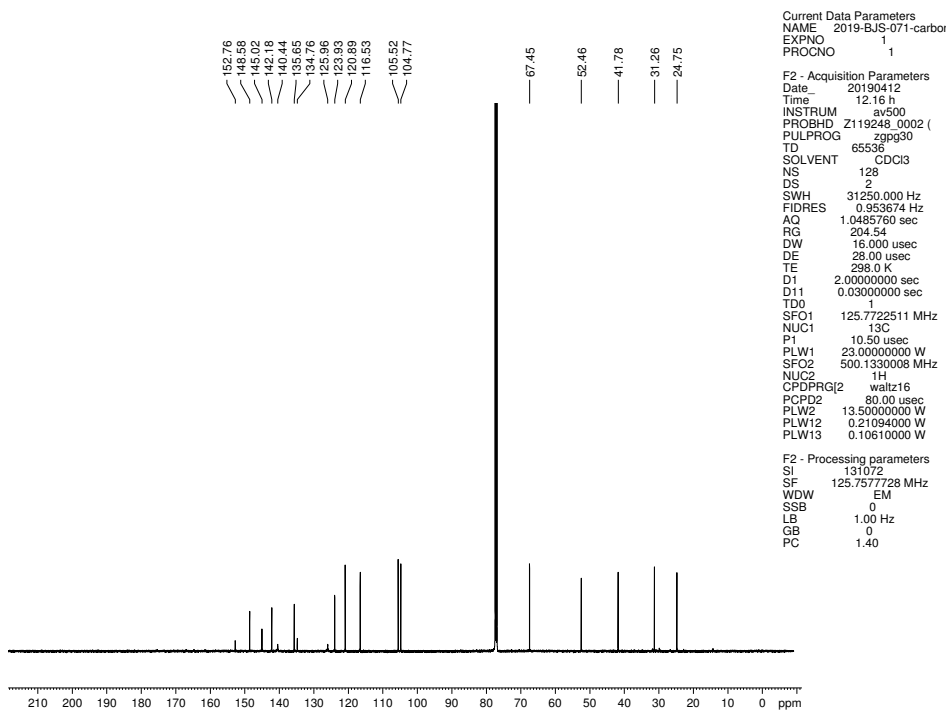
Figure 2.36. ^{13}C NMR (125 MHz, CDCl$_3$) of compound (–)-**2.11**.
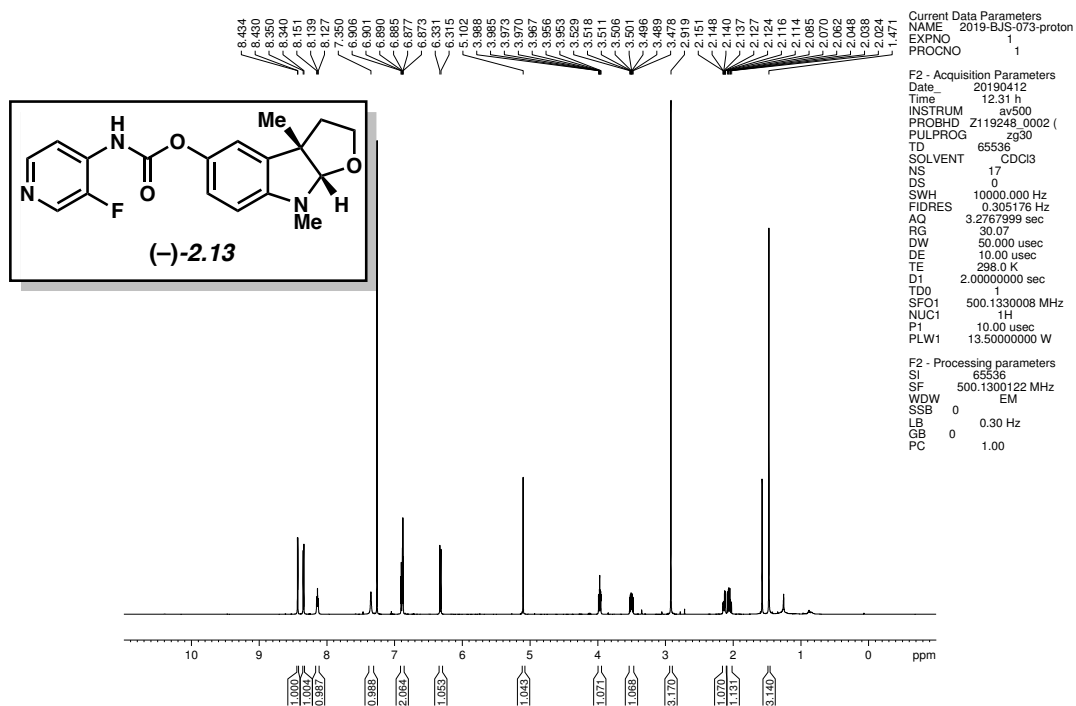
Figure 2.37. ¹H NMR (500 MHz, CDCl₃) of compound (−)-**2.13**.
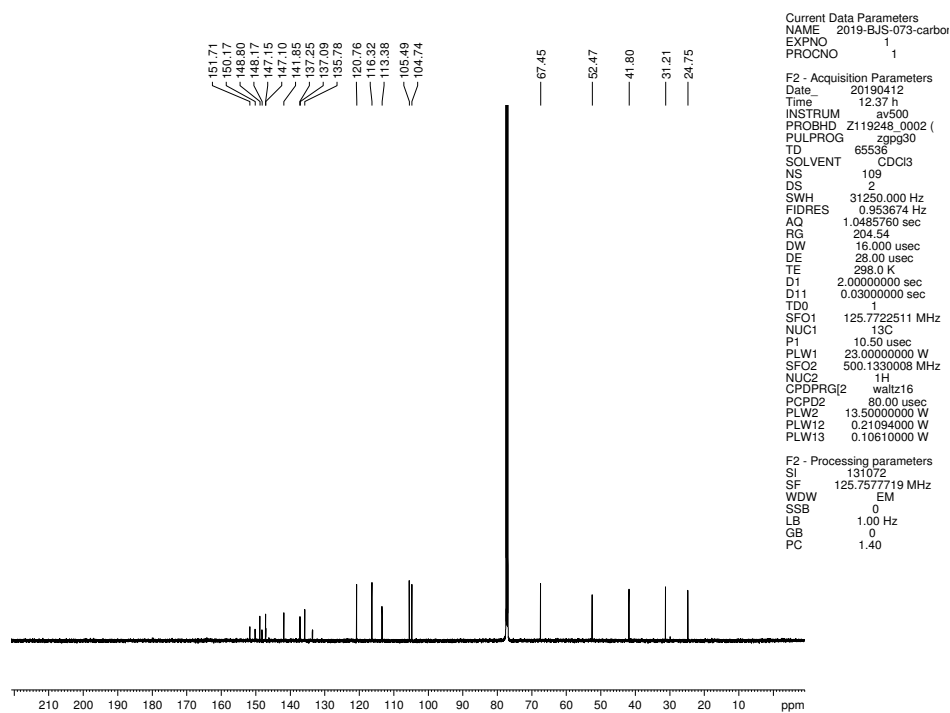
Figure 2.38. ¹³C NMR (125 MHz, CDCl₃) of compound (−)-**2.13**.
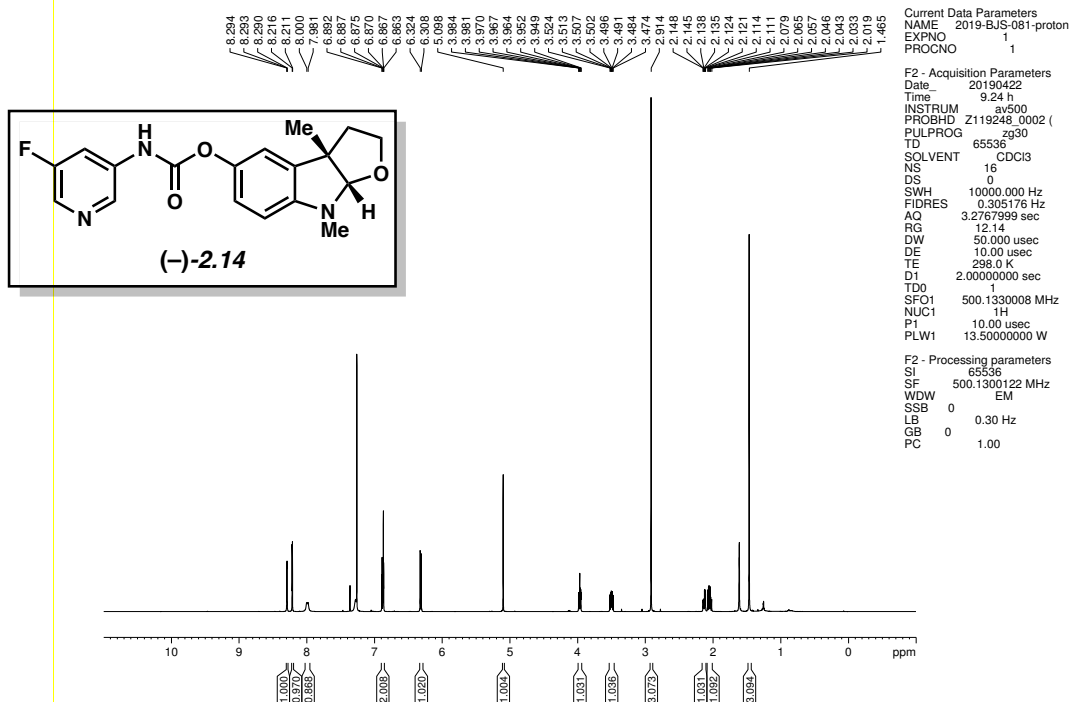
Figure 2.39. ^{1}H NMR (500 MHz, CDCl$_3$) of compound (–)-**2.14**.
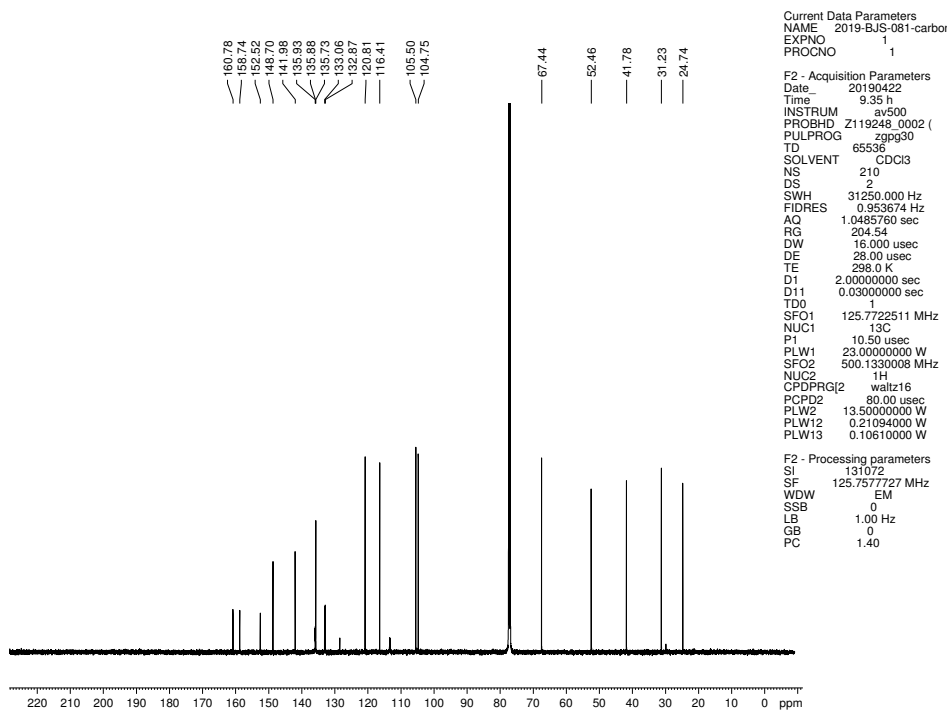
Figure 2.40. ^{13}C NMR (125 MHz, CDCl$_3$) of compound (–)-**2.14**.
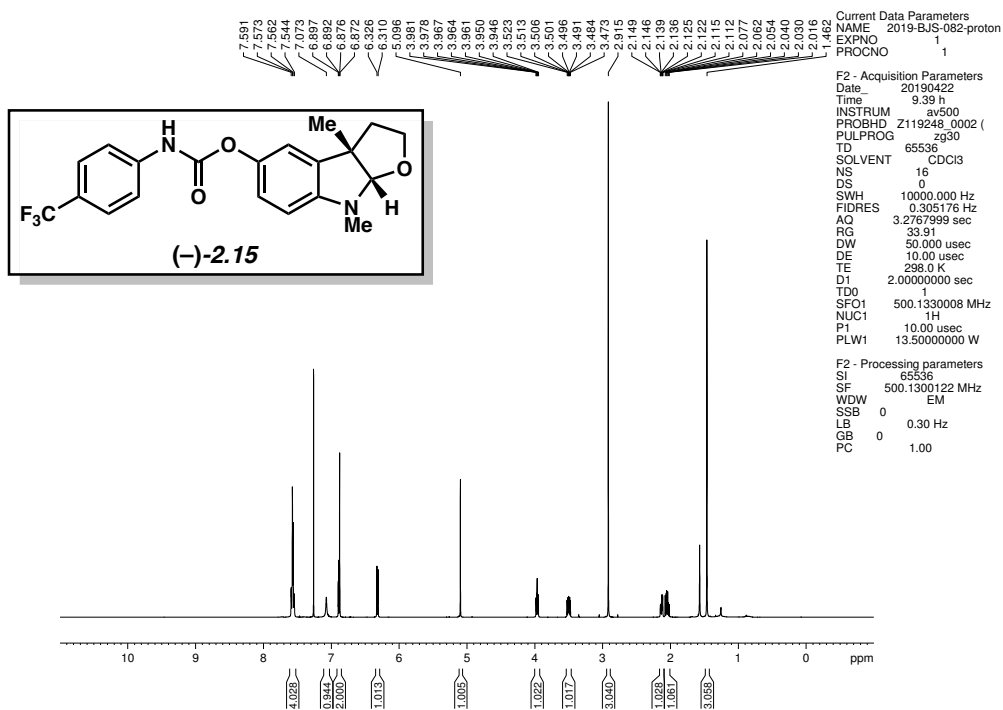
Figure 2.41. ^{1}H NMR (500 MHz, CDCl$_3$) of compound (−)-**2.15**.
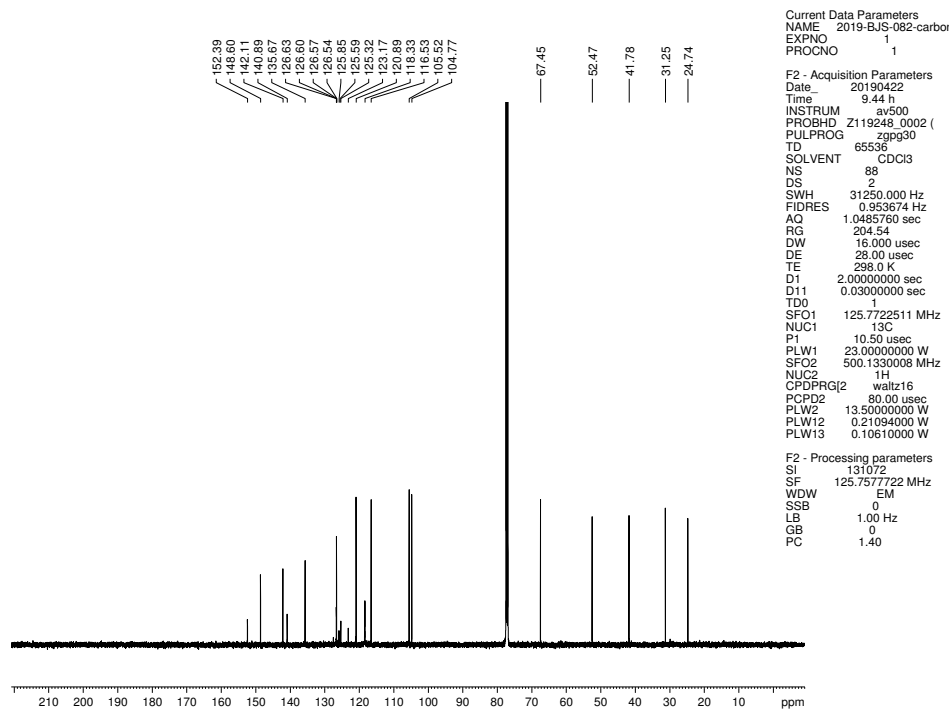
Figure 2.42. ^{13}C NMR (125 MHz, CDCl$_3$) of compound (−)-**2.15**.
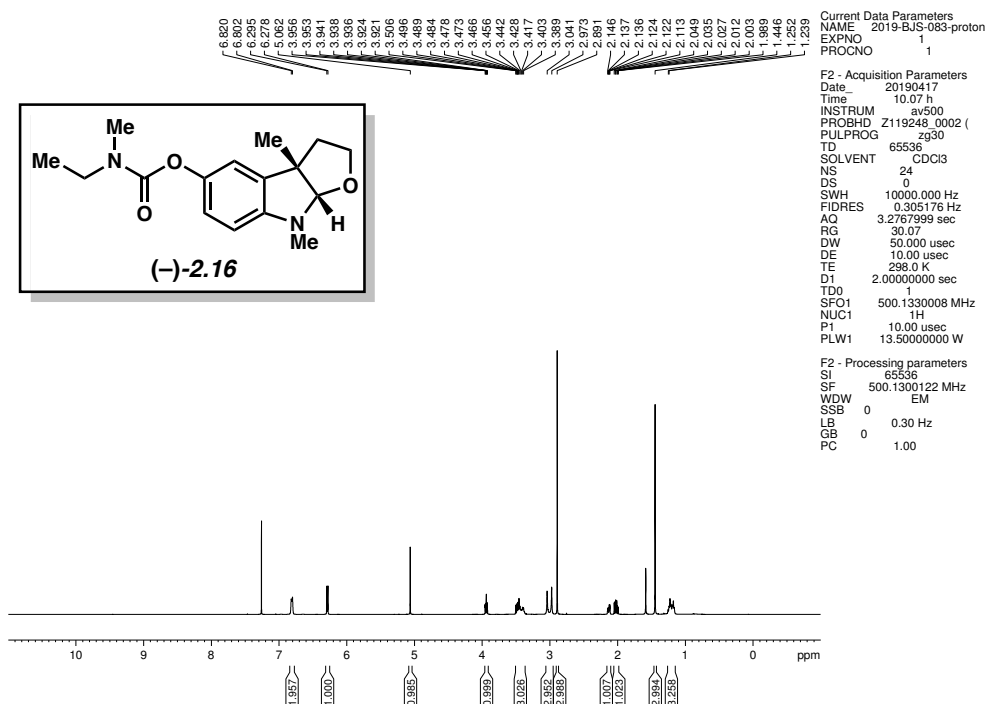
Figure 2.43. ^{1}H NMR (500 MHz, CDCl$_3$) of compound (−)-**2.16**.
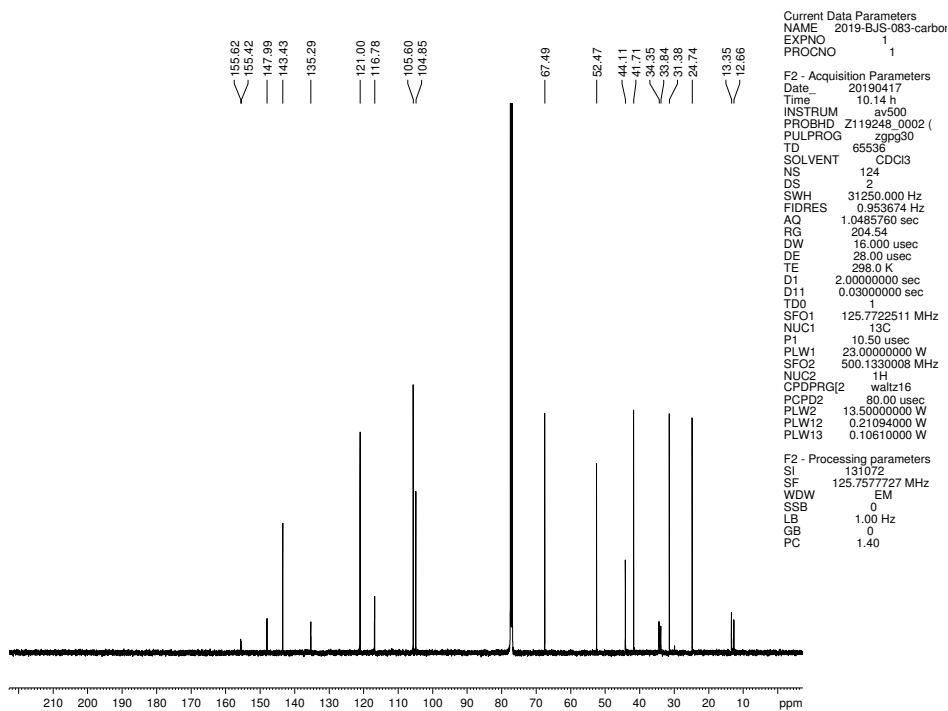
Figure 2.44. ^{13}C NMR (125 MHz, CDCl$_3$) of compound (−)-**2.16**.

2.11 SFC traces for indolines from Schemes 2.1 and 2.3

Figure 2.45 SFC trace (±)-**2.23**.
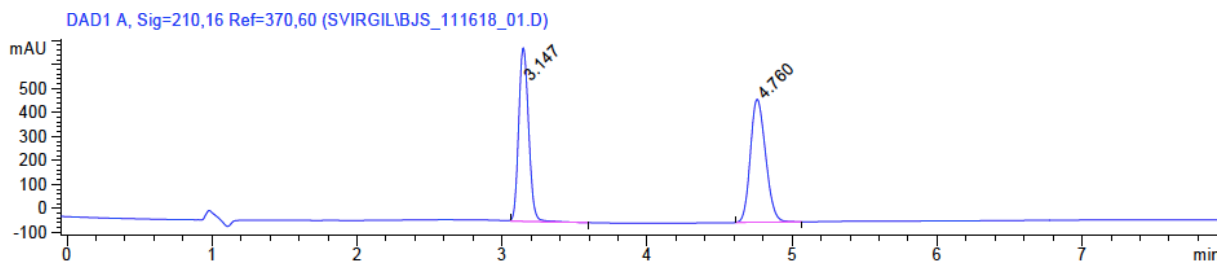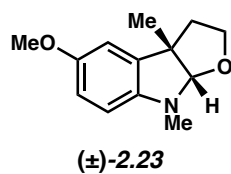
(±)-*2.23*


```
Signal 1: DAD1 A, Sig=210,16 Ref=370,60

Peak  RetTime Type   Width      Area       Height      Area
 #     [min]         [min]    [mAU*s]      [mAU]        %
----|-------|----|-------|----------|----------|--------|
  1    3.147 BB    0.0758 3457.04541  722.88733   47.9548
  2    4.760 BB    0.1134 3751.92603  512.32520   52.0452

Totals :                   7208.97144 1235.21252
```

Figure 2.46 SFC trace (–)-**2.23**.
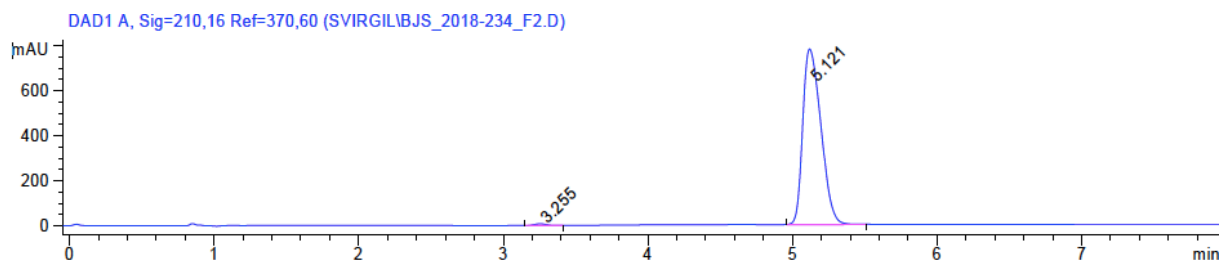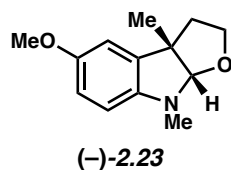
(–)-2.23


```
Signal 1: DAD1 A, Sig=210,16 Ref=370,60

Peak RetTime Type  Width      Area        Height      Area
  #    [min]        [min]    [mAU*s]       [mAU]        %
----|-------|----|-------|----------|----------|--------|
  1   3.255 BB   0.0786    41.17635    8.19597   0.5980
  2   5.121 BB   0.1383  6844.29687  780.64215  99.4020

Totals :                 6885.47323  788.83812
```

Figure 2.47 SFC trace (+)-**2.23**.
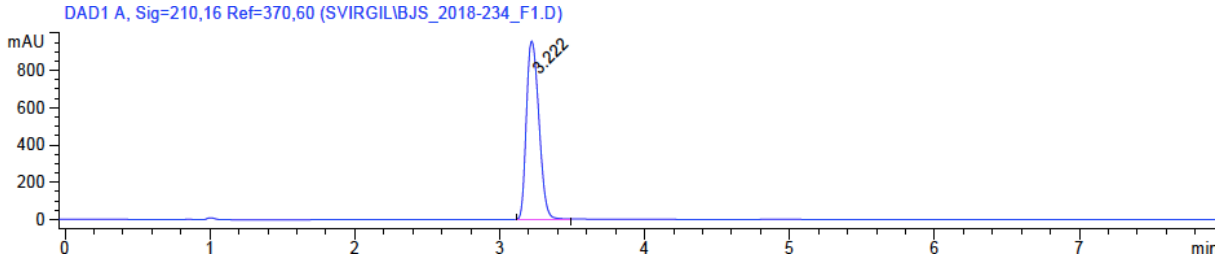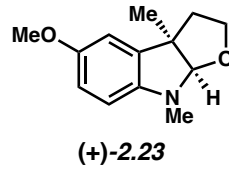
Signal 1: DAD1 A, Sig=210,16 Ref=370,60

```
Peak  RetTime  Type  Width     Area       Height     Area
  #    [min]         [min]    [mAU*s]     [mAU]        %
----|-------|----|-------|----------|----------|--------|
   1   3.222  BB   0.0987  5766.43311  951.53467  100.0000

Totals :                    5766.43311  951.53467
```

Figure 2.48 SFC trace (±)-**2.24**.
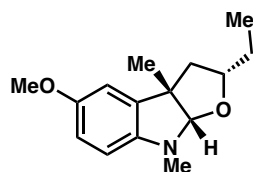
Major
(±)-2.24
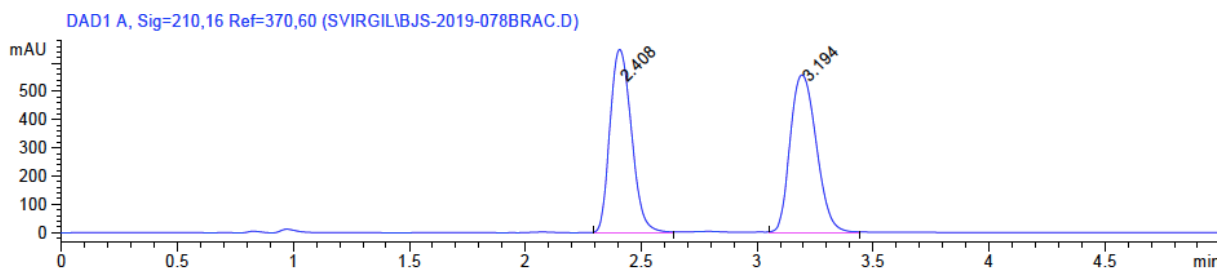

```
Signal 1: DAD1 A, Sig=210,16 Ref=370,60

Peak RetTime Type  Width      Area      Height     Area
  #    [min]        [min]    [mAU*s]     [mAU]        %
----|-------|----|-------|----------|----------|--------|
  1   2.408 BB   0.1033  4190.97412  649.47180  48.7668
  2   3.194 BB   0.1239  4402.93262  558.72266  51.2332

Totals :                 8593.90674 1208.19446
```

Figure 2.49 SFC trace (–)-**2.24**.
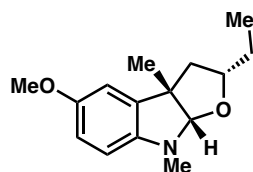
Major
(–)-2.24
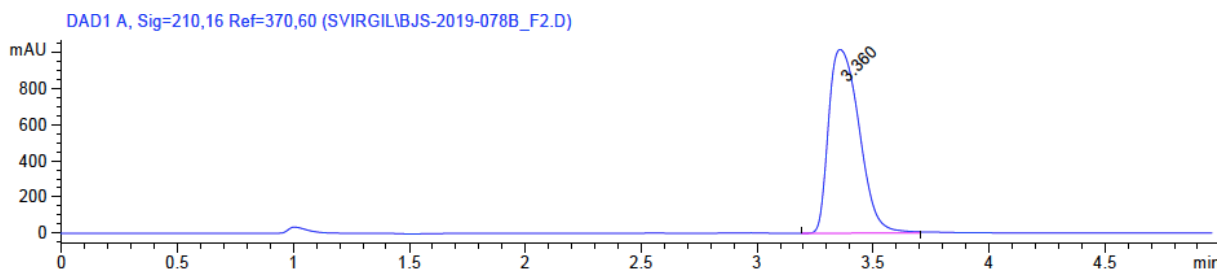
DAD1 A, Sig=210,16 Ref=370,60 (SVIRGIL\BJS-2019-078B_F2.D)

Signal 1: DAD1 A, Sig=210,16 Ref=370,60

```
Peak RetTime Type  Width     Area       Height      Area
  #    [min]        [min]    [mAU*s]      [mAU]        %
----|-------|----|-------|----------|----------|--------|
  1   3.360  BB   0.1514  9338.61230 1014.26447 100.0000

Totals :                  9338.61230 1014.26447
```

Figure 2.50 SFC trace (+)-**2.24**.
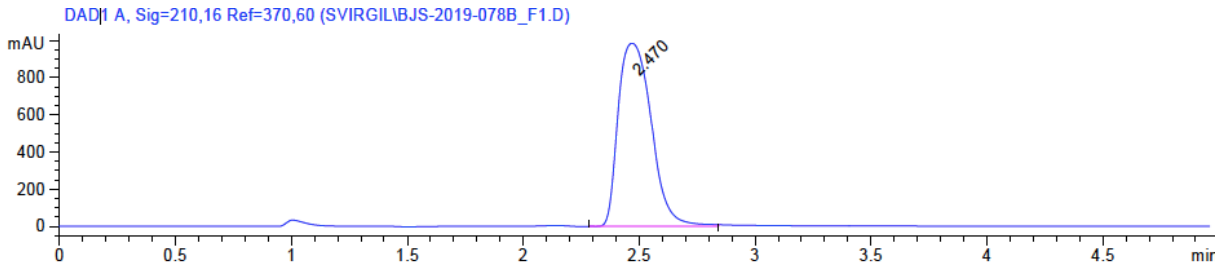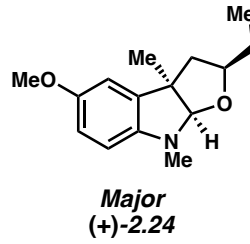
Major
(+)-*2.24*


```
Signal 1: DAD1 A, Sig=210,16 Ref=370,60

Peak RetTime Type  Width     Area      Height     Area
  #   [min]        [min]    [mAU*s]     [mAU]        %
----|-------|----|-------|----------|----------|--------|
  1   2.470 BB   0.1641 9798.25195  984.58337 100.0000

Totals :                  9798.25195  984.58337
```

Figure 2.51 SFC trace (±)-**2.25**.

Minor
(±)-**2.25**

DAD1 A, Sig=210,16 Ref=370,60 (SVIRGIL\BJS-2019-078TRAC.D)

Peak #	RetTime [min]	Type	Width [min]	Area [mAU*s]	Height [mAU]	Area %
1	2.060	BV	0.0900	3335.05176	589.90735	48.0223
2	2.409	VB	0.0988	76.34533	11.91408	1.0993
3	2.806	BB	0.1122	3460.48657	503.63641	49.8285
4	3.208	BB	0.1179	72.91069	9.46369	1.0499

Totals : 6944.79435 1114.92154

Figure 2.52 SFC trace (–)-**2.25**.

Minor
(–)-**2.25**

DAD1 A, Sig=210,16 Ref=370,60 (SVIRGIL\BJS-2019-078T_F2.D)

Signal 1: DAD1 A, Sig=210,16 Ref=370,60

```
Peak RetTime Type  Width      Area         Height       Area
 #    [min]        [min]    [mAU*s]        [mAU]          %
----|-------|----|-------|----------|----------|--------|
  1   2.920 BB    0.1222  6548.78320  847.27545 100.0000

Totals :                  6548.78320  847.27545
```

Figure 2.53 SFC trace (+)-**2.25**.

Minor
(+)-2.25

DAD1 A, Sig=210,16 Ref=370,60 (SVIRGIL\BJS-2019-078T_F1.D)

```
Signal 1: DAD1 A, Sig=210,16 Ref=370,60

Peak RetTime Type  Width      Area        Height      Area
 #    [min]        [min]    [mAU*s]       [mAU]        %
----|-------|----|-------|----------|----------|--------|
  1   2.118 BB   0.1014 5765.91357  915.86670 100.0000

Totals :                  5765.91357  915.86670
```

2.12 Biological Assays, Modeling & Permeability

Experimental details regarding biological assays, modeling and permeability studies were reported

in the literature.[60]

2.13 Notes and References

(1) El-Hayek, Y. H.; Wiley, R. E.; Khoury, C. P.; Daya, R. P.; Ballard, C.; Evans, A. R.; Karran, M.; Molinuevo, J. L.; Norton, M.; Atri, A. Tip of the iceberg: assessing the global socioeconomic costs of Alzheimer's disease and related dementias and strategic implications for stakeholders. *J. of Alzheimer's D.* **2019**, *70*, 323–341.

(2) Serrano-Pozo, A.; Frosch, M. P.; Masliah, E.; Hyman, B. T. Neuropathological alterations in Alzheimer disease. *Cold Spring Harbor Perspect. Med.* **2011**, *1*, a006189.

(3) Masters, C. L.; Bateman, R.; Blennow, K.; Rowe, C. C.; Sperling, R. A.; Cummings, J. L. Alzheimer's disease. *Nat. Rev. Dis. Primers* **2015**, *1*, 15056–15064.

(4) Olivieri, P.; Lagarde, J.; Lehericy, S.; Valabrègue, R.; Michel, A.; Macé, P.; Caillé, F.; Gervais, P.; Bottlaender, M.; Sarazin, M. Early alteration of the locus coeruleus in phenotypic variants of Alzheimer's disease. *Ann. Clin. Transl. Neurol.* **2019**, *6*, 1345–1351.

(5) Costandi, M. Ways to stop the spread of Alzheimer's disease. *Nature* **2018**, *559*, S16–S17.

(6) Selkoe, D. J.; Hardy, J. The amyloid hypothesis of Alzheimer's disease at 25 years. *EMBO Mol. Med.* **2016**, *8*, 595–608.

(7) Hardy, J.; Selkoe, D. J., The amyloid hypothesis of Alzheimer's disease: progress and problems on the road to therapeutics. *Science* **2002**, *297*, 353–356.

(8) Nelson, P. T.; Alafuzoff, I.; Bigio, E. H.; Bouras, C.; Braak, H.; Cairns, N. J.; Castellani, R. J.; Crain, B. J.; Davies, P.; Del Tredici, K.; Duyckaerts, C.; Frosch, M. P.; Haroutunian, V.; Hof, P. R.; Hulette, C. M.; Hyman, B. T.; Iwatsubo, T.; Jellinger, K. A.; Jicha, G. A.; Kovari, E.; Kukull, W. A.; Leverenz, J. B.; Love, S.; Mackenzie, I. R.; Mann, D. M.; Masliah, E.; McKee, A. C.; Montine, T. J.; Morris, J. C.; Schneider, J. A.; Sonnen, J. A.; Thal, D. R.; Trojanowski, J. Q.; Troncoso, J. C.; Wisniewski, T.; Woltjer, R. L.; Beach, T. G. Correlation of Alzheimer

disease neuropathologic changes with cognitive status: a review of the literature. *J. Neuropathol. Exp. Neurol.* **2012**, *71*, 362–681.

(9) Johnson, K. A.; Schultz, A.; Betensky, R. A.; Becker, J. A.; Sepulcre, J.; Rentz, D.; Mormino, E.; Chhatwal, J.; Amariglio, R.; Papp, K.; Marshall, G.; Albers, M.; Mauro, S.; Pepin, L.; Alverio, J.; Judge, K.; Philiossaint, M.; Shoup, T.; Yokell, D.; Dickerson, B.; Gomez-Isla, T.; Hyman, B.; Vasdev, N.; Sperling, R. Tau positron emission tomographic imaging in aging and early Alzheimer disease. *Ann. Neurol.* **2016**, *79*, 110–119.

(10) Pontecorvo, M. J.; Devous, M. D., Sr.; Navitsky, M.; Lu, M.; Salloway, S.; Schaerf, F. W.; Jennings, D.; Arora, A. K.; McGeehan, A.; Lim, N. C.; Xiong, H.; Joshi, A. D.; Siderowf, A.; Mintun, M. A.; investigators, F. A.-A. Relationships between flortaucipir PET tau binding and amyloid burden, clinical diagnosis, age and cognition. *Brain* **2017**, *140*, 748–763.

(11) Kametani, F.; Hasegawa, M., Reconsideration of amyloid hypothesis and tau hypothesis in Alzheimer's disease. *Front. Neurosci.* **2018**, *12*, 25–36.

(12) Ishiki, A.; Okamura, N.; Furukawa, K.; Furumoto, S.; Harada, R.; Tomita, N.; Hiraoka, K.; Watanuki, S.; Ishikawa, Y.; Tago, T.; Funaki, Y.; Iwata, R.; Tashiro, M.; Yanai, K.; Kudo, Y.; Arai, H. Longitudinal assessment of tau pathology in patients with Alzheimer's disease using [18F]THK-5117 positron emission tomography. *PloS One* **2015**, *10*, e0140311–e0140321.

(13) Chiotis, K.; Saint-Aubert, L.; Rodriguez-Vieitez, E.; Leuzy, A.; Almkvist, O.; Savitcheva, I.; Jonasson, M.; Lubberink, M.; Wall, A.; Antoni, G.; Nordberg, A. Longitudinal changes of tau PET imaging in relation to hypometabolism in prodromal and Alzheimer's disease dementia. *Mol. Psychiatry* **2018**, *23*, 1666–1673.

(14) Bilousova, T.; Elias, C.; Miyoshi, E.; Alam, M. P.; Zhu, C.; Campagna, J.; Vadivel, K.; Jagodzinska, B.; Gylys, K. H.; John, V. Suppression of tau propagation using an inhibitor that targets the DK-switch of nSMase2. *Biochem. Biophys. Res. Comm.* **2018**, *499*, 751–757.

(15) Asai, H.; Ikezu, S.; Tsunoda, S.; Medalla, M.; Luebke, J.; Haydar, T.; Wolozin, B.; Butovsky, O.; Kugler, S.; Ikezu, T. Depletion of microglia and inhibition of exosome synthesis halt tau propagation. *Nat. Neurosci.* **2015**, *18*, 1584–1593.

(16) Dinkins, M. B.; Dasgupta, S.; Wang, G.; Zhu, G.; Bieberich, E. Exosome reduction in vivo is associated with lower amyloid plaque load in the 5XFAD mouse model of Alzheimer's disease. *Neurobiol. Aging* **2014**, *35*, 1792–1800.

(17) Dinkins, M. B.; Enasko, J.; Hernandez, C.; Wang, G.; Kong, J.; Helwa, I.; Liu, Y.; Terry, A. V., Jr.; Bieberich, E. Neutral sphingomyelinase-2 deficiency ameliorates Alzheimer's disease pathology and improves cognition in the 5XFAD mouse. *J. Neurosci.* **2016**, *36*, 8653–8667.

(18) Wheeler, D.; Knapp, E.; Bandaru, V. V.; Wang, Y.; Knorr, D.; Poirier, C.; Mattson, M. P.; Geiger, J. D.; Haughey, N. J. Tumor necrosis factor-alpha-induced neutral sphingomyelinase-2 modulates synaptic plasticity by controlling the membrane insertion of NMDA receptors. *J. Neurochem.* **2009**, *109*, 1237–1249.

(19) Tabatadze, N.; Savonenko, A.; Song, H.; Bandaru, V. V.; Chu, M.; Haughey, N. J. Inhibition of neutral sphingomyelinase-2 perturbs brain sphingolipid balance and spatial memory in mice. *J. Neurosci. Res.* **2010**, *88*, 2940–2951.

(20) Tan, L. H.; Tan, A. J.; Ng, Y. Y.; Chua, J. J.; Chew, W. S.; Muralidharan, S.; Torta, F.; Dutta, B.; Sze, S. K.; Herr, D. R.; Ong, W. Y. Enriched expression of neutral sphingomyelinase 2 in the striatum is essential for regulation of lipid raft content and motor coordination. *Mol. Neurobiol.* **2018**, *55*, 5741–5756.

(21) Stoffel, W.; Jenke, B.; Schmidt-Soltau, I.; Binczek, E.; Brodesser, S.; Hammels, I. SMPD3 deficiency perturbs neuronal proteostasis and causes progressive cognitive impairment. *Cell Death Dis*. **2018**, *9*, 507–521.

(22) Babenko, N. A.; Shakhova, E. G. Long-term food restriction prevents aging-associated sphingolipid turnover dysregulation in the brain. *Arch. Gerontol. Geriatr*. **2014**, *58*, 420–426.

(23) Filippov, V.; Song, M. A.; Zhang, K.; Vinters, H. V.; Tung, S.; Kirsch, W. M.; Yang, J.; Duerksen-Hughes, P. J. Increased ceramide in brains with Alzheimer's and other neurodegenerative diseases. *J. Alzheimer's Dis*. **2012**, *29*, 537–547.

(24) Bandaru, V. V.; Troncoso, J.; Wheeler, D.; Pletnikova, O.; Wang, J.; Conant, K.; Haughey, N. J. ApoE4 disrupts sterol and sphingolipid metabolism in Alzheimer's but not normal brain. *Neurobiol. Aging* **2009**, *30*, 591–599.

(25) Trajkovic, K.; Hsu, C.; Chiantia, S.; Rajendran, L.; Wenzel, D.; Wieland, F.; Schwille, P.; Brugger, B.; Simons, M., Ceramide triggers budding of exosome vesicles into multivesicular endosomes. *Science* **2008**, *319*, 1244–1247.

(26) Thery, C. Exosomes: secreted vesicles and intercellular communications. *F1000 Bio. Rep*. **2011**, *3*, 15–23.

(27) Guo, B. B.; Bellingham, S. A.; Hill, A. F. The neutral sphingomyelinase pathway regulates packaging of the prion protein into exosomes. *J. Biol. Chem*. **2015**, *290*, 3455–3467.

(28) Simon, D.; Garcia-Garcia, E.; Royo, F.; Falcon-Perez, J. M.; Avila, J. Proteostasis of tau. Tau overexpression results in its secretion via membrane vesicles. *FEBS Lett*. **2012**, *586*, 47–54.

(29) Polanco, J. C.; Scicluna, B. J.; Hill, A. F.; Gotz, J. Extracellular vesicles isolated from brains of rTg4510 mice seed tau aggregation in a threshold-dependent manner. *J. Biol. Chem*. **2016**, *291*, 12445–12466.

(30) Wang, Y.; Balaji, V.; Kaniyappan, S.; Kruger, L.; Irsen, S.; Tepper, K.; Chandupatla, R.; Maetzler, W.; Schneider, A.; Mandelkow, E.; Mandelkow, E. M. The release and trans-synaptic transmission of Tau via exosomes. *Mol. Neurodegener.* **2017**, *12*, 5–30.

(31) Fiandaca, M. S.; Kapogiannis, D.; Mapstone, M.; Boxer, A.; Eitan, E.; Schwartz, J. B.; Abner, E. L.; Petersen, R. C.; Federoff, H. J.; Miller, B. L.; Goetzl, E. J. Identification of preclinical Alzheimer's disease by a profile of pathogenic proteins in neurally derived blood exosomes: A case-control study. *Alzheimers Dement.* **2015**, *11*, 600–607.

(32) Abner, E. L.; Jicha, G. A.; Shaw, L. M.; Trojanowski, J. Q.; Goetzl, E. J. Plasma neuronal exosomal levels of Alzheimer's disease biomarkers in normal aging. *Annals of clinical and translational neurology* **2016**, *3*, 399–403.

(33) Saman, S.; Kim, W.; Raya, M.; Visnick, Y.; Miro, S.; Saman, S.; Jackson, B.; McKee, A. C.; Alvarez, V. E.; Lee, N. C.; Hall, G. F. Exosome-associated tau is secreted in tauopathy models and is selectively phosphorylated in cerebrospinal fluid in early Alzheimer disease. *J. Biol. Chem.* **2012**, *287*, 3842–3849.

(34) Rojas, C.; Barnaeva, E.; Thomas, A. G.; Hu, X.; Southall, N.; Marugan, J.; Chaudhuri, A. D.; Yoo, S. W.; Hin, N.; Stepanek, O.; Wu, Y.; Zimmermann, S. C.; Gadiano, A. G.; Tsukamoto, T.; Rais, R.; Haughey, N.; Ferrer, M.; Slusher, B. S. DPTIP, a newly identified potent brain penetrant neutral sphingomyelinase 2 inhibitor, regulates astrocyte-peripheral immune communication following brain inflammation. *Scil. Rep.* **2018**, *8*, 17715–17726.

(35) Rojas, C.; Sala, M.; Thomas, A. G.; Datta Chaudhuri, A.; Yoo, S. W.; Li, Z.; Dash, R. P.; Rais, R.; Haughey, N. J.; Nencka, R.; Slusher, B. A novel and potent brain penetrant inhibitor of extracellular vesicle release. *British J. Pharmacol.* **2019**, *176*, 3857–3870.

(36) Mehta, M.; Adem, A.; Sabbagh, M. New acetylcholinesterase inhibitors for Alzheimer's disease. *Int. J. Alzheimers Dis.* **2012**, *2012*, 728983–728991.

(37) Maurer, S. V.; Williams, C. L. The cholinergic system modulates memory and hippocampal plasticity via its interactions with non-neuronal cells. *Front. Immunol.* **2017**, *8*, 1489–1503.

(38) Morozova, V.; Cohen, L. S.; Makki, A. E.; Shur, A.; Pilar, G.; El Idrissi, A.; Alonso, A. D. Normal and pathological tau uptake mediated by M1/M3 muscarinic receptors promotes opposite neuronal changes. *Front. Cell Neurosci.* **2019**, *13*, 403–415.

(39) Brunello, C.A.; Merezhko, M; Uronen, R.-L.; Huttunen, H.J. Mechanisms of secretion and spreading of pathological tau protein. *Cell. Mol. Life Sci.* **2019**, 1–24.

(40) Simmons, B. J.; Hoffmann, M.; Champagne, P. A.; Picazo, E.; Yamakawa, K.; Morrill, L. A.; Houk, K. N.; Garg, N. K. Understanding and interrupting the Fischer azaindolization reaction. *J. Am.Chem. Soc.* **2017**, *139*, 14833–14836; see also references therein.

(41) Luo, W.; Yu, Q.S.; Kulkarni, S.S.; Parrish, D.A.; Holloway, H.W.; Tweedie, D.; Shafferman, A.; Lahiri, D.K.; Brossi, A.; Greig, N. Inhibition of human acetyk and butyrylcholineesterase by novel carbamates of (–) and (+) tetrahydrofurobenzofuran and methanobenzodioxwpine. *J. Med. Chem.* **2006**, *49*, 2174–2185.

(42) Santillo, M. F.; Liu, Y. A fluorescence assay for measuring acetylcholinesterase activity in rat blood and a human neuroblastoma cell line (SH-SY5Y). *J. Pharmacol. Toxicol. Methods* **2015**, *76*, 15–22.

(43) Airola, M. V.; Shanbhogue, P.; Shamseddine, A. A.; Guja, K. E.; Senkal, C. E.; Maini, R.; Bartke, N.; Wu, B. X.; Obeid, L. M.; Garcia-Diaz, M.; Hannun, Y. A. Structure of human nSMase2 reveals an interdomain allosteric activation mechanism for ceramide generation. *Proc. Natl. Acad. of Sci.* **2017**, *114*, e5549–e5558.

(44) Park, S. J.; Kim, J. M.; Kim, J.; Hur, J.; Park, S.; Kim, K.; Shin, H.-J.; Chwae, Y.-J. Molecular mechanisms of biogenesis of apoptotic exosome-like vesicles and their roles as damage-associated molecular patterns. *Proc. Natl. Acad. of Sci.* **2018**, *115*, e11721–e11730.

(45) Zhang, X.-J.; Greenberg, D. S. Acetylcholinesterase involvement in apoptosis. *Front. Mol. Neurosci.* **2012**, *5*, 40–46.

(46) Nalivaeva, N. N.; Rybakina, E. G.; Pivanovich, I.; Kozinets, I. A.; Shanin, S. N.; Bartfai, T. Activation of neutral sphingomyelinase by IL-1beta requires the type 1 interleukin 1 receptor. *Cytokine* **2000**, *12*, 229–232.

(47) Yoshiyama, Y.; Higuchi, M.; Zhang, B.; Huang, S. M.; Iwata, N.; Saido, T. C.; Maeda, J.; Suhara, T.; Trojanowski, J. Q.; Lee, V. M. Synapse loss and microglial activation precede tangles in a P301S tauopathy mouse model. *Neuron* **2007**, *53*, 337–351.

(48) Kitazawa, M.; Cheng, D.; Tsukamoto, M. R.; Koike, M. A.; Wes, P. D.; Vasilevko, V.; Cribbs, D. H.; LaFerla, F. M. Blocking IL-1 signaling rescues cognition, attenuates tau pathology, and restores neuronal beta-catenin pathway function in an Alzheimer's disease model. *J. Immunol.* **2011**, *187*, 6539–6549.

(49) Ghosh, S.; Wu, M. D.; Shaftel, S. S.; Kyrkanides, S.; LaFerla, F. M.; Olschowka, J. A.; O'Banion, M. K. Sustained interleukin-1beta overexpression exacerbates tau pathology despite reduced amyloid burden in an Alzheimer's mouse model. *J. Neurosci.* **2013**, *33*, 5053–5064.

(50) Dickens, A. M.; Tovar-y-Romo, L. B.; Yoo, S.-W.; Trout, A. L.; Bae, M.; Kanmogne, M.; Megra, B.; Williams, D. W.; Witwer, K. W.; Gacias, M.; Tabatadze, N.; Cole, R. N.; Casaccia, P.; Berman, J. W.; Anthony, D. C.; Haughey, N. J. Astrocyte-shed extracellular vesicles

regulate the peripheral leukocyte response to inflammatory brain lesions. *Sci. Signal.* **2017**, *10*, eaai7696–7708.

(51) Vella, L. J.; Scicluna, B. J.; Cheng, L.; Bawden, E. G.; Masters, C. L.; Ang, C. S.; Willamson, N.; McLean, C.; Barnham, K. J.; Hill, A. F. A rigorous method to enrich for exosomes from brain tissue. *J. Extracell. Vesicles* **2017**, *6*, 1348885–1348898.

(52) Baietti, M. F.; Zhang, Z.; Mortier, E.; Melchior, A.; Degeest, G.; Geeraerts, A.; Ivarsson, Y.; Depoortere, F.; Coomans, C.; Vermeiren, E.; Zimmermann, P.; David, G. Syndecan-syntenin-ALIX regulates the biogenesis of exosomes. *Nat. Cell Biol.* **2012**, *14*, 677–685.

(53) Liu, X.; Nemeth, D. P.; McKim, D. B.; Zhu, L.; DiSabato, D. J.; Berdysz, O.; Gorantla, G.; Oliver, B.; Witcher, K. G.; Wang, Y.; Negray, C. E.; Vegesna, R. S.; Sheridan, J. F.; Godbout, J. P.; Robson, M. J.; Blakely, R. D.; Popovich, P. G.; Bilbo, S. D.; Quan, N., Cell-type-specific interleukin 1 receptor 1 signaling in the brain regulates distinct neuroimmune activities. *Immunity* **2019**, *50*, 317–333.

(54) Jungblut, M., Tiveron, M. C., Barral, S., Abrahamsen, B., Knobel, S., Pennartz, S., Schmitz, J., Perraut, M., Pfrieger, F. W., Stoffel, W., Cremer, H., and Bosio, A. Isolation and characterization of living primary astroglial cells using the new GLAST-specific monoclonal antibody ACSA-1. *Glia* **2012**, *60*, 894–907.

(55) Maphis, N.; Xu, G.; Kokiko-Cochran, O. N.; Jiang, S.; Cardona, A.; Ransohoff, R. M.; Lamb, B. T.; Bhaskar, K. Reactive microglia drive tau pathology and contribute to the spreading of tau in the brain. *Brain* **2015**, *138*, 1738–1755.

(56) Crotti, A.; Sait, H. R.; McAvoy, K. M.; Estrada, K.; Ergun, A.; Szak, S.; Marsh, G.; Jandreski, L.; Peterson, M.; Reynolds, T. L.; Dalkilic-Liddle, I.; Cameron, A.; Cahir-McFarland, E.;

Ransohoff, R. M. BIN1 favors the spreading of Tau via extracellular vesicles. *Sci. Rep.* **2019**, *9*, 9477–9497.

(57) Schammel, A. W.; Boal, B. W.; Zu, L.; Mesganaw, T.; Garg, N. K. *Tetrahedron* **2010**, *66*, 4687–4695.

(58) Sudhakar, G.; Satish, K.; Raghavaiah, J. *J. Org. Chem.* **2012**, *77*, 10010–10020.

(59) Yu, Q.-S.; Liu, C.; Brzostowska, M.; Chrisey, L.; Brossi, A.; Greig, N. H.; Atack, J. R.; Soncrant, T. T.; Rapoport, S. I.; Radunz, H.-E. *Helv. Chim. Acta.* **1991**, *74*, 761–766.

(60) Bilousova,T.; Simmons, B. J.; Knapp, R. R.; Elias, C. J.; Campagna, J.; Melnik, M.; Chandra, S.; Focht, S.; Zhu, C.; Vadivel, K.; Jagodzinska, B.; Cohn, W.; Spilman, P.; Gylys, K. H.; Garg, N. K.; John, V. *ACS Chem. Biol.* **2020**, *15*, 1671–1684.

CHAPTER THREE

Cyanoamidine Cyclization Approach to Remdesivir's Nucleobase

Rachel R. Knapp,[†] Veronica Tona,[†] Taku Okada, Richmond Sarpong,* and Neil K. Garg*

3.1 Abstract

We report an alternative approach to the unnatural nucleobase fragment seen in Remdesivir (Veklury®). Remdesivir displays broad-spectrum antiviral activity and is currently being evaluated in Phase III clinical trials to treat patients with COVID-19. Our route relies on the formation of a cyanoamidine intermediate, which undergoes Lewis acid-mediated cyclization to yield the desired nucleobase. The approach is strategically distinct from prior routes and could further enable the synthesis of Remdesivir and other small molecule therapeutics.

3.2 Introduction

The ongoing COVID-19 pandemic has prompted a remarkable response from the scientific community.[1] In roughly six months, numerous breakthroughs have been disclosed in testing,[2] vaccinations,[3] small molecule therapeutics,[4,5] and other areas.[6] With respect to small molecule therapeutic approaches to combat COVID-19, Remdesivir (**3.1**, Figure 3.1) has gained considerable attention from scientists and the general public.[4,7] This unnatural nucleotide analog, discovered by Gilead Sciences, Inc. and now marketed as Veklury®, displays broad-spectrum antiviral activity and is currently being evaluated in Phase III clinical trials to treat patients with COVID-19.[4h] The U.S. Food and Drug Administration has granted emergency use authorization for Remdesivir, allowing hospitalized adult and pediatric COVID-19 patients to receive Remdesivir treatments.[4a]

Remdesivir (3.1)

*Antiviral compound undergoing clinical trials
for the treatment of COVID-19*

*pyrrolo[2,1-f][1,2,4]-
triazin-4-amine
(3.2)*
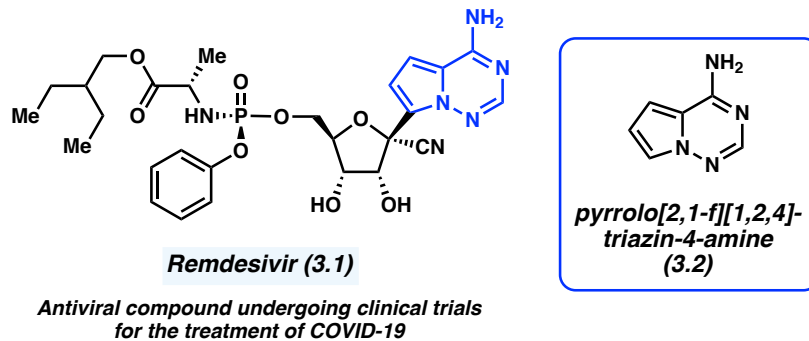
Figure 3.1. The antiviral drug Remdesivir (**3.1**) and nucleobase fragement **3.2**.

From a synthetic perspective, **3.1** (Figure 3.1) possesses several structural features that render it a challenging target.[8] In addition to the presence of a tertiary anomeric center bearing a nitrile group, the molecule contains a phosphoramidate unit with a stereogenic phosphorus center. Moreover, the nucleobase present in **3.1** is the unnatural pyrrolo[2,1-f][1,2,4]-triazin-4-amine moiety (i.e., **3.2**, Figure 3.1). This structural motif is present in a variety of other approved and experimental drugs, such as **3.3**–**3.6** (Figure 3.2).[9,10,11,12]

Avapritinib (3.3)
FDA approved chemotherapeutic

Rogaratinib (3.4)
Undergoing clinical trails for treatment of lung cancer

BMS-754807 (3.5)
IGF-1 inhibitor

BMS-690514 (3.6)
pan-HER/VEGFR2 receptor kinase inhibitor
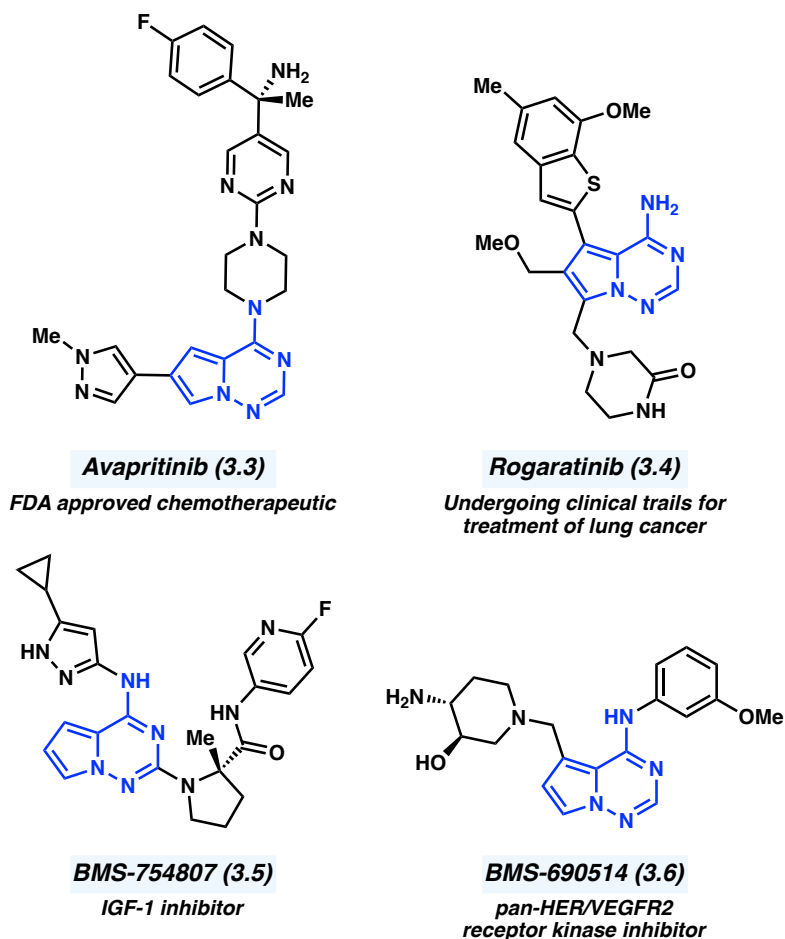
Figure 3.2. Select examples of experimental and approved drugs that possess fragment **3.2** or a derivative thereof.

With the overall aim of lowering the cost of manufacturing Remdesivir (**3.1**) or identifying alternative pathways for its synthesis, we considered the few known synthetic approaches to **3.2**.[13] As summarized in Figure 3.3, **3.2** has been generally prepared from nitrile **3.7**.[14] In turn, **3.7** can be accessed from 2-formyl pyrrole (**3.8**)[14a] or aminopyrrole derivative **3.9**.[14b–f] An exciting improvement to the synthesis of **3.2** via intermediate **3.7**, which uses pyrrole as the starting material, has recently been reported by the Medicines for All Institute.[8a] We devised a distinct, complementary approach where **3.2** would be accessed from cyanoamidine **3.10** via electrophilic aromatic substitution. Amidine **3.10** would arise from condensation of cyanamide (**3.11**) with

117

formamide **3.12**.[15] To our knowledge, this alternate strategy has not been evaluated previously. The overall conversion of **3.11** + **3.12** to **3.2** could theoretically proceed with water as the only byproduct, thus rendering the approach highly attractive.
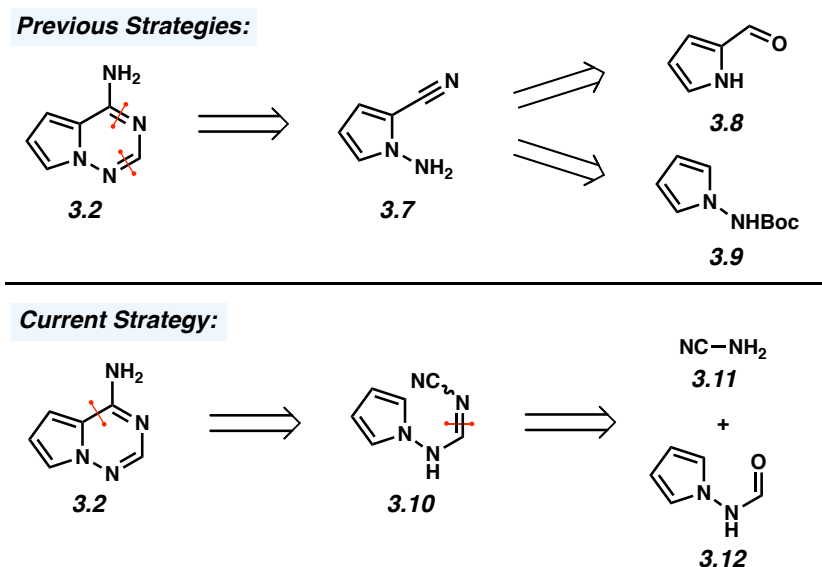
Figure 3.3. Prior and current strategies for the synthesis of **3.2**.

3.3 Synthetic Routes to Formamide (3.12)

We initiated our experimental efforts by preparing formamide **3.12** (Figure 3.4). Two distinct routes proved fruitful.[16] In the first, 1-aminopyrrole (**3.13**), which can be prepared in two steps from 2,5-dimethoxyfuran (**3.15**),[17] underwent formylation to provide **3.12**.[18] Alternatively, Boc-protected aminopyrrole **3.9** could be utilized, which is notable since it is easily accessible in a single high-yielding step from **3.15**.[14b,14f,19,20] Treatment of **3.9** with acetic anhydride in formic acid[21] at room temperature gave formamide **3.12** in 70% yield.
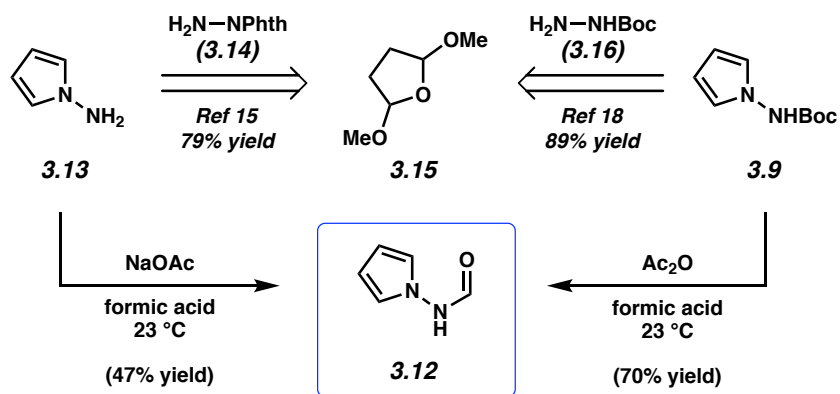
Figure 3.4. Synthetic routes to formamide **3.12** stemming from **3.15**.

3.4 Optimization of Cyanoamidine 3.10 Formation

Table 3.1 provides a sampling of conditions that were examined for the next step, which is conversion of formamide **3.12** to cyanoamidine **3.10**. Although reaction of **3.12** with 2 equiv of cyanamide and substoichiometric amounts of sodium methoxide as base did not give the desired product (entry 1), the use of stoichiometric sodium methoxide led to complete conversion, thus furnishing two isomers of cyanoamidine **3.10** in a ratio of 1.8 to 1 (entry 2), presumably favoring the depicted (*E*)-isomer.[22] We also found that only one equivalent of cyanamide was necessary. Thus, treatment of formamide **3.12** with 1 equiv of cyanamide and 1 equiv of sodium methoxide at 23 °C gave quantitative conversion to (*E*)-**3.10** and an isomer (entry 3). Although the cyanoamidine products displayed sensitivity to water, they could be easily isolated by filtering the crude reaction mixture over celite and removing the volatiles under reduced pressure.

Table 3.1. Selected conditions for the conversion of formamide **3.12**

to cyanoamidine (*E*)-**3.10.**
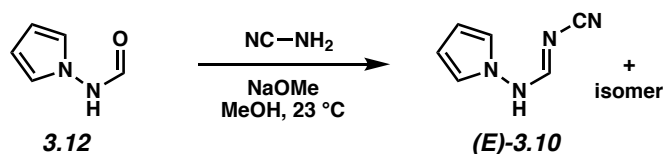
entry	equiv H₂NCN	equiv NaOMe	conversion[a]
1	2.0	0.5	0%
2	2.0	1.0	quantitative
3	1.0	1.0	quantitative

Conditions: formamide **3.12** (1.0 equiv), cyanamide (1.0–2.0 equiv), sodium methoxide (0.5–1.0 equiv), and methanol (0.5 M) stirred at 23 °C for 1 h in a sealed vial under an atmosphere of N₂. [a] Conversion to (*E*)-**3.10** and its isomer was determined by ¹H NMR analysis using 1,3,5-trimethoxybenzene as an external standard; for entries 2–3, the ratio of (*E*)-**3.10** to its isomer was observed as 1.8 to 1.

3.5 Optimization of Final Cyclization to Access 3.2

We then investigated the key cyclization.[23] Given the aforementioned sensitivity of the cyanoamidine intermediates to water, **3.12** was converted to **3.10** (presumed to be (*E*)-**3.10** and an unassigned isomer) using our optimized reaction conditions, which was carried directly into the next step without purification (see Table 3.2). The crude intermediate was subjected to a variety of acid sources with the hope of obtaining **3.2** through cyclization of the (*Z*)-isomer of **3.10**. Table 3.2 features a comparison of ¹H NMR yields obtained using 1,2-dichloroethane as solvent at 90 °C (see section 3.8.2.3 for additional results of variation of acid source, solvent, temperature, etc.). We were delighted to find that BF₃•OEt₂ could be employed as the Lewis acid (entries 1–3), with the highest yield of 22% of **3.2** being observed at a concentration of 0.1 M (entry 3). Protic acids, such as hydrochloric acid and acetic acid were ineffective (entries 4 and 5). Whereas

chlorotrimethylsilane also failed to deliver **3.2** (or a silylated derivative thereof), trace amounts or

low yields were obtained using zinc triflate, copper triflate, or titanium tetrachloride (entries 7–9).

However, subjecting crude **3.10** to tin tetrachloride furnished the desired heterocycle, **3.2**, in 28%

yield (entry 10).[24]

Table 3.2. Selected conditions for the synthesis of **3.2**.
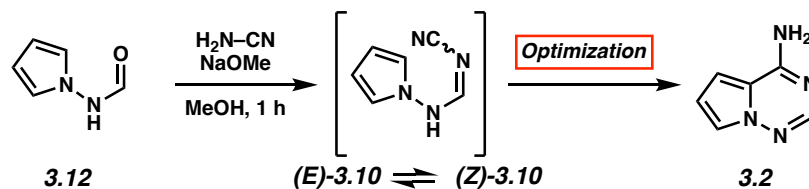
entry	acid	conc. (M.)	yield of 3.2
1	BF$_3$•OEt$_2$	1.0	4%
2	BF$_3$•OEt$_2$	0.5	3%
3	BF$_3$•OEt$_2$	0.1	22%
4	HCl	0.1	0%
5	AcOH	0.1	0%
6	TMSCl	0.1	0%
7	Zn(OTf)$_2$	0.1	trace
8	Cu(OTf)$_2$	0.1	trace
9	TiCl$_4$	0.1	7%
10	SnCl$_4$	0.1	28%

Conditions for cyclization step: crude **3.10** (1.0 equiv, assuming quantitative conversion from **3.12**), acid (2.5 equiv), and 1,2-dichloroethane (0.1 M) heated at 90 °C for 16 h in a sealed vial under an atmosphere of N$_2$; Yields were determined by ^{1}H NMR analysis using 1,3,5-trimethoxybenzene as an external standard.

3.6 1.0 mmol Scale Route to 3.2

Given the urgency and importance of efforts to alleviate the COVID-19 pandemic, coupled with currently limited research capacity at our home institutions, we opted to limit further optimization studies and instead evaluate our current protocol on mmol scale. Figure 3.5 provides an overview of the synthetic sequence with isolated yields.[25]   2,5-Dimethoxyfuran (**3.15**) is converted to formamide **3.12** in two steps. Subsequent condensation with cyanamide furnishes intermediate **3.10**, which, in turn, undergoes cyclization through its *Z* isomer to give **3.2**. We are optimistic that further optimization efforts will lead to practical improvements and welcome the expertise of process chemists worldwide to help address this challenge.
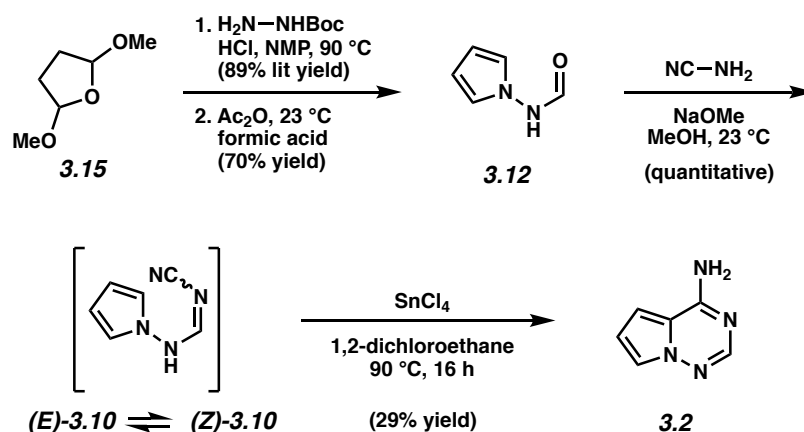
Figure 3.5. Synthesis of **3.2** on >1 mmol scale.

3.7 Conclusion

In summary, we have developed an alternative strategy to synthesize nucleobase **3.2**, a key fragment in Remdesivir and other experimental or approved small molecule therapeutics. The route relies on intermediate formamide **3.12**, which is derived in two steps from 2,5-dimethoxyfuran (**3.15**). Condensation of **3.12** with cyanamide yields an intermediate cyanoamidine (i.e., **3.10**), which then undergoes Lewis acid-mediated cyclization to deliver **3.2**. Our approach to **3.2** is atom-economical and strategically distinct from prior routes. Further

improvements to the final cyclization step can be expected in future studies. We anticipate that our synthetic route will further enable the synthesis of Remdesivir and other small molecule therapeutics that possess nucleobase **3.2**.

3.8 Experimental Section

3.8.1 Materials and Methods

Unless stated otherwise, reactions were conducted in flame-dried glassware under an atmosphere of nitrogen. Commercially obtained reagents were used as received. Formic acid, sodium acetate, acetic anhydride, cyanamide, sodium methoxide, boron trifluoride diethyl etherate, tin tetrachloride, acetic acid, zinc triflate, titanium tetrachloride, aluminum trichloride, trimethyl aluminum, *t*-butyl magnesium chloride, *n*-butyl magnesium chloride, iron trichloride, magnesium chloride, boron tribromide, boron trichloride dimethyl sulfide, and anisole were obtained from Sigma Aldrich. 1-Aminopyrrole (**3.13**), trimethylsilyl chloride, and hydrogen chloride were obtained from Oakwood Chemicals. Titanocene dichloride was obtained from TCI chemicals. Copper triflate and the Schwartz reagent were obtained from Strem Chemicals. Toluene, 1,2-dichloroethane and chlorobenzene were obtained from Fisher Scientific and purified by distillation. Nitrobenzene and nitroethane were obtained from Sigma Aldrich and were purified by distillation. 1,3,5-Trimethoxybenzene was obtained from Alfa Aesar and was used as received. A commercial sample of pyrrolo[2,1–f][1,2,3]-triazine-4-amine (**3.2**) was obtained from Ambeed. Reaction temperatures were controlled using an IKAmag temperature modulator, and unless stated otherwise, reactions were performed at room temperature (approximately 23 °C). Thin-layer chromatography (TLC) was conducted with EMD gel 60 F254 pre-coated plates (0.25 mm for analytical chromatography and 0.50 mm for preparative chromatography) and was visualized using a combination of UV and potassium permanganate staining techniques. Silicycle Siliaflash P60 (particle size 0.040–0.063 mm) was used for flash column chromatography. Uncorrected melting points were measured using a Digimelt MPA160 melting point apparatus. ^{1}H NMR spectra were recorded on Bruker spectrometers (500 and 600 MHz) and are reported relative to residual

solvent signals. Data for ^{1}H NMR spectra are reported as follows: chemical shift (δ ppm), multiplicity, coupling constant (Hz), integration. Data for ^{13}C NMR are reported in terms of chemical shift (125 MHz). IR spectra were recorded on a Perkin-Elmer UATR Two FT-IR spectrometer and are reported in terms of frequency absorption (cm^{-1}). DART-MS spectra were collected on a Thermo Exactive Plus MSD (Therm Scientific) equipped with an ID-CUBE ion source and a Vapur Interface (IonSense Inc.). Both the source and MSDwere controlled by Excalibur software version 3.0. The analyte was spotted onto OpenSpot sampling cards (IonSense Inc.) using CHCl$_3$ as the solvent. Ionization was accomplished using UHP He (Airgas Inc.) plasma with no additional ionization agents. The mass calibration was carried out using Pierce LTQ Velos ESI (+) and (–) Ion calibration solutions (Thermo Fisher Scientific).

3.8.2 Experimental Procedures

3.8.2.1 Synthesis of Formamide 3.12.
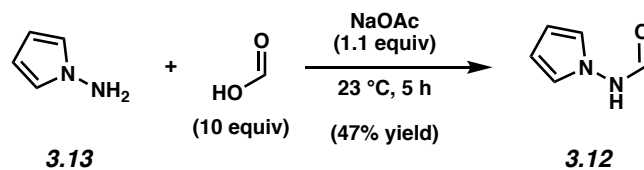
Procedure for Figure 3.4. A round bottom flask containing aminopyrrole **3.13** (2.0 g, 24.0 mmol, 1.00 equiv) and a magnetic stir bar was charged with sodium acetate (2.2 g, 27.0 mmol, 1.10 equiv) and then formic acid (9.2 mL, 0.24 mol, 10.0 equiv). The solution was stirred for 5 h at 23 °C. The reaction mixture was then diluted with water (100 mL) and dichloromethane (100 mL). The layers were then separated and the aqueous layer was extracted with dichloromethane (3 x 50 mL). The combined organic layers were then concentrated under reduced pressure. The resulting crude solid was purified by flash chromatography (20:1 CHCl$_3$:acetone then 10:1 CHCl$_3$:acetone) to afford formamide **3.12** as a white powder (1.3 g, 47% yield). Formamide **3.12**: m.p. 115–118 °C; R$_f$ 0.46

(9:1 CHCl₃:acetone). Spectroscopic data are reported for the mixture of isomers. ^{1}H NMR (500 MHz, MeOD): δ 8.29 (s), 8.21 (s) (1H total), 6.79 (t, J = 2.4), 6.66 (t, J = 2.4)(2H total), 6.12 (t , J = 2.3), 6.10 (t , J = 2.3)(2H total) ; ^{13}C NMR (100 MHz, CDCl₃): δ 164.4, 159.4, 122.5, 121.6, 108.9, 108.4; IR (film): 3295, 2973, 1664, 1048, 1376 cm^{-1}; HRMS–APCI (m/z) [M + H]$^+$ calcd for C₅H₆N₂O$^+$, 111.0553; found, 111.0551.

3.9   (70% yield)   **3.12**
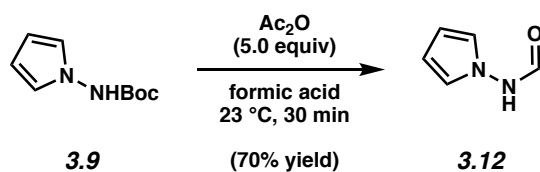
Procedure for Figure 3.4. A round bottom flask containing aminopyrrole derivative **3.9**[20] (200 mg, 1.10 mmol, 1.00 equiv) and a stir bar, was diluted with formic acid (7.3 mL, 1.92 mmol, 175.0 equiv, 0.15 M). Acetic anhydride (5.19 mL, 5.50 mmol, 5.00 equiv) was then added dropwise over 10 minutes. The solution was stirred for 30 minutes at 23 °C. The reaction mixture was then carefully basified by the addition of saturated aqueous sodium bicarbonate (50 mL over 15 minutes) until it reached pH 8. The mixture was transferred to a separatory funnel and the aqueous layer was extracted with EtOAc (4 x 50 mL). The combined organic layers were dried with sodium sulfate, filtered, and concentrated under reduced pressure. The resulting crude solid was purified by flash chromatography (2:1 hexanes:EtOAc) to afford formamide **3.12** as a white powder (85 mg, 70% yield). Spectral data match those previously reported for formamide **3.12**.[26]

3.8.2.2 Optimization of Amidine Formation.[27,28]
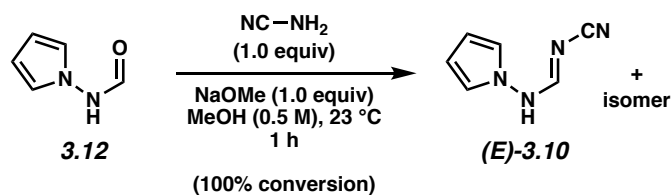
Representative Procedure for amidine formation from Table 3.1. (Entry 3.3 is used as an example). A 1-dram vial containing formamide **3.12** (40.0 mg, 0.36 mmol, 1.00 equiv) and a magnetic stir bar was charged with cyanamide (15.0 mg, 0.36 mmol, 1.00 equiv) and sodium methoxide (20.0 mg, 0.36 mmol, 1.00 equiv). Subsequently, methanol (0.73 mL, 0.50 M) was added and the reaction was stirred at 23 °C for 1 h. The mixture was filtered by passage over celite (3 cm of celite in a monster pipet), eluted with dry methanol (10 mL), and concentrated under reduced pressure to afford the crude cyanoamidine products as a white powder. The conversion (indicating full consumption of **3.12**) was determined by ^{1}H NMR analysis using 1,3,5-trimethoxybenzene as an external standard. Amidines (*E*)-**3.10** + isomer (see Figure 3.6 for possible structures). Spectroscopic data are reported for the mixture of isomers. ^{1}H NMR (500 MHz, MeOD): δ 8.34 (s), 8.09 (s)(1H total), 6.74 (t, *J* = 2.2), 6.68 (t, *J* = 2.2)(2H total), 6.08–6.05 (m)(2H total).

Any modifications of the conditions shown in the representative procedure

above are specified in Table 3.1.

Figure 3.6. Possible isomer configurations of amidine **3.10**.

(E)-3.10   (Z)-3.10

(E)-3.10 isomer   (Z)-3.10 isomer
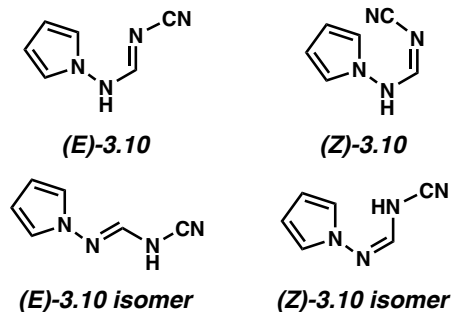
3.8.2.3 Optimization of Cyclization.
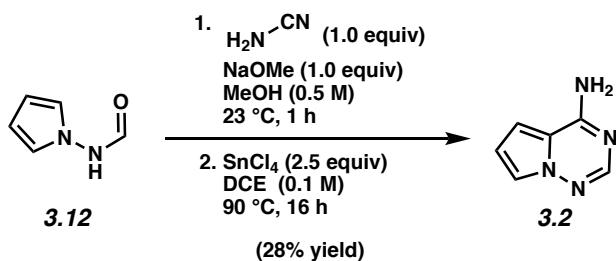
Representative Procedure for the Synthesis of Nucleobase 3.2 (Table 3.2, Entry 10 used as an example). A 1-dram vial containing formamide **3.12** (15.0 mg, 0.14 mmol, 1.00 equiv) and a magnetic stir bar was charged with cyanamide (5.7 mg, 0.14 mmol, 1.00 equiv) and sodium methoxide (7.4 mg, 0.14 mmol, 1.00 equiv). Subsequently, methanol (0.27 mL, 0.5 M) was added and the reaction was stirred at 23 °C for 1 h. The mixture was filtered (2 cm of celite in a monster pipet), eluted with dry methanol (3 mL), and concentrated under reduced pressure. To the crude cyanoamidine intermediate was added dichloroethane (0.68 mL, 0.1 M) and a magnetic stir bar. The vial was then flushed with N_2, and then $SnCl_4$ (40.0 µL, 0.34 mmol, 2.50 equiv) was added to the reaction mixture in a single portion. The vial was sealed with a Teflon-lined screw cap, placed into a preheated aluminum block on a temperature-controlled hotplate, and stirred at 90 °C for 16 h. Once the reaction was complete, the mixture was allowed to cool to 23 °C. The mixture was quenched with saturated aqueous sodium bicarbonate (5 mL) and diluted with water (5 mL) and

EtOAc (5 mL). The layers were separated, and the aqueous layer was extracted with EtOAc (3 x 8 mL). The combined organic layers were then dried over K_2CO_3, filtered, and concentrated under reduced pressure. The yield of **3.2** was determined by ^{1}H NMR analysis with anisole as an external standard.[29]

Any modifications of the conditions shown in the representative procedure

above are specified in Table 3.2 or Table 3.3.

Table 3.3. Cyclization Optimization Efforts.
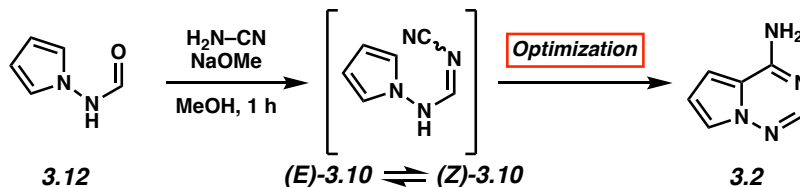
Entry	Reagent	equiv	solvent	temp. (°C)	yield of 3.2[a]
1	BF₃·Et₂O	2.5	dichloroethane	90	4%[b]
2	BF₃·Et₂O	2.5	dichloroethane	90	3%[c]
3	BF₃·Et₂O	2.5	dichloroethane	90	22%
4	HCl	2.5	dichloroethane	90	0%
5	AcOH	2.5	dichloroethane	90	0%
6	TMSCl	2.5	dichloroethane	90	0%
7	Zn(OTf)₂	2.5	dichloroethane	90	trace
8	Cu(OTf)₂	2.5	dichloroethane	90	trace
9	TiCl₄	0.5	dichloroethane	90	0%
10	TiCl₄	1.0	dichloroethane	90	7%
11	SnCl₄	2.5	dichloroethane	90	28%
12	SnCl₄	2.5	toluene	90	13%
13	SnCl₄	2.5	methanol	90	0%[d]
14	SnCl₄	2.5	nitroethane	90	13%
15	BF₃·Et₂O	1.0	dichloroethane	23	5%
16	BF₃·Et₂O	1.0	dichloroethane	45	5%
17	BF₃·Et₂O	2.5	chlorobenzene	140	4%
18	BF₃·Et₂O	2.5	nitrobenzene	180	0%

[a] Yields were determined by ^{1}H NMR analysis using 1,3,5-trimethoxybenzene as an external standard [b] 1 M concentration [c] 0.5 M concentration [d] 6 h reaction time

Additional Lewis acids screened resulting in no product formation:

AlCl₃, AlMe₃, Mg*t*-BuCl, Mg*n*-BuCl, FeCl₃, Schwartz's reagent, MgCl₂, BBr₃, BCl₃·DMS, Yb(OTf)₃, Ti(NO₃)₂, Cp₂TiCl₂

3.8.2.4 1.0 mmol-Scale Cyclization
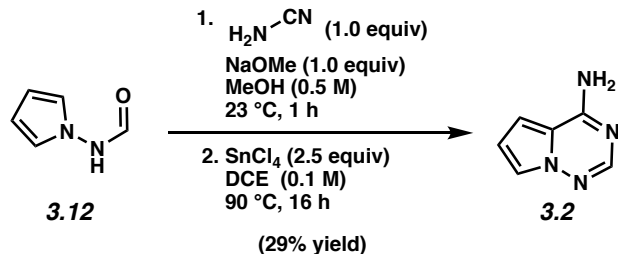
Nucleobase 3.2 (Figure 3.5). A 2-dram vial containing formamide **3.12** (110.0 mg, 1.0 mmol, 1.00 equiv) and a magnetic stir bar was charged with cyanamide (42.0 mg, 1.0 mmol, 1.00 equiv) and sodium methoxide (54.0 mg, 0.14 mmol, 1.00 equiv). Subsequently, methanol (2.0 mL, 0.5 M) was added and the reaction was stirred at 23 °C for 1 h. The mixture was filtered by passage over celite (3 cm of celite in a monster pipet) into a flame dried, round bottom flask, eluted with dry methanol (3 mL), and concentrated under reduced pressure. The flask containing the crude intermediate was charged with a stir bar and then diluted with dichloroethane (10.0 mL, 0.1 M). The reaction flask was then flushed with N_2, and then $SnCl_4$ (40.0 μL, 2.5 mmol, 2.50 equiv) was added dropwise over 1 min to the reaction mixture. The reaction flask was fitted with a reflux condenser under a positive flow of nitrogen. The mixture was then placed in a preheated oil bath and stirred at 90 °C for 16 h. Once the reaction was complete, the mixture was allowed to cool to room temperature. The mixture was quenched with saturated aqueous sodium bicarbonate (20 mL) and diluted with water (20 mL) and EtOAc (25 mL). The layers were separated, and the aqueous layer was extracted with EtOAc (3 x 30 mL). The combined organic layers were then dried over K_2CO_3, filtered, and concentrated under reduced pressure. The resulting crude solid was purified by flash chromatography (5:1 hexanes:EtOAc → 3:1 hexanes:EtOAc → 1:1 hexanes:EtOAc) to afford nucleobase **3.2** as a white powder (38 mg, 29% yield). Nucleobase **3.2**: ^{1}H NMR (500 MHz,

MeOD): δ 7.74 (s, 1H), 7.53 (dd, J = 2.6, 1.5, 1H), 6.86 (dd, J = 4.5, 1.5, 1H), 6.64 (dd, J = 4.3,

2.6, 1H). Spectral data match those previously reported.[30]

Commercial pyrrolo[2,1 –f][1,2,3]-triazine-4-amine (**3.2**) (Ambeed) ^{1}H NMR, 500 MHz, CD$_3$OD	Synthesized pyrrolo[2,1 –f][1,2,3]-triazine-4-amine (**3.2**) ^{1}H NMR, 500 MHz, CD$_3$OD
7.74 (s, 1H)	7.74 (s, 1H)
7.53 (dd, J = 2.6, 1.5, 1H)	7.53 (dd, J = 2.6, 1.5, 1H)
6.86 (dd, J = 4.5, 1.5, 1H)	6.86 (dd, J = 4.5, 1.5, 1H)
6.64 (dd, J = 4.3, 2.6, 1 H)	6.64 (dd, J = 4.3, 2.6, 1 H)

3.8.2.5 Summary of the Known Routes to 3.2

A. Klein, 1994[14a]

2 steps
28% overall yield
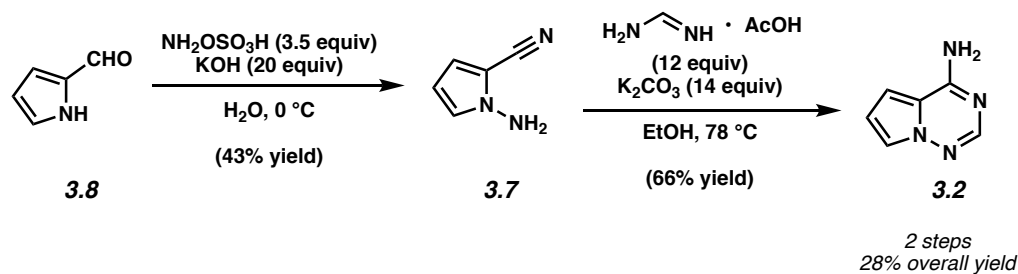
B. Bayer, 2007[14b,14c]

4 steps
31% overall yield
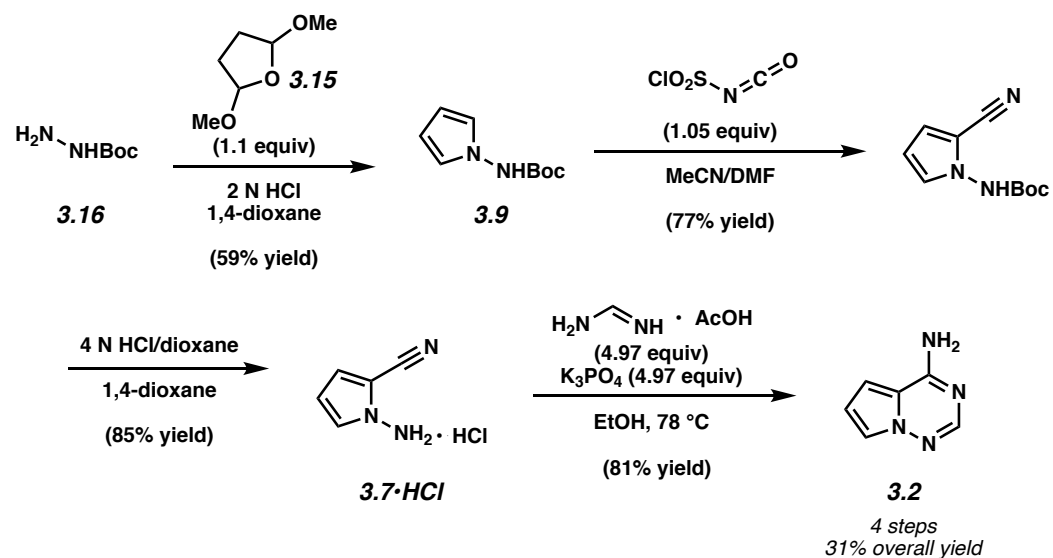
C. Medicines for All, 2020[8]

3 steps
>45% overall yield
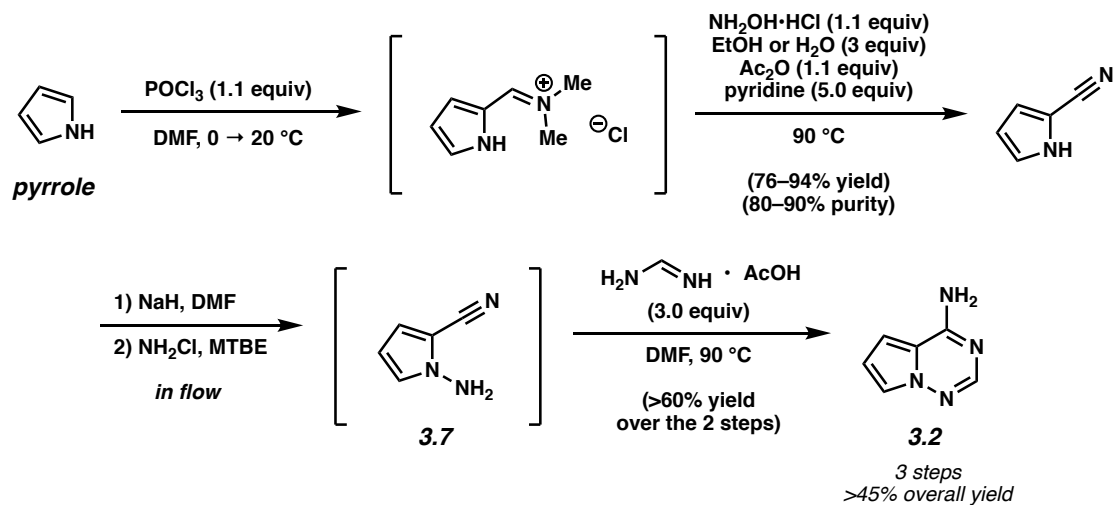
3.8.2.6 Comparison of Routes to 3.2*

Source	Number of steps	Overall Yield	Estimated bulk pricing of key compounds
Klein's synthesis, 1994[14a]	2 steps	28%	2-formylpyrrole: $214/kg hydroxylamine-O-sulfonic acid: N/A
Bayer, 2007[14b,c]	4 steps	31%	2,5-dimethoxytetrahydrofuran (**3.15**): $44/kg; *tert*-butyl carbazate: $40/kg; chlorosulfonyl isocyanate: N/A
Medicines for All Institute, 2020[8a]	3 steps	>45%	pyrrole: $17/kg hydroxylamine: $28/kg
This route	4 steps	16%	2,5-dimethoxytetrahydrofuran (**3.15**): $44/kg; *tert*-butyl carbazate: $40/kg; cyanamide: $3/kg

* As some steps/routes shown above are the result of academic studies, whereas others are from manufacturing studies (i.e., with variable levels of process chemistry optimization), some caution should be taken when analyzing the comparison data. As noted in our manuscript, extensive optimization of our route was abbreviated for reasons pertaining to the COVID-19 pandemic and the current importance of Remdesivir.

3.9 Spectra Relevant to Chapter Three:

Cyanoamidine Cyclization Approach to Remdesivir's Nucleobase

Rachel R. Knapp,[†] Veronica Tona[†] Taku Okada, Richmond Sarpong,* and Neil K. Garg*
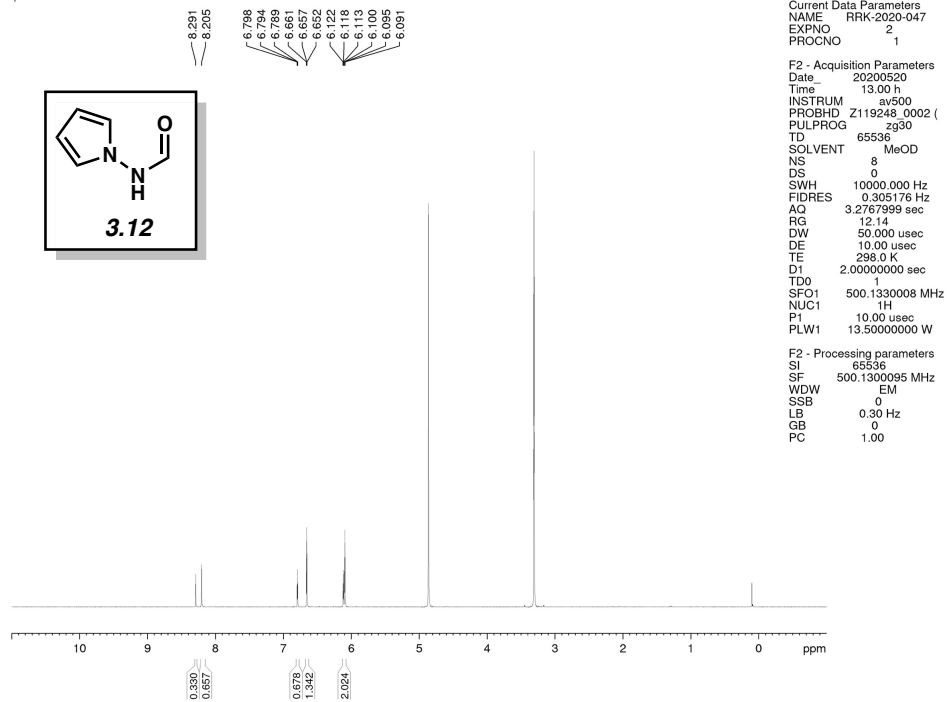
Figure 3.7. ^{1}H NMR (500 MHz, CDCl$_3$) of compound 3.12.
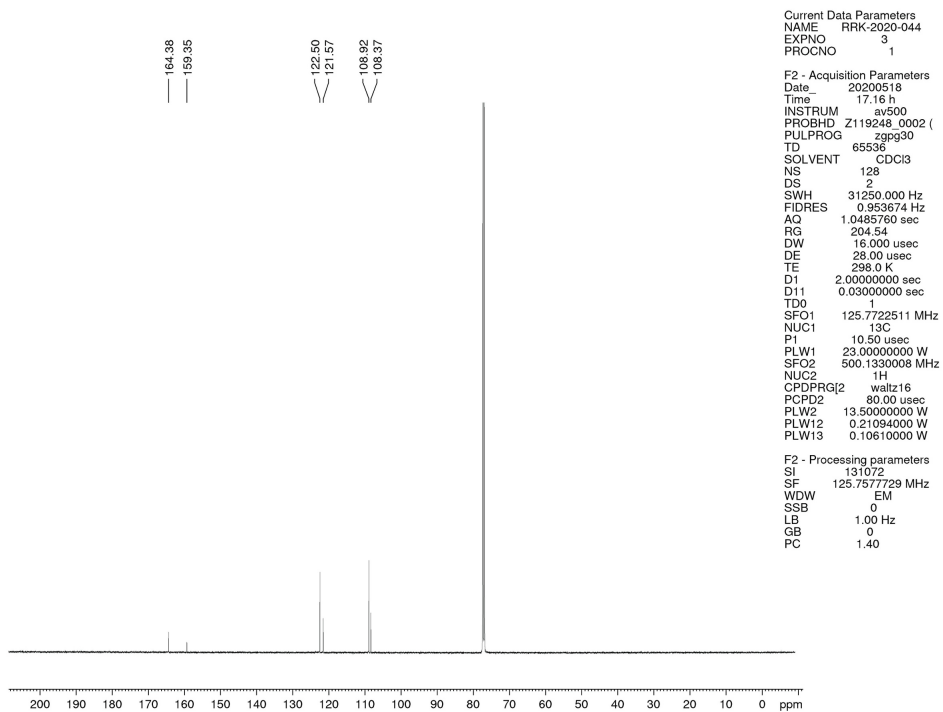
Figure 3.8. ^{13}C NMR (125 MHz, CDCl$_3$) of compound 3.12.
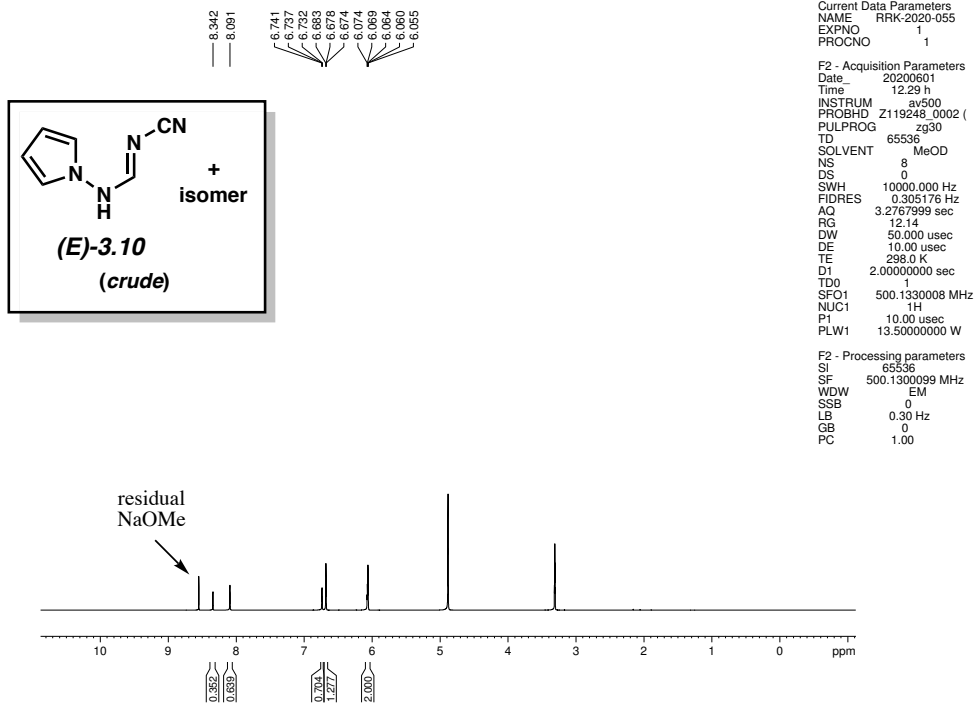
Figure 3.9. ^{1}H NMR (500 MHz, CDCl₃) of compound (*E*)-**3.10** +isomer.
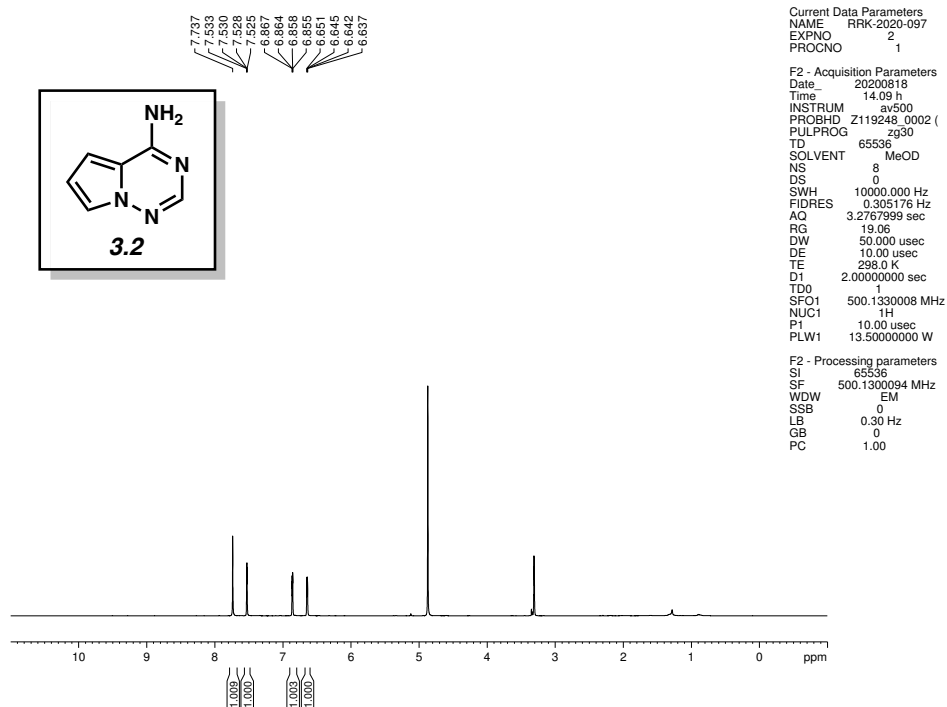
Figure 3.10. ^{1}H NMR (500 MHz, CDCl₃) of compound **3.2**.

137

Pyrrolo[2,1 –f][1,2,3]-

triazine-4-amine (**3.2**)
Comparison Spectrum
^{1}H NMR, 500 MHz, in CD$_3$OD
Top (Red): Commercial
Bottom (Blue): Synthesized
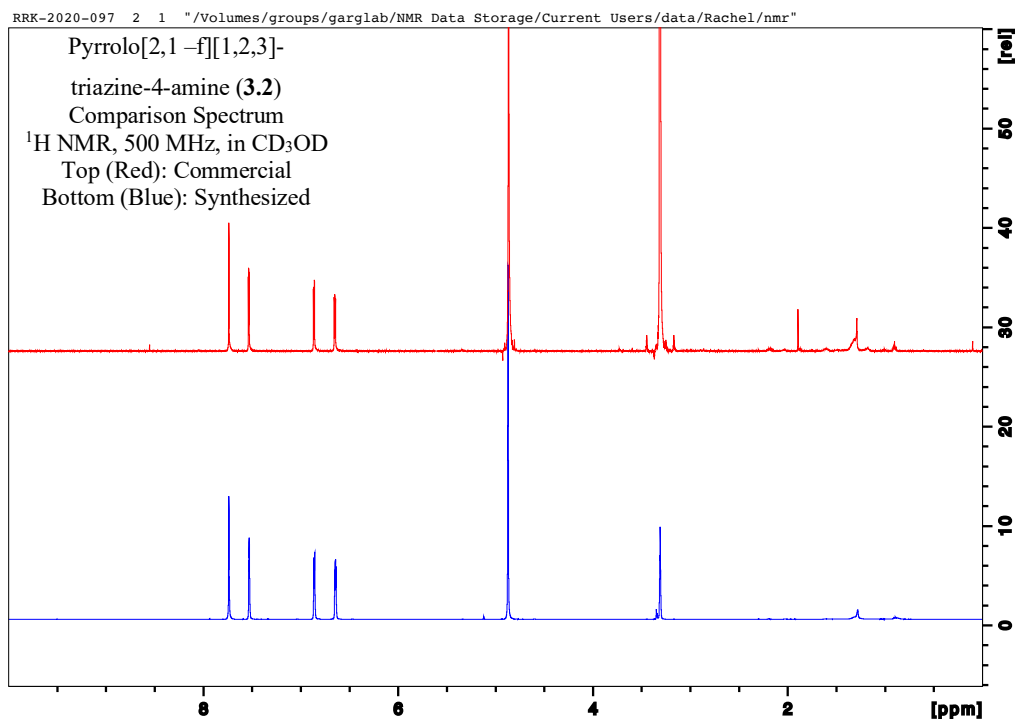
Figure 3.11. ^{1}H NMR (500 MHz, CDCl$_3$) of compound **3.2**.

3.10 Notes and References

(1) (a) Kupferschmidt, K. 'A completely new culture of doing research.' Coronavirus outbreak changes how scientists communicate, February 26, 2020. https://www.sciencemag.org/news/2020/02/completely-new-culture-doing-research-coronavirus-outbreak-changes-how-scientists/ (accessed August 30, 2020). (b) Hao, K. Over 24,000 coronavirus research papers are now available in one place; MIT Technology Review, March 16, 2020. https://www.technologyreview.com/2020/03/16/905290/coronavirus-24000-research-papers-available-open-data/ (accessed August 30, 2020). (c) Hardy, M. A.; Wright, B A.; Bachman, J. L.; Boit, T. B.; Haley, H. M. S.; Knapp, R. R.; Lusi, R. L.; Okada, T.; Tona, V.; Garg, N. K.; Sarpong, R.; Treating a global health crisis with a dose of synthetic chemistry. *ACS Cent. Sci.* **2020**, *6*, 1017–1030.

(2) (a) Peplow, M. Rapid COVID-19 testing breaks free from the lab. August 10, 2020. https://cen.acs.org/analytical-chemistry/diagnostics/Rapid-COVID-19-testing-breaks/98/web/2020/08 (accessed August 30). (b) Tromberg, B. J.; Schwetz, T. A.; Pérez-Stable, E. J.; Hodes, R. J.; Woychik, R. P.; Bright, R. A.; Fleurence, R. L.; Collins, F. S. Rapid scaling up of covid-19 diagnostic testing in the United States – The NIH RADx Initiative. *N. Engl. J. Med.* **2020**, 383, 1071–1077. (c) NIH delivering new COVID-19 testing technologies to meet U.S. demand. July 31, 2020. https://www.nih.gov/news-events/news-releases/nih-delivering-new-covid-19-testing-technologies-meet-us-demand (accessed August 30, 2020). (d) La Marca, A.; Capuzzo, M.; Paglia, T.; Roli, L.; Trenti, T.; Nelson, S. M. Testing for SARS-CoV-2 (COVID-19): A systematic review and clinical guide to molecular and serological in-vitro diagnostic assays. *Reprod. BioMed. Online* **2020**, *41*, 483–499. (e) SARS-CoV-2

Diagnostic Pipeline. Foundation for Innovative New Diagnostics (FIND), 2020. https://www.finddx.org/covid-19/pipeline/ (accessed August 30, 2020). (f) Bustin, S. A.; Benes, V.; Garson, J. A.; Hellemans, J.; Huggett, J.; Kubista, M.; Mueller, R.; Nolan, T.; Pfaffl, M. W.; Shipley, G. L.; Vandesompele, J.; Wittwer, C. T. The MIQE guidelines: Minimum information for publication of quantitative real-time PCR experiments. *Clin. Chem.* **2009**, *55*, 611−622. (g) Abbott realtime SARS-CoV-2 assay. Abbott Laboratories, 2020. https://www.molecular.abbott/us/en/products/infectious-disease/RealTime-SARS-CoV-2-Assay (accessed August 30, 2020). (h) New Rutgers saliva test for coronavirus gets FDA approval. Rutgers University, April 13, 2020. https://www.rutgers.edu/news/ new-rutgers-saliva-test-coronavirus-gets-fda-approval (accessed August 30, 2020). (i) Hahn, S. M. Coronavirus (COVID-19) update: serological tests. U.S. Food and Drug Administration, April, 7, 2020. https://www.fda.gov/news-events/press-announcements/coronavirus-covid-19-update-serological-tests (accessed August 30, 2020). (j) Kobokovich, A.; West, R.; Gronvall, G. Serology-based tests for COVID-19. Center for Health Security, Johns Hopkins Bloomberg School of Public Health, 2020. https://www.centerforhealthsecurity.org/resources/COVID-19/serology/Serology-based-tests-for-COVID-19.html (accessed August 30, 2020). (k) Bloom, J. S.; Jones, E. M.; Gasperini, M.; Lubock, N. B.; Sathe, L.; Munugala, C.; Booeshaghi, A. S.; Brandenberg, O. F.; Guo, L.; Boocock, J.; Simpkins, S. W.; Lin, I.; LaPierre, N.; Hong, D.; Zhang, Y.; Oland, G.; Choe, B. J.; Chandrasekaran, S.; Hilt, E. E.; Butte, M. J.; Damoiseaux, R.; Cooper, A. R.; Yin, Y.; Pachter, L.; Garner, O. B.; Flint, J.; Eskin, E.; Luo, C.; Kosuri, S.; Kruglyak, L.; Arboleda, V. A. Swab-Seq: A high-throughput platform for massively scaled up SARS-CoV-2 testing. *MedRxiv,* **2020** DOI: 10.1101/2020.08.04.20167874.

(3) (a) Corum, J.; Grady, D.; Wee, S.-L.; Zimmer, C. Coronavirus vaccine tracker. August 31, 2020. https://www.nytimes.com/interactive/2020/science/coronavirus-vaccine-tracker.html. (accessed August 31, 2020). (b) Deming, M. E.; Michael, N. L.; Robb, M.; Cohen, M. S.; Neuzil, K. M. Accelerating development of SARS-CoV-2 vaccines – the role for controlled human infection models. *N. Engl. J. Med.* **2020**, *383*, e63(1)-e63(4). (c) Slaoui, M.; Hepburn, M. Developing safe and effective COVID vaccines – operation warp speed's strategy and approach. *N. Engl. J. Med.* **2020**, *383*, 1701–1703. (d) Lurie, N.; Saville, M.; Hatchett, R.; Halton, J. Developing COVID-19 vaccines at pandemic speed. *N. Engl. J. Med.* **2020**, 382, 1969–1973. (e) Liu, C.; Zhou, Q.; Li, Y.; Garner, L. V.; Watkins, S. P.; Carter, L. J.; Smoot, J.; Gregg, A. C.; Daniels, A. D.; Jervey, S.; Albaiu, D. Research and development on therapeutic agents and vaccines for COVID-19 and related human coronavirus diseases. *ACS Cent. Sci.* **2020**, *6*, 315–331.

(4) For recent studies pertaining to Remdesivir, see: (a) COVID-19 update: FDA broadens emergency use authorization of Veklury (Remdesivir) to include all hospital patients for treatment of COVID-19. August, 28, 2020. https://www.fda.gov/news-events/press-announcements/covid-19-update-fda-broadens-emergency-use-authorization-veklury-remdesivir-include-all-hospitalized (accessed August 30, 2020). (b) Gilead submits new drug application to U.S. Food and Drug Administration for Veklury (Remdesivir) for the treatment of COVID-19. An open letter from our Chairman & CEO, Gilead Sciences, Inc. https://stories.gilead.com/articles/an-open-letter-from-our-chairman-and-ceo-april-29 (accessed August 30, 2020). (c) Beigel, J. H.; Tomashek, K. M.; Dodd, L. E.; Mehta, A. K.; Zingman, B. S.; Kalil, A. C.; Hohmann, E.; Chu, H. Y.; Luetkemeyer, A.; Kline, S.; Lopez de Castilla, D.; Finberg, R. W.; Dierberg, K.; Tapson, V.; Hsieh, L.; Patterson, T. F.; Paredes, R.;

Sweeney, D. A.; Short, W. R.; Touloumi, G.; Lye, D. C.; Ohmagari, N.; Oh, D.; Ruiz-Palacis, G. M.; Benfield, T.; Fätkenheuer, G.; Kortepeter, M. G.; Atmar, R. L.; Creech, B.; Lundgren, J.; Babiker, A. G.; Pett, S.; Neaton, J. D.; Burgess, T. H.; Bonnett, T.; Green, M.; Makowski, M.; Osinusi, A.; Nayak, S.; Lane, H. C. Remdesivir for the treatment of COVID-19 – preliminary report. *N. Engl. J. Med.* **2020**, *383*, 1813–1826. (d) Spinner, C. D.; Gottlieb, R. L.; Criner, G. J.; López, J. R. A.; Cattelan, A. M.; Viladomiu, A. S.; Ogbuagu, O.; Malhotra, P.; Mullane, K. M.; Castagna, A.; Chai, L. Y. A.; Roestenberg, M.; Tsang, O. T. Y.; Bernasconi, E.; Turnier, P. L.; Chang, S.-C.; SenGupta, D.; Hyland, R. H.; Osinusi, A. O.; Cao, H.; Blair, C.; Wang, H.; Gaggar, A.; Brainard, D. M.; McPhail, M. J.; Bhagani, S.; Ahn, M. Y.; Sanyal, A. J.; Huhn, G.; Marty, F. M. Effect of Remdesivir vs standard care on clinical status at 11 days in patients with moderate COVID-19. *JAMA* **2020**, 324, 1049–1057. (e) Al-Tawfiq, J. A.; Al-Homoud, A. H.; Memish, Z. A. Remdesivir as a possible therapeutic option for the COVID-19. *Travel Med. Infect. Dis.* **2020**, *34*, 101615. (f) Wang, M.; Cao, R.; Zhang, L.; Yang, X.; Liu, J.; Xu, M.; Shi, Z.; Hu, Z.; Zhong, W.; Xiao, G. Remdesivir and chloroquine effectively inhibit the recently emerged novel coronavirus (2019-nCoV) in vitro. *Cell Res.* **2020**, *30*, 269−271. (g) Sheahan, T. P.; Sims, A. C.; Leist, S. R.; Schafer, A.; Won, J.; Brown, A. J.; Montgomery, S. A.; Hogg, A.; Babusis, D.; Clarke, M. O.; Spahn, J. E.; Bauer, L.; Sellers, S.; Porter, D.; Feng, J. Y.; Cihlar, T.; Jordan, R.; Denison, M. R.; Baric, R. S. Comparative therapeutic efficacy of Remdesivir and combination Lopinavir, Ritonavir, and Interferon Beta Against MERS-CoV. *Nat. Commun.* **2020**, *222* DOI: 10.1038/s41467-019-13940-6. (h) For Remdesivir clinical trials for COVID-19, see: https://clinicaltrials.gov/ct2/results?cond=&term=remdesivir&cntry=&state=&city=&dist= (accessed August 30, 2020).

(5) For recent studies pertaining to other small molecule therapeutics, other than Remdesivir, relevant to COVID-19, see: (a) Li, G.; De Clercq, E. Therapeutic options for the 2019 novel coronavirus (2019-nCoV). *Nat. Rev. Drug Discovery* **2020**, *19*, 149–150. (b) Sheahan, T. P.; Sims, A. C.; Zhou, S.; Graham, R. L.; Pruijssers, A. J.; Agostini, M. L.; Leist, S. R.; Schäfer, A.; Dinnon III, K. H.; Stevens, L. J.; Chappell, J. D.; Lu, X.; Hughes, T. M.; George, A. S.; Hill, C. S.; Montgomery, S. A.; Brown, A. J.; Bluemling, G. R.; Natchus, M. G.; Saindane, M.; Kolykhalov, A. A.; Painter, G.; Harcourt, J.; Tamin, A.; Thernburg, N. J.; Swanstrom, R.; Dension, M. R.; Baric, R. S. An orally bioavailable broad-spectrum antiviral inhibits SARS-CoV-2 in human airway epithelial cell cultures and multiple coronaviruses in mice. *Sci. Transl. Med.* **2020**, *12*, 1–15. (c) Halford, B. An emerging antiviral takes aim at COVID-19. May, 5, 2020. https://cen.acs.org/pharmaceuticals/drug-development/emerging-antiviral-takes-aim-COVID-19/98/web/2020/05 (accessed August 30). (d) Eddy, J. Ridgeback Biotherapeutics announces launch of phase 2 trials testing EIDD-2801 as potential treatment for COVID-19. June 19, 2020. https://www.bloomberg.com/press-releases/2020-06-19/ridgeback-biotherapeutics-announces-launch-of-phase-2-trials-testing-eidd-2801-as-potential-treatment-for-covid-19 (accessed August 30, 2020). (e) De Savi, C.; Hughes, D. L.; Kvaerno, L. Quest for a COVID-19 cure by repurposing small-molecule drugs: mechanism of action, clinical development, synthesis at scale, and outlook for supply. *Org. Process Res. Dev.* **2020**, 24, 940–976. (f) Maxmen, A. More than 80 clinical trials launch to test coronavirus treatments. *Nature* **2020**, *578*, 347–348. (g) Diamond Light Source. Main protease structure and XChem fragment screen. https://www.diamond.ac.uk/covid-19/for-scientists/Main-protease-structure-and-XChem.htm (accessed August 30, 2020). (h) Moskal, M.; Beker, W.; Roszak, R.; Gajewska, E. P.; Wolos, A.; Molga, K.; Szymkuć, S.; Grynkiewicz, G.; Grzybowski, B. A. Suggestions

for second-pass anti-COVID-19 drugs based on the artificial intelligence measures of molecular similarity, shape and pharmacophore distribution. *ChemRxiv* **2020**, DOI: 10.26434/chemrxiv.12084690.v2. (i) Wang, J. Fast identification of possible drug treatment of coronavirus disease-19 (COVID-19) through computational drug repurposing study. *J. Chem. Inf. Model.* **2020**, *60*, 3277–3286.

(6) (a) FDA issues emergency use authorization for convalescent plasma as potential promising COVID-19 treatment, another achievement in administration's fight against pandemic. August, 23, 2020. https://www.fda.gov/news-events/press-announcements/fda-issues-emergency-use-authorization-convalescent-plasma-potential-promising-covid-19-treatment (accessed August 30, 2020). (b) Joyner, M. J.; Wright, R. S.; Fairweather, D.; Senefeld, J. W.; Bruno, K. A.; Klassen, S. A.; Carter, R. E.; Klompas, A. M.; Wiggins, C. C.; Shepherd, J. R. A.; Rea, R. F.; Whelan, E. R.; Clayburn, A. J.; Spiegel, M. R.; Johnson, P. W; Lesser, E. R.; Baker, S. E.; Larson, K. F.; Ripoll, J. G.; Andersen, K. J.; Hodge, D. O.; Kunze, K. L.; Buras, M. R.; Vogt, M. N. P.; Herasevich, V.; Dennis, J. J.; Regimbal, R. J.; Bauer, P. R.; Blair, J. E.; van Buskirk, C. M.; Winters, J. L.; Stubbs, J. R.; Paneth, N. S.; Verdun, N. C.; Marks, P.; Casadevall, A. Early safety indicators of COVID-19 convalescent plasma in 5000 patients. *J. Clin. Invest.* **2020**, *130*, 4791–4797. (c) Green, S.; Wigman, B.; Nistanaki, S. K.; Montgomery, H. R.; Jones, C. G.; Nelson, H. M. Chemocatalytic amplification probes enable transcriptionally-regulated Au(I)-catalysis in *E. coli* and sensitive detection of SARS-CoV-2 RNA fragments. *ChemRxiv,* **2020**, DOI: 10.26434/chemrxiv.12915761.v2.

(7) (a) Warren, T. K.; Jordan, R.; Lo, M. K.; Ray, A. S.; Mackman, R. L.; Soloveva, V.; Siegel, D.; Perron, M.; Bannister, R.; Hui, H. C.; Larson, N.; Strickley, R.; Wells, J.; Stuthman, K. S.; van Tongeren, S. A.; Garza, N. L.; Donnelly, G.; Shurtleff, A. C.; Retterer, C. J.; Gharaibeh, D.;

Zamani, R.; Kenny, T.; Eaton, B. P.; Grimes, E.; Welch, L. S.; Gomba, L.; Wilhelmsen, C. L.; Nichols, D. K.; Nuss, J. E.; Nagle, E. R.; Kugelman, J. R.; Palacios, G.; Doerffler, E.; Neville, S.; Carra, E.; Clarke, M. O.; Zhang, L.; Lew, W.; Ross, B.; Wang, Q.; Chun, K.; Wolfe, L.; Babusis, D.; Park, Y.; Stray, K. M.; Trancheva, I.; Feng, J. Y.; Barauskas, O.; Xu, Y.; Wong, P.; Braun, M. R.; Flint, M.; McMullan, L. K.; Chen, S. -S.; Fearns, R.; Swaminathan, S.; Mayers, D. L.; Spiropoulou, C. F.; Lee, W. A.; Nichol, S. T.; Cihlar, T.; Bavari, S. Therapeutic efficacy of the small molecule GS-5734 against Ebola virus in rhesus monkeys. *Nature* **2016**, *531*, 381–385. (b) Siegel, D.; Hui, H. C.; Doerffler, E.; Clarke, M. O.; Chun, K.; Zhang, L.; Neville, S.; Carra, E.; Lew, W.; Ross, B.; Wang, Q.; Wolfe, L.; Jordan, R.; Soloveva, V.; Knox, J.; Perry, J.; Perron, M.; Stray, K. M.; Barauskas, O.; Feng, J. Y.; Xu, Y.; Lee, G.; Rheingold, A. L.; Ray, A. S.; Bannister, R.; Strickley, R.; Swaminathan, S.; Lee, W. A.; Bavari, S.; Cihlar, T.; Lo, M. K.; Warren, T. K.; Mackman, R. L. Discovery and synthesis of a phosphoramidate prodrug of a pyrrolo[2,1-*f*][triazine-4-amino] adenine *C*-nucleoside (GS-5734) for the treatment of Ebola and emerging viruses. *J. Med. Chem.* **2017**, *60*, 1648–1661. (c) Mackman, R. L.; Parrish, J. P.; Ray, A. S.; Theodore, D. A. Methods and compounds for treating *paramyxoviridae* virus infections. World Patent WO 2012012776 A1, January 26, 2012. (d) Chun, B. K.; Clarke, M. O. H.; Doerffler, E.; Hui, H. C.; Jordan, R.; Mackman, R. L.; Parrish, J. P.; Ray, A. S.; Siegel, D. Methods for treating filoviridae virus infections. WO 2016069826 A1, May 6, 2016. (e) Clarke, M. O. H.; Jordan, R.; Mackman, R. L.; Ray, A. S.; Siegel, D. Methods for treating filoviridae virus infections. WO 2017184668 A1, October 26, 2017. (f) Chun, B. K.; Clarke, M. O. H.; Doerffler, E.; Hul, H. C.; Jordon, R.; Mackman, R. L.; Parrish, J. P.; Ray, A. S.; Siegel, D. Methods for treating filoviridae virus infections. US 20190275063 A1, September 12, 2019.

(8) For discussions related to cost of manufacturing Remdesivir, see references 1c and 5e, and the following: (a) Paymode, D. J.; Cardoso, F. S. P.; Sieber, J. D.; Tomlin, J. W.; Cook, D. W.; Burns, J.; Stringham, R. W; Gupton, B. F.; Snead, D.; Agrawal, T. Expanding access to Remdesivir via an improved pyrrolotriazine synthesis: supply centered synthesis. *Org. Lett.* **2020**, *22*, 7656–7661. (b) Jarvis, L. M. Scaling up Remdesivir amid the coronavirus crisis. April 20, 2020. https://cen.acs.org/biological-chemistry/infectious-disease/Scaling-remdesivir-amid-coronavirus-crisis/98/web/2020/04 (accessed August 30, 2020).

(9) For **3.3**, see: Wu, C.-P.; Lusvarghi, S.; Wang, J.-C.; Hsiao, S.-H.; Huang, Y.-H.; Hung, T.-H.; Ambudkar, S. V. Avapritinib: A selective inhibitor of KIT and PDGFRα that reverses ABCB1 and ABCG2-mediated multidrug resistance in cancer cell lines. *Mol. Pharmaceutics* **2019**, *16*, 3040–3052.

(10) For **3.4**, see: Grünewald, S.; Politz, O.; Bender, S.; Héroult, M.; Lustig, K.; Thuss, U.; Kneip, C.; Kopitz, C.; Zopf, D.; Collin, M.-P.; Boemer, U.; Ince, S.; Ellinghaus, P.; Mumberg, D.; Hess-Stumpp, H.; Ziegelbauer, K. Rogaratinib: A potent and selective pan-FGFR inhibitor with broad antitumor activity in FGFR-overexpressing preclinical cancer models. *Int. J. Cancer* **2019**, *145*, 1346–1357.

(11) For **3.5**, see: Carboni, J. M.; Wittman, M.; Yang, Z.; Lee, F.; Greer, A.; Hurlburt, W.; Hillerman, S.; Cao, C.; Cantor, G. H.; Dell-John, J.; Chen, C.; Discenza, L.; Menard, K.; Li, A.; Trainor, G.; Vyas, D.; Kramer, R.; Attar, R. M.; Gottardis, M. M. BMS-754807, a small molecule inhibitor of insulin-like growth factor-1R/IR. *Mol. Cancer Ther.* **2009**, *8*, 3341–3349.

(12) For **3.6**, see: de La Motte Rouge, T.; Galluzzi, L.; Olaussen, K. A.; Zermati, Y.; Tasdemir, E.; Robert, T.; Ripoche, H.; Lazar, V.; Dessen, P.; Harper, F.; Pierron, G.; Pinna, G.; Araujo, N.; Harel-Belan, A.; Armand, J.-P.; Wong, T. W.; Soria, J. C.; Kroemer, G. A novel epidermal

growth factor receptor inhibitor promotes apoptosis in non-small cell lung cancer cells resistant to erlotinib. *Cancer Res*. **2007**, *67*, 6253–6262.

(13) Although scaffold **3.2** is featured in a number of bioactive molecules, there are only a few known strategies to access it, all of which follow a similar bond disconnection strategy. Our strategy relies on a new bond disconnection that has the potential to further enable the synthesis of this key motif. Section 3.8.2.5 for details of known routes and key points of comparison.

(14) (a) Patil, S. A.; Otter, B. A.; Klein, R. S. Synthesis of pyrrolo[2,1-*f*][1,2,4]triazine congeners of nucleic acid purines via the *N*-amination of 2-substituted pyrroles. *J. Heterocyclic Chem*. **1994**, *31*, 781–786. (b) O'Connor, S. J.; Dumas, J.; Lee, W.; Dixon, J.; Cantin, D.; Gunn, D.; Burke, J.; Phillips, B.; Lowe, D.; Shelekhin, T., Wang, G.; Ma, X.; Ying, S.; Mcclure, A.; Achebe, F.; Lobell, M.; Ehrgott, F.; Iwuagwu, C.; Parcella, K. Preparation of pyrrolo[2, 1-*f*][1,2,4] triazin-4-ylamines as IGF-1R kinase inhibitors for the treatment of cancer and other hyperproliferative diseases. World Patent WO 2007056170 A2, May 18, 2007. (c) Dixon, J.; Phillips, B.; Achebe, F.; Kluender, H.; Newcom, J.; Parcella, K.; O'Connor, S. J.; Magnuson, S.; Hong, Z.; Zhang, Z.; Liu, Z.; Khire, U.; Wang, L.; Michels, M.; Chandler, B. Preparation of substituted 4-amino-pyrrolotriazine derivatives useful for treating hyper-proliferative disorders and diseases associated with angiogenesis. World Patent WO 2007064931 A2, June 7, 2007. (d) Duan, M.; Tian, S.; Liu, J. *N*-heterocycle-containing derivative and its pharmaceutical application. China Patent CN 110627796 A, December 31, 2019. (e) Huang, L.; Mao, W.; Wang, Z.; Liu, Y.; Huang, J.; Ouyang, F. Preparing method and application of tricyclic compounds capable of inhibiting EGFR kinase mutant. China Patent CN 110092787 A, August 6, 2019. (f) Zhang, Z.; Shen, M.; Zhao, L. Method for preparing 7-bromopyrrolo[2,

1-*f*] [1,2,4]triazin-4-amine as GS-441524 intermediate for treating feline infectious peritonitis (FIP). China Patent CN 110845502 A, February 28, 2020.

(15) For the condensation of cyanamide on a formamide, see: Dozorova, E. N.; Solov'eva N. P.; Chistyakov, V. V.; Shvarts G. Y.; Faermark, I. F.; Syubaev, R. D.; Granik, V. G.; Mashkovskii, M. D. Synthesis and biological activity of *N*-cyanoamidines and derivatives of 2,4-diaminotriazine. *Pharmaceutical Chem. J.* **1987**, *21*, 712–717.

(16) Preliminary efforts to synthesize **3.12** by Paal–Knorr pyrrole synthesis of **3.15** and formic hydrazide were unsuccessful, likely due to acid-mediated decomposition of formic hydrazide.

(17) Dey, S. K.; Lightner, D. A. 1,1'-Bipyrroles: Synthesis and stereochemistry. *J. Org. Chem.* **2007**, *72*, 9395–9397.

(18) The conversion of **3.13** to **3.12** was not fully optimized due to the greater efficiency seen in accessing **3.12** via intermediate **3.9**.

(19) Collin, M.-P.; Lobell, M.; Hübsch, W.; Brohm, D.; Schirok, H.; Jautelat, R.; Lustig, K.; Bömer, U.; Vöhringer, V.; Héroult, M.; Grünewald, S.; Hess-Stumpp, H. Discovery of Rogaratinib (BAY 1163877): a pan-FGFR inhibitor. *Chem. Med. Chem.* **2018**, *13*, 437–445.

(20) Vidal Juan, B.; Alonso Diez, J. A.; Buil A., Maria A.; Eastwood, P. R.; Esteve Trias, C.a; Lozoya Toribio, M. E.; Roberts, R. S.; Vidal Gispert, L.; Gonzalez Rodriguez, J.; Mir Cepeda, M. New CRTh2 antagonists. World Patent WO 2013010880 A1, January 24, 2013.

(21) For examples of the direct conversion of a Boc-protected amine to a formamide, see: (a) Takihiro, H.; Uruma, Y.; Usuki, Y.; Miyake, A.; Lio, H. Practical synthesis of blepharismone, a mating inducing pheromone of *Blepharisma japonicum*. *Tetrahedron: Asymmetry* **2006**, *17*, 2339–2343. (b) Zimuwandeyi, M.; Kola, F.; Lemmerer, A.; Brady, D.; Rousseau, A.; Bode,

M. L. PADAM reactions of α-aminoaldehydes: Identity of major and minor diastereomers from the Passerini reaction. *Tetrahedron* **2018**, *74*, 2925–2941.

(22) Molecular mechanics (MMFF) and DFT (B3LYP/6-31G*) equilibrium geometry calculations suggest that the *E* isomer of **3.10** is favored over the *Z* isomer of **3.10**. Amidine isomers of **3.10** were also found to be higher in energy than (*E*)- **3.10**. Thus, we surmise that the major observed isomer is (*E*)- **3.10**, as depicted. At this time, we prefer not to speculate on what the minor isomer is, but nonetheless we postulate that stereo- and amidine isomers of **3.10** can interconvert. See Figure 3.6 for a depiction of the possible products.

(23) Although the cyclization of pyrroles onto cyanoimines is not known, related cyclizations of heterocycles onto nitriles have been reported. For examples, see: (a) Outlaw, V. K.; Townsend, C. A. A practical route to substituted 7-aminoindoles from pyrrole-3-carboxaldehydes. *Org. Lett.* **2014**, *16*, 6334–6337. (b) Mizoi, K.; Mashima, Y.; Kawashima, Y.; Takahashi, M.; Mimori, S.; Hosokawa, M.; Murakami, Y.; Hamana, H. A new methodology for functionalization at the 3-position of indoles by a combination of boron lewis acid with nitriles. *Chem. Pharm. Bull.* **2015**, *63*, 538–545. (c) Zhang, L.; Xiao, Q.; Ma, C.; Xie, X.-Q.; Floreancig, P. E. Construction of a bicyclic β-benzyloxy and β-hydroxy amide library through a multicomponent cyclization reaction. *J. Combinatorial Chem.* **2009**, *11*, 640–644. (d) Neidlein, R.: Jeromin, G. Synthese neuer N-vinylpyrrole. *Chem. Ber.* **1982**, *115*, 714–721. (e) Hosmane, R. S.; Leonard, N. J. Chemical modification of nucleic acid components: reactions of cytosine, cytidine, isocytosine, and adenine with methyl *N*-cyanomethanimidate. *J. Org. Chem.* **1981**, *46*, 1457–1465. (f) Agasimundin, Y. S.; Oakes, F. T.; Leonard, N. J. Annelation of isocytosines by reaction with methyl *N*-cyanomethanimidate and sodium methoxide:

influence of substitution on the course of the reaction and rearrangements. *J. Org. Chem.* **1985**, *50,* 2474–2480.

(24) ^{1}H NMR analysis of the crude reaction mixture shows no remaining starting material and no major side products. As such, the mass balance could plausibly be attributed to decomposition or Lewis acid complexation of intermediates.

(25) Estimated bulk pricing for key compounds based on overseas import/export prices: 2,5-dimethoxytetrahydrofuran (**3.15**): $44/kg; *tert*-butyl carbazate: $40/kg; cyanamide: $3/kg.

(26) Some side products were formed in this reaction that we believe are related to the presence of Ac_2O. Although it was not possible to isolate and fully characterize these side products, this represents an opportunity for further process chemistry optimization.

(27) In our reaction conditions, we always observed the formation of the products as a 1.8:1 ratio of isomers. Safety concerns related to intermediate formamide **3.12** and cyanoamidine **3.10** are currently unknown. However, *N,N*-disubstituted formamides and cyanoamidines are well known functionalities, with reports of gram scale syntheses, without the need for any special precautions. For examples, see: (a) Garcia-Rubio, S.; Wilson, C. D.; Renner, D. A.; Rosser, J. R.; Patra, D.; Reid, J. G.; Pines, S. H. An improved process for the preparation of trimethylhydrazine and its coupling with an activated acid intermediate. *Org. Process Res. Dev.* **2004**, *8*, 360−362. (b) Golubev, P.; Krasavin, M. *N*-Isocyanodialkylamines generated in situ for the Joullié–Ugi reaction with indolenines. *Tetrahedron Lett.* **2018**, *59*, 3532−3536.

(28) Our route avoids the use of chlorosulfonyl isocyanate or hydroxylamine-*O*-sulfonic acid as a cyanation source. Instead this route employs cyanamide, which could result reduced waste generation.

(29) All attempts to synthesize **3.10** have led to an observed 1.8:1 ratio if isomers. As such, we cannot yet determine if this ratio impacts the yield of the subsequent cyclization step. In future studies, we suggest real-time reaction monitoring methods that are commonly used in process research (e.g., ReactIR, in situ NMR studies, etc.).

(30) O'Connor, S. J.; Dumas, J.; Lee, W.; Dixon, J.; Cantin, D.; Gunn, D.; Burke, J.; Philips, B.; Lowe, D.; Shelekhin, T.; Wang, G.; Ma, X.; Ying, S.; McClure, A.; Achebe, F.; Lobell, M.; Ehrgott, F.; Iwuagwu, C.; Parcella, K. WO2007056170A2. May 18, 2007. (Bayer)

CHAPTER FOUR

Diels–Alder Cycloadditions of Strained Azacyclic Allenes

Joyann S. Barber,[†] Michael M. Yamano,[†] Melissa Ramirez, Evan R. Darzi,

Rachel R. Knapp, Fang Liu, K. N. Houk, and Neil K. Garg.

4.1 Abstract

For over a century, the structures and reactivities of strained organic compounds have captivated the chemical community. Whereas triple-bond-containing strained intermediates have been well studied, cyclic allenes have received far less attention. Additionally, studies of cyclic allenes that bear heteroatoms in the ring are scarce. We report an experimental and computational study of azacyclic allenes, which features syntheses of stable allene precursors, the mild generation and Diels–Alder trapping of the desired cyclic allenes, and explanations of the observed regio- and diastereoselectivities. Furthermore, we show that stereochemical information can be transferred from an enantioenriched silyl triflate starting material to a Diels–Alder cycloadduct by way of a stereochemically-defined azacyclic allene intermediate. These studies demonstrate that heteroatom-containing cyclic allenes, despite previously being overlooked as valuable synthetic intermediates, may be harnessed for the construction of complex molecular scaffolds bearing multiple stereogenic centers.

4.2 Introduction

The chemistry of strained organic compounds has long fascinated the scientific community. Despite once being only scientific curiosities, small rings containing triple bonds can now be used in a host of applications. Breakthroughs in this area include the synthetic chemistry

of benzyne (**4.1**) and cyclohexyne (**4.2**) (Figure 4.1a), both of which were once controversial species.[1] To date, both have been utilized in a variety of synthetic applications spanning ligand synthesis, natural product synthesis, agrochemistry, and materials science.[2,3,4]

Whereas strained cyclic intermediates possessing triple bonds have gained tremendous popularity, the corresponding chemistry of cyclic allenes has remained relatively underdeveloped. The parent allene, 1,2-cyclohexadiene (**4.3**, Figure 4.1a), was first accessed by Wittig in 1966.[5] Over the subsequent five decades, the field of cyclic allene chemistry has been largely driven by theoretical studies of allene structure and chirality,[6,7,8,9,10,11] in addition to studies of cycloaddition mechanisms.[12] With regard to experiments, various methods to generate cyclic allenes have been developed,[11,13,14] and subsequently used in cycloaddition methodologies of 1,2-cyclohexadienes.[15,16,17,18,19] Taken together, these studies suggest the potential synthetic utility of cyclic allene intermediates.

A largely untapped branch of cyclic allene chemistry involves those species that contain a heteroatom. Such reactive intermediates, despite not being used commonly in synthetic chemistry today, were first studied in 1976 (Figure 4.1b). In a seminal discovery, Murata and co-workers proposed to have unintentionally accessed cyclic allene **4.4**, an isomer of benzooxepine, using a Doering–Moore–Scattebøl (DMS) ring expansion of a dihalocyclopropane precursor.[20] Despite the harsh conditions required for this rearrangement (i.e. organolithium reagents), a [2+2] cycloadduct was isolated in 33% yield, thus fueling their hypothesis for the intermediacy of a heterocyclic allene. Led by efforts from the Christl laboratory, the generation of several additional heterocyclic allenes were reported in the intervening years, such as six-membered cyclic allenes **4.5**–**4.8**. Oxacyclic allenes **4.5** and **4.6** were first reported by Christl, also using the DMS approach.[21,22] Subsequently, the groups of Schlosser[23] and Caubère,[24] respectively, demonstrated

that cyclic allene **4.6** could also be obtained by the base-mediated dehydrohalogenation of a vinylhalide precursor. With regard to azacyclic allenes, which most closely resemble the chemistry described herein, the generation of 1-aza-3,4-cyclohexadiene (**4.7**) by Christl represents a key discovery in the field.[25] Also generated by the methyllithium-promoted DMS rearrangement, this azacyclic allene underwent Diels–Alder cycloadditions and [2+2] cycloadditions, albeit in modest synthetic efficiency. More recently, efforts were put forth toward the isomeric 1-aza-2,3-cyclohexadiene. Although this was found to be unstable, *N*-borylation permitted access to azacyclic allene **4.8**.[26] Additional discoveries in this field include the synthesis of a cephalosporin-derived cyclic allene formation by Elliot and coworkers[27,28,29] and several studies pertaining to heterocyclic isoarenes.[7,30,31,32,33,34,35,36]

With the aforementioned advances in mind, we sought to provide an advance that would enable the field of heterocyclic allene chemistry to enter mainstream synthesis. Notably, all previous examples of heterocyclic allene generation require harsh, strongly basic reaction conditions and, as a consequence, often suffer from modest reaction yields. Additionally, no studies of functionalized heterocyclic allene precursors, either for the sake of synthetic utility or for the investigation of reactivity and selectivity, have been reported. As such, we sought to prepare compounds of the type **4.9** (Figure 4.1c). If intermediates **4.9** could be generated under mild conditions, they would provide a valuable tool to assemble stereochemically-complex derivatives of the medicinally-privileged piperidine scaffold. Functionalized piperidines are the most common heterocycle seen in medicines,[37] so new strategies for their synthesis are highly sought after. Moreover, the study of substituted azacyclic allenes would provide opportunities to understand and modulate various aspects of regio- and stereoselectivities using a blend of computations and experiments. Computational studies of azacyclic allenes **4.9** have not been reported.

a.

Benzyne (4.1)
1953, Roberts

Cyclohexyne (4.2)
1957, Roberts

1,2-Cyclohexadiene (4.3)
1966, Wittig

b.

4.4
1976

4.5
1987

4.6
1989

4.7
1994

4.8
2001

c.

4.9 → **4.11** or **4.12**

- Mild generation of azacyclic allenes
- Diels–Alder trapping to form sp³-rich piperidine-fused bicycles
- Computational understanding of selectivities
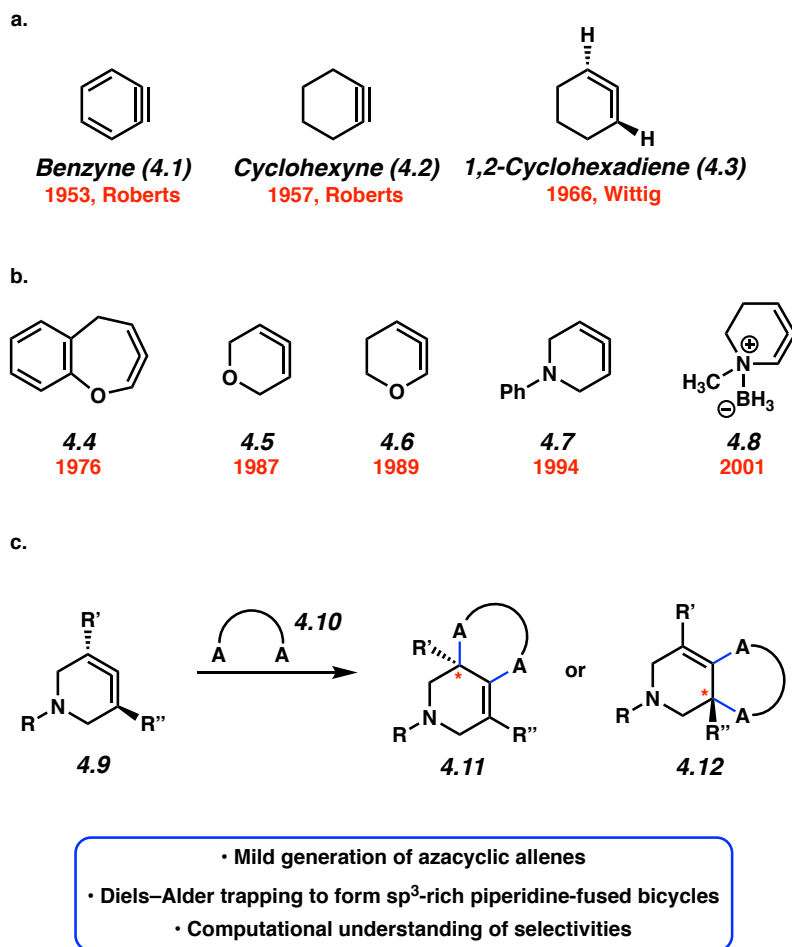
Figure 4.1. Survey of strained cyclic intermediates.

We now report (a) the syntheses of several silyl triflate precursors to azacyclic allene intermediates, (b) the mild generation and Diels–Alder trapping of the desired cyclic allenes (**4.9** + **4.10** → **4.11** + **4.12**, Figure 4.1c) to give decorated piperidine products, including some bearing quaternary stereocenters, (c) the first examples of [3+2] cycloadditions of any heterocyclic allene, and (d) computational studies, including the application of the distortion-interaction model, to explain experimentally observed selectivities. Moreover, we demonstrate that stereochemical information can be transferred from an enantioenriched silyl triflate starting material to Diels–Alder cycloadducts by way of a stereochemically-defined azacyclic allene intermediate.

4.3 Computational Analysis of Azacyclic Allene Structure

Figure 4.2 provides a comparison of linear allene **4.13** and azacyclic allene **4.14**. ωB97XD was deemed the most appropriate density functional theory (DFT) method for the cycloaddition studies (described below), and was used to optimize the ground state geometries of interest. The linear allene C=C bond length is 1.31 Å in **4.13**. As expected, the allene π orbitals are orthogonal but degenerate. In comparison, the C=C bond length of azacyclic allene **4.14** is only slightly longer (1.32 Å), with the internal angle at the central allene carbon being 133°, rather than 180°, as a result of the ring constraint. The allene π orbitals are no longer perfectly orthogonal or degenerate and the allene CH bonds are twisted out-of-plane, by 42° and 37°, respectively. Azacyclic allene **4.14** possesses 27.3 kcal/mol of strain energy (see Section 4.9.3.3) due to its distortion from linearity, an attribute that facilitates cycloaddition reactions.
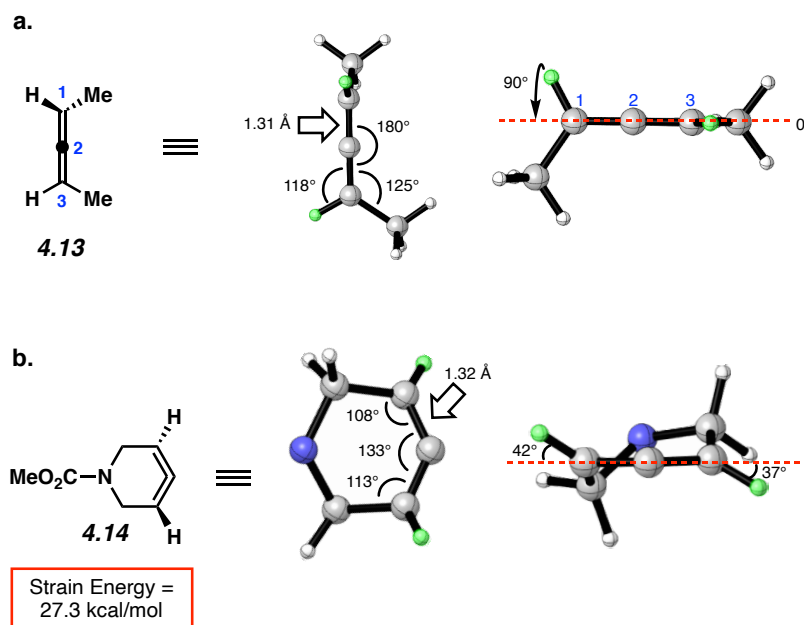
Figure 4.2. Comparison of geometry-optimized structures of allenes **4.13** and **4.14**.

4.4 Syntheses of Azacyclic Allene Precursors

With the ultimate aim of accessing azacyclic allenes **4.25**–**4.28**, we developed a divergent synthetic route to silyl triflates **4.19**, **4.20**, **4.23**, and **4.24**, stemming from common intermediate **4.16** (Figure 4.3). 4-Methoxypyridine (**4.15**) was elaborated to compound **4.16** using a straightforward sequence, analogous to that used to prepare the known trimethylsilyl derivative.[38] Subsequent 1,4-reduction proceeded smoothly using L-selectride to give an intermediate lithium enolate. Whereas acidic workup furnished silyl ketone **4.17**, trapping with methyl iodide led to α-methylated ketone **4.18**. Subsequent triflation of **4.17** and **4.18** delivered silyl triflates **4.19** and **4.20**, respectively. Alternatively, intermediates **4.17** and **4.18** could be elaborated to esters **4.21** and **4.22**, respectively, upon deprotonation and quenching with Mander's reagent. Enols **4.21** and **4.22** were readily triflated using sodium hydride and triflic anhydride, thus furnishing the corresponding silyl triflates **4.23** and **4.24**. It should be noted that by preparing four silyl triflates, we hoped to probe substituent effects on regio- and diastereoselectivities. Silyl triflate **4.19** would serve as a precursor to the parent azacyclic allene **4.25**. Allenes **4.26** and **4.27**, optimistically accessible from silyl triflates **4.20** and **4.23**, respectively, each bear one additional substituent relative to the parent allene **4.25**, but with varying electronic properties (i.e., methyl versus ester). Lastly, fully substituted allene **4.28** would be derived from silyl triflate **4.24**.
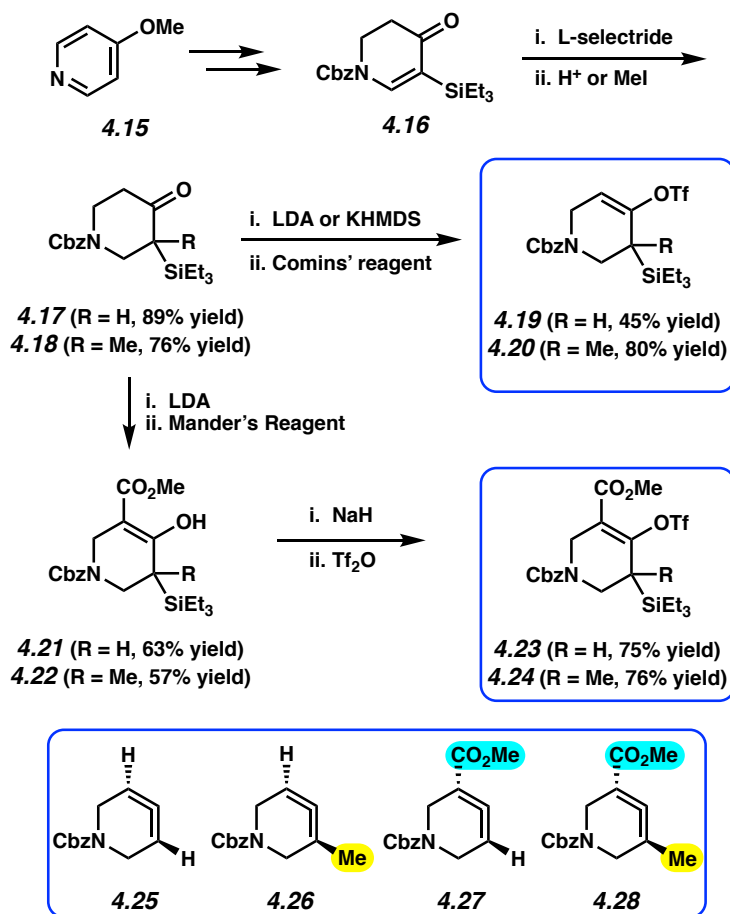
Figure 4.3. Syntheses of silyl triflates **4.19**, **4.20**, **4.23**, and **4.24**.

4.5 Scope of Methodology

With the necessary silyl triflates in hand, we sought to generate and trap azacyclic allenes

4.25–4.28 in Diels–Alder reactions (Table 4.1). This idea was realized by implementing a simple

experimental protocol, wherein CsF was added to a mixture of a given silyl triflate and a particular

diene in acetonitrile at ambient temperature, to ultimately afford a variety of cycloadducts. For

example, we found that unsubstituted allene **4.25** could be generated and trapped by

N-phenylpyrrole (**4.29a**) to furnish [2.2.1]-azabicycle **4.32** in 77% yield and 4.7:1 dr (entry 1).

Similarly, oxa-bicycles **4.33** and **4.34** were accessed by trapping of **4.25** with furans **4.30** and **4.31**,

respectively (entries 2 and 3). In all cases, the endo products were formed preferentially. We also

generated methyl-substituted allene **4.26**, which was found to undergo Diels–Alder trapping with

158

4.29a, **4.30**, and **4.31** (entries 4–6, respectively). In each case, cycloaddition occurred regioselectively on the olefin positioned distal to the methyl group, again with notable levels of diastereoselectivity. By switching to allene **4.27**, bearing an electron-withdrawing ester in place of the methyl group in **4.26**, we observed a switch in regioselectivity. As shown by the formation of **4.38**–**4.40**, cycloaddition occurred on the olefin proximal to the ester substituent (entries 7–9, respectively). It should be noted that the trapping experiments of allene **4.27** allow for the formation of quaternary centers in a controlled manner. Lastly, we examined cycloadditions between fully substituted allene **4.28** and dienes **4.29a**, **4.30**, and **4.31**. As seen in entries 10–12, the cycloadditions occurred smoothly, giving rise to cycloadducts **4.41**–**4.43** in 93–95% yield and >20:1 dr. Consistent with the regioselectivites seen in the cases of allenes **4.26** and **4.27**, cycloadditions involving allene **4.28** occur proximal to the ester and distal to the methyl group. Moreover, the trapping of **4.28** in Diels–Alder cycloadditions allows for the efficient assembly of highly functionalized piperidine scaffolds bearing quaternary stereocenters.

Table 4.1. Scope of Diels–Alder cycloadditions of azacyclic allene intermediates **4.25**–**4.28**.

Entry	Allene	Diene	Products (Yield, dr)	Entry	Allene	Diene	Products (Yield, dr)
1	**4.25**	**4.29a**	**4.32** (77% yield, 4.7:1 dr)	7	**4.27**	**4.29b**[b]	**4.38** (75% yield, >14:1 dr)
2	**4.25**	**4.30**	**4.33** (77% yield, 7.4:1 dr)	8	**4.27**	**4.30**	**4.39** (74% yield, >9:1 dr)
3	**4.25**	**4.31**	**4.34** (82% yield, 13.7:1 dr)	9	**4.27**	**4.31**	**4.40** (95% yield, >20:1 dr)
4	**4.26**	**4.29a**	**4.35** (73% yield, >20:1 dr)	10	**4.28**	**4.29a**	**4.41** (95% yield, >20:1 dr)
5	**4.26**	**4.30**	**4.36** (73% yield, 12.8:1 dr)	11	**4.28**	**4.30**	**4.42** (93% yield, >20:1 dr)
6	**4.26**	**4.31**	**4.37**[a] (56% yield, >20:1 dr)	12	**4.28**	**4.31**	**4.43** (95% yield, >20:1 dr)

Conditions unless otherwise stated: Silyl triflate substrate (1.0 equiv.), diene (5.0–10.0 equiv.), CsF (5.0 equiv.), acetonitrile (0.1 M) at 23 °C. Yields shown reflect the average of two isolation experiments. [a] The regioisomer of **4.37** was also observed (ca. 20% yield), resulting from endo cycloaddition on the more substituted olefin of allene **4.26**. [b] Pyrrole **4.29b** was employed in place of pyrrole **4.29a**, as the cycloaddition of **4.29a** with **4.27** proceeded in low yield for reasons that are not presently understood.

Several features of the allene generation and trapping experiments should be emphasized. (a) In the absence of CsF, no reaction occurs, even at elevated temperature, which is suggestive of allene formation (as opposed to Diels–Alder cycloaddition, followed by silyl triflate elimination). (b) All reactions take place at room temperature, thus allowing for azacyclic allene generation under exceptionally mild reaction conditions. (c) For all reactions with the exception of the formation of **4.37**, the opposite regioisomer was not observed. (d) This methodology provides a facile, metal-free means to access decorated piperidines, by formation of two new bonds and three stereocenters, with high levels of diastereoselectivity. (e) The substituents on the azacyclic allene have a profound effect on modulating regioselectivities in the cycloaddition reactions.

Although not the focus of the current study, it should be noted that azacyclic allene **4.25** could also be trapped in (3+2) and (2+2) cycloadditions (Table 4.2). For example, an assortment of nitrones can be employed as 1,3-dipoles. Whereas prior studies of 1,2-cyclohexadiene nitrone cycloadditions were performed optimally at elevated temperatures to accelerate reaction rates,[18] in the case of azacyclic allene **4.25**, reactions proceeded efficiently at ambient temperature (see Section 4.9.2.3 for reaction times). Moreover, comparable selectivities were seen in control experiments performed at 50 °C. Use of aldehyde-derived nitrone **4.45** provided isoxazolidine **4.46** (entry 1), whereas trapping with ketone-derived nitrone **4.47** furnished **4.48**, bearing a tertiary center and trifluoromethyl group (entry 2). When cyclic nitrones **4.49** and **4.51** were utilized, tri- and tetracyclic products **4.50** and **4.52** were obtained, respectively (entries 3 and 4). Additionally, trapping of the allene intermediate with azomethine imines[19] **4.53** and **4.55** gave the corresponding pyrazolidine products **4.54** and **4.56** (entries 5 and 6). Of note, **4.56** contains three distinct nitrogen-containing heterocycles: a piperidine, a pyrazolidine, and a pyridine ring. Nitrile oxide[19] **4.57** was also employed as a trapping agent and gave rise to isoxazoline **4.58** in 81% yield. These reactions

(entries 1–7) represent the first (3+2) cycloadditions of heterocyclic allenes. Lastly, we attempted to utilize olefin **4.59** in a (2+2) cycloaddition. This reaction proceeded smoothly to deliver cyclobutane derivative **4.60** in 78% yield as a single isomer. Collectively, the trapping experiments of azacyclic allenes shown in Tables 4.1 and 4.2 demonstrate their utility in the rapid generation of stereochemically-rich heterocycles.

Table 4.2. (3+2) and (2+2) cycloadditions of azacyclic allene intermediate **4.25**.

Entry	Trapping Agent	Products (Yield, dr)	Entry	Trapping Agent	Products (Yield, dr)
1	**4.45**	**4.46** (88% yield, >20:1 dr)	5	**4.53**	**4.54** (68% yield, 10.6:1 dr)
2	**4.47**	**4.48** (85% yield, 5.4:1 dr)	6	**4.55**	**4.56** (81% yield, 14.3:1 dr)
3	**4.49**	**4.50** (72% yield, 8.3:1 dr)	7	**4.57**	**4.58** (81% yield)
4	**4.51**	**4.52** (Quantitative yield, 5.3:1 dr)	8	**4.59**	**4.60** (78% yield)

Conditions unless otherwise stated: Silyl triflate **4.19** (1.0 equiv.), trapping agent (1.2–5.0 equiv.), CsF (5.0 equiv.), acetonitrile (0.1 M) at 23 °C. Yields shown reflect the average of two isolation experiments.

4.6 DFT Calculations

To learn about the nature of the mechanism (concerted or stepwise) and to understand how the methyl and ester groups guide selectivities, DFT calculations were performed for the Diels–Alder reactions of allenes **4.61** and **4.62** (carbomethoxy was used as a surrogate for the larger carboxybenzyl (Cbz) group to simplify computations) reacting with furan (**4.30**) (Figure 4.4). We considered pathways leading to all regio- and stereoisomers via three possible scenarios: concerted cycloaddition, stepwise zwitterionic cycloaddition, and stepwise diradical cycloaddition. B3LYP was previously used to study the mechanism of Diels–Alder cycloadditions with 1,2-cyclohexadiene. However, Brinck and coworkers have noted a tendency for B3LYP to overestimate the asynchronicity of highly asynchronous transition states and to ultimately favor stepwise pathways;[39] their recent benchmark study demonstrates that ωB97XD performs better than B3LYP for highly asynchronous Diels–Alder cycloadditions and was shown to reproduce transition state geometries obtained using a high accuracy method, CCSD(T). A variety of methods and basis sets were evaluated for this study, and ωB97XD/6-311+G(d,p)/SMD(MeCN) was selected as the computational method of choice (see Section 4.9.3.2).

Our computations reveal that pathways leading to endo products are most energetically favorable, consistent with experimental results, and proceed in an asynchronous concerted fashion. Key results are summarized in Figure 4.4a (see Section 4.9.3.4 & 4.9.3.5 for analyses of pathways leading to exo products). The $\Delta\Delta G^{\ddagger}$ for the two competing endo pathways for the Diels–Alder reaction of methyl-substituted allene **4.61** and furan (**4.30**) was calculated to be –1.5 kcal/mol, with the cycloaddition occurring on the olefin distal to the methyl group. This correlates well with the experimental result shown in Table 4.1 (see entry 5). To understand the origin of regioselectivity, we performed a distortion/interaction activation strain analysis.[40] Thus, the $\Delta E^{\ddagger}$

was calculated for the endo pathways leading to the two possible regioisomers, and $\Delta E^{\ddagger}$ was further broken down into its components, the distortion energy ($\Delta E_{dist}^{\ddagger}$, an energetic cost associated with the structural distortion of the reactants) and the interaction energy ($\Delta E_{int}^{\ddagger}$, an energetic benefit resulting from favorable orbital interactions). Whereas the $\Delta E_{dist}^{\ddagger}$ was found to be comparable for the transition states leading to the major and minor regioisomers ($\Delta\Delta E_{dist}^{\ddagger} = -0.3$ kcal/mol), ΔE_{int} was more favorable in the transition state leading to the major regioisomer ($\Delta\Delta E_{int}^{\ddagger} = -1.3$ kcal/mol). This more favorable ΔE_{int} results from more stabilizing orbital interactions between the lowest unoccupied molecular orbital (LUMO) of allene **4.61** and highest occupied molecular orbital (HOMO) of furan (**4.30**) in **TS 4.1** (Figure 4.4b), which leads to the major observed regioisomer. That is, the LUMO is more concentrated on the less substituted double bond of the allene.

The corresponding analysis was performed for the competing endo pathways for the Diels–Alder reaction of ester-substituted allene **4.62** and furan (**4.30**). The $\Delta\Delta G^{\ddagger}$ and $\Delta\Delta E^{\ddagger}$ were calculated to be -4.9 kcal/mol and -4.7 kcal/mol, respectively, with the cycloaddition occurring on the olefin proximal to the ester, consistent with experimental findings (see Table 4.1, entry 8). $\Delta E_{dist}^{\ddagger}$ was again found to be comparable for the transition states leading to the major and minor regioisomers ($\Delta\Delta E_{dist}^{\ddagger} = 0.7$ kcal/mol favoring the minor pathway), but $\Delta E_{int}^{\ddagger}$ was much more favorable in the transition state leading to the major regioisomer ($\Delta\Delta E_{int}^{\ddagger} = -5.4$ kcal/mol). More favorable orbital interactions in **TS 4.2** (Figure 4.4b) occur upon interaction with the LUMO, now concentrated on the ester-substituted double bond. As shown in Figure 4.4b, the major pathway (**TS 4.2**) is highly asynchronous with initial bond formation occurring on the central allene carbon.

To better understand the favorable electronic interactions that lead to the observed regioselectivities, Hartree-Fock molecular orbitals were calculated for allenes **4.61** and **4.62**. The

aforementioned helical LUMOs of **4.61** and **4.62** are depicted (Figure 4.4c), along with the p_z orbital coefficients for both termini of the allene, which project in the direction at which bond formation occurs. In the case of **4.61**, the less substituted terminus possesses a larger coefficient in the LUMO, which correlates to the regioselectivity we observe in experiments involving Cbz-derivative **4.26**. On the other hand, for ester **4.62**, the larger orbital coefficient resides on the more substituted allene terminus, which is also consistent with our experimental results involving allene **4.27**. The slight charge separation in the transition state also contributes to the better stabilization of those transition states leading to the observed products.

Diels–Alabel Partners		ΔG and ΔE (Major regioisomer)	ΔG and ΔE (Minor regioisomer)	ΔΔG and ΔΔE
4.61 + **4.30**	TS 4.1	$\Delta G^{\ddagger} = 19.1$ $\Delta E^{\ddagger} = 4.6$ $\Delta E_{dist}^{\ddagger} = 10.9$ $\Delta E_{int}^{\ddagger} = -6.3$	$\Delta G^{\ddagger} = 20.6$ $\Delta E^{\ddagger} = 6.2$ $\Delta E_{dist}^{\ddagger} = 11.2$ $\Delta E_{int}^{\ddagger} = -5.0$	$\Delta\Delta G^{\ddagger} = -1.5$ $\Delta\Delta E^{\ddagger} = -1.6$ $\Delta\Delta E_{dist}^{\ddagger} = -0.3$ $\Delta\Delta E_{int}^{\ddagger} = -1.3$
4.62 + **4.30**	TS 4.2	$\Delta G^{\ddagger} = 12.8$ $\Delta E^{\ddagger} = -1.6$ $\Delta E_{dist}^{\ddagger} = 8.2$ $\Delta E_{int}^{\ddagger} = -9.8$	$\Delta G^{\ddagger} = 17.7$ $\Delta E^{\ddagger} = 3.1$ $\Delta E_{dist}^{\ddagger} = 7.5$ $\Delta E_{int}^{\ddagger} = -4.4$	$\Delta\Delta G^{\ddagger} = -4.9$ $\Delta\Delta E^{\ddagger} = -4.7$ $\Delta\Delta E_{dist}^{\ddagger} = 0.7$ $\Delta\Delta E_{int}^{\ddagger} = -5.4$

b.

TS 4.1 (4.61 + 4.30) — 2.56 Å, 2.19 Å

TS 4.2 (4.62 + 4.30) — 2.83 Å, 2.16 Å

c.

R = CO$_2$Me

4.61 (−0.38, 0.24) (frontside view of LUMO)

4.62 (0.24, −0.29) (frontside view of LUMO)

Figure 4.4. Computations provide insight into regio- and diastereoselectivities (all calculated energies are reported in kcal/mol).

4.7 Enantioenriched Silyl Triflates and Transfer of Chirality Studies

We were also intrigued by the idea of accessing an enantioenriched cycloadduct by intercepting an enantioenriched heterocyclic allene intermediate. Key precedent for this idea stems from the studies of Christl and Engels, who accessed a highly enantioenriched cycloadduct from in situ-generated 1-phenyl-1,2-cyclohexadiene using a low-temperature Skattebøl rearrangement, albeit in low yield.[15,41] As an alternate approach, we hypothesized that the silyl triflate precursors

to heterocyclic allenes could be utilized in enantioenriched form. To this end, we separated gram quantities of the enantiomers of ketones **4.17** and **4.18** and elaborated them to enantioenriched silyl triflates **4.23** and **4.20**, respectively. The chiral separations were achieved using preparative chiral supercritical fluid chromatography (SFC), either by batch processing or direct purification of gram quantities, an approach also used for gram-scale purifications in industrial settings.[42] As shown in Figure 4.5, we have found that the success of this strategy is highly dependent on the nature of the heterocyclic allene substituent. When employing optically enriched ester-containing silyl triflate (+)-**4.23** in the Diels–Alder cycloaddition with pyrrole **4.29b** or furans **4.30** or **4.31**, adducts **4.38–4.40** were obtained as expected, but in racemic form (Figure 4.5a). In contrast, when enantioenriched methyl-substituted silyl triflate (+)-**4.20** was utilized in the corresponding Diels–Alder reactions, the expected cycloadducts (+)-**4.35**, (–)-**4.36**, and (+)-**4.37** were obtained in 81–98% enantiomeric excess (Figure 4.5b). As noted earlier in Table 4.1, cycloadduct **4.37** is obtained as a mixture of regioisomers in the cycloaddition between allene **4.32** and dimethylfuran (**4.31**). Interestingly, the formation of the minor regioisomer in this reaction also proceeded without significant stereochemical erosion to give the corresponding cycloadduct (+)-**4.63** bearing vicinal tetrasubstituted stereocenters in 97% ee.

Calculations were performed to assess the racemization barriers for allenes **4.62** and **4.61** to determine whether the substituent affected the barrier for racemization of the chiral allenoate intermediate generated from the corresponding silyl triflate. Prior theoretical studies on the racemization of 1,2-cyclohexadiene (**4.3**) by Johnson and coworkers showed that the racemization of 1,2-cyclohexadiene (**4.3**) occurs via a diradical transition state.[6] As shown in Figure 4.5c, the racemization barrier for ester-containing allene **4.62** was determined to be only 14.1 kcal/mol and occurs via a diaradical transition state. In the case of methyl-substituted allene **4.61**, the barrier for

racemization was calculated to be 16.4 kcal/mol, which is consistent with faster racemization of

4.62 than **4.61**, a result of greater stabilization of the diradical transition state from **4.62**. As such,

we hypothesize that allene **4.62** undergoes racemization faster than cycloaddition, thus accounting

for the formation of racemic **4.38**–**4.40** (see Figure 4.5a). With racemization being disfavorable,

the Diels–Alder reactions to give **4.35**–**4.37** proceed with significant transfer of stereochemical

information (see Figure 4.5b). At present, we cannot rule out the possibility of racemization

occurring after desilylation, but prior to allene formation. Nonetheless, these results demonstrate

that heterocyclic allenes may be employed as building blocks for enantioenriched products, while

further showcasing the key role of substituents in governing selectivities in reactions of

heterocyclic allenes.
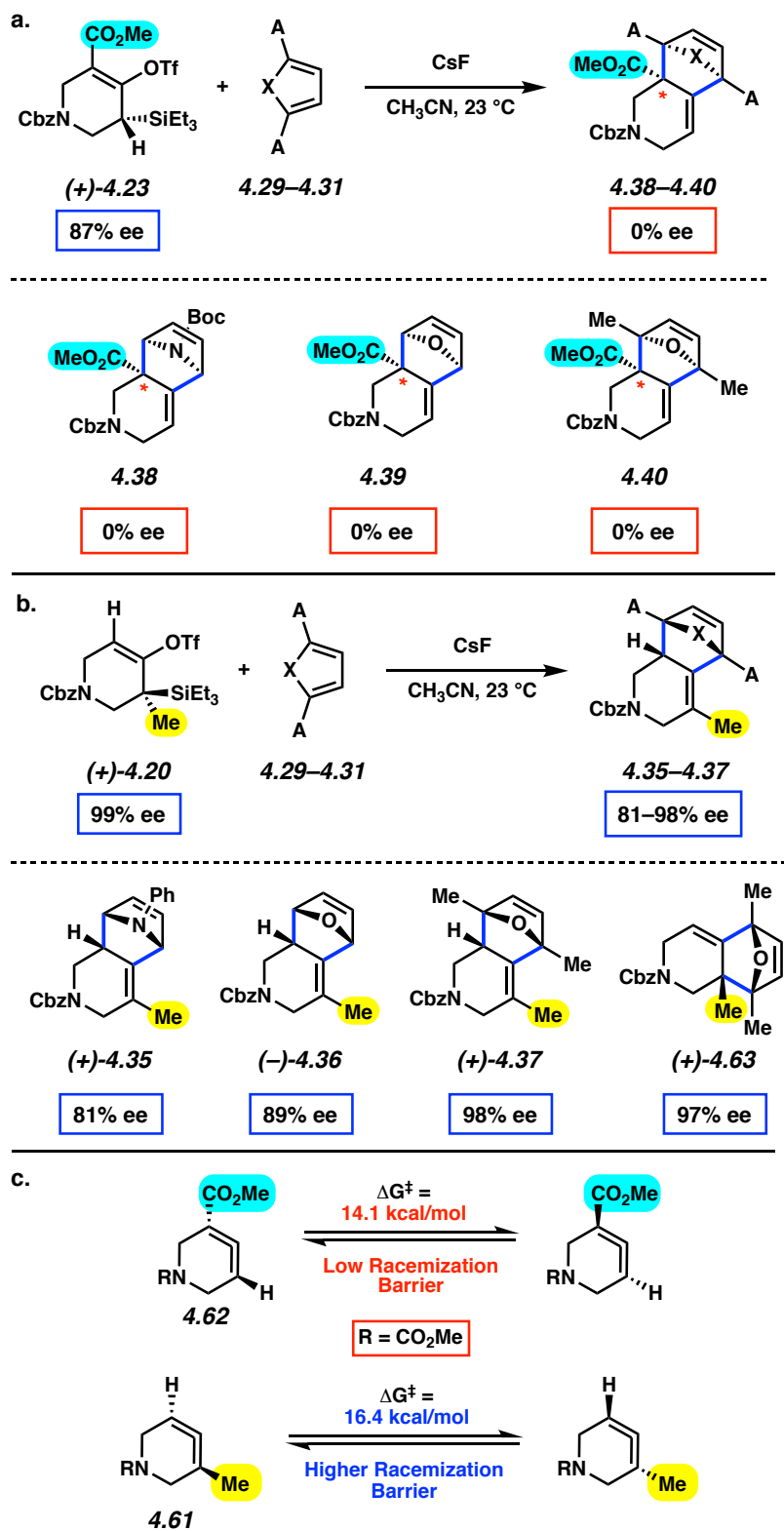
Figure 4.5. Attempted transfer of stereochemical information from silyl triflates to cycloadducts via azacyclic allene intermediates.

4.8 Conclusion

We have performed an experimental and computational study of unusual azacyclic allene intermediates. Our study includes syntheses of stable allene precursors, which in turn can be used to access the desired azacyclic allenes in situ under mild reaction conditions. Diels–Alder trapping of the allene intermediates provides an array of functionalized piperidines bearing multiple stereogenic centers, including quaternary centers in some cases. DFT studies show that computations correctly predict the observed diastereoselectivities, with cycloadditions occurring through concerted asynchronous endo transition states. A detailed distortion-interaction analysis explains the origins of the observed regiochemistry of the Diels–Alder cycloadditions. Lastly, by assessing enantioenriched silyl triflates, we found that stereochemical information can be transferred from a silyl triflate starting material to Diels–Alder cycloadducts, provided the allene is appropriately substituted.

The structure and reactivity of strained organic compounds has intrigued the chemical community for over a century. However, cyclic allenes have received relatively little attention, especially in comparison to cyclic alkynes. Our present study demonstrates that strained azacyclic allenes, although largely neglected, serve as valuable building blocks for the construction of complex molecular scaffolds bearing multiple stereogenic centers.

4.9 Experimental Section

4.9.1 Materials and Methods

Unless stated otherwise, reactions were conducted in flame-dried glassware under an atmosphere of nitrogen using anhydrous solvents (freshly distilled or passed through activated alumina columns). All commercially obtained reagents were used as received unless otherwise specified. Cesium fluoride (CsF), was obtained from Strem Chemicals. Triethylsilyl chloride (TESCl) was obtained from Oakwood Products, Inc. Iodomethane (MeI) and furan (**4.30**) were obtained from Alfa Aesar. 1,1-Diethoxyethene (**4.59**) and sodium borohydride were obtained from Fluka. L-Selectride (1 M in THF), *N*-(5-chloro-2-pyridyl)bis(trifluoromethanesulfonimide) (Comins' Reagent), potassium bis(trimethylsilyl)amide (KHMDS), hexamethylphosphoramide (HMPA), methyl cyanoformate (Mander's Reagent), lithium diisopropylamide (LDA), *N*-Boc pyrrole (**4.29b**), sodium hydride, *N*-phenylpyrrole (**4.29a**), and 2,5-dimethylfuran (**4.31**) were obtained from Sigma Aldrich. Sodium hydride was washed with pentane prior to use and stored in an Argon-filled glovebox. Trifluoromethanesulfonic anhydride (Tf$_2$O) was obtained from Combi-Blocks. Benzyl chloroformate (CbzCl) was obtained from TCI America. **4.31**, Tf$_2$O, HMPA, and diisopropylamine were distilled over CaH$_2$ prior to use. **4.30** and **4.29b** were filtered over basic alumina prior to use. Reaction temperatures were controlled using an IKAmag temperature modulator and, unless stated otherwise, reactions were performed at room temperature (approximately 23 °C). Thin layer chromatography (TLC) was conducted with EMD gel 60 F254 pre-coated plates (0.25 mm) and visualized using a combination of UV light, anisaldehyde, and potassium permanganate staining. Silicycle Siliaflash P60 (particle size 0.040–0.063 mm) was used for flash column chromatography. ^{1}H-NMR and 2D-NOESY spectra were recorded on Bruker spectrometers (at 400, 500, and 600 MHz) and are reported relative to the residual solvent signal.

Data for ^{1}H-NMR spectra are reported as follows: chemical shift (δ ppm), multiplicity, coupling constant (Hz) and integration. ^{13}C-NMR spectra were recorded on Bruker spectrometers (at 100 and 125 MHz) and are reported relative to the residual solvent signal. Data for ^{13}C-NMR spectra are reported in terms of chemical shift and, when necessary, multiplicity, and coupling constant (Hz). ^{19}F-NMR spectra were recorded on Bruker spectrometers (at 376 MHz) and reported in terms of chemical shift (δ ppm). IR spectra were obtained on a Perkin-Elmer UATR Two FT-IR spectrometer and are reported in terms of frequency of absorption (cm^{-1}). Uncorrected melting points were measured using a Digimelt MPA160 melting point apparatus. DART-MS spectra were collected on a Thermo Exactive Plus MSD (Thermo Scientific) equipped with an ID-CUBE ion source and a Vapur Interface (IonSense Inc.). Both the source and MSD were controlled by Excalibur software v. 3.0. The analyte was spotted onto OpenSpot sampling cards (IonSense Inc.) using CDCl$_3$ as the solvent. Ionization was accomplished using UHP He (Airgas Inc.) plasma with no additional ionization agents. The mass calibration was carried out using Pierce LTQ Velos ESI (+) and (−) Ion calibration solutions (Thermo Fisher Scientific). Chiral separations of compounds **4.17** and **4.18** were performed by Lotus Separations, LLC. Determination of enantiopurity was carried out on a Mettler Toledo SFC (supercritical fluid chromatography) using a Daicel ChiralPak OJ-H column and a Daicel ChiralPak IA-3 column. Optical rotations were measured with a Rudolph Autopol III Automatic Polarimeter.

*Nitrones **4.45**,[43] **4.47**,[18] **4.49**,[44] and **4.51**,[44] azomethine imines **4.53**[45] and **4.55**,[46] and nitrile oxide **4.57**[47] are all known compounds. ^{1}H-NMR spectral data matched those reported in the literature.*

4.9.2 Experimental Procedures

4.9.2.1 Syntheses of Silyl Triflate Precursors
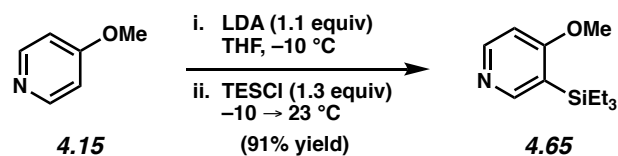
4-Methoxy-3-(triethylsilyl)pyridine (4.65). To a solution of diisopropylamine (13.9 mL, 99.0 mmol, 1.2 equiv) in THF (165 mL) at –10 °C was added *n*-BuLi (2.52 M in hexanes, 34.0 mL, 90.8 mmol, 1.1 equiv) dropwise over 1 h. The solution was stirred for 30 min at –10 °C, then 4-methoxypyridine (**4.15**, 9.00 g, 82.5 mmol, 1.0 equiv) was added dropwise over 20 min and stirred for 1 h at –10 °C. Next, TESCl (18.9 mL, 107 mmol, 1.3 equiv) was added dropwise over 1 h and was allowed to stir at –10 °C for 1 h. The reaction was allowed to warm to 23 °C. After stirring for 2 h, deionized water (1.0 mL) was added to the reaction and THF was removed under reduced pressure. The reaction was diluted with deionized water (75 mL) and was extracted with diethyl ether (3 x 50 mL). The combined organic layers were washed with deionized water (3 x 100 mL) and brine (1 x 100 mL), dried over Na_2SO_4, filtered, and concentrated under reduced pressure. The resulting crude oil was dry loaded onto SiO_2 (20.0 g) from a diethyl ether solution and was purified by flash chromatography (100% EtOAc) to afford silyl pyridine **4.65** (16.8 g, 91% yield) as a light yellow oil. Silyl pyridine **4.65**: R_f 0.52 (100% EtOAc); ^{1}H-NMR (400 MHz, CDCl$_3$): δ 8.48 (d, *J* = 5.8, 1H), 8.37 (s, 1H), 6.74 (d, *J* = 5.8, 1H), 3.84 (s, 3H), 0.96–0.91 (m, 9H), 0.86–0.81 (m, 6H); ^{13}C-NMR (100 MHz, CDCl$_3$): δ 170.5, 156.0, 152.4, 120.0, 105.4, 54.8, 7.5, 3.3; IR (film): 2952, 2874, 1571, 1559, 1271 cm^{-1}; HRMS–APCI (*m/z*) [M + H]$^+$ calcd for C$_{12}$H$_{22}$NOSi$^+$, 224.1465; found, 224.1464.
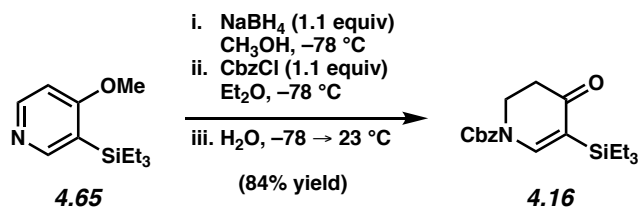
Enone 4.16. To a solution of silyl pyridine **4.65** (10.0 g, 44.5 mmol, 1.0 equiv) in methanol (100 mL) at –78 °C was added NaBH$_4$ (1.85 g, 49.0 mmol, 1.1 equiv). After stirring for 1 h at –78 °C, CbzCl (6.97 mL, 49.0 mmol, 1.1 equiv) in diethyl ether (15 mL) was transferred to the reaction via cannulation over 5 min. After stirring for 1 h at –78 °C, deionized water (15 mL) was added and the cooling bath was removed, allowing the reaction to warm to 23 °C before diluting with deionized water (100 mL). The layers were separated and the aqueous layer was extracted with Et$_2$O (3 x 50 mL). The combined organic layers were washed with deionized water (3 x 50 mL) and brine (1 x 50 mL), dried over Na$_2$SO$_4$, filtered, and concentrated under reduced pressure. The resulting crude oil was purified by flash chromatography (3:2 hexanes:Et$_2$O) to give enone **4.16** (12.9 g, 84% yield) as a colorless oil. Enone **4.16**: R$_f$ 0.43 (3:2 hexanes:Et$_2$O); ^{1}H-NMR (400 MHz, CDCl$_3$): δ 7.82 (br s, 1H), 7.44–7.34 (m, 5H), 5.27 (s, 2H), 4.00 (t, J = 7.3, 2H), 2.53 (t, J = 7.4, 2H), 0.90 (t, J = 8.0, 9H), 0.69 (q, J = 8.0, 6H); ^{13}C-NMR (125 MHz, CDCl$_3$, 9 of 13 observed): δ 196.8, 135.3, 128.9, 128.5, 69.0, 42.7, 36.2, 7.6, 3.1; IR (film): 2953, 2874, 1728, 1658, 1577, 1301 cm^{-1}; HRMS–APCI (m/z) [M + H]$^+$ calcd for C$_{19}$H$_{28}$NO$_3$Si$^+$, 346.1833; found, 346.1833.
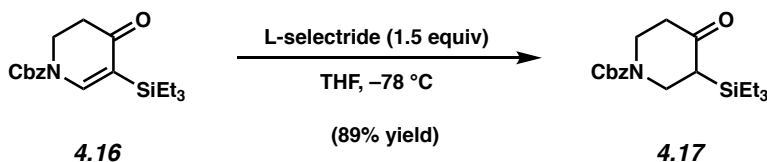
Ketone 4.17. To a solution of enone **4.16** (1.57 g, 4.55 mmol, 1.0 equiv) in THF (23 mL) at –78 °C was added L-selectride (1.0 M solution in THF, 6.83 mL, 6.83 mmol, 1.5 equiv) dropwise over 13 min. The reaction was stirred at –78 °C for 2 h, then quenched by the addition of a saturated

174

aqueous solution of NH$_4$Cl (9 mL) and allowed to warm to 23 °C. The layers were separated and the aqueous layer was extracted with Et$_2$O (3 x 40 mL). The combined organic layers were dried over Na$_2$SO$_4$, filtered, and concentrated under reduced pressure to provide the crude product, which was purified by flash chromatography (9:1 hexanes:EtOAc) to afford ketone **4.17** as a colorless oil (1.41 g, 89% yield). Ketone **4.17**: R$_f$ 0.36 (1:1 hexanes:Et$_2$O); ^{1}H-NMR (500 MHz, CDCl$_3$): δ 7.41–7.29 (m, 5H), 5.26–5.07 (m, 2H), 4.20–3.96 (m, 2H), 3.82–3.59 (m, 1H), 3.54–3.33 (m, 1H), 2.58–2.31 (m, 3H), 1.03–0.81 (m, 9H), 0.72–0.51 (m, 6H); ^{13}C-NMR (125 MHz, CDCl$_3$): δ 209.2, 208.8, 155.2, 136.6, 136.4, 128.73, 128.67, 128.5, 128.4, 128.3, 128.2, 67.8, 67.6, 42.9, 42.8, 42.5, 42.2, 40.2, 7.4, 3.0; IR (film): 2954, 2876, 1692, 1417, 1232 cm^{-1}; HRMS–APCI (*m/z*) [M + H]$^+$ calcd for C$_{19}$H$_{30}$O$_3$Si$^+$, 348.1989; found, 348.1981.

*Note: **4.17** was obtained as a mixture of rotamers. These data represent empirically observed chemical shifts from the ^{13}C-NMR spectrum.*
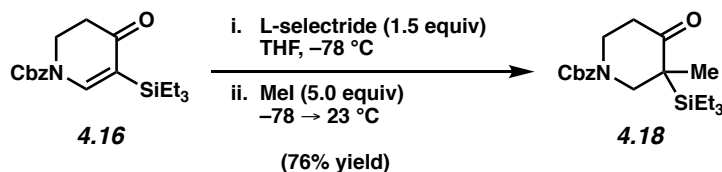
Ketone 4.18. To a solution of enone **4.16** (1.00 g, 2.89 mmol, 1.0 equiv) in THF (15.0 mL) at –78 °C was added L-selectride (1.0 M solution in THF, 4.34 mL, 4.34 mmol, 1.5 equiv) dropwise over 10 min. After stirring for 1 h, iodomethane (0.900 mL, 14.5 mmol, 5.0 equiv) was added dropwise 3 min at –78 °C, then the cold bath was removed and the reaction was warmed to 23 °C. Aluminum foil was used to cover the reaction and exclude light. After stirring for 4 h, deionized water (50 mL) was added and the layers were separated. The aqueous layer was extracted with diethyl ether (3 x 20 mL). The combined organic layers were washed with deionized water (3 x 20 mL) and brine (1 x 20 mL), dried over Na$_2$SO$_4$, filtered, and concentrated under reduced pressure.

The resulting crude oil was purified via flash chromatography (3:1 hexanes:EtOAc) to give ketone **4.18** (795 mg, 76% yield) as a colorless oil. Ketone **4.18**: R_f 0.30 (1:1 hexanes:Et$_2$O); ^{1}H-NMR (500 MHz, CDCl$_3$): δ 7.42–7.29 (m, 5H), 5.27–5.06 (m, 2H), 4.22–3.97 (m, 2H), 3.49–3.18 (m, 2H), 2.67–2.35 (m, 2H), 1.25–1.11 (m, 3H), 1.04–0.85 (m, 9H), 0.75–0.56 (m, 6H); ^{13}C-NMR (125 MHz, CDCl$_3$): δ 212.2, 211.5, 155.6, 155.2, 136.7, 136.4, 128.7, 128.5, 128.3, 128.1, 67.7, 67.5, 50.2, 49.9, 46.0, 45.6, 42.8, 42.4, 39.7, 39.6, 18.3, 7.9, 7.6, 2.4; IR (film): 2954, 2877, 1690, 1418, 1231 cm^{-1}; HRMS–APCI (*m/z*) [M + H]$^+$ calcd for C$_{20}$H$_{32}$NO$_3$Si$^+$, 362.2146; found, 362.2137.

*Note: **4.18** was obtained as a mixture of rotamers. These data represent empirically observed chemical shifts from the ^{13}C-NMR spectrum.*
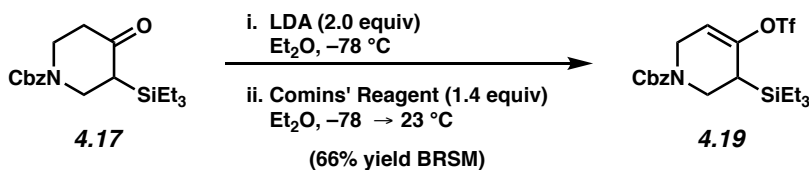
Silyl triflate 4.19. Solid LDA (142 mg, 1.33 mmol, 2.0 equiv) was added to a flame dried vial. The LDA was then suspended in diethyl ether (2.50 mL) and cooled to –78 °C for 20 min. In a separate flame-dried vial, ketone **4.17** (231 mg, 0.665 mmol, 1.0 equiv) was dissolved in diethyl ether (2.50 mL) and cooled to –78 °C for 20 min. The ketone solution was then transferred to the LDA pot via dropwise cannula transfer over 1 min and the reaction was stirred at –78 °C for 2 h. Then, Comins' Reagent (365 mg, 0.931 mmol, 1.4 equiv) in diethyl ether (2.50 mL) at –78 °C was added to the reaction flask via dropwise cannula transfer over 1 min. The cooling bath was removed and the reaction was allowed to warm to 23 °C. After stirring for 12 h, the reaction was quenched by addition of an aqueous solution of 5% (w/w) NaHCO$_3$ (5.0 mL). The layers were separated and the aqueous layer was extracted with diethyl ether (3 x 5 mL). The combined organic

layers were washed with water (3 x 5 mL) and brine (1 x 5 mL), dried over Na$_2$SO$_4$, filtered, and concentrated under reduced pressure. The resulting crude yellow oil was purified by flash chromatography (13:7 Hexanes:EtOAc) to provide silyl triflate **4.19** as a clear oil (140 mg, 45% yield, 66% yield BRSM) and single regioisomer. Unreacted starting material (76.2 mg, 33% yield) was recovered as a yellow oil. Silyl triflate **4.19**: R$_f$ 0.71 (3:1 hexanes:EtOAc); ^{1}H-NMR (500 MHz, CDCl$_3$): δ 7.45–7.29 (m, 5H), 5.68–5.55 (m, 1H), 5.27–5.08 (m, 2H), 4.29–4.16 (m, 1H), 4.11–3.89 (m, 2H), 3.52 (dd, J = 13.1, 4.4, 1H), 2.15–2.00 (m, 1H), 1.02–0.86 (m, 9H), 0.72–0.53 (m, 6H); ^{13}C-NMR (125 MHz, CDCl$_3$): δ 155.2, 154.9, 150.9, 150.4, 136.5, 136.2, 128.7, 128.5, 128.4, 128.2, 118.6 (q, J_{C-F} = 324.0), 111.3, 110.7, 67.8, 67.6, 42.6, 42.4, 42.1, 28.2, 28.0, 7.3, 2.9; ^{19}F NMR (376 MHz, CDCl$_3$): δ –73.6; IR (film): 2957, 2878, 1707, 1417, 1208 cm^{-1}; HRMS– APCI (*m/z*) [M + H]$^+$ calcd for C$_{20}$H$_{29}$F$_3$NO$_5$SSi$^+$, 480.1482; found, 480.1492.

*Note: **4.19** was obtained as a mixture of rotamers. These data represent empirically observed*

chemical shifts from the ^{13}C-NMR spectrum. While we were able to obtain only the desired

regioisomer following this procedure, during reaction optimization we often encountered a

mixture of olefin isomers. These isomers were inseparable by chromatography; however, by

heating in DMSO at 100 °C for 15 min, the undesired isomer decomposes and after purification,

***4.19** can be obtained as a single regioisomer.*
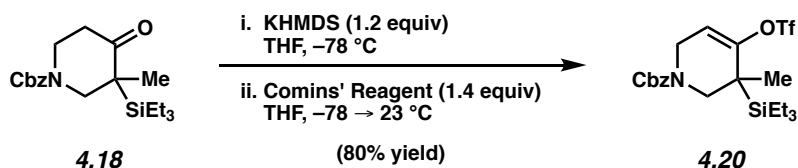
Silyl triflate 4.20. To a solution of KHMDS (1.18 g, 5.93 mmol, 1.2 equiv) in THF (7.6 mL) at –78 °C was added a solution of ketone **4.18** (1.79 g, 4.94 mmol, 1.0 equiv) in THF (7.6 mL) dropwise over 20 min. After stirring for 15 min, a solution of Comins' Reagent (2.72 g, 6.92 mmol,

1.4 equiv) in THF (7.7 mL) was added dropwise over 15 min at –78 °C, then the cooling bath was removed and reaction was allowed to warm to 23 °C. After stirring for 22 h, the reaction was quenched by addition of an aqueous solution of 5% (w/w) NaHCO$_3$ (10 mL). The layers were separated and the aqueous layer was extracted with Et$_2$O (3 x 20 mL). The combined organic layers were dried over MgSO$_4$, filtered, and concentrated under reduced pressure to provide the crude product, which was purified by flash chromatography (19:1 hexanes:EtOAc) to afford silyl triflate **4.20** as a pale yellow oil (1.95 g, 80% yield). Silyl triflate **4.20**: R$_f$ 0.32 (9:1 hexanes:EtOAc); ^{1}H-NMR (500 MHz, CDCl$_3$): δ 7.41–7.30 (m, 5H), 5.70–5.55 (m, 1H), 5.26–5.07 (m, 2H), 4.18 (d, J = 17.6, 1H), 4.00 (dd, J = 17.7, 3.0, 1H), 3.71 (d, J = 13.2, 1H), 3.52–3.39 (m, 1H), 1.24–1.11 (m, 3H), 1.03–0.90 (m, 9H), 0.75–0.60 (m, 6H); ^{13}C-NMR (125 MHz, CDCl$_3$): δ 155.4, 155.0, 154.4, 136.5, 136.4, 128.7, 128.4, 128.2, 118.5 (q, $J_{C–F}$ = 319.3), 110.1, 109.6, 67.7, 50.2, 42.6, 42.4, 31.4, 18.6, 7.8, 2.5, 2.3; ^{19}F NMR (376 MHz, CDCl$_3$): δ –74.5; IR (film): 2958, 2879, 1706, 1415, 1207 cm^{-1}; HRMS–APCI (m/z) [M + H]$^+$ calcd for C$_{21}$H$_{31}$F$_3$NO$_5$SSi$^+$, 494.1639; found, 494.1624.

*Note: **4.20** was obtained as a mixture of rotamers. These data represent empirically observed chemical shifts from the ^{13}C-NMR spectrum.*
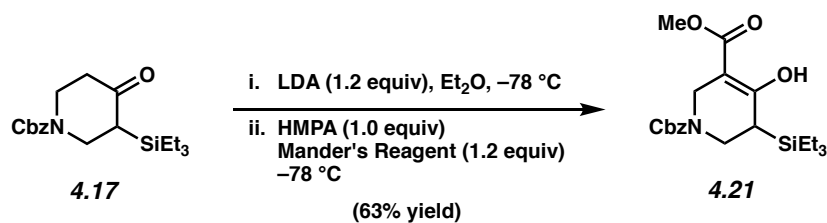
Vinylogous acid 4.21. To a solution of diisopropylamine (582 μL, 4.16 mmol, 1.2 equiv) in Et$_2$O (8.4 mL) at –78 °C was added *n*-BuLi (2.0 mL, 2.06 M in hexanes, 4.16 mmol, 1.2 equiv) dropwise over 4 min. The reaction was stirred at –78 °C for 25 min, then allowed to stir at 23 °C for 10 min. Then the reaction mixture was cooled to –78 °C and a solution of ketone **4.17** (1.3 g, 3.47 mmol,

1.0 equiv) in Et$_2$O (3.6 mL) was added dropwise over 10 min and stirred at –78 °C for 2 h. Then

HMPA (604 µL, 3.47 mmol, 1.0 equiv) and Mander's Reagent (330 µL, 4.16 mmol, 1.2 equiv)

were added dropwise sequentially over 3 min at –78 °C. The reaction was stirred at –78 °C for

1 h, then quenched by the addition of cold deionized water (0 °C, 18 mL) and allowed to warm to

23 °C. The layers were separated and the aqueous layer was extracted with Et$_2$O (3 x 30 mL). The

combined organic layers were dried over Na$_2$SO$_4$, filtered, and concentrated under reduced

pressure to provide the crude product, which was purified by flash chromatography (19:1

hexanes:EtOAc) to afford vinylogous acid **4.21** as a colorless oil (880 mg, 63% yield). Vinylogous

acid **4.21**: R$_f$ 0.45 (5:1 hexanes:Et$_2$O); ^{1}H-NMR (500 MHz, CDCl$_3$): δ 12.28 (s, 1H) 7.40–7.30 (m,

5H), 5.30–5.07 (m, 2H), 4.19 (d, J = 15.4, 1H) 4.02 (dd, J = 15.7, 1.6, 1H) 3.97–3.81 (m, 1H), 3.76

(s, 3H), 3.52–3.43 (m, 1H), 2.18–2.01 (m, 1H), 1.03–0.83 (m, 9H), 0.74–0.53 (m 6H); ^{13}C-NMR

(125 MHz, CDCl$_3$): δ 175.4, 174.6, 171.1, 155.3, 154.9, 136.8, 136.4, 128.6, 128.5, 128.4, 128.3,

128.1, 128.0, 93.0, 92.5, 67.7, 67.4, 67.2, 51.4, 41.6, 41.4, 41.0, 40.6, 29.0, 7.3, 3.1; IR (film):

2953, 2876, 1701, 1654, 1610 cm^{-1}; HRMS–APCI (*m/z*) [M + H]$^+$ calcd for C$_{21}$H$_{31}$NO$_5$Si$^+$,

406.2044; found, 406.2043.

*Note: **4.21** was obtained as a mixture of rotamers. These data represent empirically observed*

chemical shifts from the ^{13}C-NMR spectrum.
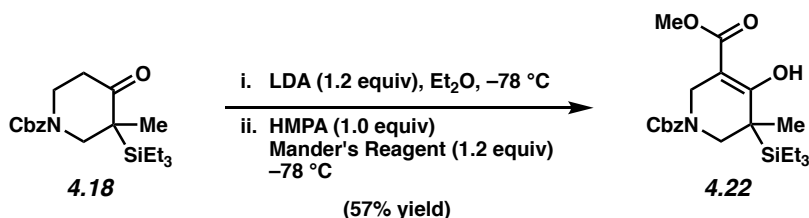
Vinylogous acid 4.22. To a solution of diisopropylamine (0.698 mL, 4.98 mmol, 1.2 equiv) in

Et$_2$O (15.0 mL) at –78 °C was added *n*-BuLi (2.49 M in hexanes, 2.00 mL, 49.8 mmol, 1.2 equiv)

dropwise over 5 min. The reaction was stirred at –78 °C for 15 min, then allowed to stir at 23 °C for 30 min. Then the reaction mixture was cooled to –78 °C and a solution of ketone **4.18** (1.50 g, 4.15 mmol, 1.0 equiv) in Et_2O (15.0 mL) was added via cannula over 30 min. After stirring for 2 h at –78 °C, HMPA (0.722 mL, 4.15 mmol, 1.0 equiv) and Mander's Reagent (0.396 mL, 4.98 mmol, 1.2 equiv) were added dropwise sequentially over 3 min at –78 °C. After stirring for 1 h, deionized water (50.0 mL) was added and the reaction was allowed to warm to 23 °C. The layers were separated and the aqueous layer was extracted with Et_2O (3 x 50 mL). The combined organic layers were then washed with deionized water (3 x 50 mL) and brine (1 x 50 mL), dried over Na_2SO_4, filtered, and concentrated under reduced pressure. The resulting crude oil was dry loaded on SiO_2 and purified via flash chromatography (17:3 hexanes:EtOAc) to give vinylogous acid **4.22** (1.00 g, 57% yield) as a colorless oil. Vinylogous acid **4.22**: R_f 0.51 (4:1 hexanes:EtOAc); ^{1}H-NMR (500 MHz, $CDCl_3$): δ 12.41 (s, 1H), 7.42–7.28 (m, 5H), 5.26–5.08 (m, 2H), 4.22–4.03 (m, 2H), 3.84–3.66 (m, 4H), 3.31–3.19 (m, 1H), 1.28–1.13 (m, 3H), 1.03–0.86 (m, 9H), 0.76–0.57 (m, 6H); ^{13}C-NMR (125 MHz, $CDCl_3$): δ 178.5, 177.7, 171.6, 168.7, 155.6, 155.2, 136.9, 136.6, 128.7, 128.61, 128.60, 128.4, 128.2, 93.1, 92.6, 67.4, 51.6, 49.2, 41.5, 41.3, 32.8, 18.7, 7.9, 2.8; IR (film): 2954, 2877, 1706, 1655, 1607, 1242 cm^{-1}; HRMS–APCI (*m/z*) [M + H]$^+$ calcd for $C_{22}H_{35}NO_5Si^+$, 420.2201; found, 420.2207.

*Note: **4.22** was obtained as a mixture of rotamers. These data represent empirically observed chemical shifts from the ^{13}C-NMR spectrum.*
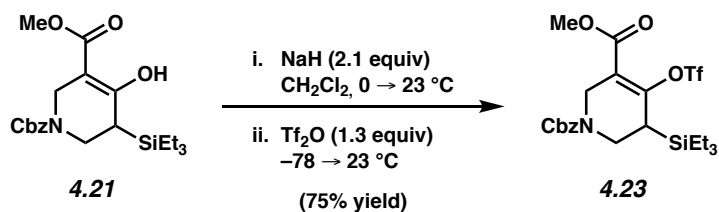
Silyl triflate 4.23. To a solution of NaH (124 mg, 5.18 mmol, 2.1 equiv) in CH_2Cl_2 (16.4 mL) at

0 °C was added a solution of vinylogous acid **4.21** (1.0 g, 2.47 mmol, 1.0 equiv) in CH_2Cl_2 (8.2

mL) dropwise over 25 min and allowed to warm to 23 °C. After stirring for 1 h, the reaction was

cooled to –78 °C and Tf_2O (540 μL, 3.21 mmol, 1.3 equiv) was added dropwise over 1 min. After

stirring for 15 min, the reaction was allowed to warm to 23 °C and stirred for 2 h. The reaction

was cooled to 0 °C and was quenched by the addition of deionized water (50 mL). The layers were

separated and the aqueous layer was extracted with CH_2Cl_2 (3 x 60 mL). The combined organic

layers were dried over Na_2SO_4, filtered, and concentrated under reduced pressure to provide the

crude product, which was purified by flash chromatography (19:1 hexanes:EtOAc) to afford silyl

triflate **4.23** as a light yellow oil (1.0 g, 75% yield). Silyl triflate **4.23**: R_f 0.23 (9:1 hexanes:EtOAc);

^{1}H-NMR (400 MHz, $CDCl_3$): δ 7.41–7.29 (m, 5H), 5.29–5.07 (m, 2H), 4.53–4.34 (m, 1H),

4.27–4.07 (m, 2H), 3.79 (s, 3H), 3.39 (dd, J = 13.1, 4.1, 1H), 2.17–2.03 (m, 1H), 0.98–0.83 (m,

9H), 0.72–0.53 (m, 6H); ^{13}C-NMR (100 MHz, $CDCl_3$): δ 163.2, 155.3, 154.9, 136.2, 128.6, 128.3,

118.3 (q, J_{C-F} = 321.0), 115.3, 67.7, 52.2, 43.4, 42.0, 30.0, 29.7, 7.0, 2.7; ^{19}F NMR (376 MHz,

$CDCl_3$): δ –74.1; IR (film): 2957, 2879, 1711, 1424, 1213 cm^{-1}; HRMS–APCI (*m/z*) [M + H]$^+$

calcd for $C_{22}H_{31}F_3NO_7SSi^+$, 538.1537; found, 538.1550.

*Note: **4.23** was obtained as a mixture of rotamers. These data represent empirically observed*

chemical shifts from the ^{13}C-NMR spectrum.
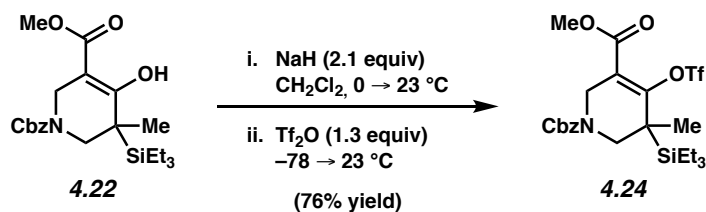
Silyl triflate 4.24. To a solution of NaH (7.2 mg, 0.300 mmol, 2.1 equiv) in CH$_2$Cl$_2$ (1.2 mL) at

0 °C was added a solution of vinylogous acid **4.22** (60.0 mg, 0.143 mmol, 1.0 equiv) in CH$_2$Cl$_2$

(0.4 mL) dropwise over 2 min and allowed to warm to 23 °C. After stirring for 1 h, the reaction

was cooled to –78 °C and Tf$_2$O (31.3 μL, 0.186 mmol, 1.3 equiv) was added dropwise over 1 min.

After stirring for 30 min, the cooling bath was removed and the reaction was stirred at 23 °C for

2 h, then the reaction was quenched by the addition of deionized water (5 mL) at 0 °C. The layers

were separated and the aqueous layer was extracted with CH$_2$Cl$_2$ (3 x 10 mL). The combined

organic layers were dried over Na$_2$SO$_4$, filtered, and concentrated under reduced pressure to

provide the crude product, which was purified by flash chromatography (19:1 hexanes:EtOAc) to

afford silyl triflate **4.24** as a colorless oil (59.7 mg, 76% yield). Silyl triflate **4.24**: R$_f$ 0.41 (4:1

hexanes:EtOAc); ^{1}H-NMR (500 MHz, CDCl$_3$): δ 7.40–7.30 (m, 5H), 5.30–5.04 (m, 2H), 4.81–

4.65 (m, 1H), 3.97–3.85 (m, 1H), 3.81–3.64 (m, 4H), 3.50–3.33 (m, 1H), 1.36–1.17 (m, 3H), 1.07–

0.91 (m, 9H), 0.79–0.61 (m, 6H); ^{13}C-NMR (125 MHz, CDCl$_3$): δ 164.2, 157.1, 155.4, 154.8,

136.3, 128.7, 128.4, 128.3, 118.3 (q, J_{C-F} = 318.7), 117.9, 117.4, 67.9, 52.5, 50.3, 44.4, 34.0, 18.2,

7.8; ^{19}F NMR (376 MHz, CDCl$_3$): δ –72.5; IR (film): 2957, 2880, 1710, 1423, 1210 cm^{-1}; HRMS–

APCI (*m/z*) [M + H]$^+$ calcd for C$_{23}$H$_{33}$F$_3$NO$_7$SSi$^+$, 552.1694; found, 552.1793.

*Note: **4.24** was obtained as a mixture of rotamers. These data represent empirically observed*

chemical shifts from the ^{13}C-NMR spectrum.

4.9.2.2 Diels–Alder Trapping Experiments

Representative Procedure (Preparation of cycloadduct 4.32 is used as an example).
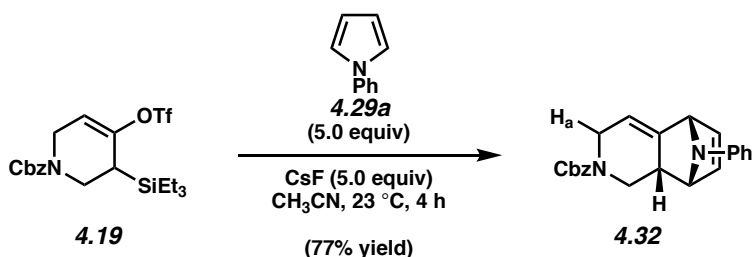
Cycloadduct 4.32. To a stirred solution of silyl triflate **4.19** (52.1 mg, 0.108 mmol, 1.0 equiv) and

N-phenylpyrrole (**4.29a**, 77.6 mg, 0.543 mmol, 5.0 equiv) in CH$_3$CN (1.1 mL) was added CsF

(82.5 mg, 0.543 mmol, 5.0 equiv). The reaction vessel was sealed and allowed to stir at 23 °C for

4 h. The reaction mixture was filtered by passage through a plug of silica gel (EtOAc eluent,

10 mL). Evaporation under reduced pressure yielded the crude residue, which was purified by

preparative thin layer chromatography (2:1 hexanes:EtOAc) to afford cycloadduct **4.32** as a light

yellow amorphous solid (77% yield, 4.7:1 dr, average of two experiments). Diastereomeric ratio

was determined by integrating the following peaks in the ^{1}H-NMR spectrum of the crude reaction

mixture (H$_a$ Major: 3.64 ppm; Minor: 3.80 ppm). Cycloadduct **4.32**: R$_f$ 0.26 (2:1 hexanes:EtOAc);

^{1}H-NMR (500 MHz, CDCl$_3$): δ 7.38–7.28 (m, 5H), 7.23–7.16 (m, 2H), 6.89–6.83 (m, 1H), 6.80

(d, J = 6.9, 2H), 6.32–6.26 (m, 1H), 6.09–5.99 (m, 1H), 5.75–5.61 (m, 1H), 5.18–5.06 (m, 2H),

4.87 (s, 1H), 4.76–4.67 (m, 1H), 4.51–4.30 (m, 1H), 4.28–4.16 (m 1H), 3.60 (d, J = 18.4, 1H),

2.56–2.46 (m, 1H), 1.91 (dt, J = 31.5, 11.3, 1H); ^{13}C-NMR (125 MHz, CDCl$_3$): δ 155.9, 155.4,

146.6, 139.3, 138.9, 136.9, 135.0, 134.7, 129.2, 129.1, 128.8, 128.6, 128.2, 128.1, 128.0, 120.8,

120.7, 117.6, 117.5, 114.8, 114.4, 67.3, 65.4, 65.3, 45.7, 45.5, 43.9, 43.5, 39.3, 39.1; IR (film):

3033, 2862, 1697, 1497, 1415 cm^{-1}; HRMS–APCI (*m/z*) [M + H]$^+$ calcd for C$_{23}$H$_{23}$N$_2$O$_2{}^+$,

359.1754; found, 359.1744.

*Note: **4.32** was obtained as a mixture of rotamers. These data represent empirically observed*

chemical shifts from the ^{13}C-NMR spectrum.

The structure of **4.32** was verified by 2D-NOESY, as the following interaction was observed:
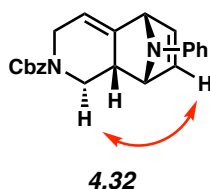
4.32

All reactions were monitored by TLC until starting material was consumed; the specific times are

listed in the reaction scheme for each reaction. Any modifications of the conditions shown in this

representative procedure are specified in the following schemes, which depict all of the results

shown in Table 4.1. For all compounds in which the diastereomeric ratios were >20:1, the minor

diastereomer was not observed in the ^{1}H-NMR of the crude reaction mixture.
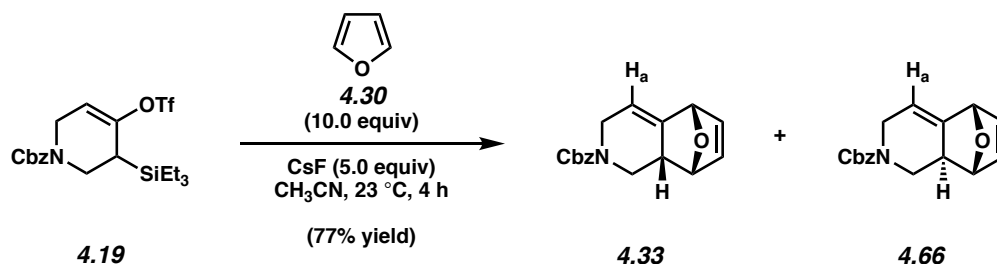
Cycloadduct 4.33. Purification by preparative thin layer chromatography (2:1:1 hexanes:CH₂Cl₂:Et₂O) afforded an inseparable mixture of cycloadducts **4.33** and **4.66** as a light yellow amorphous solid (77% yield, 7.4:1 dr, average of two experiments). Diastereomeric ratio was determined by integrating the following peaks in the ^{1}H-NMR spectrum of the crude reaction mixture (H$_a$ Major: 5.61 ppm; Minor: 5.82 ppm). Cycloadducts **4.33** and **4.66** were characterized as a mixture of diastereomers. Cycloadducts **4.33** and **4.66**: R$_f$ 0.47

(1:1 hexanes:EtOAc); ^{1}H-NMR (400 MHz, CDCl$_3$): **4.33** (major isomer): δ 7.41–7.28 (m, 5H), 6.41–6.32 (m, 1H), 6.09 (dd, J = 15.3, 5.4, 1H), 5.67–5.54 (m, 1H), 5.20–5.02 (m, 4H), 4.56–4.35 (m, 1H), 4.33–4.19 (m, 1H), 3.65–3.55 (m, 1H), 2.62–2.51 (m, 1H), 1.86–1.71 (m, 1H); **4.66** (minor isomer) δ 7.41–7.28 (m, 5H), 6.55–6.49 (m, 1H), 6.41–6.32 (m, 1H), 5.88–5.76 (m, 1H), 5.20–5.02 (m, 3H), 4.85–4.77 (m, 1H), 4.56–4.35 (m, 1H), 4.33–4.19 (m, 1H), 3.81–3.72 (m, 1H), 2.62–2.51 (m, 1H), 2.06–1.97 (m, 1H); ^{13}C-NMR (100 MHz, CDCl$_3$): δ 156.0, 155.5, 138.9, 138.6, 136.9, 136.1, 135.8, 129.5, 129.4, 128.6, 128.2, 128.0, 113.4, 113.0, 81.3, 80.1, 80.0, 79.9, 79.4, 77.4, 67.3, 45.6, 45.4, 43.8, 43.3, 40.1, 40.0; IR (film): 3008, 2866, 1691, 1414, 1229 cm^{-1}; HRMS–APCI (m/z) [M + H]$^+$ calcd for C$_{17}$H$_{18}$NO$_3{}^+$, 284.1281; found, 284.1271.

*Note: **4.33** and **4.66** were obtained as a mixture of rotamers. These data represent empirically*

observed chemical shifts from the ^{13}C-NMR spectrum.

The structures of **4.33** and **4.66** were verified by 2D-NOESY, as the following interactions were observed:

4.33   **4.66**

Cycloadduct 4.34. Purification by preparative thin layer chromatography (2:1:1 hexanes:CH$_2$Cl$_2$:Et$_2$O) afforded cycloadduct **4.34** as a colorless oil (82% yield, 13.7:1 dr,

average of two experiments). Diastereomeric ratio was determined by integrating the following peaks in the ^{1}H-NMR spectrum of the crude reaction mixture (H$_a$ Major: 5.48 ppm; Minor: 5.65 ppm). Cycloadduct **4.34**: R$_f$ 0.67 (1:1 hexanes:EtOAc); ^{1}H-NMR (500 MHz, CDCl$_3$): δ 7.42–7.27 (m, 5H), 6.15–6.09 (m, 1H), 5.88 (dd, J = 14.7, 5.2, 1H), 5.53–5.41 (m, 1H), 5.22–5.10 (m, 2H), 4.47–4.20 (m, 2H), 3.60 (ddd, J = 18.0, 4.2, 2.2, 1H), 2.37–2.30 (m, 1H), 1.80 (dt, J = 34.3, 11.3, 1H), 1.66–1.50 (m, 6H); ^{13}C-NMR (125 MHz, CDCl$_3$): δ 156.0, 155.6, 145.3, 145.0, 139.9, 139.6, 136.95, 136.90, 133.6, 133.4, 128.9, 128.7, 128.6, 128.2, 128.0, 111.6, 111.1, 87.0, 86.8, 67.3, 67.2, 47.1, 47.0, 45.3, 45.1, 43.7, 43.2, 18.1, 15.6, 15.01, 14.97; IR (film): 2974, 2931, 1702, 1606, 1416 cm^{-1}; HRMS–APCI (m/z) [M + H]$^+$ calcd for C$_{19}$H$_{22}$NO$_3{}^+$, 312.1600; found, 312.1593.

*Note: **4.34** was obtained as a mixture of rotamers. These data represent empirically observed chemical shifts from the ^{13}C-NMR spectrum.*

The structure of **4.34** was verified by 2D-NOESY, as the following interaction was observed:

4.34
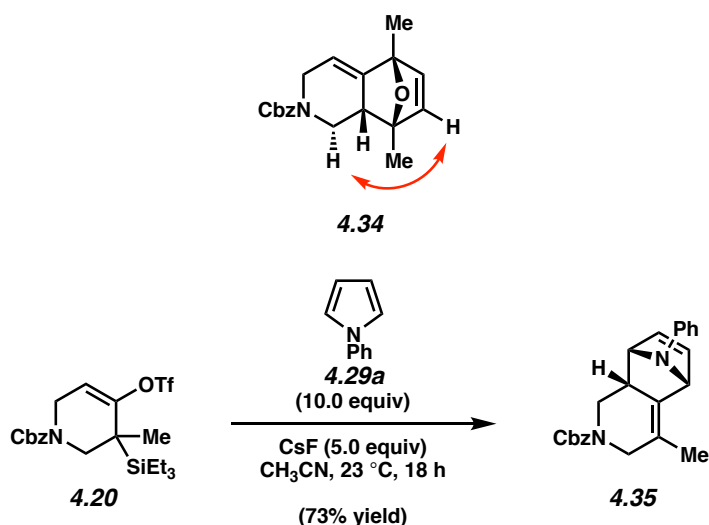
Cycloadduct 4.35. Purification by preparative thin layer chromatography (3:1 hexanes:EtOAc) afforded cycloadduct **4.35** as a colorless oil (73% yield, >20:1 dr, average of two experiments).

Cycloadduct **4.35**: R*f* 0.23 (3:1 hexanes:EtOAc); ^{1}H-NMR (500 MHz, CDCl$_3$): δ 7.39–7.29 (m, 5H), 7.23–7.17 (m, 2H), 6.89–6.83 (m, 1H), 6.80 (d, *J* = 8.2, 2H), 6.37–6.30 (m, 1H), 6.08–5.98 (m, 1H), 5.20–5.01 (m, 3H), 4.75–4.66 (m, 1H), 4.37 (ddd, *J* = 69.6, 11.4, 4.9, 1H), 4.18–4.06 (m, 1H), 3.54–3.38 (m, 1H), 2.55–2.46 (m, 1H), 1.94–1.76 (m, 4H); ^{13}C-NMR (125 MHz, CDCl$_3$): δ 155.7, 155.3, 146.8, 136.9, 134.3, 134.0, 132.3, 131.9, 129.1, 128.9, 128.70, 128.69, 128.6, 128.3, 128.12, 128.09, 122.3, 121.9, 120.8, 120.7, 117.7, 117.6, 67.25, 67.22, 65.5, 65.4, 63.8, 47.7, 47.3, 45.7, 45.5, 38.9, 38.6, 16.99, 16.97; IR (film): 3033, 2857, 1691, 1416, 1235 cm^{-1}; HRMS–APCI (*m/z*) [M + H]$^+$ calcd for C$_{24}$H$_{25}$N$_2$O$_2{}^+$, 373.1911; found, 373.1905.

*Note: **4.35** was obtained as a mixture of rotamers. These data represent empirically observed chemical shifts from the ^{1}H and ^{13}C-NMR spectra.*

The structure of **4.35** was verified by 2D-NOESY, as the following interaction was observed:

4.35
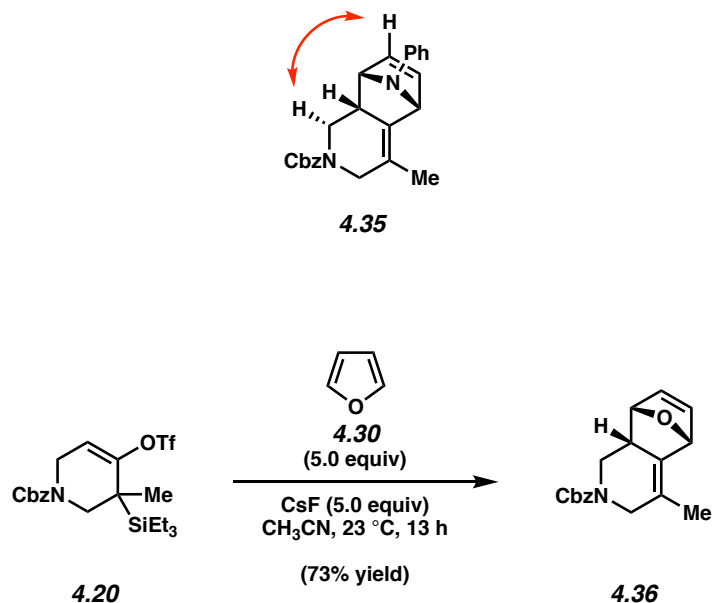
Cycloadduct 4.36. Purification by flash chromatography (2:1:1 hexanes:CH$_2$Cl$_2$:Et$_2$O) afforded cycloadduct **4.36** as a light yellow oil (73% yield, 12.8:1 dr, average of two experiments). Diastereomeric ratio was determined by integrating the following peaks in the ^{1}H-NMR spectrum

of the crude reaction mixture (Major: 6.41 ppm; Minor: 6.51 ppm). Cycloadduct **4.36**: R_f 0.71 (1:1

hexanes:Et$_2$O); ^{1}H-NMR (600 MHz, C$_6$D$_6$): δ 7.32–7.28 (m, 2H), 7.15–7.10 (m, 2H), 7.08–7.04

(m, 1H), 5.91–5.85 (m, 1H), 5.51–5.45 (m, 1H), 5.27–5.21 (m, 1H), 5.20–5.14 (m, 1H), 4.97 (br.

s, 1H), 4.60–4.55 (m, 1H), 4.52–3.93 (m, 2H), 3.30–3.03 (m, 1H), 2.41–2.29 (m, 1H), 1.46–1.36

(m, 1H), 1.22–1.13 (m, 3H); ^{13}C-NMR (125 MHz, CDCl$_3$): δ 155.7, 155.3, 136.8, 135.4, 135.2,

132.0, 131.6, 129.5, 129.3, 128.6, 128.5, 128.3, 128.04, 128.01, 127.98, 121.1, 120.6, 80.1, 80.0,

78.6, 67.2, 47.5, 47.1, 45.4, 45.2, 39.5, 39.3, 16.8; IR (film): 2923, 1697, 1416, 1236, 1115 cm^{-1};

HRMS–APCI (m/z) [M + H]$^+$ calcd for C$_{18}$H$_{20}$NO$_3^+$, 298.1438; found, 298.1433.

*Note: **4.36** was obtained as a mixture of rotamers. These data represent empirically observed*

chemical shifts from the ^{1}H and ^{13}C-NMR spectra.

The structure of **4.36** was verified by 2D-NOESY, as the following interaction was observed:

4.36
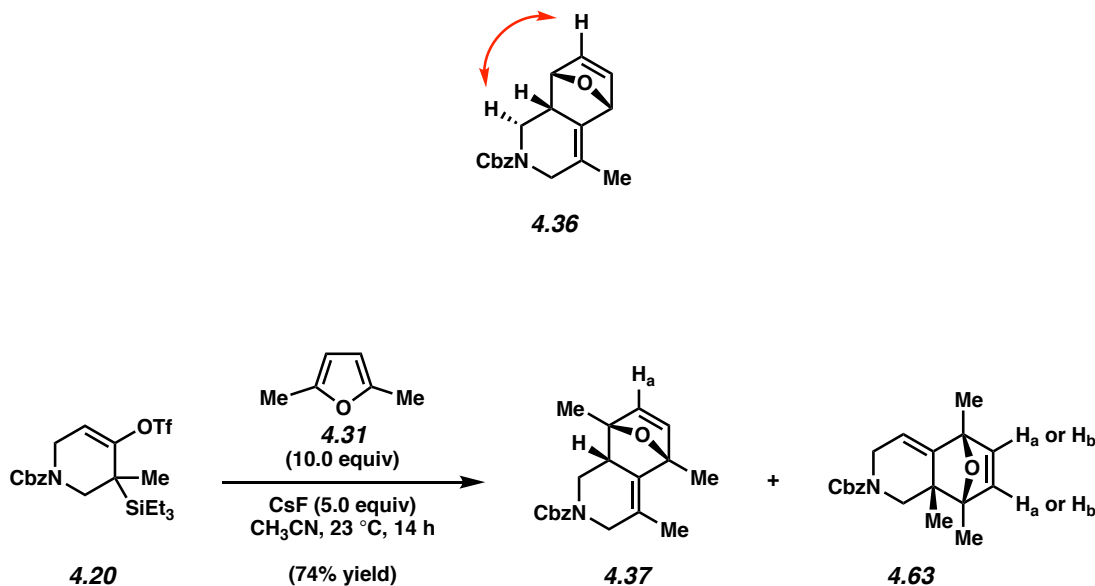
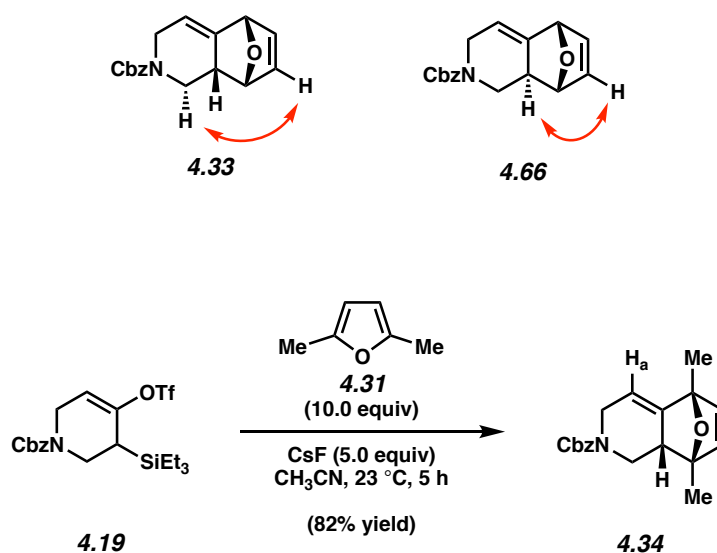**Cycloadduct 4.37.** Purification by flash chromatography (2:1:1 hexanes:CH$_2$Cl$_2$:Et$_2$O) afforded

an inseparable mixture of cycloadducts **4.37** and **4.63** as a light yellow oil (74% yield, 3.1:1 ratio

of regioisomers, >20:1 dr, average of two experiments). Regioisomeric ratio was determined by

integrating the following peaks in the ^{1}H-NMR spectrum of the crude reaction mixture (H$_a$ Major: 5.87 ppm; Minor: 5.97 ppm). Cycloadducts **4.37** and **4.63** were characterized as a mixture of regioisomers. Cycloadducts **4.37** and **4.63**: R$_f$ 0.10 (9:1 hexanes:EtOAc); ^{1}H-NMR (500 MHz, CDCl$_3$): **4.37** (major isomer): δ 7.39–7.28 (m, 5H), 6.25–6.20 (m, 1H), 5.87 (dd, J = 13.3, 5.4, 1H), 5.21–5.11 (m, 2H), 4.38–4.00 (m, 2H), 3.43–3.34 (m, 1H), 2.34–2.27 (m, 1H), 1.81–1.71 (m, 6H), 1.63–1.59 (m, 3H), 1.10 (d, J = 4.5, 1H); **4.63** (minor isomer) δ 7.39–7.28 (m, 5H), 6.06 (dd, J = 9.0, 5.4, 1H), 5.97 (dd, J = 17.3, 5.4, 1H), 5.46–5.35 (m, 1H), 5.21–5.11 (m, 2H), 4.38–4.00 (m, 2H), 3.68 (dt, J = 17.3, 5.1, 1H), 2.21–2.14 (m, 1H), 1.81–1.71 (m, 3H), 1.63–1.59 (m, 3H), 1.54–1.50 (m, 3H); ^{13}C-NMR (125 MHz, CDCl$_3$): δ 156.5, 155.7, 155.3, 149.3, 148.9, 139.7, 139.4, 139.3, 137.2, 137.0, 135.5, 133.8, 133.7, 128.9, 128.72, 128.65, 128.2, 128.14, 128.11, 128.0, 127.9, 120.2, 119.6, 110.3, 89.1, 87.4, 86.6, 86.3, 86.1, 67.9, 67.3, 67.25, 67.17, 51.7, 51.6, 48.4, 47.9, 47.5, 47.2, 45.94, 45.89, 45.1, 44.9, 43.2, 42.7, 29.8, 27.6, 18.2, 18.10, 18.09, 18.0, 17.5, 15.8, 15.2, 15.1, 14.59, 14.57; IR (film): 3032, 2932, 1701, 1416, 1239 cm^{-1}; HRMS–APCI (*m/z*) [M + H]$^+$ calcd for C$_{20}$H$_{24}$NO$_3^+$, 326.1748; found, 326.1751.

*Note: **4.37** and **4.63** were obtained as a mixture of rotamers. These data represent empirically observed chemical shifts from the ^{13}C-NMR spectrum.*

The structures of **4.37** and **4.63** were verified by 2D-NOESY, as the following interactions were observed:

4.37   4.63
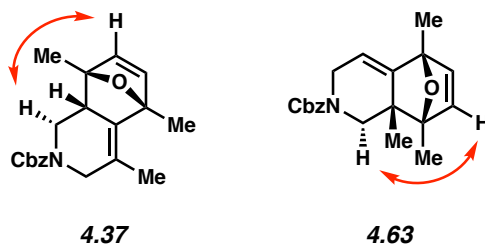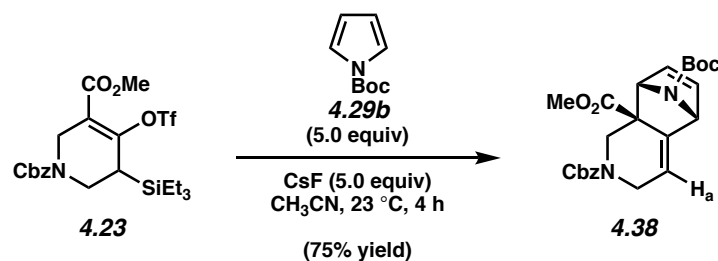
Cycloadduct 4.38. Purification by preparative thin layer chromatography (2:1 hexanes:EtOAc) afforded cycloadduct **4.38** as a colorless oil (75% yield, >14:1 dr, average of two experiments). Diastereomeric ratio was determined by integrating the following peaks in the ^{1}H-NMR spectrum of the crude reaction mixture (H$_a$ Major: 5.73 ppm; Minor: 5.86 ppm). Cycloadduct **4.38**: R$_f$ 0.29 (2:1 hexanes:EtOAc); ^{1}H-NMR (500 MHz, CDCl$_3$): δ 7.39–7.27 (m, 5H), 6.55–6.32 (m, 1H), 6.29–6.02 (m, 1H), 5.79–5.67 (m, 1H), 5.20–5.01 (m, 4H), 4.78–4.60 (m, 1H), 4.36–4.26 (m, 1H), 3.68–3.50 (m, 4H), 1.99 (dd, J = 13.7, 12.2, 1H), 1.39 (s, 9H); ^{13}C-NMR (125 MHz, CDCl$_3$): δ 171.7, 155.7, 155.1, 154.6, 139.9, 139.6, 138.0, 137.8, 136.6, 136.5, 136.0, 135.7, 131.3, 131.0, 129.5, 129.2, 128.52, 128.48, 128.1, 128.0, 127.8, 116.7, 116.4, 80.8, 67.2, 66.3, 65.6, 63.6, 62.9, 55.0, 54.5, 52.7, 49.2, 48.9, 43.8, 43.4, 28.2; IR (film): 2978, 2950, 1732, 1704, 1278 cm^{-1}; HRMS–APCI (m/z) [M + H]$^+$ calcd for C$_{20}$H$_{29}$N$_2$O$_6$$^+$, 441.2020; found, 441.2017.

*Note: **4.38** was obtained as a mixture of rotamers. These data represent empirically observed chemical shifts from the ^{1}H and ^{13}C-NMR spectra.*

The structure of **4.38** was verified by 2D-NOESY, as the following interaction was observed:

4.38

Cycloadduct 4.39. Purification by flash chromatography (2:1 hexanes:EtOAc) afforded cycloadduct **4.39** as a colorless oil (74% yield, >9:1 dr, average of two experiments). Diastereomeric ratio was determined by integrating the following peaks in the ^{1}H-NMR spectrum of the crude reaction mixture (H_a Major: 4.33 ppm; not unambiguously assigned H_a or H_b Minor: 2.86 ppm). Cycloadduct **4.39**: R_f 0.19 (2:1 hexanes:EtOAc); ^{1}H-NMR (500 MHz, CDCl$_3$): δ 7.43–7.27 (m, 5H), 6.52–6.45 (m, 1H), 6.42–6.15 (m, 1H), 5.82–5.72 (m, 1H), 5.41–5.31 (m, 1H), 5.28 (s, 1H), 5.19–5.07 (m, 2H), 4.74 (dd, J = 33.8, 11.9, 1H), 4.39–4.29 (m, 1H), 3.68–3.54 (m, 4H), 1.98 (dd, J = 19.3, 12.1, 1H); ^{13}C-NMR (100 MHz, CDCl$_3$): δ 172.4, 171.9, 155.8, 155.1, 138.6, 138.3, 137.1, 136.9, 136.7, 136.6, 129.7, 129.5, 128.52, 128.50, 128.1, 128.01, 127.98, 127.81, 116.4, 116.2, 83.6, 83.5, 79.8, 79.7, 77.4, 77.2, 77.0, 76.7, 67.2, 54.44, 54.35, 52.7, 49.3, 49.0, 43.7, 43.4, 30.0; IR (film): 3029, 2951, 2854, 1728, 1692 cm^{-1}; HRMS–APCI (*m/z*) [M + H]$^+$ calcd for C$_{19}$H$_{20}$NO$_5$$^+$, 342.1336; found, 342.1354.

*Note: **4.39** was obtained as a mixture of rotamers. These data represent empirically observed chemical shifts from the ^{1}H and ^{13}C-NMR spectra.*

The structure of **4.39** was verified by 2D-NOESY, as the following interaction was observed:


4.39
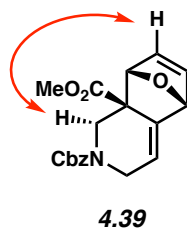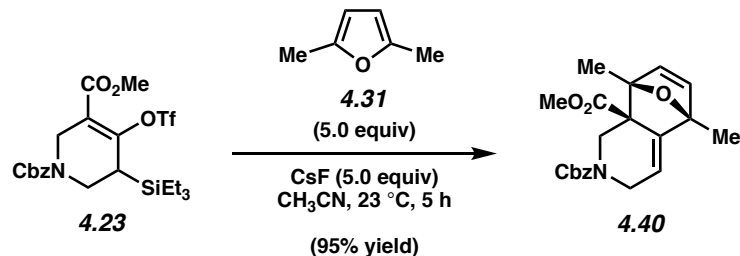
Cycloadduct 4.40. Purification by preparative thin layer chromatography (2:1 hexanes:EtOAc)

afforded cycloadduct **4.40** as a colorless oil (95% yield, >20:1 dr, average of two experiments).

Cycloadduct **4.40**: R_f 0.25 (2:1 hexanes:EtOAc); ^{1}H-NMR (500 MHz, CDCl$_3$): δ 7.43–7.28 (m,

5H), 6.20 (dd, J = 8.6, 5.4, 1H), 5.99–5.92 (m, 1H), 5.65–5.53 (m, 1H), 5.22–5.10 (m, 2H), 4.93–

4.77 (m, 1H), 4.21–4.12 (m, 1H), 3.68–3.58 (m, 4H), 1.97 (dd, J = 15.1, 11.4, 1H), 1.71 (s, 3H),

1.60–1.55 (m, 3H); ^{13}C-NMR (125 MHz, CDCl$_3$, 60 °C): δ 171.4, 155.4, 144.4, 141.5, 136.9,

134.5, 128.4 127.9, 127.8, 112.9, 88.8, 86.8, 67.1, 58.3, 52.0, 49.1, 43.3, 16.3, 14.6; IR (film):

2979, 2933, 1723, 1705, 1412 cm^{-1}; HRMS–APCI (m/z) [M + H]$^+$ calcd for C$_{21}$H$_{24}$NO$_5^+$,

370.1649; found, 370.1657.

*Note: **4.40** was obtained as a mixture of rotamers. These data represent empirically observed*

chemical shifts from the ^{1}H and ^{13}C-NMR spectra.

The structure of **4.40** was verified by 2D-NOESY, as the following interaction was observed:

4.40
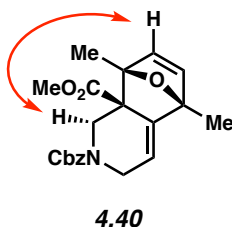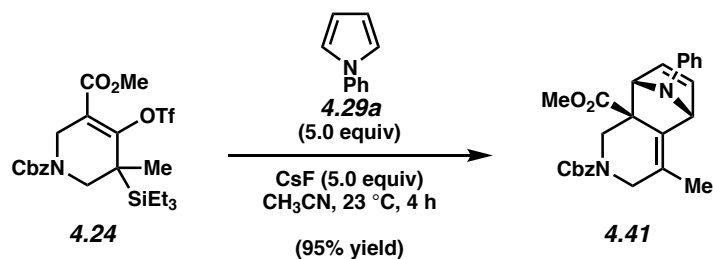
Cycloadduct 4.41. Purification by preparative thin layer chromatography (3:1 hexanes:EtOAc) afforded cycloadduct **4.41** as a white amorphous solid (95% yield, >20:1 dr, average of two experiments). Cycloadduct **4.41**: R_f 0.18 (3:1 hexanes:EtOAc); ^{1}H-NMR (500 MHz, CDCl$_3$): δ 7.40–7.29 (m, 5H), 7.21–7.15 (m, 2H), 6.86 (t, J = 7.1, 1H), 6.80 (t, J = 7.8, 2H), 6.43–6.36 (m, 1H), 5.98–5.90 (m, 1H), 5.18–5.05 (m, 4H), 4.71–4.57 (m, 1H), 4.34–4.23 (m, 1H), 3.62–3.49 (m, 3H), 3.47–3.39 (m, 1H), 2.10–2.02 (m, 1H), 1.85–1.79 (m, 3H); ^{13}C-NMR (125 MHz, CDCl$_3$): δ 173.3, 172.8, 155.8, 155.2, 146.1, 146.0, 137.0, 136.9, 136.73, 136.69, 130.8, 130.5, 128.8, 128.64, 128.62, 128.2, 128.12, 128.11, 128.0, 127.9, 127.6, 123.9, 123.5, 121.1, 118.70, 118.67, 67.31, 67.28, 64.6, 54.8, 54.6, 52.7, 52.6, 49.0, 48.6, 47.8, 47.5, 17.15, 17.12; IR (film): 3032, 2950, 1726, 1696, 1418 cm^{-1}; HRMS–APCI (*m/z*) [M + H]$^+$ calcd for C$_{26}$H$_{27}$N$_2$O$_4^+$, 431.1965; found, 431.1950.

*Note: **4.41** was obtained as a mixture of rotamers. These data represent empirically observed chemical shifts from the ^{13}C-NMR spectrum.*

The structure of **4.41** was verified by 2D-NOESY, as the following interaction was observed:

4.41

Cycloadduct 4.42. Purification by preparative thin layer chromatography (2:1 hexanes:EtOAc) afforded cycloadduct **4.42** as a colorless oil (93% yield, >20:1 dr, average of two experiments).

Cycloadduct **4.42**: R_f 0.40 (1:1 hexanes:EtOAc); ^{1}H-NMR (500 MHz, CDCl$_3$): δ 7.42–7.28 (m, 5H), 6.56–6.50 (m, 1H), 6.22–6.13 (m, 1H), 5.40 (br s, 1H), 5.39–5.30 (m, 1H), 5.18–5.06 (m, 2H), 4.76–4.63 (m, 1H), 4.27–4.17 (m, 1H), 3.65–3.53 (m, 3H), 3.43–3.37 (m, 1H), 1.98–1.90 (m, 1H), 1.79–1.74 (m, 3H); ^{13}C-NMR (125 MHz, CDCl$_3$): δ 173.0, 172.5, 155.7, 155.1, 138.1, 137.8, 136.8, 136.7, 130.8, 130.5, 130.0, 129.8, 128.6, 128.21, 128.15, 128.1, 128.0, 124.5, 124.2, 83.8, 83.7, 78.9, 78.8, 67.35, 67.32, 54.1, 54.0, 52.8, 52.7, 49.3, 49.0, 47.7, 47.3, 17.2; IR (film): 2951, 1726, 1695, 1416, 1212, 1126 cm^{-1}; HRMS–APCI (*m/z*) [M + H]$^+$ calcd for C$_{20}$H$_{22}$NO$_5^+$, 356.1493; found, 356.1495.

*Note: **4.42** was obtained as a mixture of rotamers. These data represent empirically observed chemical shifts from the ^{1}H and ^{13}C-NMR spectra.*

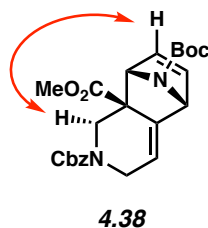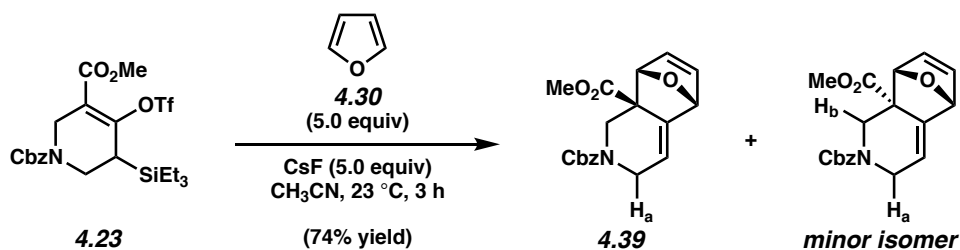The structure of **4.42** was verified by 2D-NOESY, as the following interaction was observed:

4.42
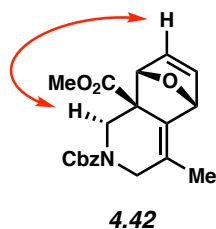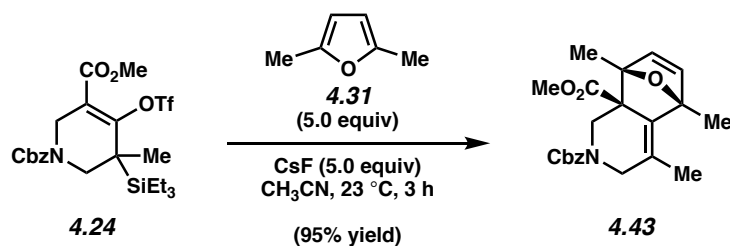
Cycloadduct 4.43. Purification by preparative thin layer chromatography (2:1 hexanes:EtOAc) afforded **4.43** as a colorless oil (95% yield, >20:1 dr, average of two experiments). Cycloadduct **4.43**: R_f 0.14 (3:1 hexanes:EtOAc); ^{1}H-NMR (500 MHz, CDCl$_3$, 50 °C): δ 7.44–7.27 (m, 5H), 6.31 (d, J = 4.8, 1H), 5.93 (d, J = 4.8, 1H), 5.19–5.12 (m, 2H), 4.83–4.69 (m, 1H), 4.02 (d, J = 18.1, 1H), 3.60 (s, 3H), 3.40 (d, J = 17.4, 1H), 2.00–1.91 (m, 1H), 1.86 (s, 3H), 1.79 (s, 3H), 1.56 (s, 3H); ^{13}C-NMR (125 MHz, CDCl$_3$): δ 171.8, 171.7, 155.7, 155.5, 144.6, 144.1, 141.8, 141.5, 136.95, 136.89, 134.6, 134.4, 128.6, 128.1, 128.05, 127.99, 113.3, 113.0, 89.0, 88.9, 87.04, 87.01, 67.3, 66.0, 58.4, 58.3, 52.5, 52.4, 49.1, 49.0, 43.5, 43.1, 16.54, 16.51, 15.4, 14.83, 14.81; IR (film): 2982, 1722, 1709, 1414, 1280 cm^{-1}; HRMS–APCI (m/z) [M + H]$^+$ calcd for C$_{22}$H$_{26}$NO$_5$$^+$, 384.1811; found, 384.1795.

*Note: **4.43** was obtained as a mixture of rotamers. These data represent empirically observed chemical shifts from the ^{13}C-NMR spectrum.*

The structure of **4.43** was verified by 2D-NOESY, as the following interaction was observed:

4.43

4.9.2.3 (3+2) and (2+2) Trapping Experiments

Representative Procedure (Preparation of isoxazolidine 4.46 is used as an example).

Isoxazolidine 4.46. To a stirred solution of silyl triflate **4.19** (51.4 mg, 0.107 mmol, 1.0 equiv) and trapping agent (nitrone **4.45**, 24.7 mg, 0.214 mmol, 2.0 equiv) in CH$_3$CN (1.1 mL) was added CsF (81.5 mg, 0.536 mmol, 5.0 equiv). The reaction vessel was sealed and allowed to stir at 23 °C for 8 h. The reaction mixture was filtered by passage through a plug of silica gel (EtOAc eluent, 10 mL). Evaporation under reduced pressure yielded the crude residue, which was purified by preparative thin layer chromatography (3:1 hexanes:EtOAc) to afford isoxazolidine **4.46** as a clear, colorless oil (88% yield, >20:1 dr, average of two experiments). Isoxazolidine **4.46**: R$_f$ 0.29 (3:1 hexanes:EtOAc); ^{1}H-NMR (500 MHz, CDCl$_3$): δ 7.40–7.28 (m, 5H), 5.49–5.36 (m, 1H), 5.15 (s, 2H), 4.76–4.54 (m, 1H), 4.44–4.42 (m, 2H), 3.72 (q, J = 6.2, 1H), 3.65–3.50, (m, 1H), 2.61–2.46 (m, 1H), 1.28 (d, J = 6.4, 3H), 1.10 (s, 9H) ; ^{13}C-NMR (100 MHz, CDCl$_3$): δ 155.6, 155.3, 146.4, 146.1, 136.5, 128.5, 128.1, 128.0, 112.5, 111.9, 70.0, 67.4, 58.7, 57.0, 44.3, 43.9, 43.2, 42.9, 26.3, 25.8, 23.9; IR (film): 2972, 2929, 2871, 1696, 1418 cm^{-1}; HRMS–APCI (*m/z*) [M + H]$^+$ calcd for C$_{19}$H$_{27}$N$_2$O$_3$$^+$, 331.2016; found, 331.2026.

*Note: **4.46** was obtained as a mixture of rotamers. These data represent empirically observed chemical shifts from the ^{13}C-NMR spectrum.*

The structure of **4.46** was verified by 2D-NOESY, as the following interaction was observed:
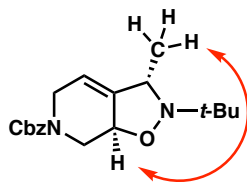
4.46

*Any modifications of the conditions shown in this representative procedure are specified in the following schemes, which depict all of the results shown in Table 4.2. Diastereomeric and regioisomeric ratios were determined by ^{1}H-NMR of the crude reaction mixtures. For all compounds in which the diastereomeric ratios were >20:1, the minor diastereomer was not observed in the ^{1}H-NMR spectra of the crude reaction mixture.*
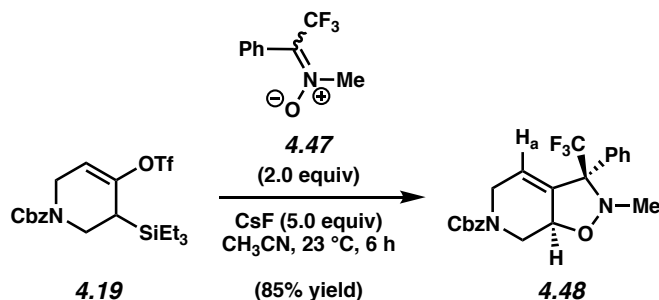
Isoxazolidine 4.48. In this reaction, nitrone **4.47** was utilized as a mixture of double bond isomers (6.4:1 ratio, major isomer depicted). Purification by preparative thin layer chromatography (5:1 hexanes:EtOAc) afforded isoxazolidine **4.48** as a colorless oil (85% yield, 5.4:1 dr, average of two experiments). Diastereomeric ratio was determined by integrating the following peaks in the ^{1}H-NMR spectrum of the crude reaction mixture (H_a Major: 5.98 ppm; Minor: 5.52 ppm). Isoxazolidine **4.48**: R_f 0.49 (3:1 hexanes:EtOAc); ^{1}H-NMR (500 MHz, CDCl$_3$): δ 7.66–7.59 (m, 2H), 7.45–7.32 (m, 8H) 6.05–5.90 (m, 1H), 5.24–5.15 (m, 2H), 4.82–4.44 (m, 3H), 3.85–3.68 (m, 1H), 2.78–2.63 (m, 1H), 2.60 (s, 3H); ^{13}C-NMR (125 MHz, CDCl$_3$): δ 155.5, 155.3, 141.3, 140.8, 136.4, 136.3, 133.1 133.0, 129.4, 128.8, 128.7, 128.4, 128.3, 128.2, 125.4 (q, J_{C-F} = 287), 121.4,

120.8, 72.1, 67.8, 44.4, 43.9, 43.7, 43.4, 41.5, 41.2; IR (film): 3032, 1704, 1497, 1111, 729 cm^{-1};

HRMS–APCI (m/z) [M + H]$^+$ calcd for C$_{22}$H$_{22}$F$_3$N$_2$O$_3$$^+$, 419.1577; found, 419.1556.

*Note: **4.48** was obtained as a mixture of rotamers. These data represent empirically observed chemical shifts from the ^{13}C-NMR spectrum.*

The structure of **4.48** was verified by 2D-NOESY, as the following interaction was observed:

4.48
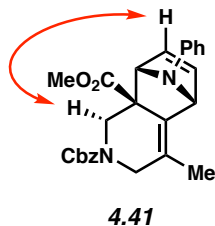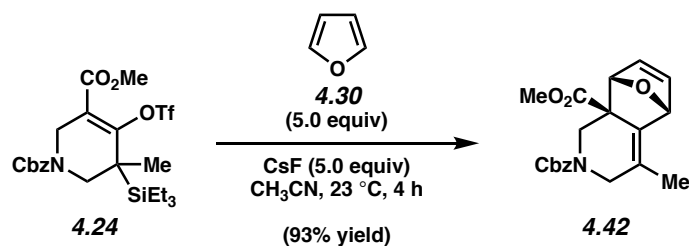

Isoxazolidine 4.50. Purification by preparative thin layer chromatography (1:1 hexanes:EtOAc) afforded isoxazolidine **4.50** as a clear, colorless oil (72% yield, 8.3:1 dr, average of two experiments). Diastereomeric ratio was determined by integrating the following peaks in the ^{1}H-NMR spectrum of the crude reaction mixture (H$_a$ Major: 5.57 ppm; Minor: 5.47 ppm). Isoxazolidine **4.50**: R$_f$ 0.41 (100% EtOAc); ^{1}H-NMR (500 MHz, CDCl$_3$): δ 7.43–7.30 (m, 5H), 5.68–5.51 (m, 1H), 5.20–5.11 (m, 2H), 4.72–4.49 (m, 1H), 4.46–4.26 (m, 2H), 4.22–4.13 (m, 1H), 3.70–3.53 (m, 1H), 3.32–3.16 (m, 2H), 2.62–2.44 (m, 1H), 2.13–2.01 (m, 1H), 1.89–1.68 (m, 3H); ^{13}C-NMR (125 MHz, CDCl$_3$): δ 155.7, 155.4, 145.5, 145.1, 135.5, 128.7, 128.3, 128.1, 114.8,

114.3, 70.5, 67.6, 67.2, 58.2, 58.1; 44.8, 44.4, 43.3, 43.0, 32.4, 25.2; IR (film) 2947, 1695, 1419, 1224, 979 cm^{-1}; HRMS–APCI (*m/z*) [M + H]$^+$ calcd for C$_{17}$H$_{21}$N$_2$O$_3{}^+$, 301.1547; found, 301.1531.

*Note: **4.50** was obtained as a mixture of rotamers. These data represent empirically observed chemical shifts from the* ^{13}*C-NMR spectrum.*

The structure of **4.50** was verified by 2D-NOESY, as the following interactions were observed:

4.50

Isoxazolidine 4.52. Purification by preparative thin layer chromatography (3:1 hexanes:EtOAc) afforded isoxazolidine **4.52** as a colorless oil (Quantitative yield, 5.3:1 dr, average of two experiments). Diastereomeric ratio was determined by integrating the following peaks in the ^{1}H-NMR spectrum of the crude reaction mixture (H$_a$ Major: 5.34 ppm; Minor: 5.94 ppm). Isoxazolidine **4.52**: R$_f$ 0.14 (3:1 hexanes:EtOAc); ^{1}H-NMR (500 MHz, CDCl$_3$): δ 7.40–7.30 (m, 5H), 7.28–7.20 (m, 2H), 7.17–7.12 (m, 2H) 5.43–5.28 (m, 1H), 5.20–5.13 (m, 2H), 5.0 (s, 1H), 4.87–4.67 (m, 1H), 4.51–4.29 (m, 2H), 3.60–3.46 (m, 1H), 3.29–3.20 (m, 1H), 3.07–2.98 (m, 1H), 2.88–2.80 (m, 1H), 2.77–2.69 (m, 1H), 2.57–2.43 (m, 1H) ; ^{13}C-NMR (100 MHz, CDCl$_3$): δ 155.4,

155.2, 142.5, 142.1, 136.4, 134.0, 131.6, 128.6, 128.5, 128.2, 128.0, 127.2, 126.3, 117.8, 117.2, 72.7, 67.5, 64.4, 51.2, 47.2, 46.8, 43.2, 42.9, 28.8; IR (film): 3030, 2850, 1707, 1223, 1417 cm^{-1}; HRMS–APCI (m/z) [M + H]$^+$ calcd for C$_{22}$H$_{23}$N$_2$O$_3$$^+$, 363.1703; found, 363.1703.
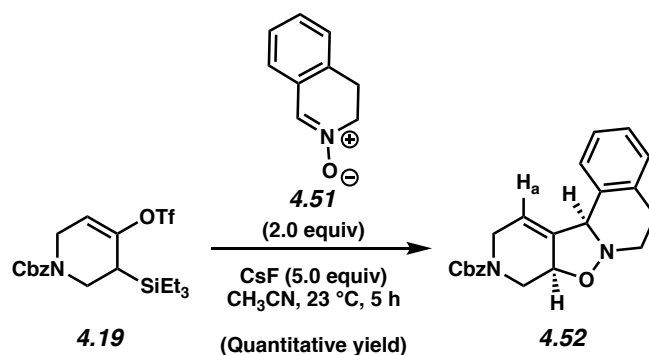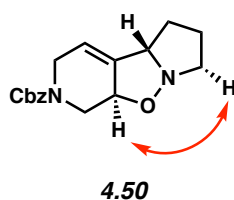
*Note: **4.52** was obtained as a mixture of rotamers. These data represent empirically observed chemical shifts from the ^{13}C-NMR spectrum.*

The structure of **4.52** was verified by 2D-NOESY, as the following interaction was observed:

4.52
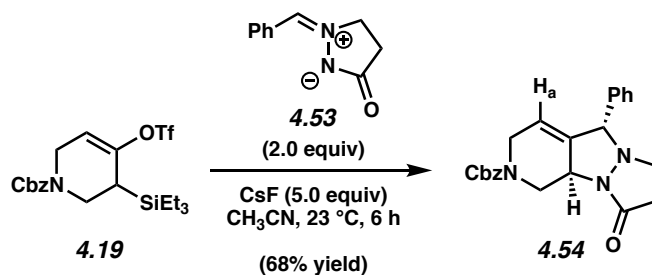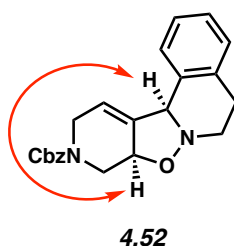
Pyrazolidine 4.54. Purification by preparative thin layer chromatography (3:1 hexanes:EtOAc) afforded pyrazolidine **4.54** as a colorless oil (68% yield, 10.6:1 dr, average of two experiments). Diastereomeric ratio was determined by integrating the following peaks in the ^{1}H-NMR spectrum of the crude reaction mixture (H$_a$ Major: 5.56 ppm; Minor: 6.05 ppm). Pyrazolidine **4.54**: R$_f$ 0.66 (100% EtOAc); ^{1}H-NMR (500 MHz, CDCl$_3$): δ 7.42–7.26 (m, 10H), 5.63–5.48 (m, 1H), 5.27–5.06 (m, 3H), 4.44–4.16 (m, 3H), 3.75–3.60 (m, 1H), 3.49–3.38 (m, 1H), 3.05 (q, J = 9.8, 1H), 2.99–2.85 (m, 1H), 2.68–2.47 (m, 2H); ^{13}C-NMR (125 MHz, CDCl$_3$): δ 168.4, 155.5, 143.1, 142.6,

138.0, 136.5, 129.1, 128.7, 128.6, 128.33, 128.27, 128.1, 118.3, 117.8, 71.8, 67.6, 52.7, 50.0, 43.52, 43.47, 43.2, 34.7; IR (film): 3032, 2251, 1683, 1417, 906 cm^{-1}; HRMS–APCI (*m/z*) [M + H]$^+$ calcd for C$_{23}$H$_{24}$N$_3$O$_3{}^+$, 390.1812; found, 390.1822.

*Note: **4.54** was obtained as a mixture of rotamers. These data represent empirically observed chemical shifts from the ^{13}C-NMR spectrum.*

The structure of **4.54** was verified by 2D-NOESY, as the following interaction was observed:
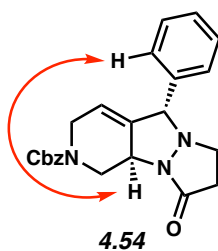
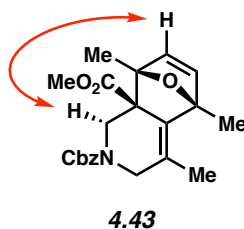*Note: The closest aromatic protons of the Cbz group are estimated to be roughly 6.7 Å away from the methine proton used for the NOE assignment. On the other hand, the distance between the shown phenyl C–H and the methine is roughly 2.2 Å (based on examination of a computed geometry-optimized structure). A correlation between the two methine protons in **4.54** was not observed.*
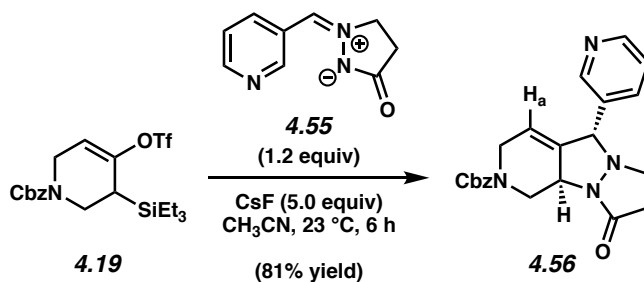
Pyrazolidine 4.56. Purification by preparative thin layer chromatography (19:1 CH$_2$Cl$_2$:MeOH) afforded pyrazolidine **4.56** as a colorless oil (81% yield, 14:3 dr, average of two experiments). Diastereomeric ratio was determined by integrating the following peaks in the ^{1}H-NMR spectrum of the crude reaction mixture (H$_a$ Major: 5.53 ppm; Minor: 6.07 ppm). Pyrazolidine **4.56**: R$_f$ 0.29 (19:1, CH$_2$Cl$_2$:MeOH); ^{1}H-NMR (300 MHz, CDCl$_3$): δ 8.62–8.53 (m, 2H), 7.70–7.61 (m, 1H), 7.43–7.27 (m, 6H), 5.62–5.46 (m, 1H), 5.32–5.07 (m, 3H), 4.48–4.30 (m, 1H), 4.27 (s, 1H), 4.14 (br s, 1H), 3.76–3.58 (m, 1H), 3.55–3.43 (m, 1H), 3.09–2.86 (m, 2H) 2.76–2.61 (m, 2H); ^{13}C-NMR (100 MHz, CDCl$_3$): δ 167.7, 155.4, 150.1, 149.4, 142.2, 136.5, 135.4, 134.2, 128.7, 128.3, 124.0, 118.9, 118.4, 69.5, 67.7, 52.7, 49.6, 43.6, 43.3, 43.0, 34.7; IR (film) 3032, 2251, 1683, 1417, 906 cm^{-1}; HRMS–APCI (*m/z*) [M + H]$^+$ calcd for C$_{23}$H$_{24}$N$_3$O$_3^+$, 390.1812; found, 390.1822.
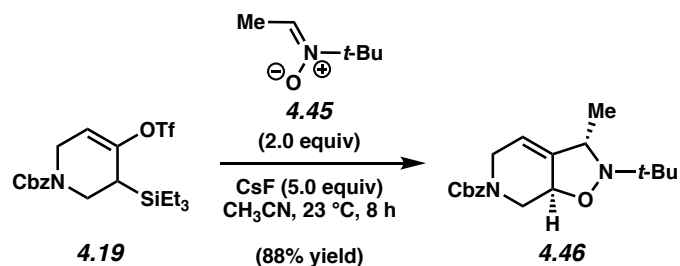
*Note: **4.56** was obtained as a mixture of rotamers. These data represent empirically observed chemical shifts from the ^{13}C-NMR spectrum.*

The structure of **4.56** was verified by 2D-NOESY, as the following interaction was observed:

4.56
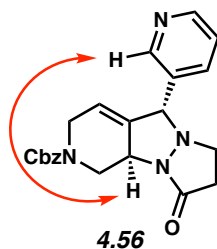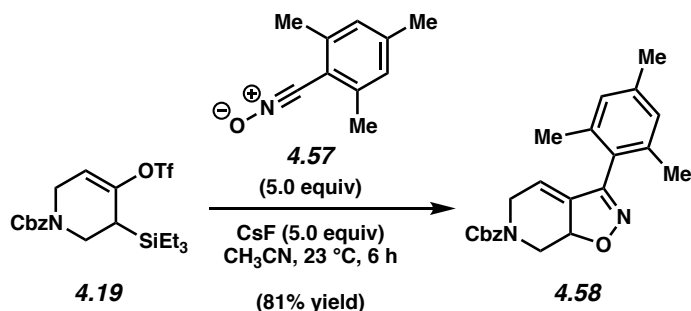
Isoxazoline 4.58. Purification by preparative thin layer chromatography (5:1 hexanes:EtOAc) afforded isoxazoline **4.58** as a colorless oil (81%, average of two experiments). Isoxazoline **4.58**: R_f 0.23 (3:1 hexanes:EtOAc); ^{1}H-NMR (500 MHz, CDCl$_3$): δ 7.42–7.30 (m, 5H), 6.91 (d, J = 4.5, 2H), 5.64–5.50 (m, 1H), 5.20 (m, 2H), 5.07–4.86 (m, 2H), 4.56–4.35 (m, 1H), 3.85–3.68 (m, 1H), 2.87–2.71 (m, 1H), 2.30 (s, 3H), 2.17 (s, 6H); ^{13}C-NMR (125 MHz, CDCl$_3$): δ 156.8, 156.6, 155.5, 155.3, 142.0, 141.7, 139.3, 137.6, 137.5, 137.2, 136.21, 136.16, 128.6, 128.53, 128.50, 128.3, 128.2, 128.1, 123.4, 123.3, 118.7, 117.9, 76.2, 76.0, 67.8, 44.9, 44.5, 43.4, 43.1, 21.1, 19.9, 19.7; IR (film): 2919, 1705, 1415, 1248, 852 cm^{-1}; HRMS–APCI (m/z) [M + H]$^+$ calcd for C$_{23}$H$_{25}$N$_2$O$_3{}^+$, 377.1860; found, 377.1842.

*Note: **4.58** was obtained as a mixture of rotamers. These data represent empirically observed chemical shifts from the ^{13}C-NMR spectrum.*
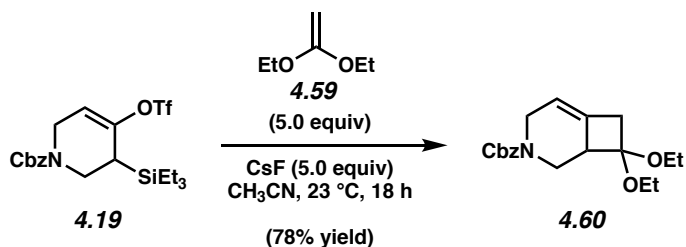
Cycloadduct 4.60. Purification by preparative thin layer chromatography (5:1 hexanes:EtOAc) afforded cycloadduct **4.60** as a colorless oil (78%, average of two experiments). Cycloadduct **4.60**: R_f 0.41 (5:1 hexanes:EtOAc); ^{1}H-NMR (500 MHz, CDCl$_3$): δ 7.39–7.29 (m, 5H), 5.51–5.40 (m,

203

1H), 5.22–5.09 (m, 2H), 4.46–4.20 (m, 2H), 3.68–3.56 (m, 1H), 3.52–3.35 (m, 4H), 3.06–2.95 (m, 1H), 2.88 (s, 2H), 2.84–2.75 (m, 1H), 1.21 (t, J = 7.1, 3H), 1.16 (t, J = 7.1, 3H); ^{13}C-NMR (125 MHz, CDCl$_3$): δ 156.2, 155.9, 137.0, 132.7, 132.2, 128.6, 128.08, 128.06, 128.03, 128.01, 114.1, 113.5, 102.3, 102.2, 67.2, 67.1, 58.1, 58.0, 50.0, 49.8, 44.1, 43.7, 41.8, 40.8, 40.4, 15.3, 15.2; IR (film): 2976, 2929, 1699, 1418, 1228 cm^{-1}; HRMS–APCI (m/z) [M + H]$^+$ calcd for C$_{19}$H$_{26}$NO$_4^+$, 332.1856; found, 332.1852.

*Note: **4.60** was obtained as a mixture of rotamers. These data represent empirically observed chemical shifts from the ^{13}C-NMR spectrum.*

The structure of **4.60** was verified by 2D-NOESY, as the following interaction was observed:

4.60
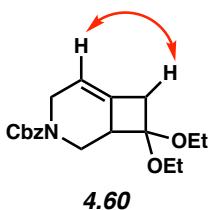
4.9.2.4 Enantiospecific Trapping Experiments

4.9.2.4.1 Separation of Ketones 4.17 and 4.18

Compound **4.17** was separated into its enantiomers by Lotus Separations on 2.0 gram scale.

Preparative Method:	Analytical Method:
AS-H (2 x 25 cm)	AS-H (25 x 0.46 cm)
10% isopropanol in CO$_2$, 100 bar	10% isopropanol/CO$_2$, 100 bar
60 mL/min, 220 nm	3 mL/min, 220 and 280 nm

Racemic **4.17**:
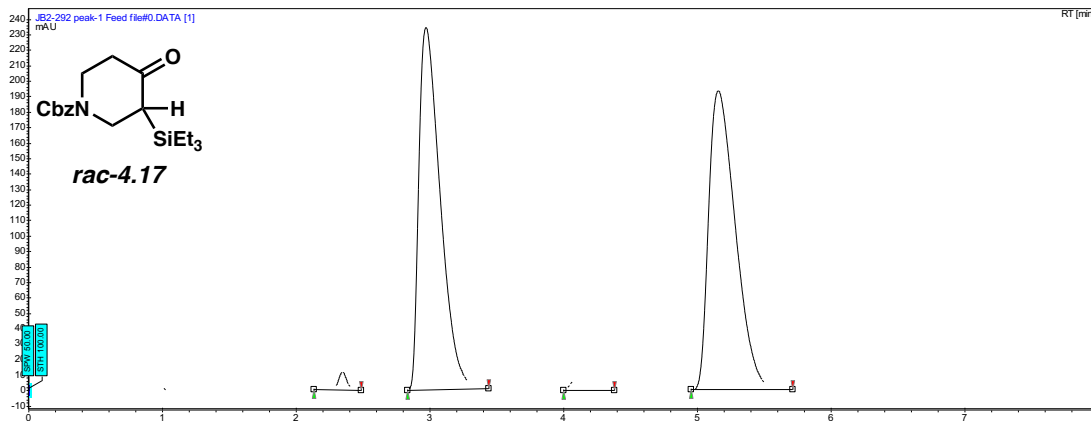
Figure 4.6. SFC trace for rac-**4.17**.

Enantioenriched **(+)-4.17** (Peak-1b was used for our studies):
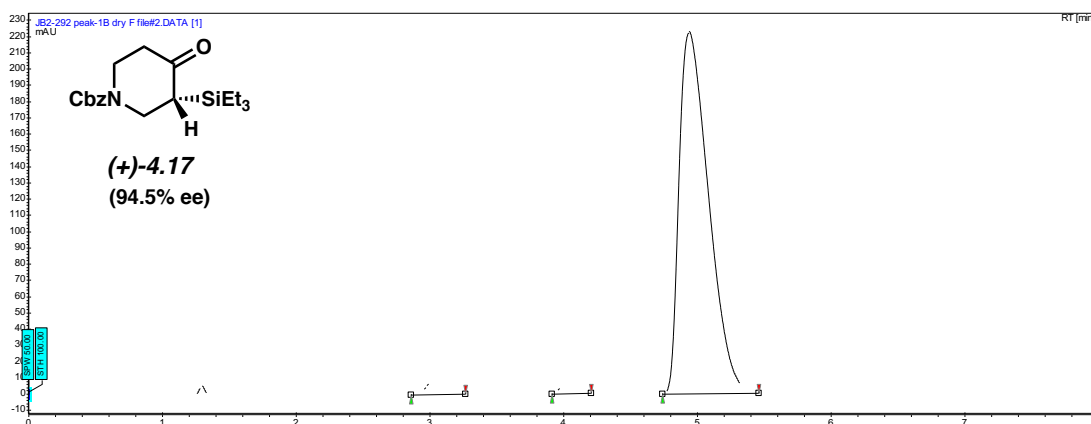
Index	Time (min)	Area (%)
Peak-1a	3.03	2.702
Imp	4.02	1.512
Peak-1b	4.94	95.786
Total		100.00

Figure 4.7. SFC trace for (+)-**4.17**.

Compound **4.18** was separated into its enantiomers by Lotus Separations (1.0 gram, batch).

Preparative Method: Analytical Method:

AD-H (3 x 25 cm)   AD-H (25 x 0.46 cm)

10% methanol/CO_2, 100 bar   15% methanol/CO_2, 100 bar

70 mL/min, 220 nm   3 mL/min, 220 and 280 nm

inj vol.: 1 mL, 20 mg/mL acetonitrile:DCM

>1.0 gram was processed using this method in batch

Racemic **4.18**:

Figure 4.8. SFC trace for rac-**4.18**.

Enantioenriched (–)-**4.18** (Peak 1 was used for cycloadditions to form (+)-**4.35** and (+)-**4.37**)

Index	Time (min)	Area (%)
Imp	1.62	6.624
Imp	2.43	1.138
Peak-1	2.62	90.770
Imp	2.77	0.745
Peak-2	2.99	0.211
Imp	3.49	0.512
Total		100.00
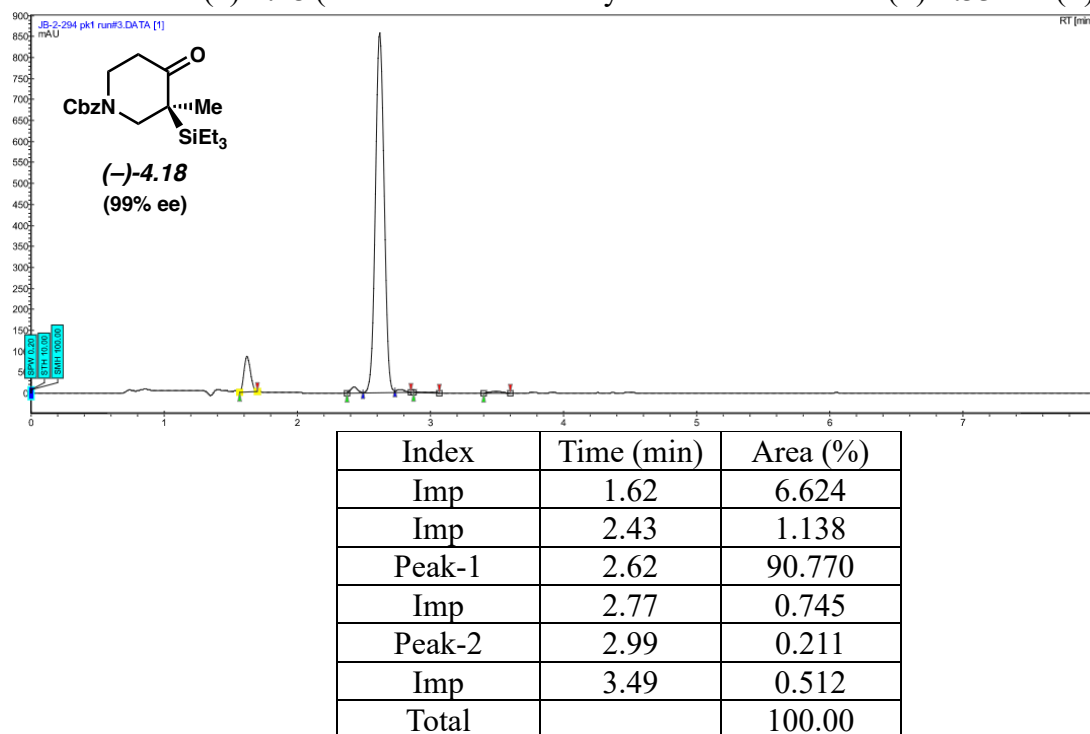
Figure 4.9. SFC trace for (–)-**4.18**.

Enantioenriched (+)-**4.18 (**Peak 2 was used for cycloaddition to form (–)-**4.36**):

Index	Time (min)	Area (%)
Imp	1.65	6.596
Peak-1	2.63	0.343
Imp	2.88	0.583
Peak-2	2.98	92.478
Total		100.00
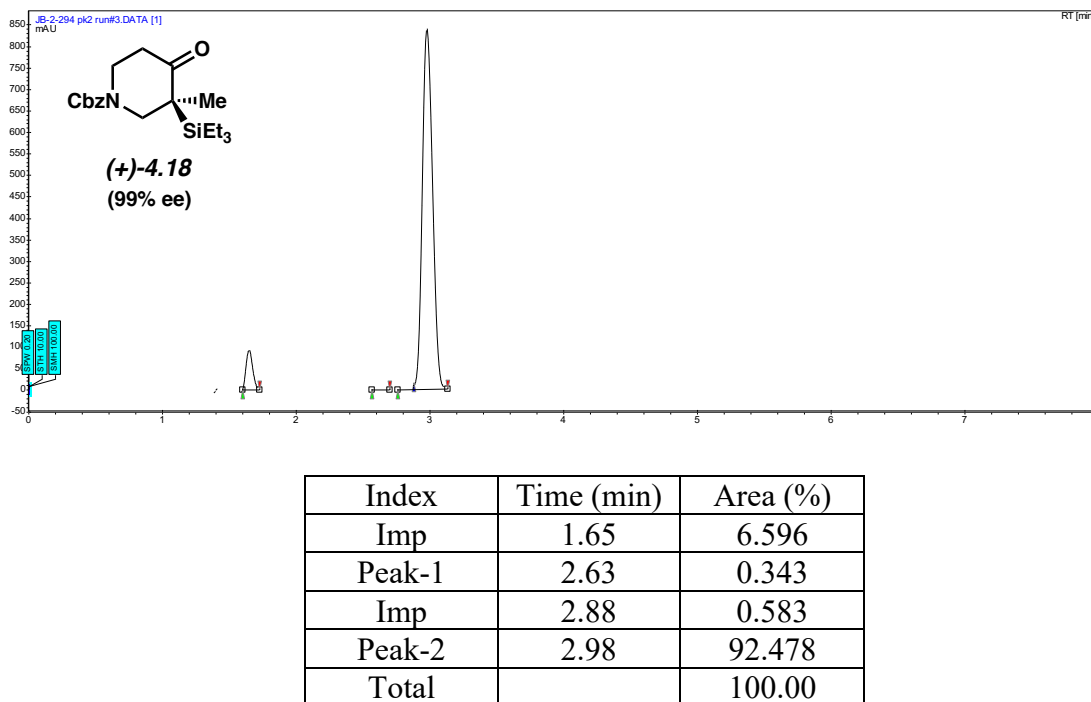
Figure 4.10. SFC trace for (+)-**4.18**.

207

4.9.2.4.2 Synthesis of Enantioenriched Silyl Triflates (+)-4.23 and (+)-4.20

(+)-4.17
(94.5% ee)

(+)-4.23
(~87% ee)
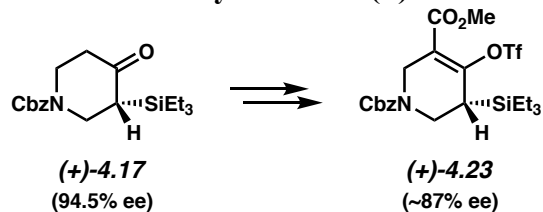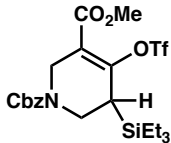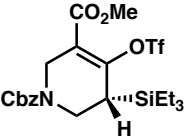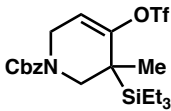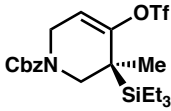
Silyl triflate (+)-4.23. Followed procedure outlined for the preparation of **4.23** in section 4.9.2.1. Spectral data matched those previously reported (see page 180). $[\alpha]^{28.0}_D$ +128.0° (c = 1.00, CH$_2$Cl$_2$).

(+)-4.18
(99% ee)

(+)-4.20
(99% ee)
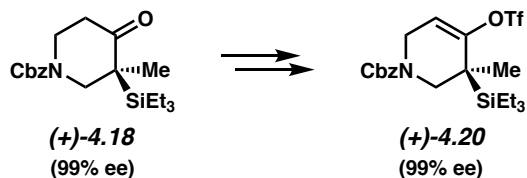
Silyl triflate (+)-4.20. Followed procedure outlined for the preparation of **4.20** on pages in section 4.9.2.1. Spectral data matched those previously reported (see page 177). $[\alpha]^{28.8}_D$ +36.0° (c = 1.00, CH$_2$Cl$_2$).

Verification of enantioenrichment of compounds 4.23 and 4.20:

Compound	Method Column/Temp.	Solvent	Method Flow Rate	Retention Times (min)	Enantiomeric Ratio (er)
(structure) rac-4.23	Daicel ChiralPak OD-H/35°C	3% isopropanol in CO_2	2 mL/min	9.96/10.71	~48.5:51.5
(structure) (+)-4.23	Daicel ChiralPak OD-H/35°C	3% isopropanol in CO_2	2 mL/min	9.76/10.34	~93.7:6.3
(structure) rac-4.20	Daicel ChiralPak AD-3/35 °C	3% isopropanol in CO_2	2 mL/min	6.17/6.80	49.9:50.1
(structure) (+)-4.20	Daicel ChiralPak AD-3/35 °C	3% isopropanol in CO_2	2 mL/min	5.95/6.66	99.6:0.4

Note: Although the two enantiomers of 4.23 were unable to be completely resolved utilizing various column conditions, this result was ultimately deemed inconsequential and not pursued further.
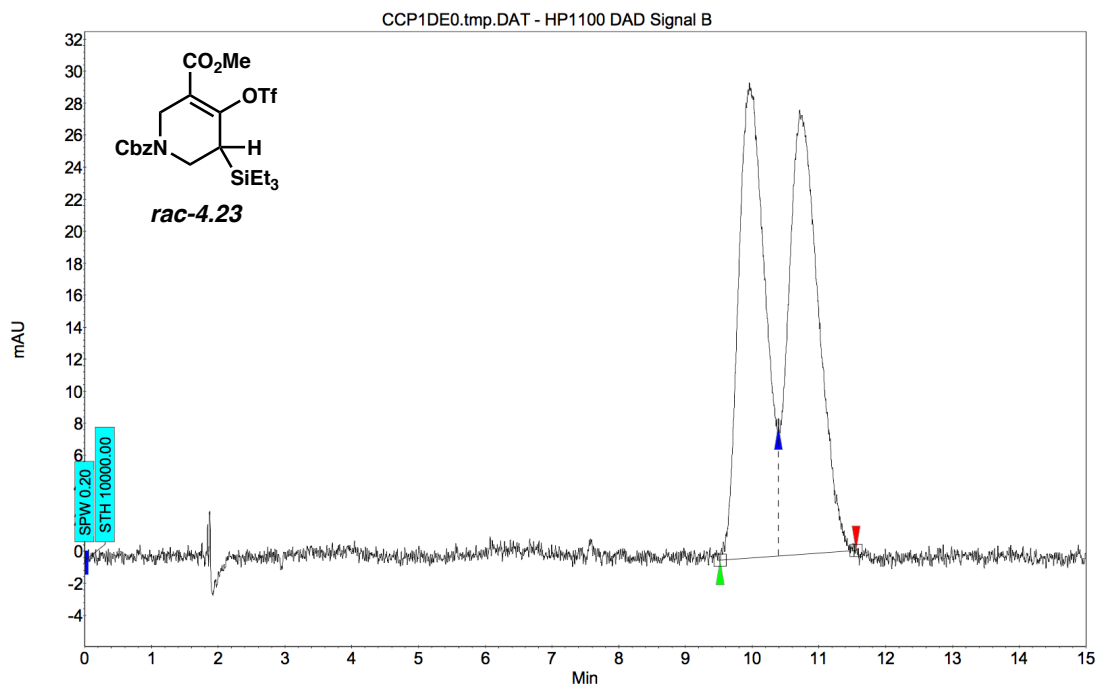
Index	Name	Start	Time	End	RT Offset	Quantity	Height	Area	Area
		[Min]	[Min]	[Min]	[Min]	[% Area]	[µV]	[µV.Min]	[%]
1	UNKNOWN	9.52	9.96	10.39	0.00	48.46	29.7	13.6	48.459
2	UNKNOWN	10.39	10.71	11.56	0.00	51.54	27.8	14.5	51.541
Total						100.00	57.5	28.1	100.000

Figure 4.11. SFC trace for rac-**4.23**.
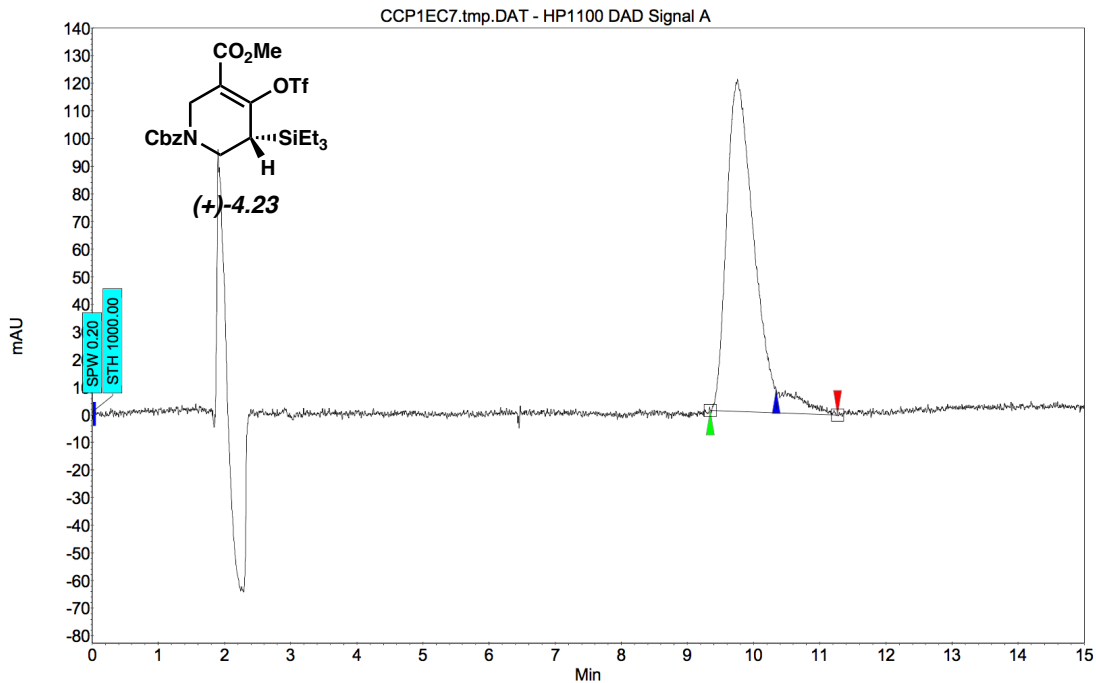
Figure 4.12. SFC trace for (+)-**4.23**.
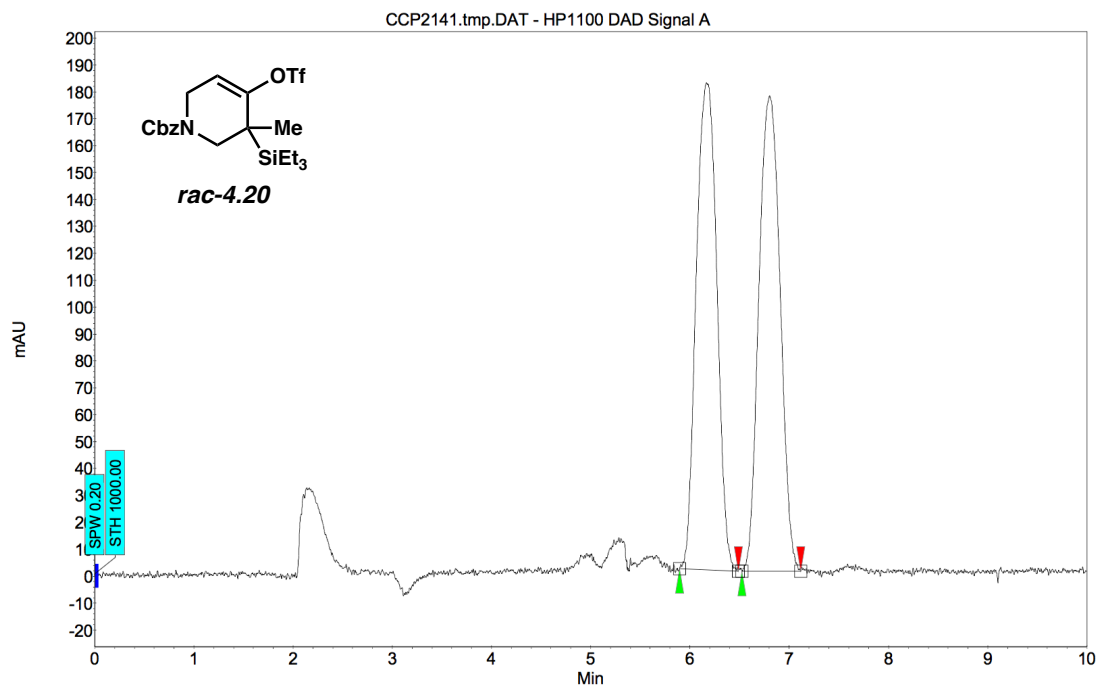
Index	Name	Start	Time	End	RT Offset	Quantity	Height	Area	Area
		[Min]	[Min]	[Min]	[Min]	[% Area]	[μV]	[μV.Min]	[%]
1	UNKNOWN	9.34	9.76	10.34	0.00	93.66	120.3	55.6	93.660
2	UNKNOWN	10.34	10.34	11.27	0.00	6.34	8.2	3.8	6.340
Total						100.00	128.6	59.4	100.000

Figure 4.13. SFC trace for rac-4.20.

Index	Name	Start	Time	End	RT Offset	Quantity	Height	Area	Area
		[Min]	[Min]	[Min]	[Min]	[% Area]	[μV]	[μV.Min]	[%]
1	UNKNOWN	5.89	6.17	6.49	0.00	49.87	181.0	43.6	49.869
2	UNKNOWN	6.53	6.80	7.12	0.00	50.13	176.8	43.9	50.131
Total						100.00	357.8	87.5	100.000
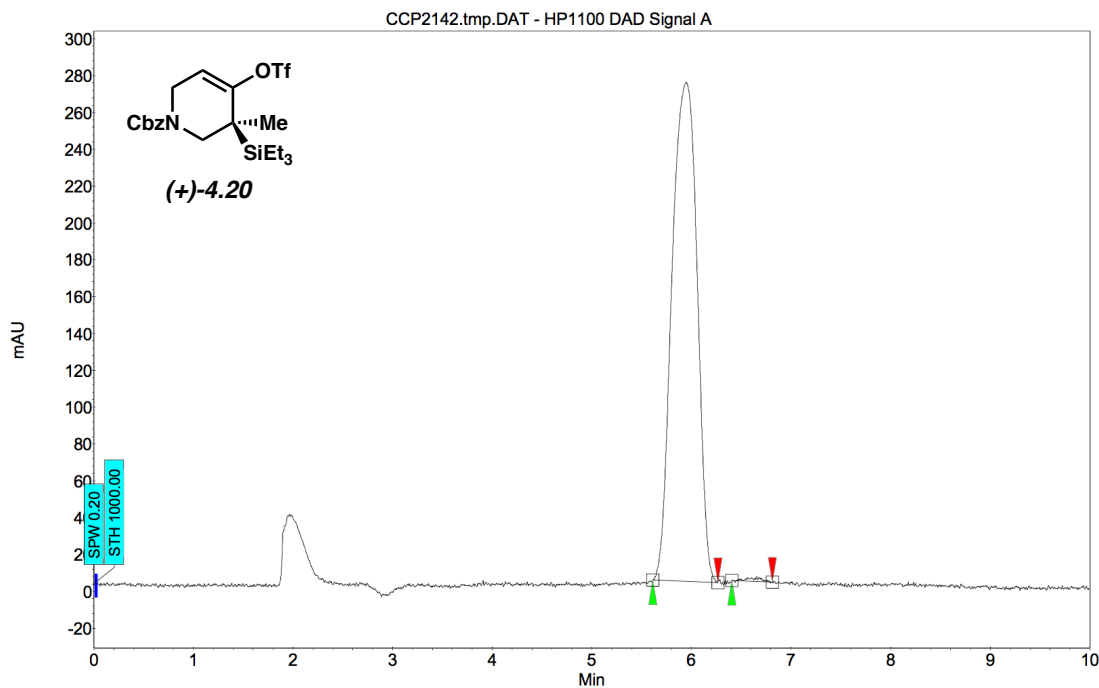
Figure 4.14. SFC trace for (+)-**4.20**.

Index	Name	Start	Time	End	RT Offset	Quantity	Height	Area	Area
		[Min]	[Min]	[Min]	[Min]	[% Area]	[µV]	[µV.Min]	[%]
1	UNKNOWN	5.61	5.95	6.27	0.00	99.61	270.9	79.2	99.612
2	UNKNOWN	6.41	6.66	6.81	0.00	0.39	2.7	0.3	0.388
Total						100.00	273.7	79.5	100.000

4.9.2.4.3 Transfer of Chirality in Cycloaddition Reactions
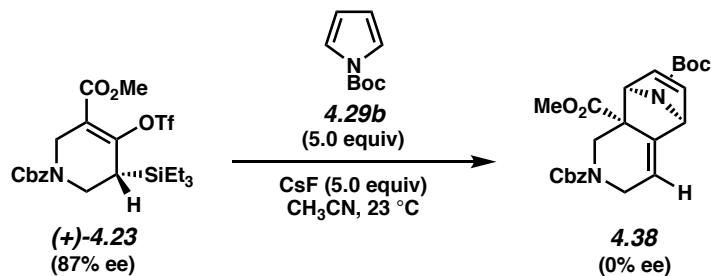
Cycloadduct 4.38. Followed procedure outlined for the preparation of **4.38** in section 4.9.2.2 (0.1 mmol scale). Spectral data matched those previously reported (see page 190). $[\alpha]^{25.6}_D$ 0.0° (c = 1.00, CH$_2$Cl$_2$).

213
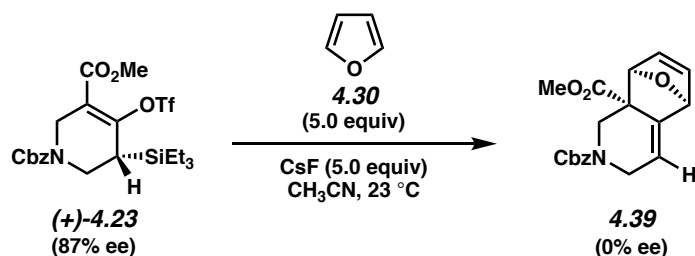
Cycloadduct 4.39. Followed procedure outlined for the preparation of **4.39** in section 4.9.2.2 (0.1 mmol scale). Spectral data matched those previously reported (see page 191).
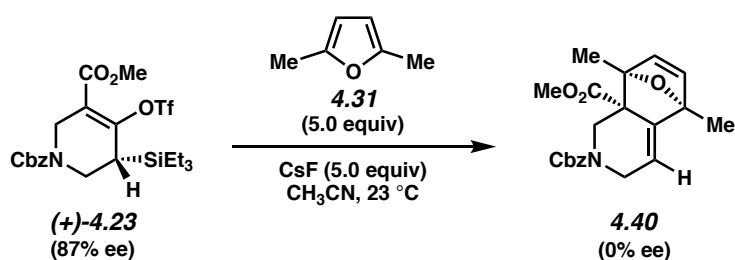
Cycloadduct 4.40. Followed procedure outlined for the preparation of **4.40** in section 4.9.2.2 (0.1 mmol scale). Spectral data matched those previously reported (see page 192). $[\alpha]^{25.9}_D$ 0.0° ($c =$ 1.00, CH$_2$Cl$_2$).
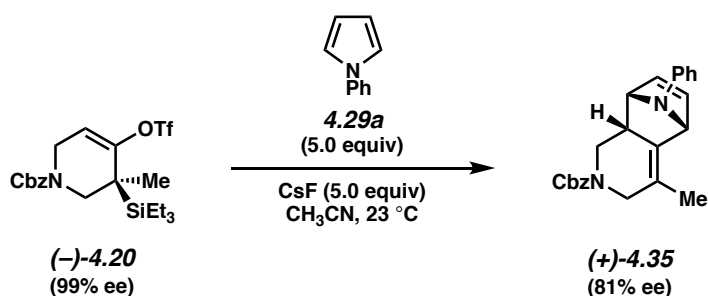
Cycloadduct (+)-4.30. Followed procedure outlined for the preparation of **4.35** in section 4.9.2.2 (0.1 mmol scale). Spectral data matched those previously reported (see page 187). $[\alpha]^{25.1}_D$ 518.0° ($c = 1.00$, CH$_2$Cl$_2$).
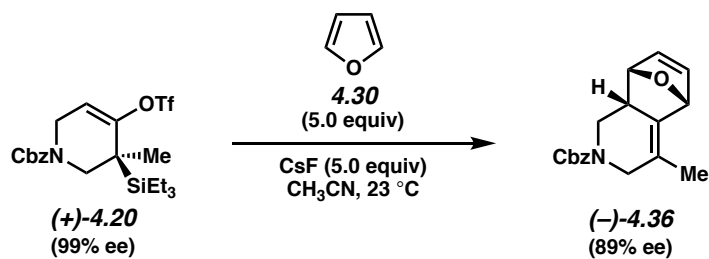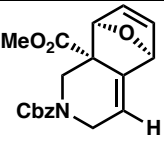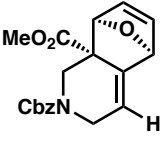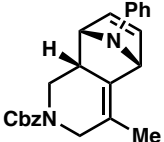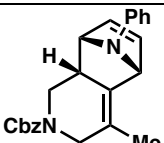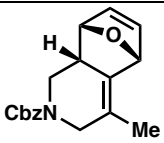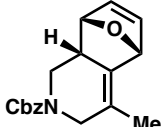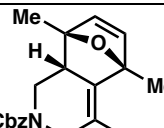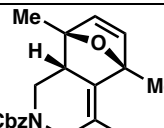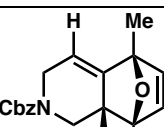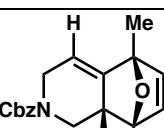
Cycloadduct (–)-4.31. Followed procedure outlined for the preparation of **4.36** in section 4.9.2.2 (0.1 mmol scale). Spectral data matched those previously reported (see page 187). $[\alpha]^{28.0}_D -56.0°$ ($c = 1.00$, CH$_2$Cl$_2$).
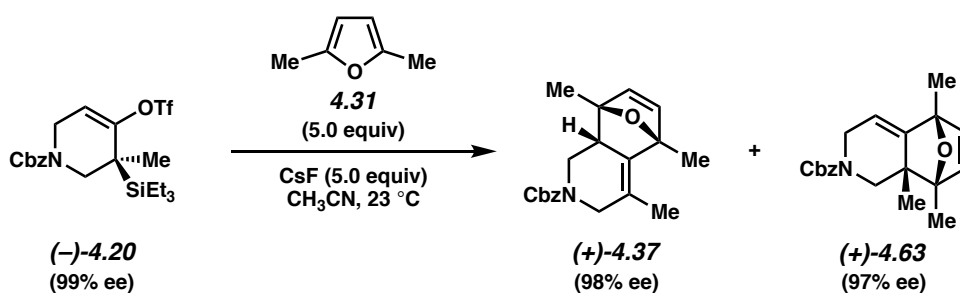
Cycloadduct (+)-4.32 and (+)-4.63. Followed procedure outlined for the preparation of **4.37** and **4.63** in section 4.9.2.2 (0.1 mmol scale). Spectral data matched those previously reported (see page 188). $[\alpha]^{25.7}_D 332.0°$ ($c = 1.00$, CH$_2$Cl$_2$).

Verification of enantioenrichment of compounds 4.39, (+)-4.35, (–)-4.36, (+)-4.37, and (+)-4.63:

Compound	Method Column/Temp.	Solvent	Method Flow Rate	Retention Times (min)	Enantiomeric Ratio (er)
rac-4.39 (from rac-4.23)	Daicel ChiralPak IA-3/35 °C	20% isopropanol in CO_2	2 mL/min	5.69/9.16	50.5:49.5
rac-4.39 (from (+)-4.23)	Daicel ChiralPak IA-3/35 °C	20% isopropanol in CO_2	2 mL/min	5.79/9.50	49.8:50.2
rac-4.35 (from rac-4.20)	Daicel ChiralPak IA-3/35 °C	20% methanol in CO_2	3.5 mL/min	6.42/8.53	49.9:50.1
(+)-4.35 (from (–)-4.20)	Daicel ChiralPak IA-3/35 °C	20% methanol in CO_2	3.5 mL/min	6.22/8.31	90.7:9.3
rac-4.36 (from rac-4.20)	Daicel ChiralPak OJ-H/35 °C	8% isopropanol in CO_2	2 mL/min	10.60/13.30	49.1:50.9

(−)-4.36 (from (+)-4.20)	Daicel ChiralPak OJ-H/35 °C	8% isopropanol in CO_2	2 mL/min	10.66/13.42	6.4:93.6
rac-4.37 (from rac-4.20)	Daicel ChiralPak IC-3/35 °C	5% methanol in CO_2	3.5 mL/min	15.67/16.63	49.4:50.6
(+)-4.37 (from (−)-4.20)	Daicel ChiralPak IC-3/35 °C	5% methanol in CO_2	3.5 mL/min	15.58/16.63	98.9:1.1
rac-4.63 (from rac-4.20)	Daicel ChiralPak IC-3/35 °C	5% methanol in CO_2	3.5 mL/min	12.28/13.06	50.6:49.4
(+)-4.63 (from (−)-4.20)	Daicel ChiralPak IC-3/35 °C	5% methanol in CO_2	3.5 mL/min	12.11/13.12	98.7:1.3
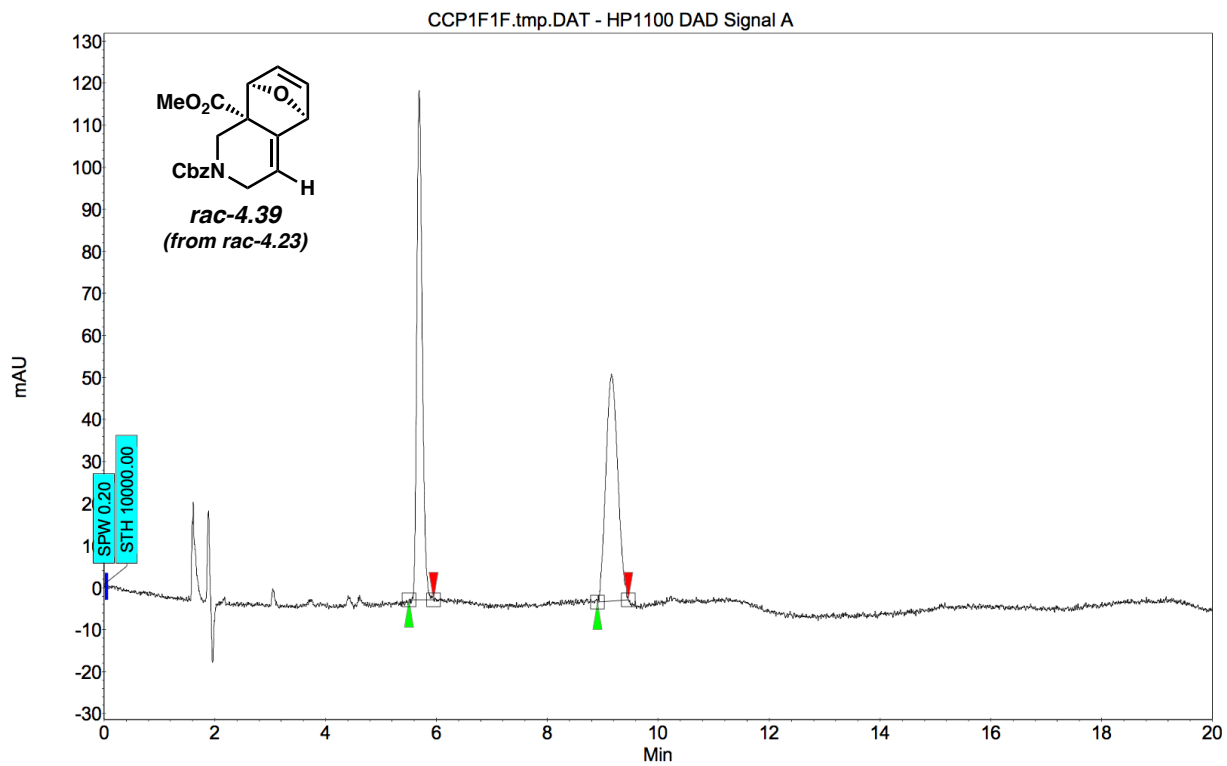
Figure 4.15. SFC trace for rac-**4.39** from rac-**4.23**.
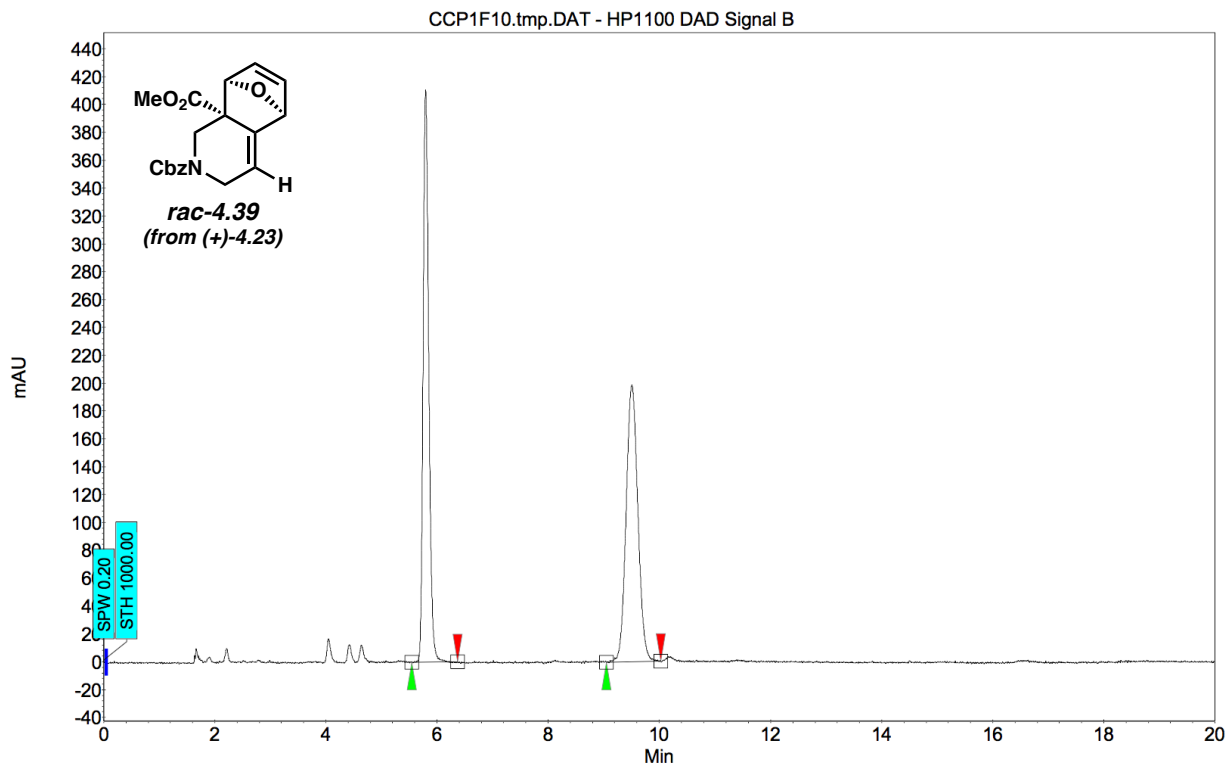
Index	Name	Start	Time	End	RT Offset	Quantity	Height	Area	Area
		[Min]	[Min]	[Min]	[Min]	[% Area]	[µV]	[µV.Min]	[%]
2	UNKNOWN	5.50	5.69	5.95	0.00	50.57	121.2	13.7	50.572
1	UNKNOWN	8.90	9.16	9.46	0.00	49.43	54.0	13.4	49.428
Total						100.00	175.2	27.1	100.000

Figure 4.16. SFC trace for rac-**4.39** from (+)-**4.23**.
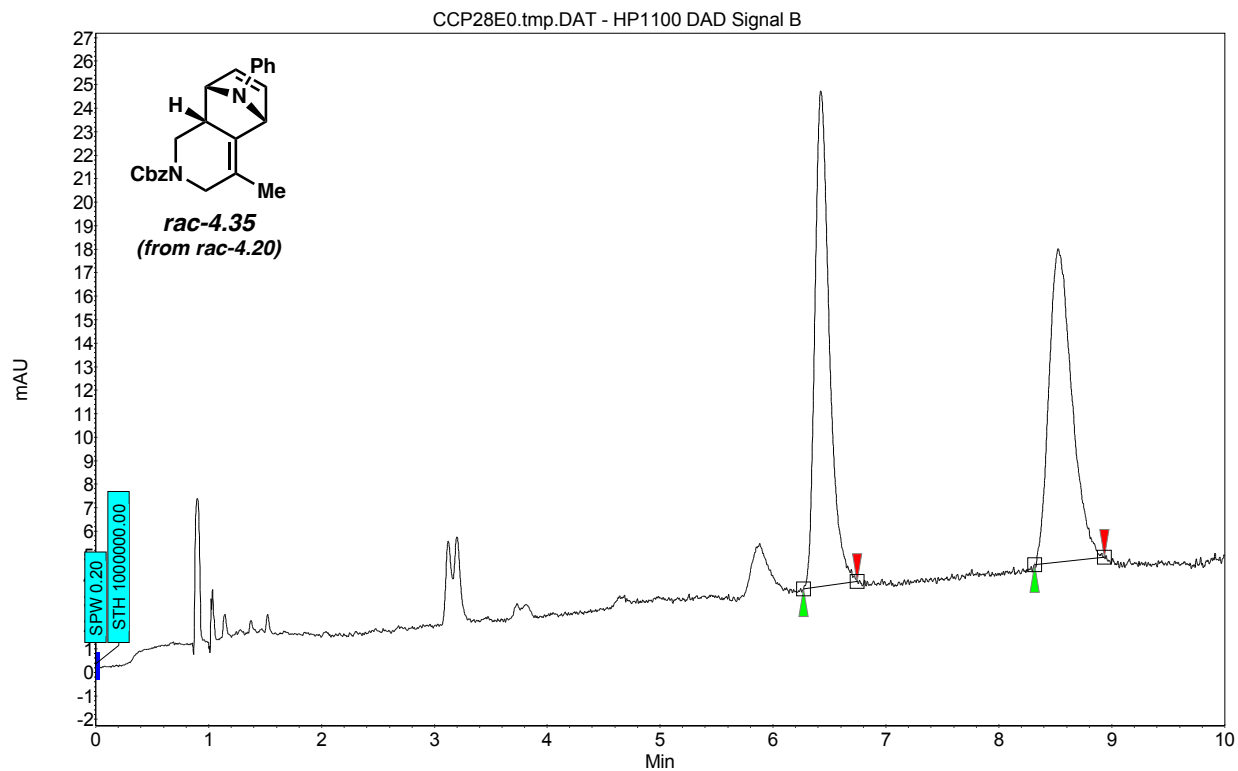
Index	Name	Start	Time	End	RT Offset	Quantity	Height	Area	Area
		[Min]	[Min]	[Min]	[Min]	[% Area]	[µV]	[µV.Min]	[%]
1	UNKNOWN	5.54	5.79	6.37	0.00	49.78	410.7	48.2	49.778
2	UNKNOWN	9.05	9.50	10.02	0.00	50.22	198.8	48.6	50.222
Total						100.00	609.5	96.9	100.000

Figure 4.17. SFC trace for rac-**4.35** from rac-**4.20**.
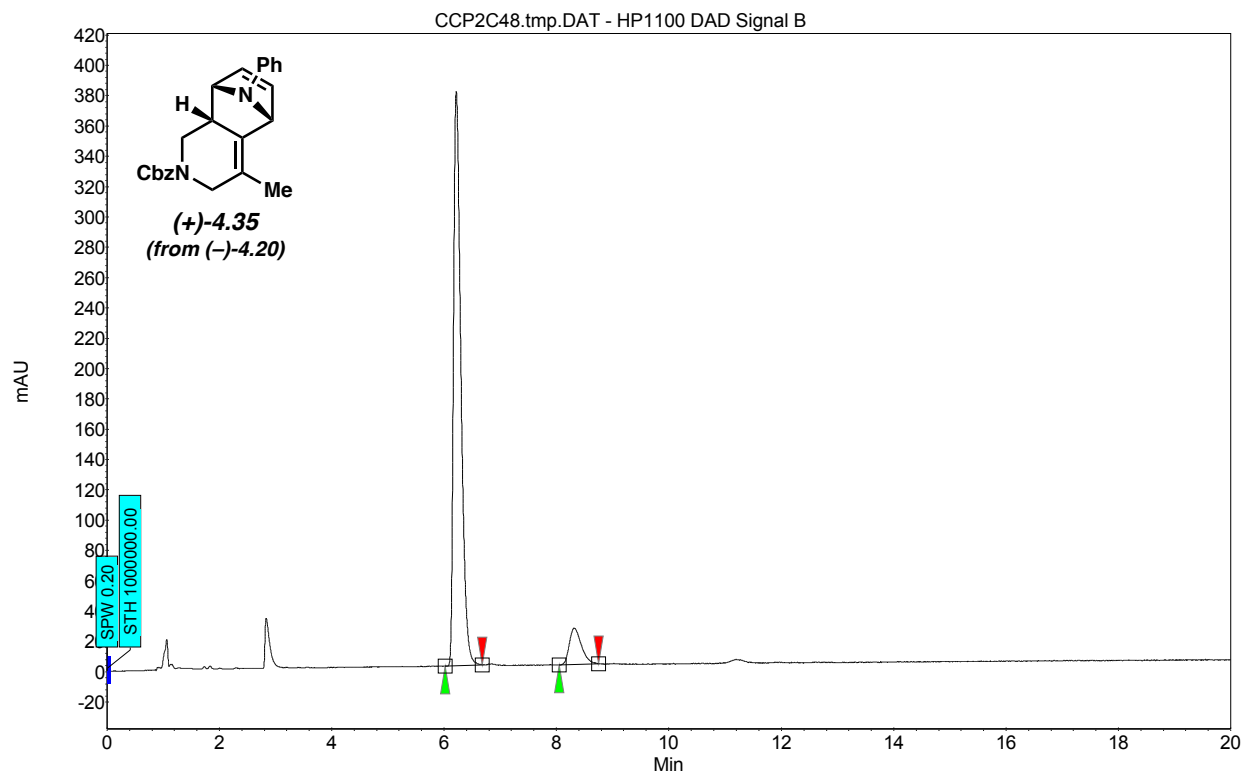
Index	Name	Start	Time	End	RT Offset	Quantity	Height	Area	Area
		[Min]	[Min]	[Min]	[Min]	[% Area]	[µV]	[µV.Min]	[%]
1	UNKNOWN	6.27	6.42	6.74	0.00	49.91	21.1	3.1	49.906
2	UNKNOWN	8.32	8.53	8.94	0.00	50.09	13.3	3.1	50.094
Total						100.00	34.4	6.3	100.000

Figure 4.18. SFC trace for (+)-**4.35** from (−)-**4.20**.
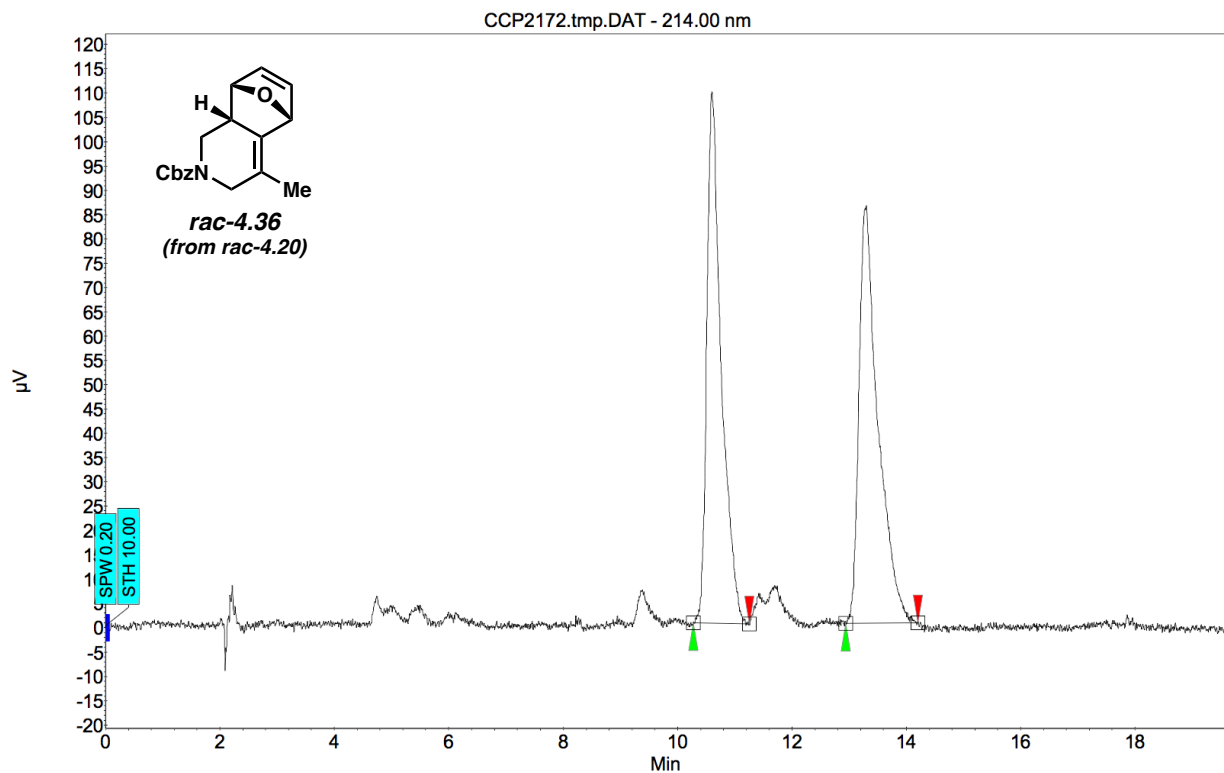
Index	Name	Start	Time	End	RT Offset	Quantity	Height	Area	Area
		[Min]	[Min]	[Min]	[Min]	[% Area]	[µV]	[µV.Min]	[%]
1	UNKNOWN	6.02	6.22	6.68	0.00	90.69	378.9	57.8	90.688
2	UNKNOWN	8.05	8.31	8.75	0.00	9.31	24.0	5.9	9.312
Total						100.00	402.8	63.7	100.000

Figure 4.19. SFC trace for rac-**4.36** from rac-**4.20**.
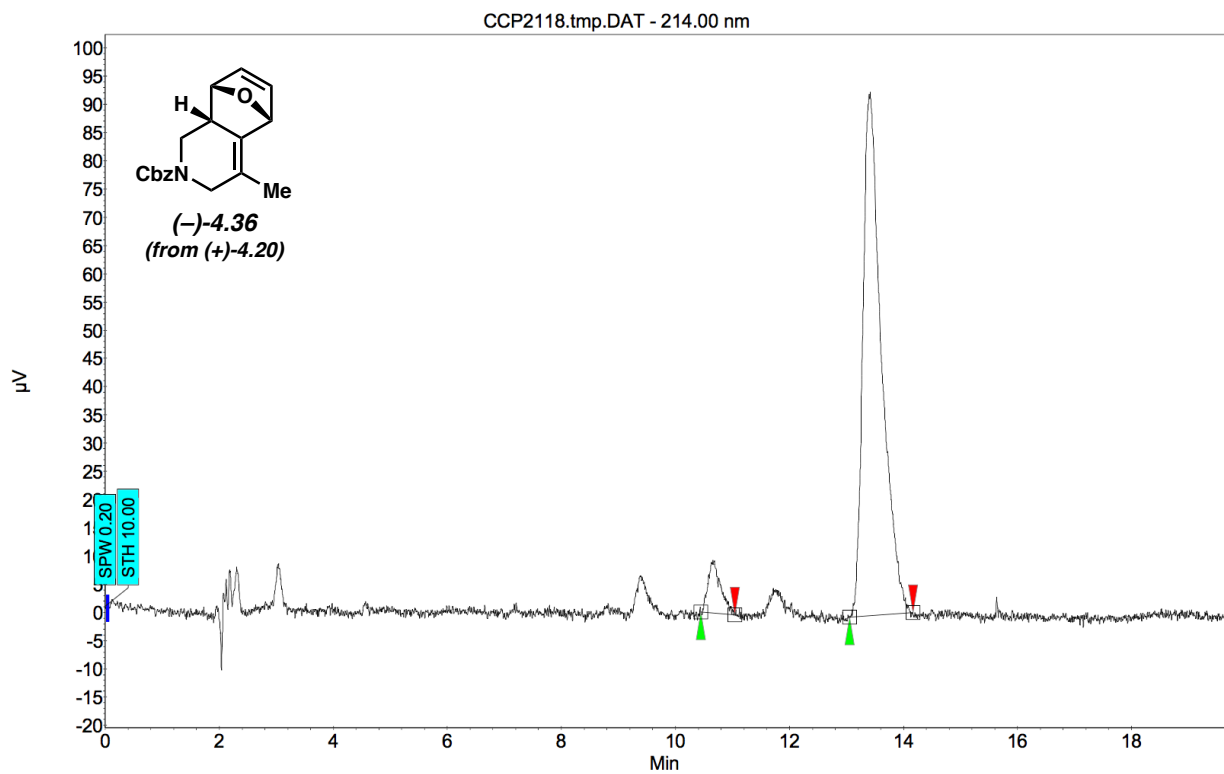
Index	Name	Start	Time	End	RT Offset	Quantity	Height	Area	Area
		[Min]	[Min]	[Min]	[Min]	[% Area]	[µV]	[µV.Min]	[%]
1	UNKNOWN	10.27	10.60	11.25	0.00	49.07	109.3	31.9	49.067
2	UNKNOWN	12.94	13.30	14.20	0.00	50.93	85.9	33.1	50.933
Total						100.00	195.3	65.1	100.000

Figure 4.20. SFC trace for (−)-**4.36** from (+)-**4.20**.
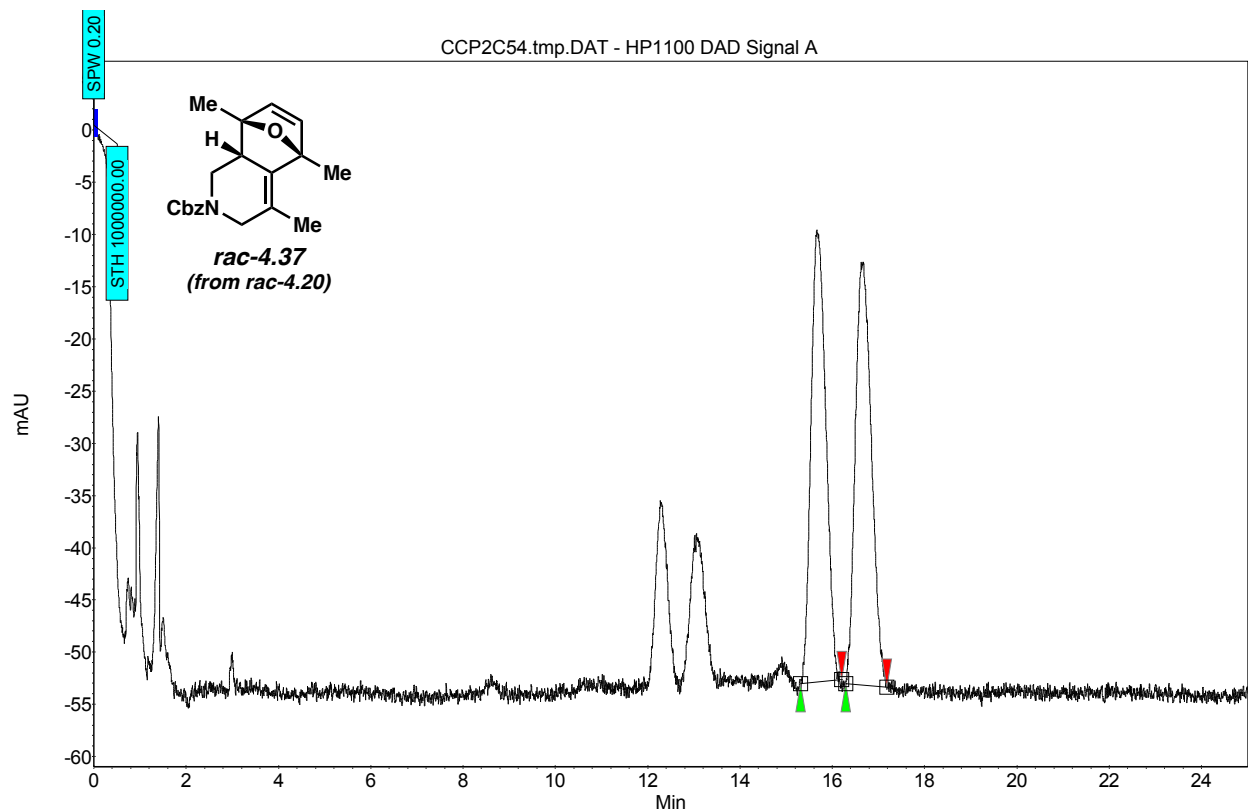
Index	Name	Start	Time	End	RT Offset	Quantity	Height	Area	Area
		[Min]	[Min]	[Min]	[Min]	[% Area]	[µV]	[µV.Min]	[%]
1	UNKNOWN	10.44	10.66	11.05	0.00	6.36	9.4	2.4	6.360
2	UNKNOWN	13.05	13.42	14.16	0.00	93.64	92.7	35.0	93.640
Total						100.00	102.1	37.4	100.000

223

Figure 4.21. SFC trace for rac-**4.37** from rac-**4.20**.
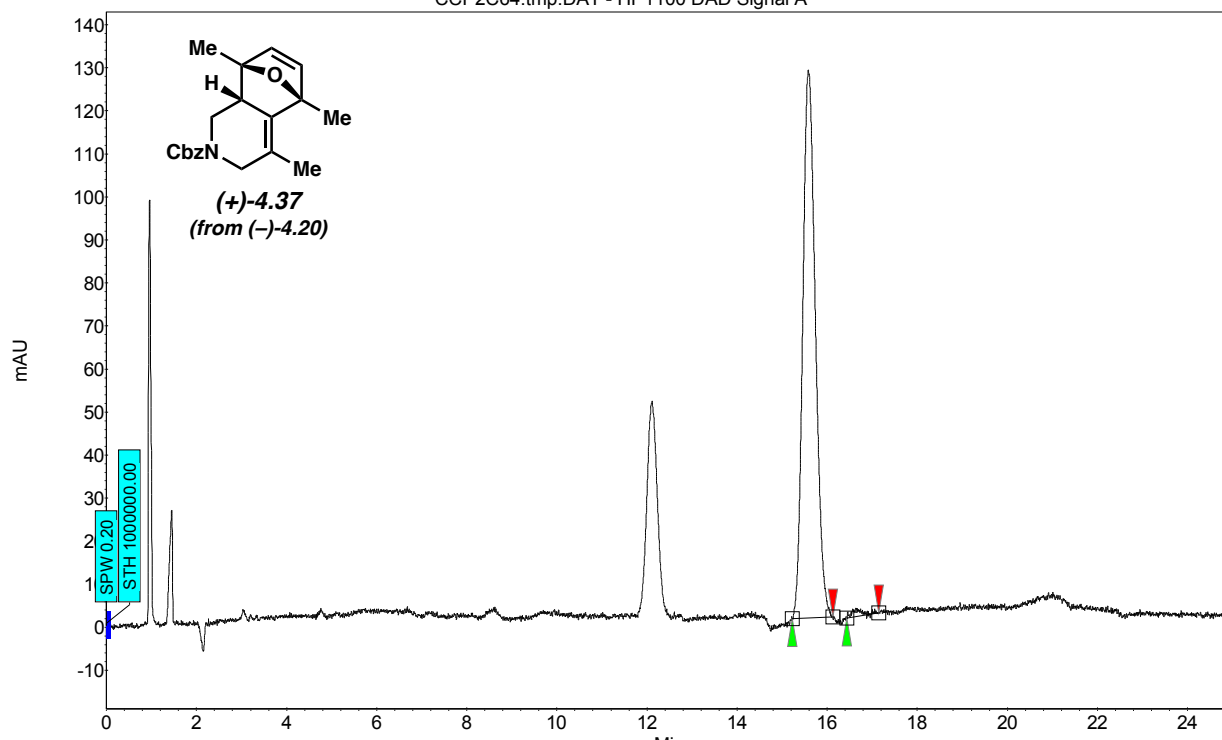
Index	Name	Start	Time	End	RT Offset	Quantity	Height	Area	Area
		[Min]	[Min]	[Min]	[Min]	[% Area]	[µV]	[µV.Min]	[%]
1	UNKNOWN	15.31	15.67	16.20	0.00	49.43	43.3	16.0	49.434
2	UNKNOWN	16.29	16.63	17.18	0.00	50.57	40.5	16.4	50.566
Total						100.00	83.8	32.4	100.000

Figure 4.22. SFC trace for (+)-**4.37** from (–)-**4.20**.
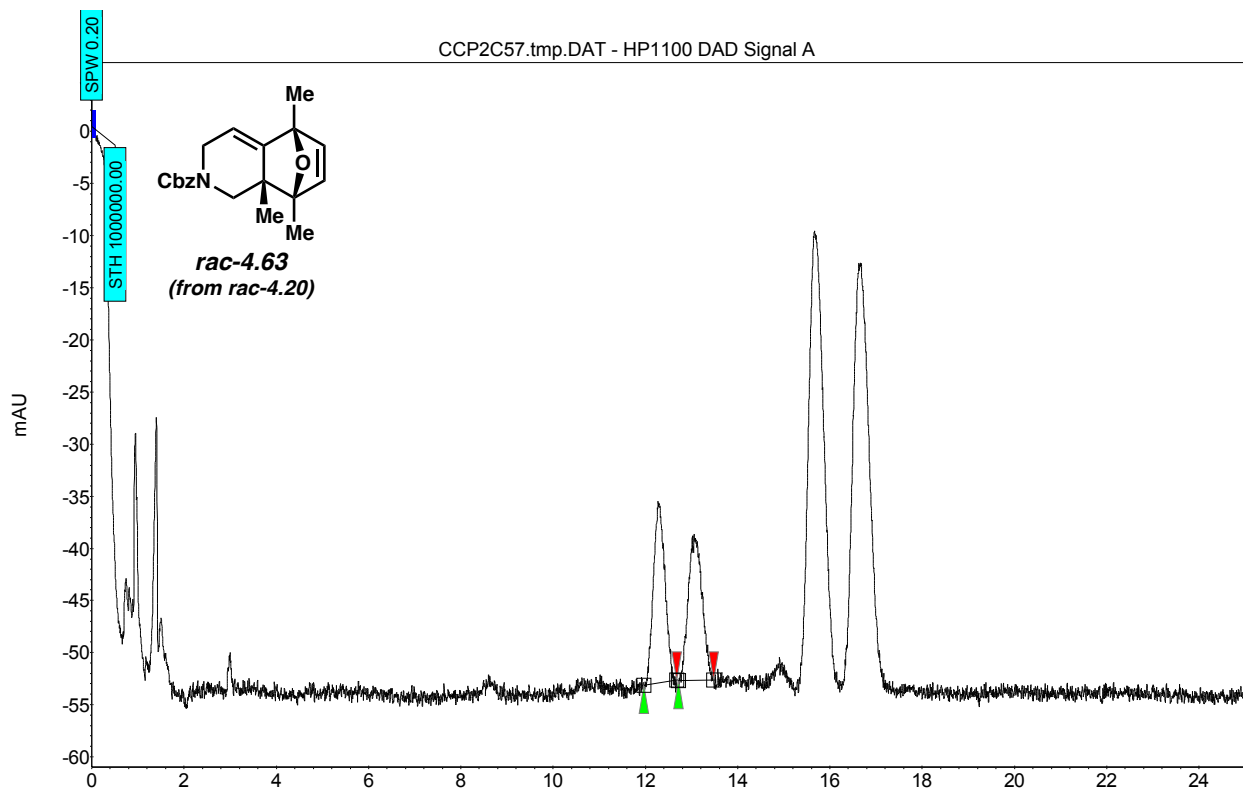
Index	Name	Start	Time	End	RT Offset	Quantity	Height	Area	Area
		[Min]	[Min]	[Min]	[Min]	[% Area]	[µV]	[µV.Min]	[%]
1	UNKNOWN	15.22	15.58	16.13	0.00	98.91	127.3	41.2	98.910
2	UNKNOWN	16.43	16.63	17.14	0.00	1.09	2.0	0.5	1.090
Total						100.00	129.3	41.6	100.000

Index	Name	Start	Time	End	RT Offset	Quantity	Height	Area	Area
		[Min]	[Min]	[Min]	[Min]	[% Area]	[µV]	[µV.Min]	[%]
1	UNKNOWN	11.97	12.28	12.68	0.00	50.56	17.4	4.9	50.564
2	UNKNOWN	12.72	13.06	13.48	0.00	49.44	14.0	4.8	49.436
Total						100.00	31.4	9.7	100.000

Figure 4.23. SFC trace for rac-**4.63** from rac-**4.20**.
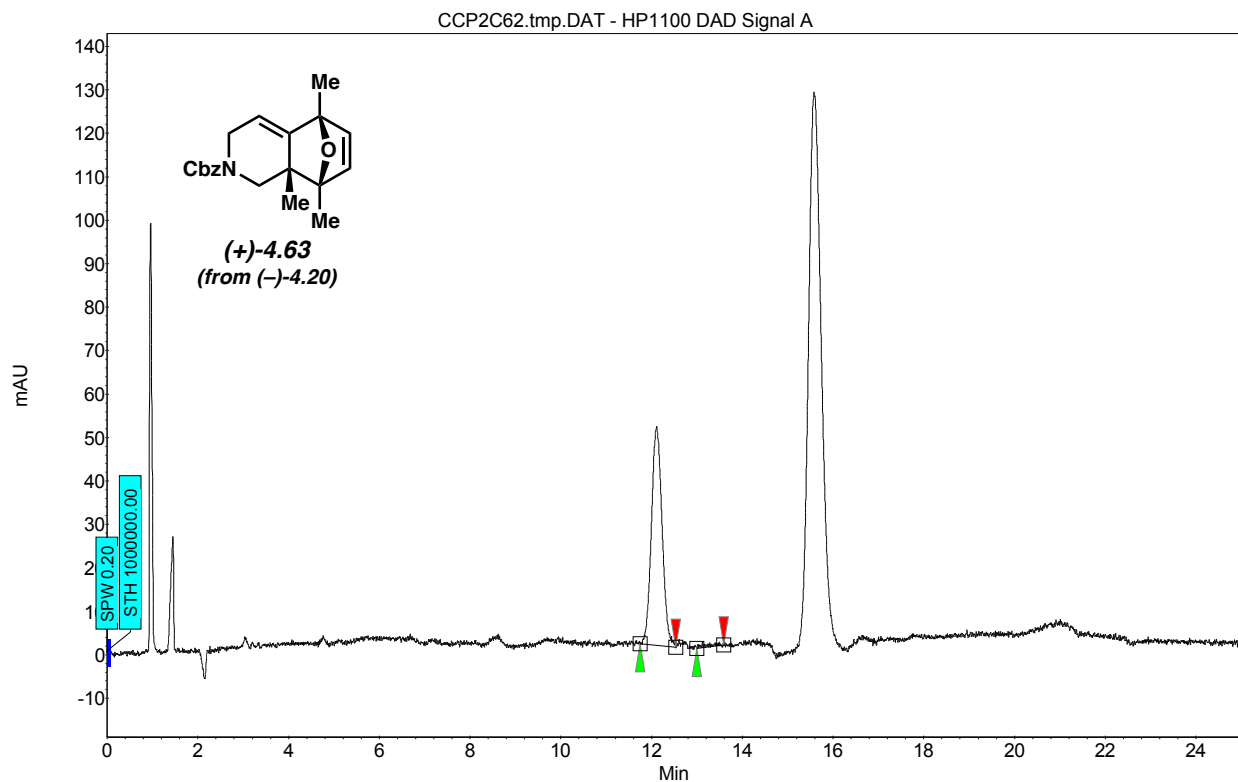
Figure 4.24. SFC trace for (+)-4.63 from (−)-4.20.

Index	Name	Start	Time	End	RT Offset	Quantity	Height	Area	Area
		[Min]	[Min]	[Min]	[Min]	[% Area]	[µV]	[µV.Min]	[%]
1	UNKNOWN	11.74	12.11	12.54	0.00	98.74	50.4	13.7	98.736
2	UNKNOWN	13.00	13.12	13.59	0.00	1.26	1.2	0.2	1.264
Total						100.00	51.6	13.9	100.000

4.9.3 Computational Methods

All calculations were carried out with the Gaussian 09 package. Geometry optimizations were performed with ωB97XD with the 6-31G(d) basis set. Frequency analysis was conducted at the same level of theory to verify the stationary points to be minima or saddle points. Free energy corrections were calculated both with and without Truhlar's quasiharmonic oscillator approximation.[48] Single-point energies and solvent effects in acetonitrile were computed with the ωB97XD/6-311+G(d,p) basis set by using SMD solvation model.[49] Molecular orbital coefficients

were obtained by single point energies at the HF/6-31G(d) level of theory. Computed structures are illustrated using CYLView.[50]

4.9.3.1 Complete Reference of Gaussian 09

Frisch, M. J.; Trucks, G. W.; Schlegel, H. B.; Scuseria, G. E.; Robb, M. A.; Cheeseman, J. R.; Scalmani, G.; Barone, V.; Mennucci, B.; Petersson, G. A.; Nakatsuji, H.; Caricato, M.; Li, X.; Hratchian, H. P.; Izmaylov, A. F.; Bloino, J.; Zheng, G.; Sonnenberg, J. L.; Hada, M.; Ehara, M.; Toyota, K.; Fukuda, R.; Hasegawa, J.; Ishida, M.; Nakajima, T.; Honda, Y.; Kitao, O.; Nakai, H.; Vreven, T.; Montgomery, Jr., J. A.; Peralta, J. E.; Ogliaro, F.; Bearpark, M.; Heyd, J. J.; Brothers, E.; Kudin, K. N.; Staroverov, V. N.; Keith, T.; Kobayashi, R.; Normand, J.; Raghavachari, K.; Rendell, A.; Burant, J. C.; Iyengar, S. S.; Tomasi, J.; Cossi, M.; Rega, N.; Millam, J. M.; Klene, M.; Knox, J. E.; Cross, J. B.; Bakken, V.; Adamo, C.; Jaramillo, J.; Gomperts, R.; Stratmann, R. E.; Yazyev, O.; Austin, A. J.; Cammi, R.; Pomelli, C.; Ochterski, J. W.; Martin, R. L.; Morokuma, K.; Zakrzewski, V. G.; Voth, G. A.; Salvador, P.; Dannenberg, J. J.; Dapprich, S.; Daniels, A. D.; Farkas, O.; Foresman, J. B.; Ortiz, J. V.; Cioslowski, J.; Fox, D. J. *Gaussian 09, Rev. D.01*; Gaussian, Inc., Wallingford, CT, **2010**.

4.9.3.2 Choice of Computational Method

DFT methods were examined to study the Diels–Alder cycloaddition of allene **4.62** with furan (**4.30**) (Figure 4.25). Calculations using B3LYP/6-31G(d) were able to successfully explain the observed diastereoselectivity, however they did not correctly account for the observed regioselectivity. M0-62X was not able to predict either the observed diastereoselectivity or regioselectivity. Computations with ωB97XD/6-31G(d) were able to predict both the observed

regioselectivity and the diastereoselectivity and was further optimized to include solvent (ωB97XD/6-311+G(d,p)/SMD(MeCN)) to give the best correlation with experimental results. We then applied this optimal level of theory to cycloaddition between allene **4.61** and furan (**4.30**) and again found good agreement with experimental results (Figure 4.26).

Level of Theory	Diastereoselectivity		Regioselectivity	
	$\Delta G_{major}{}^{\ddagger}$	$\Delta G_{minor\_exo}{}^{\ddagger}$	$\Delta G_{major}{}^{\ddagger}$	$\Delta G_{minor\_regio}{}^{\ddagger}$
B3LYP/6-31G(d)	17.2	19.2	17.2	18.2
M0-62X/6-31G(d)	11.1	11.7	11.1	11.6
ωB97XD/6-311+G(d,p)//ωB97XD/6-31G(d)	14.0	14.6	14.0	15.5
ωB97XD/6-311+G(d,p)/SMD(MeCN)//ωB97XD/6-31G(d)	12.8	14.2	12.8	17.7

agrees with experimental observation
does not agree with experimental observation
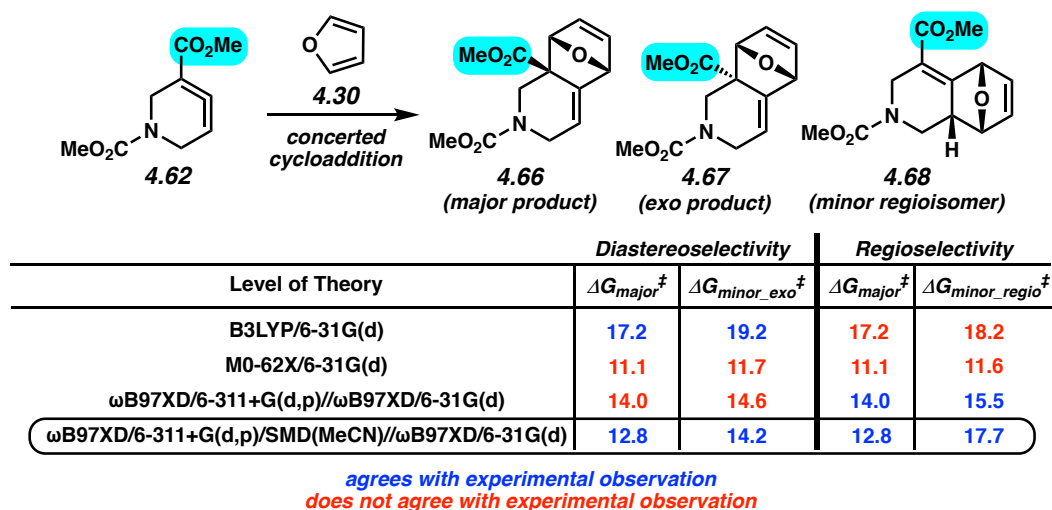
Figure 4.25. DFT methods tested to correlate experimental results on the high regioselectivity and diastereoselectivity observed in the cycloaddition between allene **4.62** and furan (**4.30**). All calculated energies are reported in kcal/mol.

Level of Theory	Diastereoselectivity		Regioselectivity	
	$\Delta G_{major}{}^{\ddagger}$	$\Delta G_{minor\_exo}{}^{\ddagger}$	$\Delta G_{major}{}^{\ddagger}$	$\Delta G_{minor\_regio}{}^{\ddagger}$
ωB97XD/6-311+G(d,p)/SMD(MeCN)//ωB97XD/6-31G(d)	19.1	21.5	19.1	20.6
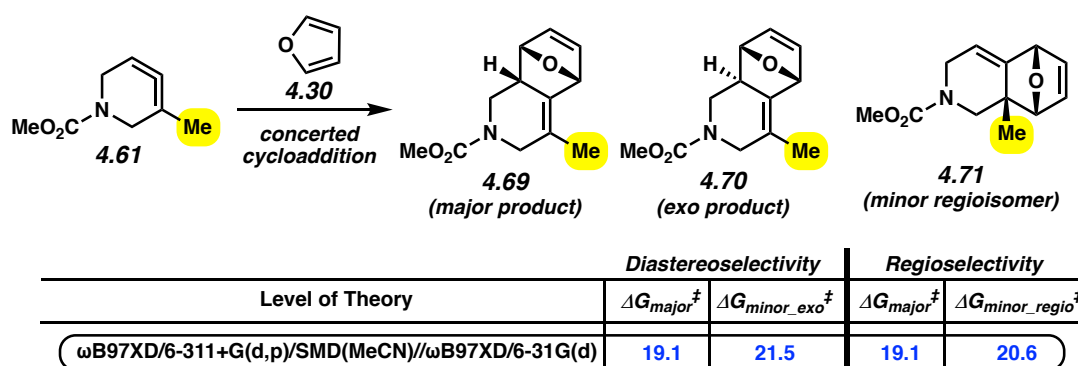
Figure 4.26. DFT methods tested to correlate experimental results on the high regioselectivity and diastereoselectivity observed in the cycloaddition between allene **4.61** and furan (**4.30**). All calculated energies are reported in kcal/mol.

4.9.3.3 Strain Energy in 3,4-Azacyclohexadiene
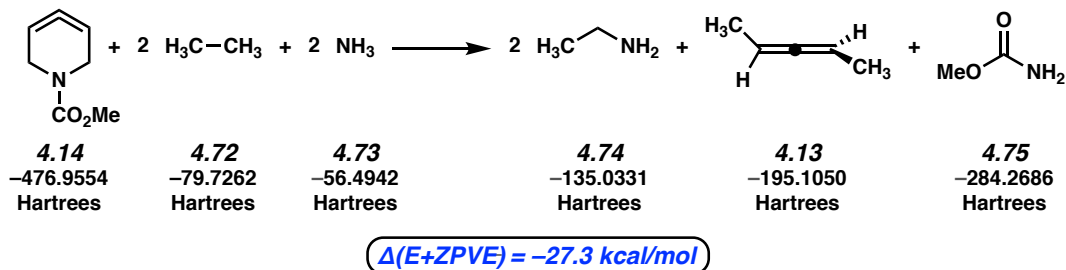
$\Delta(E+ZPVE) = -27.3$ kcal/mol

A homodesmic equation at the ωB97XD/6-31G(d)+ZPVE level of theory was used to estimate strain in 3,4-azacyclohexadiene **4.14**. Molecular strain in 3,4-azacyclohexadiene **4.14** was calculated relative to penta-2,3-diene (**4.13**).

4.9.3.4 Geometries of TS 4.1, TS 4.2, and Diastereomeric Transition States
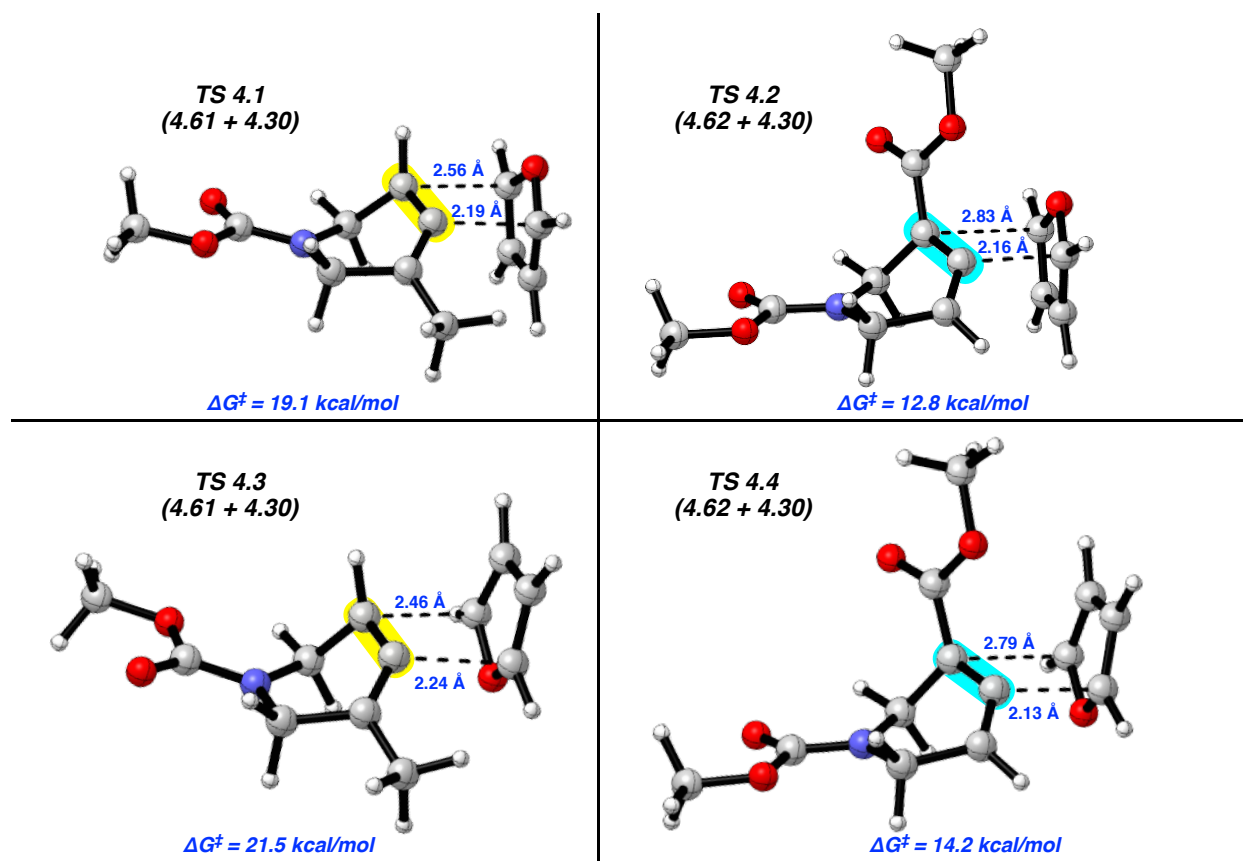
TS 4.1
(4.61 + 4.30)
2.56 Å
2.19 Å
$\Delta G^{\ddagger} = 19.1$ kcal/mol

TS 4.2
(4.62 + 4.30)
2.83 Å
2.16 Å
$\Delta G^{\ddagger} = 12.8$ kcal/mol

TS 4.3
(4.61 + 4.30)
2.46 Å
2.24 Å
$\Delta G^{\ddagger} = 21.5$ kcal/mol

TS 4.4
(4.62 + 4.30)
2.79 Å
2.13 Å
$\Delta G^{\ddagger} = 14.2$ kcal/mol

Transition states geometries for concerted cycloadditions of allenes **4.61** and **4.62** with furan (**4.30**) at the wB97XD/6-31G(d) level of theory. **TS 4.1** and **TS 4.2** lead to endo products (major diastereomers) while **TS 4.3** and **TS 4.4** lead to exo products. $\Delta G^{\ddagger}$ values are also provided (wB97XD/6-311+G(d,p)/SMD(MeCN)//wB97XD/6-31G(d)).

4.9.3.5 Geometries of Cycloadducts
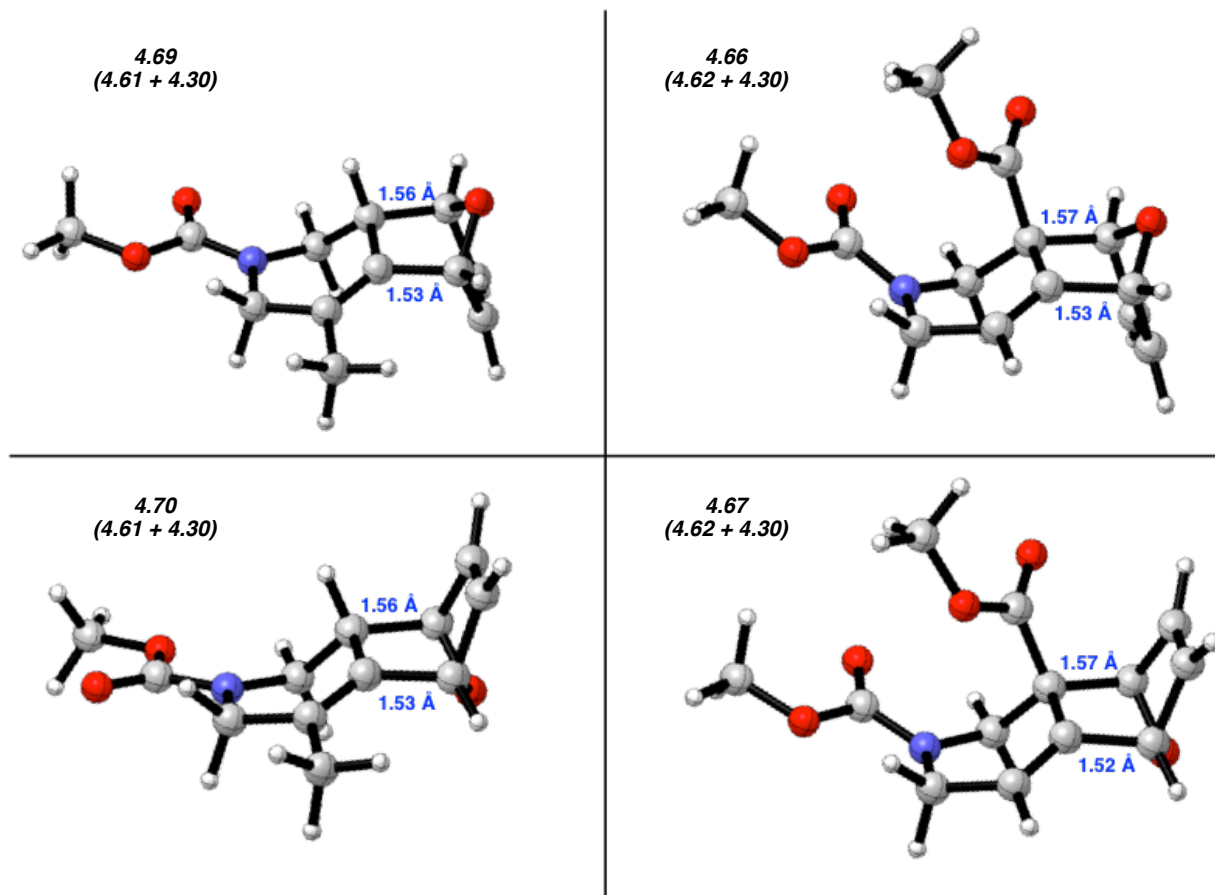
Optimized structures of endo and exo products from cycloaddition of allenes **4.61** and **4.62** with **4.30**. Cycloaddition products from Diels–Alder reaction of allenes **4.61** and **4.62** with furan (**4.30**). **4.69** and **4.66** are endo diastereomers while **4.70** and **4.67** are exo diastereomers. All of the displayed cycloadducts are considered the observed major regioisomers.

4.9.3.6 Geometries of Regioisomeric Transition States
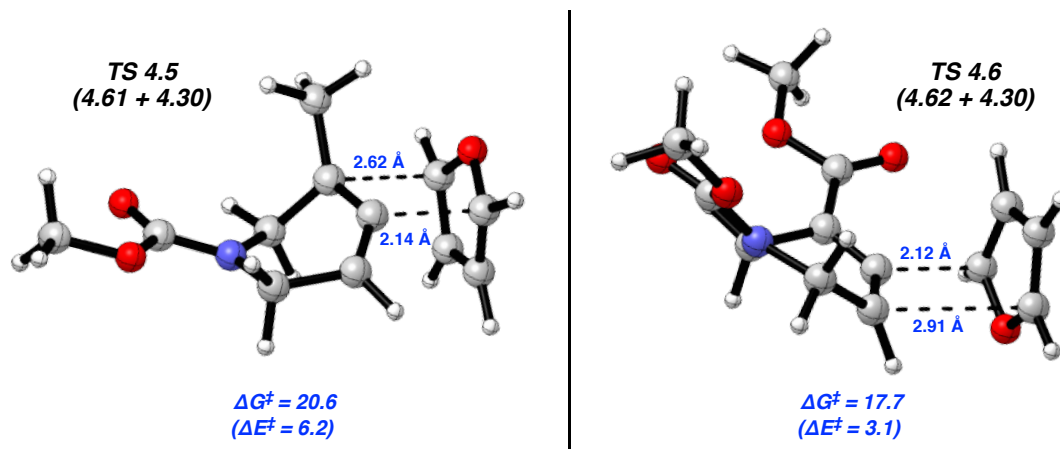
TS 4.5
(4.61 + 4.30)

2.62 Å

2.14 Å

$\Delta G^{\ddagger} = 20.6$
$(\Delta E^{\ddagger} = 6.2)$

TS 4.6
(4.62 + 4.30)

2.12 Å

2.91 Å

$\Delta G^{\ddagger} = 17.7$
$(\Delta E^{\ddagger} = 3.1)$

Transition states geometries for concerted cycloadditions of allenes **4.61** and **4.62** with furan (**4.30**) leading to minor regioisomers (endo diastereomers). **TS 4.5** and **TS 4.6** were optimized at the wB97XD/6-31G(d) level of theory. $\Delta G^{\ddagger}$ and $\Delta E^{\ddagger}$ values are also provided in kcal/mol (wB97XD/6-311+G(d,p)/SMD(MeCN)//wB97XD/6-31G(d)).

4.9.3.7 Distortion/Interaction Activation Strain Analyses

Distortion/interaction activation strain analyses were performed along the reaction coordinate for cycloadditions of allenes **4.61** and **4.62** with furan (**4.30**) at the ωB97XD/6-311+G(d,p)/SMD(MeCN)//ωB97XD/6-31G(d) level of theory. The purpose was to determine the relative importance of distortion and interaction energies along the reaction pathway.

Endo pathways leading to the two possible regioisomers were analyzed in each case. In Figures 4.27 and 4.28, the total electronic energy (ΔE), distortion energy (ΔE_{dist}), and interaction energy (ΔE_{int}) are plotted versus the average length of the two forming bonds (χ). For the reaction of allene **4.61** with furan (**4.30**), the total energies are lower as reactants proceed toward the transition state (Figure 4.27). Although distortion energies are slightly more elevated in the pathway leading to the major regioisomer, interaction energies are much lower. This indicates that

there are more stabilizing HOMO/LUMO interactions in the pathway leading to the major regioisomer.

A similar trend in interaction energies is observed for cycloaddition of allene **4.62** with furan (**4.30**) as demonstrated in Figure 4.28. Interaction energies are much more stabilizing in the pathway leading to the major regioisomer, indicating that regioselectivity is controlled by differences in interaction energies along the reaction coordinate. Additionally, distortion energies are slightly lower for the pathway leading to the major regioisomer.
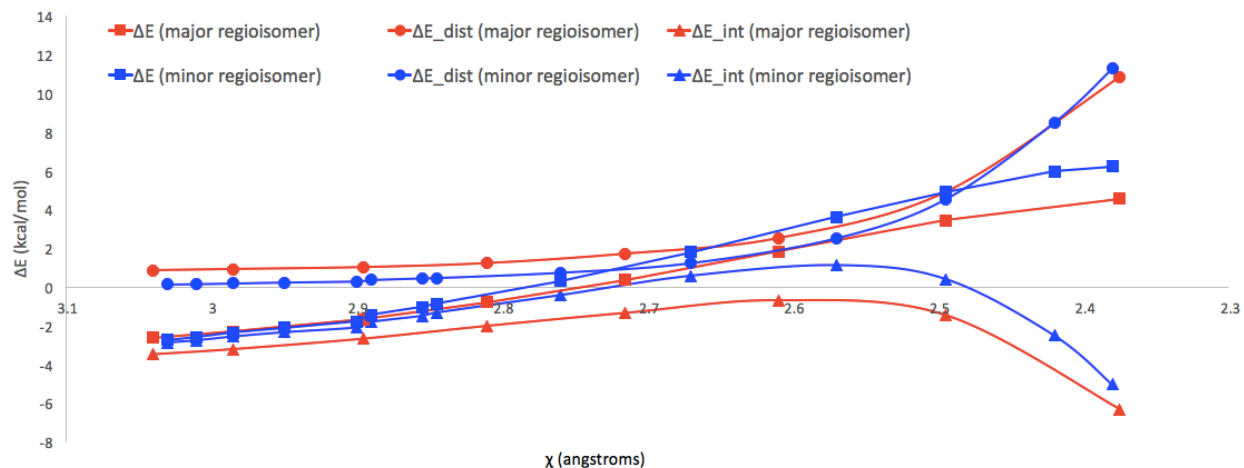
Figure 4.27. Distortion/interaction activation strain analysis along the reaction coordinate in the Diels–Alder reaction of allene **4.61** with furan (**4.30**). Concerted endo pathways leading to two possible regioisomers are plotted. The last points to the right are the respective transition states.
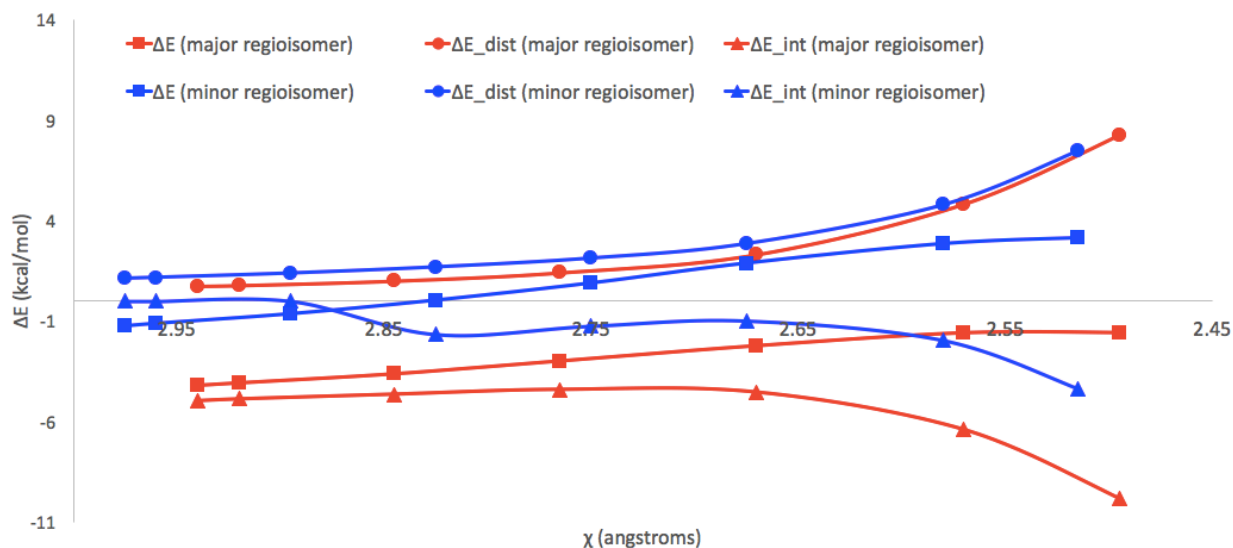
Figure 4.28. Distortion/interaction activation strain analysis along the reaction coordinate in the Diels–Alder reaction of allene **4.62** with furan (**4.30**). Concerted endo pathways leading to two possible regioisomers are plotted. The last points to the right are the respective transition states.

4.9.3.8 Racemization Barriers
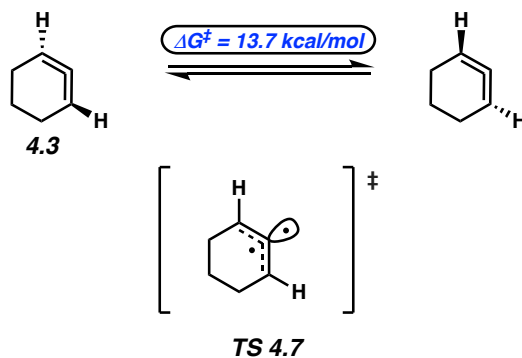
The barrier for racemization of 1,2-cyclohexadiene (**4.3**) was calculated at the ωB97XD/6-311+G(d,p)//ωB97XD/6-31G(d)/SMD(MeCN) level of theory. Racemization was found to proceed via a diradical transition state (**TS 4.7**) and with a barrier of 13.7 kcal/mol. This value is in close proximity to the literature reported value (15.0 kcal/mol).[6]
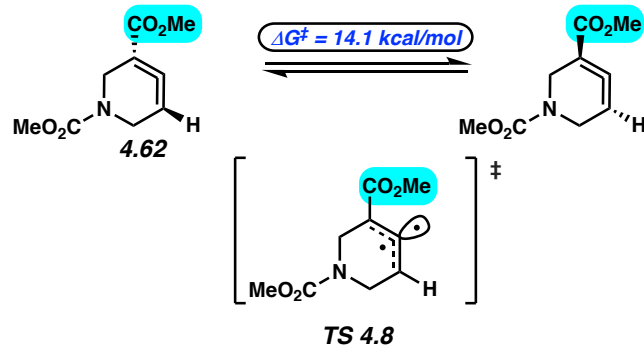
The barrier for racemization of ester allene **4.62** was calculated at the ωB97XD/6-311+G(d,p)/SMD(MeCN) level of theory. Racemization was found to proceed via a diradical transition state (**TS 4.8**) and with a barrier of 14.1 kcal/mol.
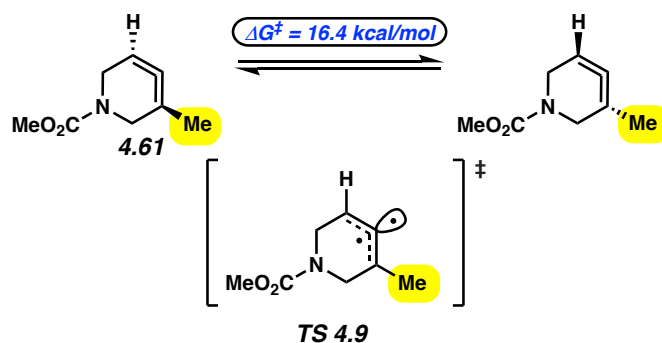
The barrier for racemization of methyl allene **4.61** was calculated at the ωB97XD/6-311+G(d,p)/SMD(MeCN) level of theory. Racemization was found to proceed via a diradical transition state (**TS 4.9**) and with a barrier of 16.4 kcal/mol.

4.9.3.9 Energies and Cartesian Coordinates for Optimized Structures

Cartesian coordinates for the optimized structures were reported in the literature.[51]

4.10 Spectra Relevant to Chapter Four:

Diels–Alder Cycloadditions of Strained Azacyclic Allenes

Joyann S. Barber,[†] Michael M. Yamano,[†] Melissa Ramirez, Evan R. Darzi,

Rachel R. Knapp, Fang Liu, K. N. Houk, and Neil K. Garg.

8.492
8.477
8.366

6.751
6.736

3.840

0.955
0.919
0.917
0.914
0.857
0.853
0.834
0.830
0.819
0.817
0.810

OMe

N

SiEt₃

4.65

Current Data Parameters
NAME   ED_1_016_2
EXPNO   1
PROCNO   1

F2 - Acquisition Parameters
Date_   20161214
Time   12.55
INSTRUM   av400
PROBHD   5 mm PABBO BB/
PULPROG   zg30
TD   52882
SOLVENT   CDCl3
NS   8
DS   0
SWH   8012.820 Hz
FIDRES   0.151523 Hz
AQ   3.2998369 sec
RG   189.85
DW   62.400 usec
DE   6.50 usec
TE   299.0 K
D1   2.00000000 sec
TD0   1

======= CHANNEL f1 =====
SFO1   400.1324008 MHz
NUC1   1H
P1   15.00 usec
PLW1   13.00000000 W

F2 - Processing parameters
SI   65536
SF   400.1300178 MHz
WDW   EM
SSB   0
LB   0.30 Hz
GB   0
PC   1.00

10   9   8   7   6   5   4   3   2   1   0   ppm

0.982
1.030

1.000

3.016

9.268
5.975

Figure 4.29. ¹H NMR (400 MHz, CDCl₃) of compound **4.65**.

170.538

156.046
152.431

120.048

105.441

54.845

7.528
3.341

Current Data Parameters
NAME   ED_1_019_pub_carb
EXPNO   1
PROCNO   1

F2 - Acquisition Parameters
Date_   20170112
Time   22.11
INSTRUM   av400
PROBHD   5 mm PABBO BB/
PULPROG   zgpg30
TD   65536
SOLVENT   CDCl3
NS   64
DS   0
SWH   25252.525 Hz
FIDRES   0.385323 Hz
AQ   1.2976128 sec
RG   189.85
DW   19.800 usec
DE   6.50 usec
TE   299.0 K
D1   2.00000000 sec
D11   0.03000000 sec
TD0   1

======= CHANNEL f1 =====
SFO1   100.6243395 MHz
NUC1   13C
P1   10.00 usec
PLW1   52.00000000 W

======= CHANNEL f2 =====
SFO2   400.1324008 MHz
NUC2   1H
CPDPRG[2   waltz16
PCPD2   90.00 usec
PLW2   13.00000000 W
PLW12   0.36111000 W
PLW13   0.29249999 W

F2 - Processing parameters
SI   65536
SF   100.6127582 MHz
WDW   EM
SSB   0
LB   1.00 Hz
GB   0
PC   1.40

230 220 210 200 190 180 170 160 150 140 130 120 110 100 90 80 70 60 50 40 30 20 10   ppm

Figure 4.30. ¹³C NMR (100 MHz, CDCl₃) of compound **4.65**.

Purified Product, 1H NMR

7.816
7.406
7.402
7.391
7.387
5.273
4.023
4.005
3.986
2.549
2.530
2.512
0.922
0.902
0.883
0.718
0.699
0.679
0.658

Current Data Parameters
NAME   ED_1_021_pub_proto
EXPNO   1
PROCNO   1

F2 - Acquisition Parameters
Date_   20170113
Time   9.12
INSTRUM   av400
PROBHD 5 mm PABBO BB/
PULPROG   zg30
TD   52882
SOLVENT   CDCl3
NS   8
DS   0
SWH   8012.820 Hz
FIDRES   0.151523 Hz
AQ   3.2998369 sec
RG   155.85
DW   62.400 usec
DE   6.50 usec
TE   299.0 K
D1   2.00000000 sec
TD0   1

======= CHANNEL f1 =====
SFO1   400.1324008 MHz
NUC1   1H
P1   15.00 usec
PLW1   13.00000000 W

F2 - Processing parameters
SI   65536
SF   400.1300176 MHz
WDW   EM
SSB   0
LB   0.30 Hz
GB   0
PC   1.00

1.000
5.075
2.070
2.080
2.070
9.098
5.988

Figure 4.31. ^{1}H NMR (400 MHz, CDCl$_3$) of compound **4.16**.

Purified Product, 13C NMR

196.802
135.277
128.885
128.463
69.021
42.677
36.220
7.554
3.068

Current Data Parameters
NAME   ED_1_021_pub_carbo
EXPNO   1
PROCNO   1

F2 - Acquisition Parameters
Date_   20170113
Time   10.01 h
INSTRUM   av500
PROBHD Z119248_0002 (
PULPROG   zgpg30
TD   65536
SOLVENT   CDCl3
NS   119
DS   2
SWH   31250.000 Hz
FIDRES   0.953674 Hz
AQ   1.0485760 sec
RG   204.54
DW   16.000 usec
DE   18.00 usec
TE   298.0 K
D1   2.00000000 sec
D11   0.03000000 sec
TD0   1
SFO1   125.7722511 MHz
NUC1   13C
P1   9.63 usec
PLW1   23.00000000 W
SFO2   500.1330008 MHz
NUC2   1H
CPDPRG[2   waltz16
PCPD2   80.00 usec
PLW2   13.50000000 W
PLW12   0.21094000 W
PLW13   0.13500001 W

F2 - Processing parameters
SI   131072
SF   125.7577724 MHz
WDW   EM
SSB   0
LB   1.00 Hz
GB   0
PC   1.40

Figure 4.32. ^{13}C NMR (125 MHz, CDCl$_3$) of compound **4.16**.

238

Purified Product, 1H NMR

7.368
7.358
7.347
7.343
7.336
7.327
7.323
7.318
5.174
5.166
5.143
5.111
4.123
4.051
4.041
4.026
4.024
4.015
3.793
3.786
3.746
3.730
3.658
3.465
3.396
3.344
2.443
2.366
0.936
0.921
0.644

4.834

2.000
1.926
1.067
0.970

3.013

8.854
5.904

Figure 4.33. ^{1}H NMR (500 MHz, CDCl$_3$) of compound **4.17**.

Purified Product, 13C NMR

209.176
208.805
155.244
136.647
136.448
128.733
128.674
128.512
128.404
128.339
128.197
67.777
67.557
42.852
42.775
42.504
42.212
40.156
7.420
2.956

Figure 4.34. ^{13}C NMR (125 MHz, CDCl$_3$) of compound **4.17**.

Figure 4.35. ¹H NMR (500 MHz, CDCl₃) of compound **4.18**.
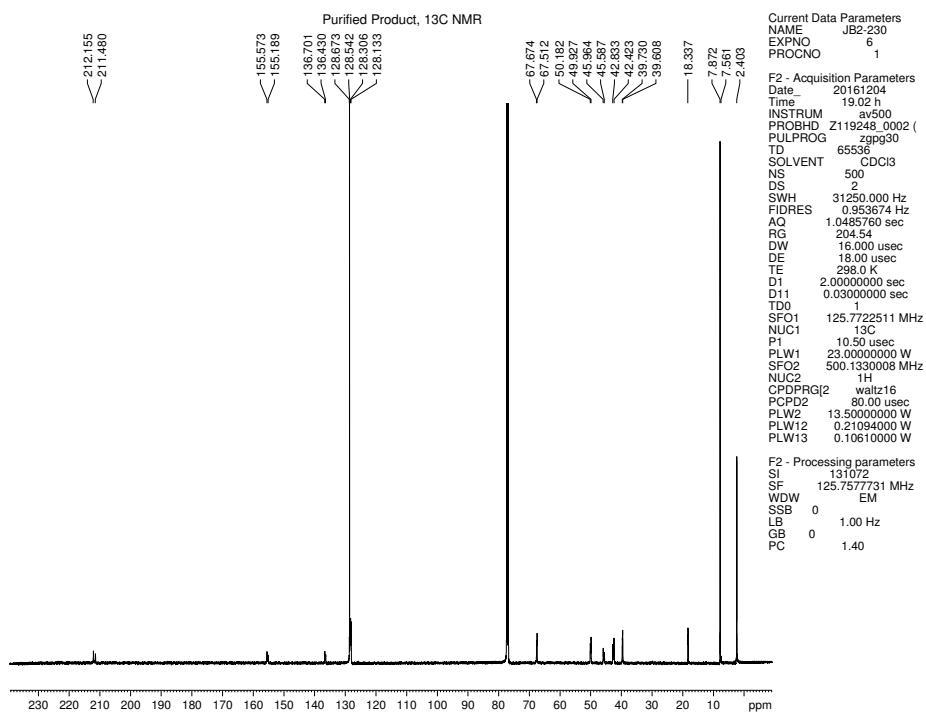
Figure 4.36. ¹³C NMR (125 MHz, CDCl₃) of compound **4.18**.
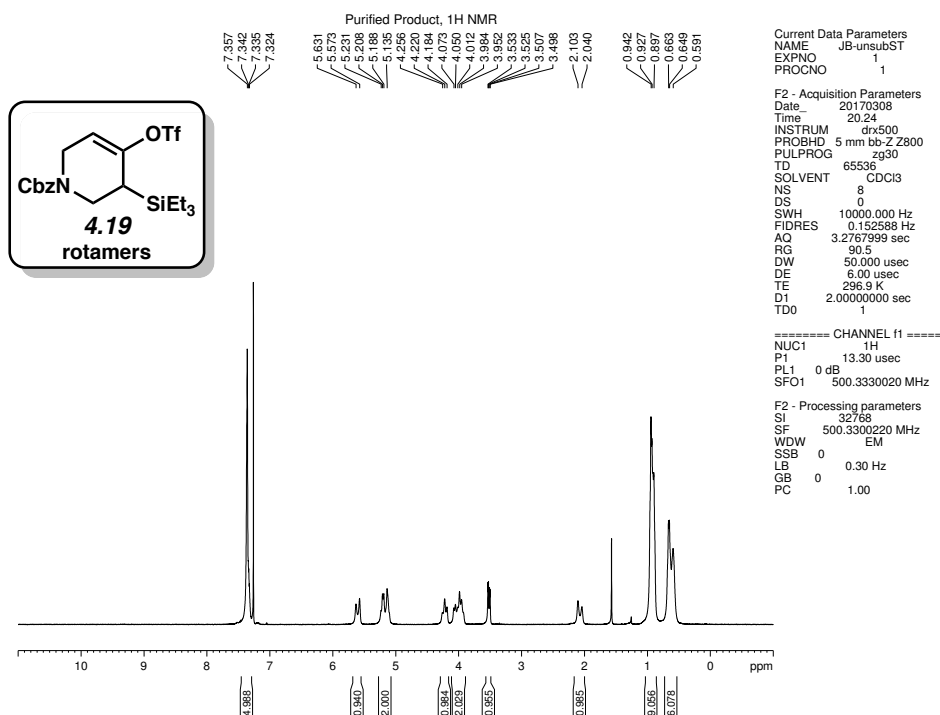
Figure 4.37. ^{1}H NMR (500 MHz, CDCl$_3$) of compound **4.19**.
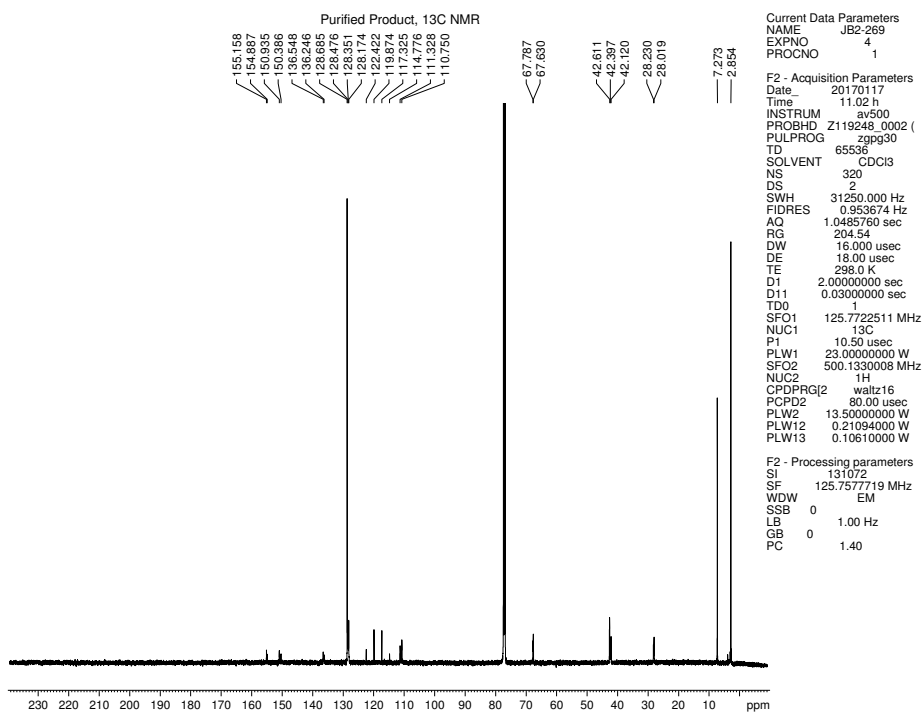
Figure 4.38. ^{13}C NMR (125 MHz, CDCl$_3$) of compound **4.19**.
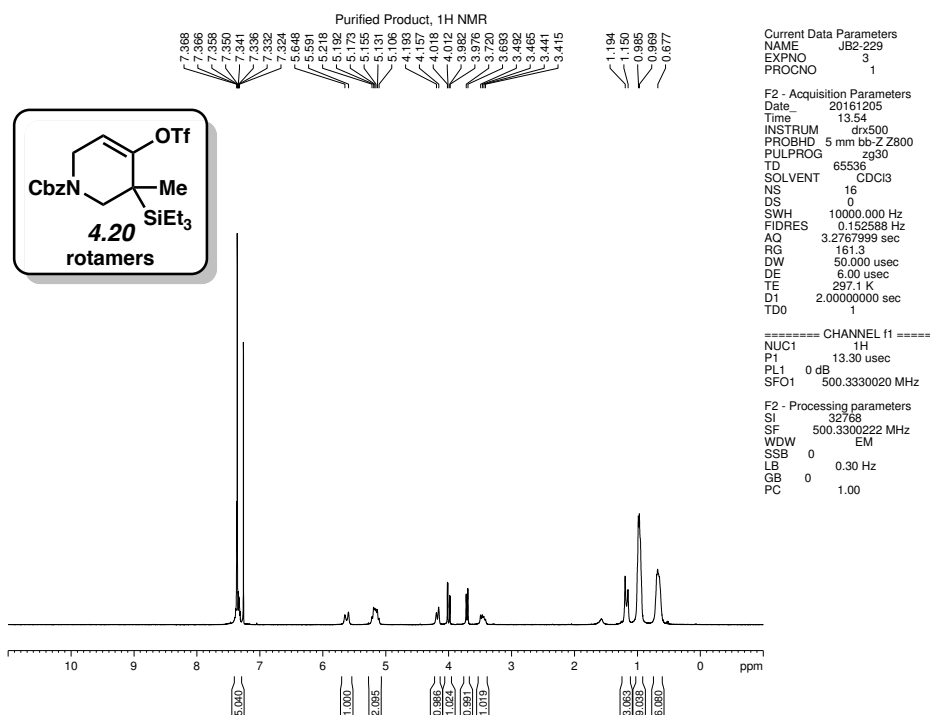
Figure 4.39. ^{1}H NMR (500 MHz, CDCl$_3$) of compound **4.20**.
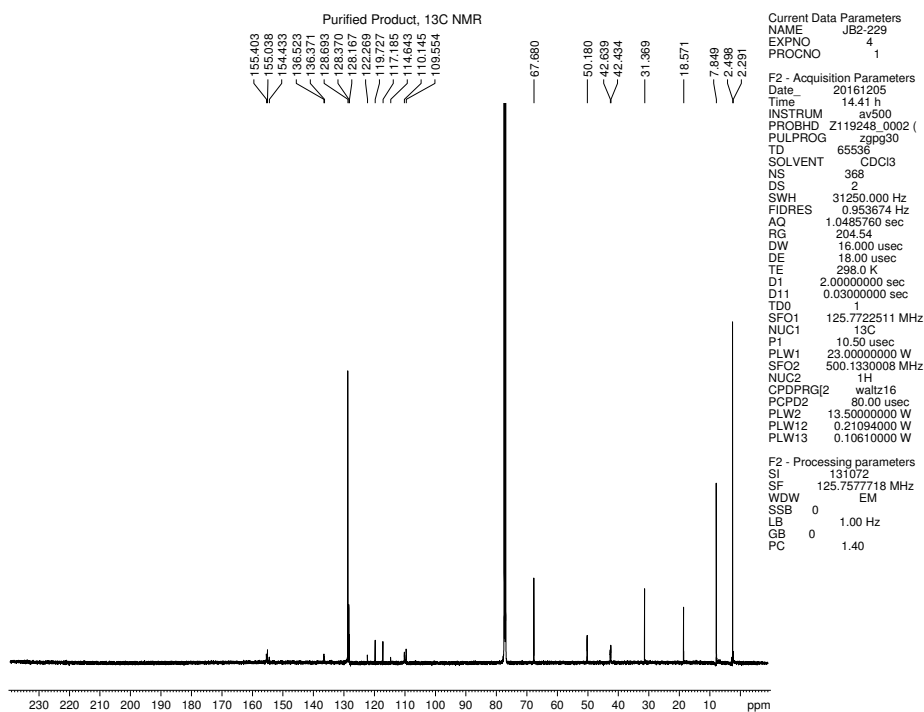
Figure 4.40. ^{13}C NMR (125 MHz, CDCl$_3$) of compound **4.20**.
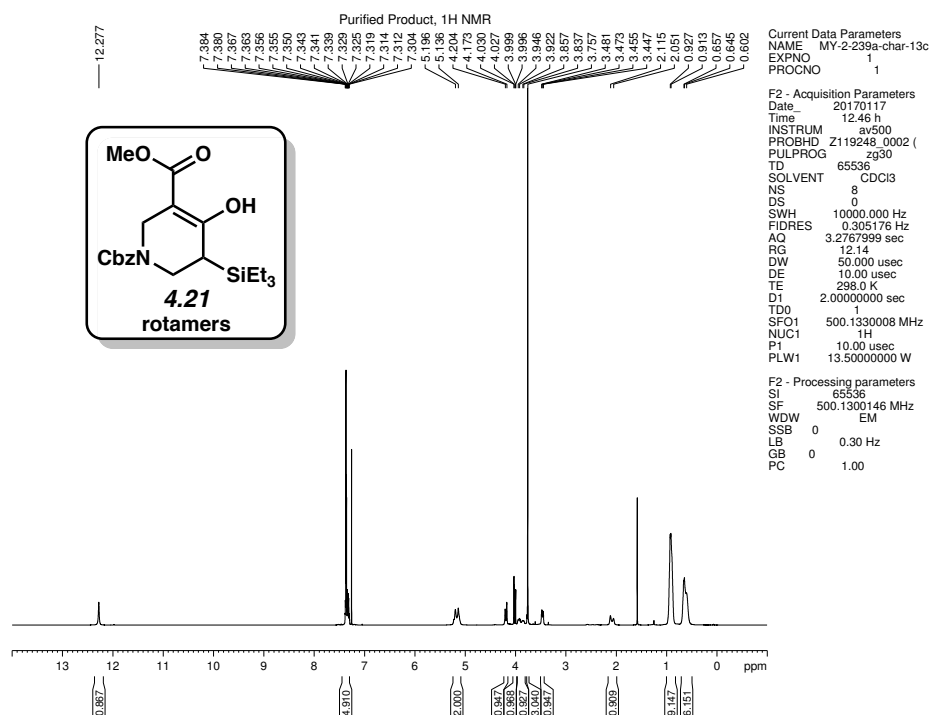
Figure 4.41. ^{1}H NMR (500 MHz, CDCl₃) of compound **4.21**.
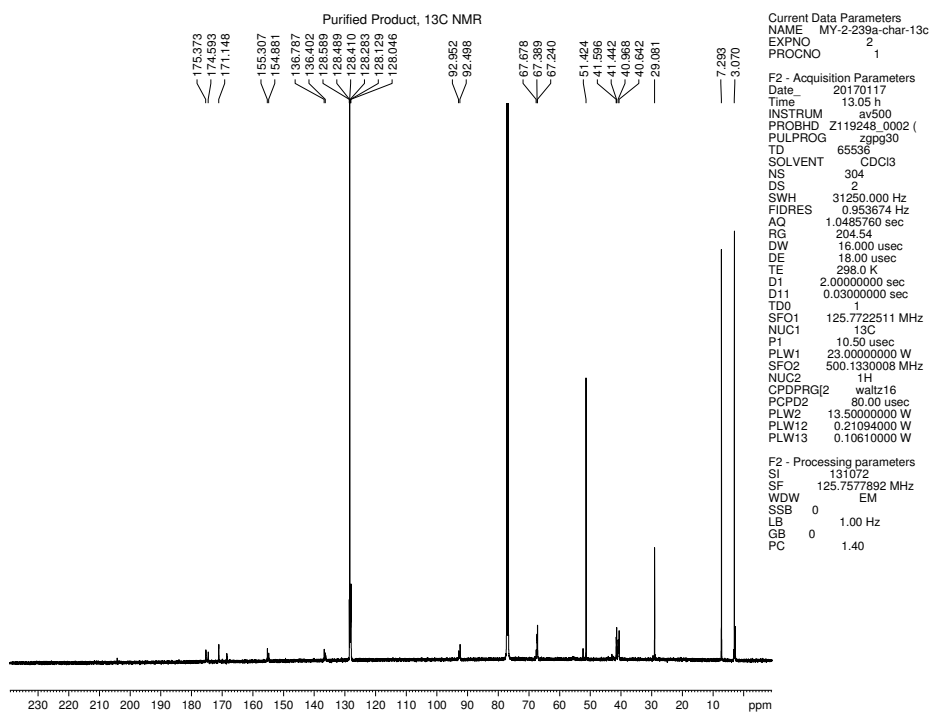
Figure 4.42. ^{13}C NMR (125 MHz, CDCl₃) of compound **4.21**.

12.412

7.373
7.368
7.361
7.345
7.334
7.329
7.324
7.317
5.233
5.208
5.167
5.150
4.167
4.135
4.094
4.062
3.798
3.780
3.737
3.706
3.677
3.259
3.233

1.222
1.178
0.957
0.943
0.692
0.678

Current Data Parameters
NAME   ED_1_034_analytical
EXPNO   1
PROCNO   1

F2 - Acquisition Parameters
Date_   20170125
Time   12.46 h
INSTRUM   av500
PROBHD   Z119248_0002 (
PULPROG   zg30
TD   65536
SOLVENT   CDCl3
NS   8
DS   0
SWH   10000.000 Hz
FIDRES   0.305176 Hz
AQ   3.2767999 sec
RG   63.27
DW   50.000 usec
DE   10.00 usec
TE   298.0 K
D1   2.00000000 sec
TD0   1
SFO1   500.1330008 MHz
NUC1   1H
P1   10.00 usec
PLW1   13.50000000 W

F2 - Processing parameters
SI   65536
SF   500.1300122 MHz
WDW   no
SSB   0
LB   0 Hz
GB   0
PC   1.00

MeO — O

OH

CbzN — Me

SiEt$_3$

4.22
rotamers

13   12   11   10   9   8   7   6   5   4   3   2   1   0   ppm

0.946

5.036

2.050

2.000
4.045
0.991

3.132
9.163
6.130

Figure 4.43. ^{1}H NMR (500 MHz, CDCl$_3$) of compound **4.22**.

178.483
177.688
171.557
168.696

155.621
155.161

136.937
136.588
128.717
128.611
128.603
128.413
128.170

93.098
92.636

67.376

51.638
49.226
41.515
41.279

32.813

18.729

7.919
2.784

Current Data Parameters
NAME   ED_1_034_analytical
EXPNO   1
PROCNO   1

F2 - Acquisition Parameters
Date_   20170127
Time   10.27 h
INSTRUM   av500
PROBHD   Z119248_0002 (
PULPROG   zgpg30
TD   65536
SOLVENT   CDCl3
NS   947
DS   2
SWH   31250.000 Hz
FIDRES   0.953674 Hz
AQ   1.0485760 sec
RG   204.54
DW   16.000 usec
DE   18.00 usec
TE   298.0 K
D1   2.00000000 sec
D11   0.03000000 sec
TD0   1
SFO1   125.7722511 MHz
NUC1   13C
P1   9.63 usec
PLW1   23.00000000 W
SFO2   500.1330008 MHz
NUC2   1H
CPDPRG[2   waltz16
PCPD2   80.00 usec
PLW2   13.50000000 W
PLW12   0.21094000 W
PLW13   0.13500001 W

F2 - Processing parameters
SI   131072
SF   125.7577726 MHz
WDW   no
SSB   0
LB   0 Hz
GB   0
PC   1.40

230 220 210 200 190 180 170 160 150 140 130 120 110 100 90 80 70 60 50 40 30 20 10   ppm

Figure 4.44. ^{13}C NMR (125 MHz, CDCl$_3$) of compound **4.22**.
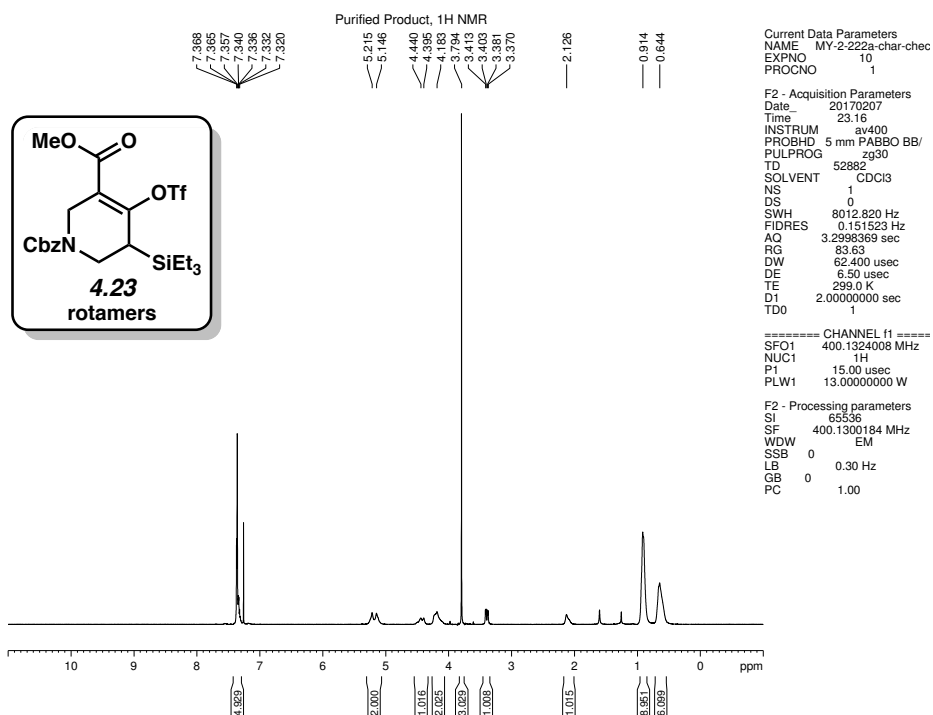
Figure 4.45. ^{1}H NMR (400 MHz, CDCl$_3$) of compound **4.23**.
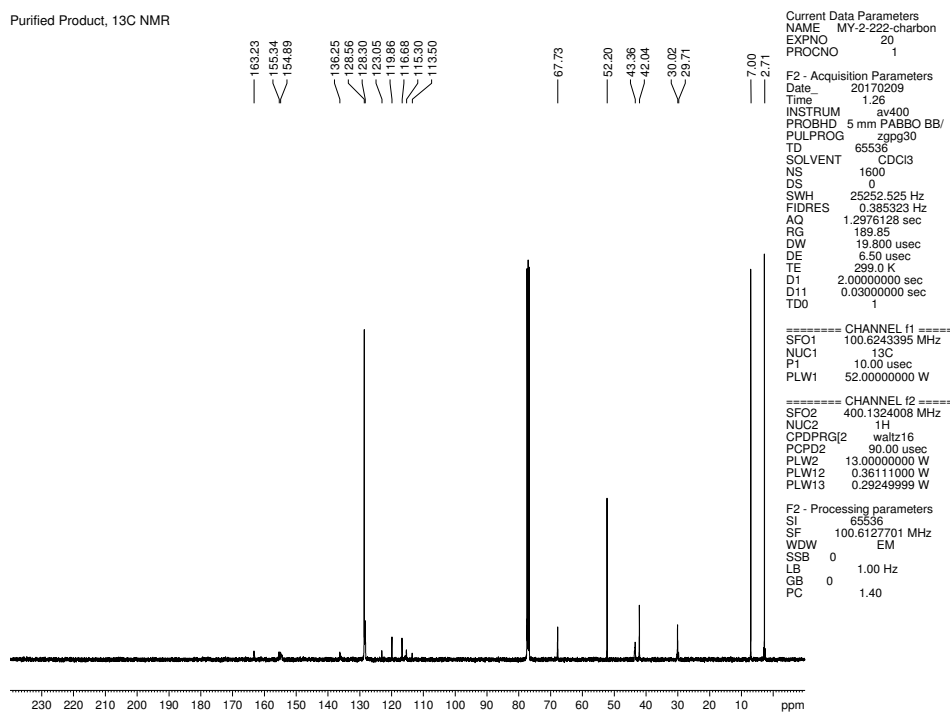
Figure 4.46. ^{13}C NMR (100 MHz, CDCl$_3$) of compound **4.23**.
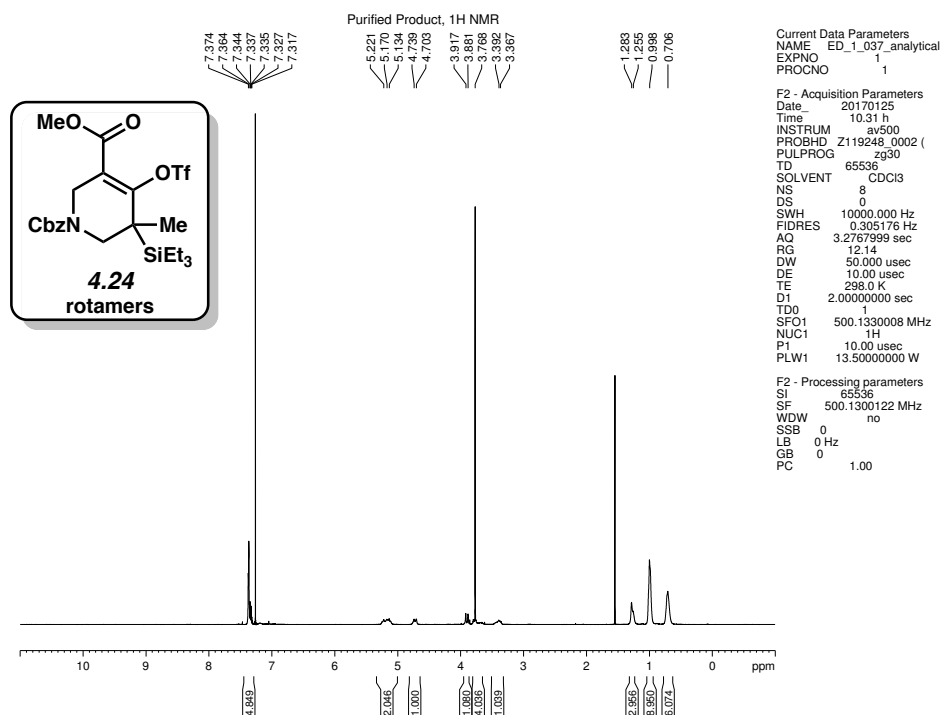
Figure 4.47. ¹H NMR (500 MHz, CDCl₃) of compound **4.24**.
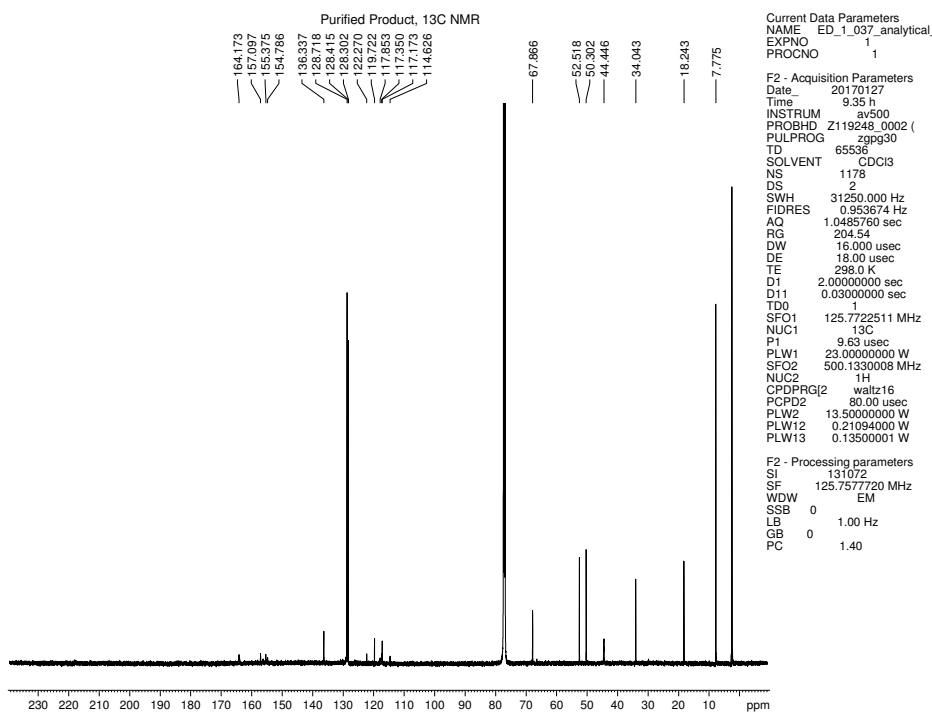
Figure 4.48. ¹³C NMR (125 MHz, CDCl₃) of compound **4.24**.
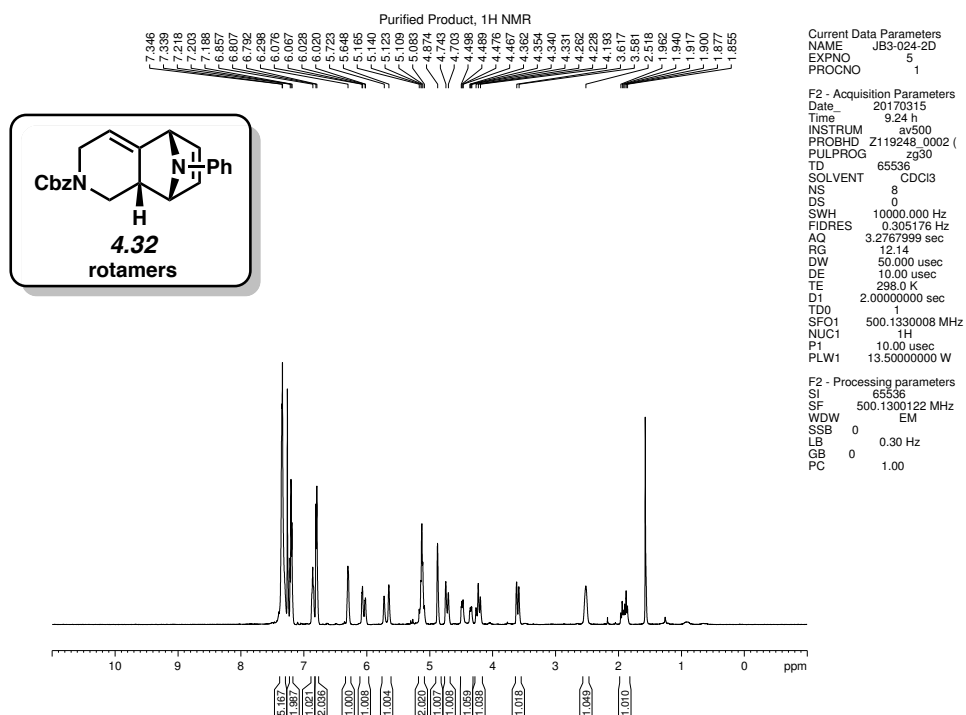
Figure 4.49. ^{1}H NMR (500 MHz, CDCl$_3$) of compound **4.32**.
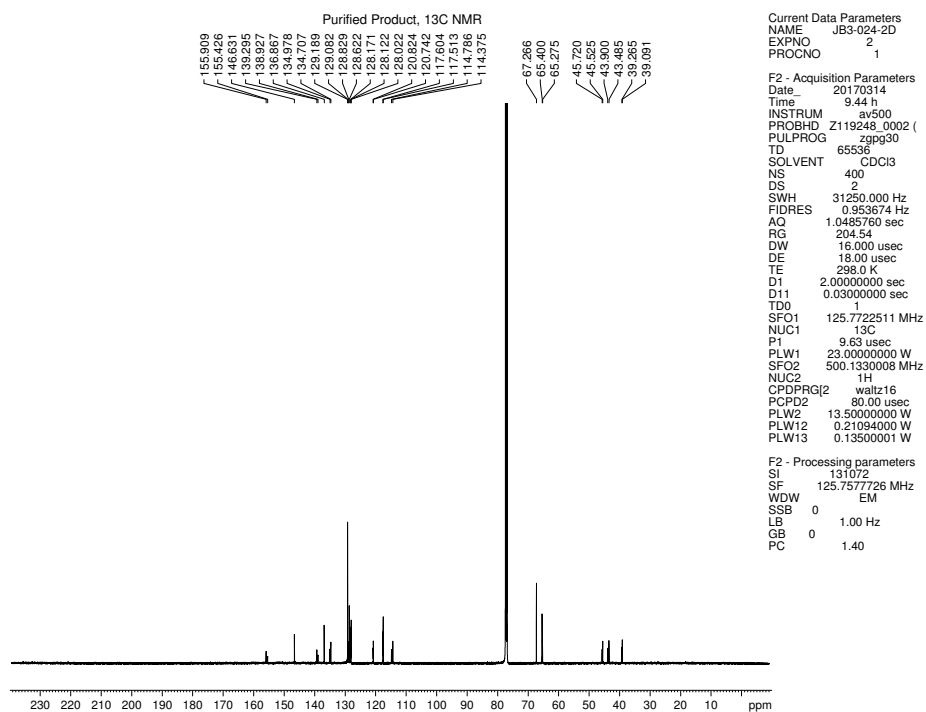
Figure 4.50. ^{13}C NMR (125 MHz, CDCl$_3$) of compound **4.32**.
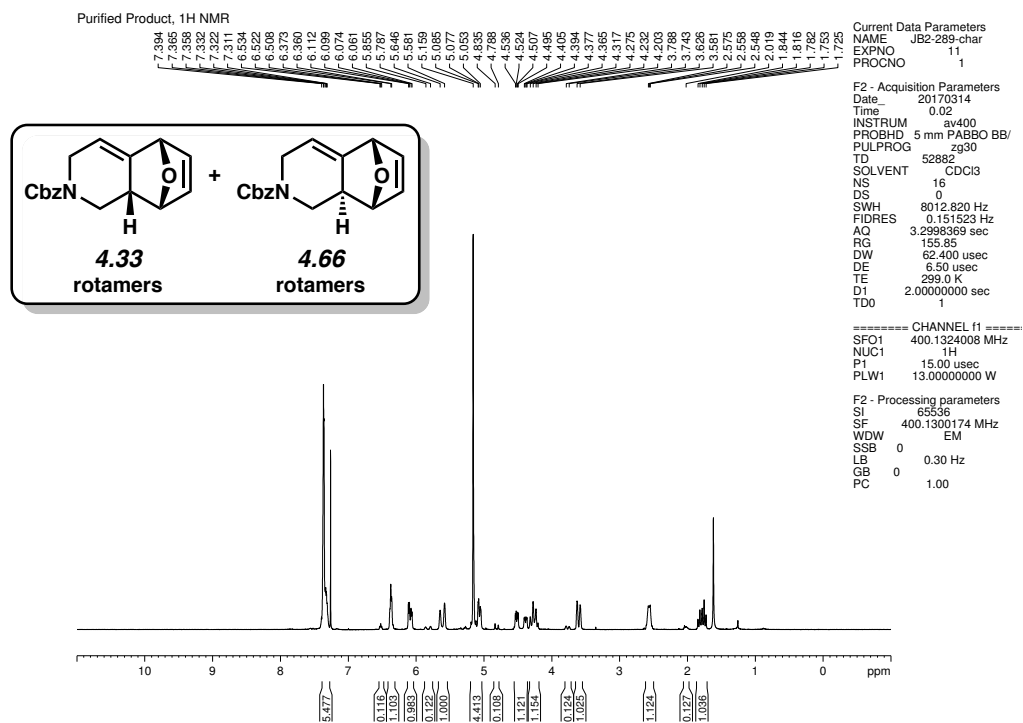
Figure 4.51. ^{1}H NMR (400 MHz, CDCl$_3$) of compounds **4.33** and **4.66**.
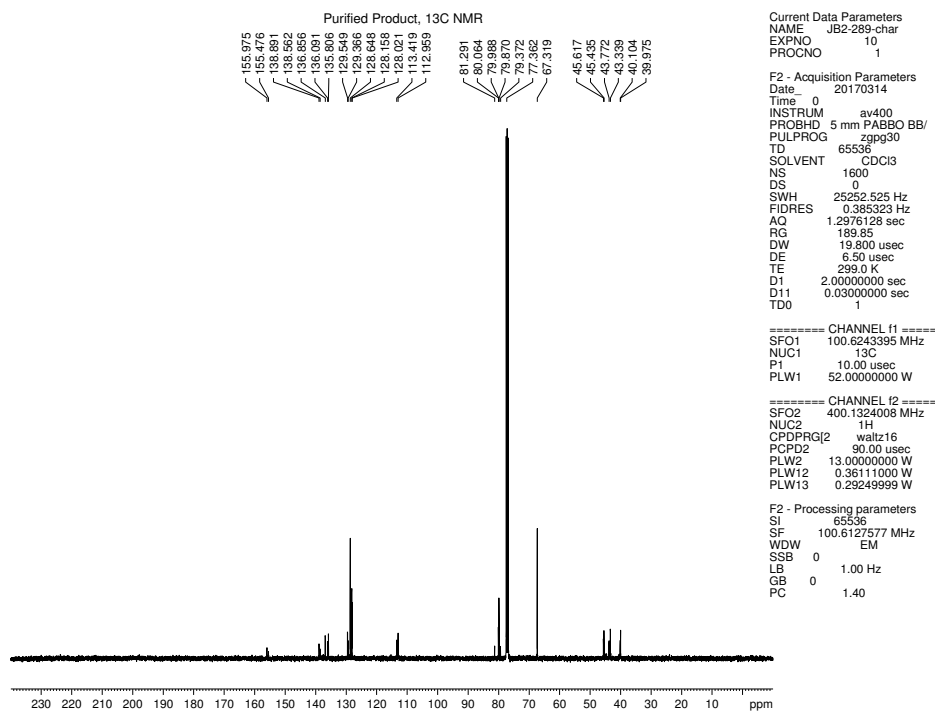
Figure 4.52. ^{13}C NMR (100 MHz, CDCl$_3$) of compounds **4.33** and **4.66**.

7.393
7.372
7.363
7.355
7.335
7.325
7.319
7.312
7.308
7.303
6.137
6.121
6.110
5.902
5.891
5.872
5.861
5.516
5.441
5.437
5.433
5.210
5.185
5.157
5.139
4.462
4.453
4.440
4.430
4.273
4.265
4.249
4.235
4.213
3.625
3.621
3.616
3.593
3.589
3.585
3.580
2.345
2.334
2.329
2.324
1.838
1.792
1.769
1.746
1.644
1.630
1.613
1.555

Me

CbzN

O

H

Me

4.34
rotamers

10 9 8 7 6 5 4 3 2 1 0 ppm

4.621

1.053
1.067
1.069
2.000
0.653
1.374
1.026
1.049
1.013
6.057
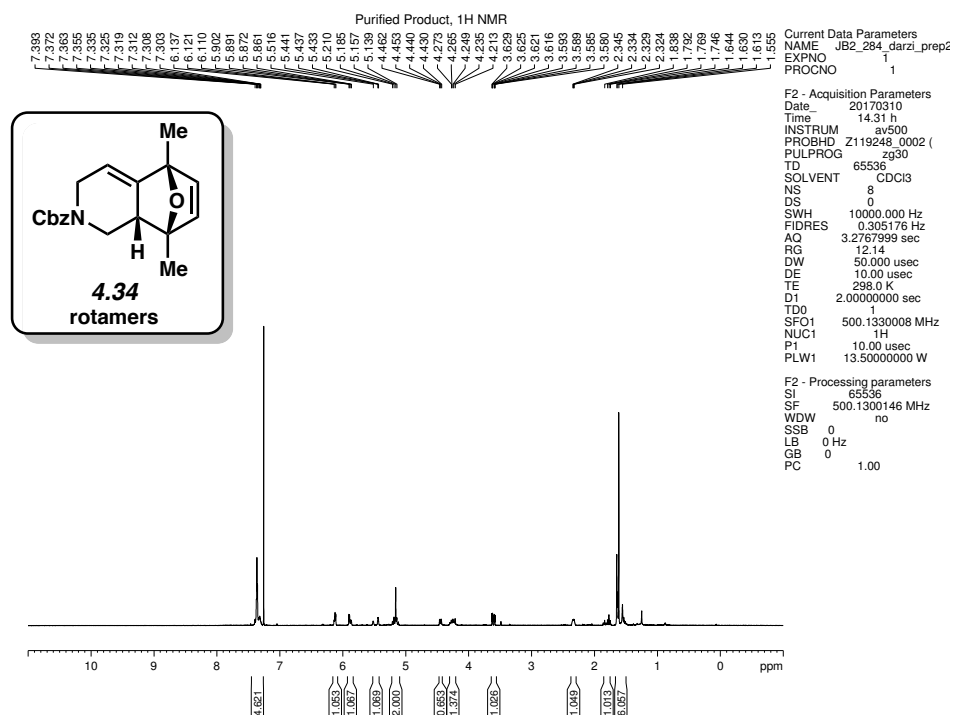
Figure 4.53. ^{1}H NMR (500 MHz, CDCl$_3$) of compound **4.34**.

156.044
155.567
145.290
144.957
139.896
139.631
136.947
136.900
133.554
133.421
128.930
128.715
128.649
128.156
128.034
111.553
111.054
86.953
86.797
67.308
67.244
47.138
46.967
45.257
45.092
43.673
43.202
18.090
15.619
15.012
14.974

230 220 210 200 190 180 170 160 150 140 130 120 110 100 90 80 70 60 50 40 30 20 10 ppm
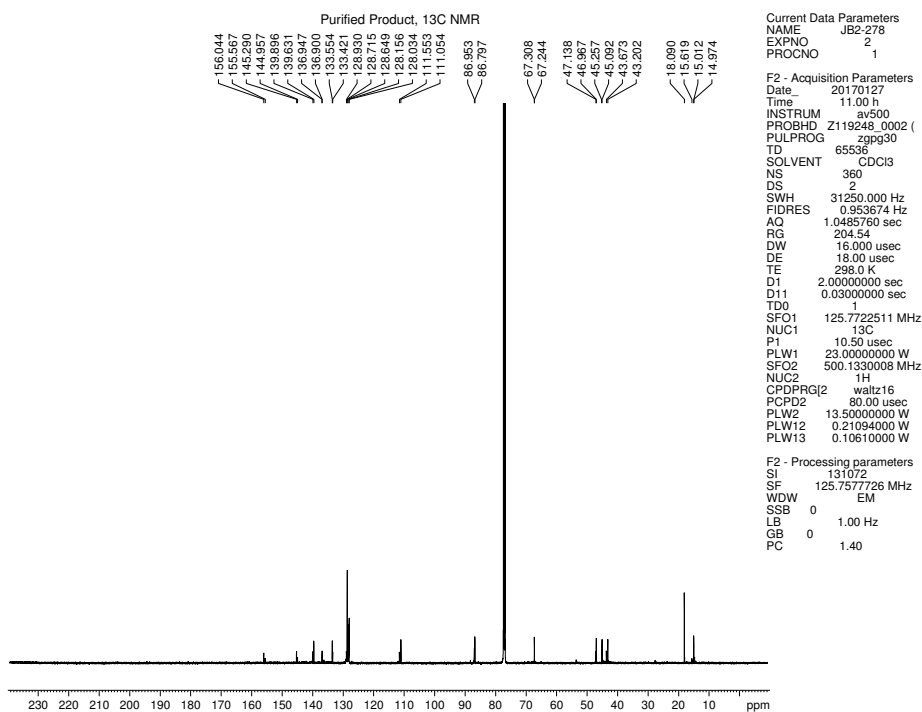
Figure 4.54. ^{13}C NMR (125 MHz, CDCl$_3$) of compound **4.34**.

Purified Product, 1H NMR

7.357, 7.350, 7.330, 7.323, 7.316, 7.214, 7.218, 7.203, 7.201, 7.186, 6.855, 6.846, 6.840, 6.810, 6.794, 6.324, 6.314, 6.053, 6.050, 6.042, 6.038, 6.006, 6.003, 5.995, 5.173, 5.166, 5.154, 5.141, 5.131, 5.126, 5.108, 5.023, 4.728, 4.686, 4.460, 4.451, 4.437, 4.428, 4.157, 4.121, 4.108, 4.073, 3.428, 3.393, 2.504, 2.495, 2.490, 1.911, 1.867, 1.844, 1.820, 1.810, 1.777

4.35
rotamers

CbzN — H — N — Ph — Me

5.036, 2.054, 1.075, 2.011, 0.998, 1.000, 3.035, 1.048, 1.027, 1.052, 0.986, 1.059, 4.078

10 9 8 7 6 5 4 3 2 1 0 ppm

Figure 4.55. ¹H NMR (500 MHz, CDCl₃) of compound **4.35**.

Purified Product, 13C NMR

155.728, 155.323, 146.768, 136.889, 134.265, 133.990, 132.329, 131.895, 129.144, 128.905, 128.702, 128.687, 128.625, 128.311, 128.129, 128.092, 122.335, 121.885, 120.758, 120.677, 117.689, 117.593, 67.249, 67.218, 65.520, 65.368, 63.789, 47.737, 47.306, 45.651, 45.453, 38.880, 38.612, 16.994, 16.969

230 220 210 200 190 180 170 160 150 140 130 120 110 100 90 80 70 60 50 40 30 20 10 ppm
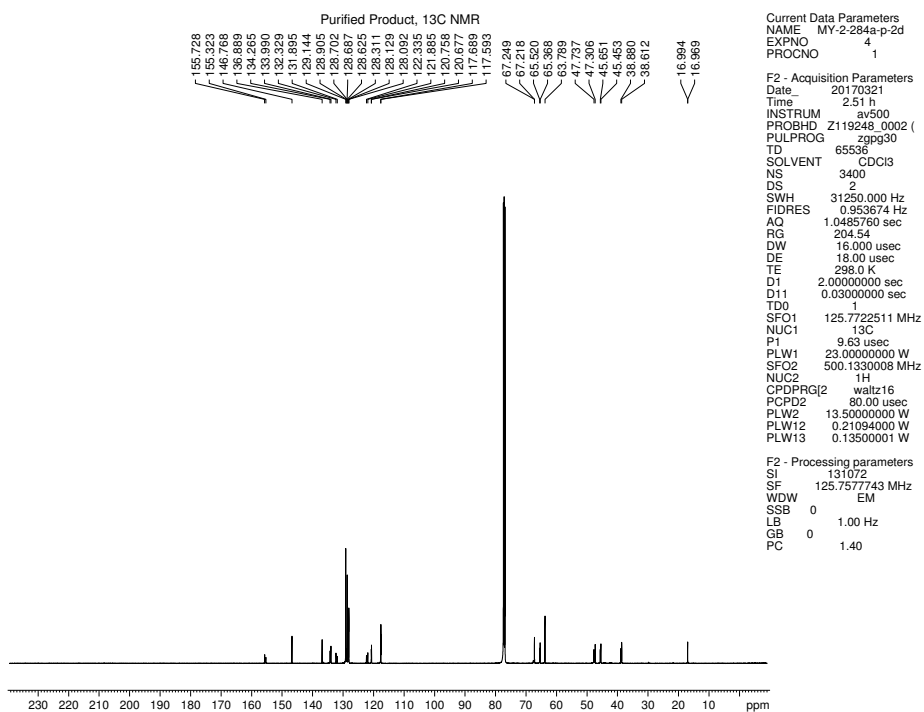
Figure 4.56. ¹³C NMR (125 MHz, CDCl₃) of compound **4.35**.
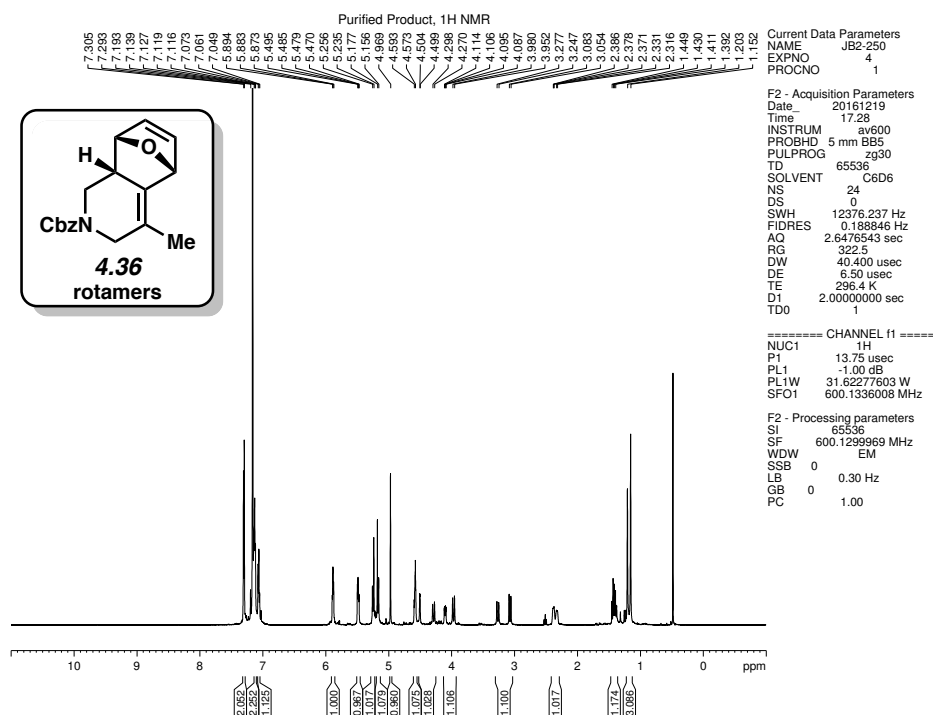
Figure 4.57. ^{1}H NMR (600 MHz, C$_6$D$_6$) of compound **4.36**.
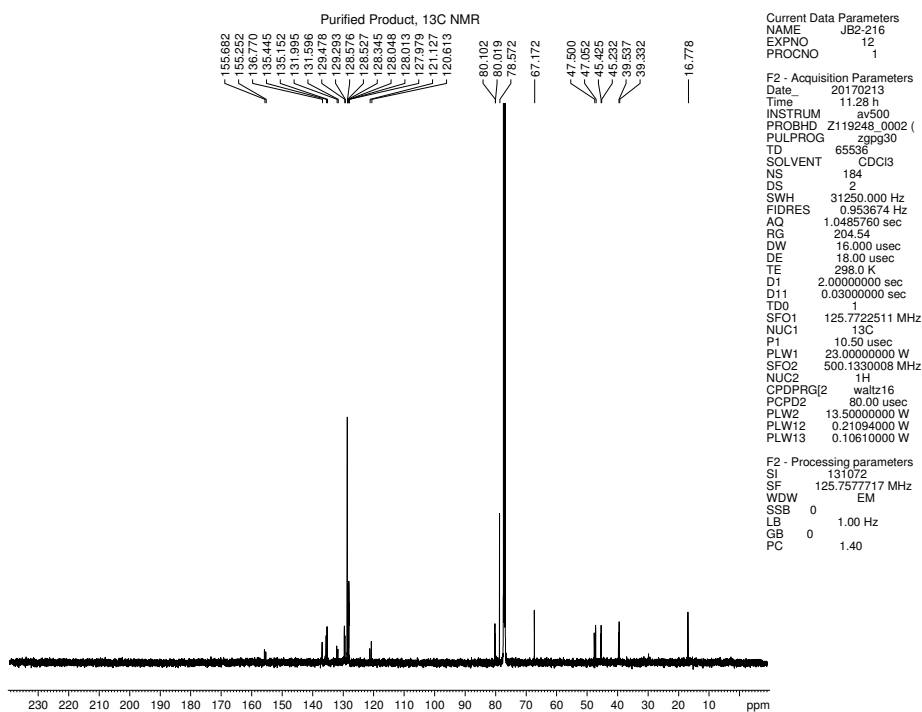
Figure 4.58. ^{13}C NMR (125 MHz, CDCl$_3$) of compound **4.36**.
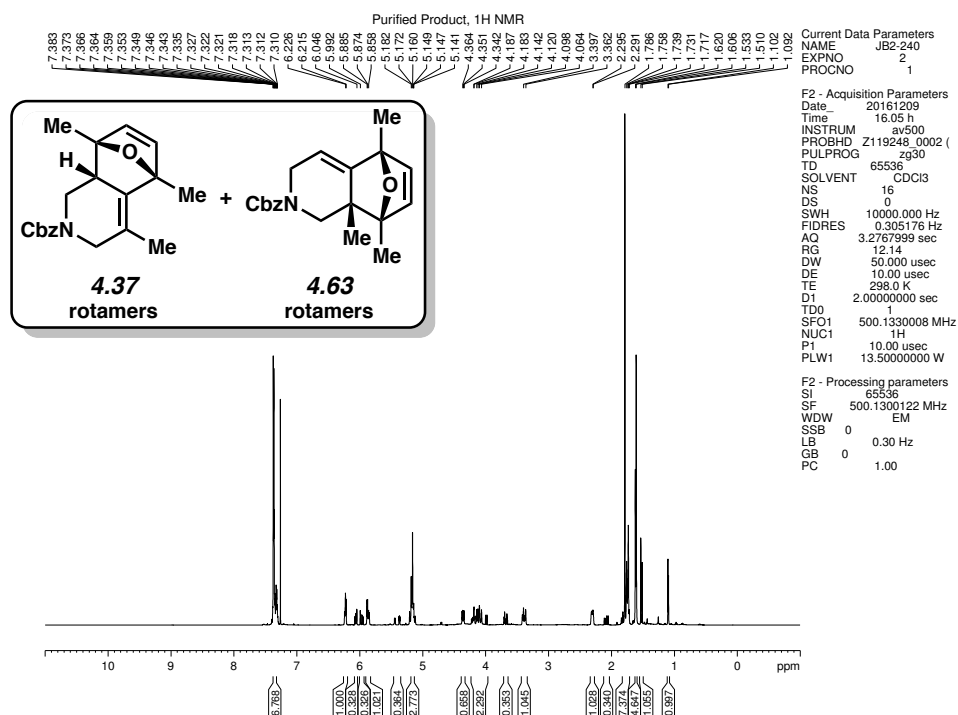
Figure 4.59. ^{1}H NMR (500 MHz, CDCl$_3$) of compounds **4.37** and **4.63**.
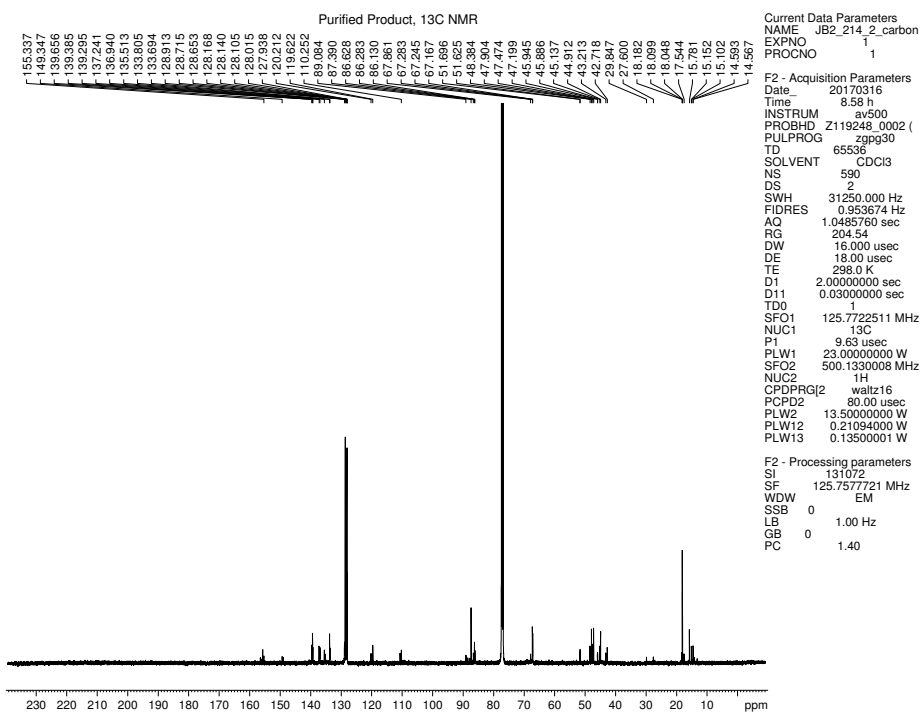
Figure 4.60. ^{13}C NMR (125 MHz, CDCl$_3$) of compounds **4.37** and **4.63**.

7.361
7.350
7.342
7.330
7.320
7.308
7.299
7.291
6.459
6.396
6.204
6.166
5.750
5.746
5.705
5.171
5.146
5.129
5.113
5.092
5.067
4.721
4.656
4.342
4.339
4.314
4.311
4.305
4.278
3.685
3.637
3.624
3.597
3.588
3.561
3.552
3.540
2.024
2.000
1.989
1.965
1.391

MeO₂C

Boc

N

CbzN

4.38
rotamers

10   9   8   7   6   5   4   3   2   1   0   ppm

4.978 | 1.000 0.992 | 1.014 | 4.082 1.012 | 1.015 | 4.067 | 0.961 | 9.011

Figure 4.61. ^{1}H NMR (500 MHz, CDCl$_3$) of compound **4.38**.

171.671
155.719
155.096
154.602
139.877
139.608
138.031
137.758
136.633
136.534
135.978
135.680
131.264
130.961
129.485
129.235
128.519
128.477
128.102
128.002
127.775
116.661
116.355
80.756
67.219
66.291
65.592
63.623
62.927
55.039
54.463
52.654
49.214
48.897
43.757
43.417
28.157

230 220 210 200 190 180 170 160 150 140 130 120 110 100 90 80 70 60 50 40 30 20 10   ppm
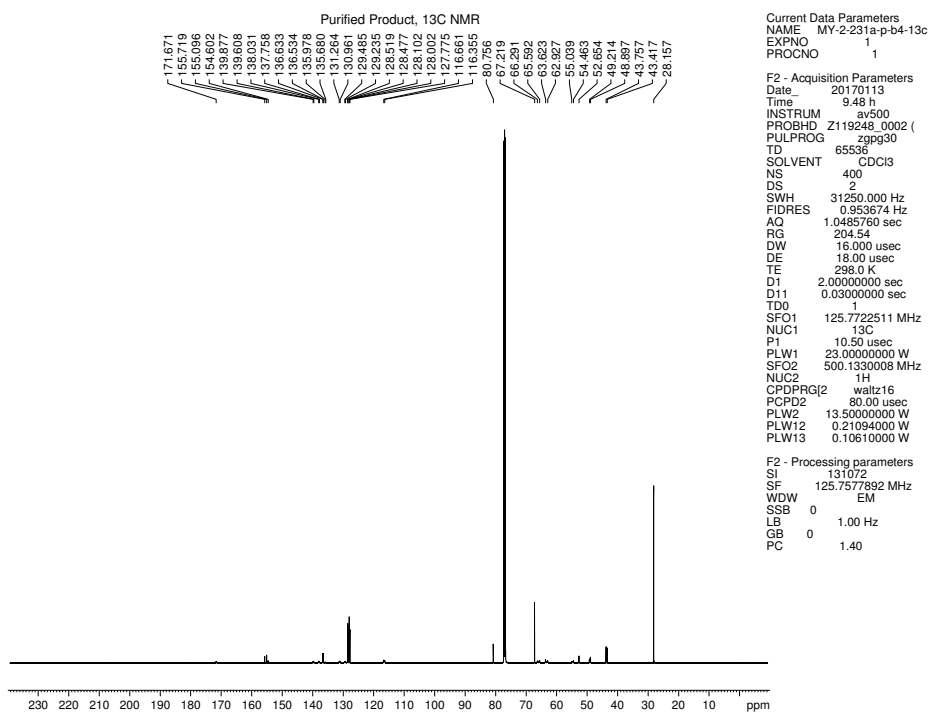
Figure 4.62. ^{13}C NMR (125 MHz, CDCl$_3$) of compound **4.38**.

Figure 4.63. ^{1}H NMR (500 MHz, CDCl$_3$) of compound **4.39**.

Figure 4.64. ^{13}C NMR (100 MHz, CDCl$_3$) of compound **4.39**.

254
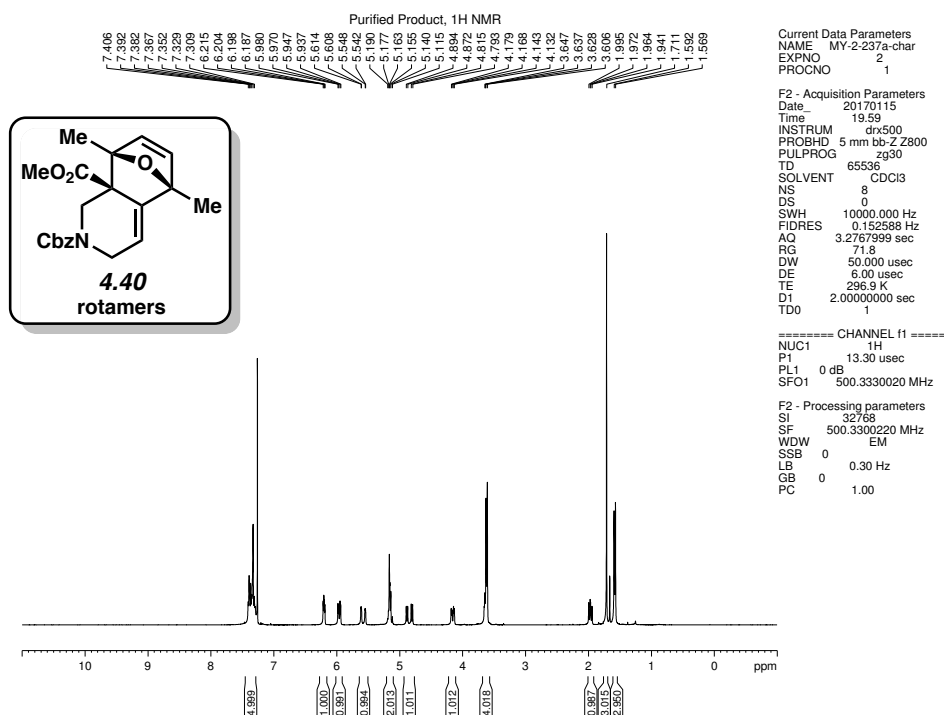
Figure 4.65. ^{1}H NMR (500 MHz, CDCl$_3$) of compound **4.40**.
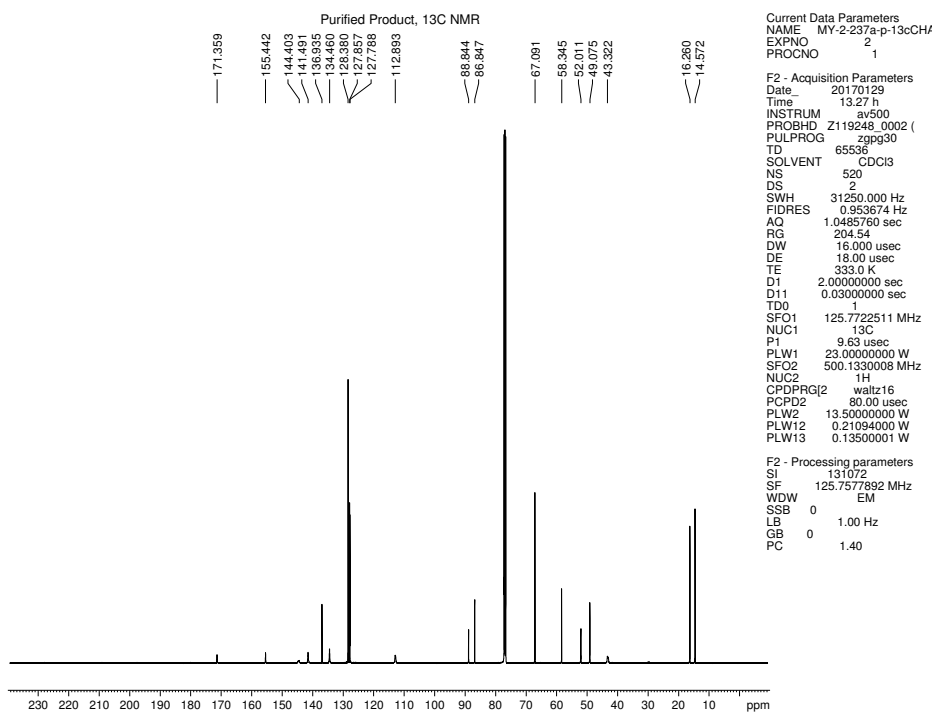
Figure 4.66. ^{13}C NMR (125 MHz, CDCl$_3$, 60 °C) of compound **4.40**.

7.368 7.363 7.360 7.327 7.319 7.310 7.195 7.180 7.167 7.164 6.878 6.864 6.849 6.816 6.801 6.411 6.400 6.391 6.389 6.381 6.378 5.963 5.956 5.953 5.924 5.917 5.914 5.180 5.153 5.139 5.123 5.117 5.068 4.692 4.668 4.615 4.590 4.321 4.285 4.279 4.243 3.610 3.509 3.462 3.437 3.428 3.402 2.095 2.070 2.054 2.030 1.835 1.814
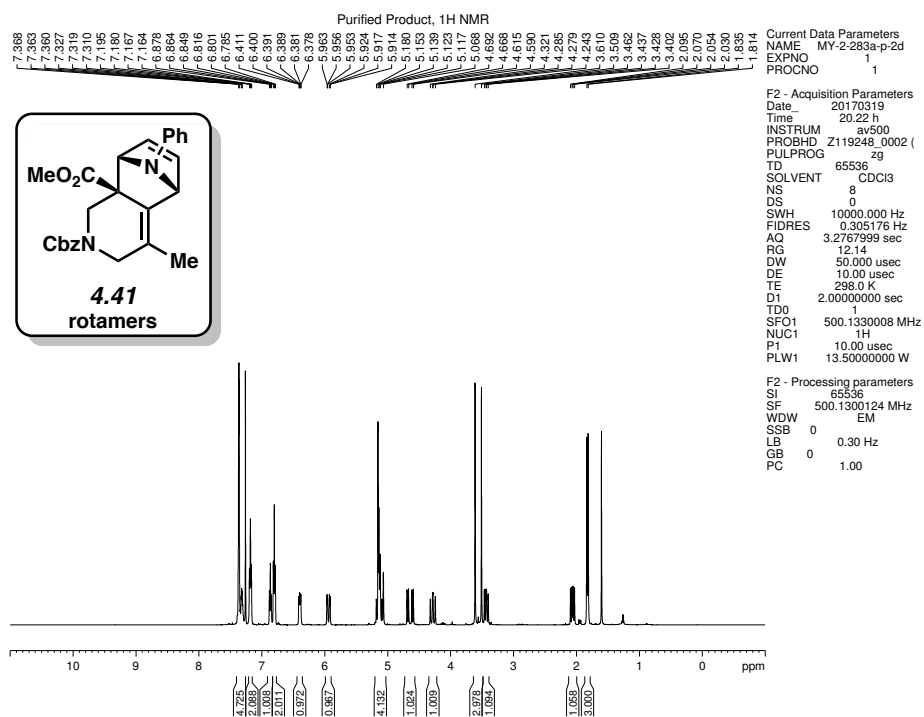
Figure 4.67. ^{1}H NMR (500 MHz, CDCl$_3$) of compound **4.41**.

173.340 172.760 155.805 155.182 146.074 146.045 137.008 136.888 136.734 136.691 130.837 130.506 128.641 128.615 128.190 128.117 128.106 127.999 127.607 127.902 123.881 123.533 121.145 118.700 118.671 67.305 67.280 64.570 54.631 54.783 52.705 52.638 48.965 48.585 47.827 47.497 17.147 17.124
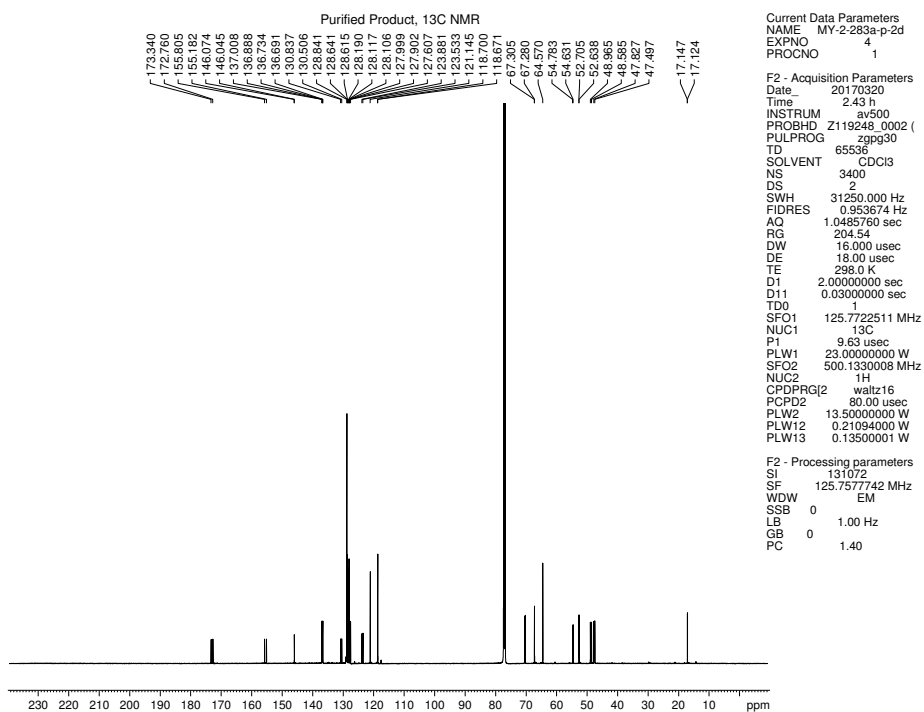
Figure 4.68. ^{13}C NMR (125 MHz, CDCl$_3$) of compound **4.41**.
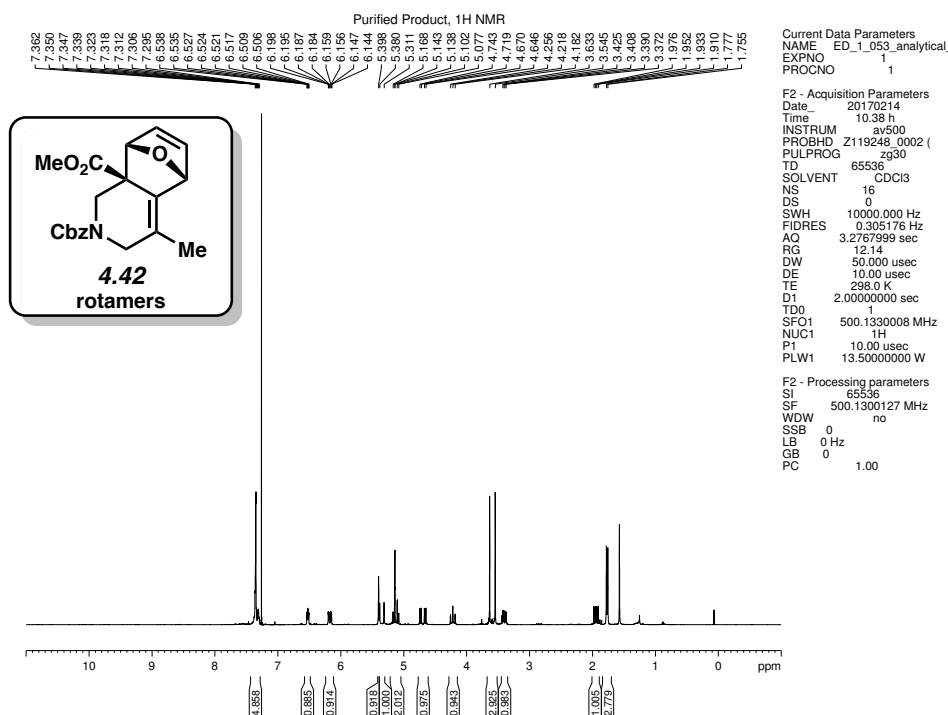
Figure 4.69. ^{1}H NMR (500 MHz, CDCl$_3$) of compound **4.42**.
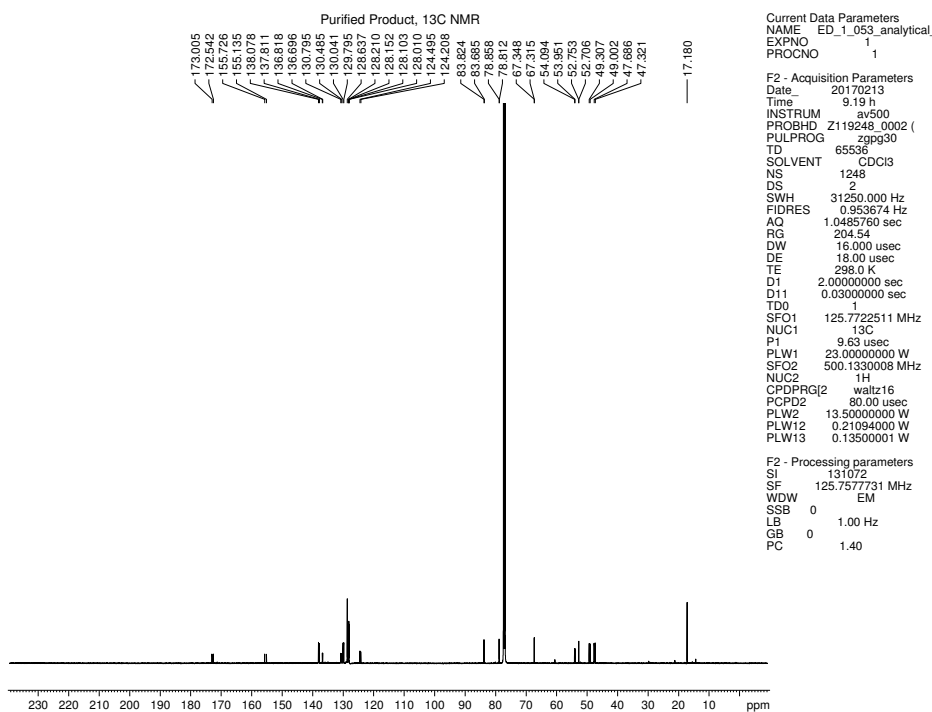
Figure 4.70. ^{13}C NMR (125 MHz, CDCl$_3$) of compound **4.42**.
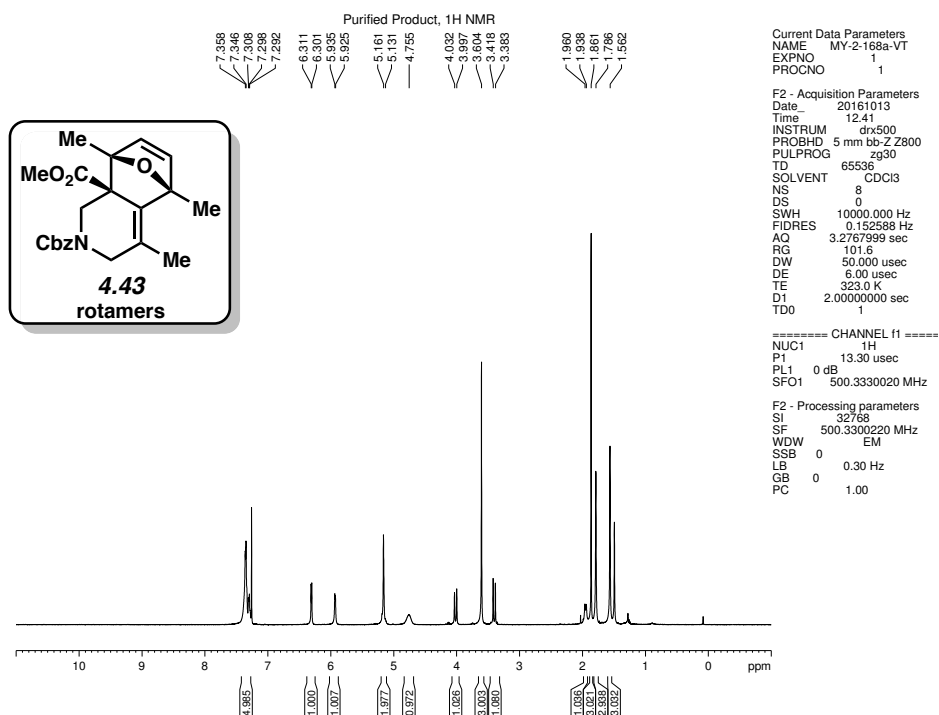
Figure 4.71. ^{1}H NMR (500 MHz, CDCl$_3$) of compound **4.43**.
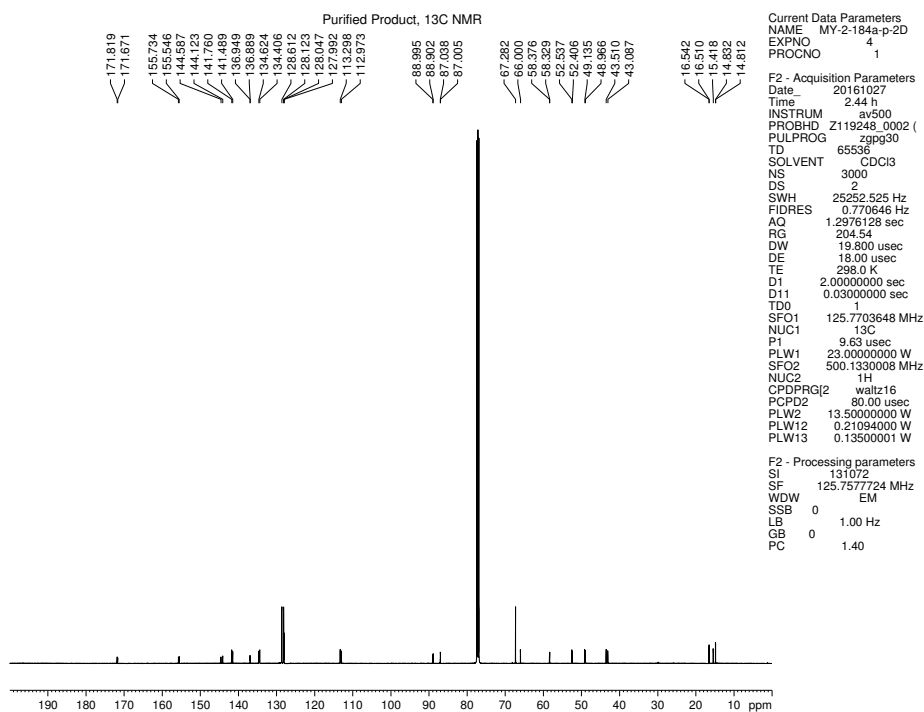
Figure 4.72. ^{13}C NMR (125 MHz, CDCl$_3$) of compound **4.43**.

7.362
7.353
7.338
7.323
7.313
7.306
7.303

5.456
5.397
5.150
4.712
4.700
4.691
4.606
4.596
4.583
4.572
4.399
4.363
4.289

3.727
3.715
3.618
3.571
3.533

2.581
2.559
2.539
2.517
2.497

1.282
1.269
1.101

Current Data Parameters
NAME   MY-3-065a-p-check
EXPNO   1
PROCNO   1

F2 - Acquisition Parameters
Date_   20171211
Time   13.20 h
INSTRUM   av500
PROBHD   Z119248_0002 (
PULPROG   zg30
TD   65536
SOLVENT   CDCl3
NS   8
DS   0
SWH   10000.000 Hz
FIDRES   0.305176 Hz
AQ   3.2767999 sec
RG   12.14
DW   50.000 usec
DE   10.00 usec
TE   298.0 K
D1   2.00000000 sec
TD0   1
SFO1   500.1330008 MHz
NUC1   1H
P1   10.00 usec
PLW1   13.50000000 W

F2 - Processing parameters
SI   65536
SF   500.1300127 MHz
WDW   EM
SSB   0
LB   0.30 Hz
GB   0
PC   1.00

4.970

1.000
1.981

1.083
2.099

1.007
1.035

0.996

3.058
9.113

Figure 4.73. ^{1}H NMR (500 MHz, CDCl$_3$) of compound **4.46**.

155.57
155.33
146.40
146.09

136.47
128.54
128.11
127.97

112.51
111.90

70.05
67.39

58.67
57.01

44.28
43.92
43.20
42.87

26.30
25.81
23.91

Current Data Parameters
NAME   MY-3-065a-p-charbon
EXPNO   10
PROCNO   1

F2 - Acquisition Parameters
Date_   20171129
Time   21.40
INSTRUM   av400
PROBHD   5 mm PABBO BB/
PULPROG   zgpg30
TD   65536
SOLVENT   CDCl3
NS   528
DS   0
SWH   25252.525 Hz
FIDRES   0.385323 Hz
AQ   1.2976128 sec
RG   189.85
DW   19.800 usec
DE   6.50 usec
TE   299.2 K
D1   2.00000000 sec
D11   0.03000000 sec
TD0   1

======== CHANNEL f1 =====
SFO1   100.6243395 MHz
NUC1   13C
P1   10.00 usec
PLW1   52.00000000 W

======== CHANNEL f2 =====
SFO2   400.1324008 MHz
NUC2   1H
CPDPRG[2   waltz16
PCPD2   90.00 usec
PLW2   13.00000000 W
PLW12   0.36111000 W
PLW13   0.29249999 W

F2 - Processing parameters
SI   65536
SF   100.6127701 MHz
WDW   EM
SSB   0
LB   1.00 Hz
GB   0
PC   1.40

Figure 4.74. ^{13}C NMR (100 MHz, CDCl$_3$) of compound **4.46**.
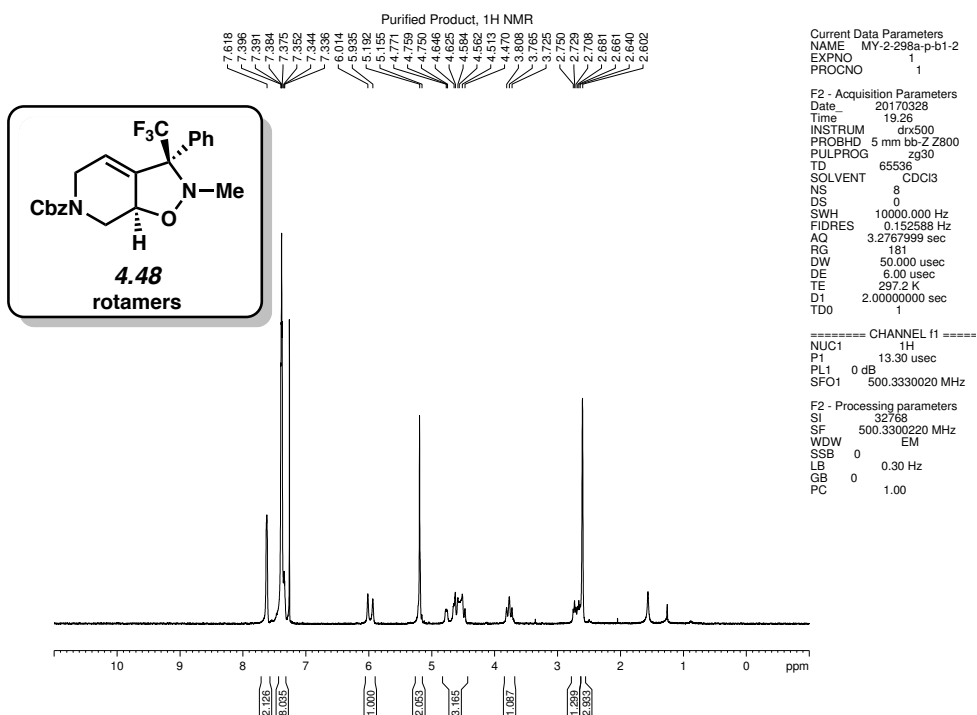
Figure 4.75. ^{1}H NMR (500 MHz, CDCl₃) of compound **4.48**.
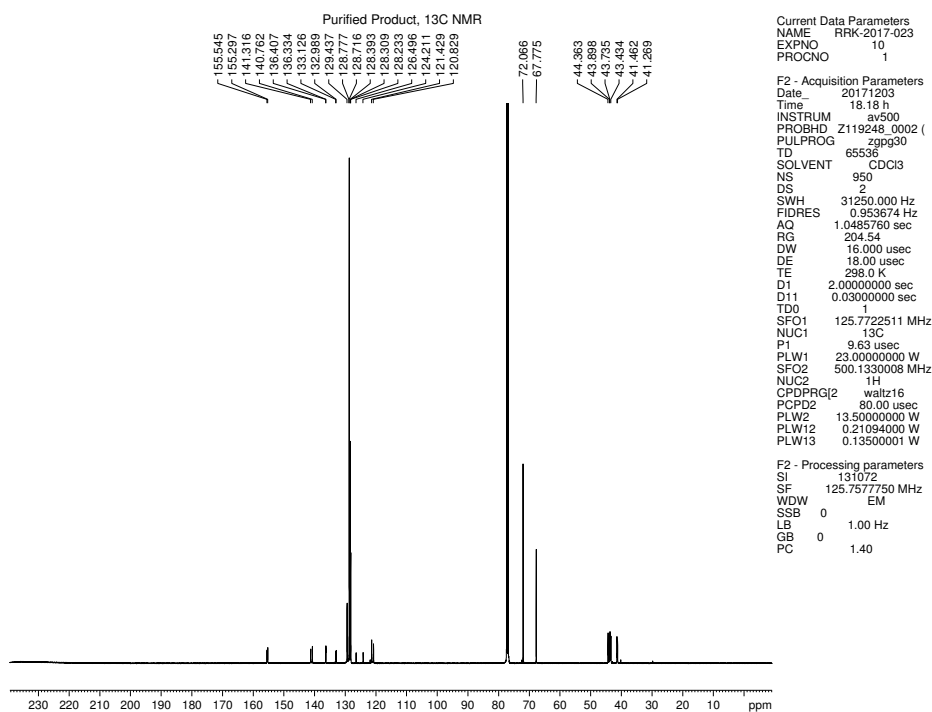
Figure 4.76. ^{13}C NMR (125 MHz, CDCl₃) of compound **4.48**.
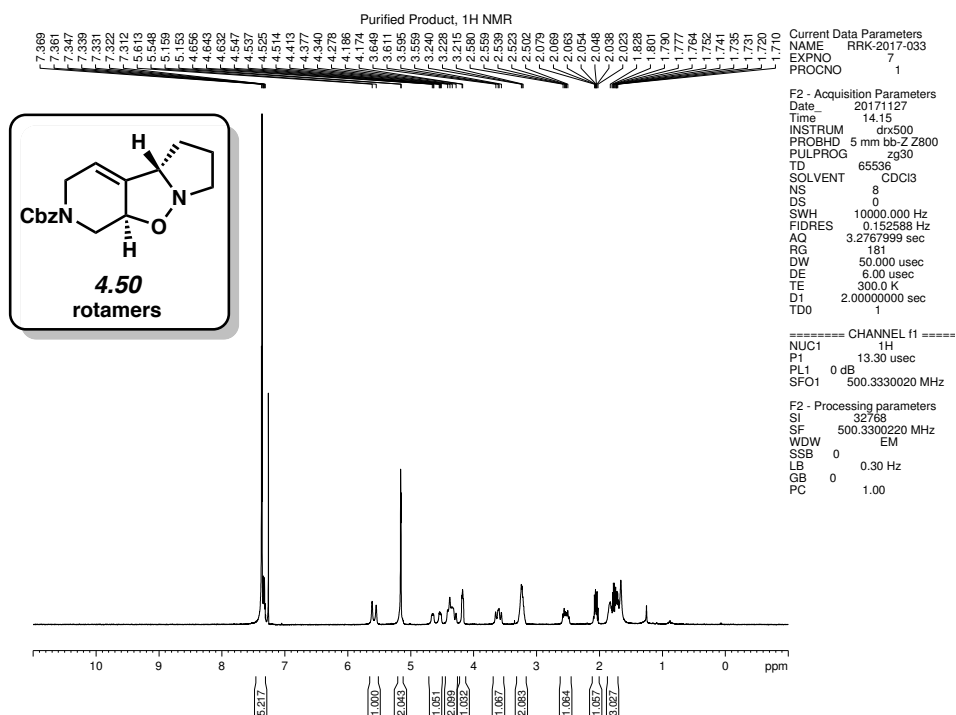
Figure 4.77. ^{1}H NMR (500 MHz, CDCl$_3$) of compound **4.50**.
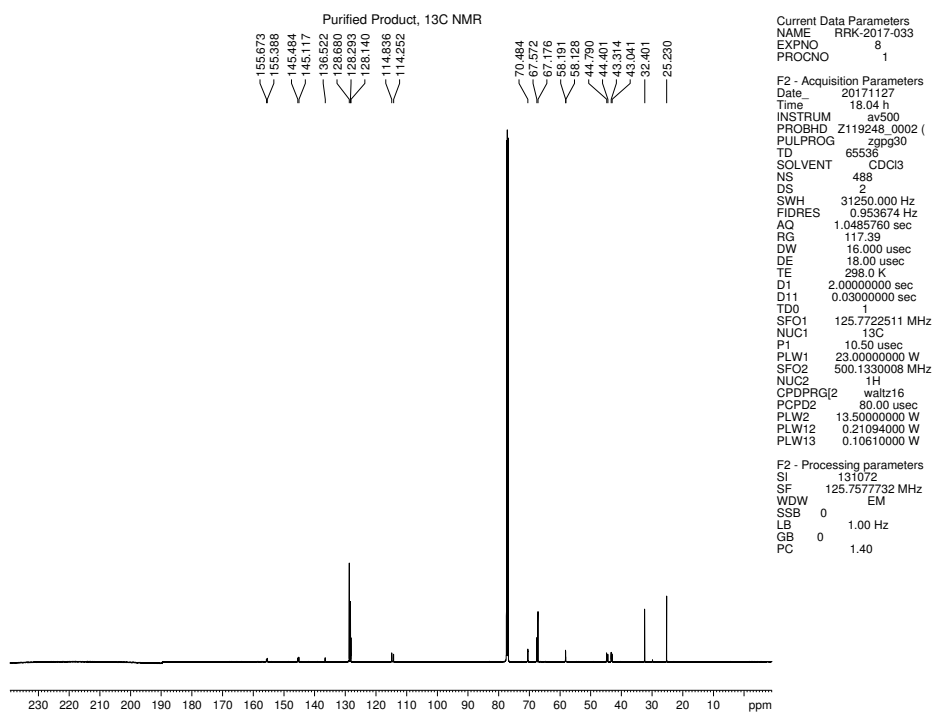
Figure 4.78. ^{13}C NMR (125 MHz, CDCl$_3$) of compound **4.50**.
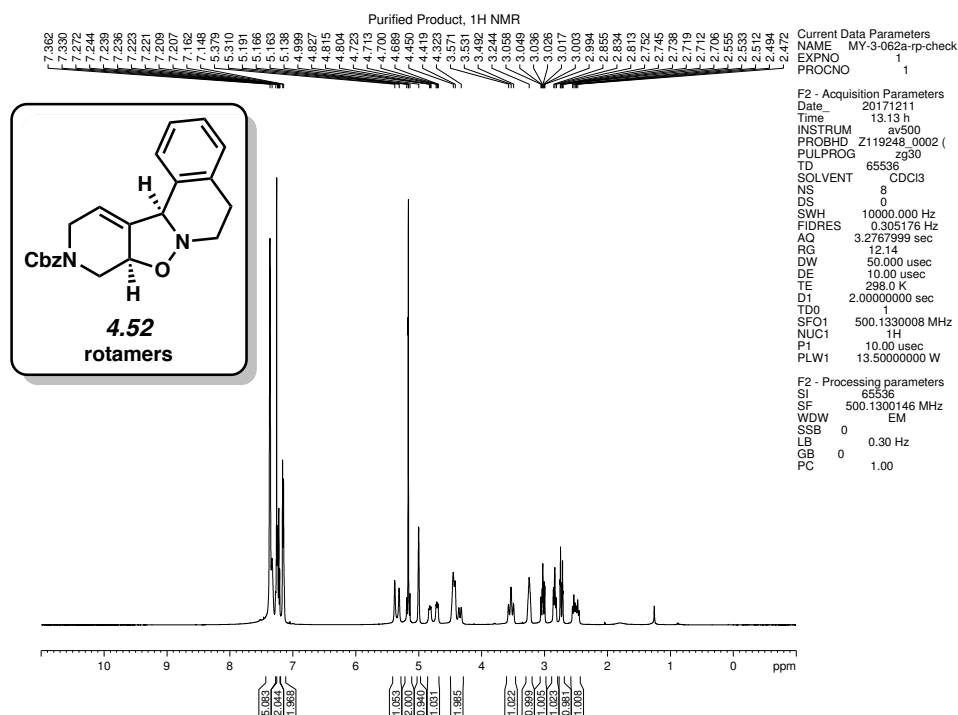
Figure 4.79. ^{1}H NMR (500 MHz, CDCl$_3$) of compound **4.52**.
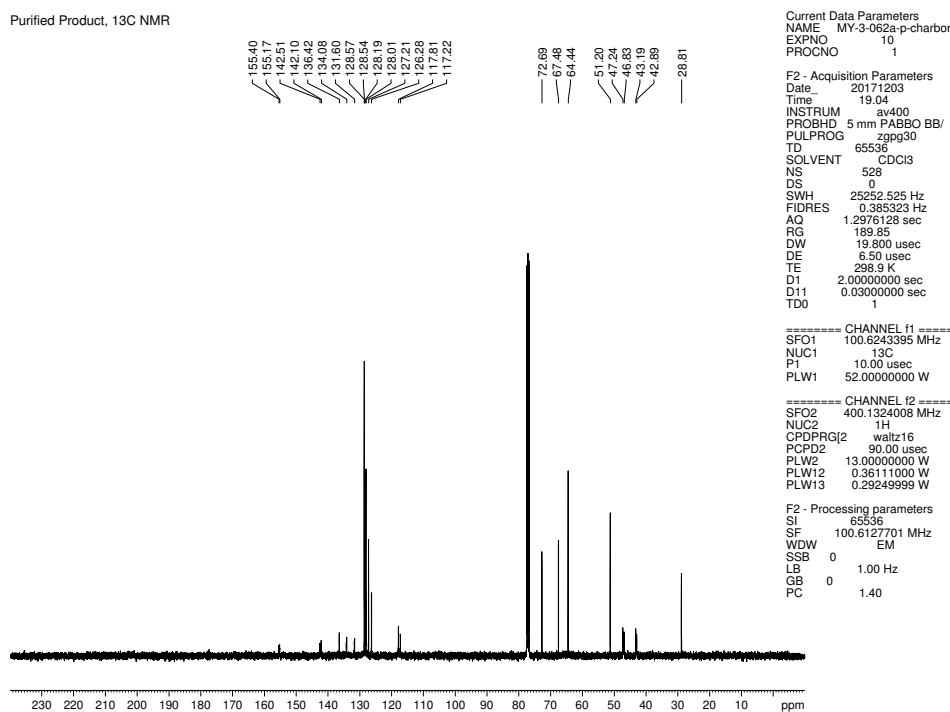
Figure 4.80. ^{13}C NMR (100 MHz, CDCl$_3$) of compound **4.52**.
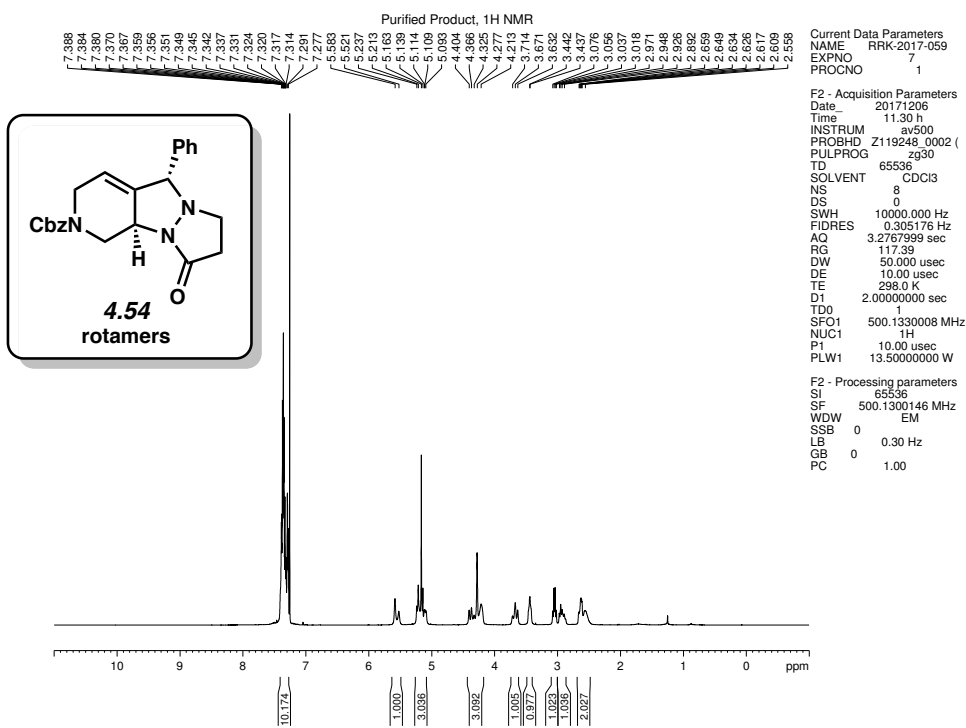
Figure 4.81. ^{1}H NMR (500 MHz, CDCl$_3$) of compound **4.54**.
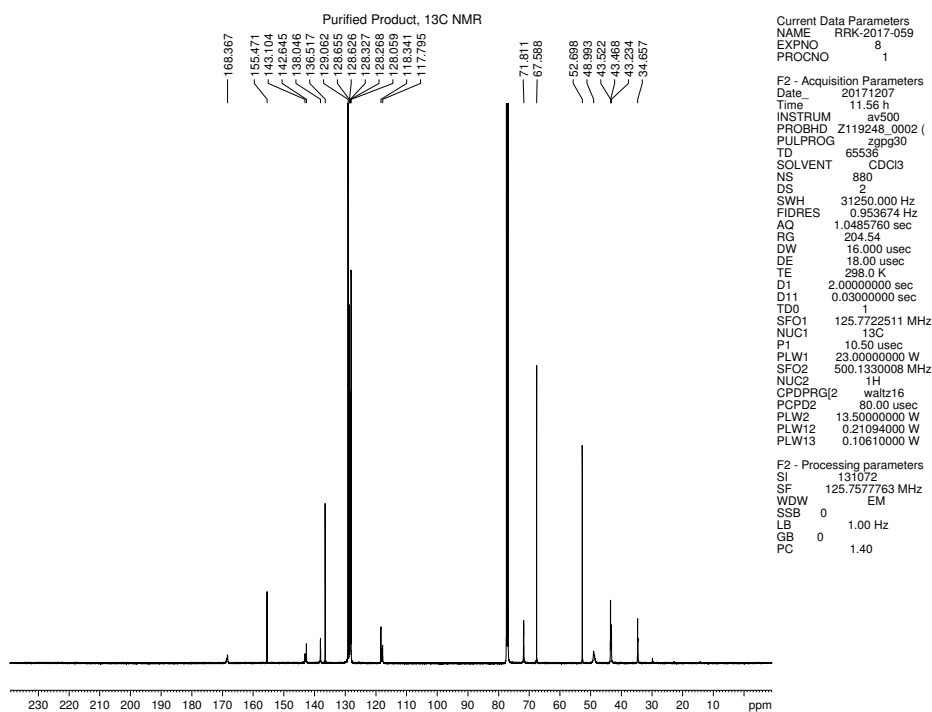
Figure 4.82. ^{13}C NMR (125 MHz, CDCl$_3$) of compound **4.54**.
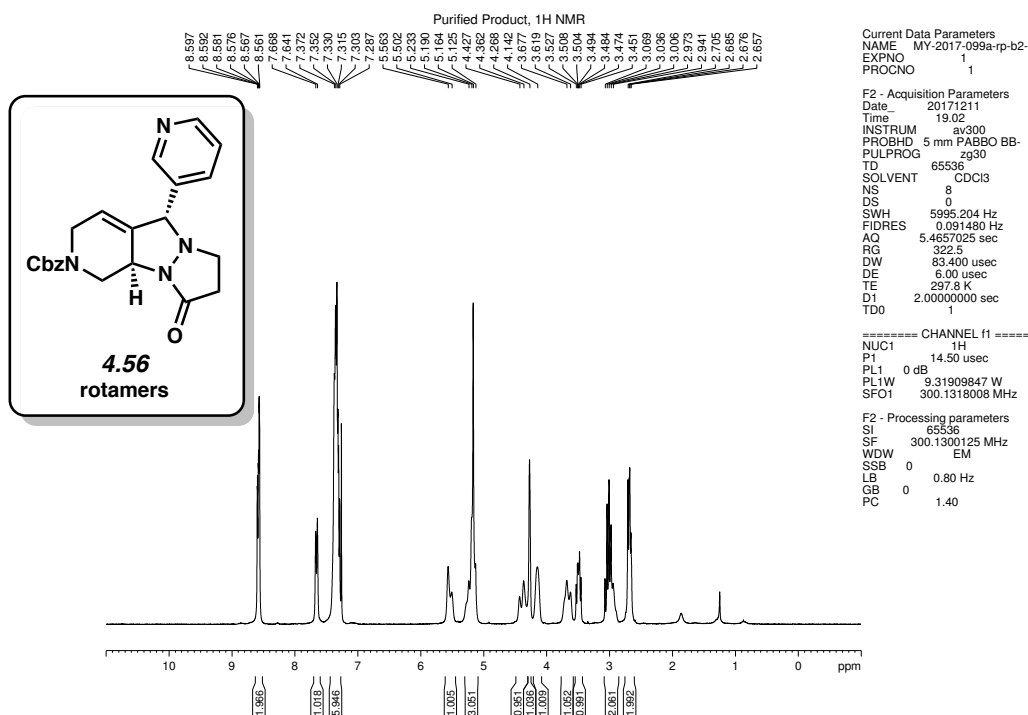
Figure 4.83. ¹H NMR (300 MHz, CDCl₃) of compound **4.56**.
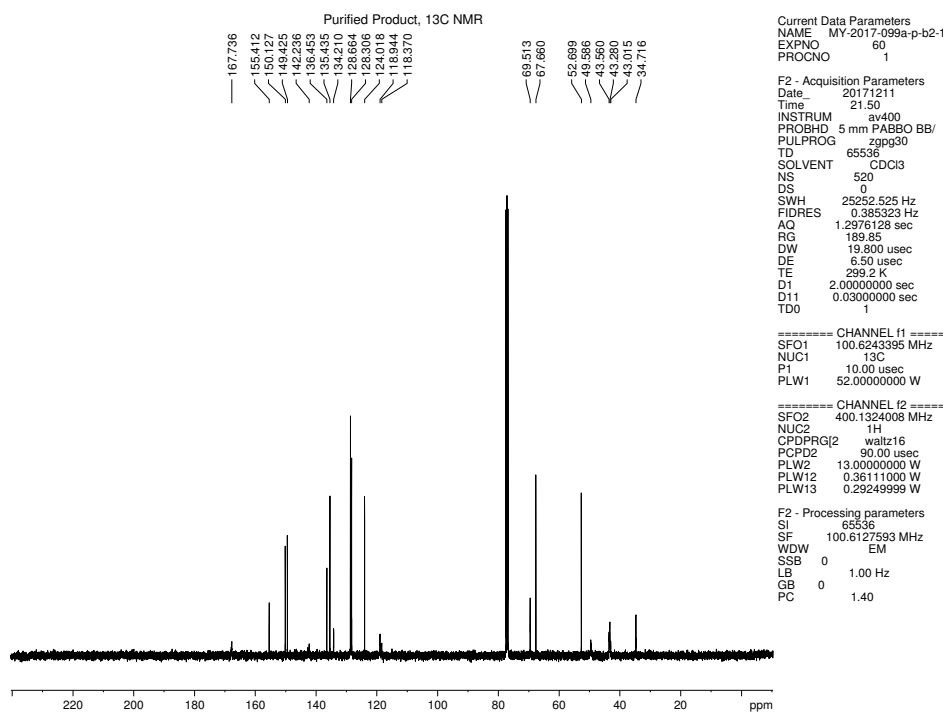
Figure 4.84. ¹³C NMR (100 MHz, CDCl₃) of compound **4.56**.
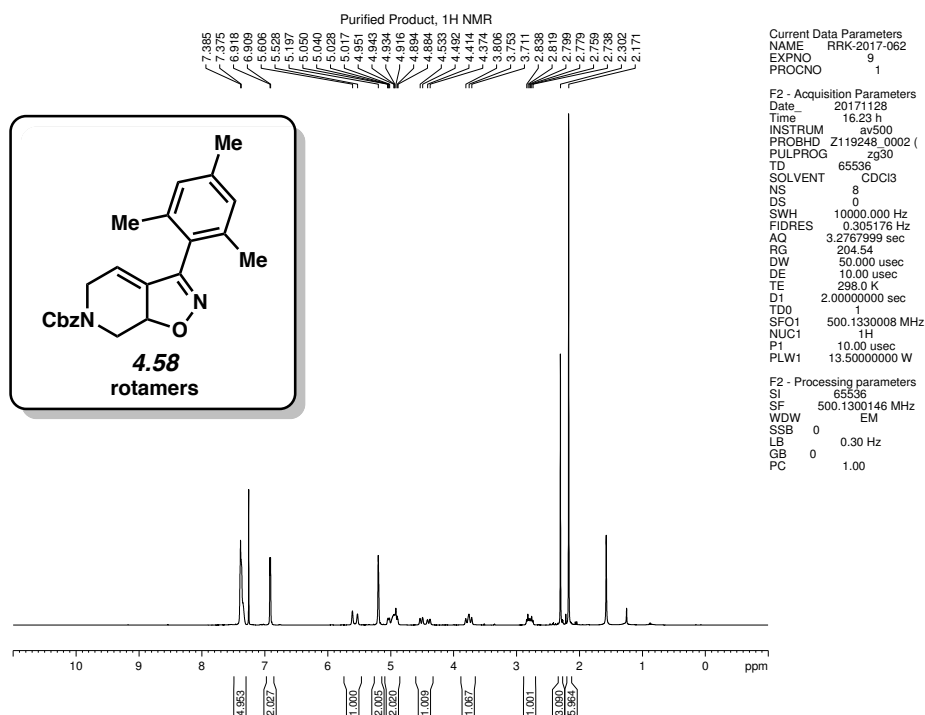
Figure 4.85. ^{1}H NMR (500 MHz, CDCl₃) of compound **4.58**.

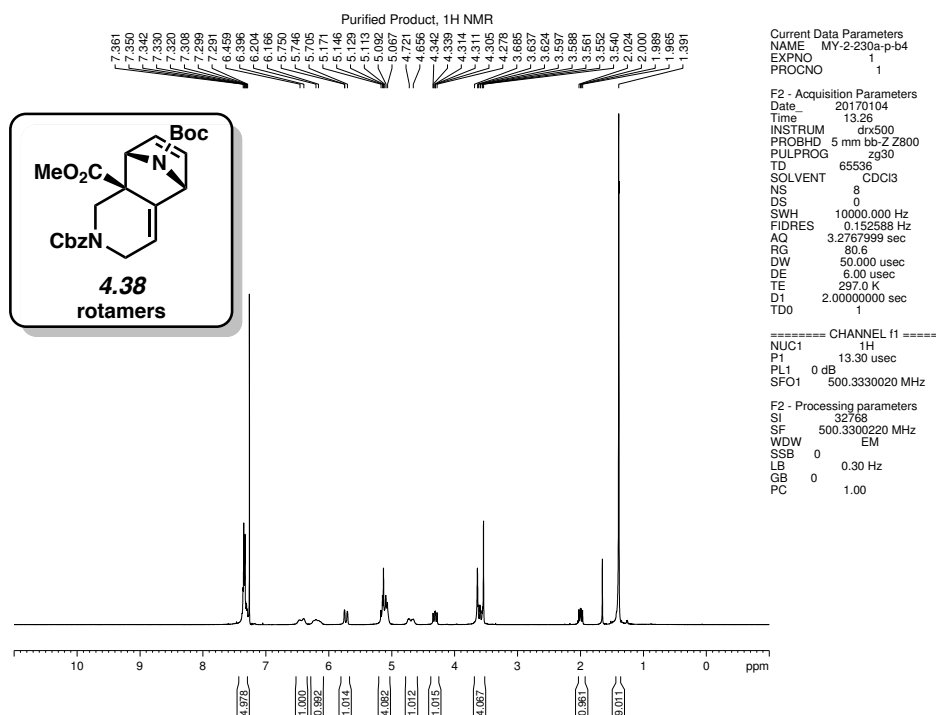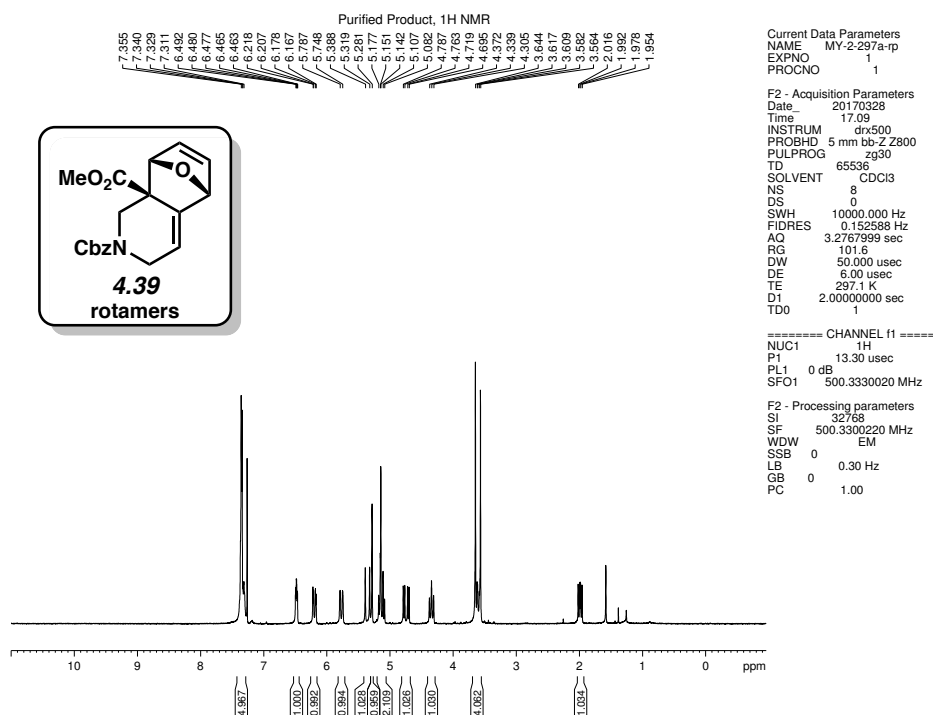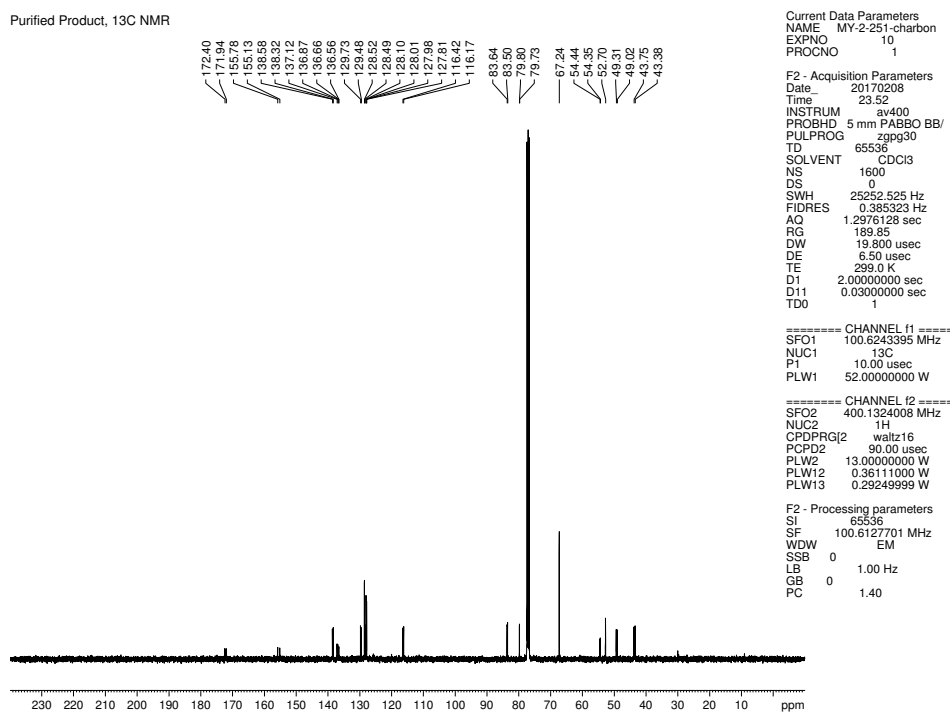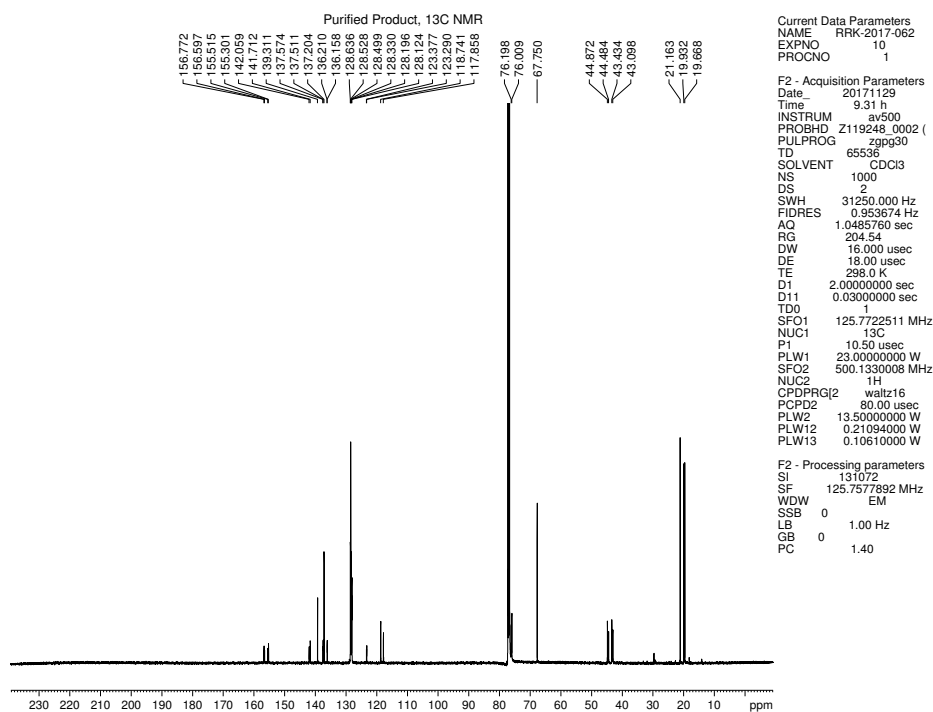*Figure 4.86.* ^{13}C NMR (125 MHz, CDCl₃) of compound **4.58**.
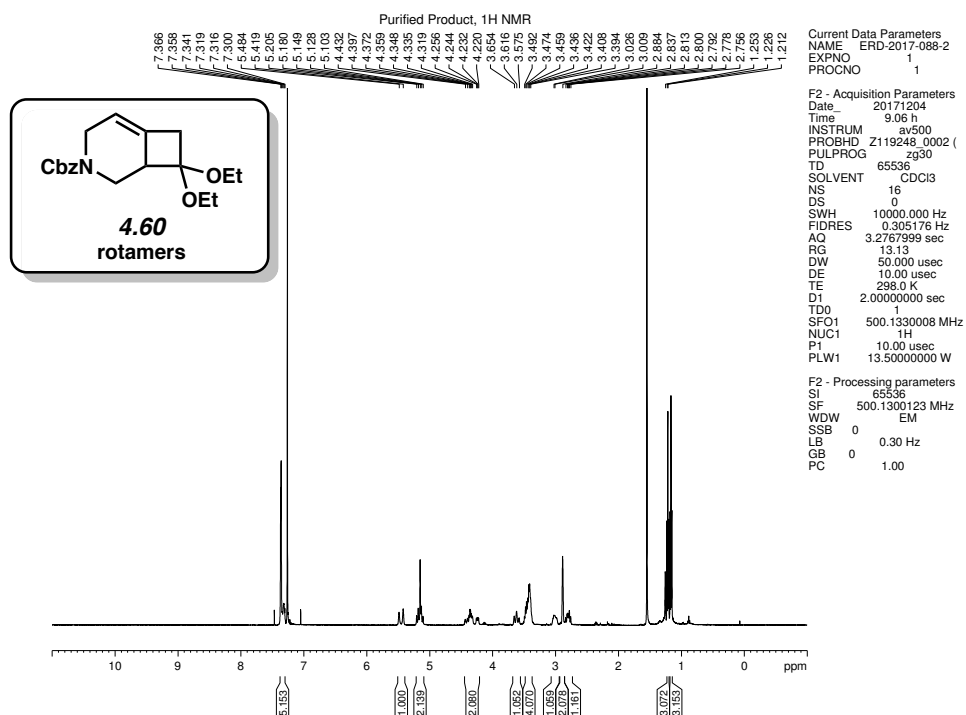
Figure 4.87. ^{1}H NMR (500 MHz, CDCl$_3$) of compound **4.60**.
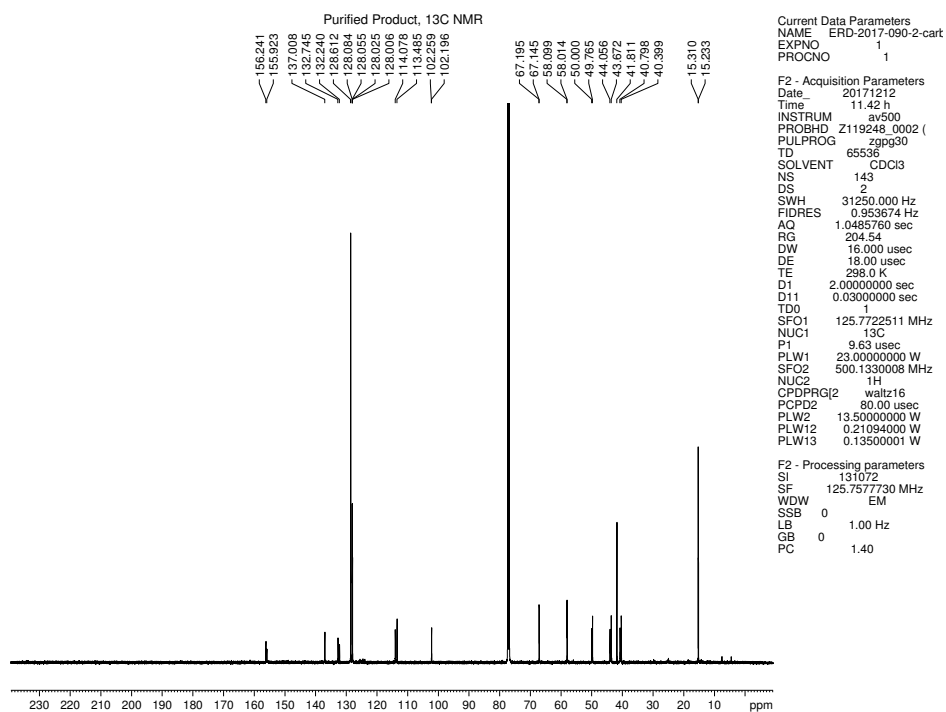
Figure 4.88. ^{13}C NMR (125 MHz, CDCl$_3$) of compound **4.60**.

4.11 Notes and References

(1) Heaney, H. *Chem. Rev.* **1962**, *62*, 81–97.

(2) Tadross, P. M.; Stoltz, B. M. *Chem. Rev.* **2012**, *112*, 3550–3557.

(3) Dubrovskiy, A. V.; Markina, N. A.; Larock, R. C. *Org. Biomol. Chem.* **2013**, *11*, 191–218.

(4) Goetz, A. E.; Shah, T. K.; Garg, N. K. *Chem. Commun.* **2015**, *51*, 34–45.

(5) Wittig, G.; Fritze, P. *Angew. Chem., Int. Ed.* **1966**, *5*, 846.

(6) Angus, R. O.; Schmidt, M. W.; Johnson, R. P. *J. Am. Chem. Soc.* **1985**, *107*, 532–537.

(7) Engels, B.; Schöneboom, J. C.; Münster, A. F.; Groetsch, S.; Christl, M. *J. Am. Chem. Soc.* **2002**, *124*, 287–297.

(8) Hänninen, M. M.; Peuronen, A.; Tuononen, H. M. *Chem. Eur. J.* **2009**, *15*, 7287–7291.

(9) Daoust, K. J.; Hernandez, S. M.; Konrad, K. M.; Mackie, I. D.; Winstanley, J.; Johnson, R. P. *J. Org. Chem.* **2009**, *71*, 5708–5714.

(10) Johnson, R. P. *Chem. Rev.* **1989**, *89*, 1111–1124.

(11) Wentrup, C.; Gross, G.; Maquestiau, A.; Flammang, R. *Angew. Chem., Int. Ed. Engl.* **1983**, *22*, 542–543.

(12) Nendel, M.; Tolbert, L. M.; Herring, L. E.; Islam, M. N.; Houk, K. N. *J. Org. Chem.* **1999**, *64*, 976−983.

(13) Moore, W. R.; Moser, W. R. *J. Am. Chem. Soc.* **1970**, *92*, 5469–5474.

(14) Quintana, I.; Peña, D.; Pérez, D.; Guitián, E. *Eur. J. Org. Chem.* **2009**, 5519−5524.

(15) Christl, M.; Fischer, H.; Arnone, M.; Engels, B. *Chem. Eur. J.* **2009**, *15*, 11266–11272.

(16) Bottini, A. T.; Hilton, L. L.; Plott, J. *Tetrahedron* **1975**, *31*, 1997−2001.

(17) Bottini, A. T.; Corson, F. P.; Fitzgerald, R.; Frost, K. A., II *Tetrahedron* **1972**, *28*, 4883−4904.

(18) Barber, J. S.; Styduhar, E. D.; Pham, H. V.; McMahon, T. C.; Houk, K. N.; Garg, N. K. *J. Am. Chem. Soc.* **2016**, *138*, 2512–2515.

(19) Lofstrand, V. A.; West, F. G. *Chem. Eur. J.* **2016**, *22*, 10763–10767.

(20) Uyegaki, M.; Ito, S.; Sugihara, Y.; Murata, I. *Tetrahedron Lett.* **1976**, *49*, 4473–4476.

(21) Schreck, M.; Christl, M. *Angew. Chem. Int. Ed.* **1987**, *26*, 690–692.

(22) Christl, M.; Braun, M. *Chem. Ber.* **1989**, *122*, 1939–1946.

(23) Ruzziconi, R.; Naruse, Y.; Schlosser, M. *Tetrahedron* **1991**, *47*, 4603–4610.

(24) Jamart-Grégoire, B.; Mercier-Girardot, S.; Ianelli, S.; Nardelli, M.; Caubère, P. *Tetrahedron* **1995**, *51*, 1973–1984.

(25) Christl, M.; Braun, M.; Wolz, E.; Wagner, W. *Chem. Ber.* **1994**, *127*, 1137–1142.

(26) Drinkuth, S.; Groetsch, S.; Peters, E.; Peters, K.; Christl, M. *Eur. J. Org. Chem.* **2001**, 2665–2670.

(27) Elliott, R. L.; Nicholson, N. H.; Peaker, F. E.; Takle, A. K.; Richardson, C. M.; Tyler, J. W.; White, J.; Pearson, M. J.; Eggleston, D. S.; Haltiwanger, R. C. *J. Org. Chem.* **1997**, *62*, 4998–5016.

(28) Elliott, R. L.; Takle, A. K.; Tyler, J. W.; White, J. *J. Org. Chem.* **1993**, *58*, 6954–6955.

(29) Elliott, R. L.; Nicholson, N. H.; Peaker, F. E.; Takle, A. K.; Tyler, J. W.; White, J. *J. Org. Chem.* **1994**, *59*, 1606–1607.

(30) Musch, P. W.; Scheidel, D.; Engles, B. *J. Phys. Chem. A* **2003**, *107*, 11223–11230.

(31) Emanuel, C. J.; Shelvin, P. B. *J. Am. Chem. Soc.* **1994**, *116*, 5991–5992.

(32) Pan. W.; Shelvin, P. B. *J. Am. Chem. Soc.* **1997**, *119*, 5091–5094.

(33) Pan, W.; Balci, M.; Shelvin, P. B. *J. Am. Chem. Soc.* **1997**, *119*, 5035–5036.

(34) Wang, J.; Sheridan, R. S. *Org. Lett.* **2007**, *9*, 3177–3180.

(35) Schöneboom, J. C.; Groetsch, S.; Christl, M.; Engles, B. *Chem. Eur. J.* **2003**, *9*, 4641–4649.

(36) Christl, M.; Drinkuth, S. *Eur. J. Org. Chem.* **1998**, *2*, 237–241.

(37) Vitaku, E.; Smith, D. T.; Njardarson, J. T. *J. Med. Chem.* **2014**, *57*, 10257–10274.

(38) McMahon, T. C.; Medina, J. M.; Yang, Y.-F.; Simmons, B. J.; Houk, K. N.; Garg, N. K. *J. Am. Chem. Soc.* **2015**, *137*, 4082–4085.

(39) Brinck, T.; Linder, M. *Phys. Chem. Chem. Phys.* **2013**, *15*, 5108–5114.

(40) Houk, K. N.; Bickelhaupt, F. M. *Angew. Chem., Int. Ed.* **2017**, *56*, 10070–10086.

(41) Christl, M.; Braun, M.; Fischer, H.; Groetsch, S.; Müller, G.; Leusser, D.; Deuerlein, S.; Stalke, D.; Arnone, M.; Engels, B. *Eur. J. Org. Chem.* **2006**, 5045–5058.

(42) Carry, J.-C.; Brohan, E.; Perron, S.; Bardouillet, P.-E. *Org. Process Res. Dev.* **2013**, *17*, 1568−1571.

(43) Lin, C.-W.; Hong, B.-C.; Chang, W.-C.; Lee, G.-H. *Org. Lett.* **2015**, *17*, 2314–2317.

(44) Murahashi, S.-I.; Shiota, T. *Tetrahedron Lett.* **1987**, *28*, 2383–2386.

(45) Shintani, R.; Fu, G. C. *J. Am. Chem. Soc.* **2003**, *125*, 10778–10779.

(46) Shintani, R.; Hayashi, T. *J. Am. Chem. Soc.* **2006**, *128*, 6330–6331.

(47) Altintas, O.; Glassner, M.; Rodriguez-Emmenegger, C.; Welle, A.; Trouillet, V.; Barner-Kowollik, C. *Angew. Chem., Int. Ed.* **2015**, *54*, 5777–5783.

(48) Ribeiro, R. F.; Marenich, A. V.; Cramer, C. J.; Truhlar, D. G. *J. Phys. Chem. B* **2011**, *115*, 14556.

(49) Marenich, A. V.; Cramer, C. J.; Truhlar, D. G. *J. Phys. Chem. B* **2009**, *113*, 6378–6396.

(50) Legault, C. Y. CYLView, 1.0b; Université de Sherbrooke: Quebec, Montreal, Canada, http://www.cylview.org (2009).

(51) Barber, J. S.; Yamano, M. M.; Ramirez, M.; Darzi, E. R.; Knapp, R. R.; Liu, F.; Houk, K. N.;

Garg, N. K. *Nat. Chem.* **2018**, *10*, 953–960.

CHAPTER FIVE

Cycloadditions of Oxacyclic Allenes and a Catalytic Asymmetric Entryway to Enantioenriched Cyclic Allenes

Michael M. Yamano, Rachel R. Knapp, Aurapat Ngamnithiporn, Melissa Ramirez,

Kendall N. Houk, Brian M. Stoltz, and Neil K. Garg.

5.1 Abstract

The chemistry of strained cyclic alkynes has undergone a renaissance over the past two decades. However, a related species, strained cyclic allenes, especially heterocyclic derivatives, have only recently resurfaced and represent another class of valuable intermediates. We report a mild and facile means to generate the parent 3,4-oxacyclic allene from a readily accessible silyl triflate precursor, and then trap it in (4+2), (3+2), and (2+2) reactions to provide a variety of cycloadducts. In addition, we describe a catalytic, decarboxylative asymmetric allylic alkylation performed on an α-silylated substrate, to ultimately permit access to an enantioenriched allene. Generation and trapping of the enantioenriched cyclic allene occurs with complete transfer of stereochemical information in a Diels–Alder cycloaddition via a point-chirality, axial-chirality, point-chirality transfer process.

5.2 Introduction

Despite once being mere scientific curiosities, strained cyclic intermediates have become a popular arena for chemical discoveries. A notable breakthrough in the field was the discovery of benzyne (**5.1**), initially proposed by Wittig in 1942 and validated by Roberts and co-workers

in 1953 (Figure 5.1).[1] In the modern era, benzyne (**5.1**) and other cyclic alkynes are readily used to make natural products,[2] medicinal agents,[3] agrochemicals,[4] materials,[5] tools for chemical biology,[6] and ligands for catalysis.[7,8] The related intermediate 1,2-cyclohexadiene (**5.2**) has generally received less attention despite being validated not long after benzyne (**5.1**) in 1966.[9] Historically, theoretical studies of **5.2** and its derivatives have been popular.[10] However, only recently has **5.2** seen synthetic use in cycloadditions.[11] This is largely due to the fact that it can be accessed under mild fluoride-mediated conditions from silyl triflate **5.3**.[12,13]

One exciting opportunity in the field of strained cyclic intermediates is the ability to access heterocyclic allenes. Early efforts in this field relied on harsh reaction conditions;[14,15] however, we recently demonstrated that azacyclic allenes **5.4** (Figure 5.1) can be accessed using mild reaction conditions. Moreover, using chiral separation technology, enantioenriched **5.4** was intercepted (R=Cbz, R'=H, R"=Me), and its stereospecific trapping allowed for a unique approach to access enantioenriched cycloadducts.[16]
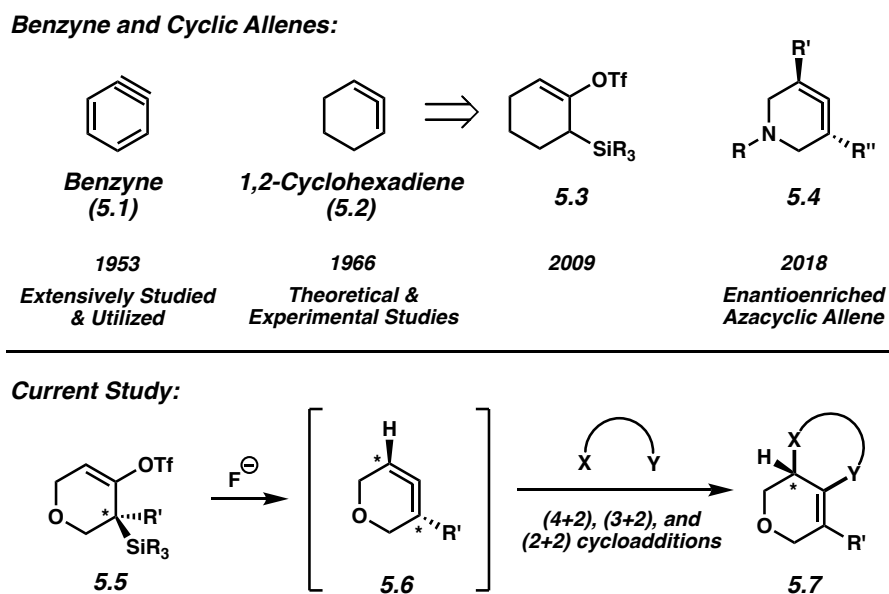
Figure 5.1. Highlights of benzyne and cyclic allene chemistry and cycloadditions of oxacyclic allenes described in this study.

Given the potential for heterocyclic allenes to provide a facile means to rapidly assemble stereochemically-rich scaffolds,[16] we wondered whether oxacyclic allenes **5.6** could be employed efficiently in cycloadditions to access oxygen-containing heterocycles.[17] Oxygenated heterocycles are often seen in natural products and drugs[18,19,20,21] and are known bioisosteres for their nitrogen and sulfur-containing counterparts.[22] A single report by Christl and Schreck demonstrated that **5.6** (R'=H) could be generated using the Doering–Moore–Skattebøl reaction, however, this required harsh organolithium-based conditions.[14] If **5.6** could be generated under mild conditions from silyl triflates **5.5**, the synthetic utility of this species could be unlocked. Additionally, we sought to access **5.6** in enantioenriched form, ideally by preparing an enantioenriched precursor to the desired allene **5.6** using asymmetric catalysis. By accessing enantioenriched **5.5**, we could explore the possibility of transferring stereochemical information from allene precursor **5.5** to cycloadduct **5.7**, through a point-chirality, axial-chirality, point-chirality transfer process. The results presented herein not only demonstrate the scope and utility of oxacyclic allene cycloadditions, but also showcase an exciting strategy that merges asymmetric catalysis with cyclic allene chemistry as a means to access enantioenriched scaffolds.

5.3 Computational Analysis of 3,4-Oxacyclohexadiene

Density functional theory (DFT) calculations on the structure of heterocyclic allene **5.8** were performed using ωB97XD/6-31G(d) (Figure 5.2).[10a,10c,10d,23] The C=C bond length of the allene is 1.32 Å, which is only slightly longer than the C=C bond length in a linear allene.[16] Furthermore, the internal angle at the central allene carbon is 133°, which is a significant deviation from the typical internal angle of 180° seen in linear allenes. The allene π orbitals in **5.8** are not perfectly orthogonal, resulting in the C–H bonds being twisted out-of-plane (i.e., 38°

and 41°). Thus, **5.8** is inherently chiral, in a manner analogous to linear allenes. The ground state geometry deviates from C2 symmetry because the molecule adopts an envelope shape; inversion of the envelope requires only 0.8 kcal/mol. Interestingly, oxacyclic allene **5.8** is calculated to possess 31.0 kcal/mol of strain energy, which is nearly 4 kcal/mol more than the azacyclic variant we previously reported.[16] This difference can be attributed to the smaller atomic radius of oxygen and the shorter C–O bond length relative to the C–N bond length in the azacyclic variant. The significant strain associated with oxacyclic allene **5.8** is expected to promote rapid cycloadditions.
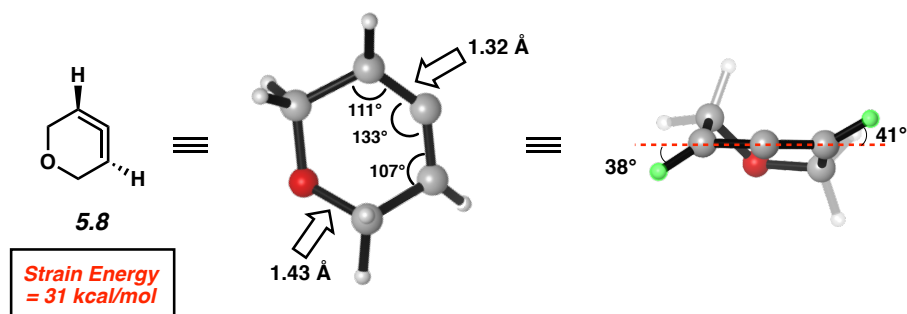
Figure 5.2. Ground state structure of oxacyclic allene **5.8**. The structure was computed using ωB97XD/6-31G(d).

5.4 Synthesis of a Silyl Triflate Precursor to 3,4-Oxacyclohexadiene

With the aim of accessing oxacyclic allene **5.8**, we first targeted silyl triflate **5.12** (Scheme 5.1), given the wide synthetic utility of silyl triflates as precursors to strained alkyne and allene intermediates.[12,24] Bromoketone **5.9** (commercially available or readily synthesized from tetrahydro-4-pyranone) was converted to triethylsilyl enol ether **5.10** upon treatment with DABCO and TESCl.[25] Subsequent retro-Brook rearrangement furnished the desired α-silyl ketone **5.11**. Finally, triflation afforded silyl triflate **5.12**.[16] Our three-step, scalable[26] synthesis of **5.12** provides a new strategy to synthesize α-silyl ketones en route to cyclic allene precursors.

Currently, α-silyl ketones are most commonly prepared by 1,4-reduction of the corresponding α,β-unsaturated ketones.[11a,12,16,27]
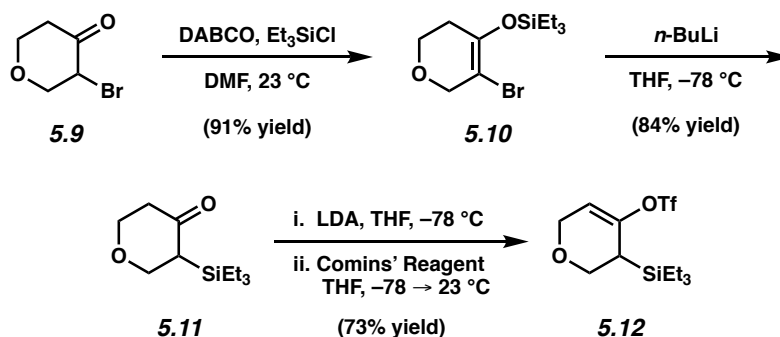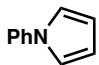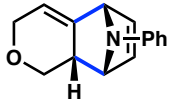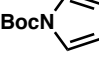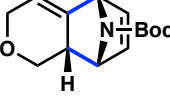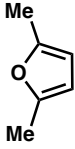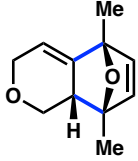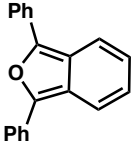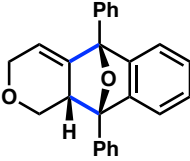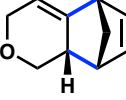
Scheme 5.1. Synthesis of silyl triflate **5.12**.

5.5 Scope of Methodology

With silyl triflate **5.12** in hand, we generated and trapped **5.8** in Diels–Alder, (3+2), and (2+2) cycloadditions. By simply employing a variety of dienes, a number of cycloadducts were prepared in good to excellent yields (Table 5.1, entries 1–5).[28] In almost all cases, the reactions were performed at 23 °C, thus highlighting the mildness of the reaction conditions. Although the diastereoselectivity was variable, in all examples, the major diastereomer observed is the endo product. The observed diastereoselectivity is supported by computations.[26] It should be noted that in each case, the products formed are considerably complex from a structural perspective, with each bearing three stereocenters, a bridged [2.2.1]-bicyclic framework, and 1 or 2 heteroatoms.

275

Table 5.1. Mild generation of oxacyclic allene **5.8** and its trapping in Diels–Alder cycloadditions.
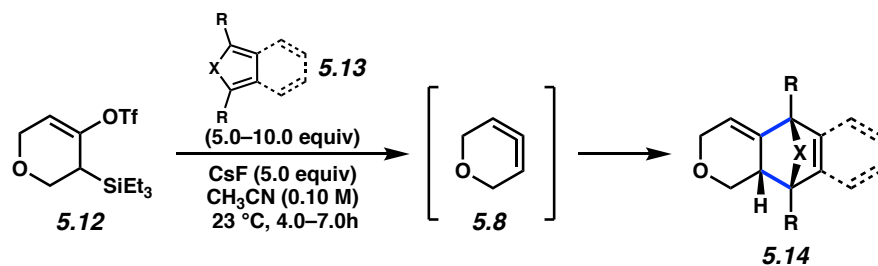
Entry	Diene	Cycloadduct[a]	Yield[b] Diastereoselectivity[c]
1	PhN (**5.15**)	**5.16**	91% 3.8 : 1 dr
2	BocN (**5.17**)	**5.18**	74% 6.2 : 1 dr
3	Me / Me (**5.19**)	**5.20**	86% 9.2 : 1 dr
4	Ph / Ph (**5.21**)	**5.22**	97%[d] 2.0 : 1 dr
5	(**5.23**)	**5.24**	83% 1.6 : 1 dr

[a]The major diastereomer is shown. [b]Yields reflect an average of two isolation experiments. [c]Diastereomeric ratios were determined by ^{1}H NMR analysis of the crude reaction mixture. [d]The reaction was performed at 60 °C for 2.5 h using 2.0 equiv of diene **5.21**.

The results of the (3+2) and (2+2) cycloadditions are shown in Figure 5.3 and Table 5.2. The use of simple nitrones gave high yields of isoxazolidine products **5.27**–**5.29**, whereas nitrones bearing either an indole or quinoline unit delivered cycloadducts **5.30** and **5.31**. We also evaluated two cyclic nitrones where R" and R'" of **5.25** were tethered, which furnished tri- and tetracyclic products **5.32** and **5.33**. Additionally, a ketone-derived nitrone was utilized, ultimately giving rise to the heteroatom-rich trifluoromethylated product **5.34**. Azomethine imines **5.37** and **5.39** were tested, giving rise to the corresponding pyrazolidines, **5.38** and **5.40,** with good to excellent diastereoselectivity (Table 5.2, entries 1 and 2). The use of nitrile oxide **5.41** led to the formation of isoxazoline **5.42** in 91% yield (entry 3). With regard to a (2+2) cycloaddition, the use of indene (**5.43**) gave cyclobutane **5.44** in excellent yield and with high regioselectivity (entry 4).
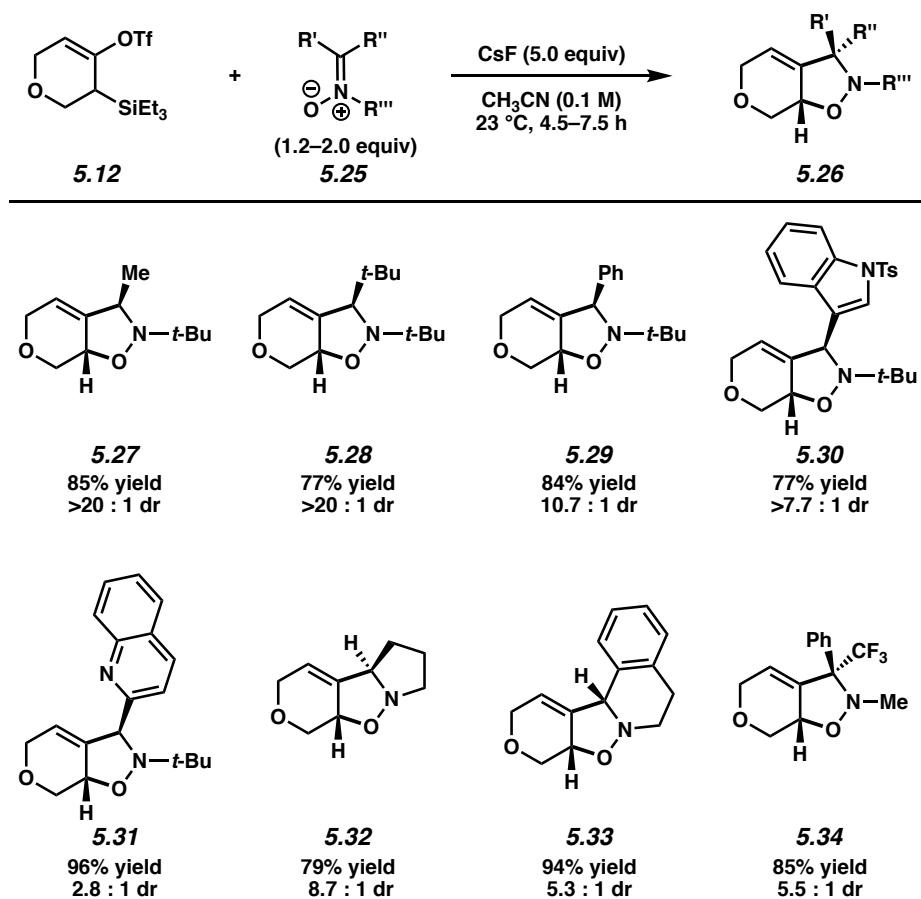
Figure 5.3. (3+2) cycloadditions with nitrones. The major diastereomeric product is shown. Yields reflect an average of two isolation experiments. Diastereomeric ratios were determined by ^{1}H NMR analysis of the crude reaction mixture.

Table 5.2. Additional (3+2) and (2+2) cycloadditions.

Entry	Trapping Agent	Cycloadduct[a]	Yield[b] Diastereoselectivity[c]
1	**5.37**	**5.38**	76% 7.6 : 1 dr
2	**5.39**	**5.40**	83% >20 : 1 dr
3	**5.41**	**5.42**	91% N/A
4	**5.43**	**5.44**	96% 5.2 : 1 dr

[a]The major diastereomer is shown. [b]Yields reflect an average of two isolation experiments. [c]Diastereomeric ratios were determined by ^{1}H NMR analysis of the crude reaction mixture.

Overall, silyl triflate **5.12** was elaborated to 17 different sp^3-rich heterocyclic cycloadducts. Several of these bear a multitude of rings, stereocenters, and heteroatoms, thus showcasing the value of oxacyclic allenes for the rapid generation of complex scaffolds. Accordingly, this method should be especially valuable in drug discovery.[17]

5.6 Catalytic Asymmetric Synthesis of an Oxacyclic Allene Precursor and Trapping

As noted earlier, one of the most exciting opportunities regarding cyclic allene chemistry is the possibility of intercepting enantioenriched allenes for the synthesis of enantioenriched cycloadducts. In a seminal study, Christl and co-workers generated 1-phenyl-1,2-cyclohexadiene in enantioenriched form, as judged by the formation of an enantioenriched cycloadduct, albeit in low yield, likely owing to the necessary use of organolithium reagents.[29] Our laboratory recently disclosed a mild, alternative strategy whereby silyl triflate precursors to the desired cyclic allenes could be employed in enantioenriched form.[16] However, in both cases, the key substrates were only accessible through chiral separation technologies. A catalytic asymmetric strategy to access enantioenriched cyclic allene precursors has not been reported.

Our efforts in this area are highlighted in Scheme 5.2. Enol carbonate **5.45** was formed by intercepting the enolate intermediate generated during the retro-Brook rearrangement of **5.10** (see Scheme 5.1). This set the stage for a Pd-catalyzed decarboxylative asymmetric allylic alkylation. Allylation was attractive, given that allyl groups serve as versatile handles for further manipulation.[30] After extensive experimentation,[26] it was found that treatment of **5.45** with Pd(dmdba)$_2$ and (*S*)-(CF$_3$)$_3$-*t*Bu-PHOX ligand **5.47** in toluene at –10 °C gave the desired ketone **5.46** in 9:1 er (81% ee) and 75% yield. This is the first example of a decarboxylative asymmetric allylic alkylation reaction being performed on an α-silyl-substituted enol carbonate. In fact, decarboxylative asymmetric allylic alkylations on substrates bearing α-heteroatoms are significantly underdeveloped.[30,31] **5.46** was converted to silyl triflate **5.48** in one-step, thus establishing the first catalytic asymmetric strategy for the synthesis of enantioenriched cyclic allene precursors.
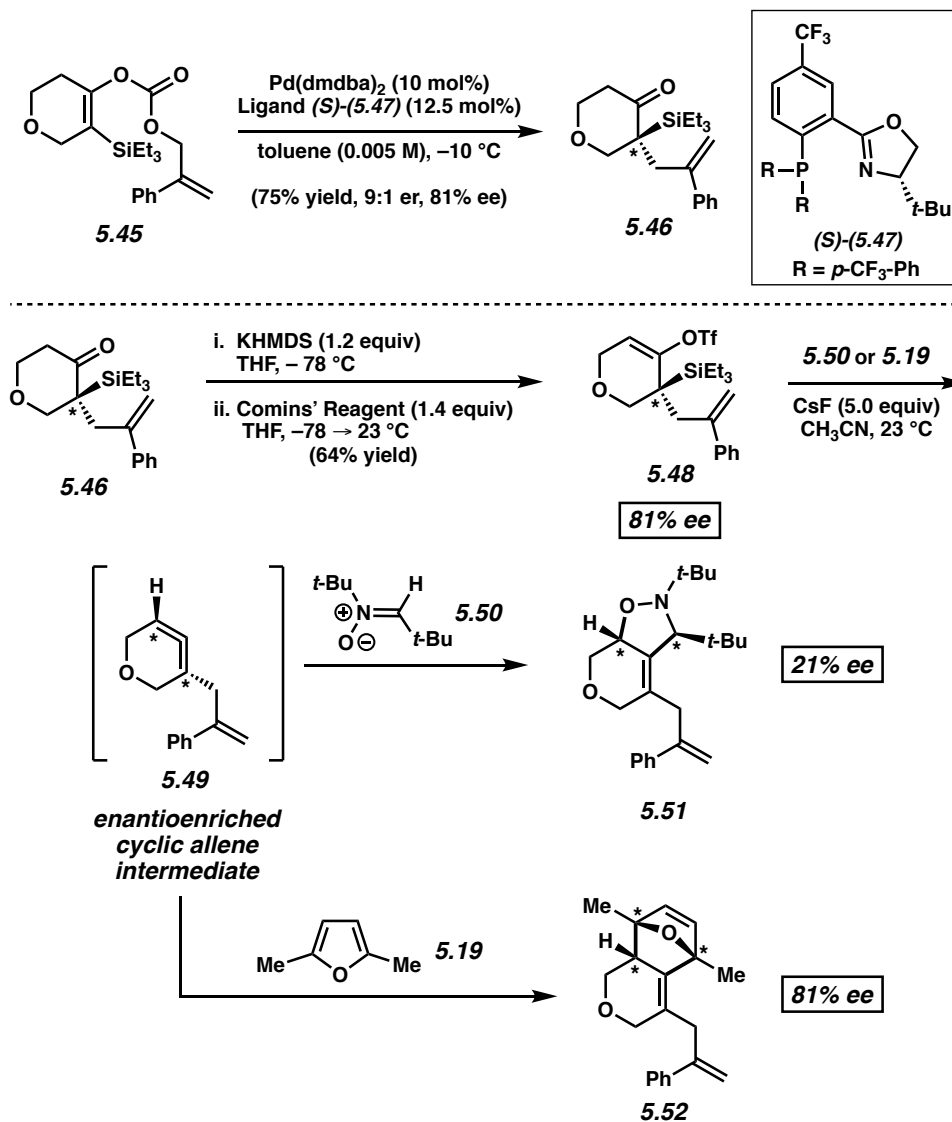
Scheme 5.2. Catalytic asymmetric approach and cycloaddition results.

5.48 was treated with trapping agent **5.50** or **5.19** in the presence of CsF in acetonitrile at 23 °C. Interestingly, the nitrone cycloadduct, isoxazolidine **5.51**, was obtained in 21% ee. On the other hand, the Diels–Alder cycloadduct, oxabicycle **5.52**, was obtained in 81% ee (>20:1 dr), which reflects complete transfer of stereochemical information. Given this latter result, we surmise that enantioenriched **5.49** is formed under the mild reaction conditions with complete transfer of stereochemical information. In the case of the nitrone trapping, previous

computational studies have demonstrated that trapping may occur through either a stepwise or concerted pathway,[11a] which accounts for the partial loss of stereochemical information.[32] However, in the case of the Diels–Alder reaction, it is likely that a concerted pathway is operative, based on our recent computational investigation of azacyclic allenes,[16] thus leading to complete transfer of stereochemical information.

The overall conversion of **5.48** to **5.49** to **5.52** deserves special attention. This is a scenario wherein the silyl-bearing stereocenter in **5.48** was ultimately accessed by asymmetric catalysis. The point chirality in **5.48** is then transferred to the axially chiral transient intermediate **5.49**, which is then relayed to product **5.52**, which possesses point chirality. Enantioenriched cycloadduct **5.52** contains three stereocenters, none of which were present in the starting material, which bears only one stereocenter. The transformation occurs preferentially at the olefin more distal to the 2-phenyl allyl group undergoing cycloaddition. This is presumably because of favorable electronic interactions in the transition state based on our prior studies,[16] however, we cannot rule out the steric impact of the 2-Ph allyl chain as a contributor to the observed regioselectivity.

5.7 Conclusion

We have discovered an efficient synthetic route to prepare a silyl triflate precursor to 3,4-oxacyclohexadiene, the first generation of an oxacyclic allene under mild conditions, and the in situ trapping of the oxacyclic allene in diastereo- and regioselective cycloadditions. These efforts collectively establish the synthetic utility of oxacyclic allenes for the rapid generation of complex heterocyclic scaffolds. In addition, we have uncovered the first catalytic, asymmetric approach to access an enantioenriched cyclic allene precursor. This relies on a Pd-catalyzed allylic allylation, performed for the first time on an α-silyl substituted substrate, which ultimately

permitted access to the necessary enantioenriched silyl triflate precursor. We show that trapping of the enantioenriched oxacyclic allene in a Diels–Alder reaction occurs with complete transfer of stereochemical information through a point-chirality, axial-chirality, point-chirality transfer process. These results showcase an exciting strategy that merges asymmetric catalysis with cyclic allene chemistry as a means to access densely functionalized, enantioenriched scaffolds.

5.8 Experimental Section

5.8.1 Materials and Methods

Unless stated otherwise, reactions were conducted in flame-dried glassware under an atmosphere of nitrogen using anhydrous solvents (freshly distilled or passed through activated alumina columns). All commercially obtained reagents were used as received unless otherwise specified. Cesium fluoride (CsF), tetrakis(triphenylphosphine)palladium(0) (Pd(PPh$_3$)$_4$), and tris(dibenzylideneacetone)dipalladium(0) (Pd$_2$(dba)$_3$) were obtained from Strem Chemicals. (1,3)-diphenylisobenzofuran (**5.21**), *N-tert*-butyl-α-phenylnitrone (**5.55**), chlorotrimethylsilane (TMSCl) were obtained from Alfa Aesar. *N*-(5-chloro-2-pyridyl)bis(trifluoromethanesulfonimide) (Comins' Reagent), *n*-butyllithium (*n*-BuLi), potassium bis(trimethylsilyl)amide (KHMDS), *N*-Boc pyrrole (**5.17**), *N*-phenylpyrrole (**5.15**), 2,5-dimethylfuran (**5.19**), dicyclopentadiene, dimethylphenylsilyl chloride (PhMe$_2$SiCl), and allyl chloroformate were obtained from Sigma Aldrich. Diisopropylamine and 1,4-diazabicyclo[2.2.2]octane (DABCO) were obtained from Acros Organics. Indene (**5.43**) was purchased from Combi-Blocks. 2,5-dimethylfuran (**5.19**), TMSCl, and diisopropylamine were distilled over CaH$_2$ prior to use. Allyl chloroformate was desiccated with CaCl$_2$ and distilled prior to use. **5.17** was filtered over basic alumina prior to use. Dicyclopentadiene was cracked and cyclopentadiene (**5.23**) was stored at –80 °C prior to use. Reaction temperatures were controlled using an IKAmag temperature modulator and, unless stated otherwise, reactions were performed at room temperature (approximately 23 °C). Thin layer chromatography (TLC) was conducted with EMD gel 60 F254 pre-coated plates (0.25 mm) and visualized using a combination of UV light, anisaldehyde, and potassium permanganate staining. Silicycle Siliaflash P60 (particle size 0.040–0.063 mm) was used for flash column chromatography. ^{1}H-

NMR and 2D-NOESY spectra were recorded on Bruker spectrometers (at 300, 400, 500, and 600 MHz) and are reported relative to the residual solvent signal. Data for ^{1}H-NMR spectra are reported as follows: chemical shift (δ ppm), multiplicity, coupling constant (Hz) and integration. ^{13}C-NMR spectra were recorded on Bruker spectrometers (at 100 and 125 MHz) and are reported relative to the residual solvent signal. Data for ^{13}C-NMR spectra are reported in terms of chemical shift and, when necessary, multiplicity, and coupling constant (Hz). ^{19}F NMR spectra were recorded on Bruker spectrometers (at 376 MHz) and reported in terms of chemical shift (δ ppm). IR spectra were obtained on a Perkin-Elmer UATR Two FT-IR spectrometer and are reported in terms of frequency of absorption (cm^{-1}). Uncorrected melting points were measured using a Digimelt MPA160 melting point apparatus. DART-MS spectra were collected on a Thermo Exactive Plus MSD (Thermo Scientific) equipped with an ID-CUBE ion source and a Vapur Interface (IonSense Inc.). Both the source and MSD were controlled by Excalibur software v. 3.0. The analyte was spotted onto OpenSpot sampling cards (IonSense Inc.) using CDCl$_3$ as the solvent. Ionization was accomplished using UHP He (Airgas Inc.) plasma with no additional ionization agents. The mass calibration was carried out using Pierce LTQ Velos ESI (+) and (–) Ion calibration solutions (Thermo Fisher Scientific). Determination of enantiopurity was carried out on a Mettler Toledo SFC (supercritical fluid chromatography) using a Daicel ChiralPak IC-3 column and a Daicel ChiralPak AD-3 column. Optical rotations were measured with a Rudolph Autopol III Automatic Polarimeter.

*Nitrones **5.54**,[33] **5.50**,[34] **5.56**, **5.57**,[11a] **5.58**,[35] **5.59**,[35] **5.60**,[11a] azomethine imines **5.37**[36] and **5.39**,[37] nitrile oxide **5.41**,[38] imidazole carboxylate **5.66**,[39] and (S)-(CF$_3$)$_3$-t-BuPHOX (**5.47**)[40] are all known compounds. ^{1}H-NMR spectral data matched those reported in the literature.*

5.8.2 Experimental Procedures

5.8.2.1 Synthesis of Silyl Triflate 5.12
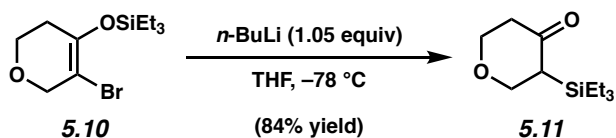
Silyl ketone 5.11. To a solution of known silyl enol ether **5.10**[25] (5.6 g, 19.1 mmol, 1.0 equiv) in THF (225 mL) at –78 °C was added *n*-BuLi (2.02 M in hexanes, 9.9 mL, 20.1 mmol, 1.05 equiv) dropwise over 18 min. The solution was stirred for 43 min at –78 °C, then the reaction was quenched with sat. aq. NaHCO$_3$ (80 mL) and allowed to warm to 23 °C. The layers were then separated and the aqueous layer was extracted with EtOAc (3 x 80 mL). The combined organic layers were then dried over Na$_2$SO$_4$, filtered, and concentrated under reduced pressure. The resulting crude oil was purified by flash chromatography (19:1 hexanes:EtOAc) to afford silyl ketone **5.11** (3.4 g, 84% yield) as a colorless oil. Silyl ketone **5.11**: R$_f$ 0.29 (9:1 hexanes:EtOAc); ^{1}H-NMR (400 MHz, CDCl$_3$): δ 4.20–4.09 (m, 2H), 3.92 (dd, *J* = 11.4, 4.6, 1H), 3.74 (ddd, *J* = 11.4, 10.9, 4.0, 1H), 2.47 (ddd, *J* = 15.6, 10.9, 6.8, 1H) , 2.38–2.31 (m, 2H), 0.97 (t, *J* = 7.7 9H), 0.68 (q, *J* = 7.7, 6H) ; ^{13}C-NMR (100 MHz, CDCl$_3$): δ 207.7, 68.1, 67.2, 44.5, 42.0, 7.4, 3.2; IR (film): 2954, 2911, 2876, 1691, 1218 cm^{-1}; HRMS–APCI (*m/z*) [M + H]$^+$ calcd for C$_{11}$H$_{23}$O$_2$Si$^+$, 215.14618; found, 215.14678.
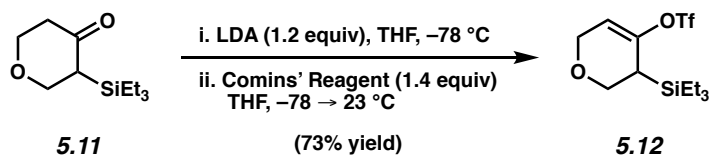
Silyl triflate 5.12. To a solution of diisopropylamine (1.30 mL, 9.1 mmol, 1.30 equiv) in THF (8.0 mL) at –78 °C was added *n*-BuLi (2.02M in hexanes, 4.20 mL, 8.4 mmol, 1.20 equiv)

dropwise over 7 min. The reaction was then stirred at –78 °C for 20 min and then allowed to warm to 23 °C. After stirring for 10 min at 23 °C, the reaction mixture was again cooled to –78 °C and a solution of silyl ketone **5.11** (1.5 g, 7.01 mmol, 1.0 equiv) in THF (8.0 mL) was added dropwise over 15 min and left to stir for 1.0 h at –78 °C. A solution of Comins' Reagent (3.86 g, 9.81 mmol, 1.4 equiv) in THF (8.2 mL) was then added dropwise over 20 min at –78 °C. The reaction was then stirred for 10 min at –78 °C before being warmed to 23 °C. After stirring for an additional 14 h, the reaction mixture was quenched by the addition of sat. aq. NaHCO$_3$ (30 mL), and the layers were separated. The aqueous layer was extracted with Et$_2$O (3 x 30 mL) and the combined organic layers were dried over Na$_2$SO$_4$, filtered, and concentrated under reduced pressure. The resulting crude oil was purified by flash chromatography (4:1 hexanes:benzene) to give silyl triflate **5.12** (1.77 g, 73% yield) as a colorless oil. Silyl triflate **5.12**: R$_f$ 0.55 (9:1 hexanes:EtOAc); ^{1}H-NMR (400 MHz, CDCl$_3$): δ 5.67–5.65 (m, 1H), 4.25 (qt, J = 16.1, 3.1, 2H), 3.96 (dd, J = 11.2, 4.7, 1H), 3.86 (dd, J = 11.2, 4.7, 1H), 2.14–2.10 (m, 1H), 0.98 (t, J = 8.2, 9H), 0.68 (q, J = 8.0, 6H); ^{13}C-NMR (125 MHz): δ 149.7, 118.7 (q, J = 318.3), 113.0, 66.7, 64.4, 28.5, 7.3, 2.9; ^{19}F-NMR (376 Hz, CDCl$_3$): –73.5; IR (film): 2957, 2880, 1681, 1418, 1245, 1207 cm^{-1}; HRMS–APCI (*m/z*) [M + H]$^+$ calcd for C$_{12}$H$_{22}$F$_3$O$_4$Si$^+$, 347.09547; found, 347.09659

5.8.2.2 Diels–Alder Trapping Experiments

Representative Procedure (Preparation of cycloadduct 5.16 is used as an example).
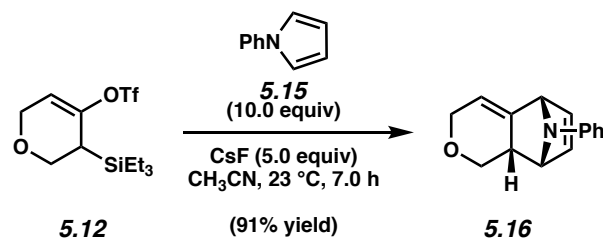
Cycloadduct 5.16. To a stirred solution of silyl triflate **5.12** (52.6 mg, 0.152 mmol, 1.0 equiv) and *N*-phenylpyrrole (**5.15**, 217 mg, 1.52 mmol, 10.0 equiv) in CH_3CN (1.52 mL) was added CsF (115.0 mg, 0.759 mmol, 5.0 equiv). The reaction vessel was sealed with a PTFE lined cap and allowed to stir at 23 °C for 7 h. The crude reaction mixture was then filtered by passage through a plug of silica gel (EtOAc eluent, 10 mL). Concentration under reduced pressure yielded the crude residue (3.8:1 dr, average of two experiments). Purification by preparative thin layer chromatography (5:1 hexanes:EtOAc) allowed for separation of the two diastereomers, which were obtained in a total yield of 91% (average of two experiments). The major diastereomer **5.16** was obtained as a light yellow amorphous solid. Cycloadduct **5.16**: R_f 0.15 (5:1 hexanes:EtOAc); ^{1}H-NMR (400 MHz, CDCl$_3$): δ 7.23–7.18 (m, 2H), 6.87–6.80 (m, 3H), 6.30 (dd, *J* = 5.6, 2.6, 1H), 5.97 (dd, *J* = 5.7, 2.1, 1H), 5.69–5.68 (m, 1H), 4.89 (br s, 1H), 4.71–4.70 (m, 1H), 4.25 (dt, *J* = 16.5, 2.1, 1H), 4.15 (dd, *J* = 9.4, 4.7, 1H), 3.96 (dt, *J* = 16.6, 3.0, 1H), 2.64–2.60 (m, 1H), 2.46 (t, *J* = 9.8, 1H); ^{13}C-NMR (125 MHz, CDCl$_3$): δ 146.8, 137.6, 135.0, 129.2, 128.4, 120.7, 117.7, 117.3, 67.9, 65.4, 64.96, 64.95, 38.6; IR (film): 3060, 3005, 2920, 1496, 1315 cm^{-1}; HRMS–APCI (*m/z*) [M + H]$^+$ calcd for $C_{15}H_{16}NO^+$, 226.12264; found, 226.12161.

The structure of **5.16** was verified by 2D-NOESY, as the following interaction was observed:
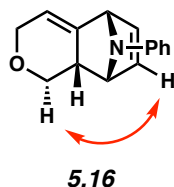
5.16

All reactions were monitored by TLC until starting material was consumed; the specific times are listed in the reaction scheme for each reaction. Any modifications of the conditions shown in this representative procedure are specified in the following schemes, which depict all of the results shown in Table 5.1. For all compounds in which the diastereomeric ratios were >20:1, the minor diastereomer was not observed in the ^{1}H-NMR spectrum of the crude reaction mixture.
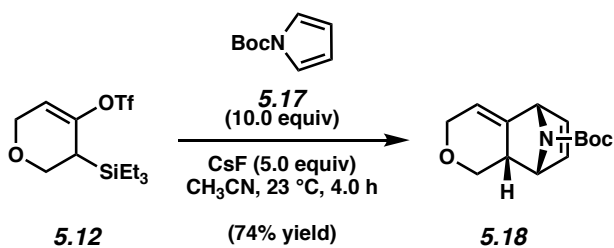
Cycloadduct 5.18. Following concentration under reduced pressure, the crude residue was obtained (6.2:1 dr, average of two experiments). Purification by preparative thin layer chromatography (5:1 hexanes:Et$_2$O) allowed for separation of the two diastereomers, which provided a total yield of 74% (average of two experiments). Major diastereomer **5.18** was obtained as a clear oil. Cycloadduct **5.18**: R$_f$ 0.28 (9:1 hexanes:EtOAc); ^{1}H-NMR (600 MHz, CDCl$_3$): δ 6.32 (br s, 1H), 5.99–5.95 (m, 1H), 5.61 (br s, 1H), 4.99–4.93 (m, 1H), 4.79–4.73 (m, 1H), 4.28 (dt, J = 16.6, 2.1, 1H), 4.14 (dd, J = 9.6, 4.8, 1H), 3.95 (dt, J = 16.6, 2.9, 1H), 2.65 (br s, 1H), 2.36 (t, J = 10.1, 1H), 1.43 (s, 9H); ^{13}C-NMR (125 MHz, CDCl$_3$): δ 155.1, 136.3, 135.5, 129.5, 128.3, 120.2, 117.0, 116.4, 80.6, 67.6, 65.0, 63.7, 63.0, 62.1, 61.6, 39.8, 39.3, 28.4; IR

(film): 2978, 1738, 1599, 1319, 1160 cm^{-1}; HRMS–APCI (*m/z*) [M + H]$^+$ calcd for C$_{14}$H$_{20}$NO$_3{}^+$, 250.14377; found, 250.14536.

*Note: **5.18** was obtained as a mixture of rotamers. These data represent empirically observed*

chemical shifts from the ^{1}H-NMR and ^{13}C-NMR spectra.

The structure of **5.18** was verified by 2D-NOESY, as the following interaction was observed:

5.18
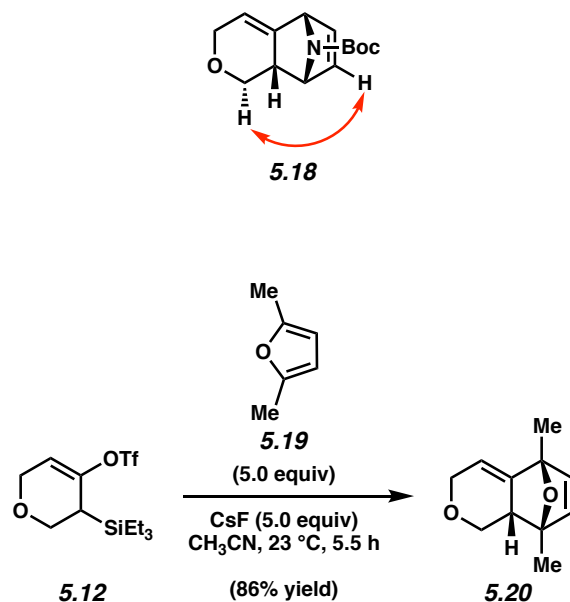
Cycloadduct 5.20. Following concentration under reduced pressure, the crude residue was obtained (9.2:1 dr, average of two experiments). Purification by flash chromatography (5:1 pentanes:Et$_2$O) allowed for separation of the two diastereomers, which afforded a total yield of 86% (average of two experiments). Major diastereomer **5.20** was obtained as a colorless oil. Cycloadduct **5.20**: R$_f$ 0.27 (9:1 hexanes:EtOAc); ^{1}H-NMR (500 MHz, CDCl$_3$): δ 6.13 (d, *J* = 5.4, 1H), 5.82 (d, *J* = 5.4, 1H), 5.48 (app q, *J* = 2.3, 1H), 4.28 (dt, *J* = 16.5, 2.1, 1H), 4.11 (dd, *J* = 9.3, 4.7, 1H), 3.94 (dt, *J* = 16.4, 2.9, 1H), 2.45–2.41 (m, 1H), 2.36–2.32 (m, 1H), 1.63 (s, 3H), 1.62 (s, 3H); ^{13}C-NMR (125 MHz, CDCl$_3$): δ 143.5, 139.9, 132.8, 113.7, 86.8, 86.6, 67.2, 64.6, 46.5, 18.2, 14.8; IR (film): 2973, 2929, 2851, 1382, 1308 cm^{-1}; HRMS–APCI (*m/z*) [M + H]$^+$ calcd for C$_{11}$H$_{15}$O$_2{}^+$, 179.10666; found, 179.10719.

The structure of **5.20** was verified by 2D-NOESY, as the following interaction was observed:

5.20
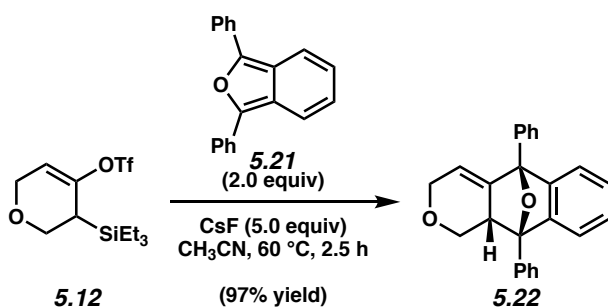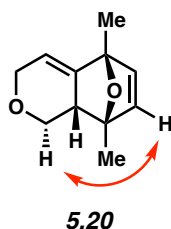
Cycloadduct 5.22. Following concentration under reduced pressure, the crude residue was obtained (2.0:1 dr, average of two experiments). Purification by preparative thin layer chromatography (9:1 hexanes:EtOAc) allowed for separation of the two diastereomers, which provided a total yield of 97% (average of two experiments). Major diastereomer **5.22** was obtained as a clear oil. Cycloadduct **5.22**: R_f 0.36 (9:1 hexanes:EtOAc); ^{1}H-NMR (500 MHz, CDCl$_3$): δ 7.88–7.86 (m, 2H), 7.65–7.63 (m, 2H), 7.53–7.45 (m, 5H), 7.43–7.41 (m, 1H), 7.25–7.21 (m, 2H), 7.17–7.14 (m, 1H), 7.01–6.99 (m, 1H), 5.71 (app q, J = 2.5, 1H), 4.45 (dd, J = 9.8, 4.9, 1H), 4.34 (dt, J = 16.9, 2.5, 1H), 3.87 (ddd, J = 16.6, 3.6, 2.9, 1H), 3.43–3.39 (m, 1H), 2.40 (t, J = 10.2, 1H); ^{13}C-NMR (125 MHz, CDCl$_3$): δ 148.1, 144.3, 142.5, 137.3, 134.1, 129.0, 128.72, 128.66, 128.6, 128.5, 127.6, 127.0, 126.4, 121.3, 118.6, 118.0, 90.2, 89.4, 67.0, 64.9, 46.3; IR (film): 3060, 2923, 1734, 1448, 734 cm^{-1}; HRMS–APCI (m/z) [M + H]$^+$ calcd for C$_{25}$H$_{21}$O$_2{}^+$, 353.15361; found, 353.15563.

The structure of **5.22** was verified by 2D-NOESY, as the following interaction was observed:

5.22

Cycloadducts 5.24 and 5.53. Following concentration under reduced pressure, the crude residue was obtained (1.6:1 dr, average of two experiments). Purification by flash chromatography (30:1 pentane:Et$_2$O), provided a total yield of 83% (average of two experiments) of **5.24** and **5.53** as an inseparable mixture. **5.24** and **5.53** (inseparable mixture) were obtained as a colorless oil. Cycloadducts **5.24** and **5.53**: R$_f$ 0.62 (9:1 hexanes:EtOAc); ^{1}H-NMR (300 MHz, CDCl$_3$): δ 6.34 (dd, J = 5.7, 3.1, 1H, 3.53), 6.09–6.02 (m, 1H, 3.24, 1H, 3.53), 5.77 (dd, J = 5.5, 2.9, 1H, 3.24), 5.59–5.54 (m, 1H, 3.53), 5.48–5.44 (m, 1H, 3.24), 4.29 (dt, J = 15.9, 2.0, 1H, 3.53), 4.26 (dt, J = 16.4, 2.2, 1H, 3.24), 4.15–4.06 (m, 1H, 3.24, 2H, 3.53), 3.97 (dt, J = 16.9, 2.9, 1H, 3.24), 3.36 (br s, 1H, 3.53), 3.26 (br s, 1H, 3.24), 2.99 (dd, J = 10.6, 9.6, 1H, 3.53), 2.95–2.90 (m, 1H, 3.24), 2.70 (br s, 1H, 3.53), 2.54–2.45 (m, 1H, 3.24), 2.41 (dd, J = 10.2, 8.7, 1H 3.24), 2.02–1.92 (m, 1H, 3.53), 1.63 (dt, J = 8.2, 1.6, 1H, 3.24), 1.59–1.54 (m, 1H, 3.53), 1.52–1.47 (m, 1H, 3.24), 1.41–1.37 (m, 1H, 3.53); ^{13}C-NMR (125 MHz, CDCl$_3$): δ 142.6, 141.3, 138.7, 136.2, 132.8, 129.8, 114.9, 114.4, 69.0, 67.8, 65.2 (2C), 50.0, 49.1, 48.7, 47.4, 43.5, 41.9, 41.2, 40.9; IR (film):

3059, 2970, 2924, 2851, 1375 cm^{-1}; HRMS–APCI (*m/z*) [M + H]$^+$ calcd for C$_{10}$H$_{13}$O$^+$, 149.09609; found, 149.09597.

The structures of **5.24** and **5.53** were verified by 2D-NOESY, as the following interaction were

observed:

5.24   **5.53**
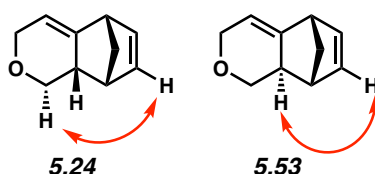
5.8.2.3 (3+2) Trappings with Nitrones

Representative Procedure (Preparation of isoxazolidine 5.27 is used as an example).
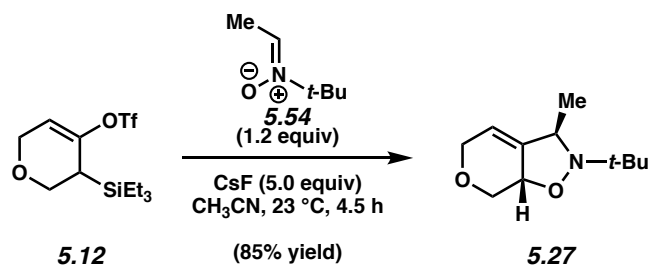
Isoxazolidine 5.27. To a stirred solution of silyl triflate **5.12** (52.2 mg, 0.151 mmol, 1.0 equiv) and nitrone **5.54** (20.8 mg, 0.181 mmol, 1.2 equiv) in CH$_3$CN (1.51 mL) was added CsF (114 mg, 0.753 mmol, 5.0 equiv). The reaction vessel was sealed with a PTFE lined cap and allowed to stir at 23 °C for 4.5 h. The reaction mixture was filtered by passage through a plug of silica gel (EtOAc eluent, 10 mL). Concentration under reduced pressure yielded the crude residue (>20:1 dr, average of two experiments). Purification by preparative thin layer chromatography (5:1 hexanes:EtOAc) afforded isoxazolidine **5.27** as a clear, colorless oil (85% yield, average of two experiments). Isoxazolidine **5.27**: R$_f$ 0.25 (9:1 hexanes:EtOAc); ^{1}H-NMR (400 MHz, CDCl$_3$): δ 5.46–5.45 (m, 1H), 4.38–4.34 (m, 1H), 4.27 (dd, *J* = 10.1, 5.9, 1H), 4.16 (dq, *J* = 16.3, 2.4, 1H),

4.07–4.01 (m, 1H), 3.74–3.70 (m, 1H), 3.11 (app t, J = 8.9, 1H), 1.29 (d, J = 6.4, 3H), 1.10 (s, 9H); ^{13}C-NMR (100 MHz, CDCl$_3$): δ 144.8, 114.1, 69.2, 66.5, 64.9, 58.8, 57.1, 25.9, 23.9; IR (film): 2971, 2929, 2865, 1361, 1129 cm^{-1}; HRMS–APCI (m/z) [M + H]$^+$ calcd for C$_{11}$H$_{20}$NO$_2^+$, 198.14886; found, 198.14936.

The structure of **5.27** was verified by 2D-NOESY, as the following interaction was observed:

5.27
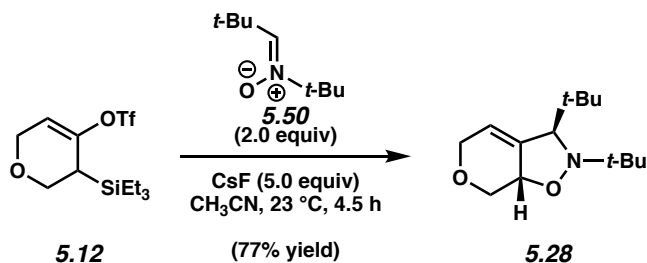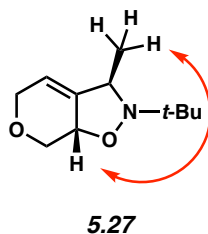
Isoxazolidine 5.28. Following concentration under reduced pressure, the crude residue was obtained (>20:1 dr, average of two experiments). Purification by flash chromatography (9:1 hexanes:EtOAc) afforded isoxazolidine **5.28** as a white powder in 77% yield (average of two experiments). Isoxazolidine **5.28**: Mp: 103–105 °C; R$_f$ 0.14 (9:1 hexanes:EtOAc); ^{1}H-NMR (500 MHz, CDCl$_3$): δ 5.45 (s, 1H), 4.30–4.28 (m, 1H), 4.23–4.20 (m, 2H), 4.05–4.02 (m, 1H), 3.31 (s, 1H), 3.17 (t, J = 9.8, 1H), 1.03 (s, 9H), 0.95 (s, 9H); ^{13}C-NMR (125 MHz, CDCl$_3$): δ 141.7, 117.6, 71.5, 70.9, 66.9, 64.7, 59.9, 34.3, 27.1, 26.9; IR (film): 2955, 2836, 1595, 1417, 1205 cm^{-1}; HRMS–APCI (m/z) [M + H]$^+$ calcd for C$_{14}$H$_{26}$NO$_2^+$, 240.19581; found, 240.19751.

The structure of **5.28** was verified by 2D-NOESY, as the following interaction was observed:
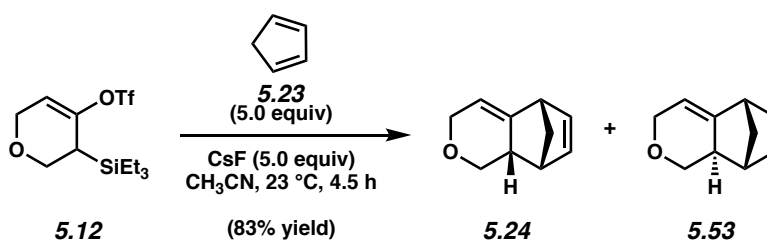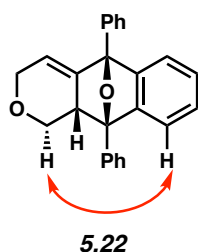

5.28
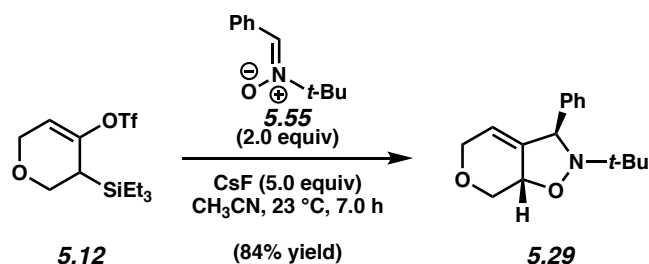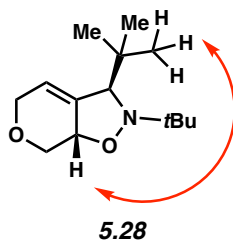
Isoxazolidine 5.29. Following concentration under reduced pressure, the crude residue was obtained (10.7:1 dr, average of two experiments). Purification by preparative thin layer chromatography (9:1 benzene:CH₃CN) allowed for separation of the two diastereomers, which provided a total yield of 84% (average of two experiments). Major diastereomer **5.29** was obtained as a white powder. Isoxazolidine **5.29**: Mp: 111–112 °C; R_f 0.43 (9:1 hexanes:EtOAc); ¹H-NMR (400 MHz, CDCl₃): δ 7.49–7.47 (m, 2H), 7.33–7.30 (m, 2H), 7.25–7.22 (m, 1H), 5.44 (app quint, J = 2.0, 1H), 4.62 (s, 1H), 4.50–4.46 (m, 1H), 4.31 (dd, J = 9.6, 5.6, 1H), 4.13–4.02 (m, 2H), 3.17 (app t, J = 9.4, 1H), 1.08 (s, 9H); ¹³C-NMR (125 MHz, CDCl₃): δ 144.8, 143.8, 128.6, 127.3, 127.0, 115.5, 70.1, 66.3, 65.7, 65.0, 59.0, 26.2; IR (film): 2972, 2931, 2867, 1492, 1453 cm⁻¹; HRMS–APCI (*m/z*) [M + H]⁺ calcd for $C_{16}H_{22}NO_2^+$, 260.16451; found, 260.16520.

The structure of **5.29** was verified by 2D-NOESY, as the following interaction was observed:

5.29
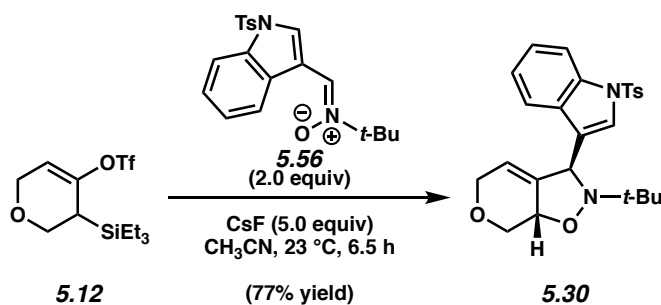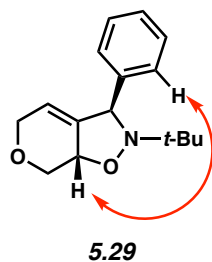
Isoxazolidine 5.30. Following concentration under reduced pressure, the crude residue was obtained (>7.7:1 dr, average of two experiments). Purification by preparative thin layer chromatography (2:2:1 hexanes:benzene:Et$_2$O) allowed for separation of the two diastereomers, which provided a total yield of 77% (average of two experiments). Major diastereomer **5.30** was obtained as a white foam. Isoxazolidine **5.30**: R$_f$ 0.27 (5:1 hexanes:EtOAc); ^{1}H-NMR (400 MHz, CDCl$_3$): δ 7.98 (d, J = 8.3, 1H), 7.75–7.70 (m, 4H), 7.33–7.29 (m, 1H), 7.25–7.21 (m, 1H), 7.21–7.16 (m, 2H), 5.55–5.52 (m, 1H), 4.87 (s, 1H), 4.51–4.45 (m, 1H), 4.30 (dd, J = 10.2, 5.6, 1H), 4.06–4.02 (m, 2H), 3.18 (app t, J = 9.0, 1H), 2.32 (s, 3H), 1.06 (s, 9H); ^{13}C-NMR (100 MHz, CDCl$_3$): δ 144.8, 142.9, 135.8, 135.3, 129.8, 129.0, 126.8, 125.0, 124.8, 124.0, 123.1, 120.3, 115.6, 114.0, 69.8, 66.1, 64.2, 58.8, 58.2, 25.8, 21.5; IR (film): 2971, 2931, 2868, 1445, 1363 cm^{-1}; HRMS–APCI (m/z) [M + H]$^+$ calcd for C$_{25}$H$_{29}$N$_2$O$_4$S$^+$, 453.18425; found, 453.18223.

The structure of **5.30** was verified by 2D-NOESY, as the following interaction was observed:

5.30
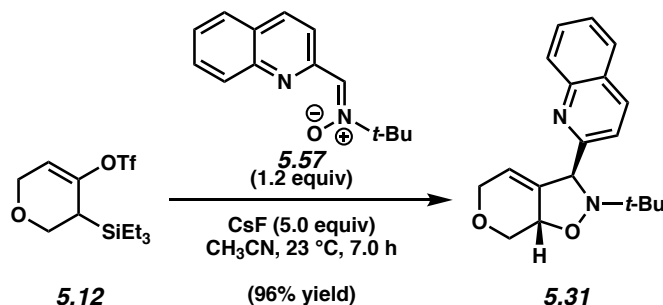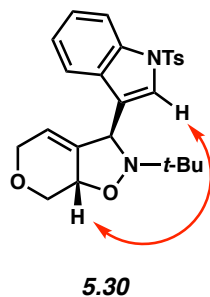
Isoxazolidine 5.31. Following concentration under reduced pressure, the crude residue was obtained (2.8:1 dr, average of two experiments). Purification by preparative thin layer chromatography (2:2:1 hexanes:CH$_2$Cl$_2$:Et$_2$O) allowed for separation of the two diastereomers, which provided a total yield of 96% (average of two experiments). Major diastereomer **5.31** was obtained as a white powder. Isoxazolidine **5.31**: R$_f$ 0.33 (5:1 hexanes:EtOAc); ^{1}H-NMR (400 MHz, CDCl$_3$): δ 8.13 (d, J = 8.5, 1H), 8.06 (d, J = 7.8, 1H), 7.86 (d, J = 8.9, 1H), 7.80 (dd, J = 8.2, 1.3, 1H), 7.70 (ddd, J = 9.0, 7.8, 1.4, 1H), 7.51 (ddd, J = 9.0, 7.5, 1.2, 1H), 5.66 (app quint, J = 2.0, 1H), 5.02–5.01 (m, 1H), 4.60–4.56 (m, 1H), 4.35 (dd, J = 10.0, 5.5, 1H), 4.07 (app q, J = 2.6, 2H), 3.21 (dd, J = 10.2, 9.0, 1H), 1.10 (s, 9H); ^{13}C-NMR (100 MHz, CDCl$_3$): δ 163.0, 147.6, 143.3, 136.8, 129.6, 129.1, 127.82, 128.76, 126.3, 120.1, 117.2, 70.5, 68.5, 66.3, 65.1, 59.1, 26.0; IR (film): 3061, 2971, 2866, 1597, 1502 cm^{-1}; HRMS–APCI (m/z) [M + H]$^+$ calcd for C$_{19}$H$_{23}$N$_2$O$_5^+$, 311.17540; found, 311.17394.

The structure of **5.31** was verified by 2D-NOESY, as the following interaction was observed:

5.31

Isoxazolidine 5.32. Following concentration under reduced pressure, the crude residue was obtained (8.7:1 dr, average of two experiments). Purification by sequential preparative thin layer chromatography (99:1 CHCl$_3$:MeOH, eluted once, then 19:1 Et$_2$O:EtOAc, eluted twice) allowed for separation of the two diastereomers, which provided a total yield of 79% (average of two experiments). Major diastereomer **5.32** was obtained as a colorless oil. Isoxazolidine **5.32**: R$_f$ 0.26 (19:1 Et$_2$O:EtOAc); ^{1}H-NMR (500 MHz, CDCl$_3$): δ 5.62–5.57 (m, 1H), 4.45–4.39 (m, 1H), 4.23–4.15 (m, 3H), 4.09–4.03 (m, 1H), 3.29–3.19 (m, 2H), 3.09 (dd, J = 10.0, 9.6, 1H), 2.11–2.03 (m, 1H), 1.91–1.82 (m, 1H), 1.81–1.71 (m, 2H); ^{13}C-NMR (125 MHz, CDCl$_3$): δ 143.5, 116.2, 69.1, 66.9, 66.6, 64.7, 58.1, 32.2, 25.3; IR (film): 3032, 1695, 1414, 1229, 1109 cm^{-1}; HRMS–APCI (m/z) [M + H]$^+$ calcd for C$_9$H$_{14}$NO$_2^+$, 168.10191; found, 168.10434.

The structure of **5.32** was verified by 2D-NOESY, as the following interaction was observed:

5.32

Isoxazolidine 5.33. Following concentration under reduced pressure, the crude residue was obtained (5.3:1 dr, average of two experiments). Purification by preparative thin layer chromatography (4:1 benzene:CH₃CN) allowed for separation of the two diastereomers, which provided a total yield of 94% (average of two experiments). Major diastereomer **5.33** was obtained as a colorless oil. Isoxazolidine **5.33**: R_f 0.53 (1:1 hexanes:EtOAc); ¹H-NMR (400 MHz, CDCl₃): δ 7.29–7.19 (m, 2H), 7.18–7.13 (m, 2H), 5.34 (app quint, J = 2.2, 1H), 5.00 (br s, 1H), 4.54–4.46 (m, 1H), 4.35 (dd, J = 10.3, 5.5, 1H), 4.25 (dq, J = 16.9, 2.4, 1H), 3.99 (dq, J = 16.9, 2.6, 1H), 3.21 (ddd, J = 10.1, 4.5, 3.8, 1H), 3.07–2.98 (m, 2H), 2.84 (ddd, J = 11.7, 10.5, 3.0, 1H), 2.73 (dt, J = 16.2, 3.5, 1H); ¹³C-NMR (100 MHz, CDCl₃): δ 141.0, 134.4, 131.9, 128.6, 128.1, 127.2, 126.3, 119.3, 71.7, 68.9, 64.7, 64.4, 51.3, 28.9; IR (film): 3023, 2964, 2923, 1494, 1454 cm⁻¹; HRMS–APCI (*m/z*) [M + H]⁺ calcd for C₁₄H₁₆NO₂⁺, 230.11756; found, 230.11828.

The structure of **5.33** was verified by 2D-NOESY, as the following interaction was observed:

5.33

**Isoxazolidine 5.34.** In this reaction, nitrone **5.60** was utilized as a mixture of double bond isomers (5:1 ratio, major isomer depicted). Following concentration under reduced pressure, the crude residue was obtained (5.5:1 dr, average of two experiments). Purification by preparative thin layer chromatography (5:1 hexanes:EtOAc) allowed for separation of the two diastereomers, which provided a total yield of 85% (average of two experiments). Major diastereomer **5.34** was obtained as a white solid. Isoxazolidine **5.34**: Mp: 67–68 °C; R$_f$ 0.37 (9:1 hexanes:EtOAc); ^{1}H-NMR (500 MHz, CDCl$_3$): δ 7.67–7.62 (m, 2H), 7.42–7.38 (m, 3H), 6.03–6.00 (m, 1H), 4.63–4.57 (m, 1H), 4.41 (dt, J = 17.3, 2.4, 1H), 4.32 (dd, J = 9.9, 5.4, 1H), 4.20 (dt, J = 17.3, 2.9, 1H), 3.25 (app t, J = 9.4, 1H), 2.62 (s, 3H); ^{13}C-NMR (125 MHz, CDCl$_3$): 139.3, 133.0, 129.3, 128.74, 128.72, 128.6, 125.2 (q, J = 287), 122.8 (q, J = 1.6), 70.7, 66.1, 64.9, 41.4; IR (film): 2971, 2875, 1450, 1268, 1157 cm^{-1}; HRMS–APCI (*m/z*) [M + H]$^+$ calcd for C$_{14}$H$_{15}$F$_3$NO$_2$$^+$, 286.10494; found, 286.10572.

The structure of **5.34** was verified by 2D-NOESY, as the following interaction was observed:

5.34

5.8.2.4 Additional (3+2) and (2+2) Trapping Experiments

Representative Procedure (Preparation of pyrazolidine 5.38 is used as an example).

Pyrazolidine 5.38. To a stirred solution of silyl triflate **5.12** (51.3 mg, 0.148 mmol, 1.0 equiv) and azomethineimine **5.37** (31.0 mg, 0.178 mmol, 1.2 equiv) in CH₃CN (1.48 mL) was added CsF (112 mg, 0.740 mmol, 5.0 equiv). The reaction vessel was sealed with a PTFE lined cap and allowed to stir at 23 °C for 5 h. Then, the crude reaction mixture was filtered by passage through a plug of silica gel (EtOAc eluent, 10 mL). Concentration under reduced pressure yielded the crude residue (7.6:1 dr, average of two experiments). Purification by preparative thin layer chromatography (2:1 benzene:CH₃CN) allowed for separation of the two diastereomers, which were obtained in a total yield of 76% (average of two experiments). The major diastereomer **5.38** was obtained as a colorless oil. Pyrazolidine **5.38**: R_f 0.12 (1:1 hexanes:EtOAc); ¹H-NMR (400 MHz, CDCl₃): δ 7.41–7.31 (m, 5H), 5.61–5.55 (m, 1H), 4.78 (dd, J = 10.2, 4.8, 1H), 4.31–4.22 (m, 3H), 4.20–4.11 (m, 1H), 3.54–3.44 (m, 2H), 3.05 (app q, J = 9.2, 1H), 2.70–2.55 (m, 2H);

^{13}C-NMR (100 MHz, CDCl$_3$): δ 167.9, 141.3, 138.5, 129.1, 128.5, 128.0, 119.7, 72.0, 65.1, 51.8, 49.7, 49.6, 34.7; IR (film): 3060, 2981, 2927, 1678, 1453 cm^{-1}; HRMS–APCI (*m/z*) [M + H]$^+$ calcd for C$_{15}$H$_{17}$N$_2$O$_2$$^+$, 257.12845; found, 257.12933.
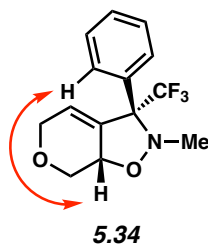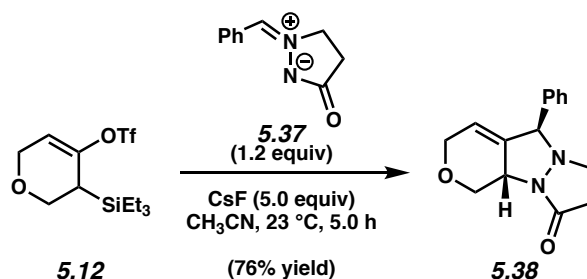
The structure of **5.38** was verified by 2D-NOESY, as the following interaction was observed:
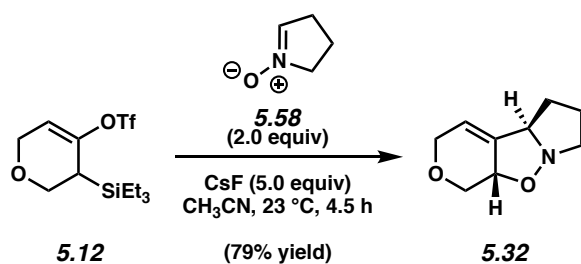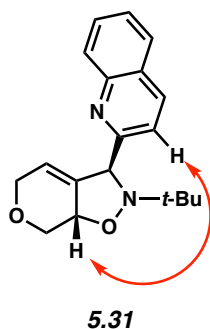

5.38
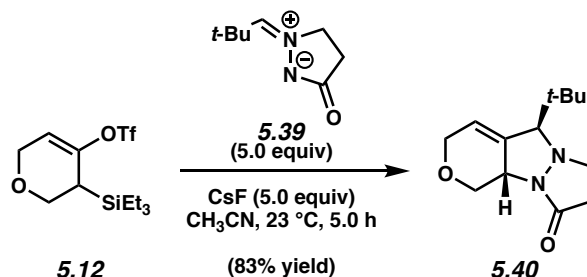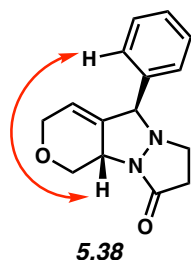
Pyrazolidine 5.40. Following concentration under reduced pressure, the crude residue was obtained (>20:1 dr, average of two experiments). Purification by preparative thin layer chromatography (2:1 benzene: CH$_3$CN) afforded Pyrazolidine **5.40** as a white powder in 83% yield (average of two experiments). Pyrazolidine **5.40**: Mp: 120–122 °C; R$_f$ 0.15 (1:1 hexanes:EtOAc); ^{1}H-NMR (400 MHz, CDCl$_3$): δ 5.57 (app quint, *J* = 2.0, 1H), 4.88 (dd, *J* = 10.7, 5.4, 1H), 4.27 (dq, *J* = 16.8, 2.4, 1H), 4.14–4.06 (m, 1H), 3.93–3.85 (m, 1H), 3.67–3.58 (m, 1H), 3.42 (dd, *J* = 10.6, 9.8, 1H), 2.91–2.77 (m, 3H), 2.57–2.45 (m, 1H), 0.93 (s, 9H); ^{13}C-NMR (100 MHz, CDCl$_3$): δ 164.0, 138.0, 120.7, 78.9, 65.7, 65.2, 56.3, 51.1, 35.3, 35.2, 26.3; IR

(film): 2955, 2868, 1679, 1445, 1421 cm^{-1}; HRMS–APCI (*m/z*) [M + H]$^+$ calcd for C$_{13}$H$_{21}$N$_2$O$_2^+$, 237.15975; found, 237.16054.

The structure of **5.40** was verified by 2D-NOESY, as the following interaction was observed:

5.40
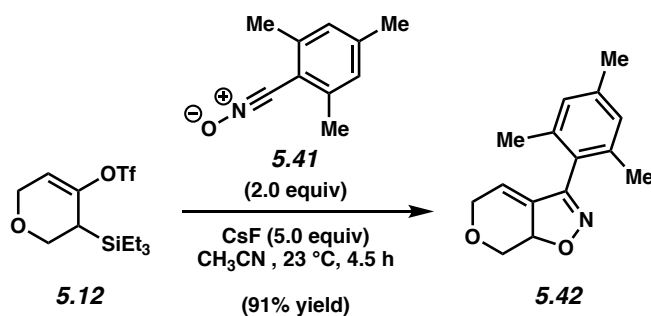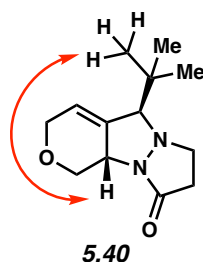
Isoxazoline 5.42. Purification by preparative thin layer chromatography (5:1 hexanes:EtOAc) afforded isoxazoline **5.42** as a clear, colorless oil (91% yield, average of two experiments). Isoxazoline **5.42**: R$_f$ 0.36 (9:1 hexanes:EtOAc); ^{1}H-NMR (500 MHz, CDCl$_3$): δ 6.94–6.90 (m, 2H), 5.60–5.58 (m, 1H), 5.02–4.96 (m, 1H), 4.55 (dd, *J* = 9.6, 5.4, 1H), 4.36 (ddd, *J* = 18.4, 4.6, 2.4, 1H), 4.20 (ddd, *J* = 18.4, 5.0, 3.0, 1H), 3.35 (app t, *J* = 9.3, 1H), 2.31 (s, 3H), 2.20 (s, 3H), 2.18 (s, 3H); ^{13}C-NMR (100 MHz, CDCl$_3$): δ 156.7, 140.6, 139.2, 137.6, 137.3, 128.51, 128.48, 123.6, 120.1, 75.0, 66.0, 64.5, 21.2, 20.0, 19.7; IR (film) 2975, 2865, 1736, 1612, 1113 cm^{-1}; HRMS–APCI (*m/z*) [M + H]$^+$ calcd for C$_{15}$H$_{18}$NO$_2^+$, 244.13321; found, 244.13475.

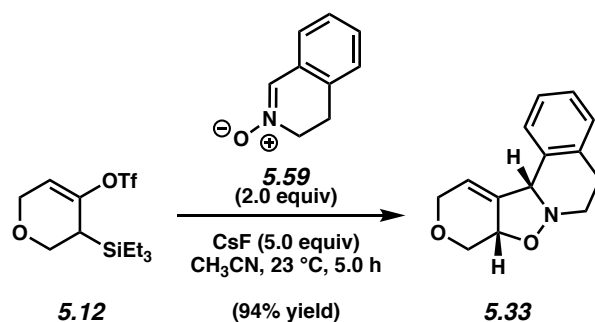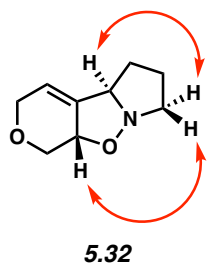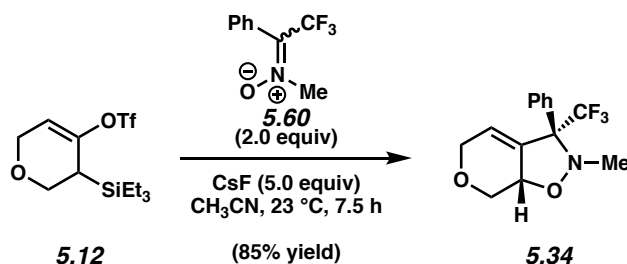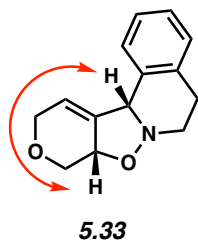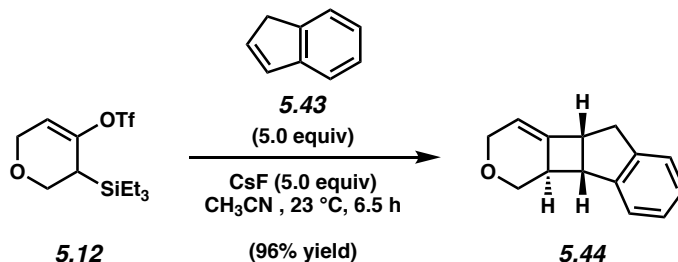**Cyclobutane 5.44.** Following concentration under reduced pressure, the crude residue was obtained (5.2:1 dr, average of two experiments). Purification by successive preparative thin layer chromatography (20:5:1 hexanes:CH$_2$Cl$_2$:Et$_2$O, eluted twice) allowed for separation of the two diastereomers, which provided a total yield of 96% (average of two experiments). Major diastereomer **5.44** was obtained as a colorless oil. Cyclobutane **5.44**: R$_f$ 0.48 (9:1 hexanes:EtOAc); ^{1}H-NMR (500 MHz, CDCl$_3$): δ 7.30–7.23 (m, 1H), 7.21–7.12 (m, 3H), 5.47–5.42 (m, 1H), 4.32–4.26 (m, 1H), 4.19–4.10 (m, 2H), 3.83–3.75 (m, 1H), 3.63–3.59 (m, 1H), 3.34–3.25 (m, 2H), 3.21 (app t, J = 9.8, 1H), 3.07–3.00 (m, 1H); ^{13}C-NMR (125 MHz, CDCl$_3$): δ 146.0, 145.9, 141.4, 126.8, 126.7, 125.3, 123.5, 113.0, 66.9, 65.5, 50.1, 49.3, 48.8, 37.3; IR (film): 3067, 3041, 2939, 2844, 1480 cm^{-1}; HRMS–APCI (*m/z*) [M + H]$^+$ calcd for C$_{14}$H$_{15}$O$^+$, 199.11174; found, 199.11236.

The structure of **5.44** was verified by 2D-NOESY, as the following interaction was observed:

5.44
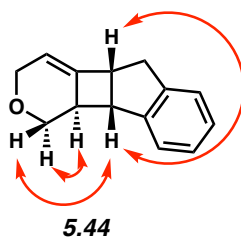
5.8.2.5 Synthesis of the Allylation Substrates

In addition to **5.45**, enol carbonates **5.63**, **5.64**, and **5.65** were prepared in order to determine the optimal substrate and conditions for the asymmetric allylic alkylation. The enol carbonates were then tested in the subsequent Pd-catalyzed allylic alkylation in Section 5.8.2.6.
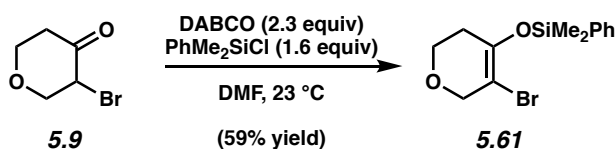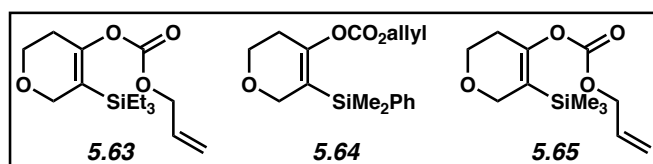
Silyl enol ether 5.61. To a stirred solution of known bromo ketone **5.9**[25] (300 mg, 1.68 mmol, 1.0 equiv) in DMF (1.52 mL) and PhMe$_2$SiCl (0.45 mL, 2.68 mmol, 1.6 equiv) was added DABCO (432 mg, 3.85 mmol, 2.3 equiv). The reaction vessel was then purged with N$_2$ and sealed with a PTFE lined cap, before allowing it to stir at 23 °C. After 12 h, the mixture was cooled to –40 °C for 10 min before quenching the reaction with sat. NaHCO$_3$ (2.0 mL) and water (4.0 mL). The layers were then separated and the aqueous layer was then extracted with EtOAc (3 x 10 mL). The combined organic layers were washed with water (2 x 10 mL) and brine (1 x 10 mL), before being dried with Na$_2$SO$_4$, filtered, and concentrated under reduced pressure. The resultant crude oil was purified via flash chromatography (19:1 hexanes:EtOAc) to afford silyl enol ether **5.61** as a colorless oil (308.5 mg, 59% yield). Silyl enol ether **5.61**: R$_f$ 0.48 (9:1 hexanes:EtOAc); ^{1}H-NMR (500 MHz, C$_6$D$_6$): δ 7.59–7.53 (m, 2H), 7.20–7.14 (m, 3H), 4.10–4.07 (m, 2H), 3.27 (t, J = 5.5, 2H), 1.83–1.77 (m, 2H), 0.37 (s, 6H); ^{13}C-NMR (125 MHz, C$_6$D$_6$): δ 145.1, 137.5, 133.7, 130.3, 98.8, 69.8, 64.7, 32.9, –0.5; IR (film): 3071, 2964, 2828, 1675,

1428 cm^{-1}; HRMS–APCI (*m/z*) [M + H]$^+$ calcd for C$_{13}$H$_{18}$BrO$_2$Si$^+$, 313.02540; found, 313.02630.
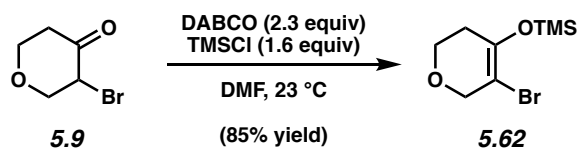
Silyl enol ether 5.62. To a stirred solution of known bromo ketone **5.9**[25] (100 mg, 0.559 mmol, 1.0 equiv) and TMSCl (0.11 mL, 0.894 mmol, 1.6 equiv) in DMF (0.51 mL) was added DABCO (144 mg, 1.28 mmol, 2.3 equiv). The reaction vessel was then purged with N$_2$ and sealed with a PTFE lined cap, before allowing it to stir at 23 °C. After 22 h, the mixture was cooled to –40 °C for 10 min and quenched with sat. aq. NaHCO$_3$ (0.5 mL) and deionized water (0.5 mL). The layers were then separated and the aqueous layer was extracted with EtOAc (3 x 3 mL). The combined organic layers were washed with water (2 x 5 mL) and brine (1 x 5 mL), before being dried with Na$_2$SO$_4$, filtered, and concentrated under reduced pressure. The resultant crude oil was purified via flash chromatography (19:1 hexanes:EtOAc) to afford silyl enol ether **5.62** as a colorless oil (119.1 mg, 85% yield). Silyl enol ether **5.62**: R$_f$ 0.49 (9:1 hexanes:EtOAc); ^{1}H-NMR (400 MHz, C$_6$D$_6$): δ 4.10 (t, *J* = 2.3, 2H), 3.35 (t, *J* = 5.5, 2H), 1.86–1.81 (m, 2H), 0.10 (s, 9H); ^{13}C-NMR (100 MHz, C$_6$D$_6$): δ 144.7, 98.2, 69.4, 64.4, 32.6, 0.4; IR (film): 2968, 2861, 1675, 1265, 1252 cm^{-1}; HRMS–APCI (*m/z*) [M + H]$^+$ calcd for C$_8$H$_{16}$BrO$_2$Si$^+$, 253.00770; found, 253.00876.
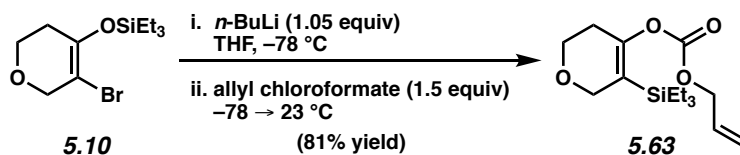
Enol carbonate 5.63. To a solution of known silyl enol ether **5.10**[25] (330 mg, 1.13 mmol, 1.00 equiv) in THF (13.2 mL) at –78 °C was added *n*-BuLi (2.24 M in hexanes, 0.527 mL, 1.18 mmol, 1.05 equiv) dropwise over 2.0 min. The solution was stirred for 34 min at –78 °C, before neat allyl chloroformate (0.180 mL, 1.69 mmol, 1.5 equiv) was then added dropwise over 1 min and the reaction was allowed to stir for 1.0 h at –78 °C, before warming to 23 °C. After stirring for 2.0 h, the reaction was quenched with water (10 mL). The layers were then separated and the aqueous layer was extracted with EtOAc (3 x 10 mL). The combined organic layers were then dried over Na_2SO_4, filtered, and concentrated under reduced pressure. The resulting crude oil was purified by flash chromatography (19:1 hexanes:EtOAc) to afford enol carbonate **5.63** (273.1 mg, 81% yield) as a colorless oil. Enol carbonate **5.63**: R_f 0.58 (5:1 hexanes:EtOAc); ^{1}H-NMR (600 MHz, $CDCl_3$): δ 5.99–5.91 (m, 1H), 5.39 (dq, *J* = 17.2, 1.4, 1H), 5.30 (dq, *J* = 1.4, 1.3, 1H), 4.66 (dt, *J* = 5.9, 1.3, 2H), 4.22 (t, *J* = 2.6, 2H), 3.85 (t, *J* = 5.6 6H), 2.41 (s, *J* = 2.6, 2H), 0.93 (t, *J* = 8.0, 9H), 0.62 (q, *J* = 8.0, 6H); ^{13}C-NMR (100 MHz, $CDCl_3$): δ 152.9, 151.7, 131.5, 120.1, 119.4, 68.8, 67.5, 64.3, 28.1, 7.4, 3.0; IR (film): 2954, 1754, 1657, 1228, 1161 cm$^{–1}$; HRMS–APCI (*m/z*) [M + H]$^+$ calcd for $C_{15}H_{27}O_4Si^+$, 299.16731; found, 299.16694.
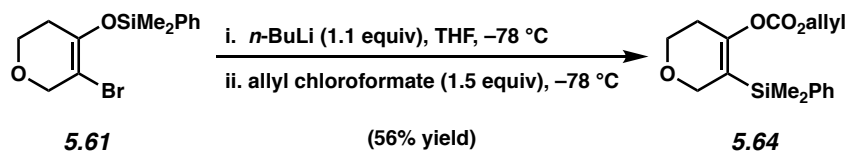
Enol carbonate 5.64. To a solution of silyl enol ether **5.61** (150.0 mg, 0.479 mmol, 1.00 equiv) in THF (5.6 mL) at –78 °C was added *n*-BuLi (2.22 M in hexanes, 0.237 mL, 0.527 mmol, 1.1

307

equiv) dropwise over 1.0 min. The solution was stirred for 20 min at –78 °C, then neat allyl

chloroformate (76.6 μL, 0.718 mmol, 1.5 equiv) was added dropwise over 1 min and the reaction

was allowed to stir at –78 °C. After stirring for 4.0 h, the reaction was quenched with water (4.0

mL) at –78 °C. The layers were then separated and the aqueous layer was extracted with EtOAc

(3 x 10 mL). The combined organic layers were dried over Na$_2$SO$_4$, filtered, and concentrated

under reduced pressure. The resulting crude oil was purified by flash chromatography (15:1

hexanes:EtOAc) to afford enol carbonate **5.64** (84.6 mg, 56% yield) as a colorless oil. Enol

carbonate **5.64**: R$_f$ 0.31 (9:1 hexanes:EtOAc); ^{1}H-NMR (500 MHz, CD$_3$CN): δ 7.54–7.49 (m,

2H), 7.39–7.31 (m, 3H), 5.92–5.82 (m, 1H), 5.33–5.27 (m, 1H), 5.25–5.21 (m, 1H), 4.47–4.43

(m, 2H), 4.17–4.14 (m, 2H), 3.78–3.75 (m, 2H), 2.32–2.27 (m, 2H), 1.92 (app quint, J = 2.4,

2H), 0.34 (s, 6H); ^{13}C-NMR (125 MHz, CD$_3$CN): δ 153.4, 153.3, 138.2, 134.7, 132.8, 130.3,

128.8, 121.8, 119.3, 69.4, 67.6, 64.8, 28.7, –2.8; IR (film): 2958, 2855, 1755, 1428, 1253 cm^{-1};

HRMS–APCI (*m/z*) [M + H]$^+$ calcd for C$_{17}$H$_{23}$O$_4$Si$^+$, 319.13601; found, 319.13757.
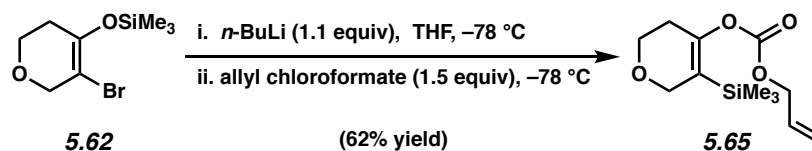
Enol carbonate 5.65. To a solution of silyl enol ether **5.62** (60.0 mg, 0.239 mmol, 1.00 equiv) in

THF (2.8 mL) at –78 °C was added *n*-BuLi (2.25 M in hexanes, 0.117 mL, 0.263 mmol, 1.1

equiv) dropwise over 2.0 min. The solution was stirred for 21 min at –78 °C, then neat allyl

chloroformate (38.2 μL, 0.385 mmol, 1.5 equiv) was added dropwise over 1 min and the reaction

was allowed to stir at –78 °C. After stirring for 3.0 h, the reaction was quenched with water (2.0

mL). The layers were then separated and the aqueous layer was extracted with EtOAc (3 x 5

mL). The combined organic layers were then dried over Na$_2$SO$_4$, filtered, and concentrated under

reduced pressure. The resulting crude oil was purified by flash chromatography (15:1 hexanes:EtOAc) to afford enol carbonate **5.65** (37.7 mg, 62% yield) as a colorless oil. Enol carbonate **5.65**: R_f 0.29 (9:1 hexanes:EtOAc); ^{1}H-NMR (500 MHz, C_6D_6): δ 5.68–5.59 (m, 1H), 5.07 (dq, J = 17.2, 1.7, 1H), 4.91 (dq, J = 10.3, 1.2, 1H), 4.36 (dt, J = 5.8, 1.4, 2H), 4.13 (t, J = 2.6, 2H), 3.55 (t, J = 5.6, 2H), 2.26–2.21 (m, 2H), 0.06 (s, 9H); ^{13}C-NMR (125 MHz, C_6D_6): δ 153.3, 152.1, 131.9, 122.4, 118.7, 68.5, 67.0, 64.2, 28.3, –1.5; IR (film): 2956, 2856, 1755, 1252, 1231 cm^{-1}; HRMS–APCI (m/z) [M + H]$^+$ calcd for $C_{12}H_{21}O_4Si^+$, 257.12036; found, 257.12173.
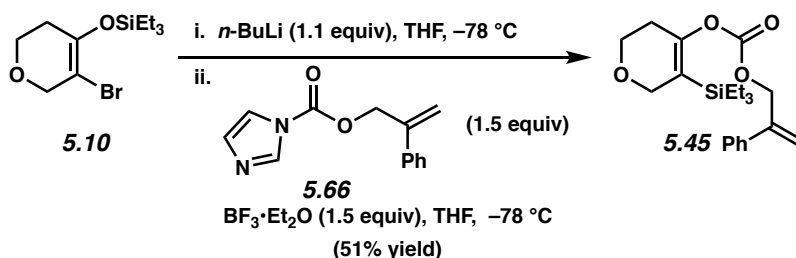
Enol carbonate 5.45. To a solution of silyl enol ether **5.10** (601.0 mg, 2.05 mmol, 1.00 equiv) in THF (24.1 mL) at –78 °C was added n-BuLi (2.19 M in hexanes, 1.03 mL, 2.25 mmol, 1.1 equiv) dropwise over 1.0 min. The solution was stirred for 45 min at –78 °C, then a solution of the known imidazole carboxylate[39] **5.66** (702 mg, 3.07 mmol, 1.50 equiv) and BF$_3$•Et$_2$O (390 µL, 2.25 mmol, 1.5 equiv) in THF (4.0 mL) that was prestirred for 35 min (at 23 °C) was added dropwise over 5 min and the reaction was allowed to stir at –78 °C. After stirring for 3.0 h the reaction was quenched with water (10.0 mL) at –78 °C. The layers were separated and the aqueous layer was extracted with EtOAc (3 x 50 mL). The combined organic layers were then dried over Na$_2$SO$_4$, filtered, and concentrated under reduced pressure. The resulting crude oil was purified by flash chromatography (19:1 hexanes:EtOAc) to afford enol carbonate **5.45** (391 mg, 51% yield) as a colorless oil. Enol carbonate **5.45**: R_f 0.54 (9:1 hexanes:EtOAc); ^{1}H-NMR (500 MHz, CDCl$_3$): δ 7.47–7.43 (m, 2H), 7.38–7.29 (m, 3H), 5.60 (br s, 1H), 5.44 (q, J = 1.0,

1H), 5.10 (d, $J = 0.9$, 2H), 4.20 (t, $J = 2.6$, 2H), 3.82 (t, $J = 5.5$, 2H), 2.39–2.34 (m, 2H), 0.89 (t,

$J = 7.8$, 9H), 0.57 (q, $J = 7.6$, 6H); ^{13}C-NMR (100 MHz, CDCl$_3$): δ 152.9, 151.6, 142.1, 137.8,

128.7, 128.3, 126.2, 120.1, 116.4, 69.6, 67.5, 64.3, 28.1, 7.4, 3.0; IR (film): 2953, 1755, 1656,

1230, 1165 cm^{-1}; HRMS–APCI (m/z) [M + H]$^+$ calcd for C$_{21}$H$_{31}$O$_4$Si$^+$, 375.19861; found,

357.20141.

5.8.2.6 Pd-Catalyzed Decarboxylative Allylic Alkylation

5.8.2.6.1 Racemic Reactions Toward α-Silyl Substituted Ketones

Representative Procedure for Racemic Reactions (Preparation of silyl ketone rac-5.67 used as an example).
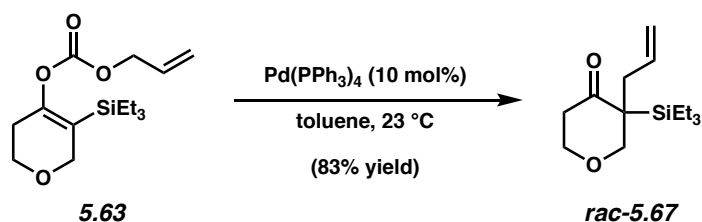
Silyl Ketone rac-5.67. In a nitrogen-filled glovebox, an oven-dried 1-dram vial was equipped

with a stir bar, enol carbonate **5.63** (100 mg, 0.335 mmol, 1.0 equiv), and toluene (1.7 mL). Then

Pd(PPh$_3$)$_4$ (38.7 mg, 0.034 mmol, 10 mol%) was added slowly in one portion, before sealing the

vial with a PTFE-lined cap. The reaction was then allowed to stir for 20 h at 23 °C before the

addition of hexanes (2 mL). After stirring for 2 min, the crude reaction mixture was filtered by

passage through a plug of silica gel (Et$_2$O eluent), and concentrated under reduced pressure. The

resulting crude oil was purified via flash chromatography (19:1 hexanes:EtOAc), to provide silyl

ketone **rac-5.67** as a colorless oil (70.5 mg, 83% yield). Silyl ketone **rac-5.67**: R$_f$ 0.58 (5:1

hexanes:EtOAc); ^{1}H-NMR (500 MHz, CDCl$_3$): δ 5.77–5.67 (m, 1H), 5.05–4.96 (m, 2H), 4.19–

4.13 (m, 1H), 4.10 (dd, $J = 11.8$, 1.3, 1H), 3.76 (d, $J = 11.7$, 1H), 3.69 (ddd, $J = 11.4$, 11.4, 4.0,

1H), 2.99–2.93 (m, 1H), 2.55 (ddd, J = 16.6, 11.5. 7.7, 1H), 3.32 (ddd, J = 16.6, 4.0, 2.0, 1H), 1.92 (dd, J = 14.1, 8.8, 1H), 1.00 (t, J = 7.9, 9H), 0.80–0.66 (m, 6H); ^{13}C-NMR (125 MHz, CDCl$_3$): δ 208.7, 135.3, 117.6, 71.2, 67.0, 50.5, 41.3, 35.1, 7.8, 2.9; IR (film): 2956, 1682, 1211, 1187, 1005 cm^{-1}; HRMS–APCI (m/z) [M + H]$^+$ calcd for C$_{14}$H$_{27}$O$_2$Si$^+$, 255.17748; found, 255.17914.
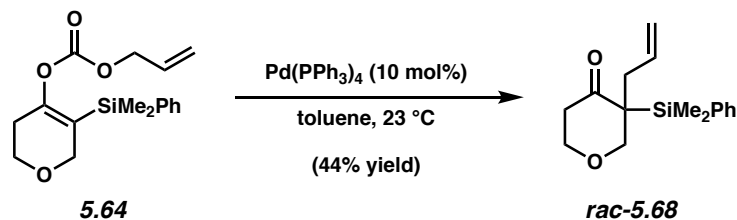
Silyl ketone rac-5.68. Purification by preparative thin layer chromatography (9:1 hexanes:EtOAc) afforded silyl ketone **rac-5.68** as a colorless oil (44% yield). Silyl ketone **rac-5.68**: R$_f$ 0.14 (3:1 hexanes:EtOAc); ^{1}H-NMR (500 MHz, CDCl$_3$): δ 7.55–7.51 (m, 2H), 7.43–7.35 (m, 3H), 5.69–5.59 (m, 1H), 5.00–4.90 (m, 2H), 4.07 (dd, J = 11.8, 1.4, 1H), 4.05–4.00 (m, 1H), 3.70 (d, J = 11.7, 1H), 3.68–3.62 (m, 1H), 2.88 (ddt, J = 14.2, 5.5, 1.6, 1H), 2.22–2.18 (m, 2H), 1.88 (dd, J = 14.3, 8.7, 1H), 0.49 (s, 3H), 0.42 (s, 3H); ^{13}C-NMR (125 MHz, CDCl$_3$): δ 208.5, 135.1, 134.8, 134.7, 129.8, 127.9, 117.6, 71.2, 67.0, 50.4, 40.7, 34.7, –3.6, –4.8; IR (film): 3071, 2963, 2853, 1681, 1428 cm^{-1}; HRMS–APCI (m/z) [M + H]$^+$ calcd for C$_{16}$H$_{23}$O$_2$Si$^+$, 275.14618; found, 275.14746.
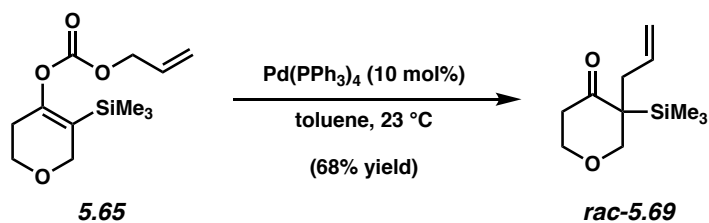
Silyl ketone rac-5.69. Purification by flash chromatography (15:1 hexanes:EtOAc) afforded silyl ketone **rac-5.69** as a colorless oil (68% yield). Silyl ketone **rac-5.69**: R$_f$ 0.26 (9:1 hexanes:EtOAc); ^{1}H-NMR (500 MHz, CDCl$_3$): δ 5.77–5.67 (m, 1H), 5.05–4.96 (m, 2H), 4.19–

4.13 (m, 1H), 4.07 (d, $J = 11.8$, 1H), 3.78 (d, $J = 11.8$, 1H), 3.70 (ddd, $J = 11.6, 11.6, 3.9$, 1H), 2.85 (dd, $J = 14.2, 5.4$, 1H), 2.54–2.45 (m, 1H), 2.36–2.29 (m, 1H), 1.89 (dd, $J = 14.3, 8.8$, 1H), 0.13 (s, 9H); ^{13}C-NMR (125 MHz, CDCl$_3$): δ 208.5, 135.0, 117.7, 71.1, 67.1, 50.1, 41.2, 34.5, –2.5; IR (film): 3076, 2925, 2853, 1682, 1251 cm^{-1}; HRMS–APCI (m/z) [M + H]$^+$ calcd for C$_{11}$H$_{21}$O$_2$Si$^+$, 213.13053; found, 213.13138.
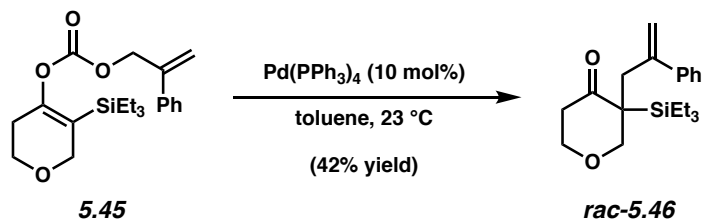
Silyl ketone rac-5.46. Purification by preparative thin layer chromatography (9:1 hexanes:EtOAc) afforded silyl ketone **rac-5.46** as a colorless oil (42% yield). Silyl ketone **rac-5.46**: R$_f$ 0.34 (9:1 hexanes:EtOAc); ^{1}H-NMR (600 MHz, CDCl$_3$): δ 7.32–7.27 (m, 4H), 7.26–7.22 (m, 1H), 5.20 (d, $J = 1.4$, 1H), 5.07 (s, 1H), 3.98–3.92 (m, 2H), 3.74–3.69 (m, 2H), 3.41 (ddd, $J = 11.1, 11.1, 4.9$, 1H), 2.44 (d, $J = 14.4$, 1H), 2.36 (ddd, $J = 17.6, 10.7, 8.2$, 1H), 1.94 (ddd, $J = 17.7, 4.8, 2.5$, 1H), 1.02 (t, $J = 7.9$, 9H), 0.84–0.69 (m, 6H); ^{13}C-NMR (125 MHz, CDCl$_3$): δ 208.3, 147.0, 141.7, 128.1, 127.5, 127.4, 116.8, 70.3, 66.1, 50.7, 40.1, 35.7, 7.8, 2.8; IR (film): 2955, 2877, 1680, 1444, 1188 cm^{-1}; HRMS–APCI (m/z) [M + H]$^+$ calcd for C$_{21}$H$_{31}$O$_4$Si$^+$, 331.20878; found, 331.20983.

5.8.2.6.2 Additional Asymmetric Allylic Alkylation Optimization Reactions

Representative Procedure for Optimization Reactions for Table 5.2, Table 5.3, Table 5.4, and Table 5.5.

In a nitrogen-filled glovebox, an oven-dried 1-dram vial was equipped with a stir bar, ligand (6.25 μmol, 12.5 mol %), Pd$_2$(dba)$_3$ (2.50 μmol, 5 mol %), and toluene (0.75 mL). The

vial was then capped with a PTFE-lined cap and stirred at 23 °C for 30 min before cooling to the desired temperature. A solution of enol carbonate starting material (0.05 mmol, 1 equiv) in toluene (0.75 mL) was slowly added over 1 min to the catalyst mixture. The vial was sealed with a PTFE-lined cap and stirred at the desired temperature for 20 h. The crude reaction mixture was filtered through a silica plug, eluted with Et$_2$O, and concentrated under reduced pressure. 1,3,5-Trimethoxybenzene was used then added and used as an external standard in quantitative NMR analysis.

Table 5.3. Additional Optimization Experiments.
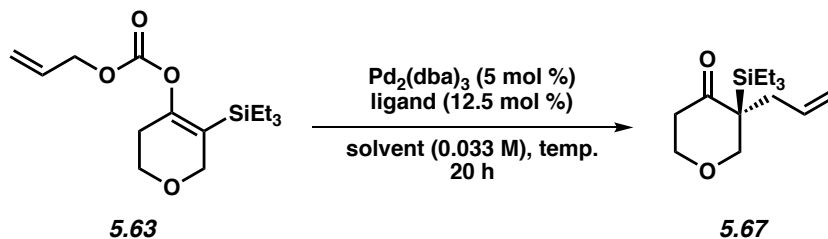
entry	ligand	solvent	temp (°C)	% conversion[b]	% ee[c]
1	*5.70*	toluene	23	>95	21
2	*5.71*	toluene	23	>95	2
3	*5.72*	toluene	23	>95	7
4	*5.73*	toluene	23	>95	13
5	*5.74*	toluene	23	>95	0
6	*5.47*	toluene	23	>95	62
7	*5.75*	toluene	23	>95	53
8	*5.76*	toluene	23	47	61
9	*5.77*	toluene	23	>95	58
10	*5.47*	THF	23	>95	47
11	*5.47*	1,4-dioxane	23	>95	57
12	*5.47*	MTBE	23	>95	52
13	*5.47*	benzene	23	>95	60
14	*5.47*	2:1 hexanes:toluene	23	>95	61
15	*5.47*	toluene	0	>95	68
16	*5.47*	toluene	−10	>95	70

[a]Conditions: enol carbonate (0.05 mmol), Pd$_2$(dba)$_3$ (5 mol %), and ligand (12.5 mol %) for 20 h. [b]Conversion determined by ^{1}H NMR analysis of the crude reaction mixture using 1,3,5-trimethoxybenzene as a standard. [c]Determined by chiral SFC analysis of the isolated product.
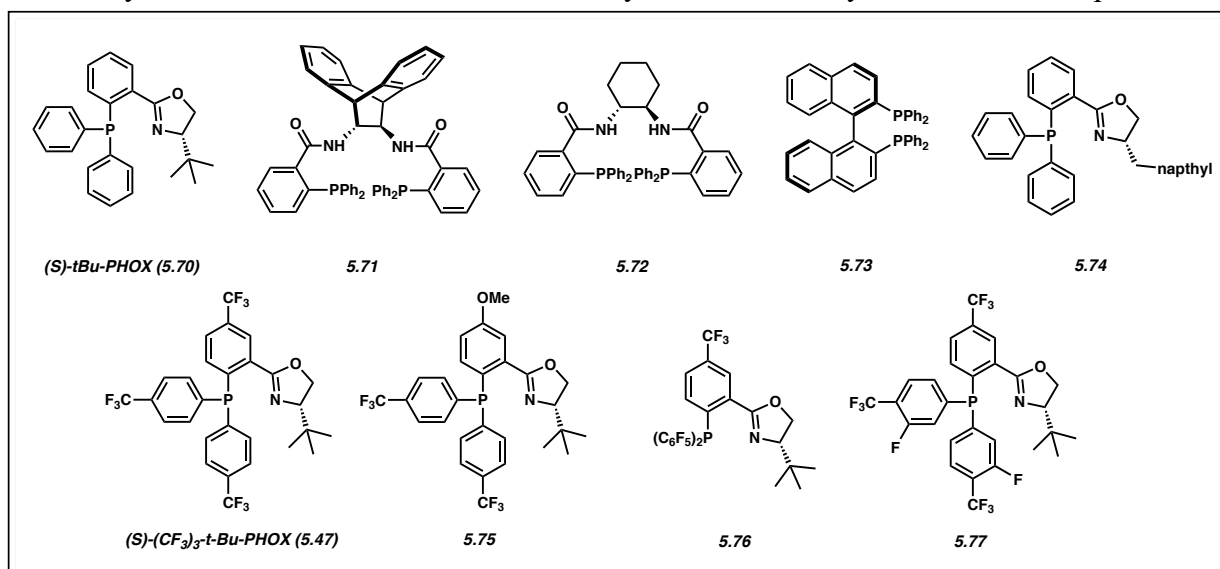
Table 5.4. Testing Alternative Palladium Sources**.**
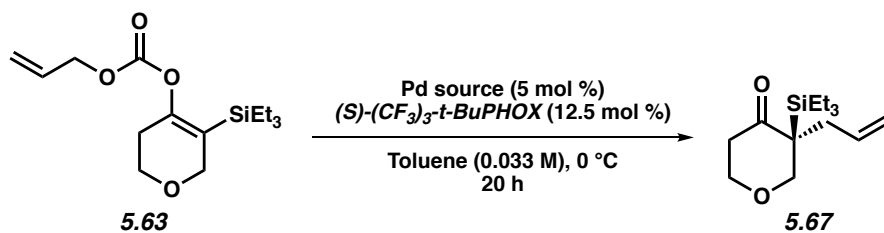
entry	Pd source	% conversion[b]	% ee[c]
1	Pd$_2$(dba)$_3$	>95	68
2	Pd(dmdba)$_2$[d]	>95	68
3	Pd$_2$(pmdba)$_3$	>95	68
4	[PdCl(allyl)]$_2$	<10	–

[a]Conditions: enol carbonate (0.05 mmol), Pd source (5 mol %), and ligand (12.5 mol %) for 20 h. [b]Conversion determined by ^{1}H NMR analysis of the crude reaction mixture using 1,3,5-trimethoxybenzene as an external standard. [c]Determined by chiral SFC analysis of isolated product. [d]Used 10 mol% of Pd source.

Table 5.5. Substrate, Temperature, and Concentration Optimization Experiments**.**
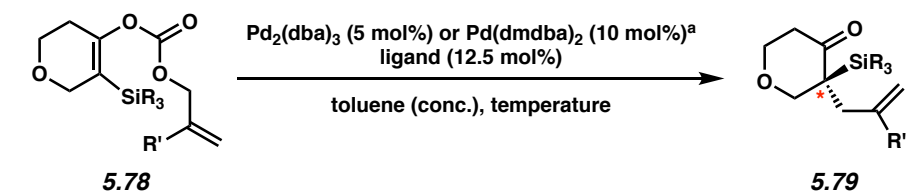
Entry	Ligand	SiR$_3$	R'	temperature	conc. (M)	%ee[b]	yield[c]
1	**5.70**	SiEt$_3$	H	23 °C	0.033	25	51%
2	**5.47**	SiEt$_3$	H	23 °C	0.033	62	85%
3	**5.47**	SiMe$_2$Ph	H	23 °C	0.033	58	69%
4	**5.47**	SiMe$_3$	H	23 °C	0.033	70	88%
5	**5.47**	SiMe$_3$	H	−10 °C	0.005	75	85%
6	**5.47**	SiEt$_3$	H	−10 °C	0.005	74	95%
7	**5.47**	SiEt$_3$	Ph	−10 °C	0.005	81	75%

(S)-tBu-PHOX (5.70)

(S)-(CF$_3$)$_3$-tBu-PHOX (5.47)
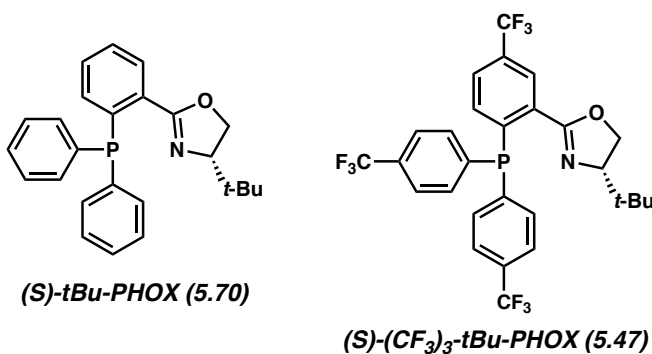
[a]Reactions performed at 23 °C utilized Pd$_2$(dba)$_3$, while reactions performed at −10 °C utilized Pd(dmdba)$_2$. Utilizing different palladium sources did not have an observable effect on enantioselectivity (see Table 5.4 for details) and was only utilized to aid purification. [b]Enantiomeric excesses (ee's) were determined by SFC analysis using a chiral stationary phase. [c]Yields were determined by ^{1}H NMR analysis using 1,3,5-trimethoxybenzene as an external standard.
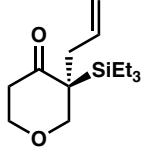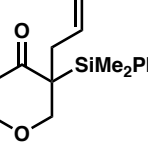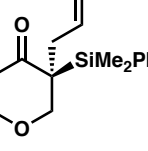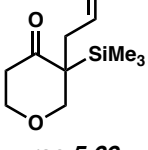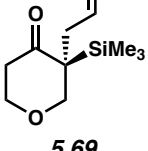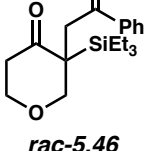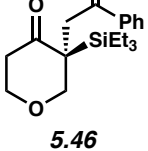
5.8.2.6.3 Optimized Decarboxylative Allylic Alkylation Reactions

Representative Procedure for Pd-Catalyzed Decarboxylative Allylic Alkylation Reactions.
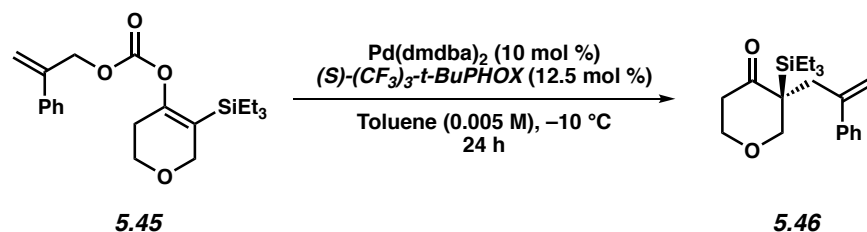
In a nitrogen-filled glovebox, an oven-dried scintillation vial was equipped with a stir bar, *(S)*-(CF₃)₃-*t*-BuPHOX ligand (3.70 mg, 6.25 μmol, 12.5 mol %), Pd(dmdba)₂ (4.08 mg, 5.00 μmol, 10 mol %), and toluene (0.75 mL). The vial was then sealed with a PTFE-lined cap and stirred at 23 °C. After 30 min, the catalyst mixture was diluted with 8.5 mL of toluene and cooled to –10 °C. A solution of enol carbonate starting material (0.05 mmol, 1 equiv) in toluene (0.75 mL) was added dropwise to the catalyst mixture. The vial was sealed with a PTFE-lined septum cap and stirred at –10 °C for 24 h. The crude reaction mixture was filtered through a silica plug (Et₂O eluent), concentrated under reduced pressure, and purified by flash chromatography to furnish the product. Silyl ketones **5.67**, **5.68**, **5.69**, **and 5.46** spectral data matched those previously reported (See Section 5.8.2.6.1).

Compound	Method Column/Temp.	Solvent	Method Flow Rate	Retention Times (min)	Enantiomeric Ratio (er)
rac-5.67	ChiralPak AD-3/40°C	3% isopropanol in CO_2	2.5 mL/min	2.81/3.13	49.1:50.9

5.67	ChiralPak AD-3/40°C	3% isopropanol in CO_2	2.5 mL/min	2.80/3.12	87.0:13.0
rac-5.68	ChiralPak IC-3/35°C	2% isopropanol in CO_2	3.5 mL/min	7.47/9.01	50.4/49.6
5.68	ChiralPak IC-3/35°C	2% isopropanol in CO_2	3.5 mL/min	9.76/11.9	77.0/23.0
rac-5.69	ChiralPak IC-3/40°C	1% isopropanol in CO_2	2.5 mL/min	7.05/7.91	49.2/50.8
5.69	ChiralPak IC-3/40°C	1% isopropanol in CO_2	2.5 mL/min	6.67/7.67	87.7/12.3
rac-5.46	Chiralcel IC-3/40°C	2% isopropanol in CO_2	2.5 mL/min	4.37/4.93	50.8/49.2
5.46	Chiralcel IC-3/40°C	2% isopropanol in CO_2	2.5 mL/min	4.47/5.05	90.3/9.7
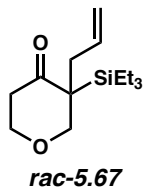
rac-5.67

Signal 1: DAD1 A, Sig=210,8 Ref=360,100

Peak #	RetTime [min]	Type	Width [min]	Area [mAU*s]	Height [mAU]	Area %
1	2.808	MF	0.1586	169.78801	17.84176	49.1226
2	3.132	FM	0.1629	175.85304	17.98790	50.8774

Figure 5.4. SFC trace for **rac-5.67**.
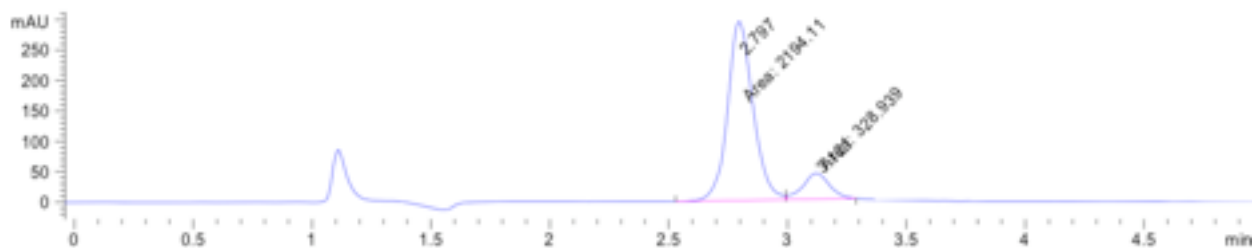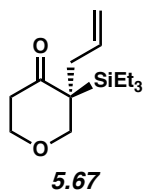
5.67

Signal 1: DAD1 A, Sig=210,8 Ref=360,100

Peak #	RetTime [min]	Type	Width [min]	Area [mAU*s]	Height [mAU]	Area %
1	2.797	MF	0.1241	2194.10840	294.65942	86.9626
2	3.121	FM	0.1286	328.93912	42.63451	13.0374

Figure 5.5. SFC trace for **5.67**.
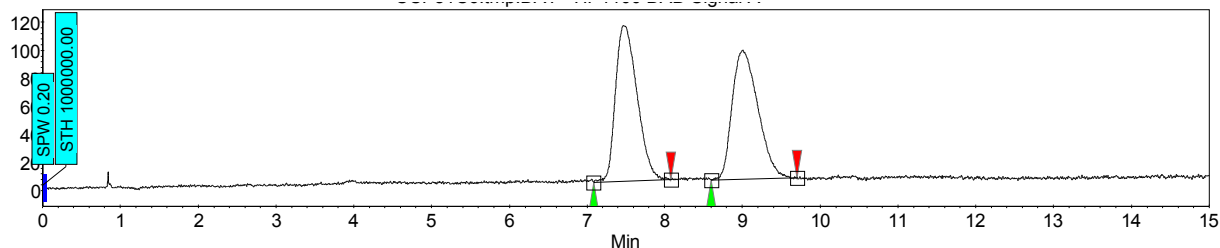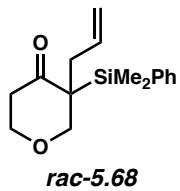
319

rac-5.68

Index	Name	Start	Time	End	RT Offset	Quantity	Height	Area	Area
		[Min]	[Min]	[Min]	[Min]	[% Area]	[μV]	[μV.Min]	[%]
1	UNKNOWN	7.09	7.47	8.09	0.00	50.38	110.9	35.9	50.385
2	UNKNOWN	8.60	9.01	9.71	0.00	49.62	92.2	35.4	49.615
Total						100.00	203.1	71.3	100.000

Figure 5.6. SFC trace for **rac-5.68**.
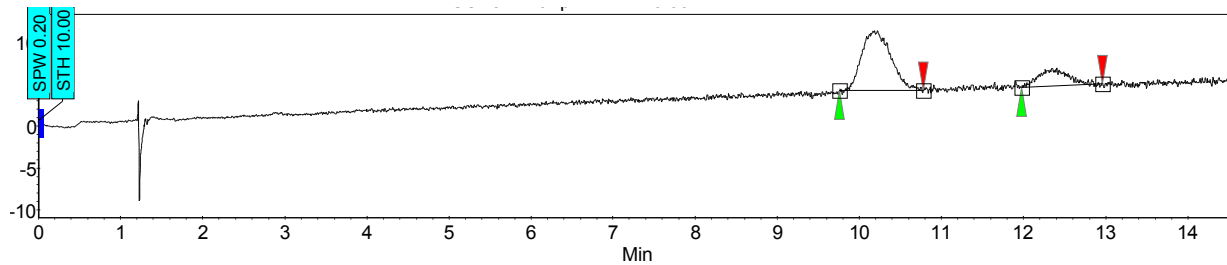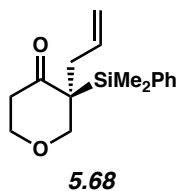
5.68

Index	Name	Start	Time	End	RT Offset	Quantity	Height	Area	Area
		[Min]	[Min]	[Min]	[Min]	[% Area]	[μV]	[μV.Min]	[%]
2	UNKNOWN	9.76	10.17	10.78	0.00	77.01	7.1	2.9	77.005
1	UNKNOWN	11.97	12.34	12.96	0.00	22.99	2.2	0.9	22.995
Total						100.00	9.3	3.8	100.000

Figure 5.7. SFC trace for **5.68**.
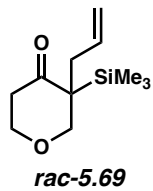
rac-5.69

Signal 1: DAD1 A, Sig=210,8 Ref=360,100

Peak #	RetTime [min]	Type	Width [min]	Area [mAU*s]	Height [mAU]	Area %
1	7.050	VV	0.2814	576.97528	29.59732	49.1807
2	7.909	VB	0.3027	596.19904	26.47661	50.8193

Figure 5.8. SFC trace for **rac-5.69**.
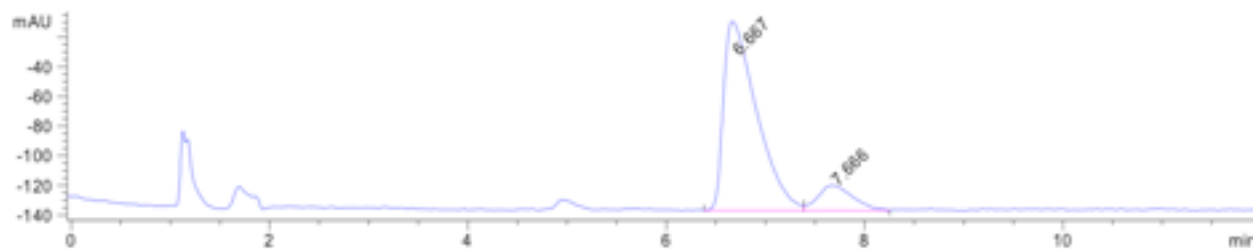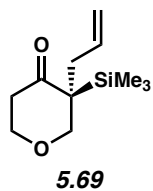
5.69

Signal 1: DAD1 A, Sig=210,8 Ref=360,100

Peak #	RetTime [min]	Type	Width [min]	Area [mAU*s]	Height [mAU]	Area %
1	6.667	BV	0.3324	2952.77930	127.38860	87.7272
2	7.666	VV	0.2993	413.08606	17.01272	12.2728

Figure 5.9. SFC trace for **5.69**.

rac-5.46

Signal 1: DAD1 A, Sig=210,8 Ref=360,100

Peak #	RetTime [min]	Type	Width [min]	Area [mAU*s]	Height [mAU]	Area %
1	4.366	MF	0.2166	696.71619	53.61436	50.7874
2	4.927	FM	0.2232	675.11218	50.40852	49.2126
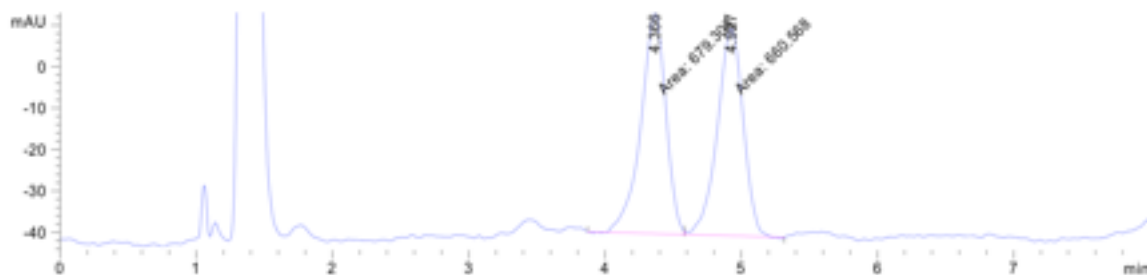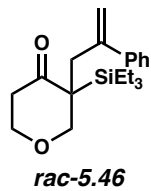
Figure 5.10. SFC trace for **rac-5.46**.

5.46

Signal 1: DAD1 A, Sig=210,8 Ref=360,100

Peak #	RetTime [min]	Type	Width [min]	Area [mAU*s]	Height [mAU]	Area %
1	4.466	MM	0.2144	1.01964e4	792.47705	90.3170
2	5.049	MM	0.2135	1093.16394	85.33304	9.6830
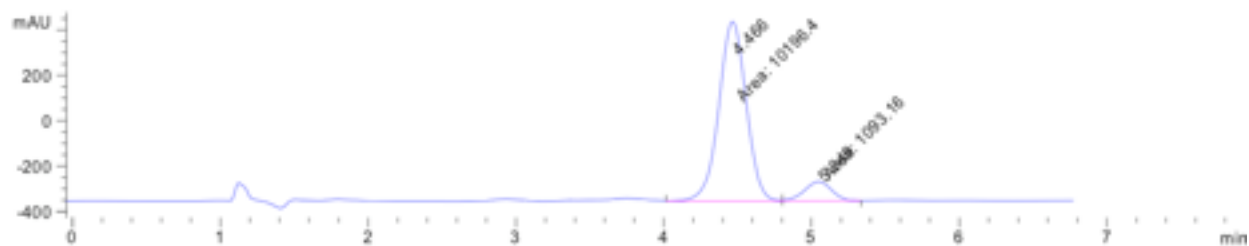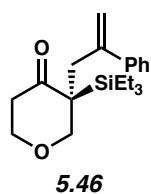
Figure 5.11. SFC trace for **5.46**.

5.8.2.7 Enantiospecific trappings

Preparation of Silyl Triflate 5.48
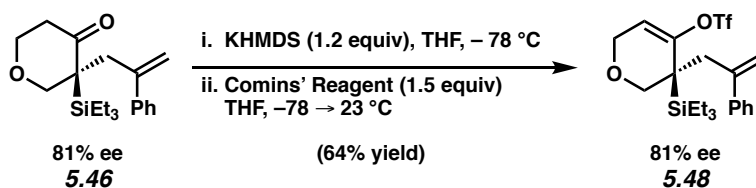
Silyl triflate 5.48. To a solution of KHMDS (7.31 mg, 0.0367 mmol, 1.20 equiv) in THF (0.1 mL) at −78 °C was added silyl ketone **5.46** (10.1 mg, 0.0306 mmol, 1.00 equiv) in THF (0.1 mL) dropwise over 1 min. The solution was stirred for 1 h at −78 °C, before a solution of Comins' Reagent (18.0 mg, 0.0458 mmol, 1.50 equiv) in THF (0.1 mL) was added dropwise over 30 sec. Following the addition, the cooling bath was removed and the reaction was allowed to stir at 23 °C. After stirring for 11 h, the reaction was quenched with sat. aq. NaHCO$_3$ (1.0 mL). The layers were then separated and the aqueous layer was extracted with EtOAc (3 x 4 mL). The combined organic layers were dried over Na$_2$SO$_4$, filtered, and concentrated under reduced pressure. The resulting crude oil was purified by preparative thin layer chromatography (9:1 hexanes:EtOAc) to afford silyl triflate **5.48** as a colorless oil (15.0 mg, 64% yield, 81% ee). Silyl Triflate **5.48**: R$_f$ 0.48 (9:1 hexanes:EtOAc); ^{1}H-NMR (500 MHz, CDCl$_3$): δ 7.36–7.22 (m, 5H), 5.49 (app t, J = 5.8, 1H), 5.23 (d, J = 1.1, 1H), 5.13 (s, 1H), 3.97 (d, J = 3.0, 2H), 3.72 (d, J = 11.8, 1H), 3.54 (d, J = 11.8, 1H), 3.02 (d, J = 14.2, 1H), 2.68 (d, J = 14.2, 1H), 1.02 (t, J = 7.9, 9H), 0.72 (q, J = 7.9, 6H); ^{13}C-NMR (100 MHz, CDCl$_3$): δ 151.3, 146.4, 143.4, 142.7, 128.2, 126.7, 118.4 (q, J = 320), 117.1, 110.7, 70.2, 64.2, 36.5, 36.3, 8.1, 2.6; ^{19}F-NMR (376 Hz, CDCl$_3$): −74.9; IR (film): 2955, 2878, 1739, 1366, 1216 cm^{-1}; [α]$^{26.3}$$_D$ −4.00° (c = 1.00, CH$_2$Cl$_2$).

Representative Procedure (Preparation of cycloadduct 5.51 is used as an example).
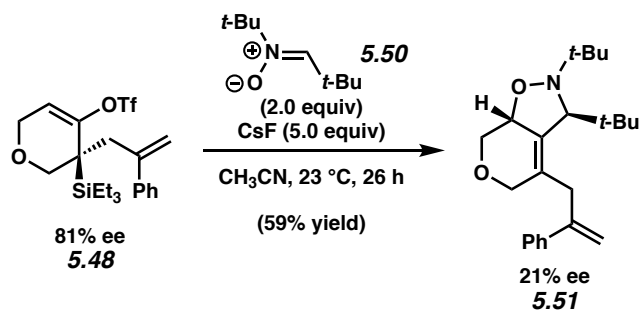
Isoxazolidine 5.51. To a stirred solution of silyl triflate **5.48** (14.2 mg, 0.031 mmol, 1.0 equiv) and nitrone **5.50** (9.7 mg, 0.0614 mmol, 2.0 equiv) in CH_3CN (0.30 mL) was added CsF (23.3 mg, 0.153 mmol, 5.0 equiv). The reaction vessel was sealed and allowed to stir at 23 °C for 26 h. The reaction mixture was filtered by passage through a plug of silica gel (EtOAc eluent, 15 mL). Concentration under reduced pressure yielded the crude residue (1.6:1 dr). Purification by preparative thin layer chromatography (1:1 hexanes:CH_2Cl_2) allowed for separation of the two diastereomers, which were obtained in a total yield of 59%. The major diastereomer **5.51** was obtained as a colorless oil (21% ee). Isoxazolidine **5.51**: R_f 0.12 (9:1 hexanes:EtOAc); ^{1}H-NMR (600 MHz, CDCl$_3$): δ 7.40–7.20 (m, 5H), 5.38 (d, $J = 0.7$, 1H), 5.13–5.11 (m, 1H), 4.40–4.34 (m, 1H), 4.23–4.17 (m, 2H), 3.82 (dd, $J = 16.2, 2.9$, 1H), 3.54 (s, 1H), 3.30 (s, 2H), 3.16 (app t, $J = 9.6$, 1H), 0.98 (s, 9H), 0.97 (s, 9H); ^{13}C-NMR (125 MHz, CDCl$_3$): δ 144.4, 141.5, 137.4, 128.5, 127.8, 126.1, 125.8, 115.0, 71.7, 67.7, 67.4, 67.2, 59.5, 53.4, 37.0, 36.0, 27.8, 26.9; IR (film): 2954, 1738, 1445, 1363, 1217, 1096 cm^{-1}; HRMS–APCI (m/z) [M + H]$^+$ calcd for $C_{23}H_{34}NO_2{}^+$, 355.25058; found, 355.25071. $[\alpha]^{29.5}{}_D$ –4.00° ($c = 1.00$, CH$_2$Cl$_2$).

The structure of **5.51** was verified by 2D-NOESY, as the following interaction was observed:

5.51
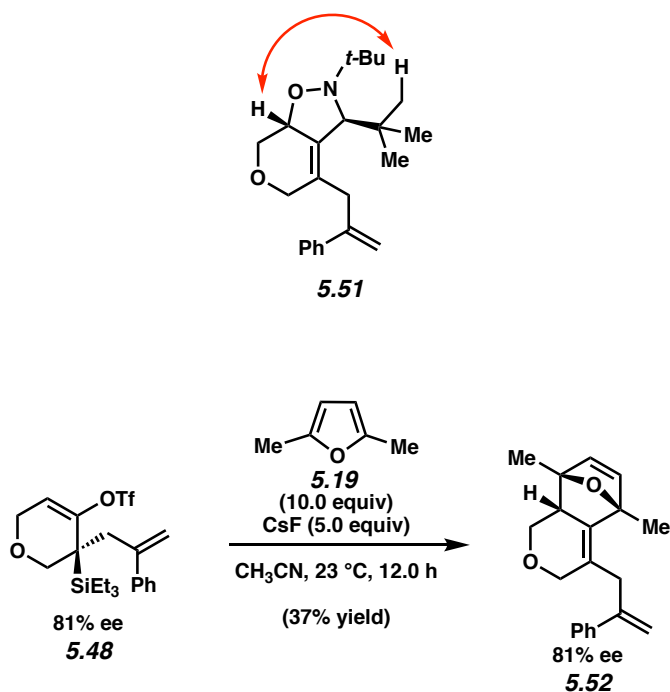
Cycloadduct 5.52. Following concentration under reduced pressure, the crude residue was obtained (>20:1 dr). Purification by preparative thin layer chromatography (5:1 hexanes:EtOAc) afforded cycloadduct **5.52** as a colorless oil in 37% yield (81% ee). Cycloadduct **5.52**: R_f 0.35 (9:1 hexanes:EtOAc); ^{1}H-NMR (500 MHz, CDCl$_3$): δ 7.42–7.38 (m, 2H), 7.36–7.27 (m, 3H), 6.17 (d, J = 5.4, 1H), 5.85 (d, J = 5.4, 1H), 5.39–5.37 (m, 1H), 5.09–5.06 (m, 1H), 4.13–4.06 (m, 2H), 3.82 (dd, J = 10.1, 2.8, 1H), 3.30 (d, J = 16.7, 1H), 3.15 (d, J = 16.7, 1H), 2.51–2.46 (m, 1H), 2.40 (dd, J = 10.6, 9.3, 1H), 1.76 (s, 3H), 1.62 (s, 3H); ^{13}C-NMR (125 MHz, CDCl$_3$): δ 145.4, 141.3, 139.8, 138.6, 133.5, 128.4, 127.7, 125.9, 123.4, 113.7, 87.4, 85.7, 67.3, 67.2, 46.7, 34.2, 18.2, 17.5; IR (film): 2924, 2852, 1741, 1632, 1380 cm^{-1}; HRMS–APCI (*m/z*) [M + H]$^+$ calcd for C$_{20}$H$_{23}$O$_2^+$, 295.16926; found, 295.17032. [α]$^{28.6}_D$ +73.3° (*c* = 1.00, CH$_2$Cl$_2$).

The structure of **5.52** was verified by 2D-NOESY, as the following interaction was observed:
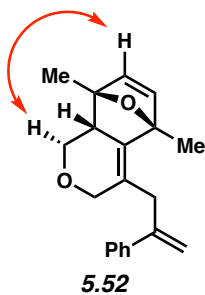
5.52

Compound	Method Column/Temp.	Solvent	Method Flow Rate	Retention Times (min)	Enantiomeric Ratio (er)
rac-5.51	ChiralPak IC-3/35°C	5% isopropanol in CO_2	3.5 mL/min	5.02/6.29	49.7/50.3
5.51	ChiralPak IC-3/35°C	5% isopropanol in CO_2	3.5 mL/min	5.29/6.55	39.2/60.8
rac-5.52	ChiralPak AD-3/35°C	5% isopropanol in CO_2	3.5 mL/min	5.41/6.80	49.9/50.1

5.52	ChiralPak AD-3/35°C	5% isopropanol in CO_2	3.5 mL/min	6.06/6.91	90.7/9.3
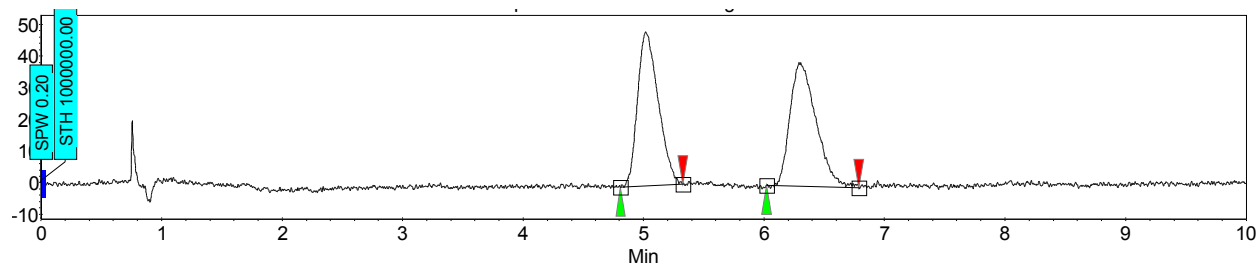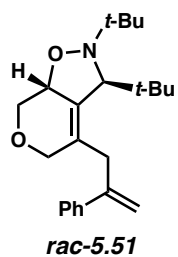
rac-5.51

Index	Name	Start	Time	End	RT Offset	Quantity	Height	Area	Area
		[Min]	[Min]	[Min]	[Min]	[% Area]	[µV]	[µV.Min]	[%]
1	UNKNOWN	4.81	5.02	5.33	0.00	49.74	48.7	9.7	49.742
2	UNKNOWN	6.02	6.29	6.79	0.00	50.26	39.3	9.8	50.258
Total						100.00	88.0	19.6	100.000

Figure 5.12. SFC trace for **rac-5.51**.
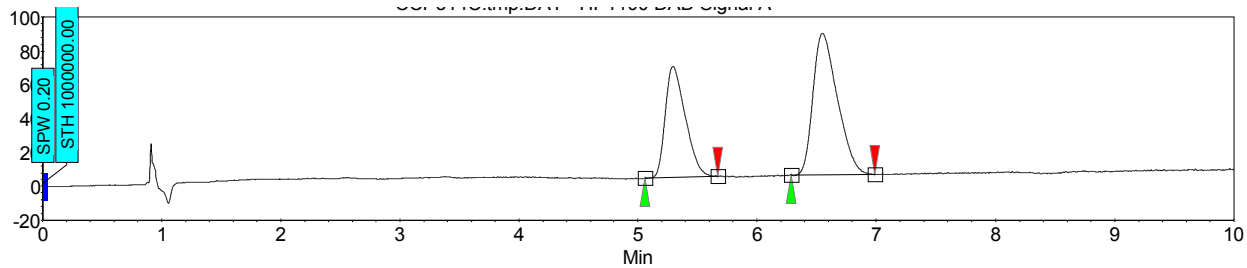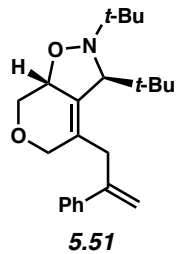
5.51

Index	Name	Start	Time	End	RT Offset	Quantity	Height	Area	Area
		[Min]	[Min]	[Min]	[Min]	[% Area]	[µV]	[µV.Min]	[%]
1	UNKNOWN	5.06	5.29	5.67	0.00	39.25	65.6	12.8	39.249
2	UNKNOWN	6.28	6.55	6.99	0.00	60.75	83.3	19.7	60.751
Total						100.00	148.9	32.5	100.000

Figure 5.13. SFC trace for **5.51**.
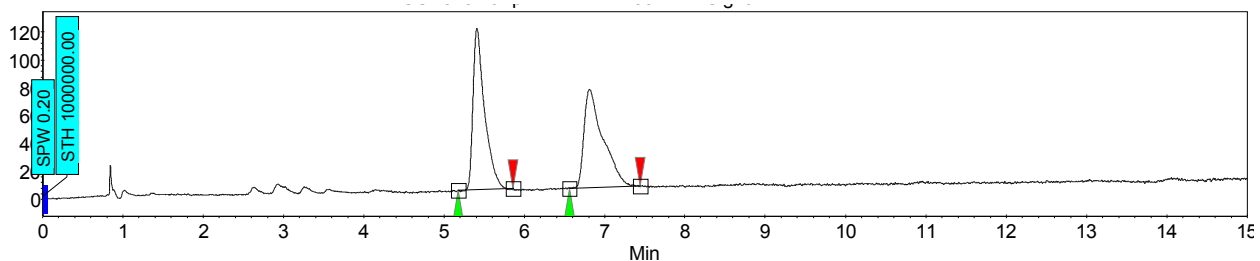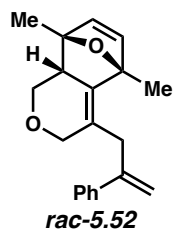
rac-5.52

Index	Name	Start	Time	End	RT Offset	Quantity	Height	Area	Area
		[Min]	[Min]	[Min]	[Min]	[% Area]	[µV]	[µV.Min]	[%]
1	UNKNOWN	5.17	5.41	5.86	0.00	49.86	115.6	19.3	49.859
2	UNKNOWN	6.56	6.80	7.45	0.00	50.14	70.3	19.4	50.141
Total						100.00	185.9	38.7	100.000

Figure 5.14. SFC trace for **rac-5.52**.
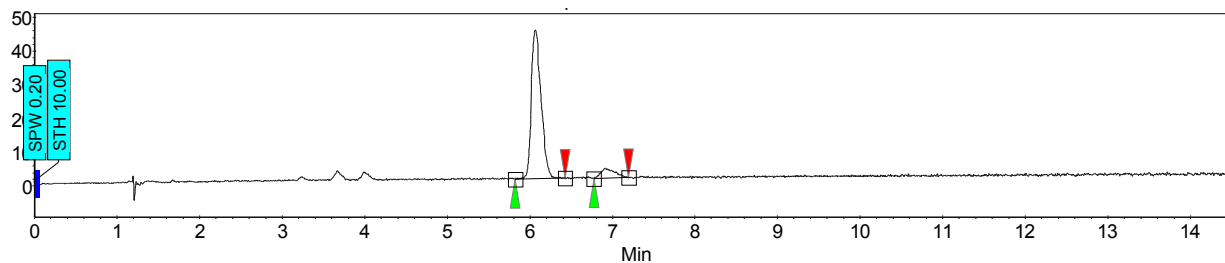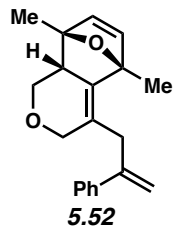
328

5.52

Index	Name	Start	Time	End	RT Offset	Quantity	Height	Area	Area
		[Min]	[Min]	[Min]	[Min]	[% Area]	[µV]	[µV.Min]	[%]
1	UNKNOWN	5.82	6.06	6.42	0.00	90.73	44.0	6.0	90.732
2	UNKNOWN	6.77	6.91	7.20	0.00	9.27	3.0	0.6	9.268
Total						100.00	47.0	6.6	100.000

Figure 5.15. SFC trace for **5.52**.

5.8.3 Computational Methods

All calculations were carried out with the Gaussian 09 package. Geometry optimizations were performed with ωB97XD and 6-31G(d) basis set. Frequency analysis was conducted at the same level of theory to verify the stationary points to be minima or saddle points. Free energy corrections were calculated with and without Truhlar's quasiharmonic oscillator approximation.[41] Single-point energies and solvent effects in acetonitrile were computed with the 6-311+G(d,p) basis set and SMD solvation model.[42] Computed structures are illustrated with CYLview. [43]

5.8.3.1 Complete Citation of Gaussian 09

Frisch, M. J.; Trucks, G. W.; Schlegel, H. B.; Scuseria, G. E.; Robb, M. A.; Cheeseman, J. R.; Scalmani, G.; Barone, V.; Mennucci, B.; Petersson, G. A.; Nakatsuji, H.; Caricato, M.; Li, X.; Hratchian, H. P.; Izmaylov, A. F.; Bloino, J.; Zheng, G.; Sonnenberg, J. L.; Hada, M.; Ehara, M.; Toyota, K.; Fukuda, R.; Hasegawa, J.; Ishida, M.; Nakajima, T.; Honda, Y.; Kitao, O.; Nakai, H.; Vreven, T.; Montgomery, Jr., J. A.; Peralta, J. E.; Ogliaro, F.; Bearpark, M.; Heyd, J. J.; Brothers, E.; Kudin, K. N.; Staroverov, V. N.; Keith, T.; Kobayashi, R.; Normand, J.; Raghavachari, K.; Rendell, A.; Burant, J. C.; Iyengar, S. S.; Tomasi, J.; Cossi, M.; Rega, N.; Millam, J. M.; Klene, M.; Knox, J. E.; Cross, J. B.; Bakken, V.; Adamo, C.; Jaramillo, J.; Gomperts, R.; Stratmann, R. E.; Yazyev, O.; Austin, A. J.; Cammi, R.; Pomelli, C.; Ochterski, J. W.; Martin, R. L.; Morokuma, K.; Zakrzewski, V. G.; Voth, G. A.; Salvador, P.; Dannenberg, J. J.; Dapprich, S.; Daniels, A. D.; Farkas, O.; Foresman, J. B.; Ortiz, J. V.; Cioslowski, J.; Fox, D. J. *Gaussian 09, Rev. D.01*; Gaussian, Inc., Wallingford, CT, **2010**.

5.8.3.2 Strain Energy in 3,4-Oxacyclohexadiene
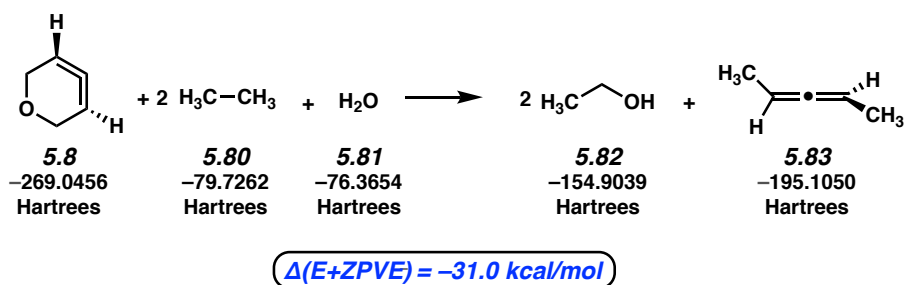
A homodesmotic equation at the ωB97XD/6-31G(d)+ZPVE level of theory was used to estimate strain in 3,4-oxacyclohexadiene **5.8**. Molecular strain in 3,4-oxacyclohexadiene **5.8** was calculated relative to penta-2,3-diene (**5.83**).

5.8.3.3 Geometries of Diasteromeric Transition States
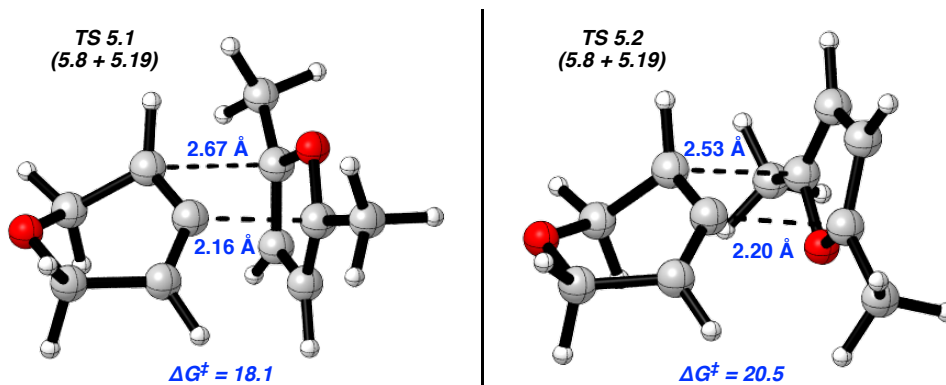
Transition states geometries for concerted cycloaddition of 3,4-oxacyclohexadiene **5.8** with dimethylfuran (**5.19**) at the ωB97XD/6-31G(d) level of theory. **TS 5.1** leads to endo product (major diastereomer) while **TS 5.2** leads to exo product (minor diastereomer). Endo and exo refer to the position of dimethylfuran (**5.19**) relative to the additional π bond in 3,4-oxacyclohexadiene **5.8**. $\Delta G^{\ddagger}$ values are provided (ωB97XD/6-311+G(d,p)/SMD(MeCN)//ωB97XD/6-31G(d)). The reaction occurs with a notable preference for formation of endo product ($\Delta\Delta G^{\ddagger}$ = 2.4 kcal/mol).

5.8.3.4 Energies and Cartesian Coordinates for Optimized Structures

Cartesian coordinates for the optimized structures were reported in the literature.[44]

5.9 Spectra Relevant to Chapter Five:

Cycloadditions of Oxacyclic Allenes and a Catalytic Asymmetric Entryway to Enantioenriched Cyclic Allenes

Michael M. Yamano, Rachel R. Knapp, Aurapat Ngamnithiporn, Melissa Ramirez

Kendall N. Houk, Brian M. Stoltz, and Neil K. Garg.

Figure 5.16. ^{1}H NMR (400 MHz, CDCl$_3$) of compound **5.11**.

Figure 5.17. ^{13}C NMR (100 MHz, CDCl$_3$) of compound **5.11**.

Purified Product 1H NMR

5.670 5.667 5.663 5.660 5.656 5.652 4.318 4.310 4.302 4.278 4.270 4.262 4.237 4.230 4.223 4.196 4.189 4.182 3.976 3.964 3.947 3.936 3.882 3.869 3.853 3.841 2.139 2.136 2.131 2.127 2.124 2.120 2.116 2.108 2.105 2.100 2.097 0.999 0.979 0.971 0.959

Current Data Parameters
NAME   MY-2017-019a-p-char
EXPNO   30
PROCNO   1

F2 - Acquisition Parameters
Date_   20180911
Time   20.27
INSTRUM   av400
PROBHD   5 mm PABBO BB/
PULPROG   zg30
TD   52882
SOLVENT   CDCl3
NS   4
DS   0
SWH   8012.820 Hz
FIDRES   0.151523 Hz
AQ   3.2998369 sec
RG   155.85
DW   62.400 usec
DE   6.50 usec
TE   298.7 K
D1   2.00000000 sec
TD0   1

======== CHANNEL f1 =====
SFO1   400.1324008 MHz
NUC1   1H
P1   15.00 usec
PLW1   13.00000000 W

F2 - Processing parameters
SI   65536
SF   400.1300184 MHz
WDW   EM
SSB   0
LB   0.30 Hz
GB   0
PC   1.00
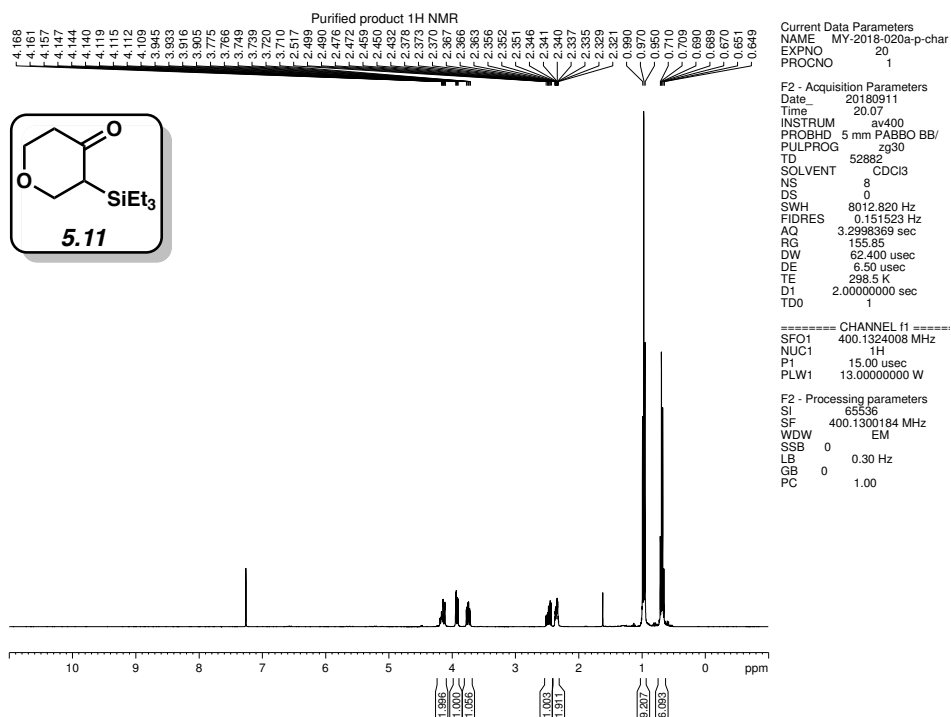
Figure 5.18. ^{1}H NMR (400 MHz, CDCl$_3$) of compound **5.12**.

Purified product 13C NMR

149.72 122.47 119.93 117.38 114.83 113.03 66.68 64.39 28.45 7.32 2.93

Current Data Parameters
NAME   ST-char-2
EXPNO   2
PROCNO   1

F2 - Acquisition Parameters
Date_   20181019
Time   10.36 h
INSTRUM   av500
PROBHD   Z119248_0002 (
PULPROG   zgpg30
TD   65536
SOLVENT   CDCl3
NS   272
DS   2
SWH   31250.000 Hz
FIDRES   0.953674 Hz
AQ   1.0485760 sec
RG   204.54
DW   16.000 usec
DE   18.00 usec
TE   298.0 K
D1   2.00000000 sec
D11   0.03000000 sec
TD0   1
SFO1   125.7722511 MHz
NUC1   13C
P1   9.63 usec
PLW1   23.00000000 W
SFO2   500.1330008 MHz
NUC2   1H
CPDPRG[2   waltz16
PCPD2   80.00 usec
PLW2   13.50000000 W
PLW12   0.21094000 W
PLW13   0.13500001 W

F2 - Processing parameters
SI   131072
SF   125.5777708 MHz
WDW   EM
SSB   0
LB   1.00 Hz
GB   0
PC   1.40

Figure 5.19. ^{13}C NMR (125 MHz, CDCl$_3$) of compound **5.12**.

7.222
7.217
7.204
7.201
7.187
7.182
6.874
6.872
6.869
6.854
6.851
6.838
6.835
6.832
6.828
6.826
6.821
6.809
6.807
6.804
6.310
6.303
6.296
6.289
5.983
5.978
5.969
5.964
5.689
5.683
4.889
4.713
4.707
4.704
4.701
4.275
4.270
4.239
4.234
4.229
4.163
4.151
4.140
4.128
3.989
3.974
3.948
3.940
3.933
3.982
2.480
2.455
2.430

2.074
3.041
1.000
1.007
1.012
1.028
1.048
1.064
1.083
1.057
1.022
1.050
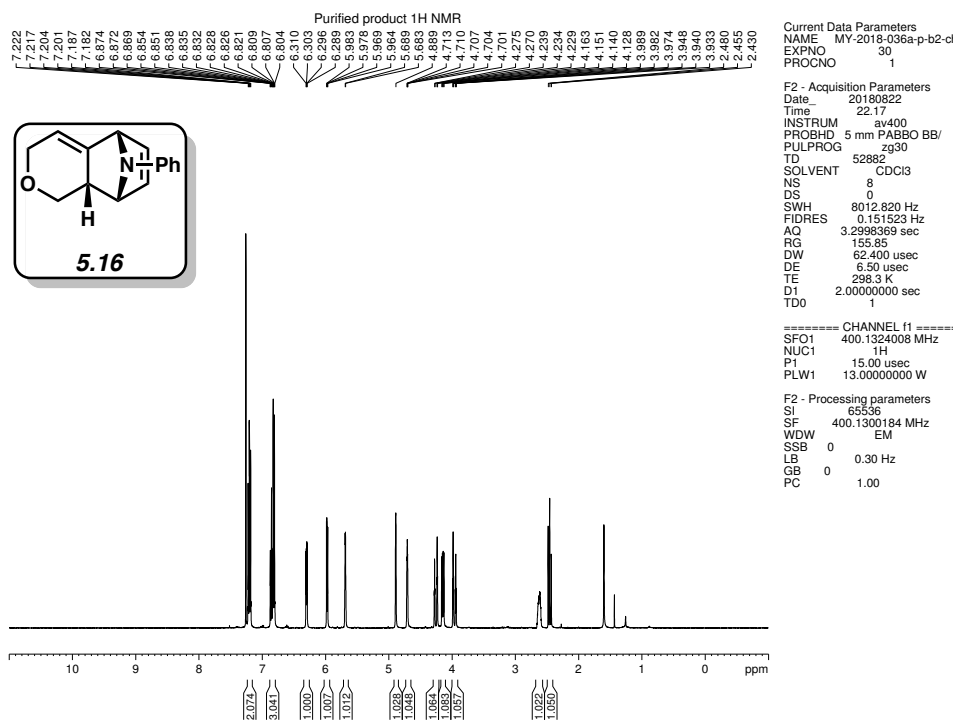
Figure 5.20. ^{1}H NMR (400 MHz, CDCl$_3$) of compound **5.16**.

146.76
137.61
135.03
129.15
128.41
120.72
117.68
117.25
67.88
65.42
64.96
64.96
38.63
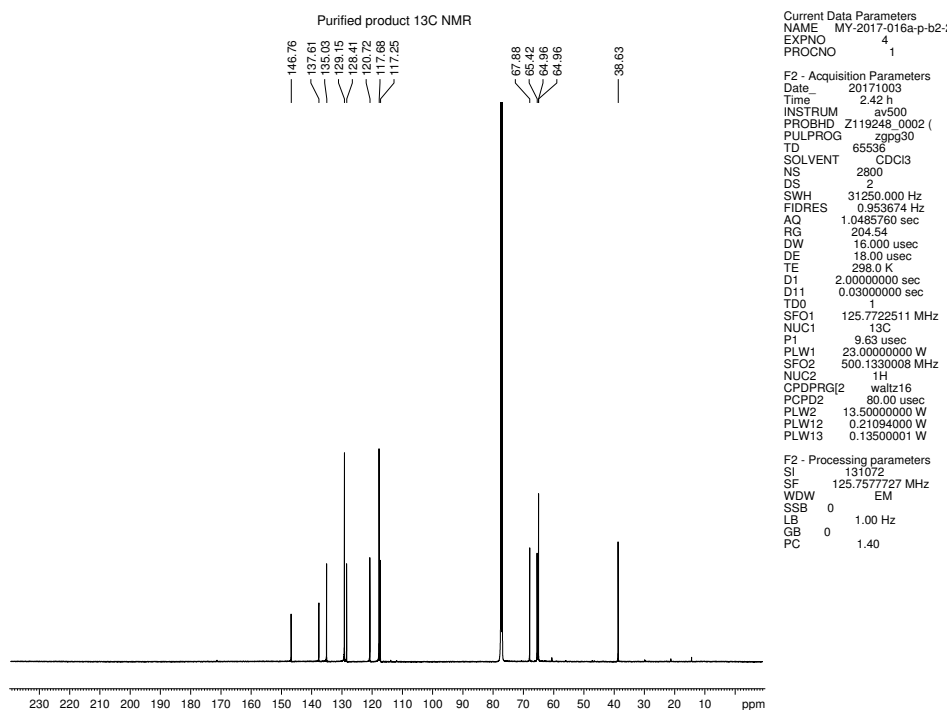
Figure 5.21. ^{13}C NMR (125 MHz, CDCl$_3$) of compound **5.16**.
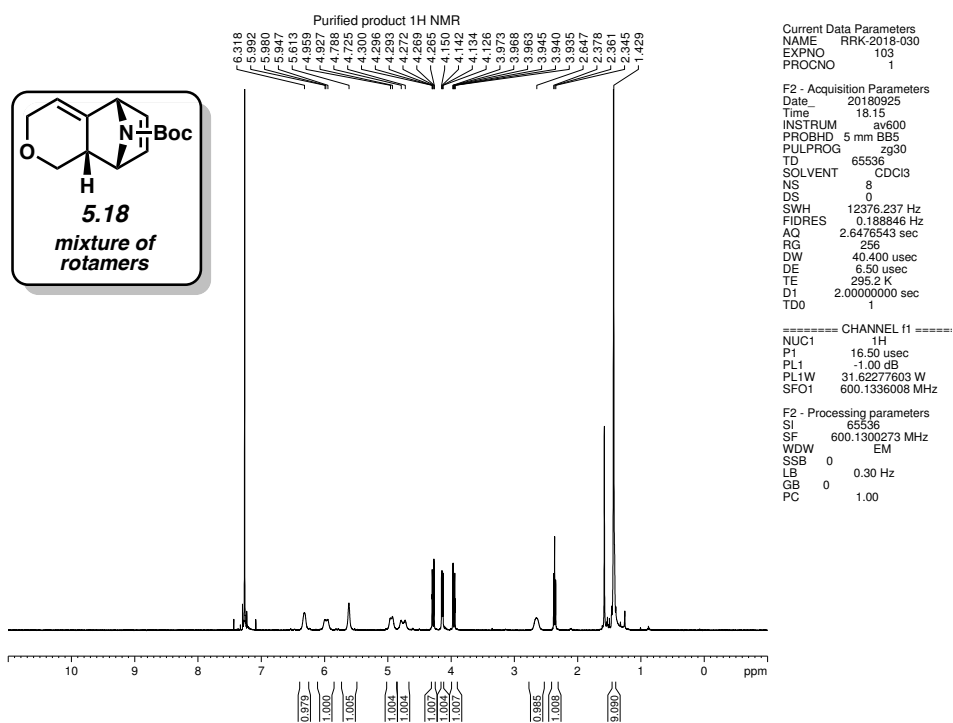
Figure 5.22. ^{1}H NMR (600 MHz, CDCl$_3$) of compound **5.18**.
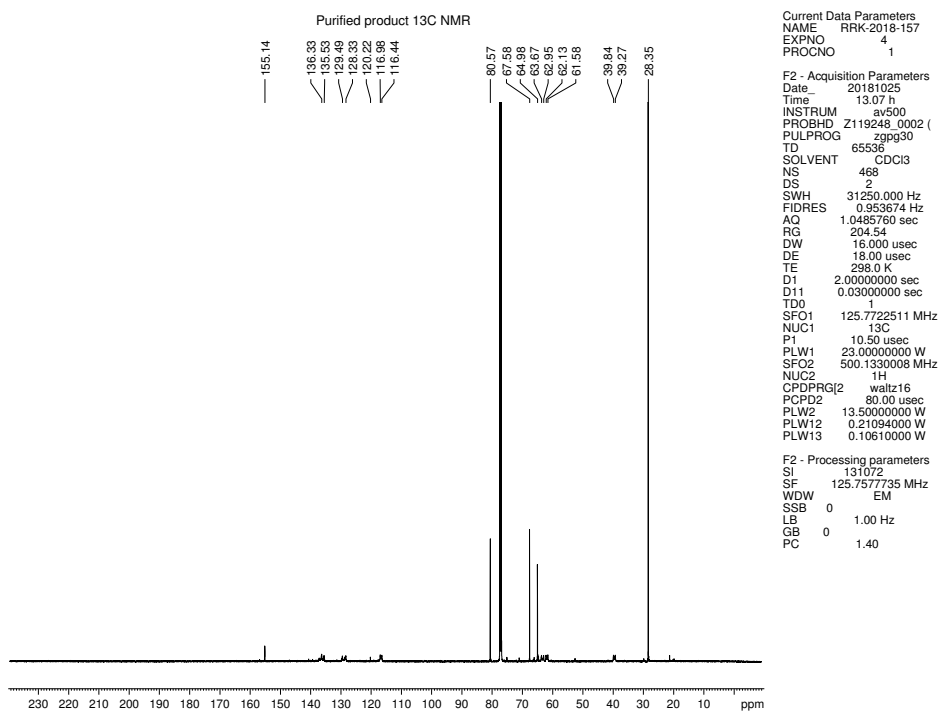
Figure 5.23. ^{13}C NMR (125 MHz, CDCl$_3$) of compound **5.18**.

Figure 5.24. ^{1}H NMR (500 MHz, CDCl$_3$) of compound **5.20**.

Figure 5.25. ^{13}C NMR (125 MHz, CDCl$_3$) of compound **5.20**.
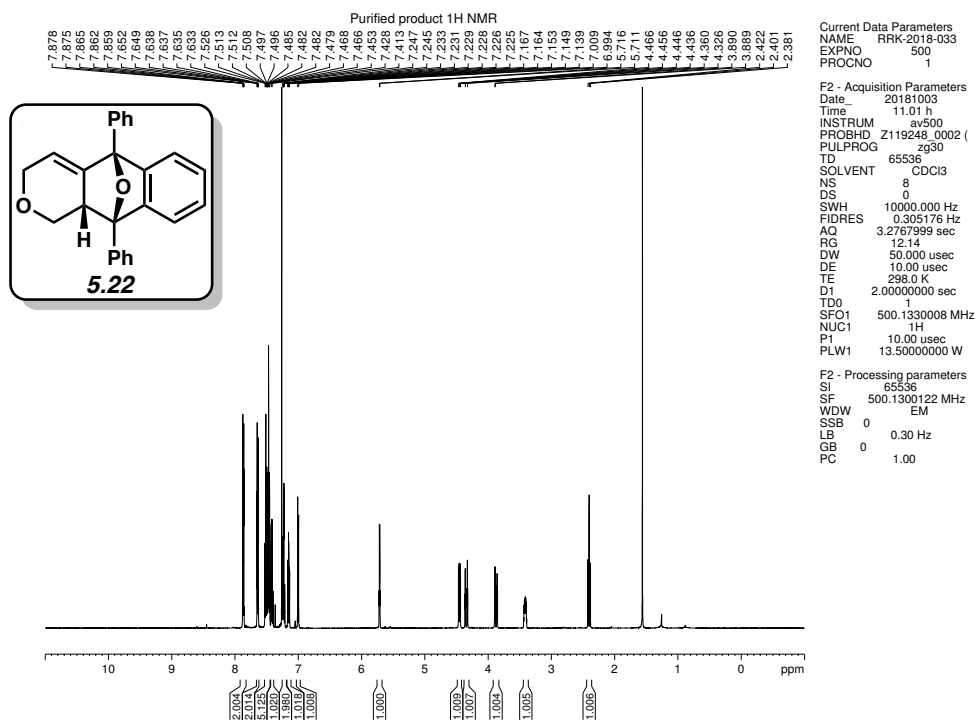
Figure 5.26. ^{1}H NMR (500 MHz, CDCl₃) of compound **5.22**.
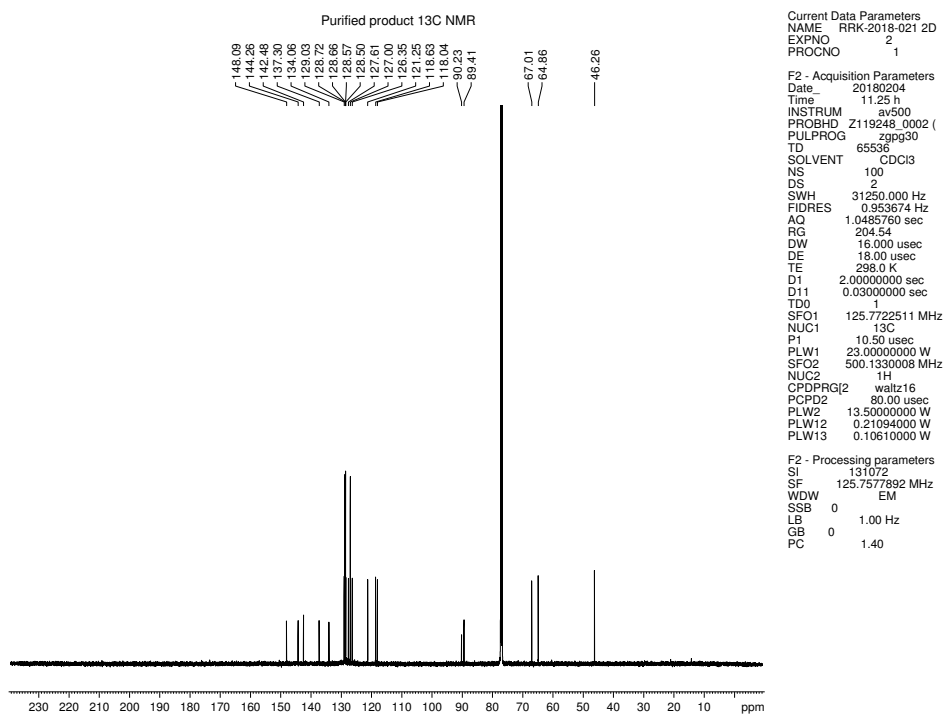
Figure 5.27. ^{13}C NMR (125 MHz, CDCl₃) of compound **5.22**.

338
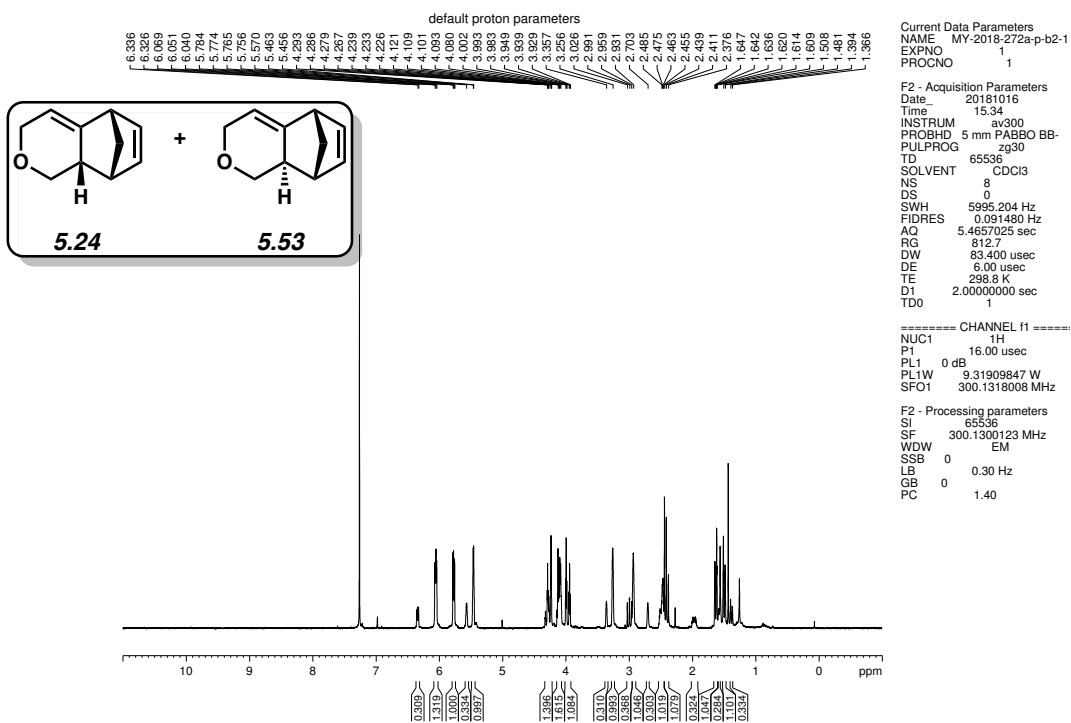
Figure 5.28. ^{1}H NMR (300 MHz, CDCl$_3$) of compound **5.24** and **5.53**.
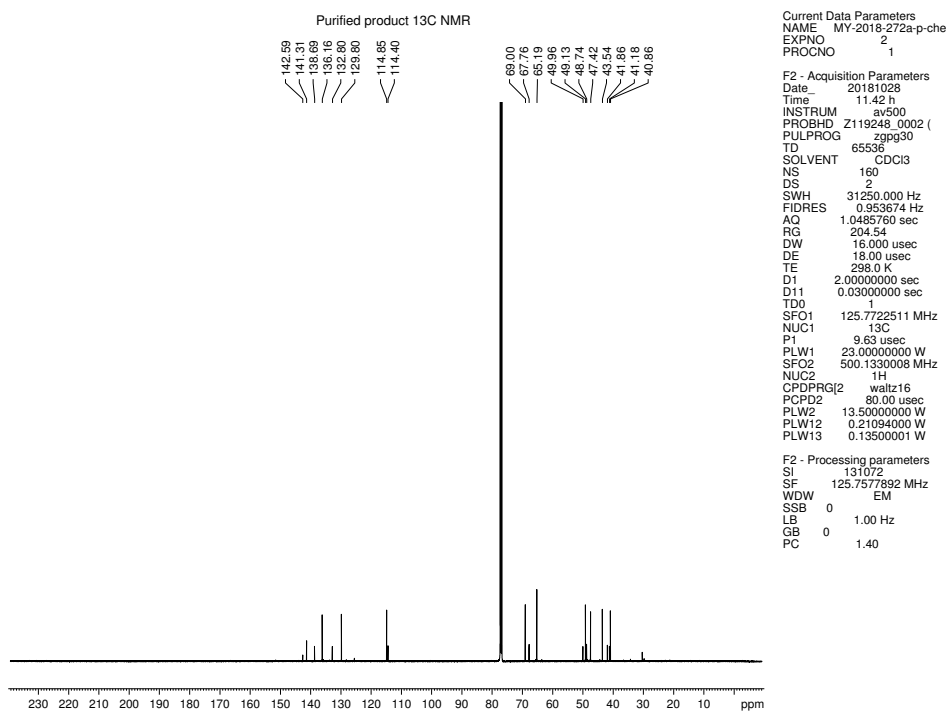
Figure 5.29. ^{13}C NMR (125 MHz, CDCl$_3$) of compound **5.24** and **5.53**.
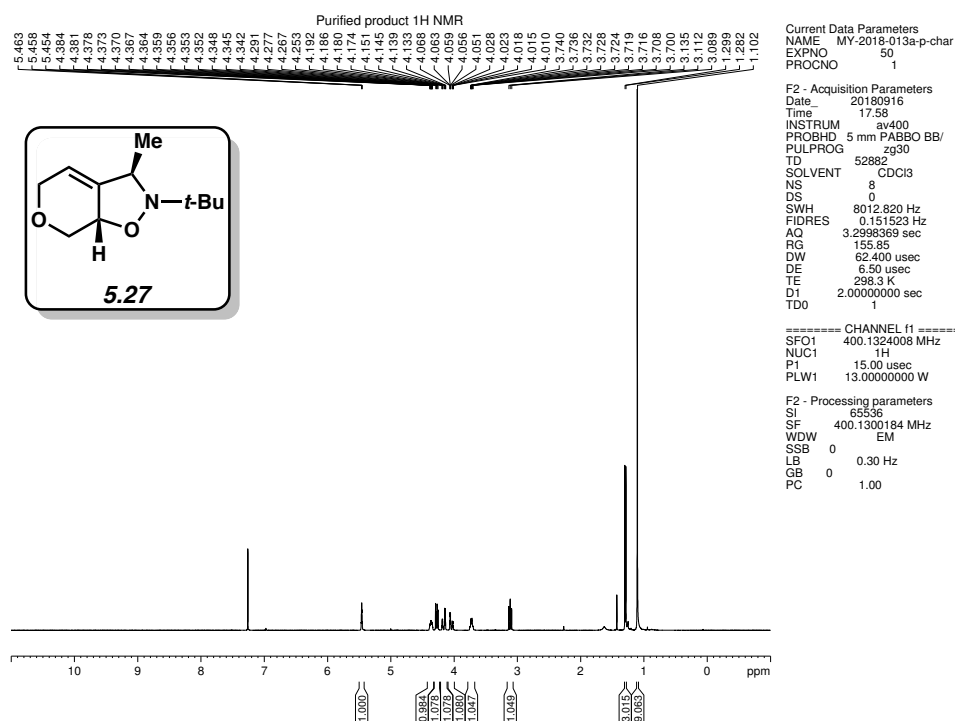
Figure 5.30. ^{1}H NMR (400 MHz, CDCl$_3$) of compound **5.27**.
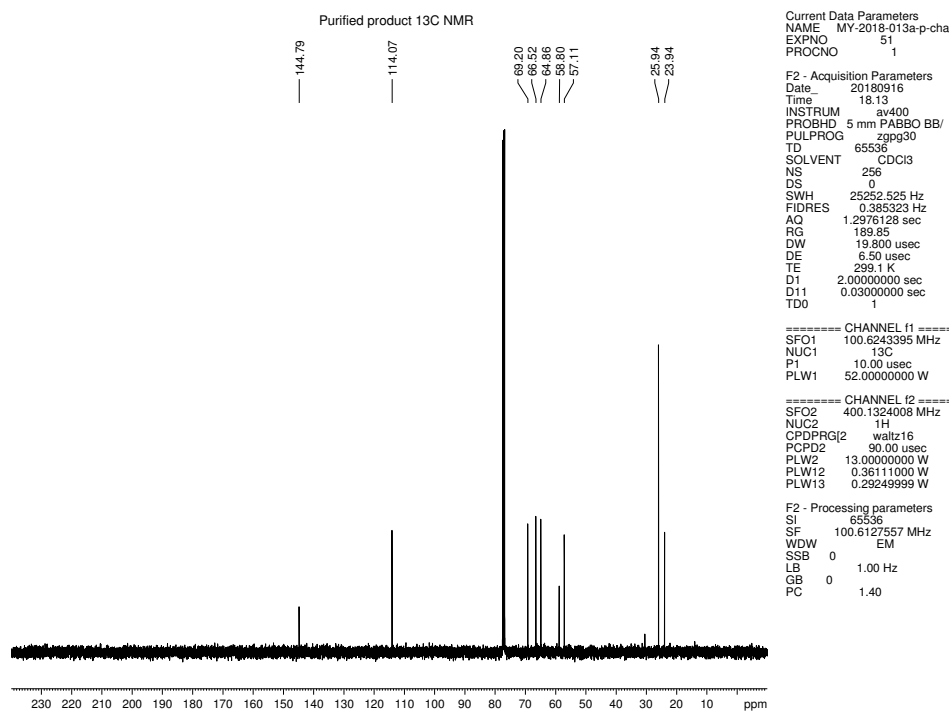
Figure 5.31. ^{13}C NMR (100 MHz, CDCl$_3$) of compound **5.27**.

340
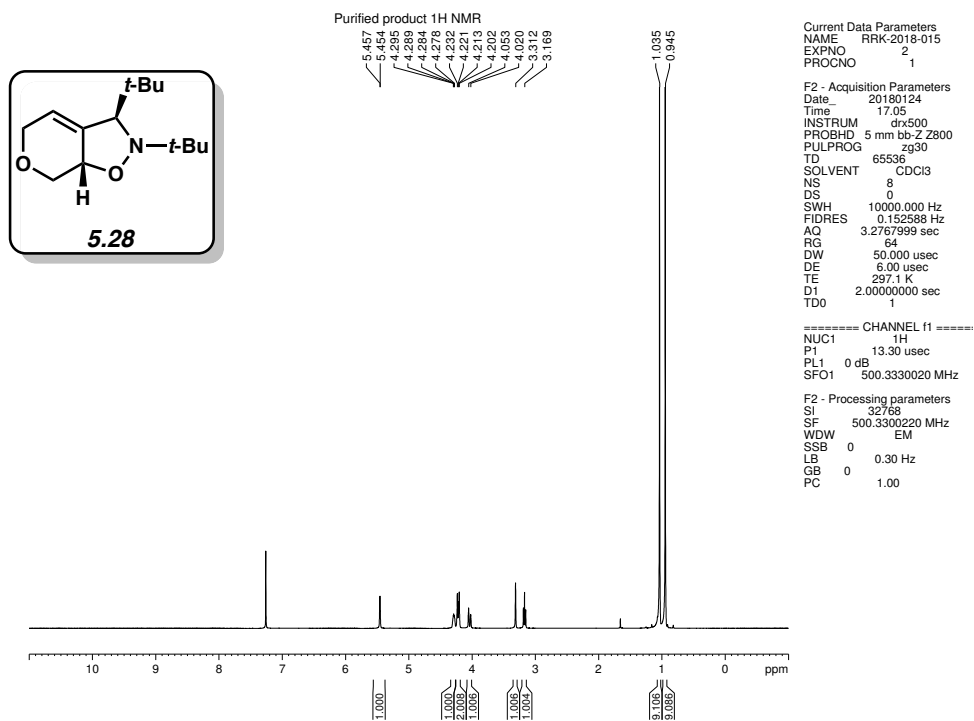
Figure 5.32. ^{1}H NMR (500 MHz, CDCl$_3$) of compound **5.28**.
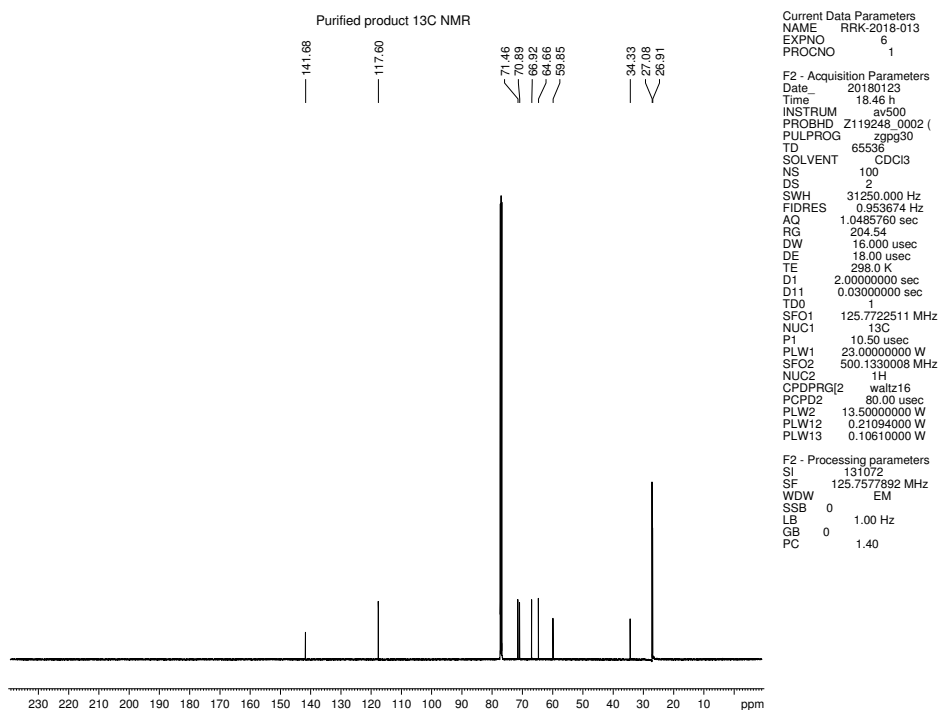
Figure 5.33. ^{13}C NMR (125 MHz, CDCl$_3$) of compound **5.28**.

341
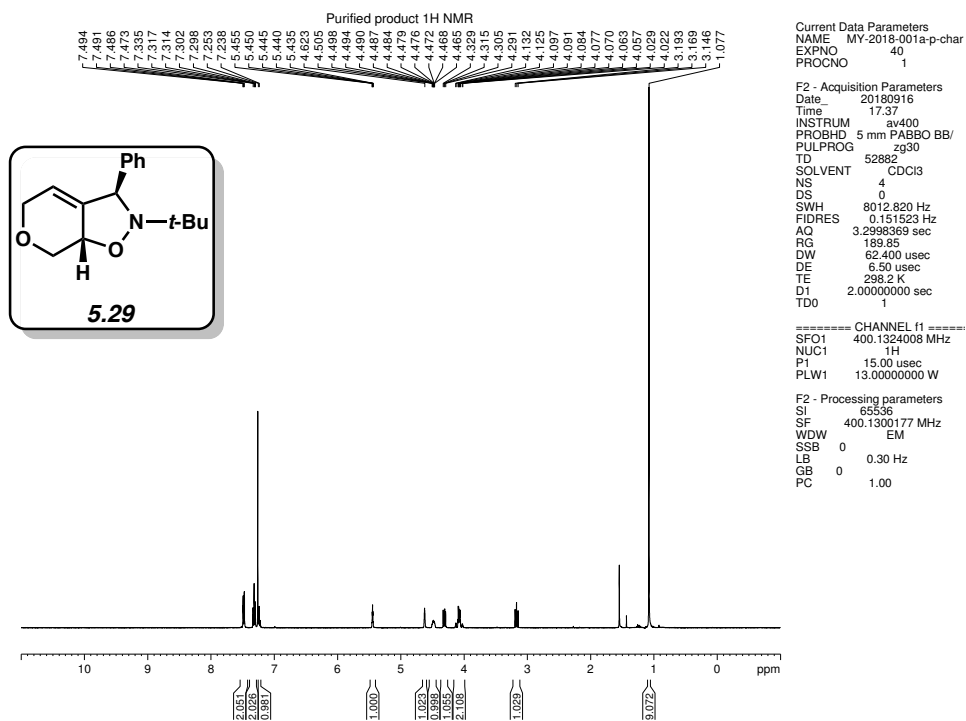
Figure 5.34. ^{1}H NMR (400 MHz, CDCl$_3$) of compound **5.29**.
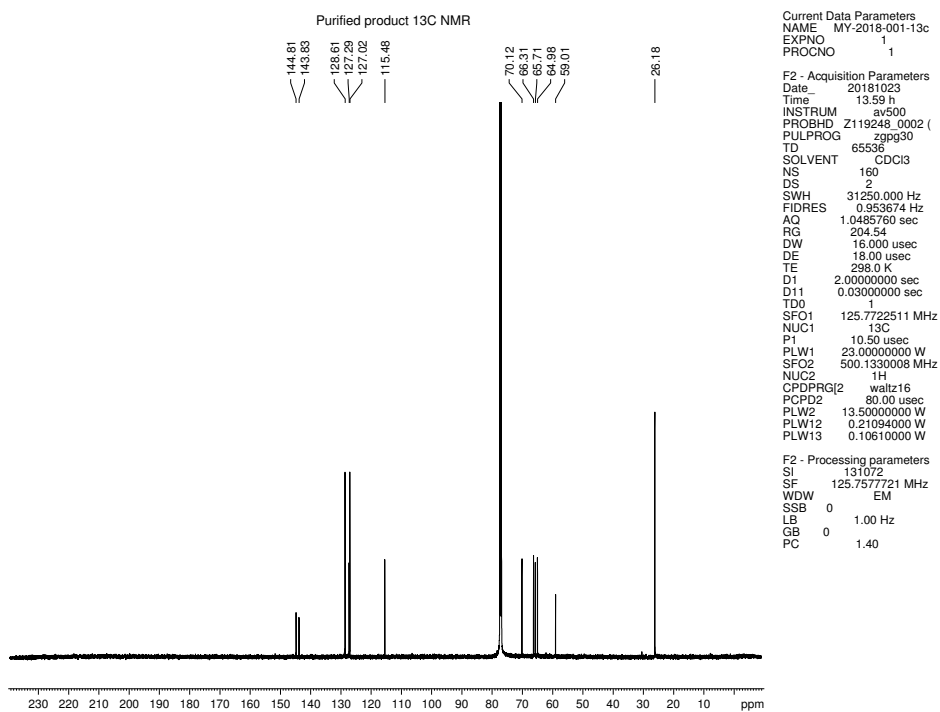
Figure 5.35. ^{13}C NMR (125 MHz, CDCl$_3$) of compound **5.29**.
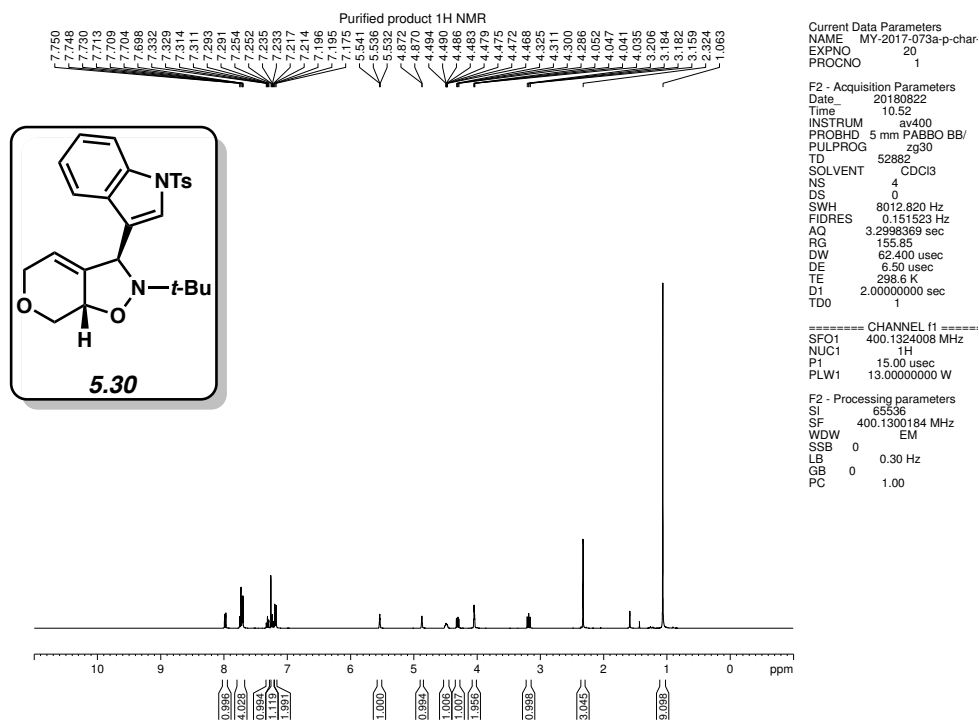
Figure 5.36. ¹H NMR (400 MHz, CDCl₃) of compound **5.30**.
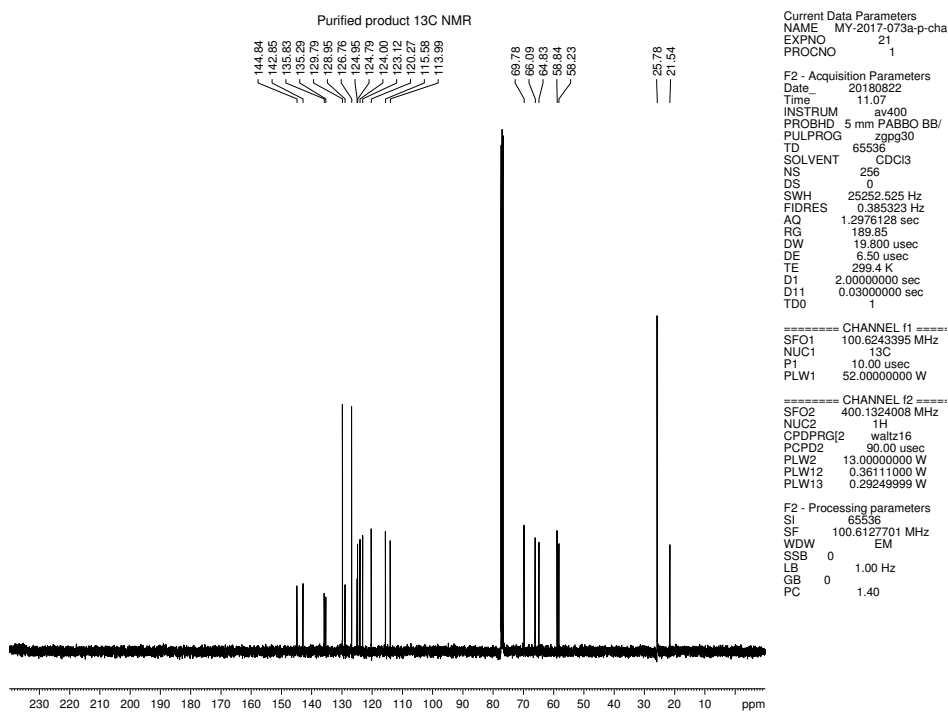
Figure 5.37. ¹³C NMR (100 MHz, CDCl₃) of compound **5.30**.

Purified product 1H NMR

8.138
8.117
8.065
8.044
7.867
7.845
7.807
7.804
7.787
7.784
7.719
7.716
7.702
7.698
7.694
7.681
7.677
7.531
7.529
7.514
7.511
7.508
7.494
7.491
5.666
5.661
5.656
5.651
5.018
5.015
5.011
4.593
4.590
4.586
4.582
4.578
4.575
4.571
4.568
4.564
4.368
4.355
4.344
4.330
4.079
4.073
4.066
4.060
3.230
3.207
3.205
3.183
1.098

5.31

Current Data Parameters
NAME   MY-2018-009a-p-char
EXPNO   10
PROCNO   1

F2 - Acquisition Parameters
Date_   20180822
Time   10.31
INSTRUM   av400
PROBHD   5 mm PABBO BB/
PULPROG   zg30
TD   52882
SOLVENT   CDCl3
NS   8
DS   0
SWH   8012.820 Hz
FIDRES   0.151523 Hz
AQ   3.2998369 sec
RG   155.85
DW   62.400 usec
DE   6.50 usec
TE   298.5 K
D1   2.00000000 sec
TD0   1

======== CHANNEL f1 =====
SFO1   400.1324008 MHz
NUC1   1H
P1   15.00 usec
PLW1   13.00000000 W

F2 - Processing parameters
SI   65536
SF   400.1300184 MHz
WDW   EM
SSB   0
LB   0.30 Hz
GB   0
PC   1.00

0.981
0.969
0.991
1.002
0.990
0.989
1.000
1.000
1.004
1.019
2.014
1.013
9.055
9.079

Figure 5.38. ^{1}H NMR (400 MHz, CDCl$_3$) of compound **5.31**.

Purified product 13C NMR

163.04
147.62
143.30
136.79
129.57
129.08
127.82
127.76
126.33
120.10
117.24
77.36
70.51
68.52
66.26
65.10
59.12
25.99

Current Data Parameters
NAME   MY-2018-009a-p-cha
EXPNO   11
PROCNO   1

F2 - Acquisition Parameters
Date_   20180822
Time   10.47
INSTRUM   av400
PROBHD   5 mm PABBO BB/
PULPROG   zgpg30
TD   65536
SOLVENT   CDCl3
NS   256
DS   0
SWH   25252.525 Hz
FIDRES   0.385323 Hz
AQ   1.2976128 sec
RG   189.85
DW   19.800 usec
DE   6.50 usec
TE   299.4 K
D1   2.00000000 sec
D11   0.03000000 sec
TD0   1

======== CHANNEL f1 =====
SFO1   100.6243395 MHz
NUC1   13C
P1   10.00 usec
PLW1   52.00000000 W

======== CHANNEL f2 =====
SFO2   400.1324008 MHz
NUC2   1H
CPDPRG[2   waltz16
PCPD2   90.00 usec
PLW2   13.00000000 W
PLW12   0.36111000 W
PLW13   0.29249999 W

F2 - Processing parameters
SI   65536
SF   100.6127574 MHz
WDW   EM
SSB   0
LB   1.00 Hz
GB   0
PC   1.40

Figure 5.39. ^{13}C NMR (100 MHz, CDCl$_3$) of compound **5.31**.

344
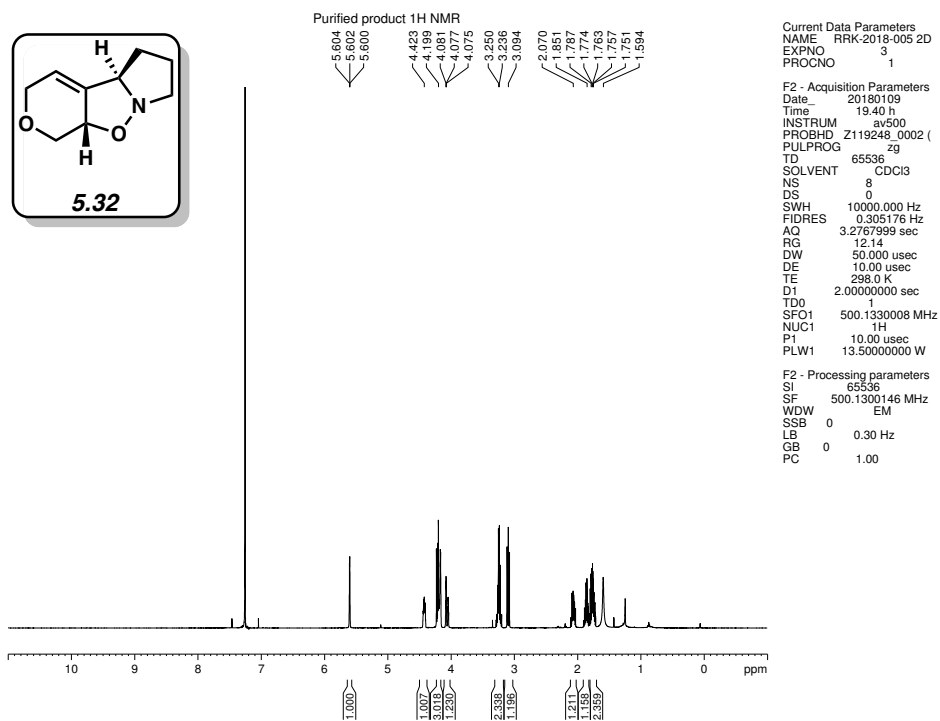
Figure 5.40. ¹H NMR (500 MHz, CDCl₃) of compound **5.32**.
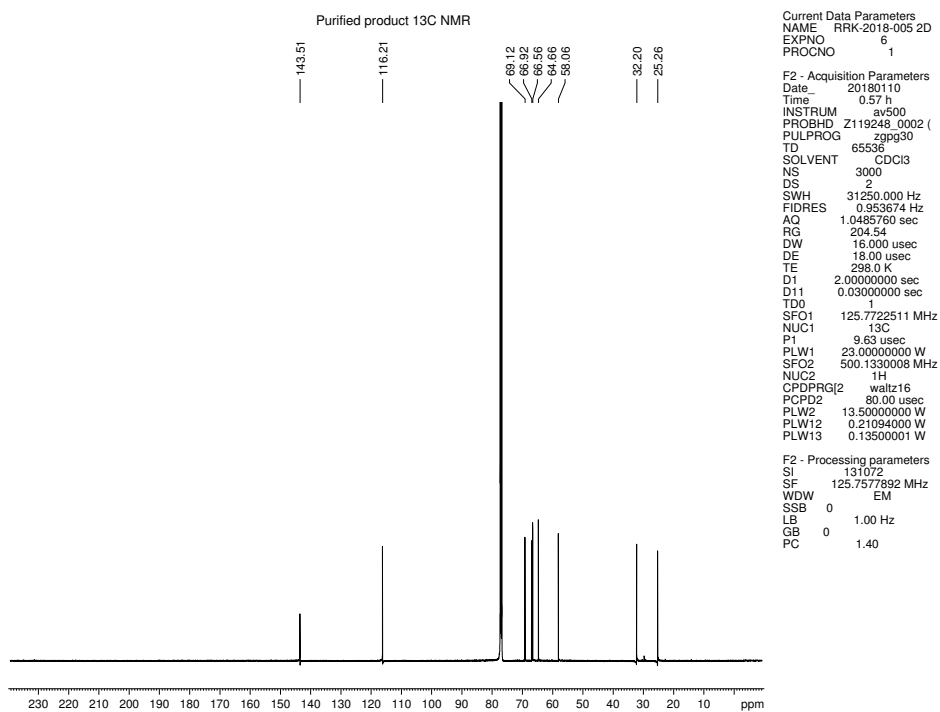
Figure 5.41. ¹³C NMR (125 MHz, CDCl₃) of compound **5.32**.
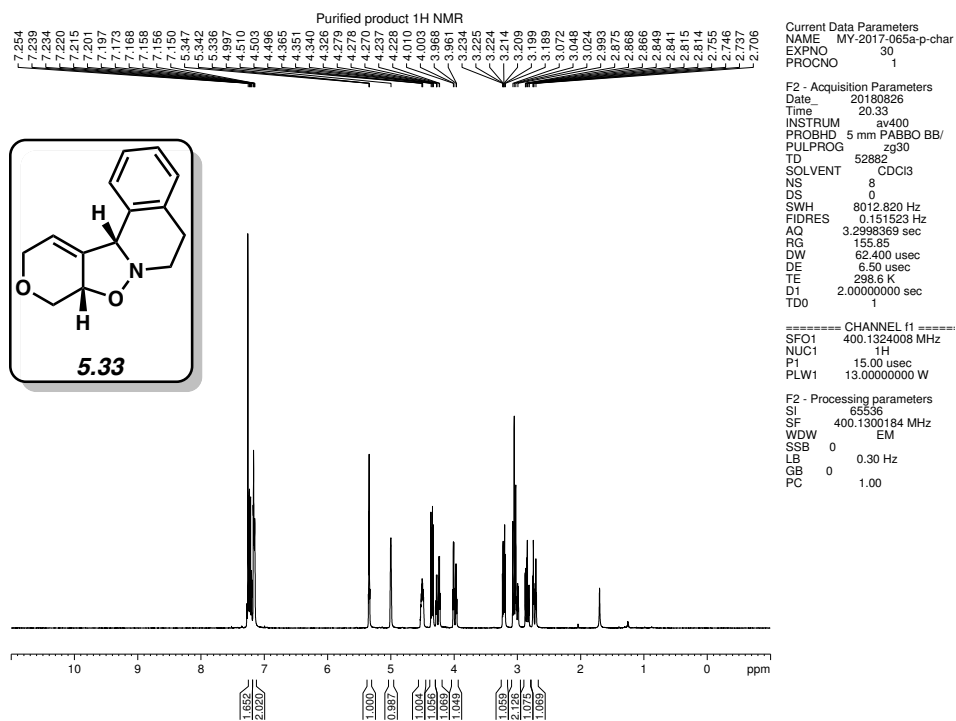
Figure 5.42. ^{1}H NMR (400 MHz, CDCl$_3$) of compound **5.33**.
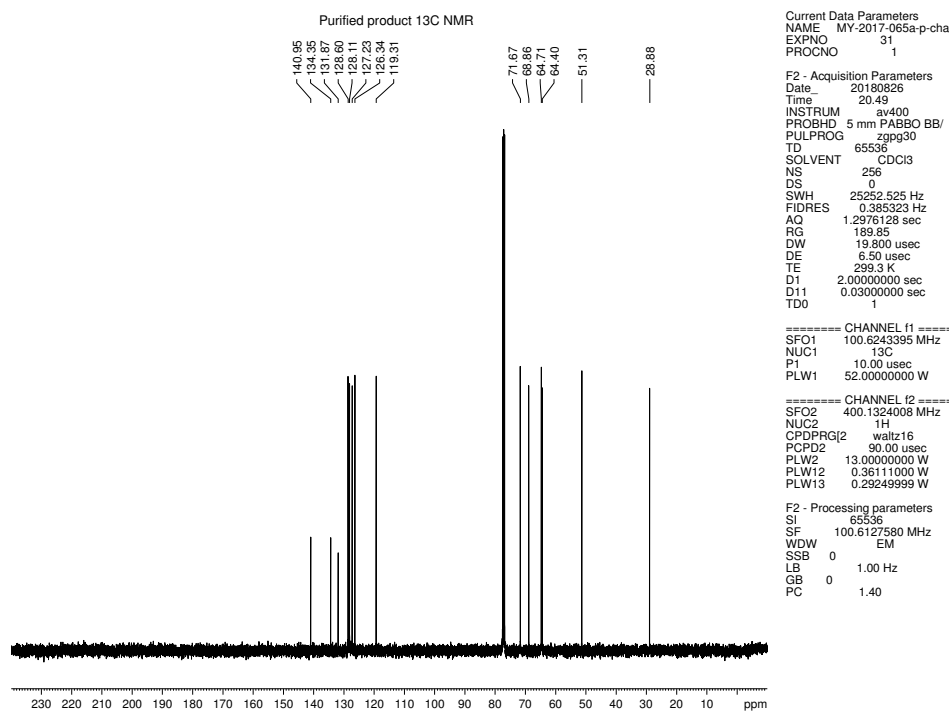
Figure 5.43. ^{13}C NMR (100 MHz, CDCl$_3$) of compound **5.33**.
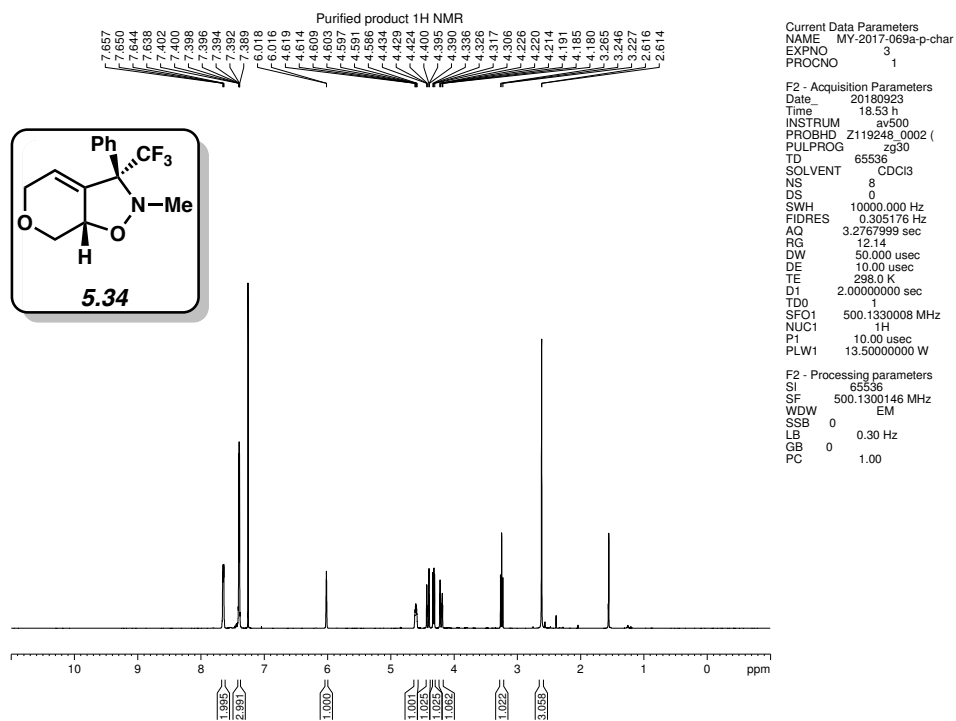
Figure 5.44. ^{1}H NMR (500 MHz, CDCl$_3$) of compound **5.34**.
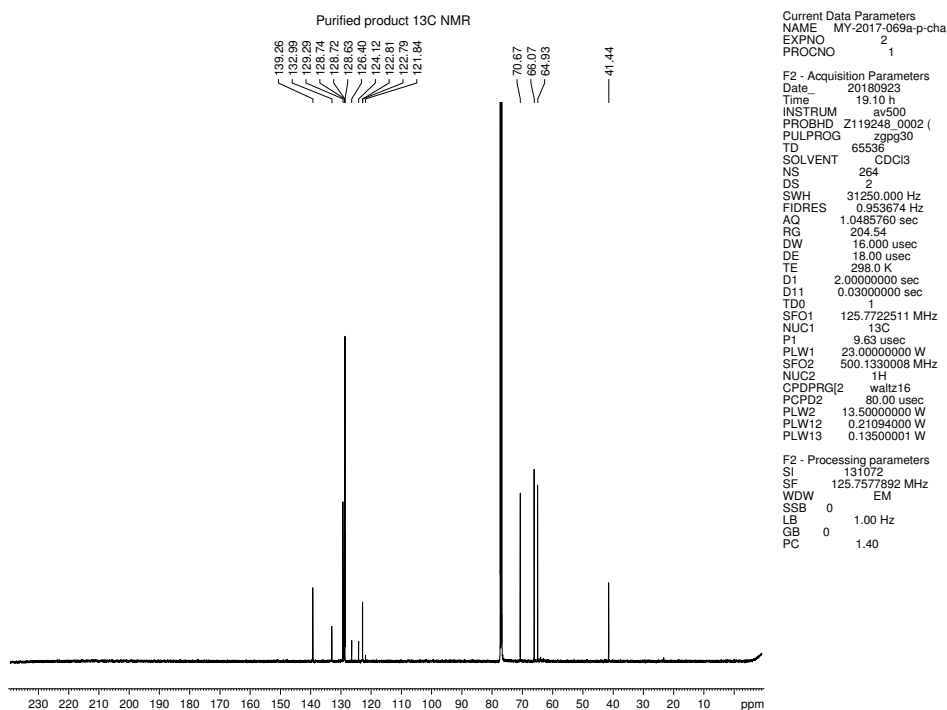
Figure 5.45. ^{13}C NMR (125 MHz, CDCl$_3$) of compound **5.34**.

347
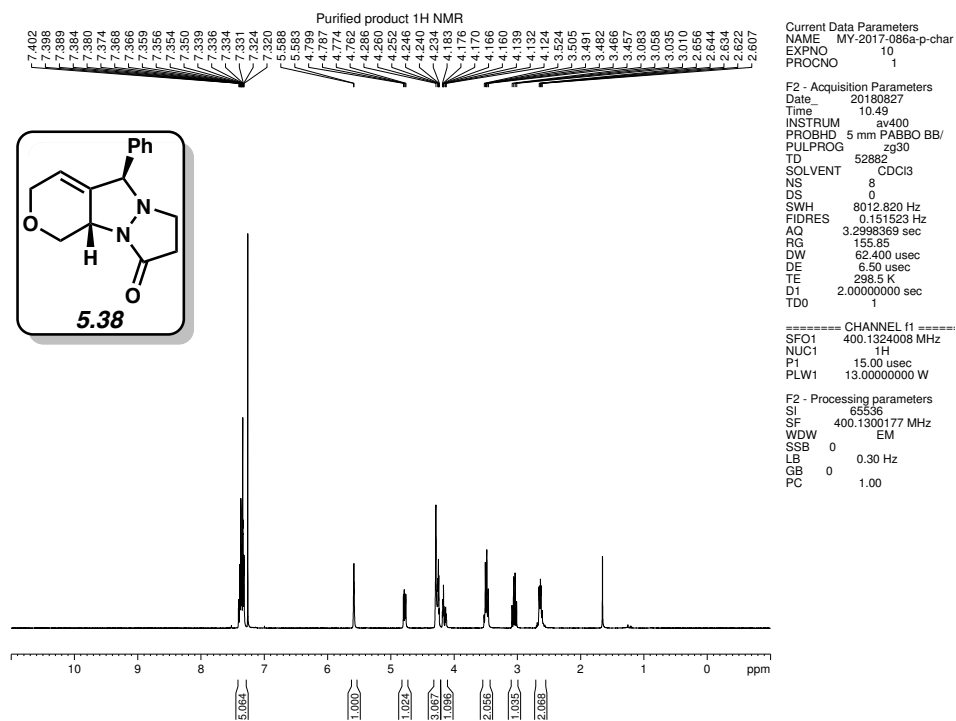
Figure 5.46. ^{1}H NMR (400 MHz, CDCl[3]) of compound **5.38**.
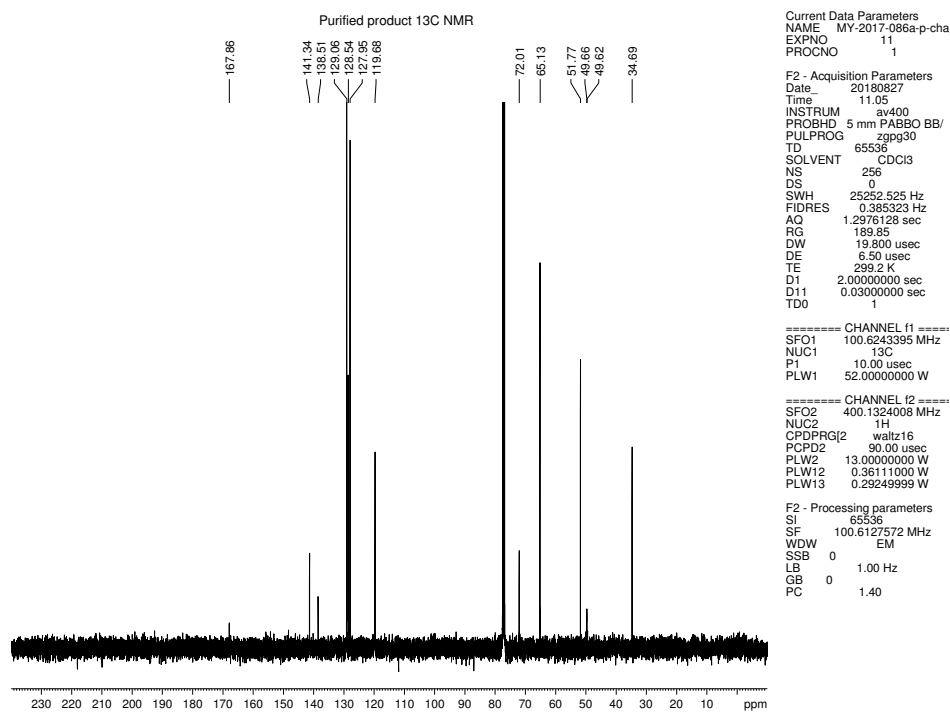
Figure 5.47. ^{13}C NMR (100 MHz, CDCl[3]) of compound **5.38**.

Purified product 1H NMR

5.576
5.571
5.566
5.561
4.898
4.884
4.871
4.858
4.295
4.289
4.259
4.253
4.247
4.240
4.135
4.129
4.126
4.124
4.121
4.115
4.087
4.084
4.079
3.892
3.889
3.646
3.628
3.625
3.610
3.447
3.423
3.421
3.397
2.899
2.894
2.890
2.887
2.881
2.865
2.855
2.851
2.846
2.834
2.830
2.816
2.812
2.524
2.513
2.510
2.494
2.491
2.477
2.476
0.938

t-Bu

5.40

Current Data Parameters
NAME   MY-2018-055a-p-char
EXPNO   10
PROCNO   1

F2 - Acquisition Parameters
Date_   20180916
Time   11.18
INSTRUM   av400
PROBHD   5 mm PABBO BB/
PULPROG   zg30
TD   52882
SOLVENT   CDCl3
NS   8
DS   0
SWH   8012.820 Hz
FIDRES   0.151523 Hz
AQ   3.2998369 sec
RG   189.85
DW   62.400 usec
DE   6.50 usec
TE   298.1 K
D1   2.00000000 sec
TD0   1

======== CHANNEL f1 =====
SFO1   400.1324008 MHz
NUC1   1H
P1   15.00 usec
PLW1   13.00000000 W

F2 - Processing parameters
SI   65536
SF   400.1300177 MHz
WDW   EM
SSB   0
LB   0.30 Hz
GB   0
PC   1.00

1.000 1.025 1.033 1.042 0.992 1.028 1.033 3.053 1.034 9.052

Figure 5.48. ^{1}H NMR (400 MHz, CDCl$_3$) of compound **5.40**.

Purified product 13C NMR

164.01
137.95
120.65
78.94
65.72
65.21
56.28
51.07
35.33
35.19
26.32

Current Data Parameters
NAME   MY-2018-055a-p-cha
EXPNO   11
PROCNO   1

F2 - Acquisition Parameters
Date_   20180916
Time   11.48
INSTRUM   av400
PROBHD   5 mm PABBO BB/
PULPROG   zgpg30
TD   65536
SOLVENT   CDCl3
NS   512
DS   0
SWH   25252.525 Hz
FIDRES   0.385323 Hz
AQ   1.2976128 sec
RG   189.85
DW   19.800 usec
DE   6.50 usec
TE   299.1 K
D1   2.00000000 sec
D11   0.03000000 sec
TD0   1

======== CHANNEL f1 =====
SFO1   100.6243395 MHz
NUC1   13C
P1   10.00 usec
PLW1   52.00000000 W

======== CHANNEL f2 =====
SFO2   400.1324008 MHz
NUC2   1H
CPDPRG[2   waltz16
PCPD2   90.00 usec
PLW2   13.00000000 W
PLW12   0.36111000 W
PLW13   0.29249999 W

F2 - Processing parameters
SI   65536
SF   100.6127557 MHz
WDW   EM
SSB   0
LB   1.00 Hz
GB   0
PC   1.40

Figure 5.49. ^{13}C NMR (100 MHz, CDCl$_3$) of compound **5.40**.

349
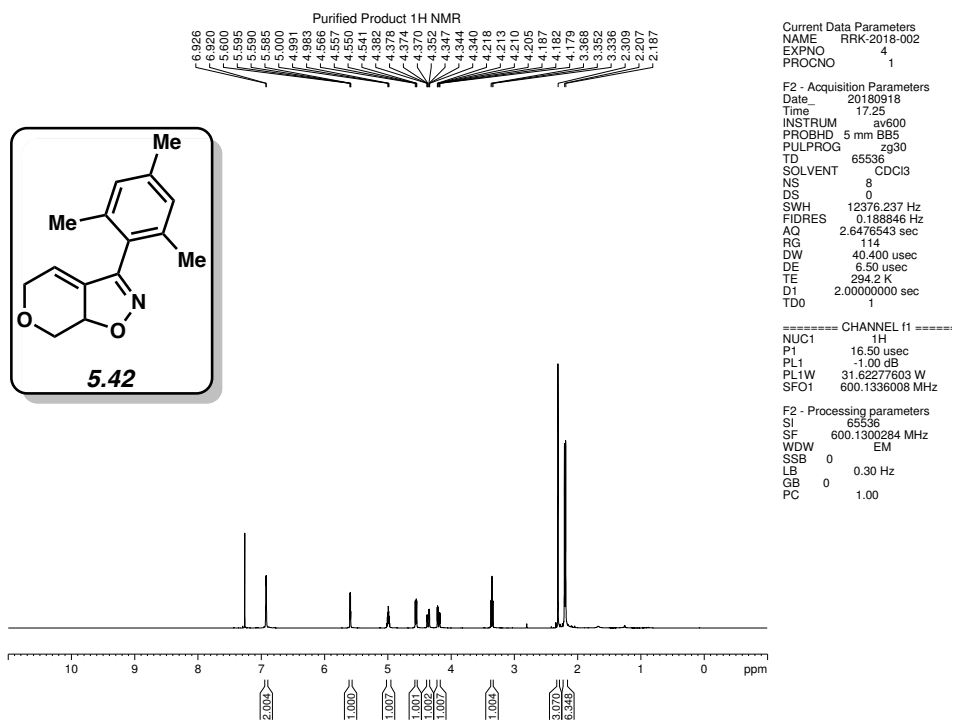
Figure 5.50. ^{1}H NMR (600 MHz, CDCl$_3$) of compound **5.42**.
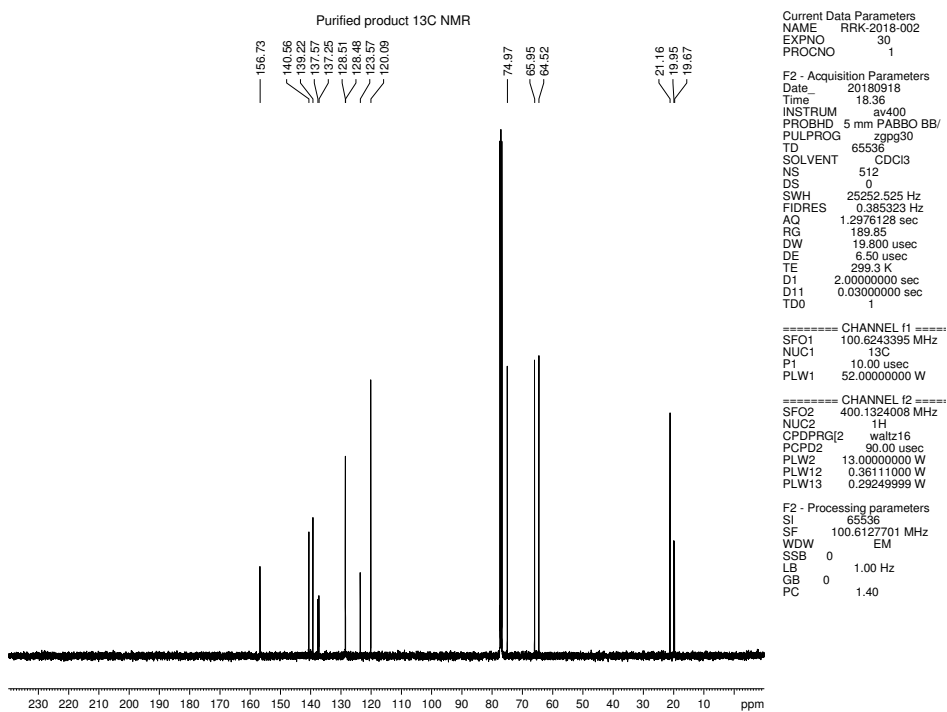
Figure 5.51. ^{13}C NMR (100 MHz, CDCl$_3$) of compound **5.42**.

350

Purified product 1H NMR

7.256
7.251
7.190
7.185
7.177
7.172
7.166
7.159
7.155
7.148
7.135
5.445
5.443
5.442
4.306
4.303
4.300
4.273
4.271
4.268
4.181
4.178
4.174
4.172
4.168
4.165
4.149
4.142
4.139
4.136
4.130
4.117
3.799
3.792
3.785
3.620
3.609
3.596
3.356
3.322
3.303
3.294
3.227
3.208
3.188
3.054
3.048
3.041
3.035
3.030
3.024
3.019
3.017
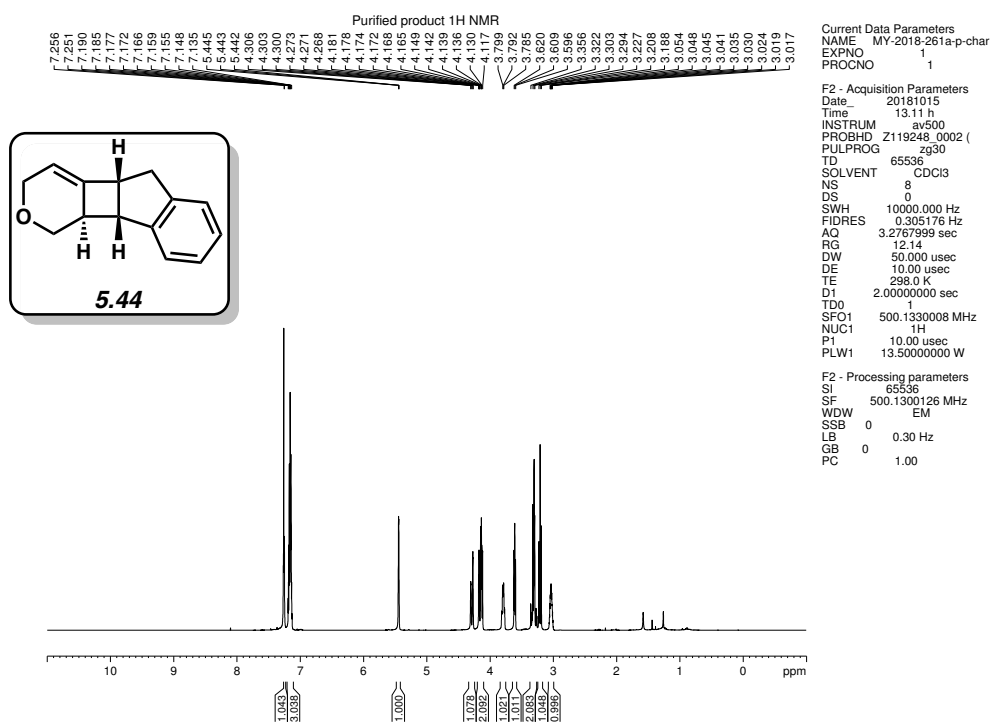
Figure 5.52. ^{1}H NMR (500 MHz, CDCl$_3$) of compound **5.44**.

Purified product 13C NMR

145.98
145.87
141.35
126.81
126.69
125.25
123.46
113.04
66.91
65.47
50.05
49.31
48.76
37.27

Figure 5.53. ^{13}C NMR (125 MHz, CDCl$_3$) of compound **5.44**.

351
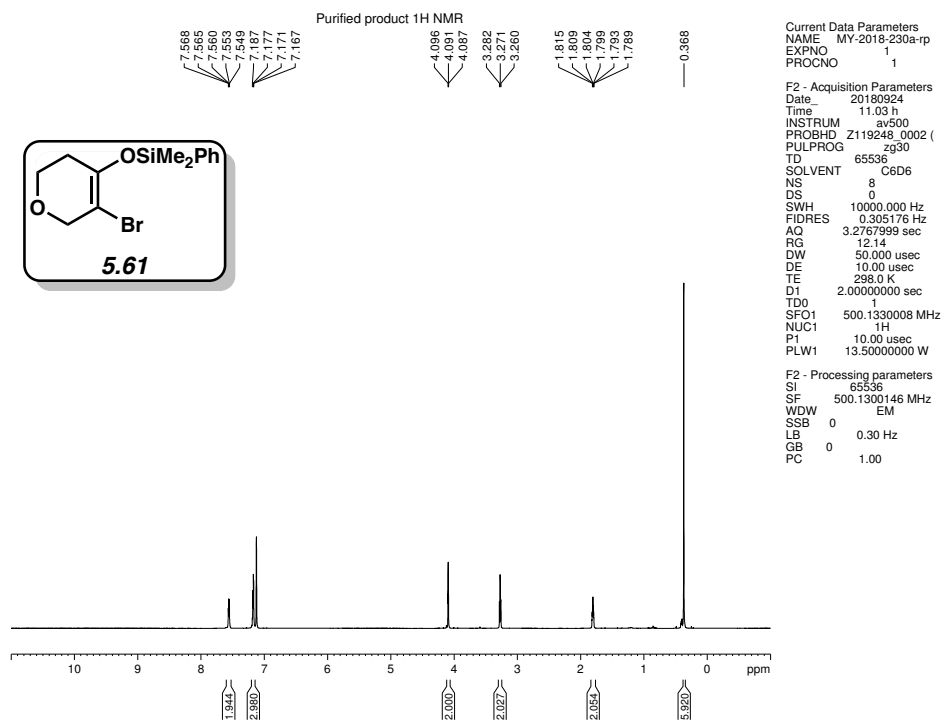
Figure 5.54. ^{1}H NMR (500 MHz, CDCl$_3$) of compound **5.61**.
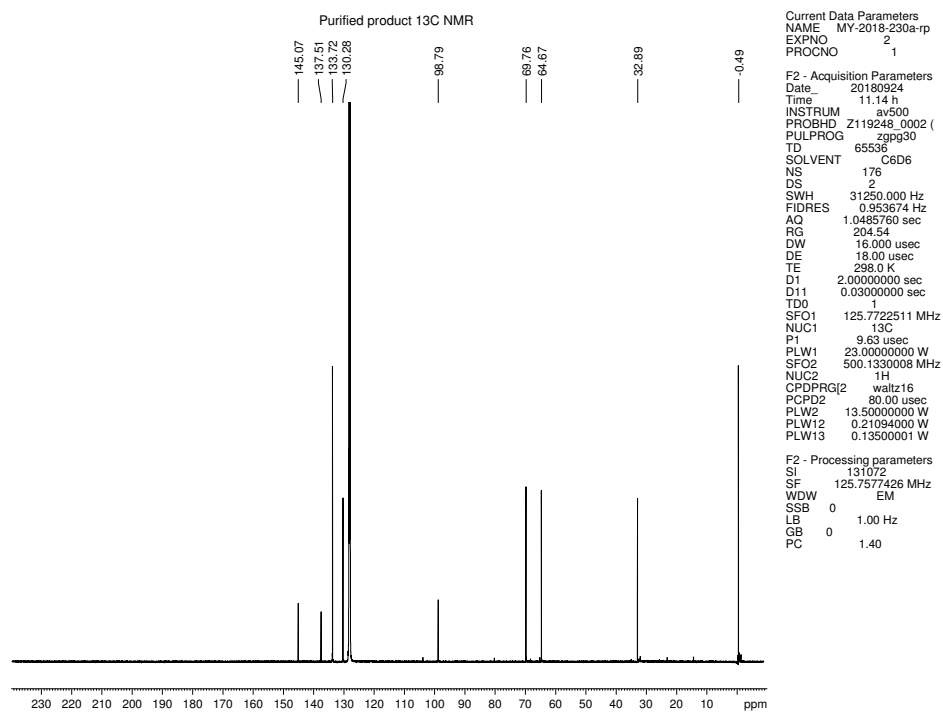
Figure 5.55. ^{13}C NMR (125 MHz, CDCl$_3$) of compound **5.61**.
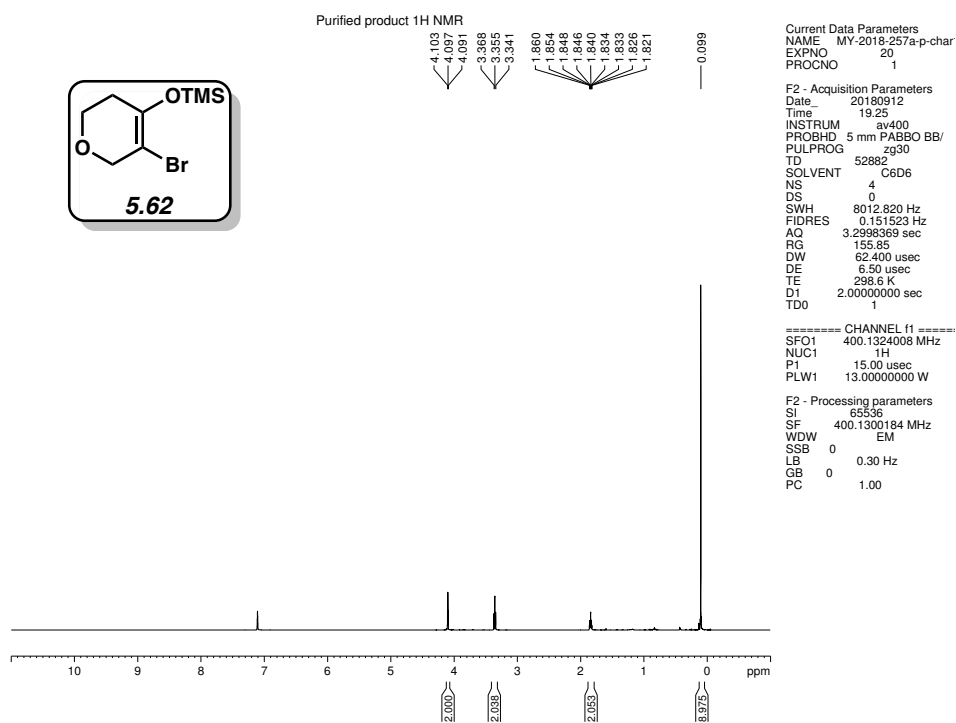
Figure 5.56. ^{1}H NMR (400 MHz, CDCl$_3$) of compound **5.62**.
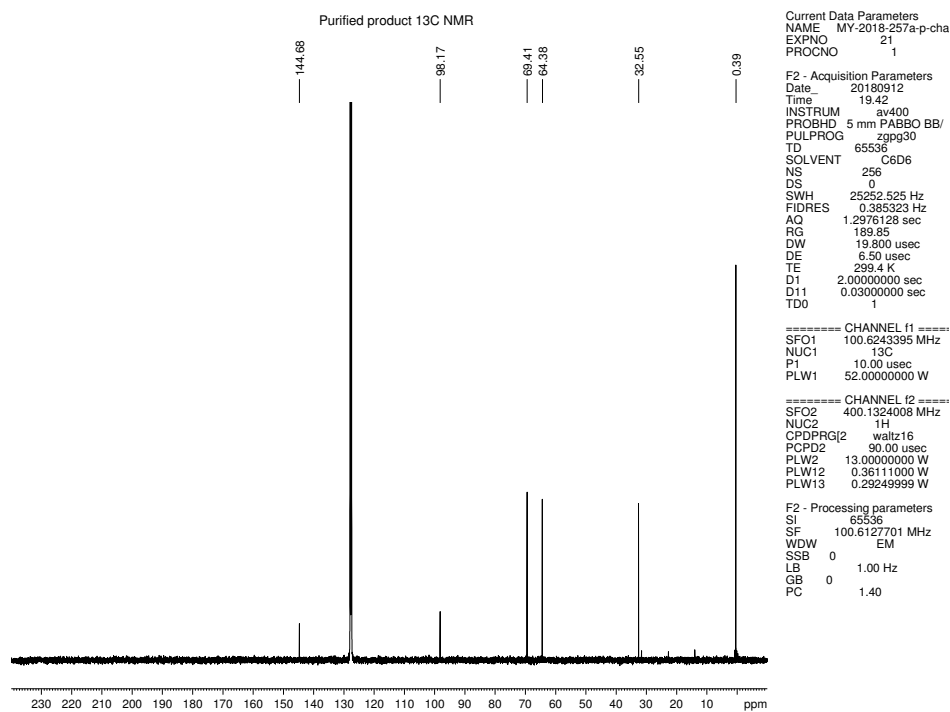
Figure 5.57. ^{13}C NMR (100 MHz, CDCl$_3$) of compound **5.62**.

353
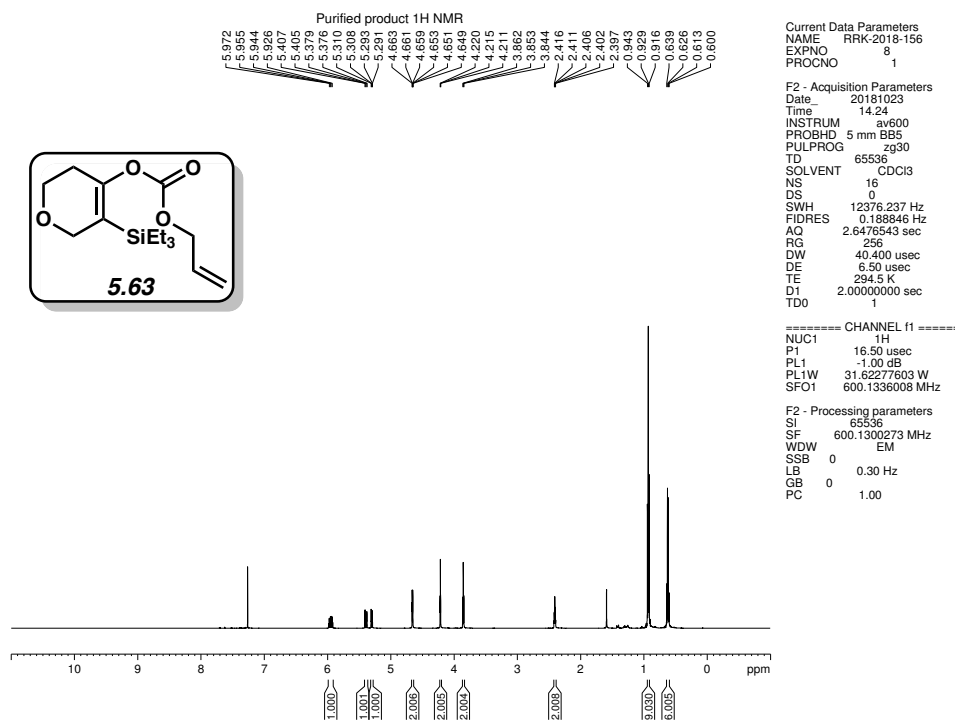
Figure 5.58. ^{1}H NMR (600 MHz, CDCl$_3$) of compound **5.63**.
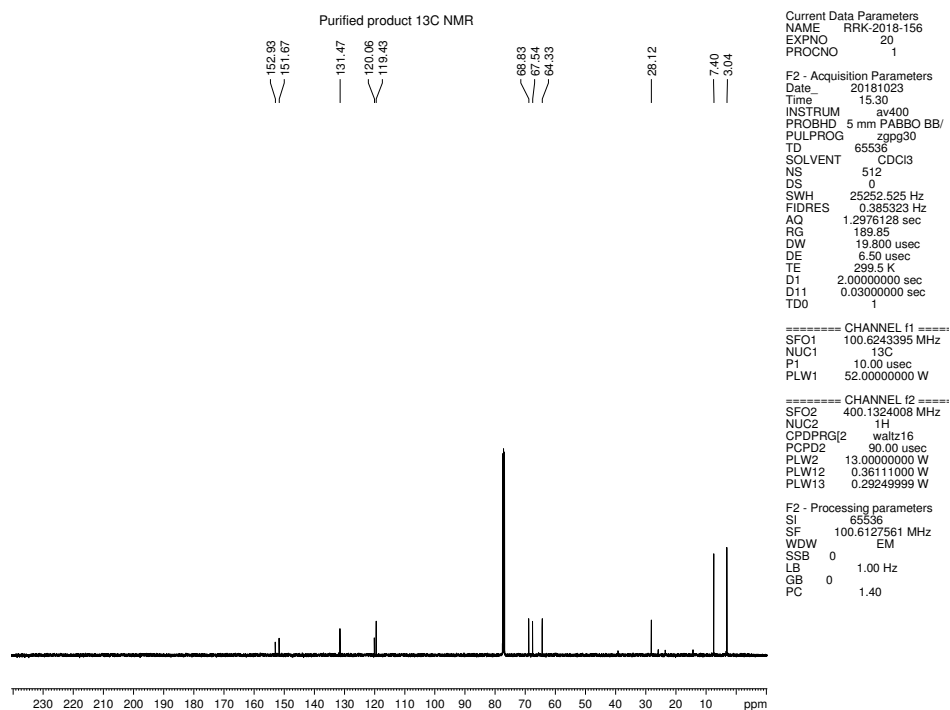
Figure 5.59. ^{13}C NMR (100 MHz, CDCl$_3$) of compound **5.63**.

354
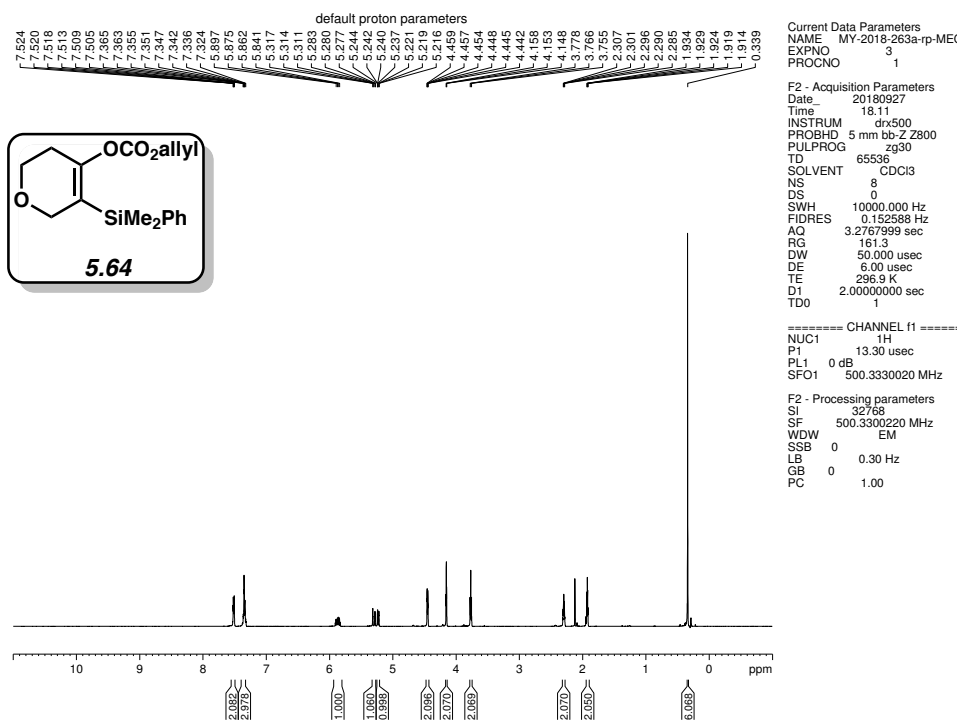
Figure 5.60. ^{1}H NMR (500 MHz, CDCl$_3$) of compound **5.64**.
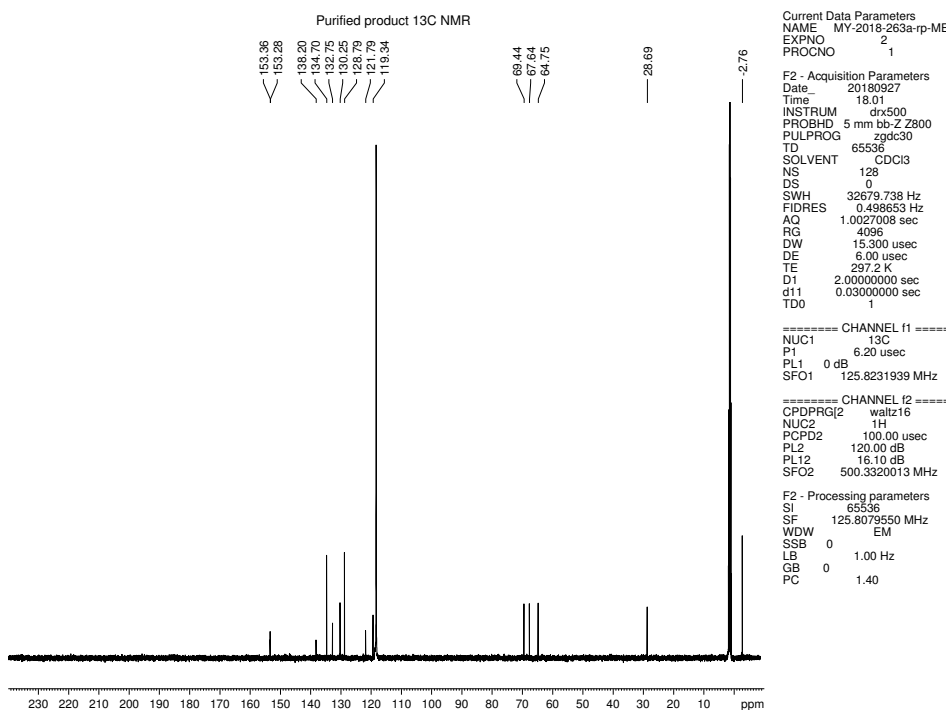
Figure 5.61. ^{13}C NMR (125 MHz, CDCl$_3$) of compound **5.64**.

355
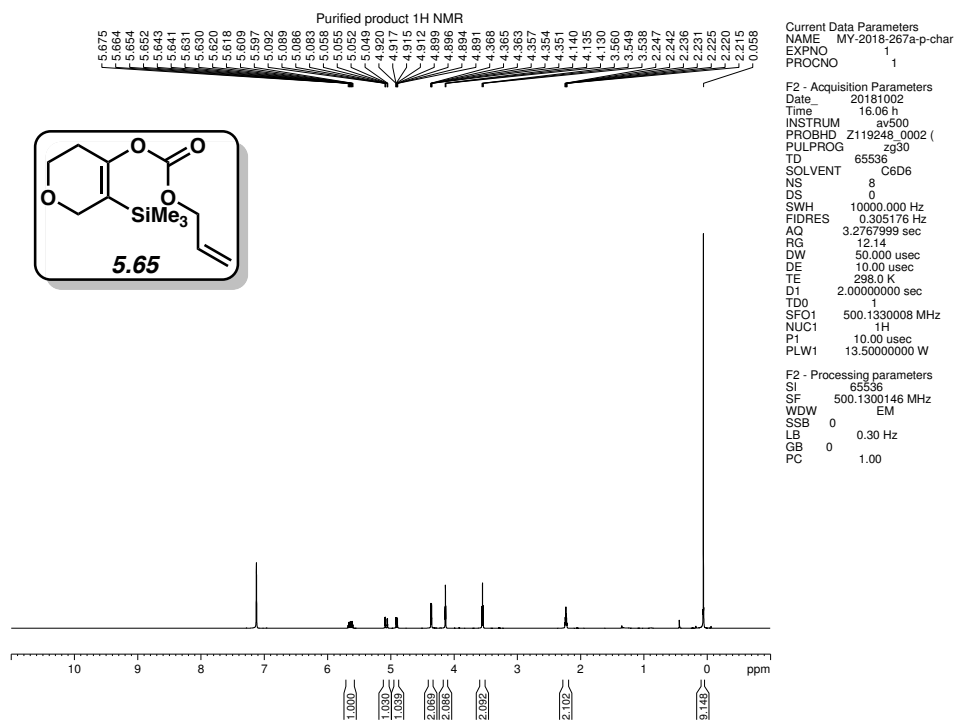
Figure 5.62. ^{1}H NMR (500 MHz, CDCl$_3$) of compound **5.65**.
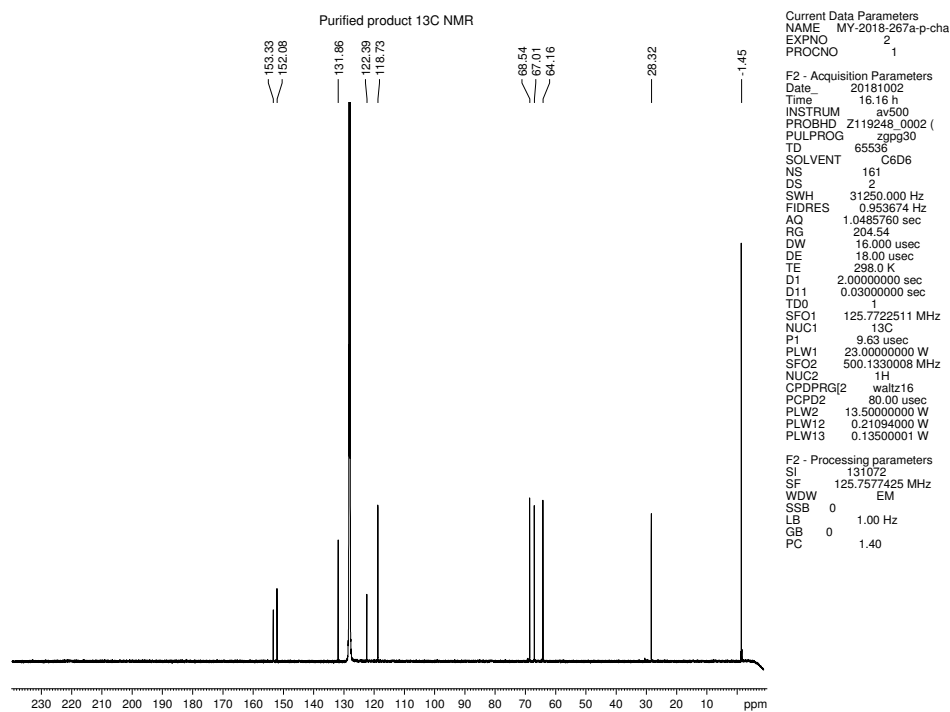
Figure 5.63. ^{13}C NMR (125 MHz, CDCl$_3$) of compound **5.65**.

Purified product 1H NMR

7.459 7.456 7.445 7.444 7.442 7.440 7.375 7.372 7.359 7.358 7.355 7.346 7.343 7.342 7.330 7.327 7.324 7.313
5.597 5.596 5.441 5.438 5.436 5.434 5.066 5.064
4.204 4.194 3.835 3.824 3.813
2.380 2.375 2.369 2.364 2.353 2.348 2.344
0.904 0.888 0.873 0.589 0.574 0.558 0.542 0.541

Current Data Parameters
NAME   RRK-2018-142
EXPNO   13
PROCNO   1

F2 - Acquisition Parameters
Date_   20180928
Time   11.32 h
INSTRUM   av500
PROBHD Z119248_0002 (
PULPROG   zg30
TD   65536
SOLVENT   CDCl3
NS   8
DS   0
SWH   10000.000 Hz
FIDRES   0.305176 Hz
AQ   3.2767999 sec
RG   12.14
DW   50.000 usec
DE   10.00 usec
TE   298.0 K
D1   2.00000000 sec
TD0   1
SFO1   500.1330008 MHz
NUC1   1H
P1   10.00 usec
PLW1   13.50000000 W

F2 - Processing parameters
SI   65536
SF   500.1300122 MHz
WDW   EM
SSB   0
LB   0.30 Hz
GB   0
PC   1.00

2.005 2.996   0.999 1.006   2.010   2.006 2.007   2.008   8.978 5.999

Figure 5.64. ^{1}H NMR (500 MHz, CDCl$_3$) of compound **5.45**.

Purified product 13C NMR

152.90 151.63 142.10 137.84 128.67 128.34 126.21 120.10 116.36
69.56 67.51 64.32
28.08
7.39 3.01

Current Data Parameters
NAME   RRK-2018-142
EXPNO   10
PROCNO   1

F2 - Acquisition Parameters
Date_   20180911
Time   13.59
INSTRUM   av400
PROBHD 5 mm PABBO BB/
PULPROG   zgpg30
TD   65536
SOLVENT   CDCl3
NS   512
DS   0
SWH   25252.525 Hz
FIDRES   0.385323 Hz
AQ   1.2976128 sec
RG   189.85
DW   19.800 usec
DE   6.50 usec
TE   299.6 K
D1   2.00000000 sec
D11   0.03000000 sec
TD0   1

======== CHANNEL f1 ======
SFO1   100.6243395 MHz
NUC1   13C
P1   10.00 usec
PLW1   52.00000000 W

======== CHANNEL f2 ======
SFO2   400.1324008 MHz
NUC2   1H
CPDPRG[2   waltz16
PCPD2   90.00 usec
PLW2   13.00000000 W
PLW12   0.36111000 W
PLW13   0.29249999 W

F2 - Processing parameters
SI   65536
SF   100.6127560 MHz
WDW   EM
SSB   0
LB   1.00 Hz
GB   0
PC   1.40

Figure 5.65. ^{13}C NMR (100 MHz, CDCl$_3$) of compound **5.45**.

357
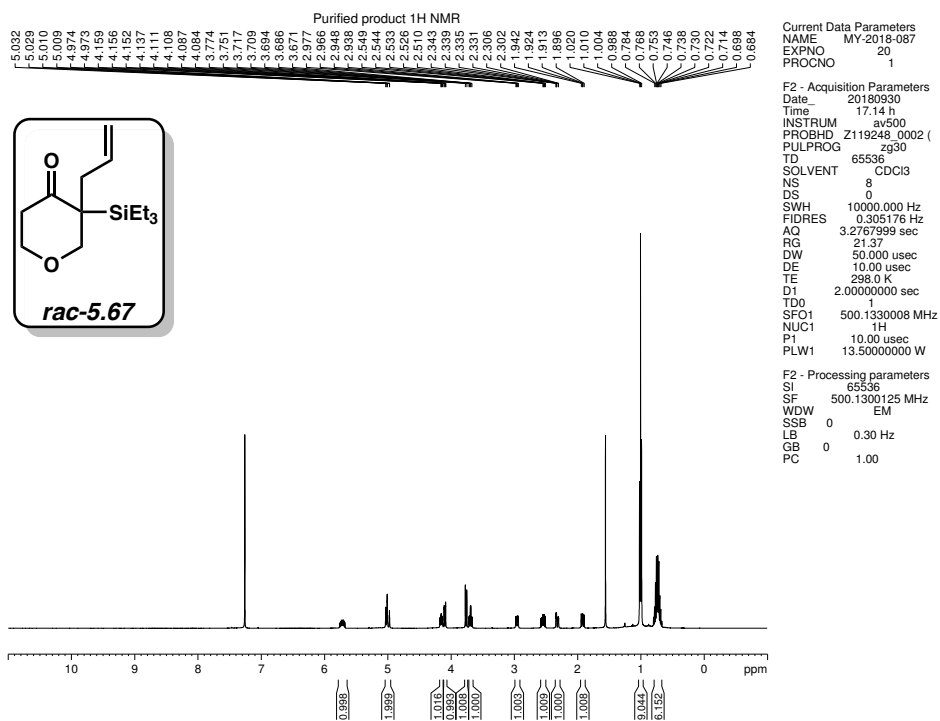
Figure 5.66. ^{1}H NMR (500 MHz, CDCl$_3$) of compound **rac-5.67**.
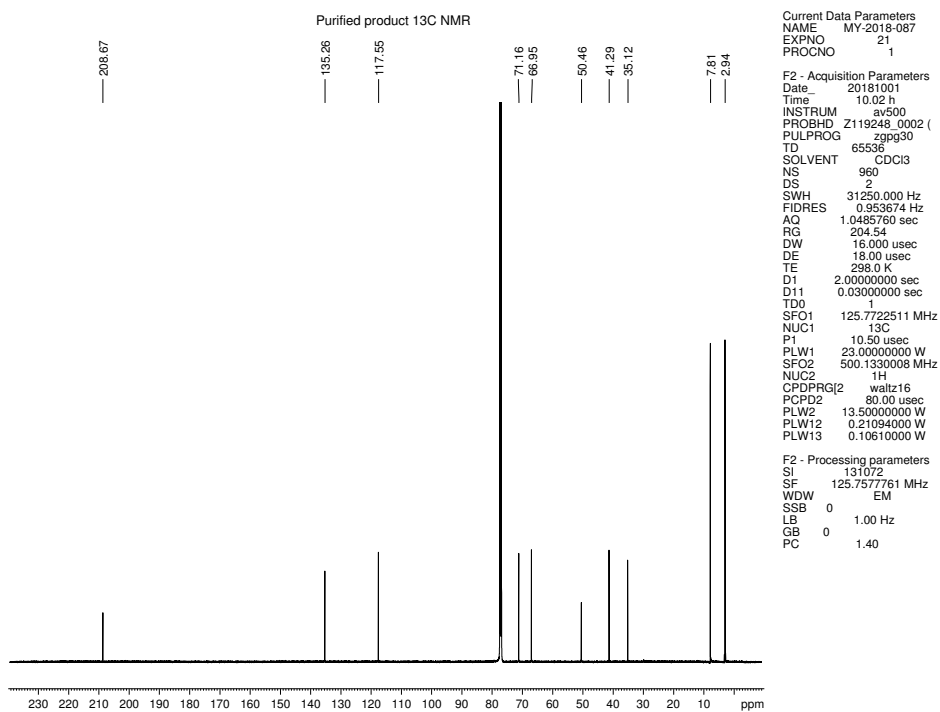
Figure 5.67. ^{13}C NMR (125 MHz, CDCl$_3$) of compound **rac-5.67**.
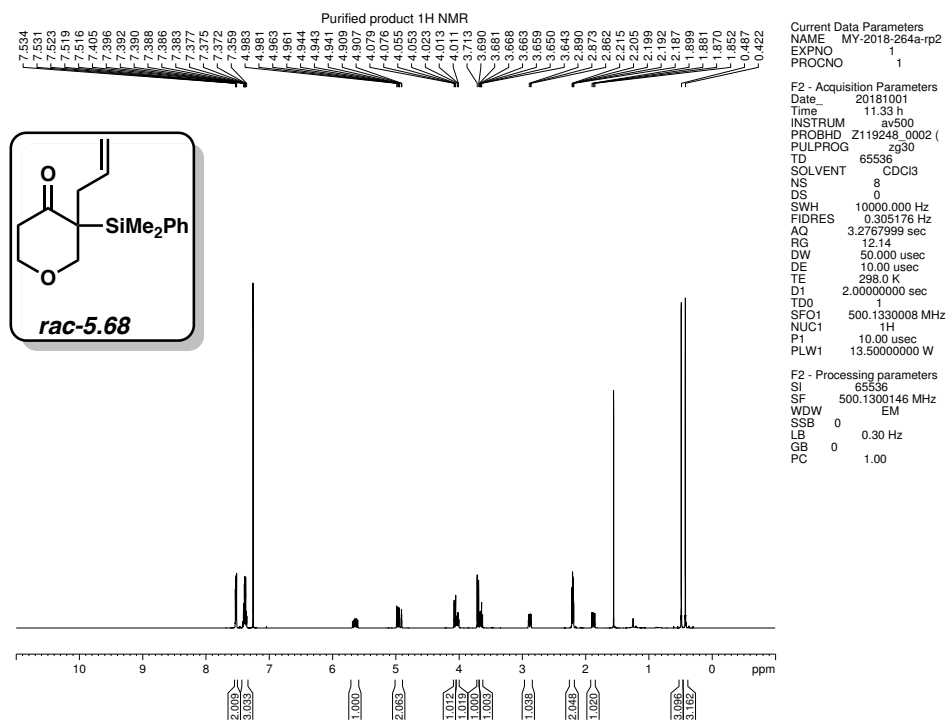
Figure 5.68. ^{1}H NMR (500 MHz, CDCl$_3$) of compound **rac-5.68**.
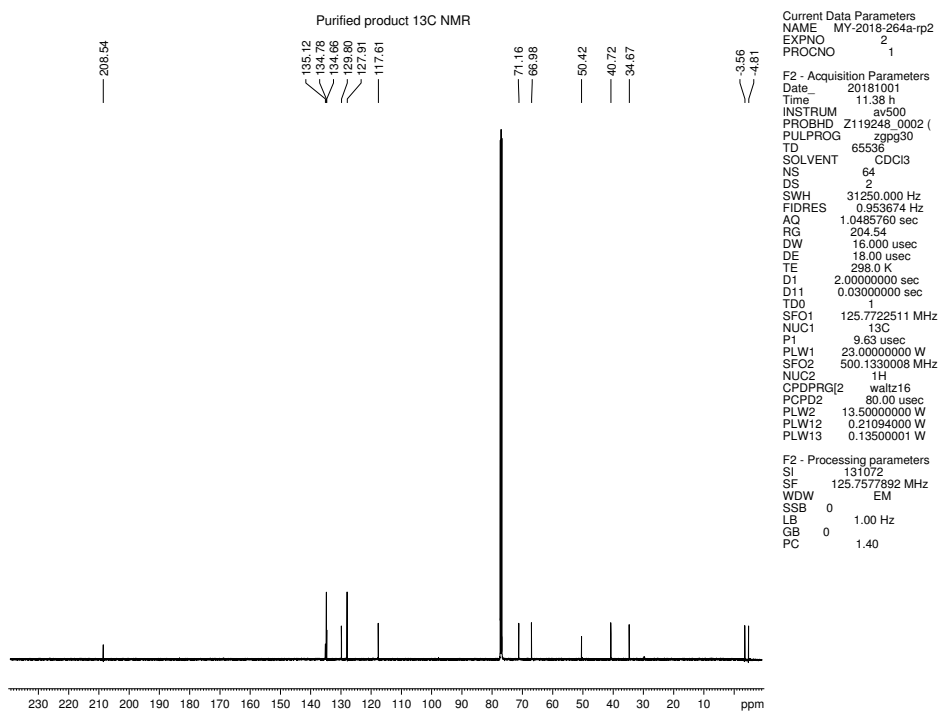
Figure 5.69. ^{13}C NMR (125 MHz, CDCl$_3$) of compound **rac-5.68**.

5.757 5.746 5.738 5.727 5.724 5.720 5.713 5.706 5.704 5.693 5.686 5.675 5.035 5.014 4.978 4.180 4.165 4.161 4.158 4.142 4.081 4.057 3.795 3.772 3.722 3.714 3.699 3.691 3.676 3.668 2.872 2.862 2.844 2.833 2.535 2.520 2.512 2.502 2.497 2.486 2.478 2.463 2.340 2.336 2.332 2.309 2.306

rac-5.69

1.000 2.006 1.020 1.020 1.022 1.083 1.013 1.138 1.099 1.039 9.101
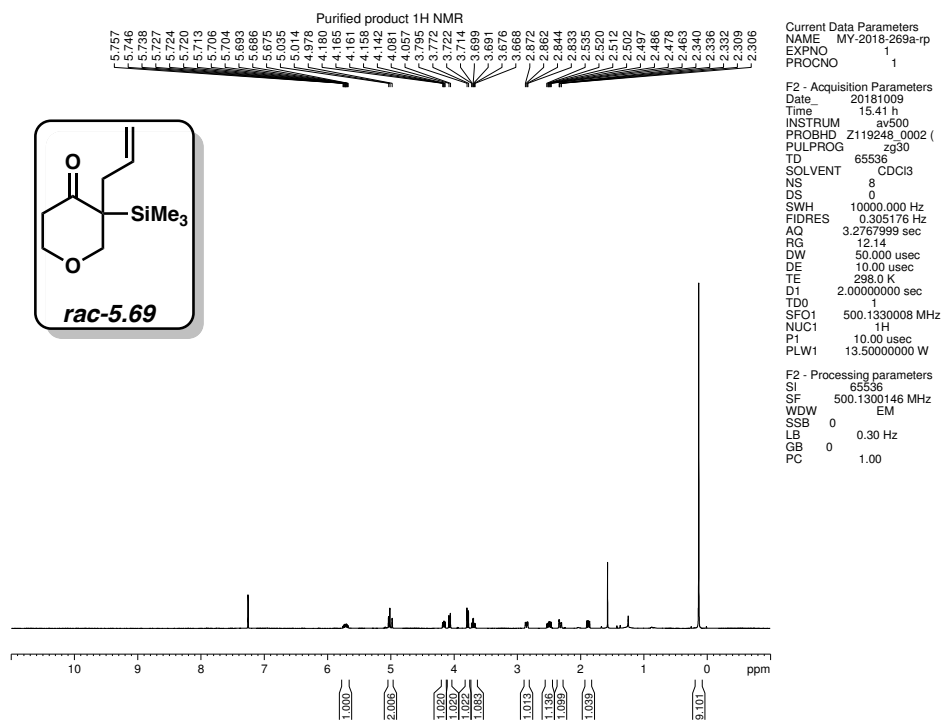
Figure 5.70. ^{1}H NMR (500 MHz, CDCl$_3$) of compound **rac-5.69**.

208.48   135.00   117.67   71.07 67.06   50.11   41.20 34.45   -2.45
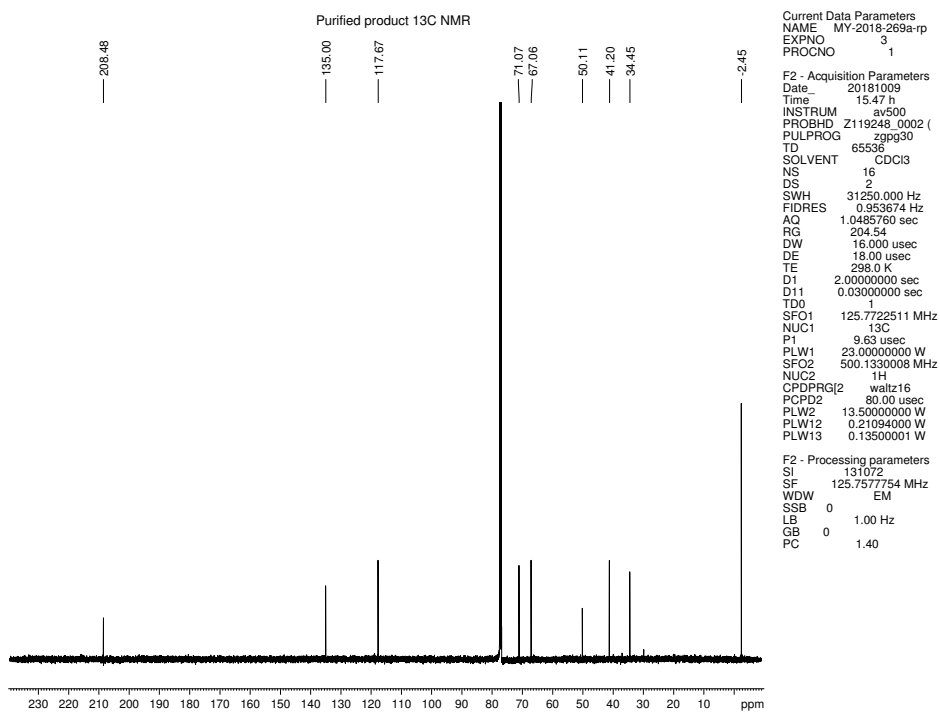
Figure 5.71. ^{13}C NMR (125 MHz, CDCl$_3$) of compound **rac-5.69**.

360
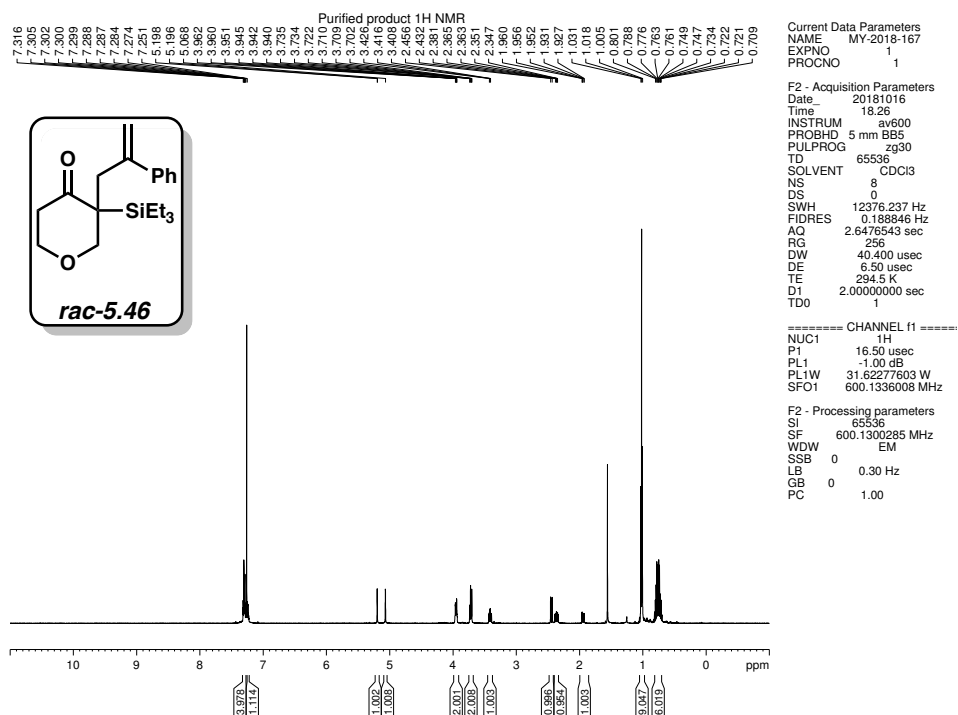
Figure 5.72. ^{1}H NMR (600 MHz, CDCl$_3$) of compound **rac-5.46**.
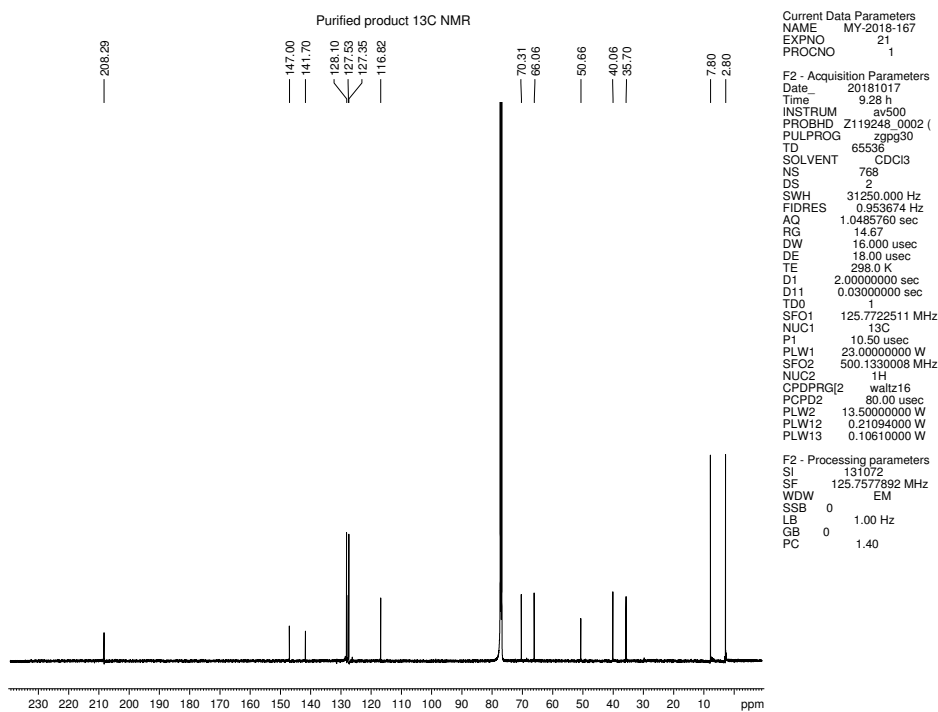
Figure 5.73. ^{13}C NMR (125 MHz, CDCl$_3$) of compound **rac-5.46**.

Figure 5.74. ^{1}H NMR (500 MHz, CDCl$_3$) of compound **5.48**.

Figure 5.75. ^{13}C NMR (125 MHz, CDCl$_3$) of compound **5.48**.
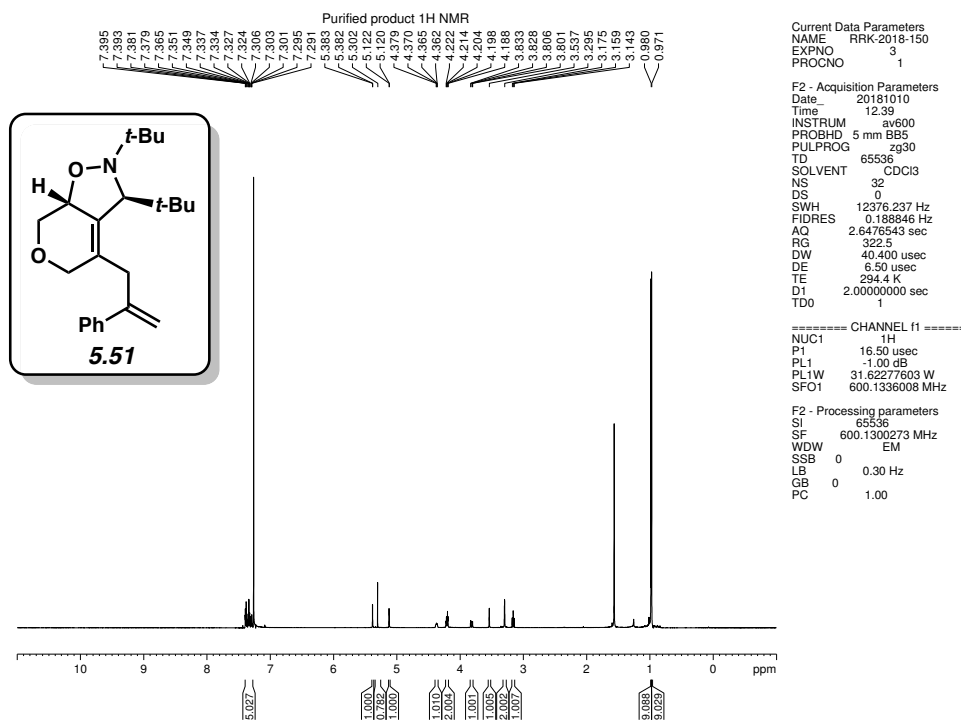
Figure 5.76. ^{1}H NMR (600 MHz, CDCl$_3$) of compound **5.51**.
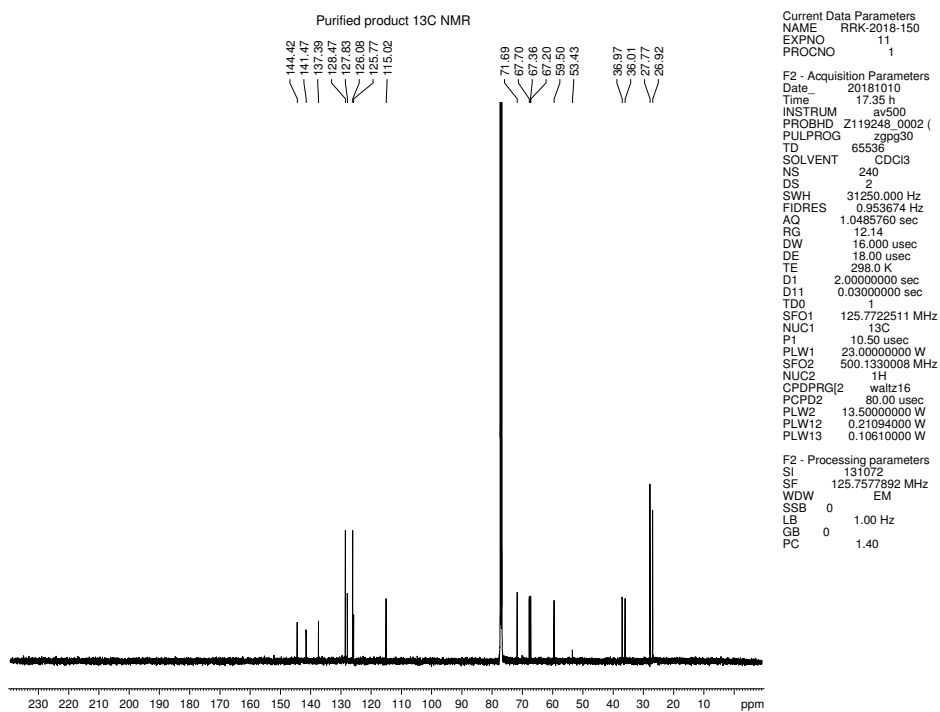
Figure 5.77. ^{13}C NMR (125 MHz, CDCl$_3$) of compound **5.51**.

363
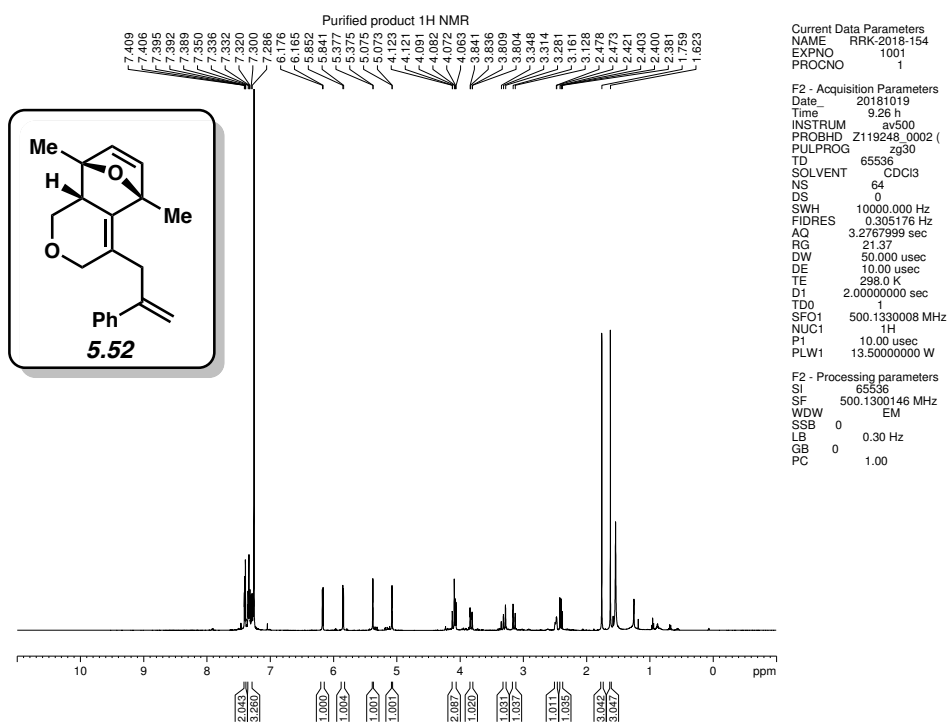
Figure 5.78. ^{1}H NMR (500 MHz, CDCl$_3$) of compound **5.52**.
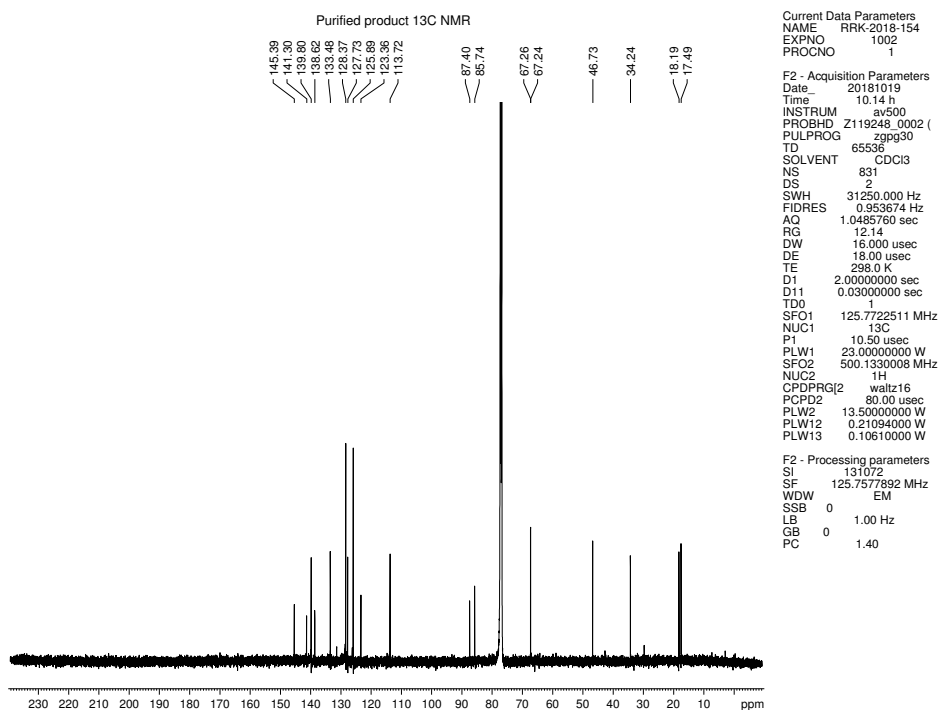
Figure 5.79. ^{13}C NMR (125 MHz, CDCl$_3$) of compound **5.52**.

5.10 Notes and References

(1) a) Wittig G. *Naturwissenschaften* **1942**, *30*, 696–703; b) Roberts, J. D.; Simmons, H. E.; Carlsmith, L. A.; Vaughn, C. W. *J. Am. Chem. Soc.* **1953**, *75*, 3290–3291.

(2) For recent examples of arynes and related species in total synthesis, see: a) Kou, K. G. M.; Pflueger, J. J.; Kiho, T.; Morrill, L. C.; Fisher, E. L.; Clagg, K.; Lebold, T. P.; Kisunzu, J. K.; Sarpong, R. *J. Am. Chem. Soc.* **2018**, *140*, 8105–8109; b) Goetz, A. E.; Silberstein, A. L.; Corsello, M. A.; Garg, N. K. *J. Am. Chem. Soc.* **2014**, *136*, 3036–3039; c) Neog, K.; Borah, A.; Gogoi, P. *J. Org. Chem.* **2016**, *81*, 11971–11977; d) Neumeyer, M.; Kopp, J.; Brückner, R. *Eur. J. Org. Chem.* **2017**, 2883–2915; e) Corsello, M. A.; Kim, J.; Garg, N. K. *Nat. Chem.* **2017**, *9*, 944–949.

(3) a) Carroll, F. I.; Robinson, T. P.; Brieaddy, L. E.; Atkinson, R. N.; Mascarella, S. W.; Damaj, M. I.; Martin, B. R.; Navarrio, H. A. *J. Med. Chem.* **2007**, *50*, 6383–6391; c) Willis, P. G.; Pavlova, O. A.; Chefer, S. I.; Vaupel, D. B.; Mukhin, A. G.; Horti, A. G. *J. Med. Chem.* **2005**, *48*, 5813–5822; d) Jacob, P. III. *J. Med. Chem.* **1981**, *24*, 1348–1353; e) Coe, J. W. et al., *Bioorg. Med. Chem. Lett.* **2005**, *15*, 4889–4897.

(4) Schleth, F.; Vettiger, T.; Rommel, M.; Tobler, H. WO2011131544 A1, **2011**.

(5) Lin, J. B.; Shah, T. J.; Goetz, A. E.; Garg, N. K.; Houk, K. N. *J. Am. Chem. Soc.* **2017**, *139*, 10447–10455.

(6) Chupakhin, E. G.; Krasavin, M. Y. *Chem. Heterocycl. Compd.* **2018**, *54*, 483–501.

(7) a) Surry, D. S.; Buchwald, S. L. *Angew. Chem. Int. Ed.* **2008**, *47*, 6338–6361; *Angew. Chem.* **2008**, *120*, 6438–6461; b) Mauger, C. C.; Mignani, G. A. *Org. Proc. Res. Dev.* **2004**, *8*, 1065–1071.

(8) For recent reviews of arynes and related intermediates, see: a) Goetz, A. E.; Garg, N. K. *J. Org. Chem.* **2014**, *79*, 846–851; b) Yoshida, S.; Hosoya, T. *Chem. Lett.* **2015**, *44*, 1450–1460; c) Bhojgude, S. S.; Bhunia, A.; Biju, A. T. *Acc. Chem. Res.* **2016**, *49*, 1658–1670; d) Shi, J.; Li, Y.; Li, Y. *Chem. Soc. Rev.* **2017**, *46*, 1707–1719; e) Asamdi, M.; Chikhalia, K. H. *Asian J. Org. Chem.* **2017**, *6*, 1331–1348; f) Idiris, F. I. M.; Jones, C. R. *Org. Biomol. Chem.* **2017**, *15*, 9044–9056; g) Takikawa, H.; Nishii, A.; Sakai, T.; Suzuki, K. *Chem. Soc. Rev.* **2018**, *47*, 8030–8056; h) Dhokale, R. A.; Mhaske, S. B. *Synthesis* **2018**, *50*, 1–16.

(9) Wittig, G.; Fritze, P. *Angew. Chem., Int. Ed.* **1966**, *5*, 846; *Angew. Chem.* **1966**, *78*, 905.

(10) a) Angus, R. O.; Schmidt, M. W.; Johnson, R. P. *J. Am. Chem. Soc.* **1985**, *107*, 532–537; b) Engels, B.; Schöneboom, J. C.; Münster, A. F.; Geoetsch, S.; Christl, M. *J. Am. Chem. Soc.* **2002**, *124*, 287–297; c) Schmidt, M. W.; Angus, R. O.; Johnson, R. P. *J. Am. Chem. Soc.* **1982**, *104*, 6838–6839; d) Dillion, P. W.; Underwood, G. R. *J. Am. Chem Soc.* **1974**, *96*, 779–787; e) Daoust, K. J.; Hernandez, S. M.; Konrad, K. M.; Mackie, I.; Winstanley, J.; Johnson, R. P. *J. Org. Chem.* **2006**, *71*, 5708–5714.

(11) a) Barber, J. S.; Styduhar, E. D.; Pham, H. W.; McMahon, T. C.; Houk, K. N.; Garg, N. K. *J. Am. Chem. Soc.* **2016**, *138*, 2512–2515; b) Lofstrand, V. A.; West, F. G. *Chem. Eur. J.* **2016**, *22*, 10763–10767.

(12) Quintana, I.; Peña, D.; Pérez, D.; Guitián, E. *Eur. J. Org. Chem.* **2009**, 5519–5524.

(13) Additionally, 1,2-cyclohexadiene has been generated through a similar silyl bromide elimination: Shakespeare, W. C.; Johnson, R. P. *J. Am. Chem. Soc.* **1990**, *112*, 8578–8579.

(14) Schreck, M.; Christl, M. *Angew. Chem. Int. Ed.* **1987**, *26*, 690–692; *Angew. Chem.* **1987**, *99*, 720–721.

(15) For heterocyclic allene generation under harsh conditions or utilizing highly basic reagents, see; a) Christl, M.; Braun, M.; Wolz, E.; Wagner, W. *Chem. Ber.* **1994**, *127*, 1137–1142; b) Ruzziconi, R.; Naruse, Y.; Schlosser, M. *Tetrahedron* **1991**, *47*, 4603–4610; c) Drinkuth, S.; Groetsch, S.; Peters, E.; Peters, K.; Christl, M. *Eur. J. Org. Chem.* **2001**, 2665–2670.

(16) Barber, J. S.; Yamano, M. M.; Ramirez, M.; Darzi, E. R.; Knapp, R. R.; Liu, F.; Houk, K. N.; Garg, N. K. *Nat. Chem.* **2018**, *10*, 953–960.

(17) Blakemore, D. C.; Castro, L.; Churcher, I.; Rees, D. C.; Thomas, A. W.; Wilson, D. M.; Wood, A. *Nat. Chem.* **2018**, *10,* 383–394.

(18) a) Atul, G.; Amit, K.; Ashutosh, R. *Chem. Rev.* **2013**, *113*, 1614–1640; b) Radadiya, A.; Shah, A. *Eur. J. Med. Chem.* **2015**, *97*, 356–376.

(19) a) Klayman, D. L. *Science* **1985**, *228*, 1049–1055; b) Dondorp, A. M., et al., *N. Engl. J. Med*. **2009**, *361*, 455–467.

(20) Montgomery, C. T.; Cassels, B. K.; Shamma, M. *J. Nat. Prod*. **1983**, *46*, 441–453.

(21) Salaski, E. J., et al., *J. Med. Chem*. **2009**, *52*, 2181–2184.

(22) a) Tomaszewski, Z., et al., *J. Med. Chem*. **2005**, *48*, 926–934; b) Nevagi, R. J.; Dighe, S. N. *Eur. J. Med. Chem*. **2015**, *97*, 561–581; c) Zhang, S.; Zhen, J.; Reith, M. E. A.; Dutta, A. K. *Bioorg. Med. Chem*. **2004**, *12*, 6301–6315; d) Zhang, S.; Reith, M. E. A.; Dutta, A. K. *Bioorg. Med. Chem. Lett*. **2003**, *13*, 1591–1595.

(23) The racemization barrier for 3,4-oxacyclohexadiene (**5.8**) was calculated to be 15.2 kcal/mol (ωB97XD/6-311+G(d,p)/SMD(MeCN)). In comparison, the racemization barrier for 3,4-azacyclohexadiene bearing an *N*-CO$_2$Me group was found to be 14.7 kcal/mol.

(24) Himeshima, Y.; Sonoda, T.; Kobayashi, H. *Chem. Lett.* **1983**, *12*, 1211–1214.

(25) Shah, T. K.; Medina, J. M.; Garg, N. K. *J. Am. Chem. Soc.* **2016**, *138*, 4948–4954.

(26) See Section 5.8.2.1 for details.

(27) Recently, an innovative approach to a 1,2-cyclohexadiene precursor was reported: Inoue, K.; Nakura, R.; Okano, K.; Mori, A. *Eur. J. Org. Chem.* **2018**, 3343–3347.

(28) In the absence of a trapping partner, (2+2) dimerization of the allene is observed.

(29) Christl, M.; Fischer, H.; Arnone, M.; Engels, B. *Chem. Eur. J.* **2009**, *15*, 11266–11272.

(30) Behenna, D. C., et. al., *Chem. Eur. J.* **2011**, *17*, 14199–14223.

(31) For recent examples, see: a) Vita, M. V.; Caramenti, P.; Waser, J. *Org. Lett.* **2015**, *17*, 5832–5835; b) Hong, A. Y.; Bennett, N. B.; Krout, M. R.; Jensen, T.; Harned, A. M.; Stoltz, B. M. *Tetrahedron* **2011**, *67*, 10234–10248; c) Kondo, H.; Maeno, M.; Hirano, K.; Shibata, N. *Chem. Commun.* **2018**, *54*, 5522–5525; d) Skardon-Duncan, J.; Sparenberg, M.; Bayle, A.; Alexander, S.; Clark, J. S. *Org. Lett.* **2018**, *20*, 2782–2786; e) Zhang, Z.-W.; Wang, C.-C.; Xue, H.; Dong, Y.; Yang, L.; Shouxin, J.-H.; Wen-Qing, L.; Wei-Dong, Z. *Org. Lett.* **2018**, *20*, 1050–1053; f) Lian, W.-F.; Wang, C.-C.; Kang, H.-P.; Li, H.-L; Feng, J.; Liu, S.; Zhang, Z.-W. *Tetrahedron Lett.* **2017**, *58*, 1399–1402.

(32) Another plausible explanation for **5.51** being obtained in diminished ee is that racemization of **5.49** occurs more readily than the nitrone cycloaddition. However, the kinetic barriers for nitrone and Diels–Alder cycloadditions on related systems have been calculated to be roughly 14 kcal / mol and 19 kcal / mol, respectively (see references 11a and 16). Since the Diels–Alder cycloaddition appears to be a more challenging process, yet proceeds with complete enantiospecificity, we disfavor racemization of **5.49** as being the cause of partial loss of ee in the case of **5.51**.

(33) C. –W. Lin, B.-C. Hong, W.-C. Chang, G.-H. Lee, *Org. Lett.* **2015**, *17*, 2314–2317.

(34) E. Drockenmuller, J.-M. Catala, *Macromolecules* **2002**, *35*, 2461–2466.

(35) S.-I. Murahashi, T. Shiota, *Tetrahedron Lett.* **1987**, *28*, 2383–2386.

(36) R. Shintani, G. C. Fu, *J. Am. Chem. Soc.* **2003**, *125*, 10778–10779.

(37) R. Shintani, T. Hayashi, *J. Am. Chem. Soc.* **2006**, *128*, 6330–6331.

(38) O. Altintas, M. Glassner, C. Rodriguez-Emmenegger, A. Welle, V. Trouillet, C. Barner-Kowollik, *Angew. Chem. Int. Ed.* **2015**, *54*, 5777–5783; *Angew. Chem.* **2015**, *127*, 5869–5875.

(39) K. M. Korch, C. Eidamshaus, D. C. Behenna, S. Nam, D. Horne, B. M. Stoltz, *Angew. Chem. Int. Ed.* **2015**, *54*, 179–183; *Angew. Chem.* **2015**, *127*, 181–185.

(40) N. T. McDougal, J. Streuff, H. Mukherjee, S. C. Virgil, B. M. Stoltz, *Tetrahedron Lett.* **2010**, *51*, 5550–5554.

(41) R. F. Ribeiro, A. V. Marenich, C. J. Cramer, D. G. Truhlar *J. Phys. Chem. B* **2011**, *115*, 14556.

(42) A. V. Marenich, C. J. Cramer, D. G. Truhlar *J. Phys. Chem. B* **2009**, *113*, 6378–6396.

(43) C. Y. Legault, CYLView, 1.0b; Université de Sherbrooke: Quebec, Montreal, Canada, http://www.cylview.org (2009**)**.

(44) Yamano, M. M.; Knapp, R. R.; Ngamnithiporn, A.; Ramirez, M.; Houk, K. N.; Stoltz, B. M.; Garg, N. K. *Angew. Chem., Int. Ed.* **2019**, *58*, 5653–5657.

CHAPTER SIX

Silyl Tosylate Precursors to Cyclohexyne, 1,2-Cyclohexadiene, and 1,2 Cycloheptadiene

Matthew S. McVeigh, Andrew V. Kelleghan, Michael M. Yamano,

Rachel R. Knapp, and Neil K. Garg

6.1 Abstract

Transient strained cyclic intermediates have become valuable intermediates in modern synthetic chemistry. Although silyl triflate precursors to strained intermediates are most often employed, the instability of some silyl triflates warrants the development of alternative precursors. We report the syntheses of silyl tosylate precursors to cyclohexyne, 1,2-cyclohexadiene, and 1,2-cycloheptadiene. The resultant strained intermediates undergo trapping in situ to give cycloaddition products. Additionally, the results of competition experiments between silyl triflates and silyl tosylates are reported.

6.2 Introduction

The chemistry of transient strained cyclic intermediates has been a popular topic of study for over a century.[1] Early efforts in the field established the existence of benzyne (**6.1**),[2] cyclohexyne (**6.2**),[3] and 1,2-cyclohexadiene (**6.3**)[4] through pioneering studies conducted by Roberts and Wittig in the 1950s and 1960s (Figure 6.1). Since their discovery, these species, along with their heterocyclic derivatives (e.g., **6.4**) have been employed in a host of synthetic applications spanning natural product synthesis,[1c,1d,1i, 5] heterocycle construction,[1e,1g,1h, 6] and materials chemistry,[1e,7] as exemplified by the syntheses of **6.5**–**6.7**.

Key Strained Intermediates:

benzyne (6.1)   cyclohexyne (6.2)   1,2-cyclohexadiene (6.3)   6.4

Applications:

Guanacastepene N (6.5)
Natural Product Synthesis

6.6
Heterocycle Synthesis

6.7
Materials Chemistry
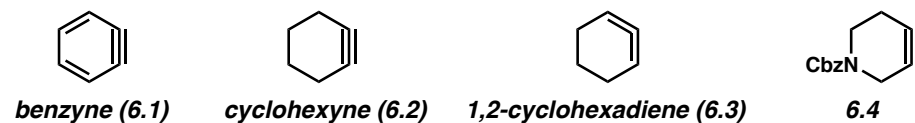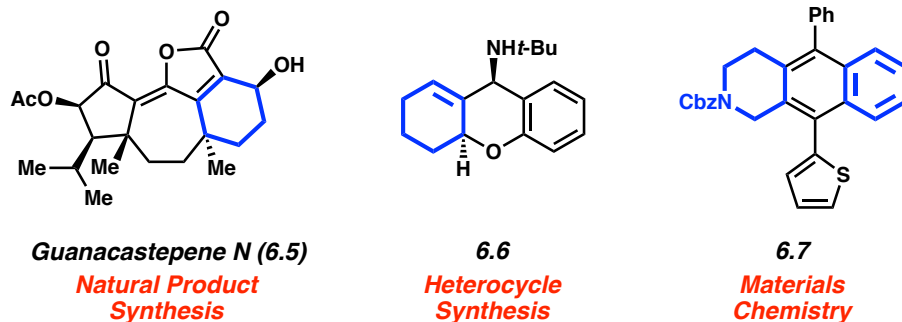
Figure 6.1. Strained cyclic intermediates and selected synthetic applications.

Many of the advanced synthetic applications of strained cyclic intermediates have been enabled by the use of silyl triflates as precursors. Initially developed by Kobayashi as precursors to benzyne (**6.1**),[8] silyl triflates have since become the most commonly employed precursors for accessing arynes, nonaromatic cyclic alkynes, and cyclic allenes.[1,9,10] However, we have encountered difficulties in preparing certain functionalized strained cyclic allene and alkyne precursors due to the instability of the corresponding silyl triflates. This instability can be attributed to the ease of triflate dissociation and cation formation in related systems.[11,12]

With the aim of circumventing silyl triflate instability and accessing a wider range of strained intermediates under Kobayashi-type conditions, we sought to develop new precursors to cyclic alkynes and allenes (i.e., **6.2** and **6.3**, Figure 6.2). As mentioned above, the most common means to access **6.2** and **6.3** is via the corresponding silyl triflates (e.g., **6.8** and **6.10**, respectively) using fluoride-induced elimination. Encouraged by the success of silyl tosylates as aryne precursors,[13] we sought to develop silyl tosylate cyclic alkyne and allene precursors **6.9** and **6.11**, respectively.[14] We hypothesized that the diminished leaving group ability of a tosylate

anion relative to a triflate[15] could alleviate difficulties associated with vinyl triflate instability, while retaining sufficient reactivity to form the desired strained intermediates.[13] These alternative precursors could also allow for new synthetic methods that leverage the differences in reactivity between tosylates and triflates.[16] Furthermore, we hoped that silyl tosylates **6.9** and **6.11** would be crystalline,[17] in contrast to silyl triflates which are often oils. This characteristic could facilitate their purification and use in process chemistry. Herein, we describe the preparation, validation, and synthetic application of the desired silyl tosylates as strained intermediate precursors.
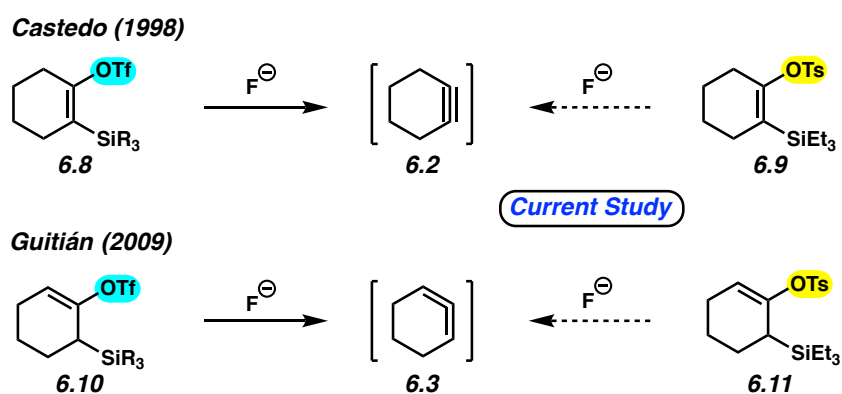
Figure 6.2. Silyl triflate (previous) and silyl tosylate (current) precursors to **6.2** and **6.3**.

6.3 Synthesis of Silyl Tosylate Precursors to Cyclohexyne and 1,2-Cyclohexadiene

Our first objective was to develop synthetic routes to the requisite silyl tosylates, which led to the preparation of **6.9** and **6.11** as shown in Figure 6.3. Following literature procedures,[18] cyclohexanone (**6.12**) was converted to silyl ketone **6.14** in good yield through a sequence involving silyl enol ether formation (**6.12**→**6.13**) and allylic deprotonation/retro-Brook rearrangement (**6.13**→**6.14**). From common intermediate **6.14**, deprotonation under either thermodynamic or kinetic control, followed by quenching with *p*-toluenesulfonic anhydride,

generated silyl tosylates **6.9** and **6.11**, respectively. Gratifyingly, both alkyne precursor **6.9** and allene precursor **6.11** were obtained as crystalline solids and could be prepared on gram-scale.
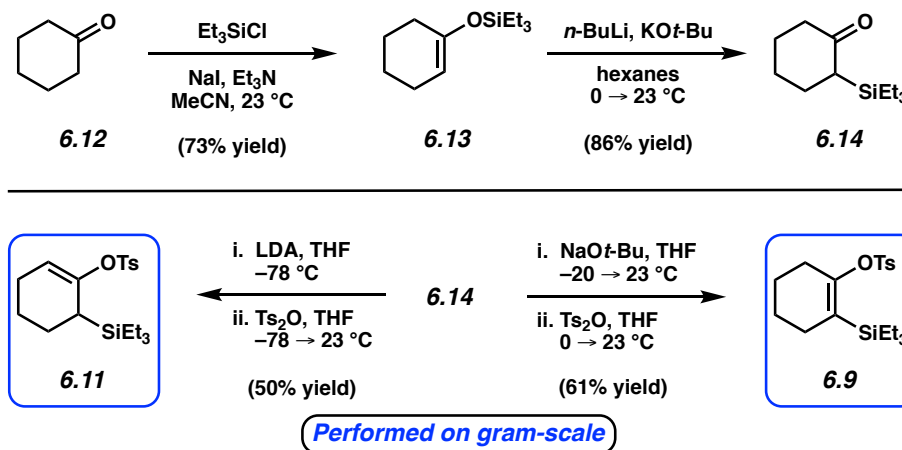
Figure 6.3. Syntheses of silyl tosylates **6.9** and **6.11**.

6.4 Comparing Silyl Tosylates and Silyl Triflates as Precursors to Cyclohexyne

As shown in Table 6.1, we found that silyl tosylate **6.9** serves as a viable precursor to generate cyclohexyne (**6.2**) with in situ trapping. It should be noted that our initial attempts to generate **6.2** from **6.9** using CsF (based on literature conditions for the corresponding trimethylsilyl triflate[6b]) led to the recovery of unreacted **6.9**. However, the use of the more soluble fluoride source tetrabutylammonium fluoride (TBAF) proved fruitful and enabled the generation of **6.2** in situ. Trapping with diene **6.16** furnished oxabicycle **6.17** via a (4+2) cycloaddition (entry 1). Similarly, the use of nitrone **6.18** as the trapping agent gave rise to isoxazolidine **6.19** by way of a (3+2) cycloaddition (entry 2). In both cases, yields were comparable to those observed using a silyl triflate precursor.[6b,18b] Lastly, nucleophilic trapping of **6.2** with imidazole (**6.20**) proved successful, generating vinyl imidazole **6.21** in moderate yield.[19] These trapping experiments demonstrate that silyl tosylate **6.9** serves as an effective precursor to **6.2**, rendering **6.9** a useful intermediate for the synthesis of heterocyclic products.

373

Table 6.1. Silyl tosylate **6.9** as a precursor to cyclohexyne (**6.2**).

Entry	Trapping Agent	Product	Yield[a] (Lit. yield from 6.8)[b]
1	6.16	6.17	76% (78%)
2	6.18	6.19	69% (61%)
3	6.20	6.21	53% (81%)

General conditions: silyl tosylate **6.9** (1.0 equiv, 0.14 mmol), trapping agent (1.5–3.0 equiv), TBAF (5.0 equiv), and THF (0.07 M) heated in a sealed vial under an atmosphere of N_2. [a]Isolated yields. [b]Literature isolated yields under comparable reaction conditions when using **6.8** (R = Me or Et)

6.5 Comparing Silyl Tosylates and Silyl Triflates as Precursors to 1,2-Cyclohexadiene

We also investigated silyl tosylate **6.11** as a precursor to strained cyclic allene **6.3** (Table 6.2). In contrast to our observations in reactions of alkyne precursor **6.9**, CsF could be utilized to induce strained intermediate formation from silyl tosylate **6.11** under the same conditions reported in the literature for the corresponding silyl triflate **6.10** (R = Et).[6a] We were delighted to find that silyl tosylate **6.11** could be employed in (4+2), (3+2), and (2+2) cycloadditions to deliver **6.23**, **6.24**, and **6.26**, respectively (entries 1–3). In all cases, yields and diastereomeric ratios were consistent with those reported in the literature for reactions employing silyl triflate

6.10 (R = Et).[6a,18b,20] The synthesis of isoxazolidine **6.24** was also carried out on mmol-scale to demonstrate scalability.

Table 6.2. Silyl tosylate **6.11** as a precursor to 1,2-cyclohexadiene (**6.3**).

Entry	Trapping Agent	Product	Yield[a] (Lit. Yield from 6.10)[b] d.r.[c] (Lit. d.r.)
1	**6.16**	**6.23**	78% (83%) 2.7:1 (2.4:1)
2	**6.18**	**6.24**	80% (88%) 9.3:1 (8.9:1) *78%, 9.0:1 d.r. on mmol-scale*
3	**6.25**	**6.26**	91%[d] (76%)[e] 2.0:1 (2.2:1)

General conditions: silyl tosylate **6.11** (1.0 equiv, 0.14 mmol), trapping agent (1.0–5.0 equiv), CsF (5.0 equiv), and MeCN (0.1 M) heated in a sealed vial under an atmosphere of N$_2$. [a]Isolated yields. [b]Literature isolated yields and diastereomeric ratios under comparable reaction conditions when using **6.10** (R = Et). [c]Diastereomeric ratios determined by ^{1}H NMR analysis of the crude reaction mixture. [d]Yield determined by ^{1}H NMR analysis using an external standard. [e]Cyclic allene generated from 6,6-dibromobicyclo[3.1.0]hexane.

6.6 Preparation of a Precursor to 1,2-Cycloheptadiene and its Subsequent Trapping

Having established silyl tosylates as effective substitutes for silyl triflates, we sought to extend this alternative method of strained intermediate generation to address a particular shortcoming in silyl triflate chemistry. As mentioned earlier, silyl triflates can sometimes be unstable due to their pronounced leaving group ability.[11,12] We have observed this type of instability when attempting to synthesize a silyl triflate precursor to 1,2-cycloheptadiene (**6.29**) (Figure 6.4).[21] Alternatively, silyl tosylate **6.28**, accessible in three steps from **6.27** (see section 6.9.2.4 for details), could be obtained as a crystalline solid. Treatment of **6.28** with isobenzofuran **6.16** under standard conditions for cyclic allene generation and trapping afforded oxabicycle **6.30** in excellent yield via the intermediacy of cyclic allene **6.29**. This example demonstrates that silyl tosylates can be used to expand the scope of strained intermediates accessible under mild fluoride-based conditions.[22]
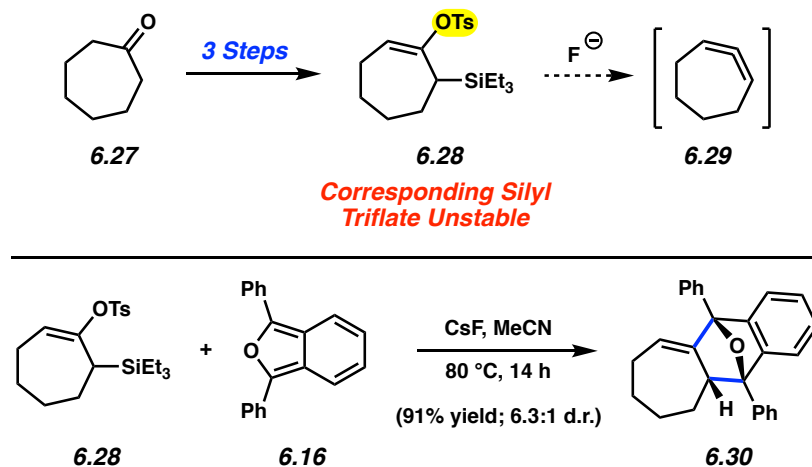
Figure 6.4. Silyl tosylate **6.28** to access 1,2-cycloheptadiene (**6.29**).

6.7 Competition Experiments Between Silyl Triflates and Silyl Tosylates

Finally, two key experiments were performed to compare the relative reactivity of our silyl tosylates to the corresponding silyl triflates (Figure 6.5). In the first, equimolar amounts of

silyl triflate **6.8a** and silyl tosylate **6.9**, both precursors to cyclohexyne (**6.2**), were treated with nitrone **6.18** under CsF-based reaction conditions. We observed that silyl triflate **6.8a** reacted selectively over silyl tosylate **6.9** to generate cycloadduct **6.19**. Silyl tosylate **6.9** did not react under these conditions. An analogous competition experiment was performed using silyl triflate **6.10a** and silyl tosylate **6.11**, both of which serve as precursors to 1,2-cyclohexadiene (**6.3**). This led to the efficient formation of **6.24** and the nearly quantitative retention of silyl tosylate **6.11**. The preferential reactivity of the silyl triflate in both cases can be rationalized based on the relative leaving group abilities of the triflate and tosylate anions.[15] This observed selectivity should prove useful in synthetic applications, analogous to prior studies in which multiple strained intermediates have been generated sequentially to synthesize complex polycyclic products.[7]
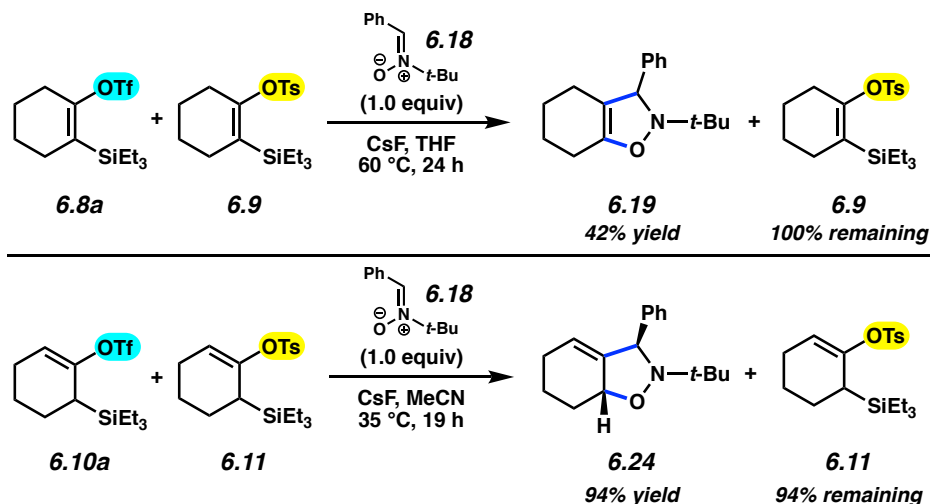
Figure 6.5. Competition experiments between silyl triflate and silyl tosylate strained intermediate precursors. Yields determined by ^{1}H NMR analysis with external standard.

6.8 Conclusion

In summary, we have developed scalable syntheses of silyl tosylate precursors to the transient strained intermediates cyclohexyne (**6.2**), 1,2-cyclohexadiene (**6.3**), and 1,2-

cycloheptadiene (**6.29**). Our synthetic routes to these precursors generate crystalline silyl tosylates, an attribute that could prove useful to process chemists. The silyl tosylate strained intermediate precursors not only replicate the chemistry attained using silyl triflates, but also can allow access to strained intermediates inaccessible using known silyl triflate chemistry, as exemplified by silyl tosylate **6.28**. Furthermore, competition experiments demonstrate that silyl triflate precursors to **6.2** and **6.3** react chemoselectively in the presence of their silyl tosylate counterparts. This selectivity should prove useful in synthetic design. Collectively, these studies demonstrate the synthetic utility of silyl tosylates as precursors to transient strained intermediates.

6.9 Experimental Section

6.9.1 Materials and Methods

Unless stated otherwise, reactions were conducted in flame-dried glassware under an atmosphere of nitrogen using anhydrous solvents (passed through activated alumina columns). All commercially obtained reagents were used as received unless otherwise specified. Imidazole (**6.20**), *p*-toluenesulfonic anhydride (Ts$_2$O), *n*-butyllithium (*n*-BuLi), tetrabutylammonium fluoride (TBAF), and potassium *tert*-butoxide (KO*t*-Bu) were obtained from Sigma-Aldrich. Sodium *tert*-butoxide (NaO*t*-Bu), 1,3-diphenylisobenzofuran (**6.16**), *N-tert*-butyl-α-phenylnitrone (**6.18**), and 1,3,5-trimethoxybenzene were obtained from Alfa Aesar. Styrene (**6.25**) was obtained from Fisher Scientific and filtered through basic alumina prior to use. Cesium fluoride (CsF) was obtained from Strem Chemicals. Diisopropylamine was obtained from Acros Organics and distilled over CaH$_2$ prior to use. Reaction temperatures were controlled using an IKAmag temperature modulator, and reactions were performed at room temperature (approximately 23 °C) unless otherwise stated. Thin-layer chromatography (TLC) was conducted with EMD gel 60 F254 pre-coated plates (0.25 mm for analytical chromatography and 0.50 mm for preparative chromatography) and visualized using a combination of UV, anisaldehyde, and potassium permanganate staining techniques. Silicycle Siliaflash P60 (particle size 0.040–0.063 mm) was used for flash column chromatography. ^{1}H NMR spectra were recorded on Bruker spectrometers (500 and 600 MHz) and are reported relative to residual solvent signals. Data for ^{1}H NMR spectra are reported as follows: chemical shift (δ ppm), multiplicity, coupling constant (Hz), integration. Data for ^{13}C NMR are reported in terms of chemical shift (at 125 MHz). IR spectra were recorded on a Perkin-Elmer UATR Two FT-IR spectrometer and are reported in terms of absorption frequency (cm^{-1}). DART-MS spectra were collected on a Thermo Exactive

Plus Orbitrap (Thermo Scientific) equipped with an ID-CUBE ion source and a Vapur Interface (IonSense Inc.). Both the source and MSD were controlled by Excalibur software v. 3.0. The analyte was spotted onto OpenSpot sampling cards (IonSense Inc.) using CH_2Cl_2 as the solvent. Ionization was accomplished using UHP He plasma with no additional ionization agents. The mass calibration was carried out using Pierce LTQ Velos ESI (+) and (–) Ion calibration solutions (Thermo Fisher Scientific).

*Note: The syntheses of silyl triflates **6.8a** and **6.10a**,[18b] silyl ketone **6.14**,[18b] and silyl enol ether **6.31**[23] have been published, and spectral data match those previously reported.*

6.9.2 Experimental Procedures

6.9.2.1 Syntheses of Silyl Tosylates 6.9 and 6.11
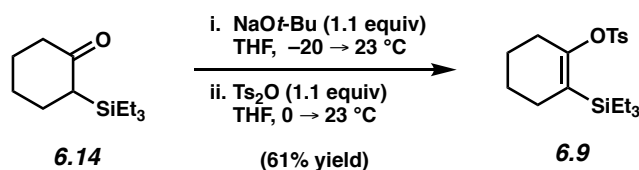
Silyl Tosylate 6.9. To a stirring suspension of sodium *tert*-butoxide (498 mg, 5.18 mmol, 1.1 equiv) in THF (5 mL) at –20 °C was added silyl ketone **6.14** (1.00 g, 4.71 mmol, 1.0 equiv) in THF (5 mL) via cannula addition over 5 min. The resulting dark orange-red solution was then warmed to 0 °C and stirred for 1 h. Next, the ice bath was removed, and the solution was stirred at 23 °C for 30 min, then recooled to 0 °C. *p*-Toluenesulfonic anhydride (1.69 g, 5.18 mmol, 1.1 equiv) in THF (7.0 mL) was then added over 7 min. The cooling bath was removed, and the off-white, heterogeneous solution was stirred at 23 °C for 5 h before being quenched with sat. aqueous NaHCO$_3$ (20 mL). The layers were separated and the aqueous layer was extracted with diethyl ether (3 x 20 mL). The organic layers were combined, washed sequentially with deionized H$_2$O (1 x 20 mL) and brine (1 x 20 mL), dried with Na$_2$SO$_4$, and concentrated under reduced pressure. The crude reaction mixture was purified via column chromatography (3:97 Et$_2$O:hexanes) to provide silyl tosylate **6.9** (1.06 g, 61% yield) as a white, crystalline solid. Silyl tosylate **6.9**: R$_f$ 0.55 (9:1 hexanes:EtOAc); ^{1}H NMR (500 MHz, CDCl$_3$): δ 7.82–7.79 (m, 2H), 7.34–7.30 (m, 2H), 2.44 (s, 3H), 2.23–2.20 (m, 2H), 2.11–2.06 (m, 2H), 1.64–1.58 (m, 2H), 1.53–1.47 (m, 2H), 0.88 (t, J = 8.1, 9H), 0.61 (q, J = 7.5, 6H); ^{13}C NMR (125 MHz, CDCl$_3$): δ 154.5, 144.4, 135.8, 129.6, 127.6, 121.9, 28.8, 28.2, 23.0, 22.1, 21.7, 7.5, 3.1; IR (film): 2950, 2875, 1642, 1368, 1191 cm^{-1}; HRMS–APCI (*m/z*) [M + H]$^+$ calcd for C$_{19}$H$_{31}$O$_3$SSi$^+$, 367.1755; found 367.1754.

i. LDA (2.0 equiv)
   THF, –78 °C

ii. Ts₂O (1.5 equiv)
    THF, –78 → 23 °C

(50% yield)

6.14

6.11
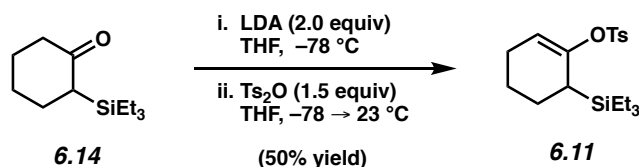
Silyl Tosylate 6.11. To a stirring solution of diisopropylamine (1.41 mL, 9.88 mmol, 2.1 equiv) in THF (14 mL) at –78 °C was added *n*-butyllithium (2.50 M in hexanes, 3.78 mL, 9.44 mmol, 2.0 equiv) dropwise over 3 min. After stirring for 20 min, the reaction was warmed to 23 °C and stirred for 10 min, before recooling the reaction to –78 °C. Next, silyl ketone **6.14** (1.00 g, 4.72 mmol, 1.0 equiv) in THF (14 mL) was added dropwise via cannula addition over 10 min. The resulting pale-yellow solution was stirred for 1 h. Then, a solution of *p*-toluenesulfonic anhydride (2.31 g, 7.08 mmol, 1.5 equiv) in THF (18 mL) was added dropwise via cannula addition over 6 min. The cooling bath was allowed to melt, gradually warming the reaction to 23 °C over 18 h, at which point it was quenched with sat. aqueous NaHCO₃ (40 mL). The layers were separated and the aqueous layer was extracted with diethyl ether (3 x 40 mL). The combined organic layers were then dried over Na₂SO₄, filtered, and concentrated under reduced pressure to provide a yellow oil. The crude oil was passed through a silica plug (3:97 Et₂O:hexanes), and the eluate was concentrated to give a pale-yellow oil. This oil was dissolved in refluxing hexanes and cooled gradually to –78 °C over 4 h to induce crystallization. The crystals were filtered off, washed with cold hexanes, and the mother liquor was concentrated to give a clear oil. This oil was subjected to the same crystallization procedure, and both crops of crystals were combined to afford silyl tosylate **6.11** (860 mg, 50% yield) as a white, crystalline solid. Silyl tosylate **6.11**: R$_f$ 0.57 (1:1 hexanes:benzene); ^{1}H NMR (500 MHz, CDCl₃): δ 7.78 (d, *J* = 8.1, 2H), 7.32 (d, *J* = 8.1, 2H), 5.19–5.16 (m, 1H), 2.45 (s, 3H), 2.01–1.90 (m, 2H), 1.82–1.74 (m, 2H), 1.62–1.56 (m, 1H), 1.53–1.45 (m, 1H), 1.36–1.27 (m, 1H), 0.92 (t, *J* = 7.9, 9H), 0.60 (q, *J* = 8.2, 6H); ^{13}C NMR (125 MHz, CDCl₃): δ 151.4, 144.7, 133.5, 129.4, 128.5, 114.3,

25.5, 25.3, 24.1, 21.8, 21.7, 7.5, 3.0; IR (film): 2954, 2877, 1370, 1179, 1191 cm^{-1}; HRMS–APCI (*m/z*) [M + H]$^+$ calcd for C$_{19}$H$_{31}$O$_3$SSi$^+$, 367.1755; found 367.1758.

6.9.2.2 Cyclohexyne Trapping Experiments

Representative Procedure 6.1 (Table 6.1, entry 1 is used as an example).
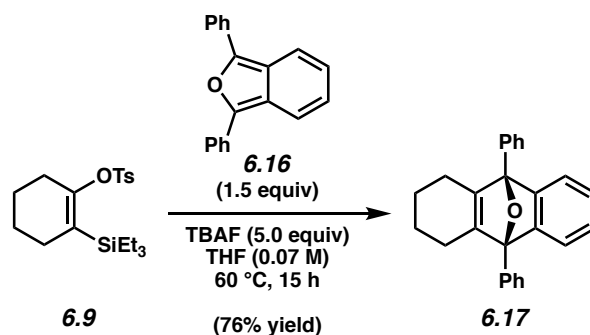
Cycloadduct 6.17. To a stirred solution of silyl tosylate **6.9** (49.6 mg, 135 µmol, 1.0 equiv), and 1,3-diphenylisobenzofuran (**6.16**) (54.9 mg, 203 µmol, 1.5 equiv) in THF (1.35 mL, 0.07 M) was added TBAF (1.0 M in THF, 677 µL, 677 µmol, 5.0 equiv). The reaction vessel was purged with N$_2$, sealed with a teflon cap, and placed in a preheated, 60 °C aluminum heating block. After stirring for 15 h, the reaction was cooled to 23 °C. The resultant yellow solution was filtered through a plug of silica gel (EtOAc eluent, 10 mL) and concentrated under reduced pressure to afford a crude yellow solid. Purification by preparative thin layer chromatography (3:2 benzene:hexanes) provided cycloadduct **6.17** (36.2 mg, 76% yield, average of two experiments) as a pale-yellow solid. Cycloadduct **6.17**: Spectral data match those previously reported.[18b]
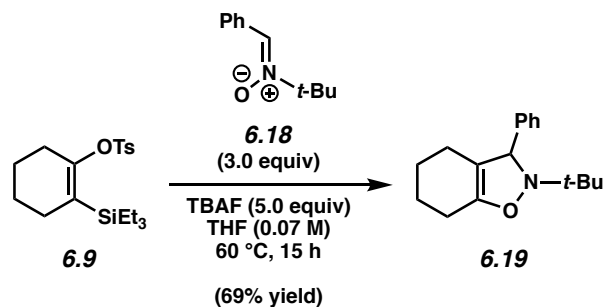
Cycloadduct 6.19. Followed Representative Procedure 5.1. Purification by preparative thin layer chromatography (9:1 Hexanes:EtOAc) provided cycloadduct **6.19** (24.2 mg, 69% yield, average of two experiments) as a white solid. Cycloadduct **6.19**: Spectral data match those previously reported.[6b]
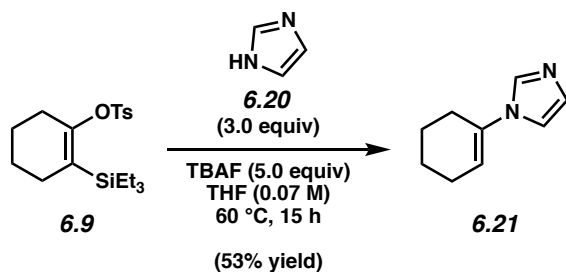
Imidazole adduct 6.21. Followed Representative Procedure 5.1. Purification by preparative thin layer chromatography (EtOAc) provided cycloadduct **6.21** (10.7 mg, 53% yield, average of two experiments) as an off-white solid. Imidazole adduct **6.21**: Spectral data match those previously reported.[6b]

6.9.2.3 1,2-Cyclohexadiene Trapping Experiments

Representative Procedure 6.2 (Table 6.2, entry 1 is used as an example).
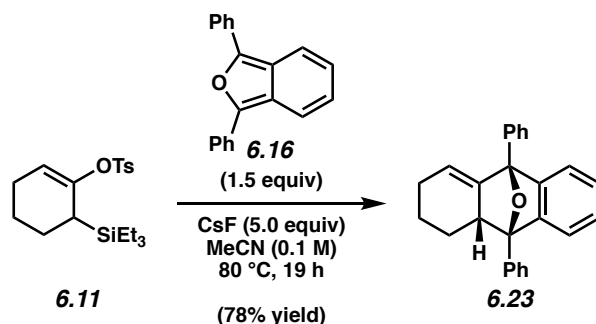
Cycloadduct 6.23. To a stirred solution of silyl tosylate **6.11** (49.7 mg, 136 μmol, 1.0 equiv) and 1,3-diphenylisobenzofuran (**6.16**) (55.5 mg, 205 μmol, 1.5 equiv) in MeCN (1.40 mL, 0.1 M) was added CsF (100 mg, 0.68 mmol, 5.0 equiv). The reaction vessel was purged with N_2, sealed with a teflon cap and teflon tape, and placed in a preheated, 80 °C aluminum heating block. The reaction was allowed to stir at this temperature for 19 h. After cooling to 23 °C, the yellow, heterogenous solution was filtered through a plug of silica gel (EtOAc eluent, 10 mL) and concentrated under reduced pressure to afford a crude yellow solid. Purification by preparative thin layer chromatography (2:1 hexanes:CH_2Cl_2 with 2% acetone) provided cycloadduct **6.23** as a pale-yellow solid (36.9 mg, 78% yield, 2.7:1 d.r. by ^{1}H NMR analysis of the crude material, average of two experiments). Cycloadduct **6.23**: Spectral data match those previously reported.[18b]

Any modification of the conditions shown in the representative procedure above are

specified in the following scheme
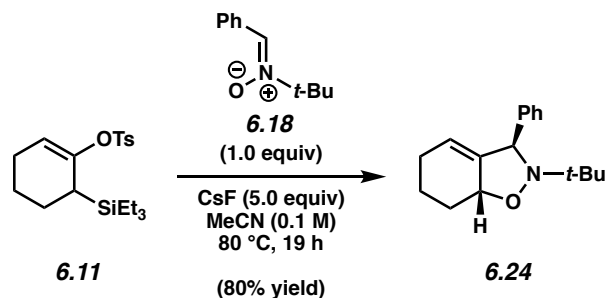
Cycloadduct 6.24. Followed Representative Procedure 5.2. Purification by preparative thin layer chromatography (1:1 hexanes:benzene) provided cycloadduct **6.24** as a white solid (30.2 mg, 80% yield, 9.3:1 d.r. by ^{1}H NMR analysis of the crude material, average of two experiments). Cycloadduct **6.24**: Spectral data match those previously reported.[6a]
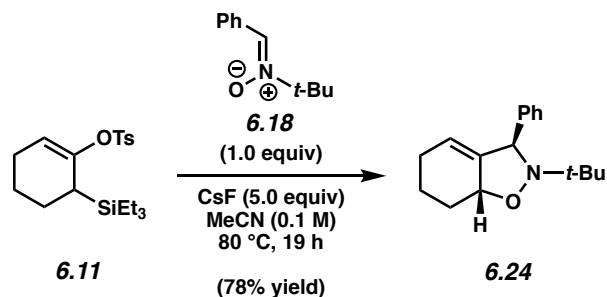
Cycloadduct 6.24 (mmol scale). To a stirred solution of silyl tosylate **6.11** (367 mg, 1.00 mmol, 1.0 equiv) and *N-tert*-butyl-α-phenylnitrone (**6.18**) (181 mg, 1.02 mmol, 1.0 equiv) in MeCN (10.0 mL, 0.1 M) was added CsF (761 mg, 5.01 mmol, 5.0 equiv). The reaction vessel was purged with N$_2$, sealed with a teflon cap and teflon tape, and placed in a preheated, 80 °C aluminum heating block. The reaction was allowed to stir at this temperature for 19 h. After cooling to 23 °C, the white, heterogenous solution was filtered through a plug of silica gel (EtOAc eluent, 30 mL) and concentrated under reduced pressure to afford a crude off-white solid. Purification by flash chromatography (4:1 to 1:1 hexanes:benzene) provided cycloadduct **6.24** as a white solid (200.2 mg, 78% yield, 9.0:1 d.r.). Cycloadduct **6.24**: Spectral data match those previously reported.[6a]

6.25
(5.0 equiv)

6.11

CsF (5.0 equiv)
MeCN (0.1 M)
80 °C, 19 h

(91% yield)

6.26
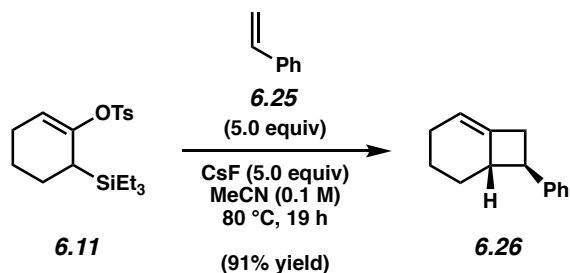
Cycloadduct 6.26. Followed a modified Representative Procedure 5.2 by adding 1,3,5-trimethoxybenzene as an external standard to the crude residue obtained by filtration of the reaction mixture. ^{1}H NMR analysis of this crude mixture showed cycloadduct **6.26** (91% yield, 2.0:1 d.r., average of two experiments). The volatility of **6.26** hampered isolation attempts. Cycloadduct **6.26**: Spectral data match those previously reported.[20]

6.9.2.4 Synthesis of Silyl Tosylate 6.28

6.31

n-BuLi (2.0 equiv)
KOt-Bu (2.5 equiv)

hexanes, 0 → 23 °C

(95% yield)

6.32
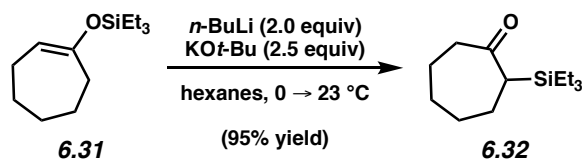
Silyl ketone 6.32. To a heterogeneous solution of potassium *tert*-butoxide (186 mg, 1.66 mmol, 2.5 equiv) in hexanes (1.3 mL) at 0 °C was added *n*-butyllithium (2.36 M in hexanes, 0.561 mL, 1.32 mmol, 2.0 equiv) dropwise over 2 min. The solution was removed from the ice bath and stirred at 23 °C for an additional 20 min. A solution of silyl enol ether **6.31** (150 mg, 0.662 mmol, 1.0 equiv) in hexanes (1.3 mL) was then added dropwise over 5 min and stirred at 23 °C. After stirring for 2 h, deionized H_2O (5.0 mL) was added to the reaction, and the aqueous layer was extracted with diethyl ether (3 x 5 mL). The combined organic layers were dried over Na_2SO_4, filtered, and concentrated under reduced pressure. The resulting crude oil was purified by flash chromatography (1.5:98.5 EtOAc:hexanes) to afford silyl ketone **6.32** (142 mg, 95%

yield) as a clear, colorless oil. Silyl ketone **6.32**: R_f 0.36 (99:1 benzene:Et$_2$O); ^{1}H NMR (500 MHz, CDCl$_3$): δ 2.63–2.56 (m, 1H), 2.37 (dd, J = 11.9, 4.9, 1H), 2.33–2.27 (m, 1H), 2.03–1.95 (m, 1H), 1.93–1.82 (m, 3H), 1.72–1.61 (m, 1H), 1.46–1.29 (m, 2H), 1.18–1.07 (m, 1H), 0.94 (t, J = 8.0, 9H), 0.60 (q, J = 7.5, 6H); ^{13}C NMR (125 MHz, CDCl$_3$): δ 215.9, 47.6, 43.6, 31.1, 30.5, 25.9, 25.7, 7.3, 2.4; IR (film): 2880, 1670, 1417, 1208, 879 cm^{-1}; HRMS-APCI (m/z) [M + H]$^+$ calcd for C$_{13}$H$_{27}$OSi$^+$, 227.1826; found 227.1826.
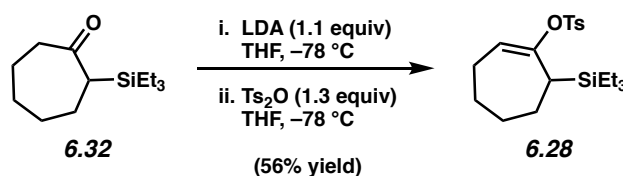
Silyl tosylate 6.28. To a solution of diisopropylamine (0.110 mL, 0.762 mmol, 1.15 equiv) in THF (0.5 mL) at –78 °C was added n-butyllithium (2.36 M in hexanes, 0.309 mL, 0.729 mmol, 1.1 equiv) dropwise over 2 min. The solution was stirred for 30 min at –78 °C, then warmed to 23 °C over 15 min before being cooled to –78 °C. Silyl ketone **6.32** (150 mg, 0.662 mmol, 1.0 equiv) in THF (0.5 mL) was added dropwise over 5 min and stirred for 1 h at –78 °C. Next, p-toluenesulfonic anhydride (281 mg, 0.861 mmol, 1.3 equiv) in THF (2.0 mL) was added dropwise over 5 min and allowed to stir at –78 °C. After stirring for 1 h, sat. aqueous NaHCO$_3$ (3.0 mL) was added to the reaction, and the stirring solution was warmed to 23 °C. The aqueous layer was then extracted with diethyl ether (3 x 3 mL), and the combined organic layers were dried over Na$_2$SO$_4$, filtered, and concentrated under reduced pressure. The resulting crude solid was dissolved and passed through a plug of silica gel (2:1 hexanes:benzene eluent, 100 mL). The eluate was concentrated and divided into three equal portions. Each portion was purified by preparative thin layer chromatography (7:3 benzene:hexanes), and the individual portions were

recombined to afford silyl tosylate **6.28** (141 mg, 56% yield) as a white solid. Silyl tosylate **6.28**:

M.p. 39.9–40.8 °C; R_f 0.79 (99:1 benzene:Et$_2$O); ^{1}H NMR (500 MHz, CDCl$_3$): δ 7.82–7.79 (m,

2H), 7.35–7.31 (m, 2H), 5.22 (dd, J = 9.2, 4.4, 1H), 2.45 (s, 3H), 2.10 (t, J = 5.7, 1H), 2.07–2.00

(m, 1H), 1.94–1.87 (m, 1H), 1.83–1.76 (m, 1H), 1.75–1.65 (m, 2H), 1.55–1.49 (m, 1H), 1.49–

1.41 (m, 1H), 1.37–1.28 (m, 1H), 0.94 (t, J = 8.1, 9H), 0.63 (q, J = 7.7, 6H); ^{13}C NMR (125

MHz, CDCl$_3$): δ 154.3, 144.6, 133.6, 129.5, 128.5, 118.4, 33.0, 28.2, 27.6, 26.0, 23.9, 21.7, 7.5,

3.6; IR (film): 2929, 2876, 1368, 1177, 994 cm^{-1}; HRMS-APCI (m/z) [M + H]$^+$ calcd for

C$_{20}$H$_{33}$O$_3$SSi$^+$, 381.1914; found 381.1907.

5.9.2.5 1,2-Cycloheptadiene Trapping Experiment
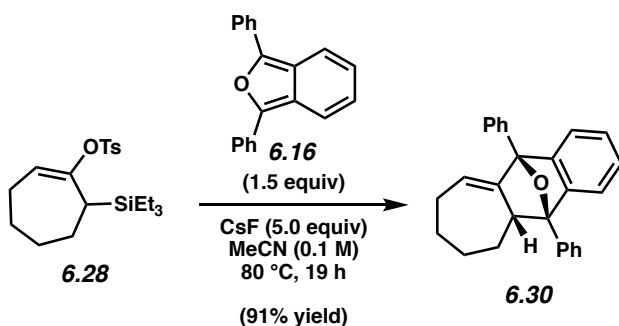
Cycloadduct 6.30. To a stirred solution of silyl tosylate **6.28** (19.8 mg, 52.0 µmol, 1.0

equiv) and 1,3-diphenylisobenzofuran (**6.16**) (21.1 mg, 78.0 µmol, 1.5 equiv) in MeCN (0.52

mL, 0.1 M) was added CsF (39.5 mg, 260 µmol, 5.0 equiv). The reaction vessel was purged with

N$_2$, sealed with a teflon cap and teflon tape, and placed in a preheated, 80 °C aluminum heating

block. The reaction was allowed to stir at this temperature for 14 h. After cooling to 23 °C, the

yellow, heterogeneous solution was filtered through a plug of silica gel (EtOAc eluent, 10 mL)

and concentrated under reduced pressure to afford a crude yellow solid. Purification by

preparative thin layer chromatography (2:1 hexanes:CH$_2$Cl$_2$ with 2% acetone) provided

cycloadduct **6.30** (17.3 mg, 91% yield, 6.3:1 d.r. by ^{1}H NMR analysis of the crude material).

Cycloadduct **6.30**: Spectral data match those previously reported.[22]

6.9.2.6 Silyl Tosylate and Silyl Triflate Competition Experiments
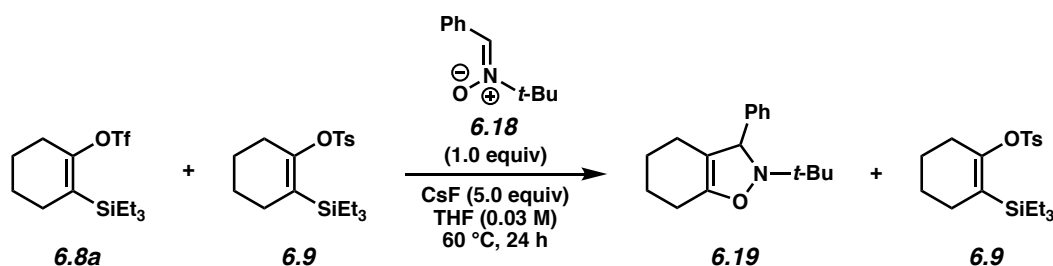
Alkyne precursor competition experiment. To a stirred solution of silyl triflate **6.8a** (25.0 mg, 72.6 μmol, 1.0 equiv), silyl tosylate **6.9** (26.6 mg, 72.6 μmol, 1.0 equiv), and *N*-*tert*-butyl-α-phenylnitrone (**6.18**) (12.9 mg, 72.6 μmol, 1.0 equiv) in THF (2.4 mL, 0.03 M) was added CsF (55.1 mg, 363 μmol, 5.0 equiv). The reaction vessel was purged with N$_2$, sealed with a teflon cap, and placed in a preheated, 60 °C aluminum heating block. The reaction was allowed to stir at this temperature for 24 h. After cooling to 23 °C, the solution was filtered through a plug of silica gel (EtOAc eluent, 10 mL) and concentrated under reduced pressure to afford the crude reaction mixture. 1,3,5-trimethoxybenzene was added as an external standard. ^{1}H NMR analysis of the crude reaction mixture showed cycloadduct **6.19** (42% yield) and silyl tosylate **6.9** (100% remaining).
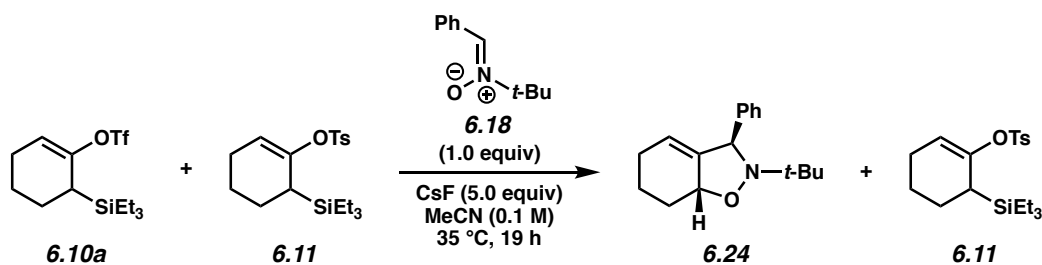
Allene precursor competition experiment. To a stirred solution of silyl triflate **6.10a** (25.0 mg, 72.6 μmol, 1.0 equiv), silyl tosylate **6.11** (26.6 mg, 72.6 μmol, 1.0 equiv), and *N-tert*-butyl-α-phenylnitrone (**6.18**) (12.9 mg, 72.6 μmol, 1.0 equiv) in MeCN (0.73 mL, 0.1 M) was added CsF (55.1 mg, 363 μmol, 5.0 equiv). The reaction vessel was purged with N₂, sealed with a teflon cap, and placed in a preheated, 35 °C aluminum heating block. The reaction was allowed to stir at this temperature for 19 h. After cooling to 23 °C, the solution was filtered through a plug of silica gel (EtOAc eluent, 10 mL) and concentrated under reduced pressure to afford the crude reaction mixture. 1,3,5-trimethoxybenzene was added as an external standard. ¹H NMR analysis of the crude reaction mixture showed cycloadduct **6.24** (94% yield, 12.2:1 d.r.) and silyl tosylate **6.11** (94% remaining).

6.10 Spectra Relevant to Chapter Six:

Silyl Tosylate Precursors to Cyclohexyne, 1,2-Cyclohexadiene, and 1,2-Cycloheptadiene

Matthew S. McVeigh, Andrew V. Kelleghan, Michael M. Yamano, Rachel R. Knapp, and Neil K. Garg.
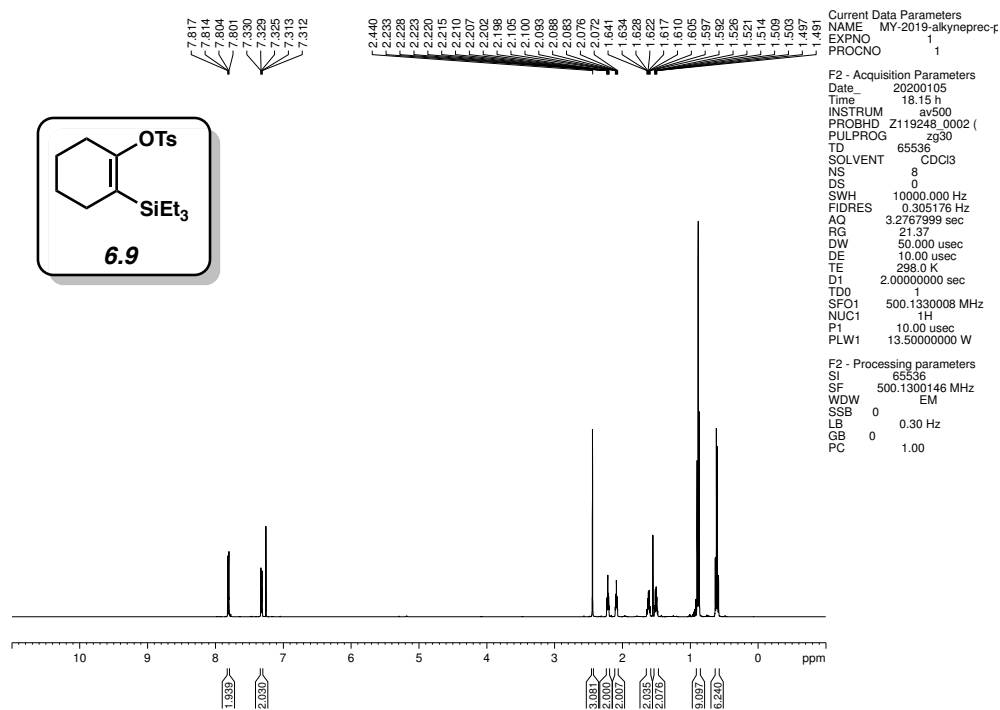
Figure 6.6. ^{1}H NMR (500 MHz, CDCl$_3$) of compound **6.9**.
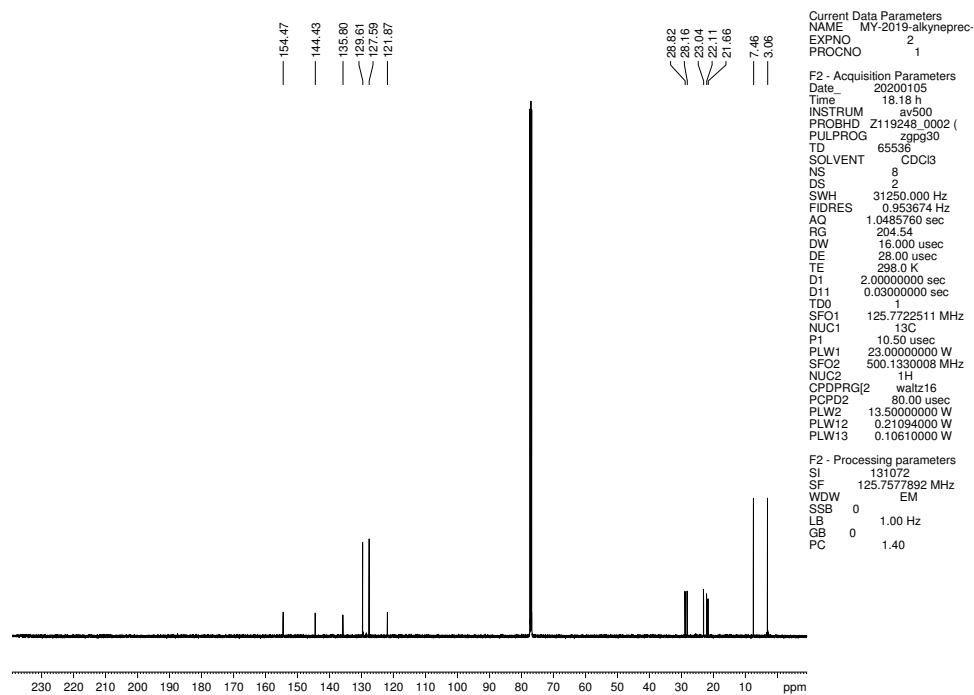
Figure 6.7. ^{13}C NMR (125 MHz, CDCl$_3$) of compound **6.9**.
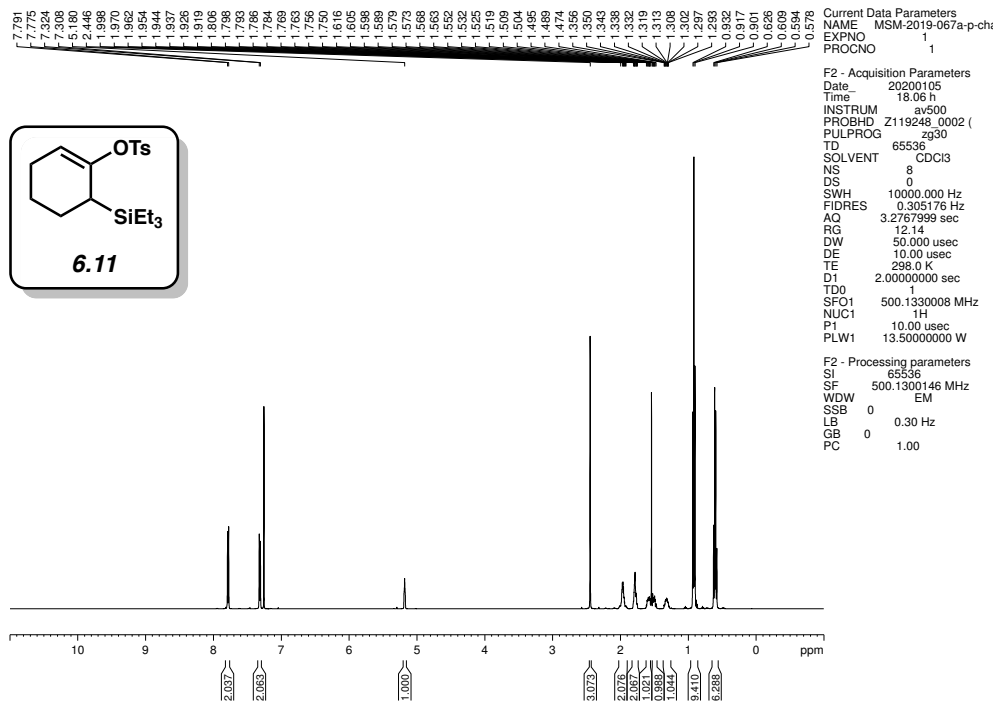
Figure 6.8. ¹H NMR (500 MHz, CDCl₃) of compound **6.11**.
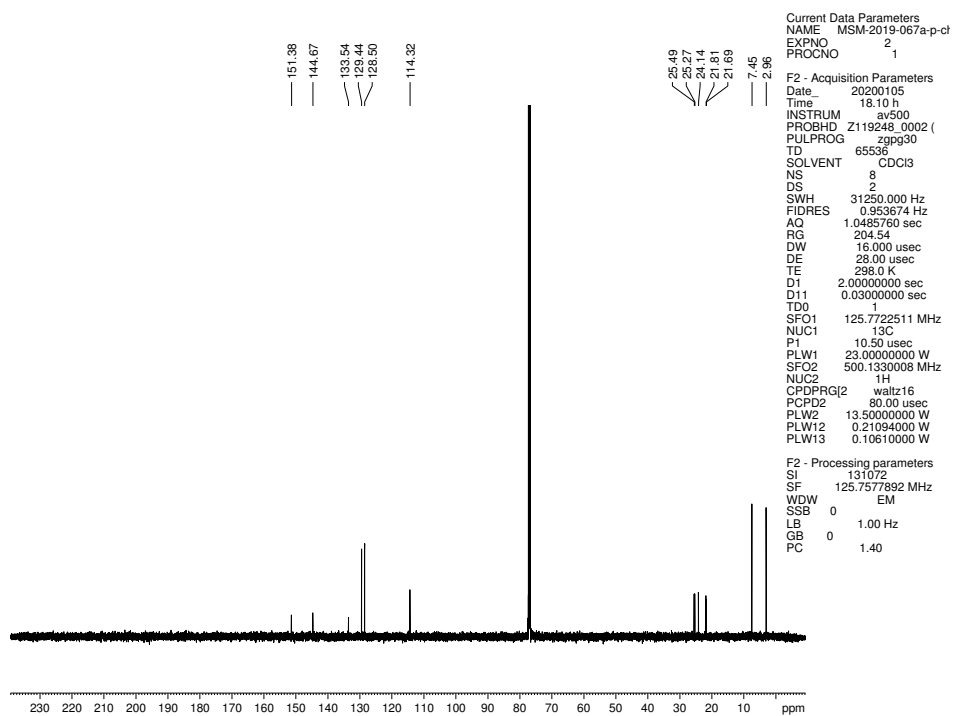
Figure 6.9. ¹³C NMR (125 MHz, CDCl₃) of compound **6.11**.
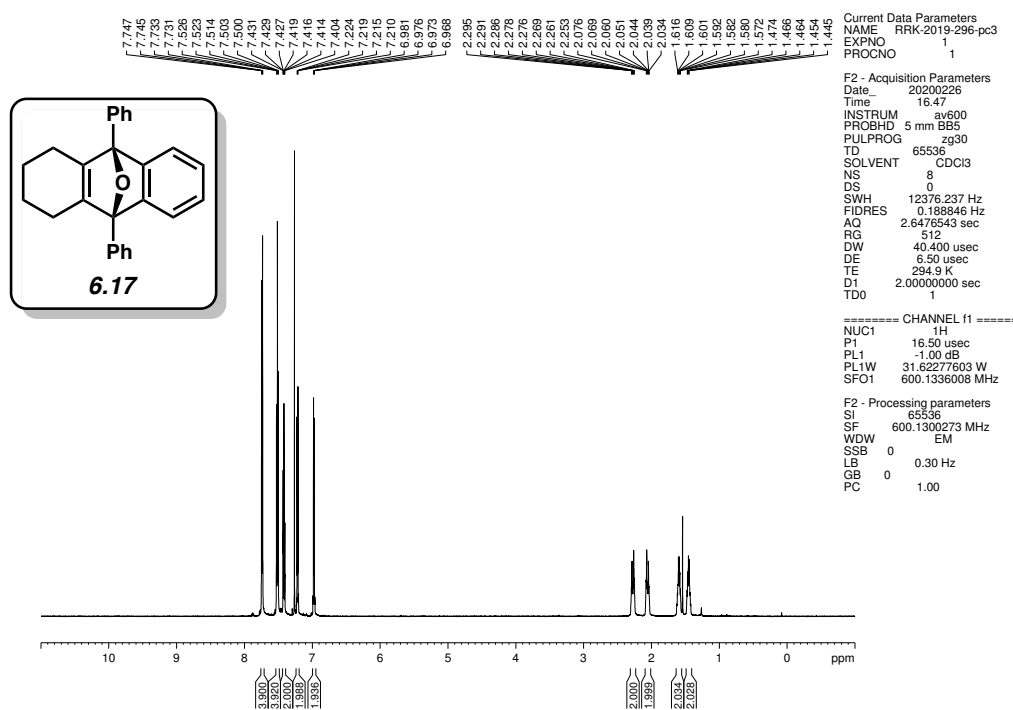
Figure 6.10. ^{1}H NMR (600 MHz, CDCl$_3$) of compound **6.17**.
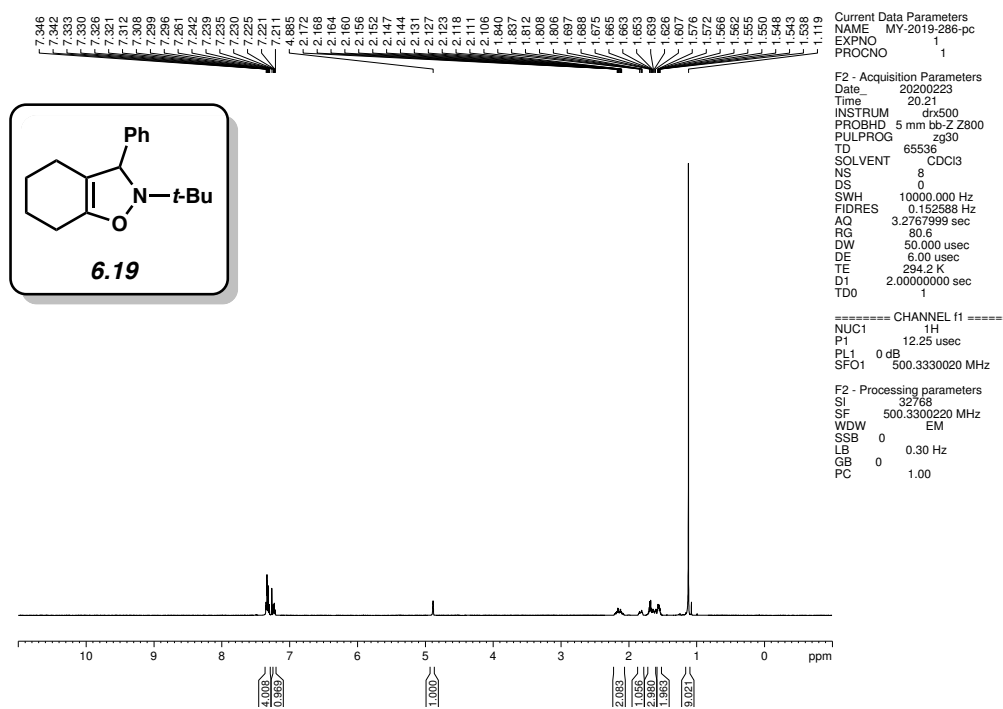
Figure 6.11. ^{1}H NMR (500 MHz, CDCl$_3$) of compound **6.19**.

395
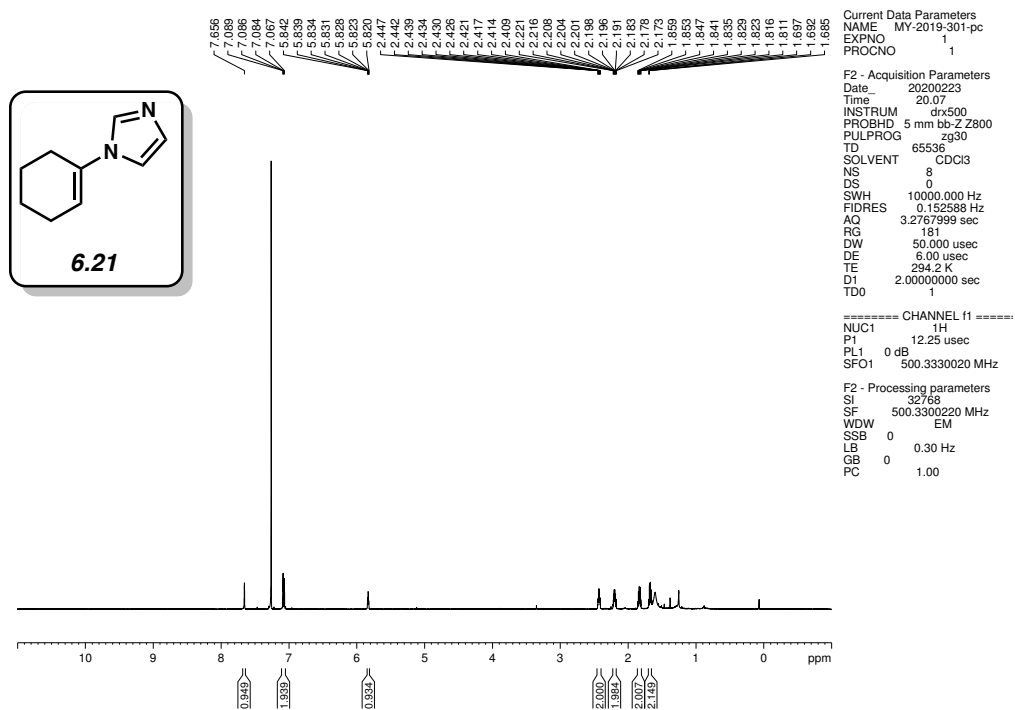
Figure 6.12. ^{1}H NMR (500 MHz, CDCl$_3$) of compound **6.21**.
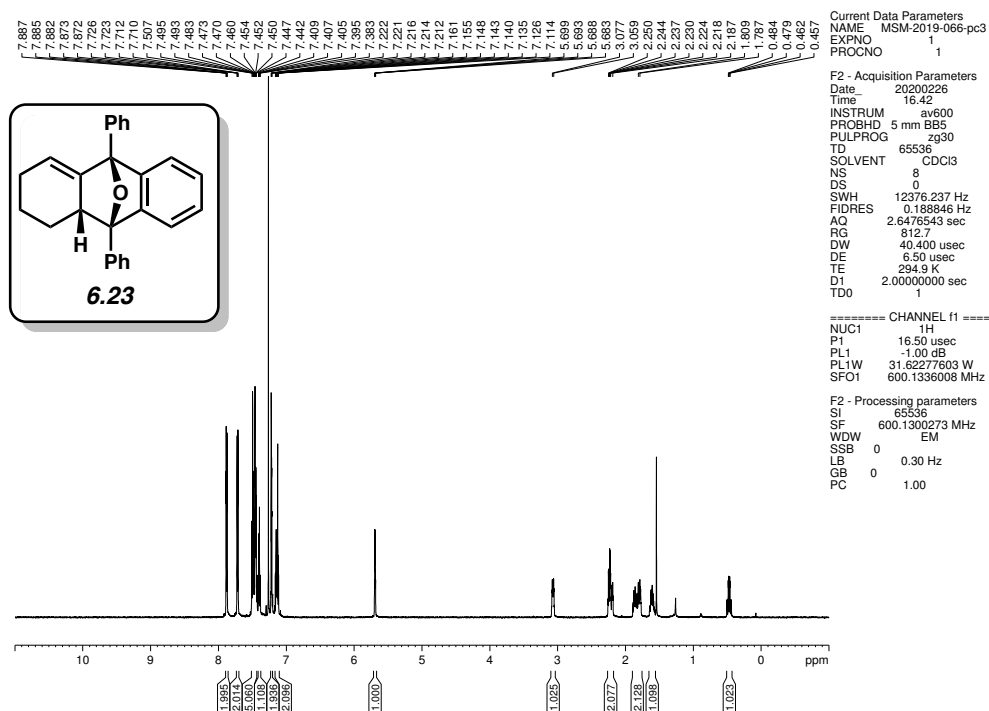
Figure 6.13. ^{1}H NMR (600 MHz, CDCl$_3$) of compound **6.23**.
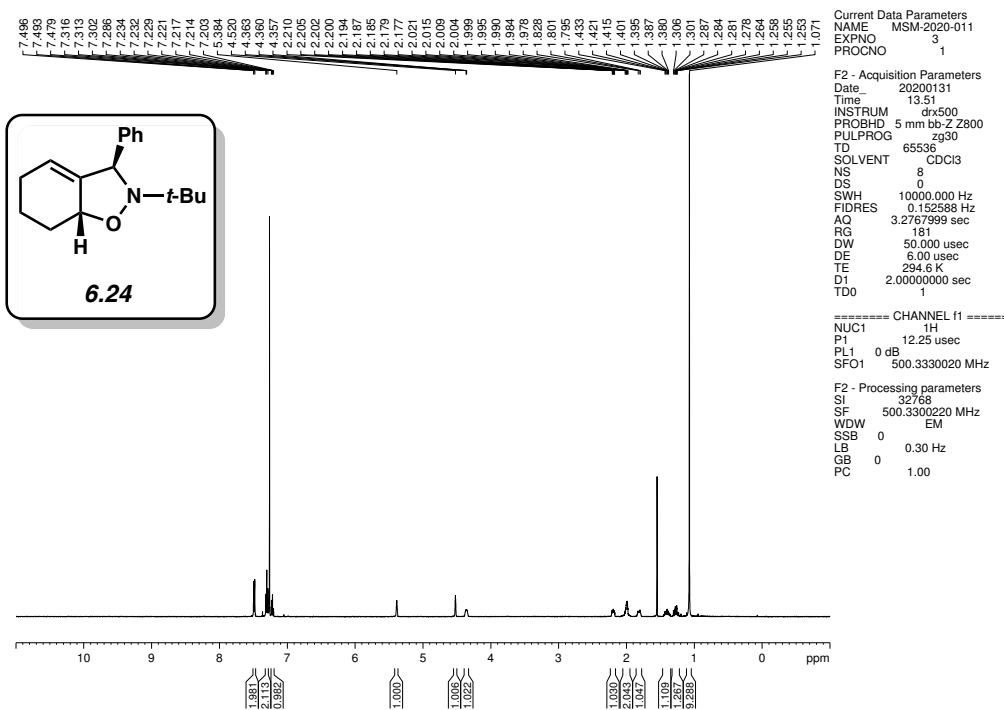
Figure 6.14. ¹H NMR (500 MHz, CDCl₃) of compound **6.24**.
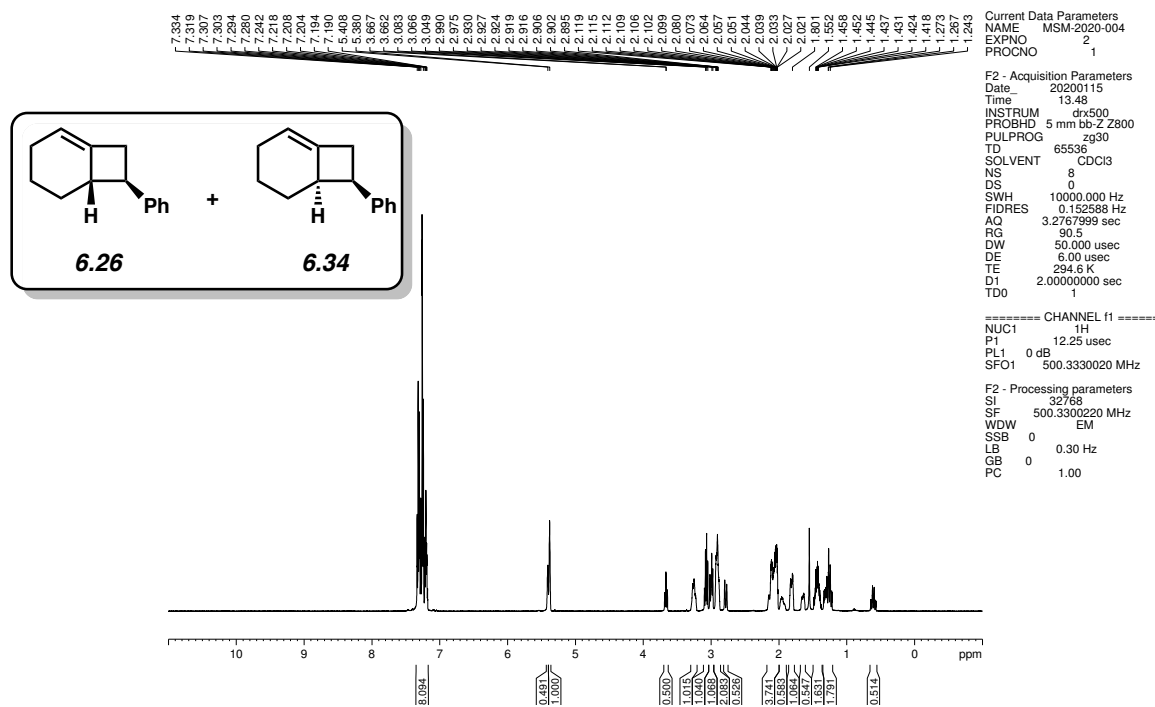
Figure 6.15. ¹H NMR (500 MHz, CDCl₃) of compounds **6.26** and **6.34**.
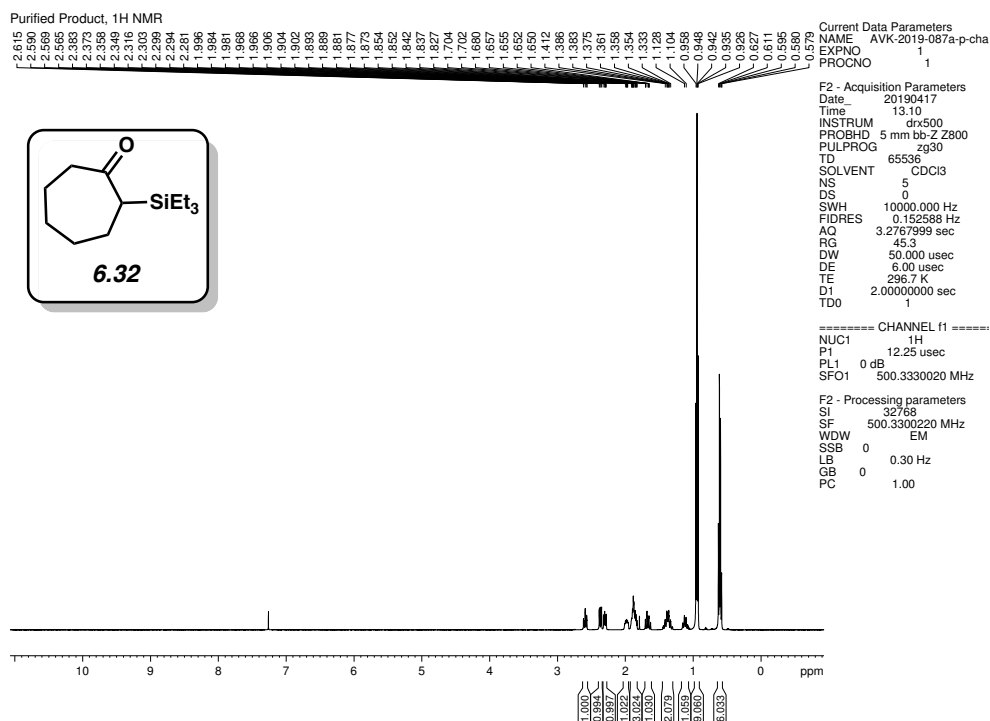
Figure 6.16. ^{1}H NMR (500 MHz, CDCl$_3$) of compounds **6.32**.
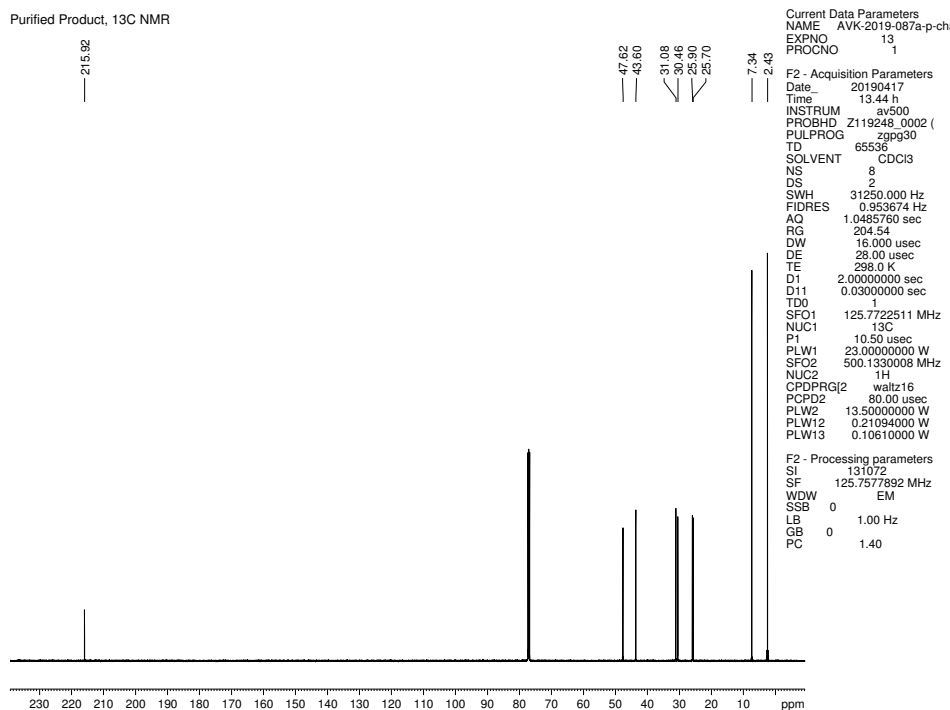
Figure 6.17. ^{13}C NMR (125 MHz, CDCl$_3$) of compound **6.32**.
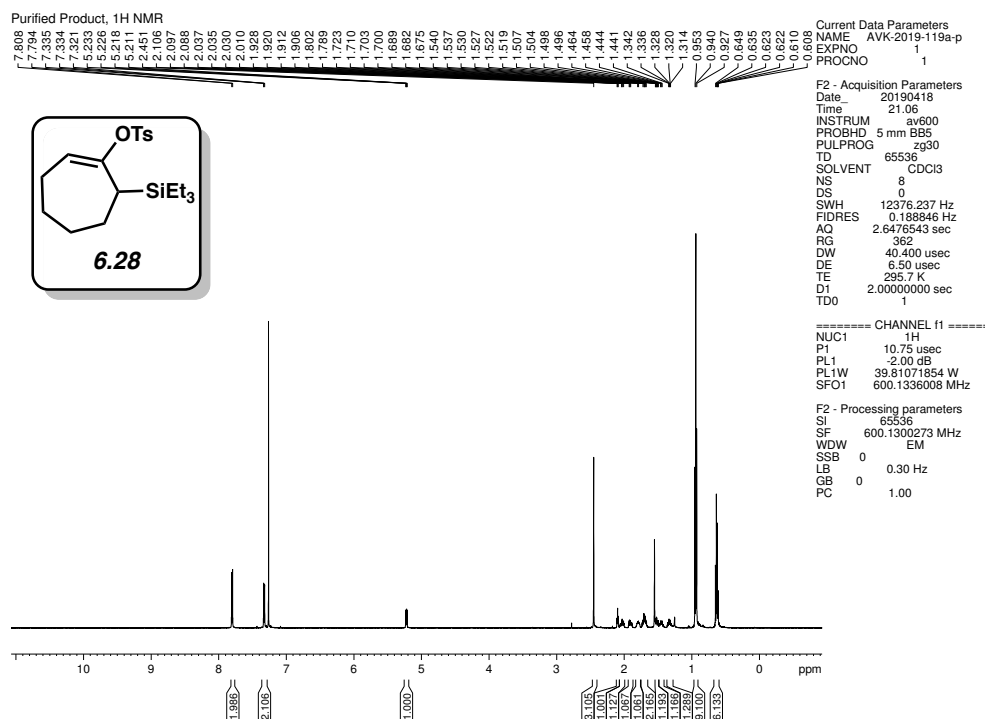
Figure 6.18. ^{1}H NMR (600 MHz, CDCl$_3$) of compounds **6.28**.
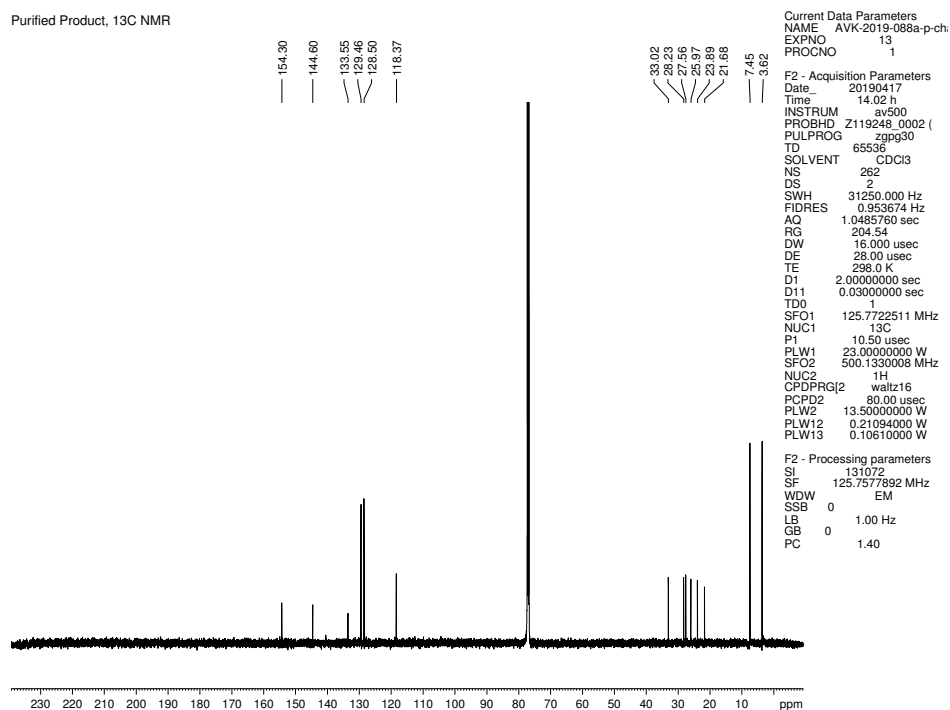
Figure 6.19. ^{13}C NMR (125 MHz, CDCl$_3$) of compound **6.28**.
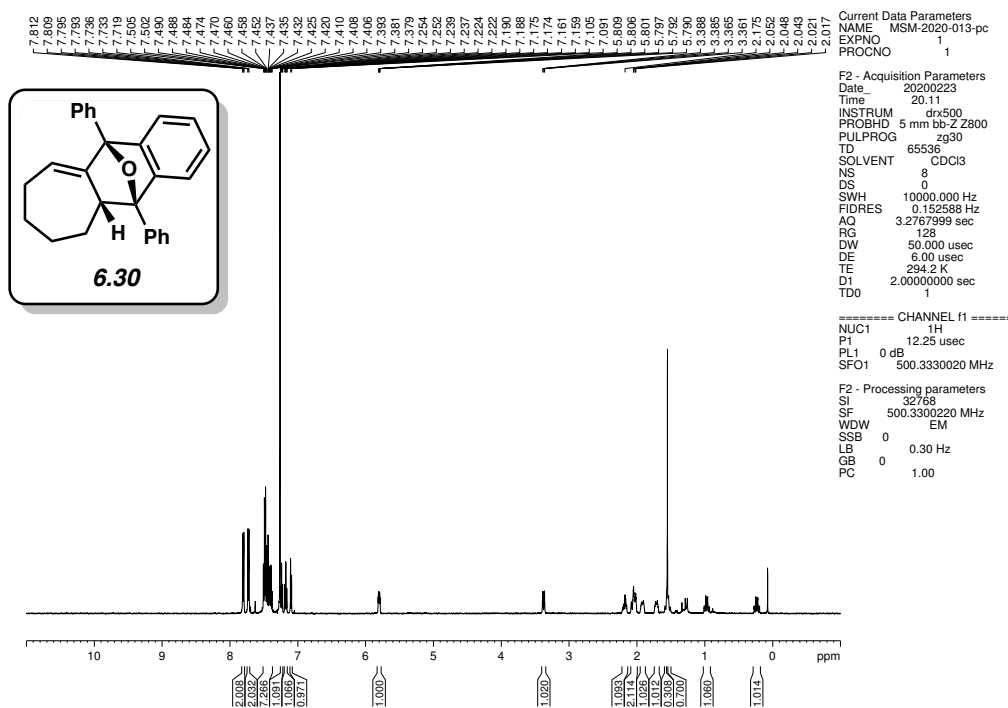
Figure 6.20. ^{1}H NMR (500 MHz, CDCl$_3$) of compounds **6.30**.

6.11 Notes and References

(1) For reviews of transient strained cyclic intermediates, see: (a) Wenk, H. H.; Winkler, M.; Sander, W. One century of aryne chemistry. *Angew. Chem., Int. Ed.* **2003**, *42*, 502–528. (b) Bronner, S. M.; Goetz, A. E.; Garg, N. K. Understanding and modulating indolyne regioselectivities. *Synlett* **2011**, *18*, 2599–2604. (c) Tadross, P. M.; Stoltz, B. M. A comprehensive history of arynes in natural product total synthesis. *Chem. Rev.* **2012**, *112*, 3550–3577. (d) Gampe, C. M.; Carreira, E. M. Arynes and cyclohexyne in natural product synthesis. *Angew. Chem., Int. Ed.* **2012**, *51*, 3766–3778. (e) Dubrovskiy, A. V.; Markina, N. A.; Larock, R. C. Use of benzynes for the synthesis of heterocycles. *Org. Biomol. Chem.* **2013**, *11*, 191–218. (f) Hoffmann, R. W.; Suzuki, K. A "hot, energized" benzyne. *Angew. Chem., Int. Ed.* **2013**, *52*, 2655–2656. (g) Goetz, A. E.; Garg, N. K. Enabling the use of heterocyclic arynes in chemical synthesis. *J. Org. Chem.* **2014**, *79*, 846–851. (h) Yoshida, S.; Hosoya, T. The renaissance and bright future of synthetic aryne chemistry. *Chem. Lett.* **2015**, *44*, 1450–1460. (i) Takikawa, H.; Nishii, A.; Sakai, T.; Suzuki, K. Aryne-based strategy in the total synthesis of naturally occurring polycyclic compounds. *Chem. Soc. Rev.* **2018**, *47*, 8030–8056. (j) Dhokale, R. A.; Mhaske, S. B. Transition-metal-catalyzed reactions involving arynes. *Synthesis* **2018**, *50*, 1–16.

(2) (a) Wittig, G. Phenyl-lithium, der Schlüssel zu einer neuen Chemie metallorganischer Verbindungen. *Naturwissenschaften* **1942**, *30*, 696–703. (b) Roberts, J. D.; Simmons, H. E.; Carlsmith, L. A.; Vaughan, C. W. Rearrangement in the reaction of chlorobenzene-1-C^{14} with potassium amide. *J. Am. Chem. Soc.* **1953**, *75*, 3290–3291.

(3) Scardiglia, F.; Roberts, J. D. Evidence for cyclohexyne as an intermediate in the coupling of phenyllithium with 1-chlorocyclohexene. *Tetrahedron* **1957**, *1*, 343–344.

(4) Wittig, G.; Fritze, P. On the intermediate occurrence of 1,2-cyclohexadiene. *Angew. Chem., Int. Ed.* **1966**, *5*, 846.

(5) (a) Gampe, C. M.; Carreira, E. M. Total syntheses of guanacastepenes N and O. *Angew. Chem., Int. Ed.* **2011**, *50*, 2962–2965. (b) Kou, K. G. M.; Pflueger, J. J.; Kiho, T.; Morrill, L. C.; Fisher, E. L.; Clagg, K.; Lebold, T. P.; Kisunzu, J. K.; Sarpong, R. A benzyne insertion approach to hetisine-type diterpenoid alkaloids: synthesis of cossonidine (davisine). *J. Am. Chem. Soc.* **2018**, *140*, 8105–8109. (c) Goetz, A. E.; Silberstein, A. L.; Corsello, M. A.; Garg, N. K. Concise enantiospecific total synthesis of tubingensin A. *J. Am. Chem. Soc.* **2014**, *136*, 3036–3039. (d) Neog, K.; Borah, A.; Gogoi, P. Palladium(II)-catalyzed C–H bond activation/C–C and C–O bond formation reaction cascade: Direct synthesis of coumestans. *J. Org. Chem.* **2016**, *81*, 11971–11977. (e) Neumeyer, M.; Kopp, J.; Brückner, R. Controlling the substitution pattern of hexasubstituted naphthalenes by aryne/siloxyfuran Diels–Alder additions: regio and stereocontrolled synthesis of arizonin C1 analogs. *Eur. J. Org. Chem.* **2017**, 2883–2915. (f) Corsello, M. A.; Kim, J.; Garg, N. K. Total synthesis of (–)-tubingensin B enabled by the strategic use of an aryne cyclization. *Nat. Chem.* **2017**, *9*, 944–949.

(6) (a) Barber, J. S.; Styduhar, E. D.; Pham, H. V.; McMahon, T. C.; Houk, K. N.; Garg, N. K. Nitrone cycloadditions of 1,2-cyclohexadiene. *J. Am. Chem. Soc.* **2016***, 138*, 2512–2515. (b) Medina, J. M.; McMahon, T. C.; Jiménez-Osés, G.; Houk, K. N.; Garg, N. K. Cycloadditions of cyclohexynes and cyclopentyne. *J. Am. Chem. Soc*. **2014**, *136*, 14706–14709. (c) McMahon, T. C.; Medina, J. M.; Yang, Y.-F.; Simmons, B. J.; Houk, K. N.; Garg, N. K. Generation and regioselective trapping of a 3,4-piperidyne for the synthesis of functionalized heterocycles. *J. Am. Chem. Soc.* **2015**, *137*, 4082–4085. (d) Tlais, S. F.;

Danheiser, R. L. *N*-Tosyl-3-azacyclohexyne. Synthesis and chemistry of a strained cyclic ynamide. *J. Am. Chem. Soc.* **2014**, *136*, 15489–15492. (e) Shah, T. K.; Medina, J. M.; Garg, N. K. Expanding the strained alkyne toolbox: generation and utility of oxygen-containing strained alkynes. *J. Am. Chem. Soc.* **2016**, *138*, 4948–4954. (f) Barber, J. S.; Yamano, M. M.; Ramirez, M.; Darzi, E. R.; Knapp, R. R.; Liu, F.; Houk, K. N.; Garg, N. K. Diels–Alder cycloadditions of strained azacyclic allenes. *Nat. Chem.* **2018**, *10*, 953–960. (g) Nendel, M.; Tolbert, L. M.; Herring, L. E.; Islam, M. N.; Houk, K. N. Strained allenes as dienophiles in the Diels–Alder reaction: an experimental and computational study. *J. Org. Chem.* **1999**, *64*, 976–983. (h) Lofstrand, V. A.; West, F. G. Efficient trapping of 1,2-cyclohexadienes with 1,3-dipoles. *Chem. Eur. J.* **2016***, 22*, 10763–10767. (i) Yamano, M. M.; Knapp, R. R.; Ngamnithiporn, A.; Ramirez, M.; Houk, K. N.; Stoltz, B. M.; Garg, N. K. Cycloadditions of oxacyclic allenes and a catalytic asymmetric entryway to enantioenriched cyclic allenes. *Angew. Chem., Int. Ed.* **2019**, *58*, 5653–5657.

(7) (a) Darzi, E. R.; Barber, J. S.; Garg, N. K. Cyclic alkyne approach to heteroatom-containing polycyclic aromatic hydrocarbon scaffolds. *Angew. Chem., Int. Ed.* **2019**, *58*, 9419–9424. (b) Pérez, D.; Peña, D.; Guitián, E. Aryne cycloaddition reactions in the synthesis of large polycyclic aromatic compounds. *Eur. J. Org. Chem.* **2013**, 5981–6013. (c) Xiao, X.; Hoye, T. R. The domino hexadehydro-Diels–Alder reaction transforms polyynes to benzynes to naphthynes to anthracynes to tetracynes (and beyond?). *Nat. Chem.* **2018**, *10*, 838–844. (d) Suh, S.-E.; Barros, S. A.; Chenoweth, D. M. Triple aryne–tetrazine reaction enabling rapid access to a new class of polyaromatic heterocycles. *Chem. Sci.* **2015**, *6*, 5128–5132. (e) Mizukoshi, Y.; Mikami, K.; Uchiyama, M. Aryne polymerization enabling straightforward synthesis of elusive poly(*ortho*-arylene)s. *J. Am. Chem. Soc.* **2015**, *137*, 74–77.

(8) Himeshima, Y.; Sonoda, T.; Kobayashi, H. Fluoride-induced 1,2-elimination of *o*-trimethylsilylphenyl triflate to benzyne under mild conditions. *Chem. Lett.* **1983**, *12*, 1211–1214.

(9) Atanes, N.; Escudero, S.; Pérez, D.; Guitián, E.; Castedo, L. Generation of cyclohexyne and its Diels–Alder reaction with α-pyrones. *Tetrahedron Lett.* **1998**, *39*, 3039–3040.

(10) Quintana, I.; Peña, D.; Pérez, D.; Guitián, E. Generation and reactivity of 1,2-cyclohexadiene under mild reaction conditions. *Eur. J. Org. Chem*. **2009**, 5519–5524.

(11) For a review related to vinyl triflate dissociation, see: Stang, P. J. Vinyl triflate chemistry: Unsaturated cations and carbenes. *Acc. Chem. Res.* **1978**, *11*, 107–114.

(12) For references related to β-silyl stabilized vinyl cations, see: (a) Siehl, H.-U.; Kaufmann, F. P. Carbon-13 NMR spectroscopic determination of the magnitude of the β-silyl stabilization effect in 1-mesitylvinyl cations. *J. Am. Chem. Soc.* **1992**, *114*, 4937–4939. (b) Müller, T.; Meyer, R.; Lennartz, D.; Siehl, H.-U. Unusually stable vinyl cations. *Angew. Chem., Int. Ed.* **2000**, *39*, 3074–3077. (c) McGibbon, G. A.; Brook, M. A.; Terlouw, J. K. Stabilization energies for α- and β-silyl substituents on vinyl cations determined using mass spectrometric techniques. *J. Chem. Soc., Chem. Commun.* **1992**, *4*, 360–362.

(13) (a) Cunico, R. F.; Dexheimer, E. M. Generation of 1,2-dehydrobenzene from the dehalosilylation of (*o*-halophenyl)trimethylsilanes. *J. Organomet. Chem.* **1973**, *59*, 153–160. (b) Lv, C.; Wan, C.; Liu, S.; Lan, Y.; Li, Y. Aryne trifunctionalization enabled by 3-silylaryne as a 1,2-benzdiyne equivalent. *Org. Lett.* **2018**, *20*, 1919–1923.

(14) Although silyl triflates **6.8** and **6.10** do not suffer from instability, their known reactivity provides a useful point of comparison for developing the complementary precursors **6.9** and **6.11**, respectively.

(15) (a) Streitwieser, A., Jr.; Wilkins, C.; Kiehlmann, E. Kinetics and isotope effects in solvolyses of ethyl trifluoromethanesulfonate. *J. Am. Chem. Soc.* **1968**, *90*, 1598–1601. (b) Noyce, D. S.; Virgilio, J. A. The synthesis and solvolysis of 1-phenylethyl disubstituted phosphinates. *J. Org. Chem.* **1972**, *37*, 2643–2647.

(16) For methods that leverage the reactivity differences between triflates and tosylates to achieve selective, sequential functionalization of arynes, see: (a) Hamura, T.; Arisawa, T.; Matsumoto, T.; Suzuki, K. Two-directional annelation: dual benzyne cycloadditions starting from bis(sulfonyloxy)diiodobenzene. *Angew. Chem., Int. Ed.* **2006**, *45*, 6842–6844. (b) Xu, H.; He, J.; Shi, J.; Tan, L.; Qiu, D.; Luo, X.; Li, Y. Domino aryne annulation via a nucleophilic-ene process. *J. Am. Chem. Soc.* **2018**, *140*, 3555–3559.

(17) The introduction of tosyl groups is known to impart crystallinity; for examples, see: (a) Kazemi, F.; Massah, A. R.; Javaherian, M. Chemoselective and scalable preparation of alkyl tosylates under solvent-free conditions. *Tetrahedron* **2007**, *63*, 5083–5087. (b) Jiang, X.; Li, J.; Zhang, R.; Zhu, Y.; Shen, J. An improved preparation process for gemcitabine. *Org. Proc. Res. Dev.* **2008**, *12*, 888–891.

(18) (a) Corey, E. J.; Rücker, C. The 1,3 O→C silyl rearrangement of silyl enol ether anions – synthesis of α-silyl ketones. *Tetrahedron Lett.* **1984**, *25*, 4345–4348. (b) Inoue, K.; Nakura, R.; Okano, K.; Mori, A. One-pot synthesis of silylated enol triflates from silyl enol ethers for cyclohexynes and 1,2-cyclohexadienes. *Eur. J. Org. Chem.* **2018**, 3343–3347.

(19) The yield of **6.21** from **6.9** is lower than when using the analogous trimethylsilyl triflate (see ref 6b). This may be attributed to an empirically observed inhibitory effect of excess imidazole on the consumption of **6.9**.

(20) Christl, M.; Schreck, M. 7-Arylbicyclo[4.2.0]oct-1-ene – Synthese durch [2 + 2]-Cycloadditionen von 1,2-Cyclohexadien sowie 1-Methyl-1,2-cyclohexadien und thermische Äquilibrierung der *exo/endo*-Isomeren. *Chem Ber.* **1987**, *120*, 915–920.

(21) Attempts to synthesize the corresponding silyl triflate precursor to 1,2-cycloheptadiene (**6.29**) were unsuccessful due to rapid degradation of the desired vinyl triflate upon attempted purification.

(22) For methods to access **6.29** under harsher reaction conditions, see: (a) Bottini, A. T.; Hilton, L. L. Relative reactivities of bicyclo[3.2.1]octa-2,3-diene and 1,2-cycloheptadiene with conjugated dienes and styrene. *Tetrahedron* **1975**, *31*, 2003–2006. (b) Sutbeyaz, Y; Ceylan, M.; Secen, H. A novel synthesis of transient 1,2-cyclohexadiene and 1,2-cycloheptadiene via β-halosilanes. *J. Chem. Res. (M)* **1993**, *8*, 2189–2196.

(23) Chen, Q.; Tanaka, S.; Fujita, T.; Chen, L.; Minato, T.; Ishikawa, Y.; Chen, M.; Asao, N.; Yamamoto, Y.; Jin, T. The synergistic effect of nanoporous AuPd alloy catalysts on highly chemoselective 1,4-hydrosilylation of conjugated cyclic enones. *Chem. Comm.* **2014**, *50*, 3344–3346.

CHAPTER SEVEN

Progress Toward the Total Synthesis of Alstilobanine A

7.1 Abstract

Monoterpene indole alkaloids represent the largest classes of natural products, many of which possess biological activity for the treatment of human diseases. One such alkaloid, alstilobanine A (**7.1**), is the focus of this chapter. Our synthetic strategy hinges on a on a key (4+2) cycloaddition between a pyrone and an azacyclic allene to construct the core of the natural product. Herein, we detail the current experimental progress toward the synthesis of alstilobanine A and outline future studies.

7.2 Introduction

Indole alkaloids comprise one of the largest groups of natural products with biological activity for the treatment of human diseases.[1] One such alkaloid, (–)-alstilobanine A (**7.1**, Figure 7.1), first isolated in 2008 by Morita and co-workers,[2] consists of an unusual 2-azadecalin core appended to the indole fragment. The stereochemical complexity of **7.1** renders it a formidable synthetic target. In particular, the 2-azadecalin core contains four vicinal stereogenic centers, two of which are fully substituted, as well as a number of potentially sensitive functional groups. To highlight these challenges, only a single racemic synthesis of **7.1** has been reported, which provided access to the natural product in 20 linear steps.[3] Intrigued by the structure of alstilobanine A (**7.1**), we pursued a concise synthesis of **7.1**. Our proposed synthesis hinges on a (4+2) cycloaddition of a strained cyclic allene **7.3** to rapidly prepare a highly functionalize azadecalin.

Strained cyclic intermediates have long fascinated the scientific community[4] and despite once being curiosities, small rings containing a triple bond can now be used in a host of applications.[5] Specifically, synthetic strategies leveraging the reactivity of strained intermediates can be advantageous. Despite the high reactivity due to the ring strain found in these intermediates, they react regioselectively and can form multiple bonds in a single step. Additionally, they can be formed under mild reaction conditions. These characteristics make the use of strained intermediates well suited for complex molecule synthesis and strained cyclic intermediates possessing triple bonds have been utilized in a number natural product syntheses.[5f–h]

Interestingly, the corresponding cyclic allenes, despite being first reported in 1976[6] and possessing similar strategic advantages as cyclic alkynes, has seen little application in the realm of complex molecule synthesis.[7] From a strategic standpoint, the strain of cyclic allenes can also be harnessed to introduce complexity as the allene can be substituted and subsequent trapping gives rise to sp^3-rich products.[8] Furthermore, akin to linear allenes, cyclic allenes are chiral and this chirality can be leveraged to control the absolute stereochemistry found in the corresponding products. Our group and others have gained insights into the fundamental reactivity of these intermediates through methodology development.[9] There have been a number of insights into the regio- and steroselecitivty trends as well as methods to control the absolute stereochemistry found in the products.[10] With these synthetic advantages in mind, our proposed synthesis of alstilobanine A (**7.1**) strategically relies on a (4+2) cycloaddition with a substituted azacyclic allene **7.3** and pyrone **7.2** to rapidly access the azadecalin core of **7.1** (Figure 7.1). The key step would form two bonds and install three of the four stereocenters, two of which are fully substituted. The success of these studies would push the scope and limitations of this reaction methodology while enabling efficient access to alstilobanine A (**7.1**).
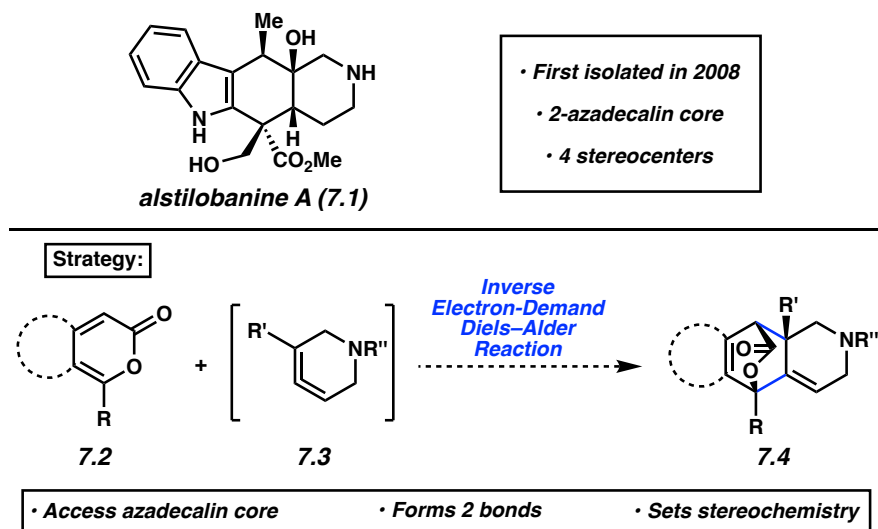
Figure 7.1. The structure of alstilobanine A (**7.1**) and overview of current approach.

7.3 Retrosynthetic Analysis

A concise retrosynthetic analysis for alstilobanine A (**7.1**) is shown in Figure 7.2. Retrosynthetically, **7.1** was envisioned to arise from **7.5** through functional group manipulations to install the methyl ester and primary alcohol moieties. **7.5**, in turn, could be prepared from **7.6** via a reduction. Triol **7.6** could be accessed from **7.8** via a reductive opening of the lactone and cleavage of the acetate group. Next, it was envisioned that the key intermediate **7.8** could be prepared by a (4+2) cycloaddition between an indole 2-pyrone **7.9** and acetoxy-substituted aza cyclicallene **7.10**. Notably, this key step would form two new bonds and set three of the four stereocenters. Overall, the strategic usage of a strained cyclic allene would enable the rapid generation of structural complexity and is expected to facilitate a concise synthesis of **7.1**.
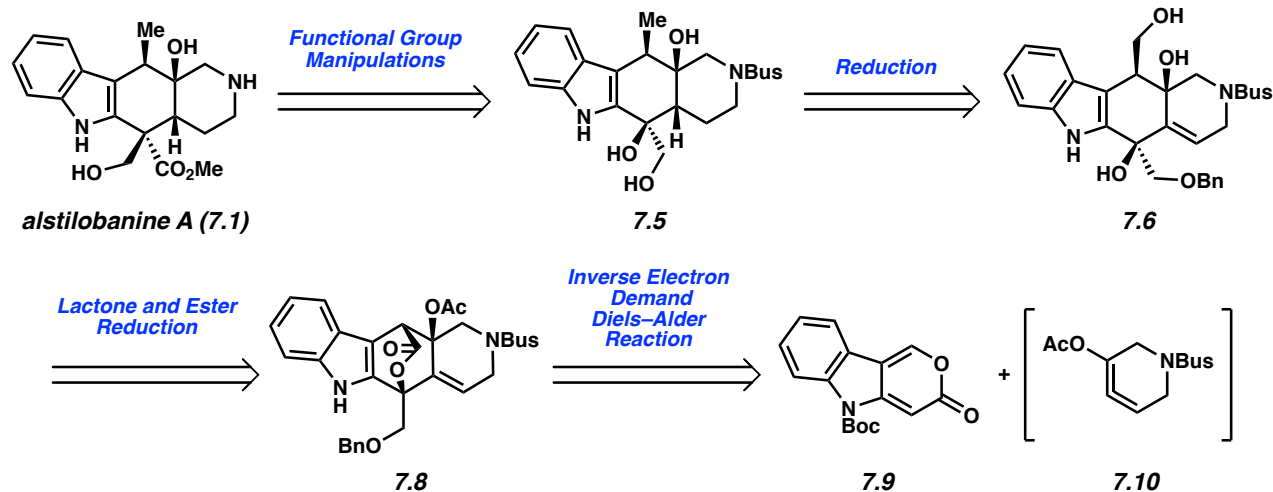
Figure 7.2. Retrosynthetic analysis of alstilobanine A (**7.1**).

7.4 (4+2) Cycloadditions with Indole Pyrone 7.9

Studies toward the total synthesis of alstilobanine A (**7.1**) commenced by evaluating the regio- and stereoselectivity of the (4+2) cycloaddition between pyrone **7.9** (known in 6 steps)[23] and in situ-generated azacyclic allene **7.10**, shown in Figure 7.3. To achieve this goal, acetoxy-substituted azacyclic allene **7.11** precursor was prepared (see Section 7.9.2.1). Subjection of **7.9** and **7.11** to mild fluoride-mediated conditions led to the formation of undesired cycloadduct **7.12** in 80% yield. This unexpected adduct is proposed to arise through generation of cyclic allene **7.10** and trapping with **7.9**, followed by spontaneous decarboxylation and aromatization. Of note, the undesired regioisomer was observed in this transformation as cycloaddition occurred on the double bond of the cyclic allene distal to the acetoxy substituent. It was hypothesized that shifting from an electron-donating group (acetoxy group) to an electron-withdrawing group (ester) could reverse the regioselectivity, and lead to cycloaddition at the olefin proximal to the substituent. Of note, a previous study by our group has demonstrated the regioselectivity of (4+2) cycloadditions of azacyclic allenes is guided by the electronic nature of the substituents.[11] To investigate this hypothesis, ester-substituted azacyclic allene precursor **7.13** was synthesized and treated with

pyrone **7.9** in the presence of CsF. Unfortunately, cycloaddition of cyclic allene **7.14** again occurred at the undesired double bond of the allene, giving **7.15** was obtained as the major product in 56% yield.
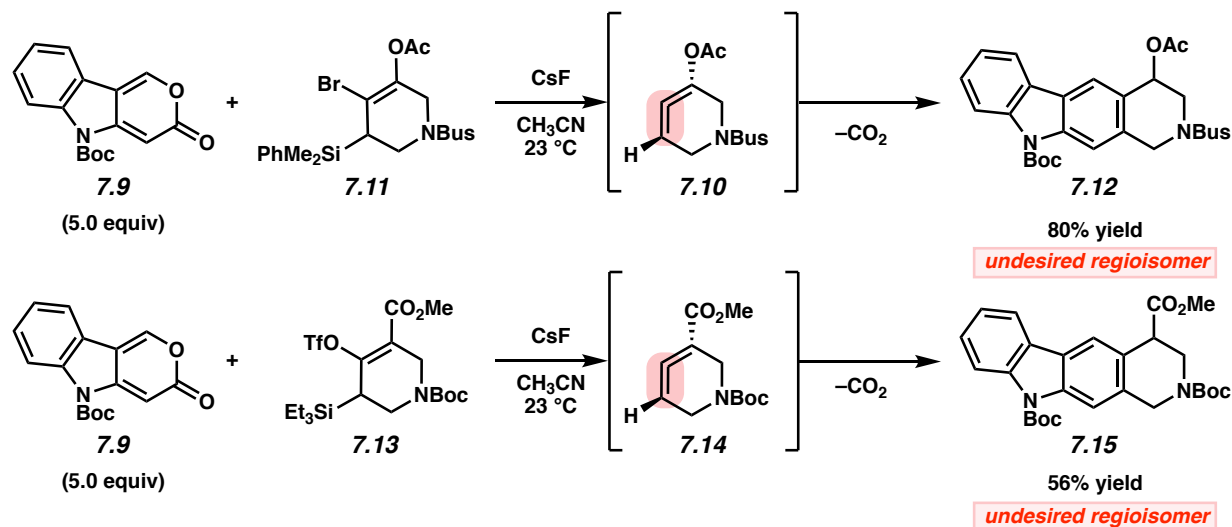
Figure 7.3 Initial studies of the (4+2) cycloaddition of azacyclic allenes with indole pyrone **7.9** give rise to the undesired regioselectivity.

7.5 Revised Route to Alstilobanine A (7.1)

To overcome the regioselectivity challenges observed in cycloadditions of the azacyclic allene with indole pyrone **7.9**, a revised retrosynthetic analysis was designed. Retrosynthetically, compound **7.6** would still be accessed through the proposed route, however, it was envisioned to arise from *o*-nitro arene **7.16** via a reductive indolization. **7.16** could then be traced back to **7.17** through reduction of the lactone and ester moieties. Key intermediate **7.17** could, in turn, be generated by a (4+2) cycloaddition between pyrone **7.18** and acetoxy-substituted azacyclic allene **7.10**. Key to the revised synthetic strategy is the use of an electron-poor diene **7.18**. Studies within our group have validated pyrone dienes to participate in inverse electron-demand Diels–Alder reactions and cyclize on the alkene proximal to the electron-donating substituent. While the revised strategy does not incorporate the indole moiety in the key (4+2) cycloaddition, the reaction does

411

install all but one of the carbons found in the framework of alstilobanine A (**7.1**) and sets the stereochemistry.
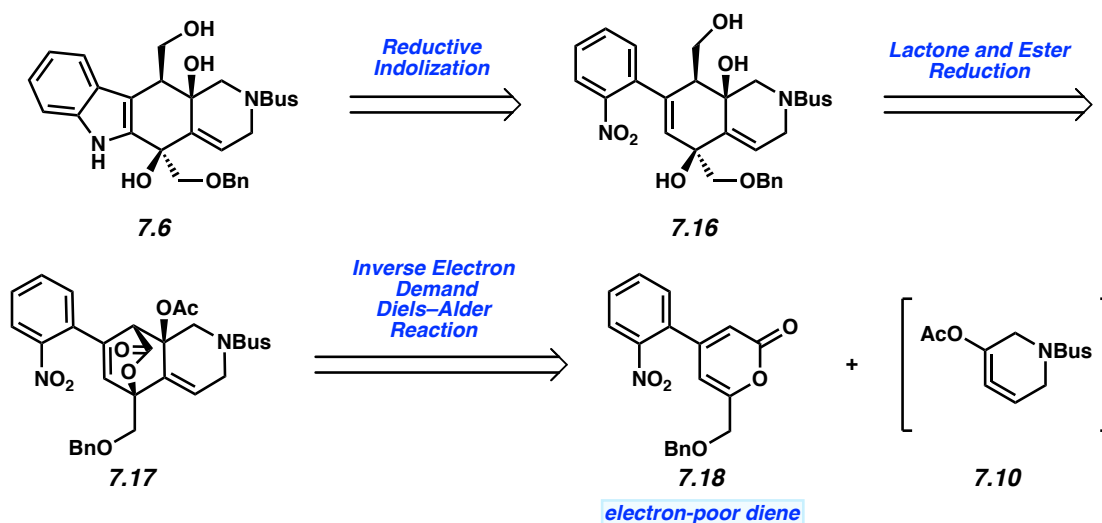
Figure 7.4 Revised retrosynthetic analysis of alstilobanine A (**7.1**).

With the revised retrosynthesis in hand, our attention turned to investigating the regioselectivity of the redesigned (4+2) cycloaddition (Figure 7.5). We were excited to find that exposure of silyl bromide **7.11** and pyrone **7.18** to mild fluoride-based conditions led to formation of cycloadduct **7.17** in 46% yield (>20:1 d.r.), via the proposed transition structure **7.19**. Of note, the cycloaddition occurs on the olefin proximal to the acetoxy substituent, generating two fully substituted stereocenters in the process. Furthermore, this transformation assembles the core framework of alstilobanine A (**7.1**) in one step, giving a product that contains all but one of the carbon atoms present in the natural product.
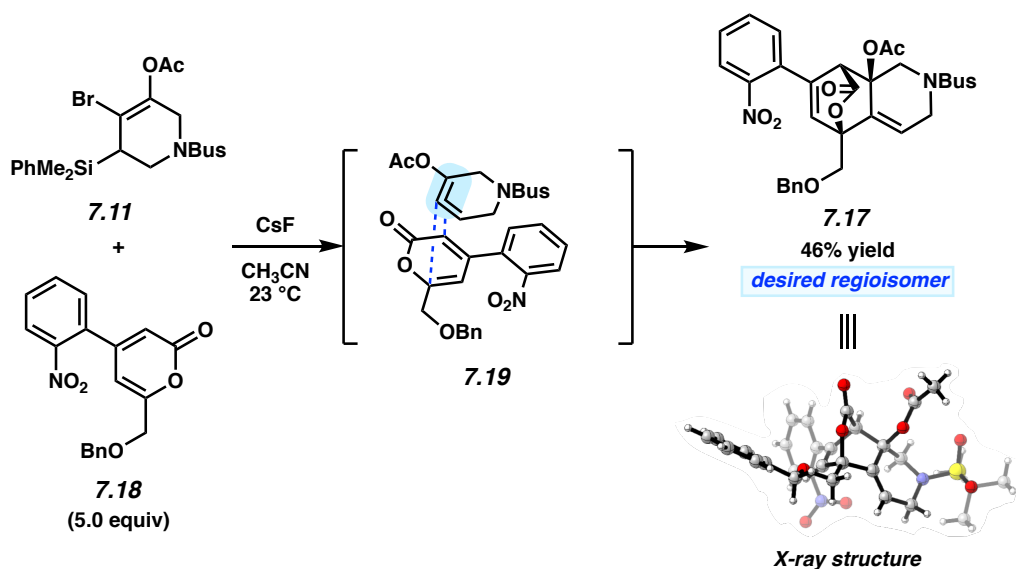
Figure 7.5 Key (4+2) cycloaddition to access the core of alstilobanine A (**7.1**).

7.6 Current Directions

With **7.17** in hand, the lactone bridge and acetate groups were reduced using lithium borohydride to afford triol **7.16** in 48% yield. Current efforts are focused on achieving a reductive indolization to forge the C–N bond of **7.6** and access the indole fragment present in alstilobanine A (**7.1**). Initial experiments employing TiCl₃ as a reductant[12] are promising, and assessment of alternative reducing conditions[13] to optimize this transformation is ongoing.
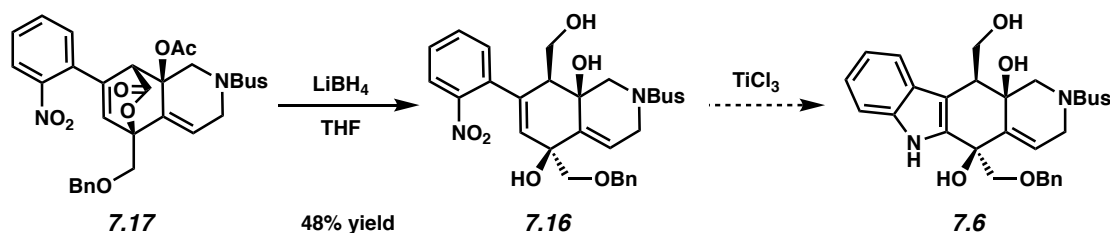
Figure 7.6 Current efforts en route to alstilobanine A (**7.1**).

7.7 Future Directions

Many options for endgame studies can be envisioned, some of which are shown in Figure 7.7. Following the installation of the indole moiety, the triol **7.6** will subjected to Appel reaction conditions to convert the primary alcohol to an alkyl iodide. Subsequent reduction is expected to

413

result in hydrodeiodination, benzyl group removal, and alkene reduction in one step to afford **7.5**.
[14] In the ideal scenario, the *cis*-decalin configuration is preferred, however, if this proves challenging, an alcohol-directed reduction using Crabtree's catalyst can be employed.[15] Treatment of **7.5** with TFA is expected to induce removal of the Bus group and dehydration of the activated alcohol, forming carbocation **7.20**. Notably, dehydrations of this nature have been reported previously.[16] The carbocation **7.20** is then proposed to be trapped by sodium cyanide (Route A),[17] whereby the approach of the nucleophile is expected to take place from the α-face. Following formation of **7.21**, a Pinner reaction would be executed using HCl in methanol to convert the nitrile group to the methyl ester and give rise to alstilobanine A (**7.1**).[18] If approach of the nucleophile from the concave α-face is challenging, an alternative route is proposed (Route B). Namely, the carbocation **7.20** could be trapped with a hydride source to give **7.22**[19] and subsequent oxidation should generate **7.23**. Finally, α-deprotonation and trapping of the resultant enolate with formaldehyde is expected to deliver the natural product. [14] In this final step, alkylation is anticipated to occur on the less sterically hindered β-face.
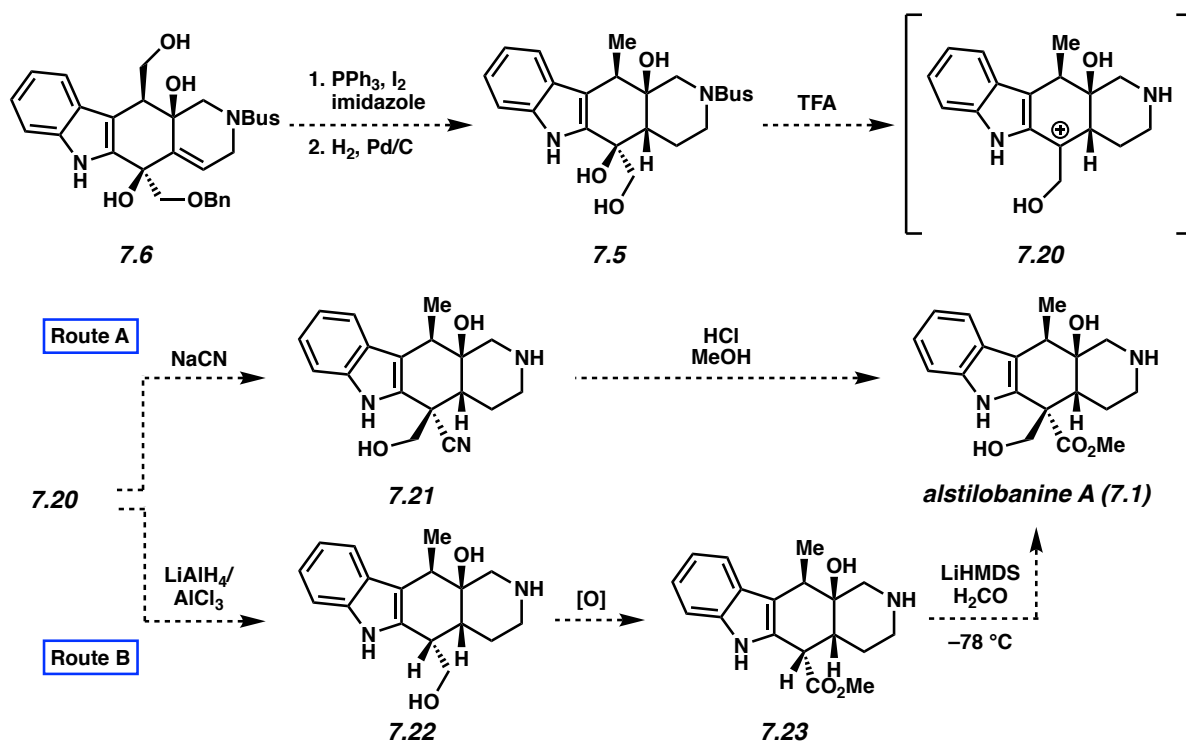
Figure 7.7 Proposed strategy to complete the total synthesis of alstilobanine A (**7.1**).

7.8 Conclusions

We have conceived an ambitious plan to synthesize alstilobanine A (**7.1**). Our route leverages a key (4+2) cycloaddition using an azacyclic allene to generate two bonds and set two stereocenters found in the natural product. Thus far, we have accessed key intermediate **7.16** in four steps from known starting materials. Current efforts are aimed at performing a reductive indolization to complete the core indole framework of the natural product. The success of this synthesis will underscore the synthetic advantages of employing strained cyclic allenes strategically in complex molecule synthesis and should facilitate a concise synthesis of **7.1**.

7.9 Experimental Section

7.9.1 Materials and Methods

Unless stated otherwise, reactions were conducted in flame-dried glassware under an atmosphere of nitrogen using anhydrous solvents (freshly distilled or passed through activated alumina columns). All commercially obtained reagents were used as received unless otherwise specified. Cesium fluoride (CsF), copper bromide•dimethyl sulfide complex, and PdCl$_2$(dppf)•CH$_2$Cl$_2$ were obtained from Strem Chemicals. Titanium trichloride, acetic anhydride, and lithium borohydride were obtained from Sigma-Aldrich. Potassium carbonate was obtained from Alfa Aesar. Reaction temperatures were controlled using an IKAmag temperature modulator and, unless stated otherwise, reactions were performed at room temperature (approximately 23 °C). Thin layer chromatography (TLC) was conducted with EMD gel 60 F254 pre-coated plates (0.25 mm) and visualized using a combination of UV light and potassium permanganate staining. Silicycle Siliaflash P60 (particle size 0.040–0.063 mm) was used for flash column chromatography. ^{1}H-NMR and 2D-NOESY spectra were recorded on Bruker spectrometers (at 500 and 600 MHz) and are reported relative to the residual solvent signal. Data for ^{1}H-NMR spectra are reported as follows: chemical shift (δ ppm), multiplicity, coupling constant (Hz) and integration. ^{13}C-NMR spectra were recorded on Bruker spectrometers (at 125 MHz) and are reported relative to the residual solvent signal. Data for ^{13}C-NMR spectra are reported in terms of chemical shift and, when necessary, multiplicity, and coupling constant (Hz). IR spectra were obtained on a Perkin-Elmer UATR Two FT-IR spectrometer and are reported in terms of frequency of absorption (cm^{-1}). Uncorrected melting points were measured using a Digimelt MPA160 melting point apparatus. DART-MS spectra were collected on a Thermo Exactive Plus MSD (Thermo Scientific) equipped with an ID-CUBE ion source and a Vapur Interface (IonSense Inc.).

Both the source and MSD were controlled by Excalibur software v. 3.0. The analyte was spotted onto OpenSpot sampling cards (IonSense Inc.) using CDCl$_3$ as the solvent. Ionization was accomplished using UHP He (Airgas Inc.) plasma with no additional ionization agents. The mass calibration was carried out using Pierce LTQ Velos ESI (+) and (–) Ion calibration solutions (Thermo Fisher Scientific).

Enone **7.24**[20] *Benzyl propargyl ether (***7.27***)*[21] *and 3-bromopropiolic acid (***7.26***)*[22],

pyrone **7.9**[23],*and silyl triflate* **7.13**[11] *are known compounds.*

7.9.2 Experimental Procedures

7.9.2.1 Synthesis of Silyl Bromide 7.11.
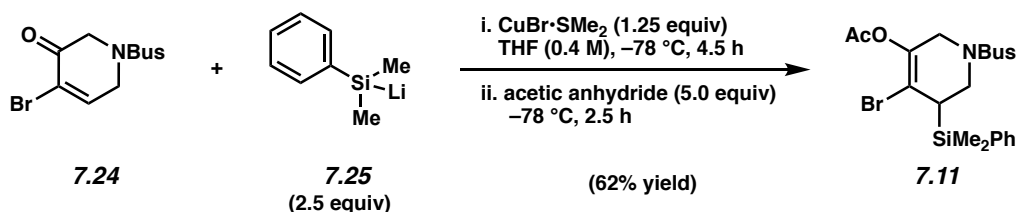
Silyl bromide 7.11. A solution of copper bromide•dimethyl sulfide complex (356 mg, 1.73 mmol, 1.25 equiv) suspended in THF (9.23 mL, 0.15 M) was cooled to 0 °C. Then, a previously prepared solution of **7.25**[24] (0.32M in THF, 10.8 mL, 3.46 mmol, 2.5 equiv) was added to the solution to give a deep red color dropwise via syringe over 7 mins. The resulting silyl cuprate solution was stirred for 30 min at 0 °C before being cooled to –78 °C. Once at –78 °C, a cooled (–78 °C) solution of known enone **7.24**[25] (0.25 M in THF, 410 mg, 1.38 mmol, 1.0 equiv) was added dropwise via a syringe over 5 mins. The reaction mixture stirred at –78 °C for 1 h. After 1 h, distilled acetic anhydride (0.653 mL, 6.92 mmol, 5.0 equiv) was added dropwise via syringe over 2 mins. The solution was allowed to stir at –78 °C for 5 h. The reaction was then quenched with diethyl ether (5 mL) and water (5 mL) and allowed to warm to 23 °C. The layers were then separated and the

aqueous layer was extracted with EtOAc (3 x 10 mL). The combined organic layers were dried

Na$_2$SO$_4$, filtered, and concentrated under reduced pressure. The resulting crude oil was purified by

flash chromatography (4:1 hexanes:EtOAc → 10:1 hexanes:EtOAc) to afford silyl bromide **7.11**

(410 mg, 62% yield) as a colorless oil. Silyl bromide **7.11**: R$_f$ 0.31 (100% benzene); ^{1}H-NMR (400

MHz, CDCl$_3$): δ 7.57–7.52 (m, 2H), 7.40–7.34 (m, 3H), 4.00–3.84 (m, 2H), 3.54 (dd, J = 9.1, 5.4,

1H) , 3.42–3.33 (m, 1H), 2.65–2.55 (m, 1H), 2.18 (s, 3H), 1.32 (s, 9H), 0.53 (s, 3H), 0.48 (s, 3H);

^{13}C-NMR (125 MHz, CDCl$_3$): δ 168.0, 136.7, 134.1, 129.6, 128.0, 112.8, 62.1, 48.4, 48.0, 35.0,

24.7, 20.7, –2.5, –3.5; IR (film): 3070, 2976, 1772, 1368, 1320 cm^{-1}; HRMS–APCI (*m/z*) [M +

H]$^+$ calcd for C$_{19}$H$_{28}$BrNO$_4$SSi$^+$, 476.07440; found, 476.07952.

7.9.2.2 Synthesis of Pyrone 7.18.
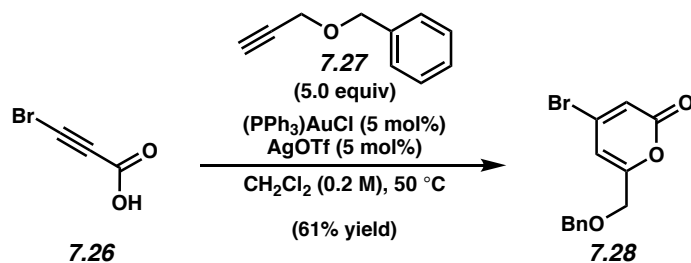
4-Bromo pyrone 7.28. To a solution of 3-bromopropiolic acid (**7.26**, 991 mg, 1.00 equiv, 6.65

mmol), benzyl propargyl alcohol (**7.27**, 4.86 g, 5.00 equiv, 33.3 mmol), and (PPh$_3$)AuCl (165 mg,

5 mol%, 0.333 mmol) in CH$_2$Cl$_2$ (34 mL, 0.20 M) was added AgOTf (85.5 mg, 5 mol%, 0.333

mmol). Then, the reaction was heated to 50 °C and allowed to stir for 14.5 h. After 14.5 h, the

reaction was allowed to cool to 23 °C, filtered over celite (1 cm) with CH$_2$Cl$_2$ (~20 mL) to remove

the black precipitate, and concentrated under reduced pressure to a crude oil. The crude oil was

purified by flash chromatography (19:1 hexanes:EtOAc → 9:1 hexanes:EtOAc) to obtain pyrone

7.28 (1.21 g, 61% yield) as an orange oil. Pyrone **7.28**: R$_f$ 0.31 (9:1 hexanes:EtOAc); ^{1}H NMR

(600 MHz, CDCl$_3$): δ 7.39–7.31 (m, 5H), 6.50–6.49 (m, 2H), 4.62 (s, 2H), 4.28 (t, J = 7.9, 2H);

^{13}C NMR (150 MHz, CDCl$_3$): δ 161.4, 159.7, 141.0, 136.7, 128.6, 128.3, 127.9, 116.0, 107.4, 73.5,

67.2; IR (film): 3090, 3031, 2863, 1732, 1622, 1549, 1107 cm^{-1}; HRMS-APCI (*m/z*) [M + H]$^+$ calcd for C$_{13}$H$_{12}$BrO$_3^+$, 294.9964; found 294.9964.
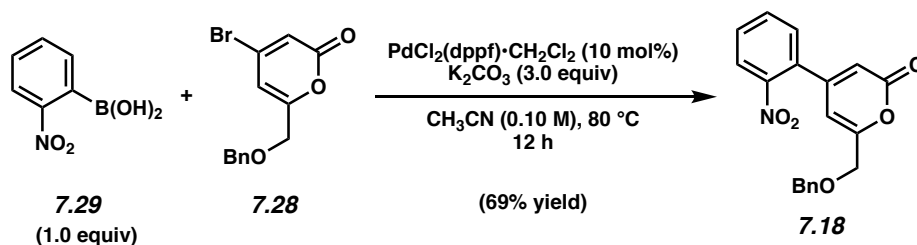
Pyrone 7.18. A 1-dram vial was charged with potassium carbonate (50 mg, 0.36 mmol, 3.0 equiv) and flame-dried under reduced pressure. After cooling to room temperature, the vial was charged with boronic acid **7.29** (20 mg, 0.12 mmol, 1.0 equiv), pyrone **7.28** (35 mg, 0.12 mmol, 1.0 equiv) and PdCl$_2$(dppf)•CH$_2$Cl$_2$ (9.8 mg, 0.012 mmol, 10 mol%). The vial was purged with N$_2$ and diluted with acetonitrile (0.1 M). The vial then was sealed with a PTFE-lined cap under a flow of N$_2$ and placed in a preheated 80 °C aluminum block and stirred for 12 h. After 12 h, the reaction was allowed to cool to 23 °C. The reaction was concentrated under reduced pressure and then diluted with water (4 mL) and EtOAc (4 mL). The layers were then separated and the aqueous layer was extracted with EtOAc (3 x 5 mL). The combined organic layers were dried Na$_2$SO$_4$, filtered, and concentrated under reduced pressure. The resulting crude reaction mixture was purified by preparative TLC (1:1 hexanes:EtOAc) to afford pyrone **7.18** (28 mg, 69% yield) as a white solid. Pyrone **7.18**: R$_f$ 0.19 5:1 hexanes:EtOAc); ^{1}H-NMR (500 MHz, CDCl$_3$): δ 8.14–8.08 (m, 1H), 7.75–7.69 (m, 1H), 7.66–7.60 (m, 1H), 7.43–7.28 (m, 6H) , 6.21–6.18 (m, 2H), 4.63 (s, 1H), 4.35 (s, 1H); ^{13}C-NMR (100 MHz, CDCl$_3$): δ 161.6, 161.2, 154.4, 147.4, 137.0, 133.9, 132.7, 130.7. 130.6, 128.7, 128.3, 128.1, 125.2, 112.2, 103.9, 73.5, 67.8; IR (film): 3066, 2862, 1726, 1524, 1346 cm^{-1}; HRMS–APCI (*m/z*) [M + H]$^+$ calcd for C$_{19}$H$_{15}$NO$_5$Si$^+$, 338.10230; found 338.10531.

7.9.2.3 Diels–Alder Trapping Experiments.

Representative Procedure (Cycloadduct 7.12 is used as an example).
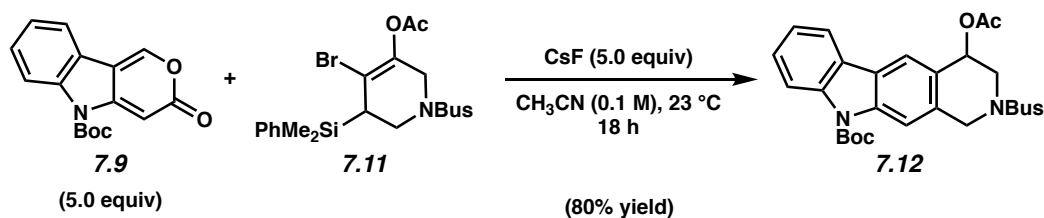
Cycloadduct 7.12. To a stirred solution of silyl bromide **7.11** (5 mg, 0.01 mmol, 1.0 equiv) and

pyrone **7.9** (20 mg, 0.05 mmol, 5.0 equiv) in CH_3CN (0.1 mL) was added CsF (8 mg, 0.05 mmol,

5.0 equiv) as a singular portion. The reaction vessel was sealed with a PTFE-lined cap and allowed

to stir at 23 °C for 18 h. The crude reaction mixture was then filtered by passage through a plug of

silica gel (EtOAc eluent, 10 mL) and then concentration under reduced pressure. The crude

reaction mixture was purificated by preparative thin layer chromatography (2:1 hexanes:EtOAc)

afford the cycloadduct **7.12** (3.1 mg, 80% yield). Cycloadduct **7.12**: R_f 0.54 (2:1 hexanes:EtOAc);

^{1}H-NMR (400 MHz, $CDCl_3$): δ 8.23 (d, J = 4.3, 1H), 8.2 (s, 1H), 7.99–7.94 (m, 2H), 7.50–7.45

(m, 1H), 7.38–7.33 (m, 1H), 6.06 (s, 1H), 5.03–4.89 (m, 1H), 4.62 (d, J = 17.4, 1H), 4.21–4.11 (m,

1H), 3.60 (dd, J = 7.1, 2.3, 1H), 2.13 (s, 3H), 1.76 (s, 9H), 1.45 (s, 9H); ^{13}C-NMR (125 MHz,

$CDCl_3$): δ 151.0, 138.8, 132.9, 128.3, 127.5, 126.4, 125.4, 125.2, 123.3, 121.0, 119.9, 116.3, 113.6,

84.4, 67.9, 61.9, 49.6, 28.4, 24.6, 21.4; IR (film): 2978, 2918, 1728, 1455, 1320 cm^{-1}; HRMS–

APCI (*m/z*) [M + H]$^+$ calcd for $C_{26}H_{32}N_2O_6S^+$, 502.20874; found, 502.21183.

All reactions were monitored by TLC until starting material was consumed; the specific times

are listed in the reaction scheme for each reaction. Any modifications of the conditions shown in

this representative procedure are specified in the following Figures. For all compounds in which

the diastereomeric ratios were >20:1, the minor diastereomer was not observed in the ^{1}H-NMR

spectrum of the crude reaction mixture.
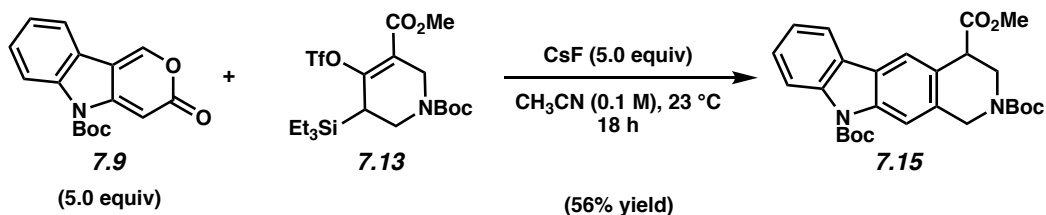
Cycloadduct 7.15. The crude reaction mixture was purified by preparative thin layer chromatography (5:1 hexanes:EtOAc) afford the cycloadduct **7.15** (11.7 mg, 56% yield). Cycloadduct **7.15**: R_f 0.35 (5:1 hexanes:EtOAc); ^{1}H-NMR (500 MHz, CDCl₃): δ 7.8.34–8.07 (m, 2H), 7.93 (d, J = 7.5, 1H), 7.79 (s, 1H), 7.45 (t, J = 7.5, 1H), 7.79 (s, 1H), 7.34 (t, J = 7.4, 1H), 5.01–4.88 (m, 1H), 4.65 (d, J = 8.4, 1H), 4.37 (d, J = 5.8, 1H), 4.07–3.96 (m, 1H), 3.73 (s, 3H), 3.61 (dd, J = 6.5, 4.1, 1H), 1.76 (s, 9H), 1.50 (s, 9H); ^{13}C-NMR (125 MHz, CDCl₃): δ 173.0, 154.7, 1515.2, 139.0, 138.8, 138.4, 133.0, 128.5, 127.3, 124.9, 123.2, 119.9, 116.4, 114.5, 114.2, 84.3, 80.3, 52.5, 47.0, 46.2, 45.2, 44.9, 44.4, 43.4, 28.6, 28.5; IR (film): 2977, 1726, 1697, 1366, 1153 cm^{-1}; HRMS–APCI (m/z) [M + H]$^+$ calcd for $C_{27}H_{32}N_2O_6{}^+$, 481.2331; found, 481.23567.
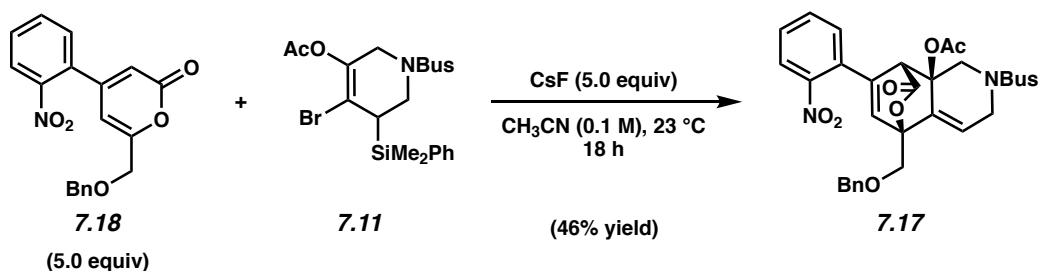
Cycloadduct 7.17. The crude reaction mixture was purified by flash chromatography (1:1 hexanes:EtOAc) afford the cycloadduct **7.17** (62.7 mg, 46% yield). Cycloadduct **7.17**: R_f 0.15 (1:1 hexanes:EtOAc); ^{1}H-NMR (400 MHz, CDCl₃): δ 7.80 (dd, J = 4.1, 1.1, 1H), 7.64 (td, J = 7.6, 1.3, 1H), 7.51 (td, J = 7.8, 1.3, 1H), 7.42 (dd, J = 4.3, 1.3, 1H), 7.40–7.31 (m, 5H), 6.42–6.40 (m, 1H), 5.93 (t, J = 3.0, 1H), 5.08–5.06 (m, 1H), 4.83 (d, J = 6.7, 1H), 4.83 (d, J = 1.5, 2H), 4.13 (d, J = 5.3, 1H), 4.00 (d, J = 5.3, 1H), 3.78 (dd, J = 10.0, 3.0, 1H), 3.05 (d, J = 6.7, 1H), 2.07 (s, 3H), 1.33 (s, 9H); ^{13}C-NMR (125 MHz, CDCl₃): δ 170.66, 168.7, 148.4, 137.0, 135.1, 133.1, 132.9, 131.5,

130.13, 130.10, 129.7, 128.6, 128.2, 128.0, 124.5, 122.1, 82.8, 74.1, 67.6, 62.0, 52.0, 47.0, 45.1, 24.6, 22.0; IR (film): 2925, 1767, 1751, 1318, 1219 cm^{-1}; HRMS–APCI (*m/z*) [M + H]$^+$ calcd for C$_{30}$H$_{32}$N$_2$O$_9$S$^+$, 597.19013; found, 597.18917.

7.9.2.4 Reduction of 7.17.

7.17   LiBH$_4$ (3.0 equiv)   THF (0.03 M), 23 °C   2.5 h   (48% yield)   **7.16**
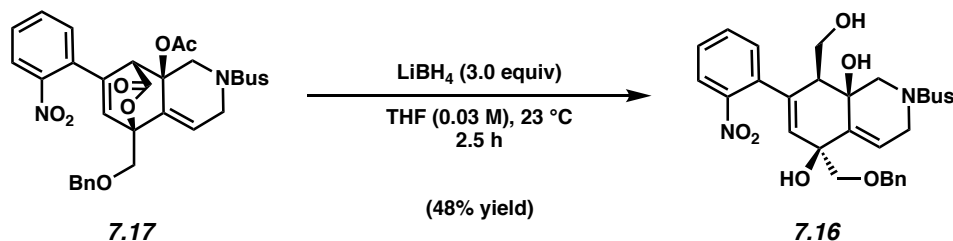
Triol 7.16. To a stirred solution of lactone **7.16** (14.5 mg, 0.24 mmol, 1.0 equiv) in THF (0.03 M) was added LiBH$_4$ (2.0 M in THF, 36.5 μL, 3.0 equiv) dropwise and the reaction stirred at 23 °C for 2.5 h. After 2.5 h, the reaction was quenched with ammonium chloride (2 mL) at 23 °C in one portion. The layers were then separated and the aqueous layer was extracted with EtOAc (3 x 2 mL). The combined organic layers were dried Na$_2$SO$_4$, filtered, and concentrated under reduced pressure. The resulting crude reaction mixture was purified by preparative thin layer chromatography (2:1 benzene:EtOAc) to afford triol **7.16** (4.9 mg, 48% yield) as a clear oil. Triol **7.16**: R$_f$ 0.12 (2:1 benzene:EtOAc); ^{1}H-NMR (500 MHz, CDCl$_3$): δ 7.94–7.86 (m, 1H), 7.62–7.51 (m, 2H), 7.49–7.42 (m, 1H), 7.37–7.27 (m, 5H), 5.97 (s, 1H), 5.78 (d, *J* = 0.1, 1H), 5.51 (brs, 1H), 5.51 (brs, 1H), 4.57 (s, 2H), 4.25–4.03 (m, 3H), 4.02–3.89 (m, 2H), 3.72–3.51 (m, 4H), 3.42 (brs, 1H), 3.06 (s, 1H), 1.41 (s, 9H); ^{13}C-NMR (125 MHz, CDCl$_3$): δ 149.1, 137.5, 137.0, 135.2, 132.9, 131.8, 128.64, 128.62, 128.5, 128.13, 128.12, 124.4, 122.1, 74.0, 73.7, 72.9, 72.6, 70.6, 62.2, 61.9, 60.9, 53.3, 46.7, 46.5, 32.1, 24.86, 22.84, 14.3; IR (film): 3398, 2928, 1525, 1314, 1121 cm^{-1}; HRMS–APCI (*m/z*) [M + H]$^+$ calcd for C$_{28}$H$_{34}$N$_2$O$_6$S$^+$, 559.21086; found, 559.20276.

7.10 Spectra Relevant to Chapter Seven:

Progress Toward the Total Synthesis of Alstilobanine A
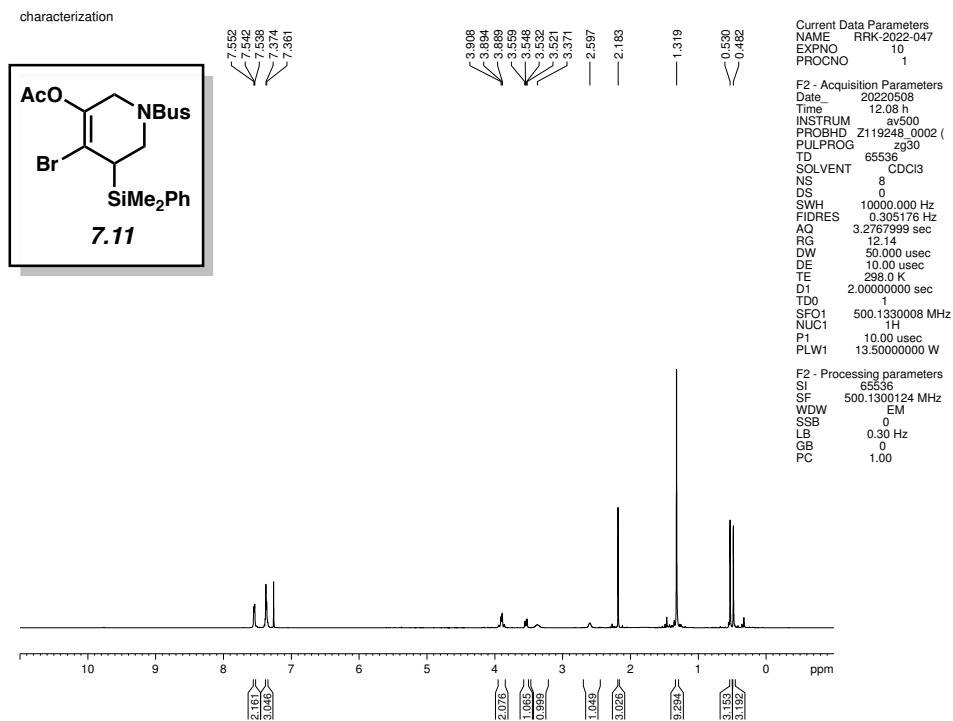
Figure 7.8 ^{1}H NMR (500 MHz, CDCl₃) of compound **7.11**.
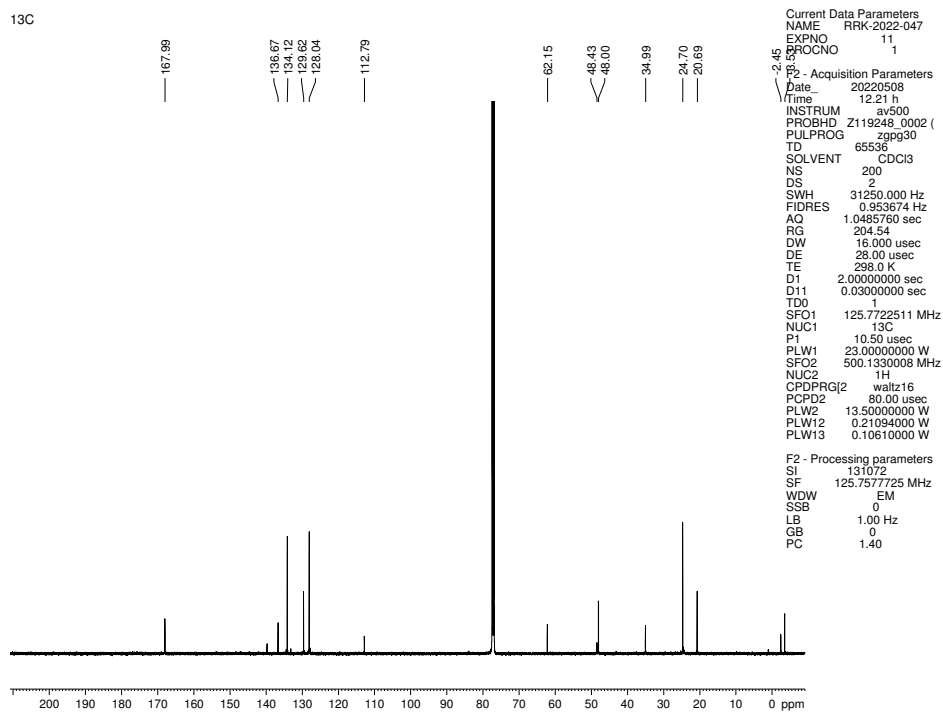
Figure 7.9 ^{13}C NMR (125 MHz, CDCl₃) of compound **7.11**.

Purified Product, 1H NMR

7.388
7.386
7.375
7.374
7.372
7.365
7.362
7.349
7.345
7.337
7.335
7.331
7.327
7.323
7.311
6.496
6.494
6.493
6.490
6.488
6.486
6.486
4.620
4.281
4.280
4.279

Current Data Parameters
NAME   FMI-2018-123
EXPNO   10
PROCNO   1

F2 - Acquisition Parameters
Date_   20190117
Time   18.10
INSTRUM   av600
PROBHD 5 mm BB5
PULPROG   zg30
TD   65536
SOLVENT   CDCl3
NS   8
DS   0
SWH   12376.237 Hz
FIDRES   0.188846 Hz
AQ   2.6476543 sec
RG   45.3
DW   40.400 usec
DE   6.50 usec
TE   295.3 K
D1   2.00000000 sec
TD0   1

======== CHANNEL f1 =====
NUC1   1H
P1   18.25 usec
PL1   -1.00 dB
PL1W   31.62277603 W
SFO1   600.1336008 MHz

F2 - Processing parameters
SI   65536
SF   600.1300280 MHz
WDW   EM
SSB   0
LB   0.30 Hz
GB   0
PC   1.00

Br

O

O

BnO

7.28

10 9 8 7 6 5 4 3 2 1 0 ppm

5.482   2.000   2.171 2.235

Figure 7.10 ^{1}H NMR (500 MHz, CDCl$_3$) of compound **7.28**.

Purified Product, 13C NMR

161.42
159.68
141.05
136.74
128.63
128.25
127.88
116.00
107.40
73.51
67.18

Current Data Parameters
NAME   FMI-2018-123
EXPNO   11
PROCNO   1

F2 - Acquisition Parameters
Date_   20190117
Time   18.13
INSTRUM   av600
PROBHD 5 mm BB5
PULPROG   zgdc30
TD   65536
SOLVENT   CDCl3
NS   25
DS   0
SWH   37593.984 Hz
FIDRES   0.573639 Hz
AQ   0.8716288 sec
RG   18390.4
DW   13.300 usec
DE   6.50 usec
TE   295.5 K
D1   2.00000000 sec
D11   0.03000000 sec
TD0   1

======== CHANNEL f1 =====
NUC1   13C
P1   9.75 usec
PL1   0 dB
PL1W   75.35659027 W
SFO1   150.9209173 MHz

======== CHANNEL f2 =====
CPDPRG[2   waltz16
NUC2   1H
PCPD2   80.00 usec
PL2   -1.00 dB
PL12   14.14 dB
PL2W   31.62277603 W
PL12W   0.96827775 W
SFO2   600.1336008 MHz

F2 - Processing parameters
SI   65536
SF   150.9028181 MHz
WDW   EM
SSB   0
LB   1.00 Hz
GB   0
GC   1.40

190 180 170 160 150 140 130 120 110 100 90 80 70 60 50 40 30 20 10 ppm

Figure 7.11 ^{13}C NMR (125 MHz, CDCl$_3$) of compound **7.28**.
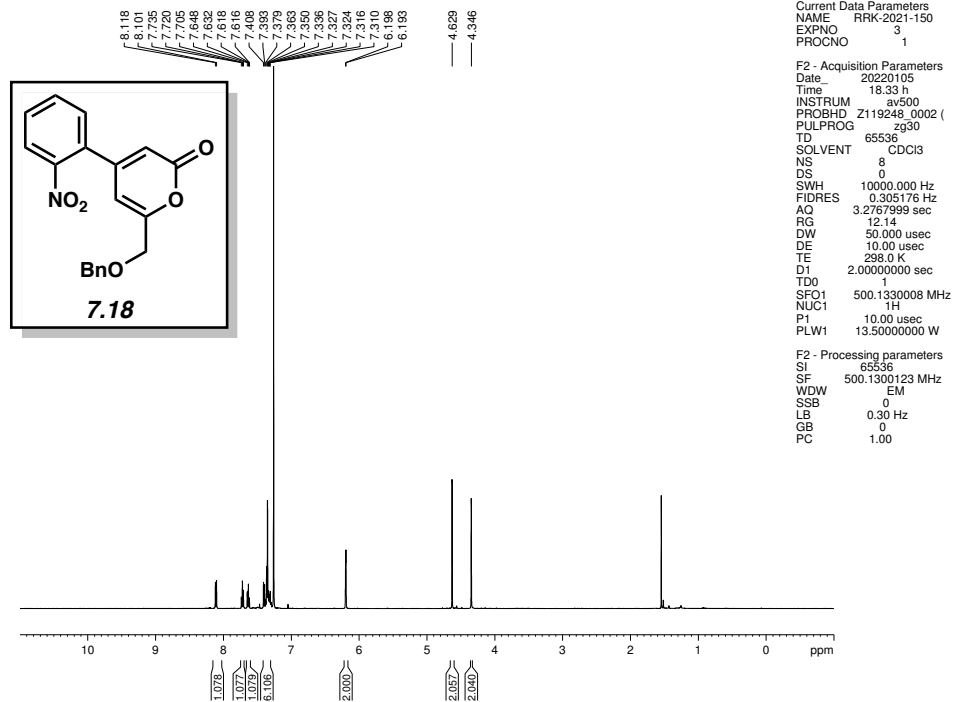
Figure 7.12 ^{1}H NMR (500 MHz, CDCl$_3$) of compound **7.18**.
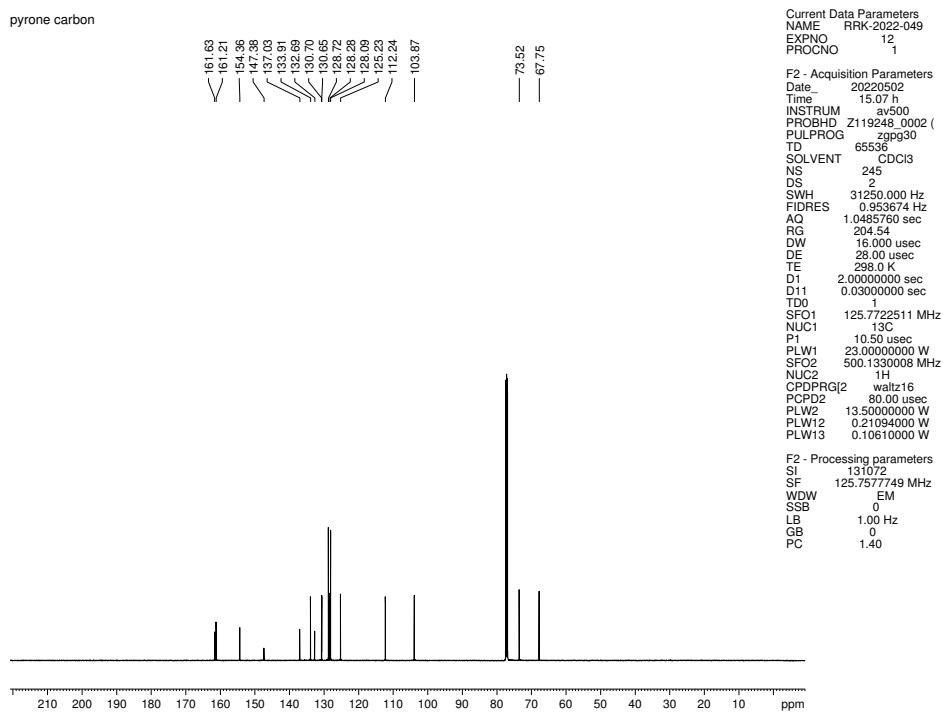
Figure 7.13 ^{13}C NMR (125 MHz, CDCl$_3$) of compound **7.18**.

426
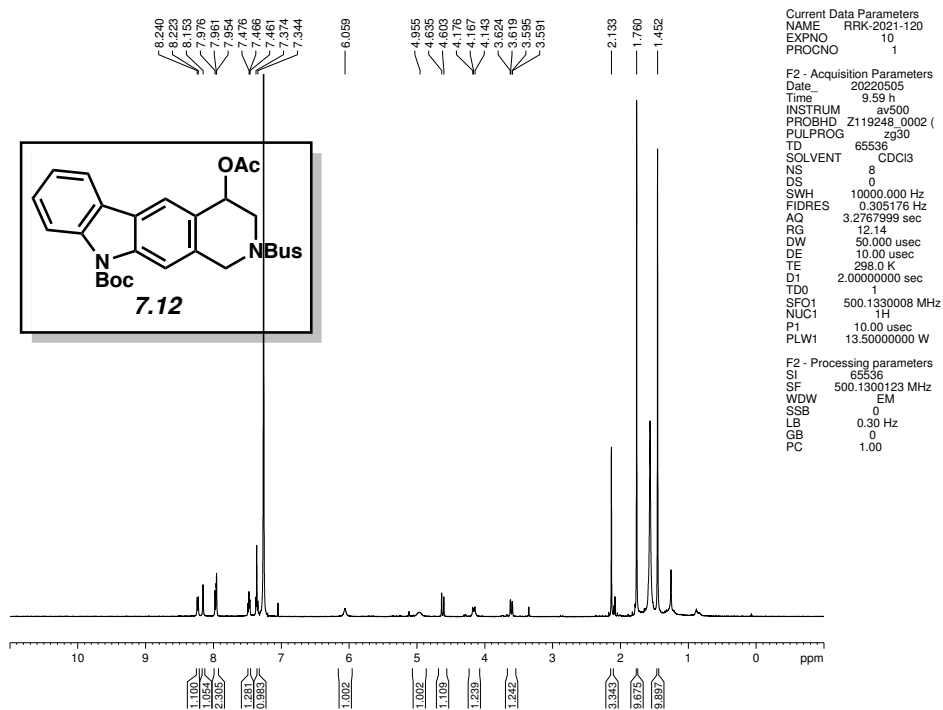
Figure 7.14 ^{1}H NMR (500 MHz, CDCl$_3$) of compound **7.12**.
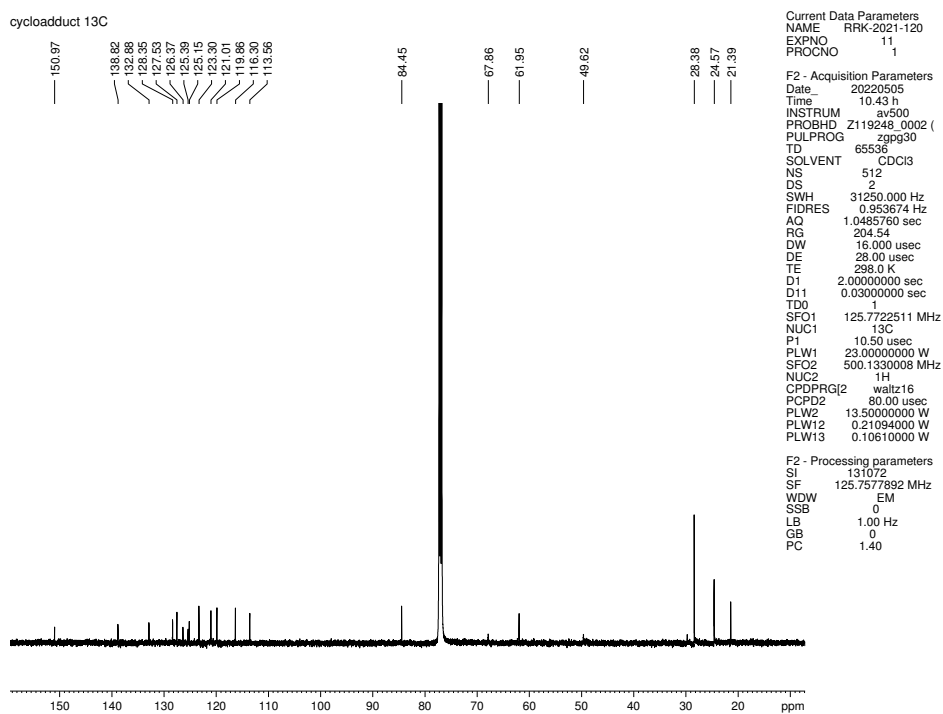
Figure 7.15 ^{13}C NMR (125 MHz, CDCl$_3$) of compound **7.12**.
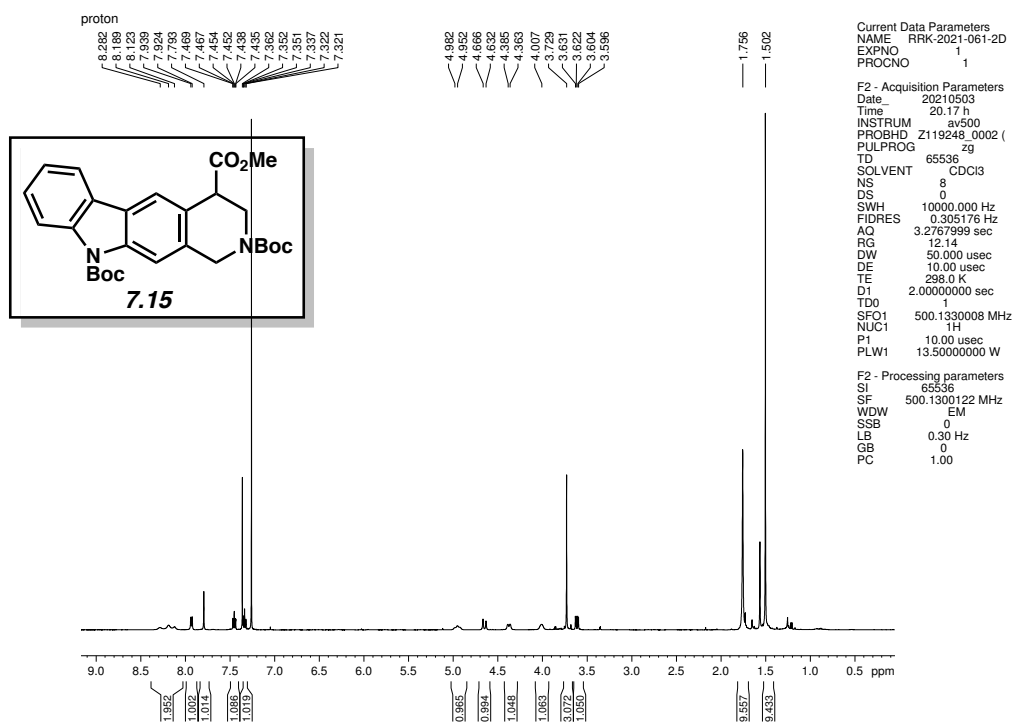
Figure 7.16 ^{1}H NMR (500 MHz, CDCl$_3$) of compound **7.15**.
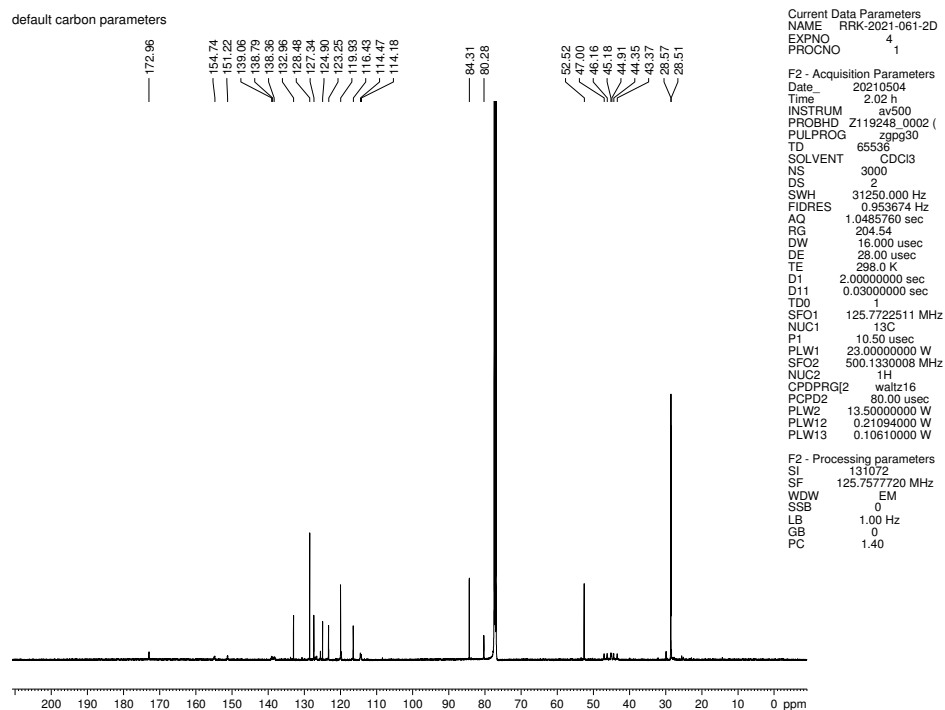
Figure 7.17 ^{13}C NMR (125 MHz, CDCl$_3$) of compound **7.15**.

428

7.639
7.627
7.624
7.525
7.522
7.509
7.507
7.494
7.491
7.430
7.427
7.414
7.412
7.392
7.380
7.376
7.369
7.364
7.363
7.358
7.355
7.345
7.341
7.340
7.337
7.323
6.411
6.407
5.945
5.939
5.933
5.074
5.070
4.851
4.824
4.687
4.681
4.137
4.116
4.013
3.991
3.810
3.804
3.772
3.766
3.059
3.032
2.074
1.327

7.17

10 9 8 7 6 5 4 3 2 1 0 ppm

1.013
1.061
1.139
1.084
5.291

0.999

1.010

1.038
1.026
2.281

1.185
1.040
1.000

1.004

3.045

9.290
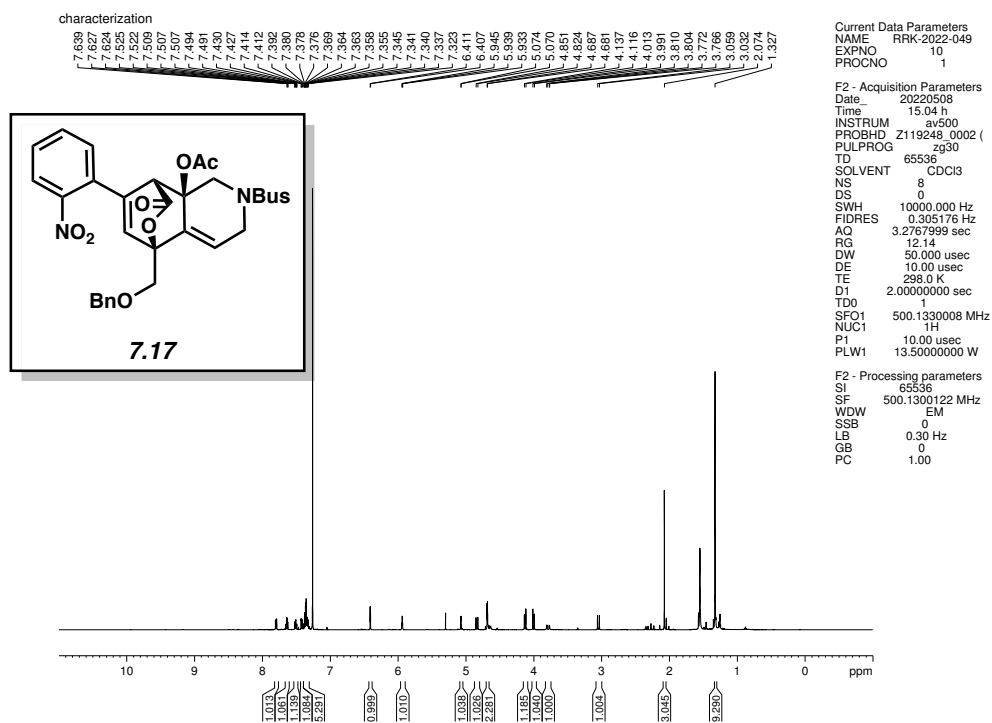
Figure 7.18 ^{1}H NMR (500 MHz, CDCl$_3$) of compound **7.17**.

170.66
168.68
148.40
137.01
135.08
133.14
132.92
131.52
130.09
130.14
129.73
128.65
128.19
128.04
124.50
122.10
82.84
74.14
67.59
61.97
52.03
47.05
45.13
24.64
22.02

200 190 180 170 160 150 140 130 120 110 100 90 80 70 60 50 40 30 20 10 0 ppm
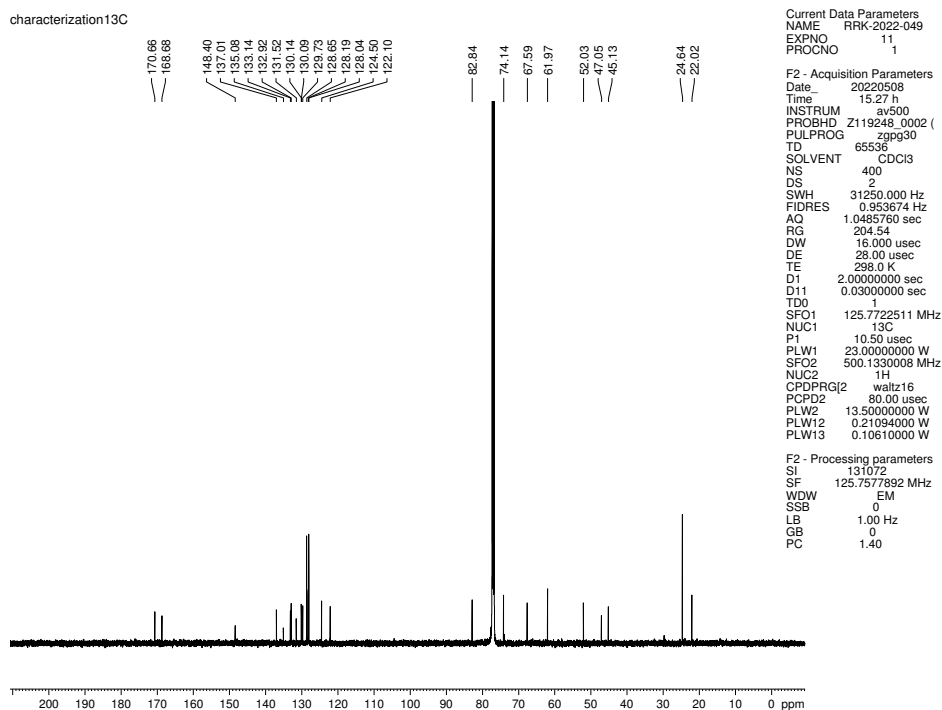
Figure 7.19 ^{13}C NMR (125 MHz, CDCl$_3$) of compound **7.17**.

429

7.900
7.884
7.601
7.586
7.572
7.547
7.472
7.457
7.441
7.314
7.302
7.289

5.971
5.786
5.783

4.572
4.189
4.167
4.079
3.971
3.942
3.691
3.672
3.639
3.630
3.622
3.609
3.554
3.535
3.422
3.056

1.418

10   9   8   7   6   5   4   3   2   1   0   ppm

0.909
2.082
1.106
4.984

1.012
1.000
0.693

2.252
1.538
1.282
2.029
1.299
1.948
1.357
1.020
0.969

9.979
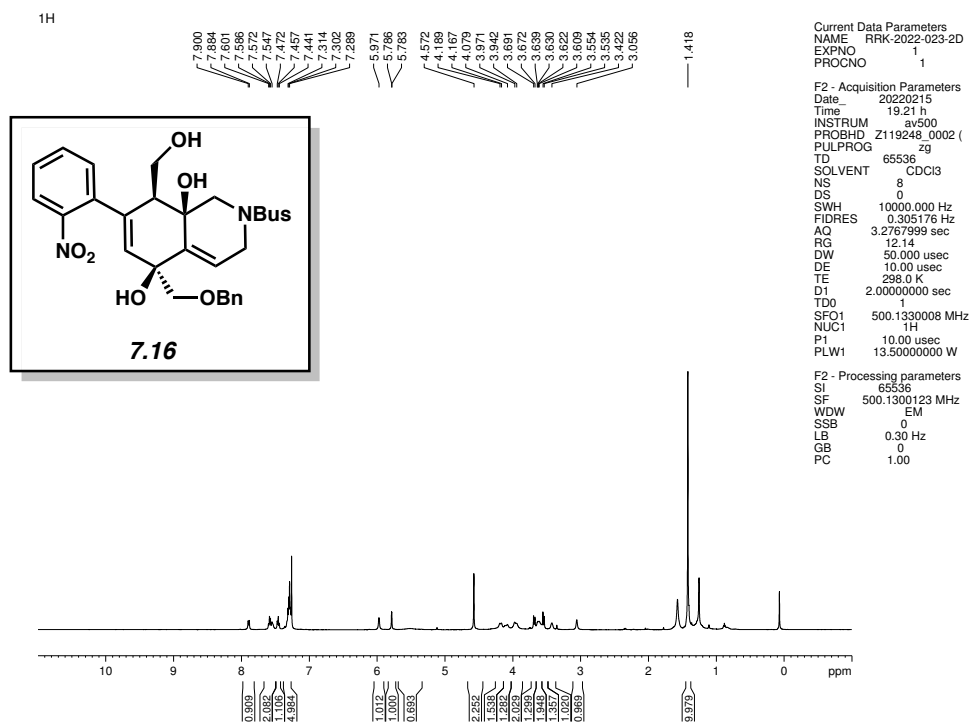
Figure 7.20 ^{1}H NMR (500 MHz, CDCl$_3$) of compound **7.16**.

default carbon parameters

149.07
137.51
137.04
135.24
132.87
131.85
128.65
128.63
128.48
128.13
128.12
124.39
122.11

73.99
73.74
72.91
72.64
70.59
62.23
61.93
60.90
53.32
46.65
46.47

32.07

24.87
22.84

14.27

200 190 180 170 160 150 140 130 120 110 100 90 80 70 60 50 40 30 20 10 0 ppm
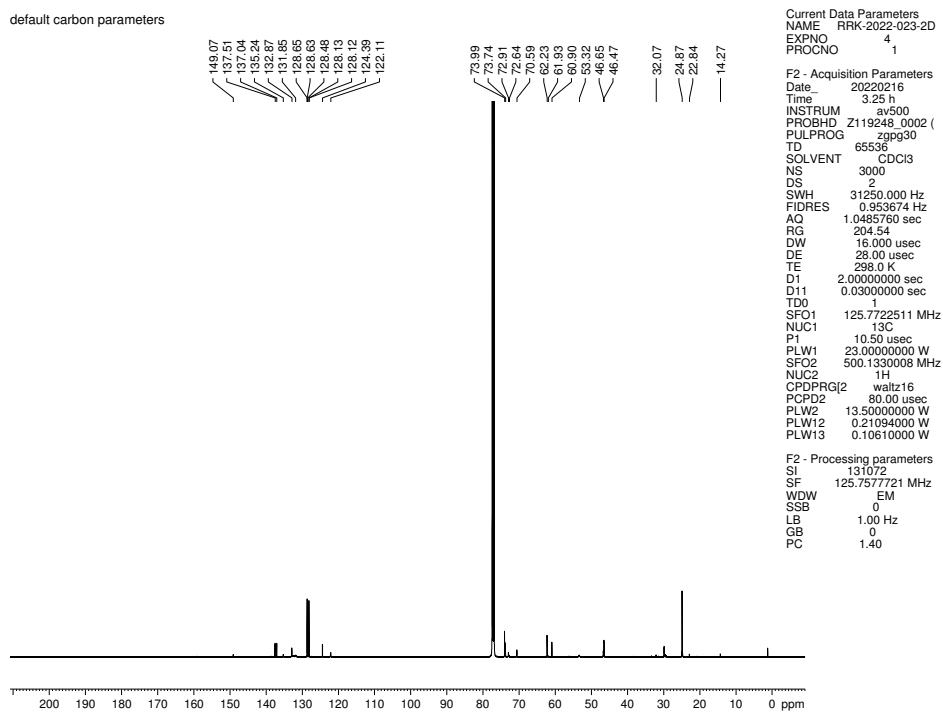
Figure 7.21 ^{13}C NMR (125 MHz, CDCl$_3$) of compound **7.16**.

430

7.11 Notes and References

(1) (a) Gul, W.; Hamann, M. T. Indole alkaloid marine natural products: an established source of cancer drug leads with considerable promise for the control of parasitic, neurological and other diseases. *Life Sciences* **2005**, *78*, 442–453. (b) O' Connor, S. E.; Maresh, J. J. Chemistry and biology of monoterpene indole alkaloid biosynthesis. *Nat. Prod. Rep.* **2006**, *23*, 532–547. (c) Kochanowska-Karamyan, A. J.; Hamann, M. T. Marine indole alkaloids: potential new drug leads for the control of depression and anxiety. *Chem. Rev.* **2010**, *110*, 4489–4497. (d) Ishikura, M.; Abe, T.; Choshi, T.; Hibino, S. Simple indole alkaloids and those with a nonrearranged monoterpenoid Unit. *Nat. Prod. Rep.* **2015**, *32*, 1389–1471. (e) Sravanthi, T. V.; Manju, S. L. Indoles — a promising scaffold for drug development. *Eur. J. Pharm. Sci.* **2016**, *91*, 1–10.

(2) Koyama, K.; Hirasawa, Y.; Zaima, K.; Hoe, T. C.; Chan, K.-L.; Morita, H. Alstilobanines A–E, new indole alkaloids from Alstonia Angustiloba. *Bioorg. Med. Chem.* **2008**, *16*, 6483–6488.

(3) (a) Feng, Y.; Majireck, M. M.; Weinreb, S. M. Total synthesis of the unusual monoterpenoid indole alkaloid (±)-alstilobanine A. *Angew. Chem. Int. Ed.* **2012**, *51*, 12846–12849. (b) Feng, Y.; Majireck, M. M.; Weinreb, S. M. Total syntheses of the monoterpene indole alkaloids (±)-alstilobanine A and E and (±)-angustilodine. *J. Org. Chem.* **2014**, *79*, 7–24.

(4) Wenk, H. H.; Winkler, M.; Sander, W. One century of aryne chemistry. *Angew. Chem., Int. Ed.* **2003**, *42*, 502−528.

(5) Dubrovskiy, A. V.; Markina, N. A.; Larock, R. C. Use of benzynes for the synthesis of heterocycles. *Org. Biomol. Chem.* **2013**, *11*, 191−218. (b) Mauger, C. C.; Mignani, G. A. An efficient and safe procedure for the large-scale Pd-catalyzed hydrazonation of aromatic chlorides using Buchwald technology. *Org. Process Res. Dev.* **2004**, *8*, 1065− 1071. (c) Takikawa, H.; Nishii, A.; Sakai, T.; Suzuki, K. Aryne-based strategy in the total synthesis of naturally occurring polycyclic compounds. *Chem. Soc. Rev.* **2018**, *47*, 8030−8056. (d) Tadross, P. M.; Stoltz, B. M. A comprehensive history of arynes in natural product total synthesis. *Chem. Rev.* **2012**, *112*, 3550−3577. (e) Schleth, F.; Vettiger, T.; Rommel, M.; Tobler, H. Process for the preparation of pyrazole carboxylic acid amides. International patent WO 2011131544 A1, Oct 27, 2011. (d) Lin, J. B.; Shah, T. J.; Goetz, A. E.; Garg, N. K.; Houk, K. N. Conjugated trimeric scaffolds accessible from indolyne cyclotrimerizations: synthesis, structures, and electronic properties. *J. Am. Chem. Soc.* **2017**, *139*, 10447−10455. (f) Takikawa, H.; Nishii, A.; Sakai, T.; Suzuki, K. Aryne-based strategy in the total synthesis of naturally occurring polycyclic compounds. *Chem. Soc. Rev.* **2018**, *47*, 8030−8056. (g) Tadross, P. M.; Stoltz, B. M. A comprehensive history of arynes in natural product total synthesis. *Chem. Rev.* **2012**, *112*, 3550−3577. (h) Gampe, C. M.; Carreira, E. M. Arynes and cyclohexyne in natural product synthesis. *Angew. Chem., Int. Ed*. **2012**, *51*, 3766–3778.

(6) Wittig, G.; Fritze, P. On the intermediate occurrence of 1,2- cyclohexadiene. *Angew. Chem., Int. Ed. Engl.* **1966**, *5*, 846.

(7) Whereas cyclic allenes have not seen synthetic development to the extent that their alkyne counterparts have, invaluable studies on methods for allene generation and trapping have been put forward by Christl, Balci and Jones, Elliot, Guitian, West, and many others. For a´

comprehensive view of strained cyclic allene chemistry through 2003, see: Christl, M. Cyclic allenes up to seven-membered rings. *Modern Allene Chemistry*; Krause, N., Kashmi, S. A. K., Eds.; Wiley-VCH: Weinheim, 2004; pp 243−357.

(8) Lovering, F.; Bikker, J.; Humblet, C. Escape from flatland: Increasing saturation as an approach to improving clinical success. *J. Med. Chem.* **2009**, *52*, 6752−6756.

(9) Anthony, S. M.; Wonilowicz, L. G.; McVeigh, M. S.; Garg, N. K. Leveraging fleeting strained intermediates to access complex scaffolds. *JACS Au* **2021**, *1*, 897–912.

(10)   (a) Yamano, M. M.; Knapp, R. R.; Ngamnithiporn, A.; Ramirez, M. R.; Houk, K. N.; Stoltz, B. M.; Garg, N. K. Cycloadditions of oxacyclic allenes and a catalytic asymmetric entryway to enantioenriched cyclic allenes. *Angew. Chem., Int. Ed.* **2019**, *58*, 5653–5657. (b) Yamano, M. M. Kelleghan, A. V.; Shao, Q.; Giroud, M.; Simmons, B. J.; Li, B.; Chen, S.; Houk, K. N.; Garg, N. K. *Nature* **2020**, *586*, 242–247. (c) Kelleghan, A. V.; Witkowski, D. C.; McVeigh, M. S.; Garg, N. K. *J. Am. Chem. Soc.* **2021**, *143*, 25, 9338–9342.

(11) Barber, J. S.; Yamano, M. M.; Ramirez, M.; Darzi, E. R.; Knapp, R. R.; Liu, F.; Houk, K. N.; Garg, N. K. Diels–Alder cycloadditions of strained azacylic allenes. *Nat. Chem.* **2018**, *10*, 953–960.

(12) Tong, S.; Xu, Z.; Mamboury, M.; Wang, Q.; Zhu, J. Aqueous titanium trichloride promoted reductive cyclization of *o*-nitrostyrenes to indoles: development and application to the synthesis of rizatriptan and aspidospermidine. *Angew. Chem., Int. Ed.* **2015**, *54*, 11809–11812.

(13) (a) Shevlin, M.; Guan, X.; Driver, T. G. Iron-catalyzed reductive cyclization of *o*-nitrostyrenes using phenylsilane as the terminal reductant. *ACS Catal.* **2017**, *7*, 5518–5522.

(b) Nykaza, T. V.; Ramirez, A.; Harrison, T. S.; Luzung, M. R.; Radosevich, A. T. Biphilic organophosphorus-catalyzed intramolecular C_{sp2}–H amination: evidence for a nitrenoid in catalytic Cadogan cyclization. *J. Am. Chem. Soc.* **2018**, *140*, 3103–3113. (c) Song, H.; Yang, Z.; Tung, C.-H.; Wang, W. Iron-catalyzed reductive coupling of nitroarenes with olefins: intermediate of iron–nitroso complex. *ACS Catal.* **2020**, *10*, 276–281.

(14) Feng, Y.; Majireck, M. M.; Weinreb, S. M. Total synthesis of monoterpene indole alkaloids (±)-alstilobanine A and E and (±)-angustilodine. J. Org. Chem. **2014**, *79*, 7–24.

(15) Brown, H. B. Directed homogeneous hydrogenation. *Angew. Chem., Int. Ed. Engl.* **1987**, *26*, 190–203.

(16) (a) Tang, F.; Banwell, M. G.; Willis, A. C. A Raney cobalt mediated reductive cyclization route to the uleine alkaloid gilbertine. *J. Org. Chem*. **2016**, *81*, 10551–10557. (b) Hock, S.; Borschberg, H.-J. Enantioselective synthesis of (–)-(19*R*)-ibogamin-19-ol. *Helvetica Chimica Acta* **2006**, *89*, 542–557.

(17) Chou, S.-Y.; Tseng, C.-L.; Chen, S.-F. The formal synthesis of chiral etodolac using chiral 1,2-di(alkylcarbonyl)oxypentan-3-one as chiral building block. *Heterocycles* **1999**, *51*, 1527–1541.

(18) Alekseeva, N. V.; Bokanov, A. I.; Alekseeva, L. M.; Budanova, L. I.; Synthesis of 1,6-carbazoledicarboxylic and 1,2,3,4-tetracarbazole-1,6-dicarboxylic acid esters. *Pharm. Chem. J.* **2003**, *37*, 26–29.

(19) Hock, S.; Borschberg, H.-J. Enantioselective synthesis of (–)-(19*R*)-ibogamin-19-ol. *Helvetica Chimica Acta* **2006**, *89*, 542–557.

(20) Furkert, D. P.; Husbands, S. M. First Asymmetric Synthesis of *trans*-3,4-dimethyl-4-arylpiperidines. *Org. Lett.* **2007**, *9*, 3769–3771.

(21) Ishikawa, T.; Mizuta, T.; Hagiwara, K.; Aikawa, T.; Kudo, T.; Saito, S. Catalytic alkynylation of ketones and aldehydes using quaternary ammonium hydroxide base. *J. Org. Chem.* **2003**, *68*, 3702–3705.

(22) Luo, T.; Dai, M.; Zheng, S.-L.; Schreiber, S. L. Syntheses of α-pyrones using gold-catalyzed coupling reactions. *Org. Lett*. **2011**, *13*, 2834–2836.

(23) Moody, J. C.; Kulsum, F. Diels–Alder reactivity of pyrano[4,3-*b*]indol-3-ones, indole 2,3,-quinodimethane analogues. *J. Chem. Soc. Perkin Trans.* **1990**, 673–679.

(24) Lofstrand, V. A.; West, F. G.; Efficient trapping of 1,2-cyclhexadienes with 1,3-dipoles. *Angew. Chem., Int. Ed.* **2015**, *54*, 11809–11812.

(25) Furkert, D. P.; Husbands, S. M. First Asymmetric Synthesis of trans-3,4-dimethyl-4-arylpiperidines. *Org. Lett.* **2007**, *9*, 3769–3771.

CHAPTER EIGHT

Catalysis in Modern Drug Discovery: Insights from a Graduate Student-Taught Undergraduate Course

Jason V. Chari,[†] Rachel R. Knapp,[†] Timothy B. Boit, and Neil K. Garg.

8.1 Abstract

A course centered around transition-metal catalysis in modern drug discovery was designed to illustrate the central role of organic chemistry in driving small-molecule drug development. The course highlighted both fundamental and applied concepts, first with a focus on the drug discovery process, followed by foundational principles in catalysis and modern catalytic methods. Finally, these topics were unified in the last portion of the course, where case studies served to highlight the use of transition-metal catalysis in the synthesis of modern drugs. Three graduate students designed and taught the course, with mentorship from a faculty member, leading to several notable teaching outcomes. Additionally, experts in the fields of catalysis and drug discovery served as guest lecturers throughout the duration of the course. This approach spotlighted the various careers that organic chemists play in the development of new medicines. We hope that this course motivates the creation of other courses in STEM that unify fundamental concepts with applications and career outcomes.

8.2 Introduction

Organic synthesis plays an integral role in small molecule drug development.[1] Indeed, chemists trained in organic synthesis execute both the design and synthesis of small molecules that treat widespread ailments and address global health crises.[2] Comprising 71% of the 53 drugs

approved by the FDA in 2020,[3] small molecule therapeutics continue to represent the majority of drugs approved in the US. In addition, multiple phases of the drug development pipeline require expertise in synthetic organic chemistry. For example, the discovery phase of small molecule drug development necessitates the synthesis and design of numerous analogs, whereas the process chemistry phase warrants the creation and optimization of a highly efficient synthetic route to the desired drug molecule.

In spite of the connections between organic synthesis and the drug discovery process, this fundamental relationship is not always directly or thoroughly explored in undergraduate courses. Traditionally, undergraduate organic chemistry coursework centers around fundamental synthetic transformations, whereas discussions of applications are often limited or receive minimal context. Although there have been exciting advances that bring these connections into organic laboratory courses,[4] as well as courses in computational drug design,[5] considerably fewer initiatives have been reported in lecture-based courses. This can leave undergraduate students with a narrow perspective on the relevance of organic chemistry, as well as career opportunities. Articulating both the modern drug discovery process and careers in organic chemistry can serve to both empower students to consider its connection to human health and lead to greater student engagement overall.

In addition to connecting organic chemistry to improving human health, an area that is often underemphasized or omitted from undergraduate coursework is transition-metal catalysis. As reflected in the awarding of three Nobel Prizes in chemistry over the past two decades,[6] transition-metal catalysis has had a widespread impact across many disciplines of science, enabling access to new pharmaceuticals, polymers, agrochemicals, and materials. In the area of drug discovery, transition-metal catalysis represents a ubiquitous and indispensable tool that has greatly

improved the ability to establish structure–activity relationships in drug leads.[7] As an example, 22% of representative medicinal chemistry publications in 2014 described a Suzuki–Miyaura cross-coupling reaction.[8] In comparison, data from 1984 revealed no examples of transition-metal catalysis in medicinal chemistry publications.[8] In spite of the dramatic impact and evolution of transition-metal catalysis in drug development, it often receives less attention than "classical" reactions (e.g., S_N2, Diels–Alder, etc.) and their fundamental principles in undergraduate lecture courses.[9] As such, students may not have the opportunity to learn fundamental concepts in catalysis, or perhaps more importantly, understand the applications of these concepts in important areas such as pharmaceutical development. Teaching transition-metal catalysis in the context of drug discovery offers a means for students to connect chemistry to human health, and to equip students with the conceptual tools necessary to devise syntheses of drug scaffolds. By clearly articulating the direct connection between transition-metal catalysis and improving human health, students can begin to appreciate the driving force of organic chemistry in the world around them.

8.3 Course Rationale

We sought to design a virtual course that teaches fundamental concepts in both drug discovery and catalysis, while also being engaging and impactful for students from diverse backgrounds. To achieve this, we pursued an approach that highlights both young researchers and established experts in the field. First, rather than being led by a professor or lecturer, the course was designed and taught by senior graduate students, under the advisement of a faculty member. This offered notable advantages for both the undergraduate students in the course and the graduate student instructors themselves. Indeed, previous studies have demonstrated that "undergraduates who take their first course in a given subject from a graduate student are nearly twice as likely to subsequently major in that subject compared to their peers who take the same course from full-

time faculty."[10] This finding supports the idea that receiving instruction from graduate students can serve as a valuable supplement to professor-led courses. Of note, this model is by no means meant to replace faculty teaching responsibilities, nor should it be used by faculty to skirt or delegate their teaching responsibilities. Additionally, this approach is likely most suitable for summer course offerings, when faculty are ordinarily not expected to teach and greater flexibility may be available. This can also positively impact the graduate student instructors themselves, as "graduate students who teach more frequently are more likely to graduate in a timely manner and more likely to subsequently be employed by a college or university in their early careers."[10] To ensure that the graduate students were well-equipped to lead this course, they received important mentorship from a faculty member in teaching, scientific communication, and management. In particular, the faculty member provided insight and advice on refining the course design as well as depth and difficulty of content, managing student issues, and providing advice on grading. In addition to this mentorship, the senior graduate students who led the course were also either pursuing research directly involved in transition-metal catalysis or had career aspirations of entering the pharmaceutical industry. This ensured that the instructors were both confident in the material and passionate about the topics discussed.

It should also be noted that graduate student instructors are often similar in age to their undergraduate counterparts and can therefore appear more approachable, and additionally offer insight into the motivations and experiences of a graduate student. Demystifying the graduate student experience[11] proved to be a defining feature of the course, as the majority of those enrolled were third- or fourth-year undergraduate students in the process of making important decisions about their post-graduation plans.

In addition to placing a focus on graduate student instruction, we also sought to include perspectives, insights, and stories from established leaders in the fields of drug discovery and catalysis through invited guest lectures.[12] We envisioned that this would allow the course to more fully and accurately portray the field of drug discovery by serving as a supplement to the graduate student-produced lectures. Furthermore, this would provide an opportunity to showcase scientists from diverse backgrounds, including women and scientists of color, highlighting their unique experiences and career trajectories.[13] Achieving diversity and inclusion in science remains a critical goal, and showcasing the empowering stories of chemists from underrepresented backgrounds in leadership positions has proven to be a powerful mechanism to address equity in chemistry.[14] Indeed, many of the guest lecturers featured in our course had non-linear career paths and stories, but that still led to successful outcomes. Hearing these stories can provide important inspiration for students considering potential career paths and create an open space for students to pose questions and interact directly with leaders in the field. This fostered a unique environment for the students, who may not have otherwise had the opportunity to connect with chemists in this capacity. In addition to the positive impact on students, this design also appealed to the guest lecturers by providing a space for them to gain more exposure and visibility for their company or research group, as well as connect with students who are early in their careers. Likewise, the graduate student instructors for the course were able to broaden their professional network by connecting with leaders in industry.

Beyond the overall learning experience of the undergraduate students, several administrative benefits can arise through the creation of virtual courses led by graduate students. Namely, the virtual, asynchronous design enables students outside of the university to participate in the course. Of note, this can provide students from smaller schools, which may have fewer

available elective courses, exposure to applications of organic chemistry in drug discovery. Moreover, individuals outside of academia would also have the opportunity to participate. This course garnered enrollment from the University of California, Los Angeles (UCLA) students as well as non-UCLA-enrolled undergraduate students and even individuals currently working in the pharmaceutical industry. In so doing, the virtual approach brought visibility to the department and university at large. Overall, the course was designed to not only better contextualize important concepts in organic chemistry, but also to provide a unique and positive experience for all participating groups.

8.4 Course Design

Catalysis in Modern Drug Discovery was offered as a 4-unit elective course that would take place over six weeks. The course was designed at UCLA and garnered an enrollment of 53 students in its first year (summer of 2020) and 43 students in its second year (summer of 2021). The prerequisites for the course were general chemistry and introductory organic chemistry.

The decision to render this course virtual, which was made prior to the COVID-19 pandemic, was motivated by several guiding factors.[15] First, this would offer UCLA students who were not on campus during the summer the opportunity to complete the course remotely. Moreover, this format would allow students outside of the UCLA community, both in academia and in industry, to participate. The virtual format would additionally provide flexibility regarding time commitment. In particular, the lectures, which were 30 to 60 minutes in length, were posted three times per week, and could be viewed at any time. These lectures were provided in the form of pre-recorded videos featuring narrated presentations and interactive clips. The lectures were supplemented with small-group, virtual discussion sections. Two one-hour sessions were offered per week, each of which was attended by 20–30 students. These sessions were focused on

answering questions from students, as well as reviewing challenging course content. These discussion sections served to maintain student engagement, provide important support to students, and create a sense of community, given the virtual nature of the course. As mentioned earlier, these sessions were optional, but attendance was rewarded with extra credit. Office hours were also conducted virtually in a one-on-one setting by student request.

As mentioned, in addition to the core pre-recorded lecture content, a guest lecture series was incorporated into the course and featured five guest lectures delivered by experts in academia and the pharmaceutical industry. These live, virtual lectures featured a vice president at a major pharmaceutical company, an established academic medicinal chemist, a rising star at a small biotechnology company, a prominent process chemist, and an established academic researcher in the area of catalysis. The faculty advisor for the course provided important suggestions for potential guest lecturers and, in some cases, directly connected the graduate student instructors with these individuals. The first guest lecture took place during the second week of the course, ensuring that students were introduced to key principles in drug discovery prior to this lecture. The format of the guest lectures varied depending on the invited individual, but generally involved a 30-minute lecture followed by a 30-minute question-and-answer session. The guest lecturers typically placed a large emphasis on illustrating the story of their journey to their current career, as well as providing advice and insights along the way. In addition to detailing empowering success stories in catalysis or drug discovery, these guest lectures and question-and-answer sessions sprouted meaningful discussions around topics such as diversity in STEM, how to engage in undergraduate research, and even advice on applying and interviewing for jobs. By conducting the course in a virtual setting, several speakers were able to attend from various parts of the country.

8.5 Course Content

The course was segmented into three main parts, as illustrated in Figure 8.1. Overall, this structure would allow students to gain a foundational understanding of the drug discovery process (Part I) before learning about catalysis as a field, and more specifically, the principles of transition-metal catalysis (Part II). Equipped with knowledge of both drug development and important concepts in catalysis, the students would then be capable of combining all elements of these topics in the final portion of the course (Part III). More specifically, this latter section would challenge students to apply their knowledge of transition-metal catalysis in order to strategically build drug molecules. With three graduate students teaching the course, each graduate student spearheaded one of the three sections and was tasked with designing course content, recording lecture content, and leading discussion sections for those two weeks.

Part I: Introduction to the Drug Discovery Process

Week 1 ——————————————————— *Week 2*

| **History of Key Landmarks in Drug Discovery** | **Blueprint of Modern Drug Discovery: From Concept to Market**
• Overview of key concepts in medicinal & process chemistry | **Case Studies in Drug Discovery**
• Lipitor • Antiviral drugs
• Thalidomide (e.g., COVID-19
• The Pill Therapeutics) |

Focus of Guest Lecture: Career path to becoming a medicinal chemist

---

Part II: Transition-Metal Chemistry

Week 3 ——————————————————— *Week 4*

| **Transition-Metal Chemistry I**
• Introduction to catalysis
• Pd-catalyzed C–C bond-forming cross-couplings | **Transition-Metal Chemistry II**
• Pd-Catalyzed C–O & C–N Cross-Couplings
• Transition metal-catalyzed alkene metathesis
• Enantioselective catalysis |

Focus of Guest Lectures: Career path to becoming a process chemist & academic research in catalysis

---

Part III: Catalysis in Drug Discovery

Week 5 ——————————————————— *Week 6*

| **Introduction to catalysis in drug discovery**
• Metal-catalyzed C–C & C–N bond-forming reactions in drug syntheses
• Concepts & strategies
• Case studies | **Olefin Metathesis & Stereoselective Reactions**
• Review of key concepts & strategies
• Case studies
• Future directions |

Focus of Guest Lectures: Tips and advice for applying and interviewing for post-graduation positions & academic research in drug discovery

Figure 8.1. Structure of course content, including core lecture content and guest lecture topics.

8.5.1 Part I: Introduction to the Drug Discovery Process

The objective of the first part of the course was to provide students with an understanding of drug discovery and development, and to specify the role of the organic chemist in these processes.[16] To begin, a brief history of drug discovery was described, showcasing key landmarks in the field. This included discussions of impactful drugs such as ephedrine, morphine, and penicillin. Important terms and drug categorizations (e.g., small molecules vs. biologics) were defined to clarify the scope of the course and relevant terminology. During the remainder of the first week, the students were presented with a blueprint of drug discovery in the modern era. This included a detailed overview of medicinal chemistry and techniques for target selection (e.g., identifying a particular protein to inhibit), lead discovery, and lead optimization. This was

followed by an introduction to process chemistry, which included guiding principles in route design, optimization, and scale-up, as well as brief industrial examples. Clear contrasts were drawn between the objectives and route design strategies pursued by medicinal chemists (e.g., design of diversifiable routes) in comparison to process chemists (e.g., design of a convergent route). In week two, in-depth case studies in drug discovery served to apply concepts from the first week by conveying the stories behind the discovery of particularly impactful drugs, from concept to market. As delineated in Figure 8.2, this included the discovery and development of therapeutics such as atorvastatin (Lipitor), norethindrone (the Pill), and antiviral drugs developed to treat global health crises such as HIV, influenza, and COVID-19. These case studies were typically structured in the form of a story, first capturing background on the ailment and key biological mechanisms of action before describing strategic features of target selection, lead discovery, hit-to-lead optimization, route optimization, scale-up, and lastly broader impacts of the therapeutic developed. Overall, the objective of these case studies was to solidify and contextualize key concepts in hit-to-lead optimization and the development of process routes. More broadly, we hoped to highlight the strategic aspects of drug discovery and development, as well as the long-term impact of therapeutics developed in part by organic chemists.
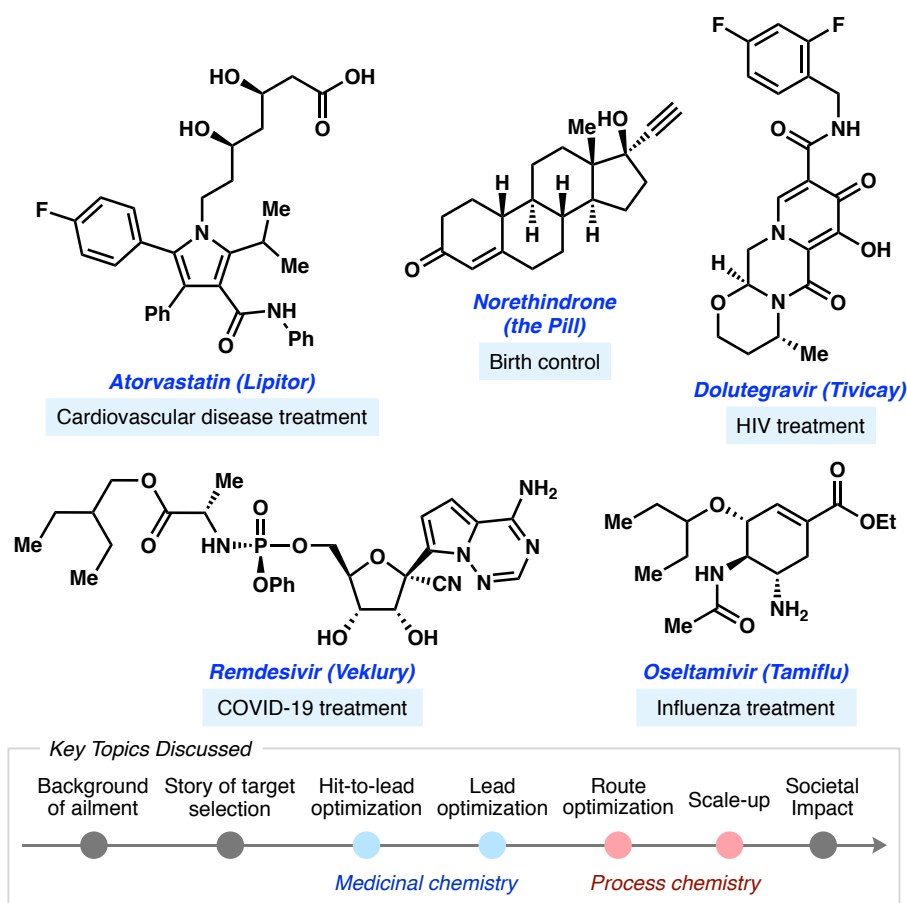
Figure 8.2. Exemplary drug scaffolds discussed in Part I of the course, and generalized flow of lecture content.

8.5.2 Part II: Transition-Metal Chemistry

In Part II of Catalysis in Modern Drug Discovery, the focus of the course shifted from drug discovery into transition-metal catalysis. To introduce this new topic, basic principles of catalysis and transition-metal chemistry (e.g., definition of a catalyst, kinetics versus thermodynamics, and electron counting of metal complexes) were described in the first lecture of this section.[17] Following this introduction, a series of lectures dedicated to important bond-forming methodologies was presented. This included the Suzuki–Miyaura cross-coupling reaction, the Mizoroki–Heck reaction, olefin metathesis, and enantioselective processes such as the Sharpless asymmetric epoxidation. As illustrated in Figure 8.3, the organization of each topic featured an

introduction of the reaction, its mechanism, guiding principles, and scope studies and insights. Overall, this structure allowed students to develop a conceptual understanding of key C–C, C–O, and C–N bond-forming processes in organic chemistry that rely upon transition-metal catalysis. In addition, the focus on the scope and limitations of a particular reaction served to highlight the challenges that organic chemists still face in the synthesis of small molecule therapeutics.

8.5.3 Part III: Catalysis in Modern Drug Discovery

Following Parts I and II, the final section of the course was focused on highlighting the use of transition-metal catalysis in the syntheses of notable pharmaceuticals.[8,18] This section served to link together all aspects of the course up to this point by incorporating transition-metal catalysis into the students' retrosynthetic toolbox. Each case study first introduced a small molecule therapeutic and described the disease or condition that it treats. Following this introduction, the development of the drug was described and a key aspect of the drug discovery process was highlighted in each case study. Examples included the rational design of lead structures, SAR studies, and process scale optimization. The compound was then analyzed from a synthetic chemistry perspective, with a focus on identifying particular bonds that were formed using the methodologies identified in Part II. By identifying these key disconnections, the students were exposed to strategy level retrosynthetic analysis. The final lecture provided a future outlook within the field of catalysis, underscoring the importance of developing new synthetic methods to accelerate the process of drug development.
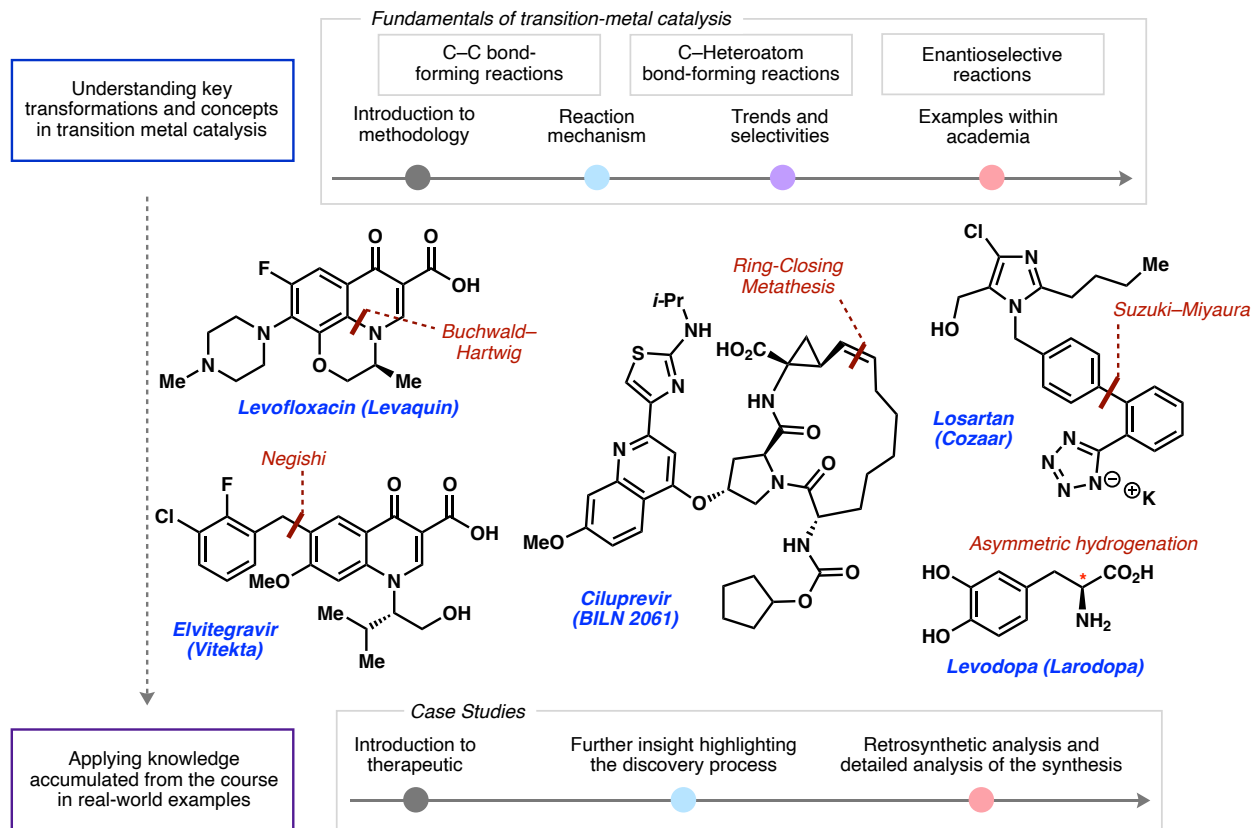
Figure 8.3. Fundamentals of transition-metal catalysis (Part II of the course) and case studies presented (Part III of the course).

8.6 Course Grading

Students were assessed through a combination of exams, quizzes, problem sets, and participation, weighted as follows: weekly problem sets 30%, weekly quizzes 20%, midterm exam 20%, final exam 30%, and up to 5% extra credit. The extra credit, which served to incentivize participation and engagement from the students, was offered on the basis of attendance at the discussion sections and guest lectures, as well as posing questions for the guest speakers live (via Zoom) or via the course's online forum. The problem sets and quizzes, which were based on the previous week's course material, were comprised of multiple-choice questions that assessed students' understanding of the content and evaluated critical thinking skills toward solving applied problems. Following week three of the course, a midterm exam was administered and consisted of

multiple choice and short answer questions based on course content from weeks 1–3. At the end of the course, a cumulative final exam was administered that consisted of multiple choice questions.

8.7 Student Reflections

At the end of the course, the students completed an anonymous feedback report through UCLA's course evaluation form. The responses were collected from students who attended the course in summer 2020 (number of responses, $n = 19$) and summer 2021 ($n = 39$).[19] Across the two terms, the "overall rating" average for the course was 8.43 out of 9.00 (94%), demonstrating a strongly positive overall response. Additionally, it was found that student interest in the subject grew substantially upon completion of the course, increasing from a score of 2.22 to 2.71 (where $1 = $ low, $2 = $ medium, and $3 = $ high interest). At the end of the course evaluation, open-form comments provided by students reflected highly on two major aspects of the course: the structure/design of the course and its impact on students' perspectives of career paths post-graduation.

Regarding the course structure, students' comments displayed an appreciation for the three sections and how they were ultimately unified to highlight real-world applications:

"I really enjoyed the structure of the course, as well as the guest lectures that have been integrated throughout the 6 weeks. It was such an eye opening and amazing experience to be able to hear from both medicinal and process chemists, and learn more about their work experience."

"Before, I didn't really have much interest in the subject, but after seeing so many examples of how these reactions were used, I saw the importance and applicability of catalysis in

drug synthesis. I feel like the class was structured very very well, and the schedule was very logical."

"I liked the real-world applications included throughout the lectures and how practical the material was."

"In [the third] part of the course we are taking what we learned about transition metal catalysis and applying it to some case studies of real drugs that use these methods. It was very interesting to see how what we are learning is applied to drugs that are being used in the market."

Additionally, the students described the impact the course had on them in showcasing career paths post-graduation:

"This is perhaps the first organic chemistry-based course that I've taken that I have thoroughly enjoyed! Learning about actual applications of organic chemistry and hearing from experts in the field of drug discovery has been very rewarding and has helped me narrow down potential career choices."

"Ultimately, this course was fairly interesting and showed me that the pharmaceutical industry may be a route for me to think about going into later on in my career."

"The first two weeks of this course piqued my interest in the pharmaceutical industry, especially in the synthesis of various drug molecules, which I haven't thought much about prior to the course, giving me something to think about as I continue to decide on what to do with my education in chemistry."

"I appreciated hearing his unique backstory in terms of what led to him becoming a grad student."

Overall, the feedback from students highlighted the impact of connecting chemistry concepts to real world applications and career avenues.

8.8 Personal Reflections

This course was created to serve as a bridge between fundamental organic chemistry curricula and real-world applications. Toward this end, the course focused on the centrality of organic chemistry in the discovery of new medicines and the importance of transition-metal catalysis in the modern synthetic chemists' toolbox. Despite the broad impact of transition-metal catalysis, which has been reflected in the awarding of multiple Nobel Prizes over the past two decades,[6] it can often be overlooked or considered a minor focus in introductory coursework. Furthermore, the unique reaction mechanisms of these transformations require a deeper analysis of reaction mechanism and selectivity principles, as well as compel students to consider new disconnections in the synthesis of small molecule drugs.

Due to the diverse range of skillsets required in drug development, a number of career opportunities are achievable for students majoring in fields such as chemistry or biochemistry. However, when these career avenues are not made clear to students, they may be unaware of these potential opportunities. In our multi-pronged approach, we sought to incorporate discussions of career opportunities into the video lectures, guest lectures, and discussion sections. The guest lectures provided a glimpse into what the careers of successful scientists might look like, from chemists at small biotechnology companies to large pharmaceutical companies, as well as those in academia. We sought to showcase diverse roles in our selection of guest lecturers, which included process chemists, medicinal chemists, and scientists in management-type roles. We also placed an important emphasis on selecting guest lecturers from diverse backgrounds, including women, scientists of color, and individuals with non-linear career paths. We hope to have inspired students

to follow their interests and pursue careers in drug discovery that they may not have considered previously.

As described, the course was led by graduate student instructors, who in turn received guidance from a faculty member, representing a fairly uncommon feature in undergraduate curricula. This provided an environment in which the students enrolled in the course could relate more to the instructors and lowered the barrier for communication about the course or related topics. Moreover, creating this direct interface allowed the undergraduate students to gain insight into the day-to-day lifestyle of graduate students in chemistry. This additionally sparked meaningful conversations about how to get involved in research, reasons for pursuing a Ph.D. program, and perspective on the instructors' own personal career plans. We would encourage the design of other STEM elective courses that are organized and led by senior graduate students.

Given the COVID-19 pandemic, instructors globally have been required to transition into online learning. We remained highly focused on maintaining an interactive environment, despite the challenges of the virtual setting, and explored several avenues to achieve this. An illustrative example from the course was the incorporation of QR codes (powered by QRChem.net[20]) into the lecture content that link to the 3D structure of a particular chemical compound, which the students can interact with on their smartphones. This not only sought to make the lectures feel more immersive to the students, but also aided in conveying key chemical concepts that require 3D visualization. We also incorporated exciting video content into the lectures that served to make the course content more vibrant. The small group setting of the discussion sections also provided students an opportunity to ask questions. Finally, we utilized an online forum which allowed students to pose questions about course content or guest lecture material.

8.9 Conclusion

In conclusion, we have described the rationale, design, and structure of a new graduate student-led course on drug discovery with a focus on transition-metal catalysis. Addition of this course to UCLA's curriculum exposed students to the importance of organic synthesis in the development of novel medicines. Through this exposure, undergraduate students were introduced to potential avenues for careers within chemistry and engaged in direct interactions with leaders in the field. We hope this course encourages the development of new courses in STEM that sharpen the connection between fundamental concepts and their applications, while also highlighting career avenues. Moreover, we look forward to the development of new graduate student-led courses that serve to reduce barriers to higher education in STEM and curate an environment where students can explore potential avenues for their careers post-graduation.

8.10 Notes and References

(1)   Rotella, D. P. The Critical Role of Organic Chemistry in Drug Discovery. *ACS Chem. Neurosci.* **2016**, *7*, 1315–1316.

(2)   Hardy, M. A.; Wright, B. A.; Bachman, J. L.; Boit, T. B.; Haley, H. M. S.; Knapp, R. R.; Lusi, R. F.; Okada, T.; Tona, V.; Garg, N. K.; Sarpong, R. Treating a Global Health Crisis with a Dose of Synthetic Chemistry. *ACS Cent. Sci.* **2020**, *6*, 1017−1030.

(3)   Mullard, A. 2020 FDA Drug Approvals. *Nature Rev. Drug Discov.* **2021**, *20*, 85–90.

(4)   (a) Dorn, S. K.; Newman, J. D.; van Kessel, J. C.; Brown, L. C. Synthesis and Biological Assay of Small-Molecule Quorum Sensing Inhibitors: A Three-Week Course-Based Undergraduate Research Experience. *J. Chem. Educ.* **2021**, *98*, 3533–3541. (b) Bailie, A. E.; Nortcliffe, A. Synthesis of Quinolone Antibiotic Analogues: A Multistep Synthetic Chemistry Experiment for Undergraduates. *J. Chem. Educ.* **2021**, *98*, 3333–3340. (c) Funicello, M.; Cerminera, I.; Chiummiento, L.; Lupattelli, P.; Felluga, F.; Berti, F. Biginelli Reaction and β-Secretase Inhibition: A Multicomponent Reaction as a Friendly Educational Approach to Bioactive Compounds. *J. Chem. Educ.* **2021**, *98*, 1756–1761. (d) Yang, J.; Yuan, Y.; Gu, J.; Li, A.; Wei, Z.; Ouyang, Q. Drug Synthesis and Analysis of an Acetylcholinesterase Inhibitor: A Comprehensive Medicinal Chemistry Experience for Undergraduates. *J. Chem. Educ.* **2021**, *98*, 991–995.

(5)   For recent examples and reviews of computer-aided drug design courses, see: (a) Sydow, D.; Wichmann, M.; Rodríguez-Guerra, J.; Goldmann, D.; Landrum, G.; Volkamer, A. TeachOpenCADD-KNIME: A Teaching Platform for Computer-Aided Drug Design Using KNIME Workflows. *J. Chem. Inf. Model.* **2019**, *59*, 4083–4086. (b) Romero, R. M.; Bolger,

M. B.; Morningstar-Kywi, N.; Haworth, I. S. Teaching of Biopharmaceutics in a Drug Design Course: Use of GastroPlus as Educational Software. *J. Chem. Educ.* **2020**, *97*, 2212–2220. (c) Ragno, R.; Esposito, V.; Di Mario, M.; Masiello, S.; Viscovo, M.; Cramer, R. D. Teaching and Learning Computational Drug Design: Student Investigations of 3D Quantitative Structure–Activity Relationships through Web Applications. *J. Chem. Educ.* **2020**, *97*, 1922–1930. (d) Shi, X.-X.; Li, J.-Y.; Chen, Q.; Zhu, X.-L.; Hao, G.-F.; Yang, G.-F. Development of a Web-Based Laboratory Class to Reduce the Challenges in Teaching Fragment-Based Drug Design. *J. Chem. Educ.* **2020**, *97*, 427–436. (e) Tuvi-Arad, I. Computational Chemistry in the Undergraduate Classroom – Pedagogical Considerations and Teaching Challenges. *Isr. J. Chem.* **2021**, *61*, 1–10. (f) Clent, B.; Wang, Y.; Britton, H. C.; Otto, F.; Swain, C. J.; Todd, M. H.; Wilden, J. D.; Tabor, A. B. Molecular Docking with Open Access Software: Development of an Online Laboratory Handbook and Remote Workflow for Chemistry and Pharmacy Master's Students to Undertake Computer-Aided Drug Design. *J. Chem. Educ.* **2021**, *98*, 2899–2905. (g) Tantillo, D. J.; Siegel, J. B.; Saunders, C. M.; Palazzo, T. A.; Painter, P. P.; O'Brien, T. E.; Nuñez, N. N.; Nouri, D. H.; Lodewyk, M. W.; Hudson, B. M.; Hare, S. R.; Davis, R. L. Computer-Aided Drug Design for Undergraduates. *J. Chem. Educ.* **2019**, *96*, 920–925.

(6)   Nobelprize.org: The Official Web Site of the Nobel Prize. All Nobel Prizes in Chemistry. https://www.nobelprize.org/prizes/lists/all-nobel-prizes-in-chemistry (accessed Nov 2021).

(7)   Buskes, M. J.; Blanco, M.-J. Impact of Cross-Coupling Reactions in Drug Discovery and Development. *Molecules* **2020**, *25*, 3493–3514.

(8)   Brown, D. G.; Boström, J. Analysis of Past and Present Synthetic Methodologies on Medicinal Chemistry: Where Have All the New Reactions Gone? *J. Med. Chem.* **2016**, *59*, 4443−4458.

(9)   For notable examples of successful laboratory-based undergraduate courses in transition-metal catalysis, see: (a) Hie, L.; Chang, J. J.; Garg, N. K. Nickel-Catalyzed Suzuki−Miyaura Cross-Coupling in a Green Alcohol Solvent for an Undergraduate Organic Chemistry Laboratory. *J. Chem. Educ.* **2015**, *92*, 571–574. (b) Costa, N. E.; Pelotte, A. L.; Simard, J. M.; Syvinski, C. A.; Deveau, A. M. Discovering Green, Aqueous Suzuki Coupling Reactions: Synthesis of Ethyl (4-Phenylphenyl)acetate, a Biaryl with Anti-Arthritic Potential. *J. Chem. Educ.* **2012**, *89*, 1064−1067. (c) Aktoudianakis, E.; Chan, E.; Edward, A. R.; Jarosz, I.; Lee, V.; Mui, L.; Thatipamala, S. S.; Dicks, A. P. "Greening Up" the Suzuki Reaction. *J. Chem. Educ.* **2008**, *85*, 555−557. (d) Hamilton, A. E.; Buxton, A. M.; Peeples, C. J.; Chalker, J. M. An Operationally Simple Aqueous Suzuki−Miyaura Cross-Coupling Reaction for an Undergraduate Organic Chemistry Laboratory. *J. Chem. Educ.* **2013**, *90*, 1509−1513. (e) Horikoshi, R. Illustrating Catalysis with Interlocking Building Blocks: A BINAP−Ruthenium Complex Catalyzed Asymmetric Hydrogenation. *J. Chem. Educ.* **2015**, *92*, 332–335. (f) Dander, J. D.; Morrill, L. A.; Nguyen, M. M.; Chen, S.; Garg, N. K. Breaking Amide C–N Bonds in an Undergraduate Organic Chemistry Laboratory. *J. Chem. Educ.* **2019**, *96*, 776–780. (g) Wathen, B.; Lanehart, E.; Woodis, L. A.; Rojas, A. J. Buchwald−Hartwig Amination, High-Throughput Experimentation, and Process Chemistry: An Introduction via Undergraduate Laboratory Experimentation. *J. Chem. Educ.* **2021**, *98*, 996–1000.

(10) Bettinger, E. P.; Long, B. T.; Taylor, E. S. When Inputs Are Outputs: The Case of Graduate Student Instructors. *Econ. Educ. Rev.* **2016**, *52*, 63–76.

(11) Wang, L.; Arnaud, C. H. Grad School, in Students' Own Words. *C&E News* https://cen.acs.org/education/graduate-education/Grad-school-in-students-own-words/96/i36# (accessed 2022-01-06).

(12) Of note, guest lectures serving to highlight the expertise of academic and industrial professionals have been implemented previously in undergraduate coursework; for an example, see Ref 5g.

(13) Reisman, S. E.; Sarpong, R.; Sigman, M. S.; Yoon, T. P. Organic Chemistry: A Call to Action for Diversity and Inclusion. *J. Org. Chem.* **2020**, *85*, 10287–10292.

(14) For a comment on the importance of storytelling in chemical education to help address equity in chemistry, see: Collins, S. N. The Importance of Storytelling in Chemical Education. *Nat. Chem.* **2021**, *13*, 1–2.

(15) Since the beginning of the COVID-19 pandemic, several successful virtual courses have been reported. For pertinent examples, see: (a) Giordano, A. N.; Gardner, D.; Kennerly, W. W.; Bruce, C. D. Conversations Among Physical Chemists: Strategies and Resources for Remote Teaching and Learning Catalyzed by a Global Pandemic. *J. Chem. Educ.* **2021**, *98*, 2228–2235. (b) Accettone, S. L. W. Student Perceptions of Remote Chemistry Lecture Delivery Methods. *J. Chem. Educ.* **2021**, *98*, 3667–3679. (c) Silverberg, L. J. Three-Part Approach to Remote/Residential Organic Chemistry Lab During the COVID-19 Pandemic. *J. Chem. Educ.* **2021**, *98*, 3898–3903. (d) Kimble-Hill, A. C.; Rivera-Figueroa, A.; Chan, B. C.; Lawal, W. A.; Gonzalez, S.; Adams, M. R.; Heard, G. L.; Gazley, J. L.; Fiore-Walker, B. Insights

Gained into Marginalized Students Access Challenges During the COVID-19 Academic Response. *J. Chem. Educ.* **2020**, *97,* 3391–3395. (e) Alright, H.; Stephenson, C. R. J.; Schindler, C. S. Converting a Two-Week Chemistry Course for High School Students to a Virtual Format During COVID. *J. Chem. Educ.* **2021**, *98,* 2457–2464. (f) Anzovino, M. E.; Mallia, V. A.; Morton, M. S.; Barker Paredes, J. E.; Pennington, R.; Pursell, D. P.; Rudd, G. E. A.; Shepler, B.; Villanueva, O.; Lee, S. Insights and Initiatives While Teaching Organic Chemistry I and II with Laboratory Courses in the Time of COVID-19. *J. Chem. Educ.* **2020**, *97,* 3240–3245. (g) Ramachandran, R.; Rodriguez, M. C. Student Perspectives on Remote Learning in a Large Organic Chemistry Lecture Course. *J. Chem. Educ.* **2020**, *97,* 2565–2572. (h) For an editorial summarizing ideas and approaches for virtual instruction arising from the response of chemistry educators to the COVID-19 pandemic, see: Holme, T. A. Introduction to the *Journal of Chemical Education* Special Issue on Insights Gained While Teaching Chemistry in the Time of COVID-19. *J. Chem. Educ.* **2020**, *97,* 2375–2377.

(16)   For an excellent introductory textbook describing the modern drug discovery process, see: Stevens, E. *Medicinal Chemistry: The Modern Drug Discovery Process, 1st ed.*; Pearson Education, 2013.

(17)   (a) Hegedus, L. S.; Söderberg, B. C. G. *Transition Metals in the Synthesis of Complex Organic Molecules, 3rd ed.*; University Science Books, 2009. (b) *White Lab; Lecture Notes.* http://faculty.scs.illinois.edu/white/index.php?p=lectures (accessed 2022-01-06).

(18)   Crawley, M. L.; Trost, B. M. *Applications of Transition Metal Catalysis in Drug Discovery and Development: An Industrial Perspective, 1st ed.*; John Wiley & Sons, Inc., 2012.

(19) The increase in student response rate from 2020 to 2021 is likely due to the offering of a small extra credit incentive.

(20) Dang, J.; Lin, B.; Yuan, J.; Schwartz, S. T.; Shah, R. M.; Garg, N. K. Smart Access to 3D Structures. *Nat. Rev. Chem.* **2018**, *2*, 95–96.